UCRL-19530

c-2

NUCLEAR CHEMISTRY
Annual Report 1969

Lawrence Radiation Laboratory
University of California - Berkeley

UCRL-19530

c.2

DISCLAIMER

UCRL-19530
UC-4 Chemistry
TID 4500 (55th Ed.)

UNIVERSITY OF CALIFORNIA

Lawrence Radiation Laboratory
Berkeley, California

AEC Contract No. W-7405-eng-48

NUCLEAR CHEMISTRY DIVISION ANNUAL REPORT, 1969

January 1970

I. Perlman, Director, Nuclear Chemistry Division
Editors: Norman Edelstein, David Hendrie, and Maynard Michel

Work done under the auspices of the U. S. Atomic Energy Commission

Printed in the United States of America
Available from
Clearinghouse for Federal Scientific and Technical Information
National Bureau of Standards, U. S. Department of Commerce
Springfield, Virginia 22151
Price: Printed Copy $3.00; Microfiche $0.65

NUCLEAR CHEMISTRY DIVISION ANNUAL REPORT, 1969*

Contents

*Preceding Annual Reports: UCRL-18667, UCRL-17989.

PHYSICAL AND INORGANIC CHEMISTRY

RADIATION CHEMISTRY

CHEMICAL ENGINEERING

I. Nuclear Structure and Nuclear Properties

Nuclear Spectroscopy and Radioactivity

ENERGY LEVELS IN ^{235}Np

D. J. Gorman and Frank Asaro

We have studied the energy levels in ^{235}Np populated in the alpha decay of ^{239}Am and in the electron-capture decay of ^{235}Pu.

The alpha spectrum of ^{239}Am was studied with 18-keV (FWHM) resolution, using a surface barrier Au-Si detector, and with 13-keV (FWHM) resolution in a magnetic α-particle spectrograph. We have determined three alpha groups which have not been previously observed.[1,2] Table I gives our alpha energies, intensities, and hindrance factors. The alpha spectrum obtained with the solid-state detector is shown in Figs. 1 and 2. Figure 1 shows the raw data and Fig. 2 the spectrum after a smoothing operation has been performed in the computer. A γ ray of 49 keV energy was observed in coincidence with the unresolved alpha spectrum. This γ ray had been previously observed and determined to have E1 multipolarity.[1]

Table I. ^{239}Am alpha groups

α-Particle energy (MeV)	Excited state energy (keV)	Intensity (%)	Hindrance factor
5.825 ± 0.004	0	0.33 ± 0.02	1300
5.776 ± 0.002	49.0 ± 0.1	83.7 ± 0.4	2.9
5.734 ± 0.002	91.6 ± 0.3	13.75 ± 0.07	10
5.680 ± 0.002	146.8 ± 0.7	1.98 ± 0.03	36

From the alpha and gamma spectra we determined energy levels in ^{235}Np at 49.0 ± 0.1, 91.6 ± 0.3 and 146.8 ± 0.7 keV. These levels give a good fit to the simple rotational formula $E = E_0 + (\hbar^2/2\Im)\, I(I+1)$. Taking the spin of the 49-keV level as 5/2 (Ref. 1) and assuming the 91.6-keV level to be the 7/2 member of the rotational band, one obtains a value for the rotational constant of 6.09 ± 0.04 keV. Using this value we would predict the 9/2 member of the band to lie at an energy of 146.4 ± 0.5 keV, which fits the 146.8-keV level within the experimental error.

The electron-capture decay of ^{235}Pu was studied by using Ge(Li) detectors in singles and coincidence measurements. In the gamma singles spectrum we observed copious K and L x rays and two γ rays of energies 49.0 ± 0.1 and 34.1 ± 0.1 keV. The lifetime of the 49.0-keV γ ray was measured as $(6.0 \pm 0.5) \times 10^{-9}$ sec. The half-life of ^{235}Pu was redetermined to be 24.3 ± 0.1 min. Table II gives the energies and intensities of the γ rays obtained in both singles and coincidence measurements.

Table II. Intensities of γ rays in ^{235}Pu per 100 K x rays.

Energy (keV)	Singles	Coincidence
49.0 ± 0.1	2.05 ± 0.02	1.1
34.1 ± 0.1	0.186 ± 0.014	0.12

The intensity of the 49-keV transition in coincidence with K x rays is 1.1%. It had been previously determined[1] from ^{239}Am alpha decay that this γ ray was E1 with an intensity of 0.5 per alpha disintegration. The theoretical conversion coefficient is 1 for an E1 transition of that energy. Therefore about 2% of the K capture populates the 49-keV state directly or via higher states. Approximately 98% of the K-capture processes then bypass this state and very likely

populate the ground-state rotational band. The energy levels of ^{235}Np are similar to those of ^{237}Np and ^{239}Np.[3,4] The first excited state in each of these latter two nuclides lies at about 32 keV and decays to the ground state by predominantly M1 radiation with some E2 admixture. If we assume the same admixture as for ^{237}Np (1.4% E2) (Ref. 3) the theoretical conversion coefficient for the 34.1-keV γ ray should be 195. The intensity of the 34.1-keV transition in coincidence with K x rays is then ≈ 24%. This intensity is sufficiently large that it cannot come from de-excitation of the 49.0-keV state, and hence it very likely represents K capture to the 34.1-keV level. The remaining ≈ 74% of the K capture very likely populates the ground state. We do not feel the coincidence intensities are sufficiently accurate to obtain a meaningful K/L ratio.

The ground-state band for ^{235}Np is very likely the same 5/2+ [642] as for ^{237}Np and ^{239}Np, as previously indicated.[4] For similar reasons the band based on the 49.0-keV state likely has the Nilsson assignment 5/2- [523]. The K-capture process populates the 5/2 and 7/2 members of the ground-state rotational band, indicating that ^{235}Pu should have spin 5/2 or 7/2. This spin would be consistent with the K-capture population to the 5/2- [523] band also. By analogy to ^{233}U, which has the same number of neutrons, the ^{235}Pu ground state probably has the Nilsson assignment 5/2+ [633].

The proposed decay scheme is shown in Fig. 3.

References

1. Frank Asaro, F. S. Stephens, Jr., W. M. Gibson, R. A. Glass, and I. Perlman, Phys. Rev. 100, 1541 (1955).
2. R. A. Glass, R. J. Carr, and W. M. Gibson, J. Inorg. Nucl. Chem. 13, 181 (1960).
3. C. M. Lederer, J. M. Hollander, and I. Perlman, Table of Isotopes, 6th edition (John Wiley and Sons, New York, 1967).
4. C. M. Lederer, J. K. Poggenburg, F. Asaro, J. O. Rasmussen, and I. Perlman, Nucl. Phys. 84, 481 (1966).

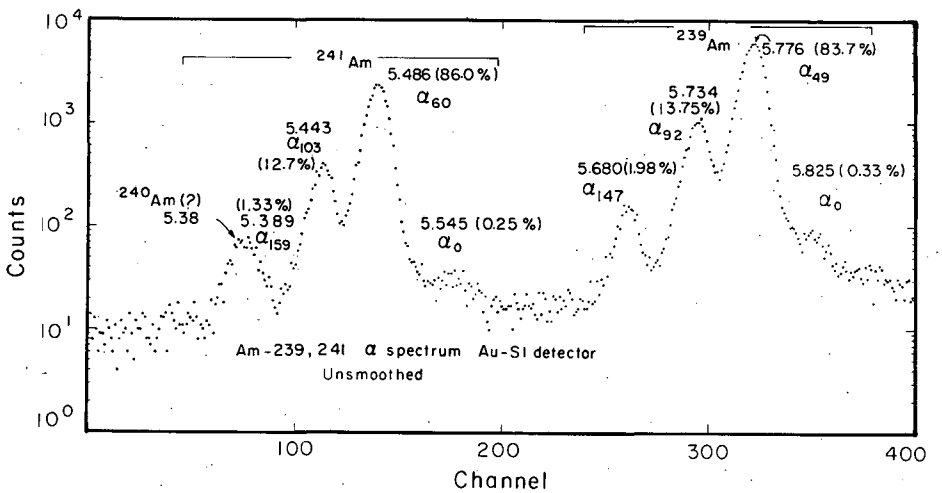

Fig. 1. ^{239}Am alpha spectrum--raw data.
(XBL6912-6404)

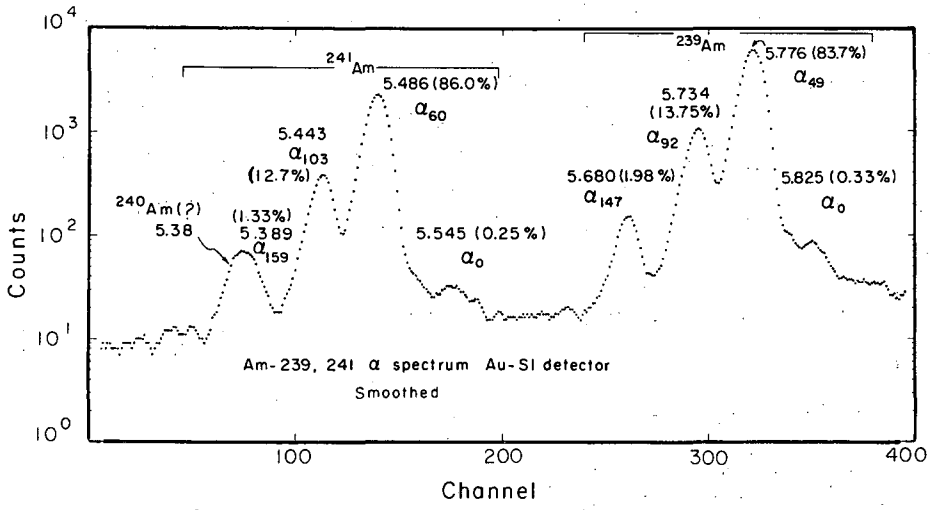

Fig. 2. ^{239}Am alpha spectrum -- result of computer smoothing. (XBL6912-6403)

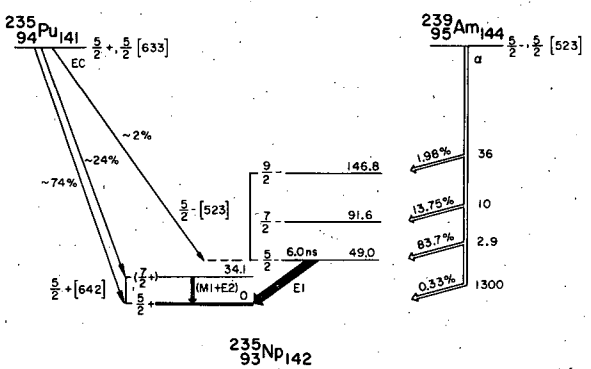

Fig. 3. Partial decay schemes of ^{239}Am and ^{235}Pu. (XBL701-2127)

THE ALPHA DECAY OF ^{235}Np AND THE DECAY OF ^{231}Th

E. Browne† and F. Asaro

We have studied the alpha spectrum of ^{235}Np, using a Au-Si surface-barrier detector with 14.5-keV (FWHM) resolution. Coincidences between conversion electrons and α particles occurring within the resolving time of the electronic system were considerably reduced by applying a permanent magnetic field to the source in order to deflect the electrons from striking the detector. Our alpha spectrum is shown in Fig. 1, and the α-particle energies, intensities, and hindrance factors are given in Table I.

Table I. Alpha-particle groups emitted by ^{235}Np.

α-Particle energy[a] (MeV)	Excited state (keV)	Abundance (%)	Hindrance factor
5.097 ± 0.003	0	1.5 ± 0.2	5.2×10^2
5.089 ± 0.003	8	≈ 0.2	3.5×10^3
5.040 ± 0.002	58	1.8 ± 0.3	1.9×10^2
5.014 ± 0.002	84	53 ± 10	4.3
4.996 ± 0.004	103	24	7
4.986 ± 0.004	113	6 } ± 8	2.4×10
4.930 ± 0.006	170	≈ 0.6	1.0×10^2
4.915 ± 0.002	185	11.5 ± 0.5	4.3
4.852 ± 0.003	249	0.7 ± 0.1	2.6×10
4.800 ± 0.007	302	≈ 0.1	7×10

The γ-ray spectra in coincidence with all the α particles, with ($\alpha_{113} \rightarrow \alpha_0$) and with ($\alpha_{185} \rightarrow \alpha_{170}$), were measured with a 5-cm^3 Ge(Li) detector. The α-particle gates used in these measurements are indicated in Fig. 1. Gamma rays of 58.5, 84.2, 81.2, 102.2, and 110.4 keV and three very weak ones of 125, 165, and 184 keV were observed in coincidence with all the α particles (Fig. 2). The first two γ rays were also observed in coincidence with ($\alpha_{113} \rightarrow \alpha_0$). In coincidence with ($\alpha_{185} \rightarrow \alpha_{170}$) were observed γ rays of 81.2, 84.2, 102, 110, and 125 keV.

A 102.2-keV state is definitely established by these measurements. This state receives at the most 0.015% direct alpha population; it is populated mostly through a 183.4-keV state by an 81.2-keV transition. Our γ-ray energies and absolute intensities are given in Table II.

^{231}Th singles γ-ray spectrum was measured at very high resolution [710 eV (FWHM) for γ rays of 122 keV] with a Ge(Li) detector, and γ-γ coincidence measurements were performed with Ge(Li) detectors using a bidimensional coincidence setup of 1600 × 1600 channels.

A 93.1-keV γ ray was observed both in our singles spectrum and in coincidence with ($\gamma_{81.2} + \gamma_{82.1}$) (Fig. 3). This γ ray de-excites the 102.30-keV even-parity state populating a state at 9.3 keV. If (as assumed) this latter state is the I = 1/2 member of the ground-state rotational band, the spin of the 102.30-keV level is definitely 3/2, since it is populated by an 81.2-keV M1 transition[1,2] from an I = 5/2 state at 183.4 keV.[1] Our experimental data indicate that the 84.17-, 101.38-, and 111.62-keV levels are the I = 5/2, 7/2, and 9/2 members of a K = 3/2 rotational band. This confirms the suggestion of Hoekstra and Wapstra[3] that the levels at 102.30 and 183.47 keV be assigned the Nilsson states 3/2 3/2+ [651] and 5/2 5/2+[642] respectively. The anomalous order of the levels in the K = 3/2 band and the low hindrance factor of the alpha group that populates the 84.2-keV state in the alpha decay of ^{235}Np are due to the Coriolis coupling of this band with the 1/2+ [660] and 5/2+ [642] rotational bands respectively. The lack of appreciable alpha population to the 102.2-keV level is consistent with this interpretation, since this state cannot be mixed with the favored one.

Table II. ^{235}Np γ rays measured in coincidence with all the α particles.

γ-Ray energy (keV)	Intensity per α (%)
58.5 ± 0.4	0.8 ± 0.2
81.2 ± 0.2	1.5 ± 0.1
84.2 ± 0.1	8.6 ± 0.6
102.2 ± 0.4	0.30 ± 0.06
110.4 ± 0.4	0.20 ± 0.05
125 ± 1	0.07 ± 0.03
165 ± 1	0.05 ± 0.03
184 ± 1	0.04 ± 0.03

Complete Coriolis calculations that include all the positive-parity interacting rotational bands were performed in order to obtain the energies and the admixtures of the pertubed states. The secular equations for each spin were solved by using a computer program written by Thomas P. Clements of this Laboratory. This program solved the secular determinants for all the I values involved, simultaneously adjusting all the parameters until a least-squares fit to the experimental levels was made. We used seven parameters in our

calculations. The final values of these parameters were reasonable, except the decoupling constant of the 1/2+ [660] rotational band, which had to be reduced by a factor of about 2.

Our final wave functions were tested with the reduced M1 electromagnetic transition probability ratios. The agreement between the experimental and the calculated values is good, except for the ratio B_{146}/B_{163} (Table III).

The Nilsson orbital 5/2- [523] was assigned to an odd-parity rotational band at 174.10 keV populated in the β decay of ^{231}Th.

The best ^{231}Th and ^{235}Np decay schemes are shown in Figs. 4 and 5 respectively. The energy levels are similar to those found by Holtz[1] in the decay of ^{231}Th.

Footnote and References

†Present address: care of Gloria Lando, P. O. Box 760, Asuncion, Paraguay.

1. M. Holtz, in Table of Isotopes, 6th edition (John Wiley & Sons, New York, 1967), p. 421.
2. J. M. Hollander, F. S. Stephens, F. Asaro, and I. Perlman, unpublished information, 1961.
3. W. Hoekstra and A. H. Wapstra, Phys. Rev. Letters 22, 16, 859 (1969).
4. M. Holtz, private communication.

Table III. Reduced M1 gamma transition probability ratios in the decay of ^{231}Th.

	K_i, K_f	I_i, I_f, I_f	$\langle \ \rangle^{2a} / \langle\langle \ \rangle\rangle$	Theoretical value[b]	Experimental value[c]
$\frac{B_{82}}{B_{81}}$	$\frac{5}{2}, \frac{3}{2}$	$\frac{5}{2}, \frac{7}{2}, \frac{3}{2}$	0.0714	0.36	0.49 ± 0.07
$\frac{B_{99}}{B_{81}}$	$\frac{5}{2}, \frac{3}{2}$	$\frac{5}{2}, \frac{5}{2}, \frac{3}{2}$	0.428	0.021	0.032 ± 0.004[d]
$\frac{B_{135.7}}{B_{163}}$	$\frac{5}{2}, \frac{3}{2}$	$\frac{7}{2}, \frac{7}{2}, \frac{5}{2}$	0.156	0.87	0.87 ± 0.12
$\frac{B_{146}}{B_{163}}$	$\frac{5}{2}, \frac{3}{2}$	$\frac{7}{2}, \frac{9}{2}, \frac{5}{2}$	0.710	0.88	0.31 ± 0.05

a. These values are the ratios of the squares of the appropriate Clebsch-Gordan Coefficients.
b. These values were obtained by taking into account the mixing of the rotational bands.
c. From our ^{231}Th singles gamma spectrum.
d. The M1-E2 mixing ratio for the 99-keV transition was taken from the conversion-electron data of Holtz (Ref. 4).

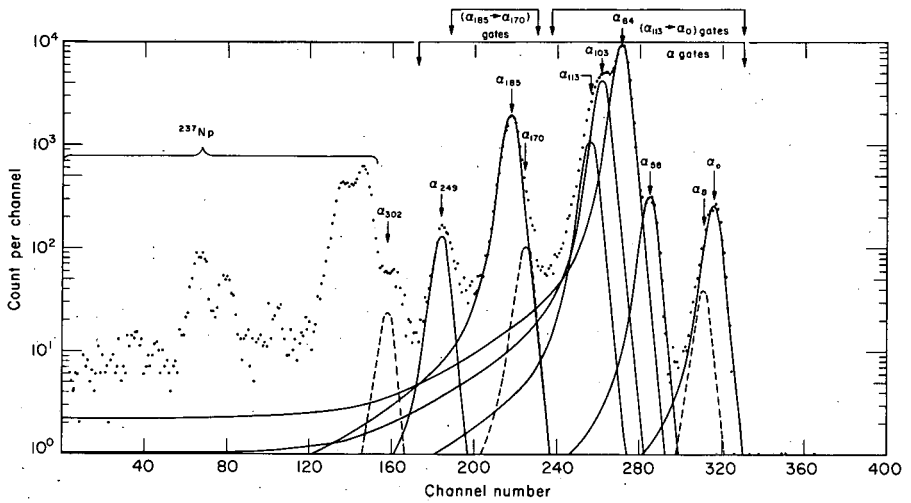

Fig. 1. ^{235}Np alpha spectrum. (XBL6910-3882)

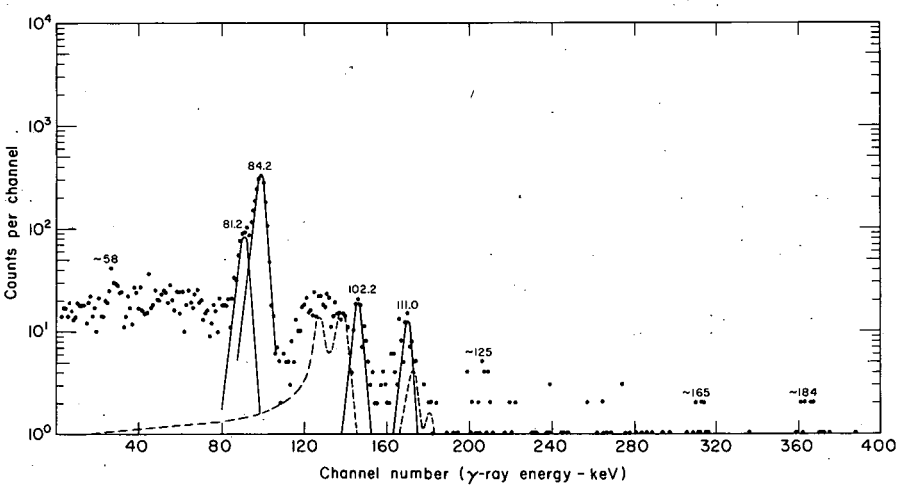

Fig. 2. ^{235}Np γ-ray spectrum measured in coincidence with all the α particles. The accidental coincidence spectrum due to U K x rays is drawn with a dashed line. (XBL6910-3881)

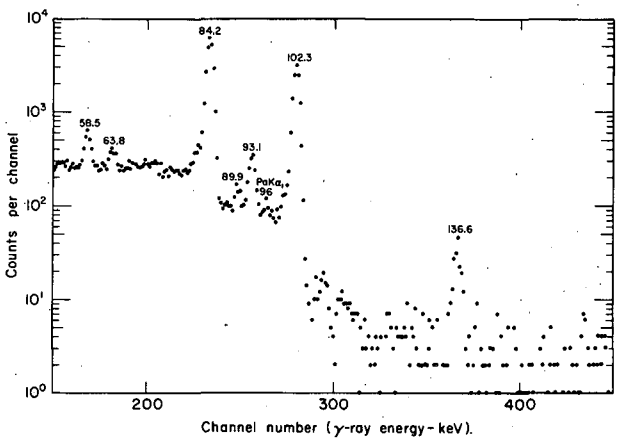

Fig. 3. ^{231}Th γ-ray spectrum in coincidence with ($\gamma_{81} + \gamma_{82}$). (XBL6910-3908)

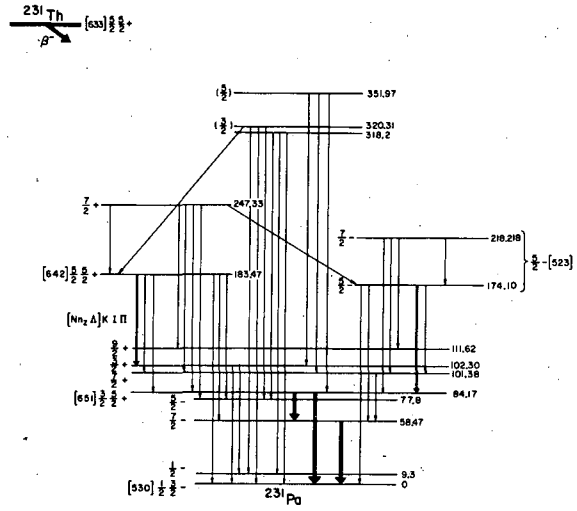

Fig. 4. ^{231}Th decay scheme. (XBL701-2012)

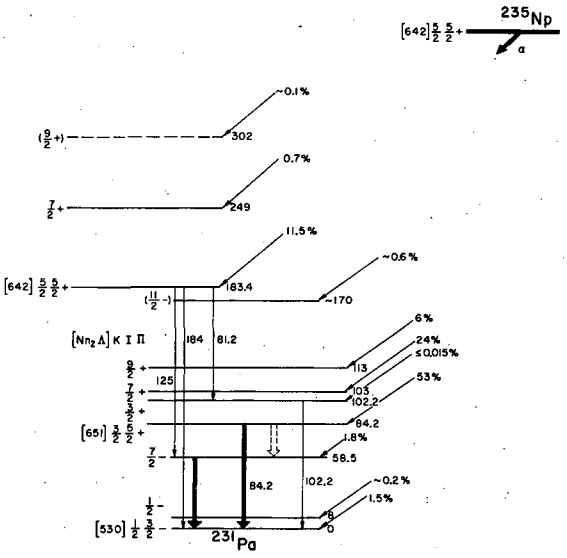

Fig. 5. ^{235}Np decay scheme. (XBL701-2010)

NUCLEAR SPECTROSCOPY STUDIES ON ^{251}Cf

E. Browne† and F. Asaro

We have studied the alpha spectrum of ^{251}Cf with 15-keV (FWHM) resolution, using a Au-Si surface barrier detector. The relatively high resolution of the spectrum led to a more accurate determination of alpha group energies and intensities. The alpha spectrum is shown in Fig. 1, and our α-particle energies, abundances, and hindrance factors are given in Table I.

Gamma rays were measured in coincidence with all the α particles, with α_{227} and with α_{406}, by use of a coincidence unit with a resolving time of 100 μsec. Alpha particles were detected with a Au-Si detector and γ rays with a 5-cm^3 Ge(Li) detector. The α-particle gates used in these measurements are indicated in Fig. 1. We have also measured the γ-ray spectrum in coincidence with all the α particles with a coincidence unit of 0.8 μsec resolving time. In this latter measurement the α particles were detected with a ZnS screen coupled to a photomultiplier tube. The γ-ray spectra in coincidence with all the α particles and with α_{227} are shown in Figs. 2 and 3 respectively. Gamma ray energies and intensities are given in Tables II and III.

The conversion electrons were measured in coincidence with all the α particles by using coincidence units of 100 and 0.5 μsec resolving time, respectively. Electrons were detected with a Si(Li) detector and α particles with a Au-Si surface barrier detector. The long resolving time was necessary to detect the electrons from the 227-keV delayed transition. The coincidence spectrum measured with the long resolving time is shown in Fig. 4, and the corresponding electron energies and intensities are listed in Table IV. The conversion coefficients of the 177- and 227-keV transitions obtained from this measurement confirm the respective E2 and M2 multipolarities previously assigned.[1]

A 285-keV γ ray detected in coincidence with α_{227} and also with all the α particles probably originates at a state of the same energy which receives direct alpha population. No transition from this state to the I = 11/2 member of the ground-state rotational band was observed. This indicates that the maximum spin of the 285-keV state is probably 7/2.

An M1 or E2 γ ray of 118 keV was observed in coincidence with α_{227}. The total intensity of this transition shows that the only possible state where it could originate is the 227-keV level. This is consistent with the intensity balance of the transitions which de-excite such a state. Both the γ ray and the conversion electrons of the 118-keV transition were found to be delayed. Therefore this transition must be preceded by a delayed one. Delayed γ rays of 113 and 132 keV were also observed in coincidence with α_{227}.

A possible interpretation of these γ rays is the following: The 118-keV γ ray de-excites from a 213-keV state to a 95-keV state. These two states could be the I = 5/2 and I = 3/2 members respectively of a K = 1/2 rotational band. The 95-keV state could also be populated from the 227-keV level by the 132-keV γ ray. A 114-keV state populated by a 113-keV γ ray from the 227-keV state could be the I = 7/2 member of this band. The experimental decoupling constant is -7.5, and the rotational constant 6.3 keV. This band could be the Nilsson orbital 1/2-[761]. The rotational constant is reasonable and the decoupling constant has the right sign. The magnitude of the latter, however, is larger than the theoretical value, which is -4.6 to -1.6 for deformations of η = 4 and 6 respectively.

If this interpretation is correct, the 95-keV state could be an isomeric state with a half-life of about 1 sec, the half-life of a possible M3 transition to the ground state. The best ^{251}Cf decay scheme is shown in Fig. 5.

Footnote and Reference

†Present address: care of Gloria Lando, P. O. Box 760, Asuncion, Paraguay.

1. A. Chetham-Strode, Jr., R. J. Silva, J. R. Tarrant, and I. R. Williams, Nucl. Phys. A107, 645-654 (1968).

Table I. Alpha-particle groups emitted by ^{251}Cf.

α-Particle energy (MeV)	Excited state (keV)	Abundance (%)	Hindrance factor
6.067 ± 0.003	0	2.7 ± 0.3	4.2×10^3
6.007 ± 0.003	60	11.6 ± 0.5	4.8×10^2
5.935 ± 0.005	134	0.6 ± 0.1	3.8×10^3
5.843 ± 0.003	227	27 ± 1	2.7×10
5.805 ± 0.005	266	4.2 ± 0.4	1.1×10^2
5.783 ± 0.005	288	2.0 ± 0.3	1.7×10^2
5.753 ± 0.005	318	3.8 ± 0.4	6.2×10
5.728 ± 0.007	344	1.0 ± 0.3	1.7×10^2
5.667 ± 0.003	406	35 ± 1	2.2
5.637 ± 0.007	436	3.5 ± 1.3	1.5×10
5.622 ± 0.005	452	4.5 ± 1.0	9.3
5.592 ± 0.007	482	≈ 0.22	1.3×10^2
5.556 ± 0.004	519	1.5 ± 0.2	1.1×10
5.489 ± 0.007	587	0.3 ± 0.1	2.3×10

Alpha particle energies are relative to the values of 5.160 and 5.115 MeV for the alpha groups of ^{240}Pu, and 5.760 and 5.802 MeV for the alpha groups of ^{244}Cm.

Table II. ^{251}Cf γ rays measured in coincidence with all the α particles (2τ = 0.8 μsec).

γ-Ray energy (keV)	Intensity per α (%)
K-X rays	4.0 ± 0.4
61.5 ± 0.3	0.56 ± 0.22
68 ?	≈ 0.2
73 ?	≈ 0.3
83 ?	≈ 0.1
135 ?	≈ 0.1
144 ?	≈ 0.1
154 ?	≈ 0.2
176.6 ± 0.1	17 ± 1
214 ?	≈ 0.2
227 ?	≈ 0.2
255 ?	≈ 0.2
262 ?	≈ 0.2
266.0 ± 0.3	0.5 ± 0.2
270 ?	≈ 0.2
285.0 ± 0.2	1.4 ± 0.3
291.0 ± 0.3	0.4 ± 0.2

Table III. ^{251}Cf γ rays measured in coincidence with (5.737 → 5.885)-MeV alpha groups (2τ = 100 μsec).

γ-Ray energy (keV)	Intensity per α (%)
K x rays	35 ± 3
113 ± 2	2.0 ± 0.5
118 ± 2	2.1 ± 0.4
132 ± 2	1.0 ± 0.4
227 ± 1	5.4 ± 0.8
≈284 ?	≈ 2

Table IV. ^{251}Cf conversion electrons measured in coincidence with all the α particles ($2\tau = 100$ μsec).

E_e (keV)	I_e (%)	Conversion shell	E (keV)	I_γ (%)	α	Multipolarity	Remarks
≈ 48	4.1 ± 0.6	K			0.24 ± 0.05		
152.8	18 ± 1	L_I+L_{II}			1.0 ± 0.1		
157.3	9 ± 1	L_{III}			0.5 ± 0.1		
170.6	12 ± 1	M			0.7 ± 0.1		
175.1	6.4 ± 1.0	N	176.4	17.3 ± 1.7	0.37 ± 0.05	E2	
98.8	37 ± 2	K			7 ± 2		
202.5	19 ± 1	L_I+L_{II}			3.7 ± 0.6		
208.5	3.0 ± 0.7	L_{III}			0.6 ± 0.2		
221.4	11 ± 1	M			2.1 ± 0.4		
226.0	4.4 ± 0.7	N	227.3	5.1 ± 1.3	0.85 ± 0.15	M2	
85	2.3 ± 0.4	Auger($KL_{II}L_{III}$ - KL_IL_{III})					
94.0	7.2 ± 0.7	L_I+L_{II}			7.2 ± 0.9		
112.0	5 ± 1	M			5 ± 1		
117	2.5 ± 0.5	N	118.0	1.0 ± 0.2	2.5 ± 0.7	M1 or E2	delayed
140.7	3.2 ± 0.6	K(269) or L_I+L_{II}(165)					delayed
163.0	2.8 ± 0.6	K ?	291				delayed
≈ 186 ?	0.6						
≈ 192 ?	0.9						
≈ 218 ?	1.5						

E_e = electron energy

I_e = electron intensity per α decay

E = transition energy

I_γ = γ-ray intensity

α = conversion coefficient.

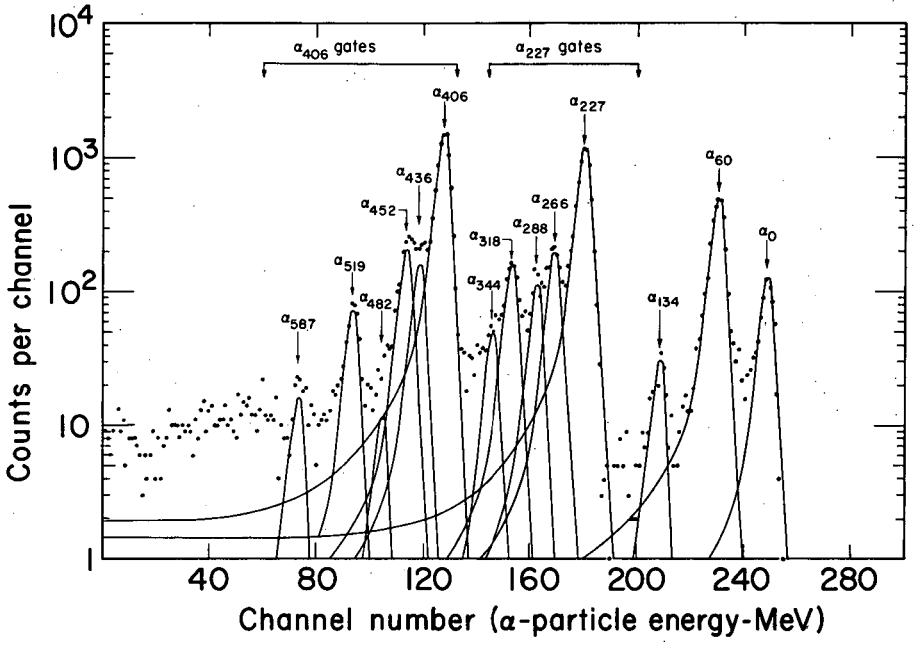

Fig. 1. ^{251}Cf alpha spectrum. (XBL701-2003)

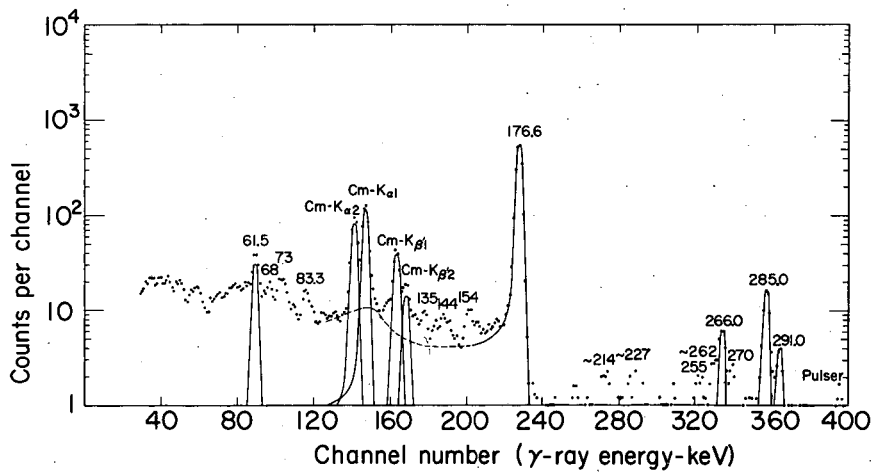

Fig. 2. ^{251}Cf γ-ray spectrum measured in coincidence with all the α particles (2τ = 0.8 μsec). (XBL701-2002)

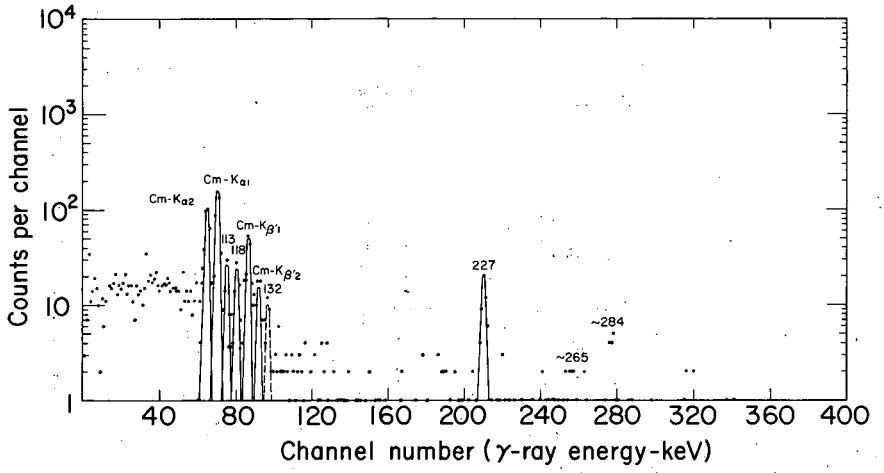

Fig. 3. ^{251}Cf γ-ray spectrum measured in coincidence with α_{227} (2τ = 100 μsec). (XBL7012007)

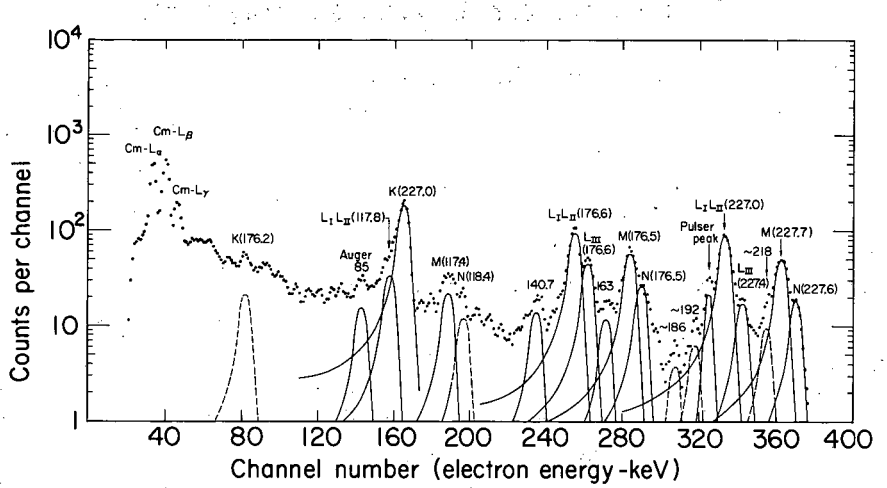

Fig. 4. ^{251}Cf conversion-electron spectrum measured in coincidence with all the α particles (2τ = 100 μsec). (XBL701-2008)

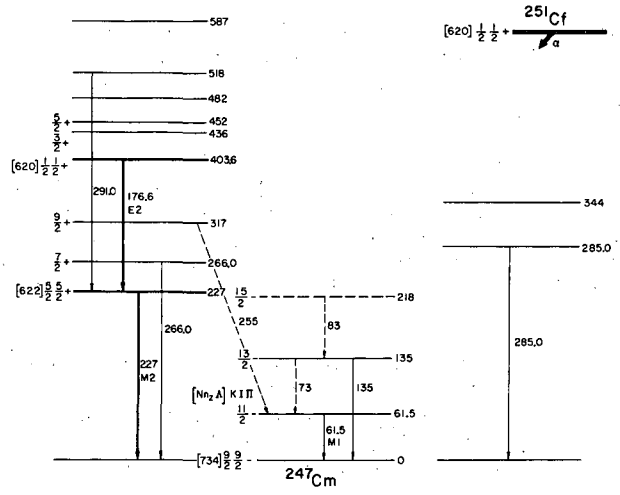

Fig. 5. ^{251}Cf decay scheme. (XBL701-2009)

GAMMA-RAY ENERGIES AND INTENSITIES IN THE DECAY OF ^{131}Ba AND ^{124}Sb

Leo D. Brown,† F. Asaro, and I. Perlman

In the determination of chemical composition by neutron activation analysis, one of the uncertainties in the method is caused by interferences of γ rays from different nuclides with each other. Although this effect can be minimized with high-resolution γ-ray detectors, there are still instances in which the extent of the interference must be determined and removed. This necessitates an accurate knowledge of γ-ray energies and intensities for the various radioactive species present. The incidence of interferences is greater statistically for a nuclide with many γ rays, as also is the chance that a γ ray has eluded detection through lack of resolving power of the instrumentation.

This work on ^{124}Sb and ^{131}Ba is part of a general program of determining energies and intensities, where either is insufficiently well known, of gamma spectra likely to cause problems in neutron activation.

Kelly and Horen[1] measured the energies of conversion electrons produced in ^{131}Ba decay. Horen, Hollander, and Graham[2] did similar studies and also measured the relative intensities. Karlsson[3] made a study of the energies and relative intensities of ^{131}Ba γ rays with a Li-drifted Ge detector.

Earlier work on the decay of ^{124}Sb using low-resolution scintillation spectroscopy has been tabulated.[4] Recently, Stelson,[5] utilizing Ge detector techniques, made a thorough investigation of the decay scheme of ^{124}Sb, including γ-γ coincidence and angular correlation measurements to help verify his proposed level scheme.[5]

The γ-ray energies and intensities in this experiment were measured with a 1-cm^3 high-resolution Ge(Li) detector (0.68 keV half width at 130 keV) connected to a 4096-channel pulse-height analyzer. An efficiency curve for the detector was made using calibrated γ-ray sources of ^{57}Co, ^{60}Co, ^{137}Cs, ^{54}Mn, ^{88}Y, ^{241}Am, and ^{203}Hg. In addition, ^{180m}Hf was used as a relative intensity standard.

Barium-131 was prepared by neutron irradiation in the Triga Research Reactor of the University of California–Berkeley. The sample was allowed to "cool" for several days, during which time the short-lived radioactive species had virtually disappeared. The only detectable species other than the 12.0-day half-life ^{131}Ba was the 7.2-year half-life ^{133}Ba. The large difference in the half-life allowed easy differentiation between γ rays of the two species (^{133}Ba γ-ray peaks were barely evident in the spectra taken). The attenuation of the γ rays due to self-absorption was found to be insignificant except for the lower-energy peaks, for which corrections were made.

^{124}Sb and ^{122}Sb were produced by neutron irradiation in the Berkeley Reactor. Since ^{124}Sb has a 60.4-day half-life and ^{122}Sb has a 2.80-day half-life,[4] the γ rays of each isotope were easily distinguished. As the energies measured were rather high and the amount of sample was small, no correction for γ-ray attenuation needed to be made.

The measured energies and relative intensities of ^{131}Ba γ rays in this work are given in Table I and compared with the energies of Horen, Hollander, and Graham[2] and the γ-ray intensities of Karlsson.[3] The energy values determined in this experiment agree quite well with those accurately determined by Horen and his co-workers. In addition, other radiations of energies 154.51, 158.66, 527.12, and 531.45 keV were observed. These were due to coincidences with Cs K x rays from ^{131}Ba K capture. The abundances of the 247-, 249-, and 404-keV γ rays were corrected for coincidence contributions.

As shown in Table I, there are some disagreements between this work and that of Karlsson[3] in the relative intensities of the ^{131}Ba γ rays. When the γ-ray spectrum obtained by Karlsson[3] was examined, it was readily apparent that some of the weaker peaks (for which much of the disagreement occurs) had very high background counts compared with the peak height. Because of the better detector resolution and greater number of channels in the analyzer used in this work, better counting statistics were probably obtained.

Table I. Gamma rays of ^{131}Ba.

Energy (keV)		Relative intensity	
This work	Horen et al (Ref. 2)	This work	Karlsson (Refs. 5, 6)
	54.84	0.23	
	78.69	1.6	1.7
	82.43	0.056	
	92.25	1.3	1.2
	123.73	63	78
	133.54	4.6	5.7
137.1 ± 0.3	137.26	0.098	
157.12 ± 0.15	157.01	0.45	0.53
216.01 ± 0.1	216.01	46	50
239.54 ± 0.1	239.56	5.3	5.9
246.80 ± 0.15	246.83	1.4	1.5
249.40 ± 0.1	249.36	9.5	7.7
294.5 ± 0.3	294.45	0.27	0.37
351.1 ± 0.3	351.21	0.23	0.26
373.26 ± 0.1	373.15	30	31
404.04 ± 0.1	404.3	2.9	3.0
427.6 ± 0.3	427.7	0.19	0.35
451.8 ± 0.4	451.7	0.06	
461.2 ± 0.3	461.3	0.13	0.45
	462.9		
480.6 ± 0.2	480.6	0.82	1.6
486.57 ± 0.1	486.6	4.4	5.9
496.36 ± 0.1	496.3	100	100
572.9 ± 0.4	573.3	0.30	0.42
585.15 ± 0.15	585.1	2.5	2.7
620.20 ± 0.1	620.2	3.9	3.6
674.8 ± 0.5	674.2	0.26	0.28
696.9 ± 0.3	696.5	0.36	0.31
832.1 ± 0.4	832.0	0.38	0.44

In Table II the energies and relative intensities of the decay of ^{124}Sb are presented for this work and for that of Stelson.[5] The agreement is fairly close for most of the γ-ray energies and intensities. The increased precision in this work is due mainly to the higher resolution of the detector and the high linearity of energy distribution per channel in the analyzer. The major differences in the γ-ray intensities are attributed to large counting errors in the low-intensity peaks.

Footnotes and References

†Visiting student from Department of Chemistry, Baylor University, Waco, Texas 76703.

1. W. H. Kelly and D. J. Horen, J. Nucl. Phys. 47, 454 (1963).
2. D. J. Horen, J. M. Hollander, and R. L. Graham, Phys. Rev. 135, 302 (1964).
3. K. Karlsson, Arkiv Fysik 33, 47 (1967).
4. C. M. Lederer, J. M. Hollander, and I. Perlman, Table of Isotopes (John Wiley & Sons, New York, 1967).
5. P. H. Stelson, Phys. Rev. 157, 1098 (1967).
6. These values were normalized from the original work to facilitate comparison.

Table II. Gamma rays of ^{124}Sb.

Energy (keV)		Relative intensity	
This work	Stelson[a]	This work	Stelson[a]
602.72 ± 0.1	602.5 ± 0.3	100	100
645.81 ± 0.1	645.1 ± 0.3	7.7	8.5
709.30 ± 0.15	709.0 ± 0.5	1.4	1.8
713.71 ± 0.1	713.3 ± 0.5	2.3	2.8
722.72 ± 0.1	722.3 ± 0.3	11	12.5
790.7 ± 0.4	790.2 ± 0.5	0.66	0.8
968.21 ± 0.15	967.8 ± 0.3	2.2	2.3
1045.1 ± 0.3	1044.8 ± 0.3	1.9	2
1325.4 ± 0.3	1325.5 ± 0.5	2.0	1.6
1355.2 ± 0.4	1354 ± 1	1.1	1.2
1368.1 ± 0.3	1368 ± 1	2.8	3
1436.6 ± 0.4	1434 ± 1	0.89	1.4
1445.0 ± 0.6	1445 ± 1	0.68	0.3
1489.0 ± 0.4	1488 ± 1	0.85	0.8
1525.8 ± 0.4	1525 ± 1	0.55	0.5
1690.90 ± 0.1	1691 ± 0.5	56	50

a. From Stelson, Ref. 5.

MEASUREMENTS OF MICROSECOND HALF-LIVES OF ALPHA-EMITTING ISOTOPES

Jørn Borggreen† and Earl K. Hyde

Alpha-emitting nuclei with neutron numbers just above the N = 126 closed shell have been prepared by heavy-ion reactions and isolated by use of the helium-gas jet collection technique.[1] During the course of this investigation, many of the half-lives were found to be shorter than ≈ 2 msec, which is the lower limit for a half-life to be measured by our present transportation technique. In several instances it was possible to isolate a parent activity with a half-life of many msec that gave rise to a daughter with a half-life in the μsec range. For such daughter products we developed a method for half-life determination by use of a single detector and a time-to-amplitude converter (TAC). In the following, two methods are described which were used according to whether the half-life to be measured was longer or shorter than ≈ 1 μsec.

The first method (method I) makes use of the TAC incorporated in the electronic system shown in Fig. 1. One unconventional feature is the use of signals from the same detector as input to both start and stop sides of the TAC. To prevent an individual pulse from serving simultaneously as start and stop, a delay was inserted on the start side. Any pulse on the start input could fire the TAC for its preset cycle time, and any second pulse reaching the stop input during this cycle time could cause the appearance of a pulse on the time output of the TAC. This time pulse was passed to a computer interface unit. The valid-start and valid-stop output signals were used to gate the passage of the linear signals associated with the start and stop pulses to the same computer interface. The pulse-stretching and gating circuitry shown in Fig. 1 was required to insure time coincidence of the three pulses presented to the computer interface.

A computer program, MULTID, was used to control the acceptance and processing of the pulses by a PDP-7 computer. Whenever signals appeared simultaneously on the three inputs the pulse amplitudes were coded and stored as an event record on magnetic tape. The distributions over the three parameters were shown on-line during data recording. After the experiment the events on the magnetic tape record were analyzed with the program MULTIS by setting selection criteria (windows) on any two of the three parameters and examining the corresponding distribution of the third. For example, windows could be set on specific alpha peaks in the start (parent) and stop (daughter) spectra and the corresponding time spectrum examined to determine the half-life of a specific nuclide.

An application of this technique is shown in Figs. 2 and 3. In the singles spectrum of the α-decay products isolated from the reaction of 87-MeV ^{16}O and ^{208}Pb there occur about a dozen activities that include the mother-daughter pair 1.8-msec ^{221}Th and 1.6-μsec ^{217}Ra. In the spectra from a TAC experiment made on these products the major peaks in the start spectrum were those of ^{221}Th and the dominant peak in the stop spectrum was that of ^{217}Ra. With the MULTIS program the data were sorted with a window set on the 8.995-MeV α peak of ^{217}Ra in the stop spectrum; this resulted in the clean spectrum for ^{221}Th shown in Fig. 2. The corresponding time-parameter data are shown in Fig. 3.

The above-described experimental technique could not be used for submicrosecond half lives because it was not possible with the available pulse-shaping settings of the amplifier to obtain distinct pulses containing the energy information on the start and stop pulses. A second method (method II) outlined schematically in Fig. 4 was used in such cases. In this, use is made of the fact that in most cases the two α particles are emitted within 1 or 2 μsec; when time constants chosen for the linear amplifier are very long (5 msec) compared with the half-life, a pile-up pulse occurs and is registered by the ADC as a single pulse with an energy equal to the sum of the two α energies. Also by this method it was necessary to insert a delay in the start side of the TAC; the length of this delay has no influence on the measured half-life.

No pulse stretcher was needed for these short half-lives, since the acceptance time for the multidimensional computer interface was 3 μsec and the TAC was operated at range 3μsec or less.

After the experiment the information stored on magnetic tape could be analyzed as described above, except that here there is only one energy spectrum and consequently there is no information on which α pulse came first.

In Fig. 5 is shown a sum spectrum obtained when the method is applied to the products of the $^{208}Pb + ^{19}F$ reaction. Although the quality of α-peak resolution is somewhat reduced by the long time constants used, it is possible to distinguish three main groups in the spectrum. They are sum peaks of α decays of $^{220}Ac + ^{216}Fr$, $^{217}Fr + ^{213}At$, and $^{219}Ac + ^{215}Fr$. The positions and lengths of the arrows show the expected location and relative intensity of the sum peaks computed from the known complex structure of the alpha decay of the mother and daughter. Figure 6 shows the half-life curves obtained by off-line sorts of the data with windows as indicated in Fig. 5.

Experiments were performed by TAC methods I and II on the products from a variety of reaction systems at the Hilac. Results are summarized in Tables I and II.

The authors acknowledge a private communication from R. D. Macfarlane and D. Torgerson which stimulated them to employ TAC techniques, and thanks are extended to Mr. Al Wydler for help with equipment development and Dr. Lloyd Robinson for computer equipment and program development.

Table I. Summary of results (odd Z).

	E_α (MeV)	Branching (%)	$t_{1/2}$ (μsec)	Method
^{221}Ac decay chain:				
^{221}Ac	7.645	70 ± 2		
	7.440	20 ± 2		
	7.375	10 ± 2		
^{217}Fr	8.315	100	22 ± 5	I
^{213}At	9.080		0.11 ± 0.02	II
^{220}Ac decay pair:				
^{220}Ac	8.19	3		
	8.06	6		
	8.00	5		
	7.98	4		
	7.94, 7.89	3		
	7.85, (7.82)	23		
	7.79	13		
	7.68	20		
	7.61	22		
^{216}Fr	9.005	100	0.70 ± 0.02	I
^{223}Pa decay pair:				
^{223}Pa	8.005			
	8.190			
^{219}Ac	8.665		7 ± 2	I
^{215}Fr	9.365		< 0.5	I
^{222}Pa decay pair:				
^{222}Pa	8.16-8.54			
^{218}Ac	9.205		0.27 ± 0.04	I

Table II. Summary of results (even Z).

	E_α (MeV)	Branching (%)	$t_{1/2}$ (μsec)	Method
^{219}Ra decay pair				
^{219}Ra	7.980	35 ± 2		
	7.675	65 ± 5		
^{215}Rn	8.675	100	2.30 ± 0.15	I
^{222}Th decay chain				
^{222}Th	7.980	100		
^{218}Ra	8.385	100	14 ± 2	I
^{214}Rn	9.035	100	0.27 ± 0.02	II
^{221}Th decay pair				
^{221}Th	8.470	30 ± 5		
	8.145	62 ± 5		
	7.73	8 ± 3		
^{217}Ra	8.995		1.6 ± 0.2	I

Footnote and Reference

†On leave from Niels Bohr Institute, Risø, Denmark.

1. K. Valli, E. K. Hyde, and J. Borggreen, Production and Decay Properties of Thorium Isotopes of Mass 221 through 224 Formed in Heavy-Ion Reactions, UCRL-18992, Oct. 1969, and J. Borggreen, K. Valli, and E. K. Hyde, Production and Decay Properties of Protactinum Isotopes of Mass 222 to 225 Formed in Heavy Ion Reactions, UCRL-19539, Feb. 1970.

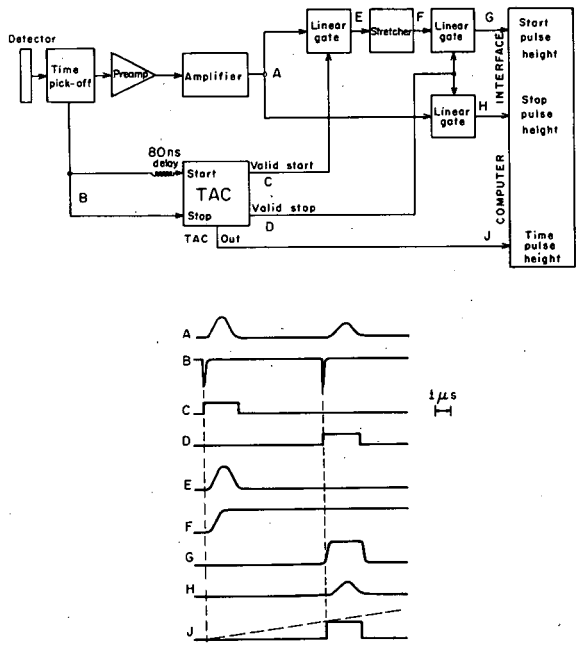

Fig. 1. Schematic diagram of electronics used in Method I to study time correlation of α particles from a single detector. (TAC stands for time-to-amplitude converter.) The time sequence of pulse forms at points A, B, C, etc. in the diagram is displayed in the lower part of the figure.
A. Two linear (energy) signals.
B. The analogous time signals.
C. Gate signal generated if the start pulse is accepted by the TAC, i.e., if the TAC is not busy.
D. Gate signal generated if the stop pulse is accepted by the TAC, i.e., if it has been preceded by a start pulse (accepted) within the time range of the TAC.
E. The linear signal corresponding to the "start α" after passing first gate.
F. The same (start α) stretched for a time equal to the TAC time range.
G. Section of this stretched signal gated through to the analyzer by the valid stop signal D.
H. Linear signal corresponding to the "stop α" gated through to the analyzer by the valid stop signal D.
J. The TAC output proportional to the time B elapsed between the emission of the two α particles. (XBL6911-6164)

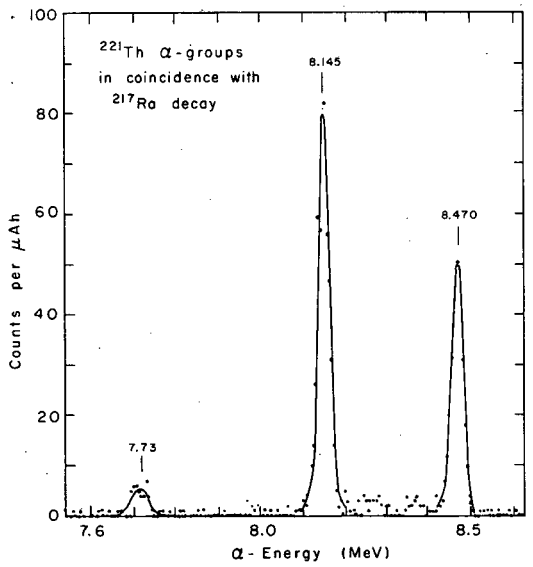

Fig. 2. ^{221}Th alpha groups associated with 8.995-MeV alphas from ^{217}Ra. Results of TAC experiment on products isolated from ^{16}O + ^{208}Pb reaction. (XBL6910-3962)

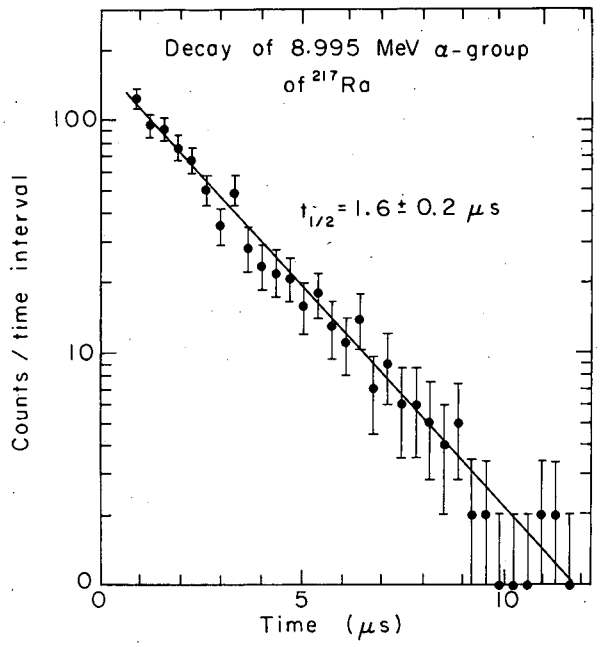

Fig. 3. Time relationship between ^{221}Th α particles of 8.470 and 8.145 MeV and ^{217}Ra alphas of 8.995 MeV. (XBL6910-3951)

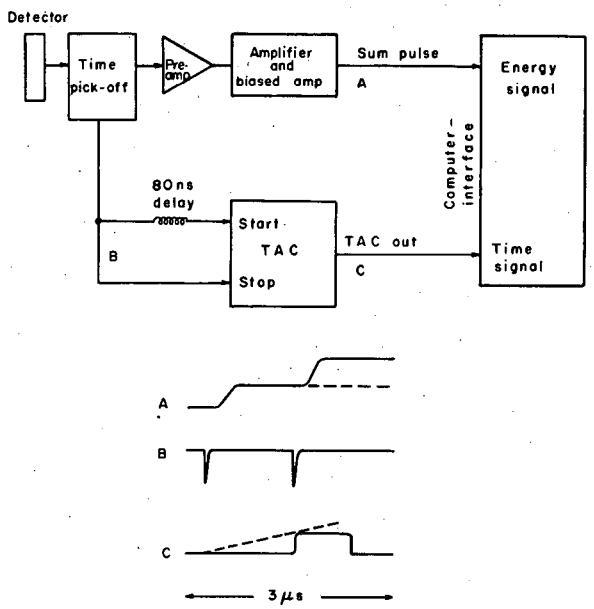

Fig. 4. Schematic diagram of electronics used in method II to study time correlation of α particles from a single detector. (TAC stands for time-to-amplitude converter.) The time sequence of pulse forms at points A, B, and C in the diagram is displayed in the lower part of the figure.
A. Two linear (energy) signals added in the linear amplifier.
B. The analogous time signals.
C. The TAC output proportional to the time elapsed between the emission of the two α particles. (XBL701-2055)

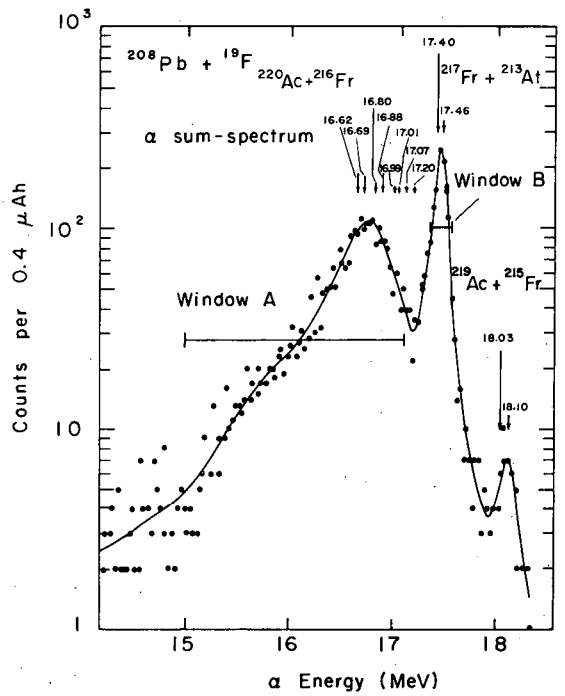

Fig. 5. Alpha sum spectrum, showing three different sum peaks from the products of the reaction ^{208}Pb + ^{19}F. (XBL701-2054)

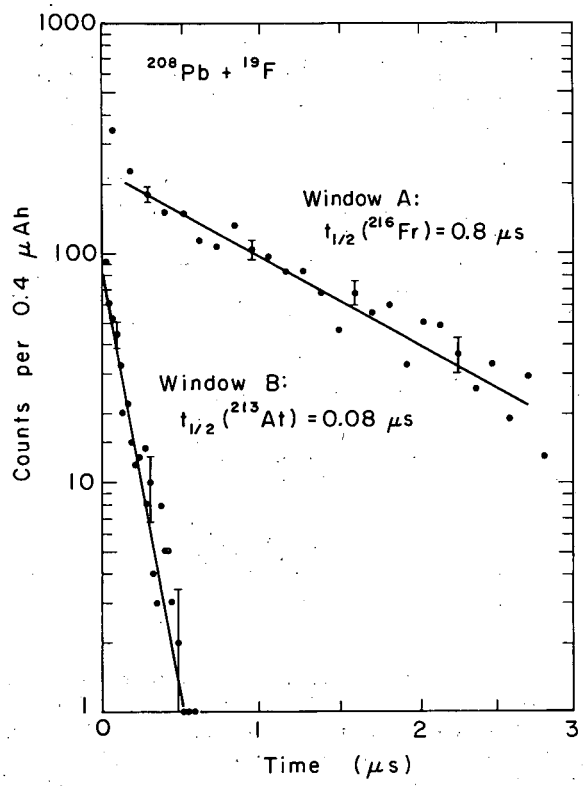

Fig. 6. Half-life curves obtained from sorts with windows A and B in Fig. 5. More accurate values for $t_{1/2}$ were obtained in experiments in which the TAC range was adjusted to optimize only one of the half-lives. (XBL701-2053)

ON ALPHA DECAY OF ^{255}No AND ^{257}No

Pirkko Eskola,† Kari Eskola,* Matti Nurmia, and Albert Ghiorso

In our previous work[1] on alpha decay of nobelium isotopes, ^{255}No was produced by the nuclear reaction ^{246}Cm(^{13}C, 4n)^{255}No. Its alpha energy was reported to be 8.11 ± 0.02 MeV and half-life 185 ± 20 sec. ^{257}No was produced by the reaction ^{248}Cm(^{13}C, 4n)^{257}No. Two α-particle groups of 8.23 ± 0.02 MeV (50%) and 8.27 ± 0.02 MeV (50%) were assigned to ^{257}No, and its half-life was found to be 23 ± 2 sec.

Flerov et al.[2] have produced ^{255}No using the reaction ^{238}U(^{22}Ne, 5n)^{255}No. Their values for alpha energy and half-life of ^{255}No was 8.08 ± 0.03 MeV and 3.0 ± 0.2 min. Flerov's group has not reported any results on ^{257}No.

In this work ^{255}No and ^{257}No were produced in much larger amounts than earlier. In experiments on rutherfordium (element 104) we noticed that ^{255}No is produced in greater yield by bombarding ^{249}Cf with ^{12}C ions than by bombarding ^{246}Cm with ^{13}C ions. This made it possible to investigate the fine structure in the alpha decay of ^{255}No in considerable detail.

The ^{249}Cf target was the same as used in our rutherfordium work:[3] 60 μg of ^{249}Cf in an area of 0.21 cm^2, or 290 μg/cm^2. The 47-μg ^{248}Cm target, used to produce ^{257}No from ^{248}Cm(^{13}C, 4n)^{257}No, was electrodeposited from an isopropyl alcohol solution in an area of 0.13 cm^2 on a substrate sandwich consisting of 0.1 mg/cm^2 Pd sputtered onto 2.2 mg/cm^2 Be. According to the mass analysis, this 350-μg/cm^2 target contained 93.7% ^{248}Cm, less than 0.2% ^{247}Cm, 3.2% ^{246}Cm, 0.6% ^{245}Cm, and 2.4% ^{244}Cm. The targets were bombarded mainly by ^{12}C and ^{13}C ions accelerated by the Berkeley Hilac. Currents in the range of 2 to 4 μA dc (as completely stripped ions) were used.

The apparatus used was the same as that used in our rutherfordium work[3] and similar to that described in our previous papers about nobelium.[1,4]

In ^{12}C bombardments of ^{249}Cf target several nobelium isotopes were produced by (^{12}C, αxn) reactions. In Fig. 1 there is a series of spectra of such a bombardment. The energy of ^{12}C ions was 70 MeV. There are four consecutive spectra, 200 sec each, and the topmost spectrum is the sum of the four. The prominent α-particle group at 8.11 MeV is partly due to the alpha decay of ^{254}No, although at this energy it mostly beongs to ^{255}No. Besides this peak there are four other α-particle groups with energies 7.76, 7.92, 8.25, and 8.30 MeV which decay with the same half-life, 200 ± 10 sec, as the 8.11-MeV α-particle group of ^{255}No, and in addition they have excitation functions similar to that of the 8.11-MeV peak. These two features together with some cross-bombardments indicate that the four peaks are due to the alpha decay of ^{255}No, too. The energies and relative intensities of the α-particle groups were determined by submitting the spectra to a computer analysis[5] using the SAMPO program written for the analysis of gamma spectra by Routti and Prussin. The results are presented in Table I. For alpha energy calibration, the 7.04-MeV peak of ^{252}Fm and the 7.43-MeV peak of ^{250}Fm were used. Excitation curves of several activities produced by bombardment of ^{249}Cf with ^{12}C ions are presented in Fig. 2.

A decay scheme for ^{255}No is proposed in Fig. 3. The decay scheme of ^{253}Fm (Ref. 6) is presented for comparison. Numbers to the right of the levels are the energy of the level in keV, corresponding alpha energy in MeV, relative intensity of the alpha transition, and the alpha-decay hindrance factor. Hindrance factor calculations are based on spin-independent (ℓ = 0) equations of Preston.[7] The radius parameter was evaluated from data on nearest two-even-even alpha emitters.

Although no gamma spectroscopic studies have been done, spin and parity assignments are suggested on the basis of expected analogy with the decay of ^{253}Fm. Judging by the gross features of the level scheme and considering the hindrance factors for the alpha transitions, it seems probable that the ground state of ^{255}No is the same as that of ^{253}Fm and the ground state of ^{251}Fm is the same as that of ^{249}Cf. The 50-keV state is then the first member of the ground-state rotational band. The 190-keV state may be the same as the 145-keV 5/2 + [622↑] hole state in ^{253}Fm decay scheme. The hindrance factor for the 7.76-MeV alpha transition is 1.6, and indicates a favored alpha transition. It then seems probable that the 550-keV state is the same as the ground state of ^{255}No, or 1/2 + [620↑], and corresponds to the 417-keV state in ^{253}Fm decay. Then according to the Nilsson diagram the 380-keV state might be the 7/2 + [624↑] hole state or the 7/2 + [613↓] particle state, neither of which has been observed in ^{253}Fm alpha decay. However, the hindrance factor 5.2 of the 7.92-MeV alpha transition is much too small for an L = 4 alpha transition. On the basis of the hindrance factor a possible candidate for the 380-keV state is the 3/2 + [622↑] particle state.

^{257}No was produced by bombarding ^{248}Cm with ^{13}C ions. The series of spectra in Fig. 4 is the sum of four different experiments with ^{13}C ion energies ranging from 66 MeV to 74 MeV. The top spectrum is the sum of the individual 20-sec spectra from the four detectors. The three alpha groups at 8.22, 8.27, and 8.32 MeV are assigned to ^{257}No. The 8.43-MeV peak is due to the alpha decay of ^{256}No, and because of the 3-sec half-life it is seen only in the first spectrum. Lighter nobelium isotopes are not seen in these spectra. Excitation curves for ^{257}No and ^{256}No are presented in Fig. 5. ^{257}No is produced by the (^{13}C, 4n) reaction and ^{256}No by the (^{13}C, 5n) reaction. The half-life of ^{257}No was measured and found to be 26 ± 2 sec. The energies and relative intensities of the three α-particle groups of ^{257}No were determined with help of the SAMPO program.[5] The 7.04 MeV-peak of ^{252}Fm and the 8.43-MeV peak of ^{256}No served as energy calibration values. The results are presented in Table II together with assumed level energies and calculated hindrance factors. The value of the radius parameter of ^{256}No was used in hindrance factor calculations.

Table I. Alpha groups of ^{255}No.

Alpha-particle energy (MeV)	Excited-state energy (keV)	Intensity (%)	Hindrance factor
8.30 ± 0.02	0	3 ± 1	620
8.25 ± 0.02	50	6 ± 1	210
8.11 ± 0.01	190	57 ± 3	7.8
7.92 ± 0.01	380	19 ± 2	5.2
7.76 ± 0.01	550	15 ± 2	1.6

Table II. Alpha groups of ^{257}No.

Alpha-particle energy (MeV)	Excited-state energy (keV)	Intensity (%)	Hindrance factor
8.32 ± 0.02	0	(19 ± 2)	(19)
8.27 ± 0.02	50	(26 ± 2)	(9.6)
8.22 ± 0.02	100	(55 ± 3)	(3.1)

If the decay scheme of ^{277}No is analogous to that of ^{255}Fm there should be a favored alpha transition to a level around 100 keV, whereas the transition to the ground state of ^{253}Fm should be strongly hindered. In ^{255}Fm alpha decay[8] 93% of the alpha transitions lead to a 107-keV state and the hindrance factor of the transition is 1.2, but only 0.09% of the transitions lead to the ground state of ^{251}Cf and the hindrance factor is 3500. Considering the hindrance factors for ^{257}No alpha transitions it seems probable that the 8.22-MeV alpha group corresponds to the favored transition mentioned above. The 8.32-MeV alpha transition, then, should lead to the ground state of ^{253}Fm, but the hindrance factor 19 of this transition is much too small for an L = 4 alpha transition. Also, the hindrance factor 9.6 for the 8.27-MeV alpha group is too small compared with the value 460 for the transition leading to a 48-keV state in ^{255}Fm alpha decay. It seems probable to us that in our ^{257}No spectra the 8.27-MeV and 8.32-MeV peaks are too intense because of summation of the signals from the conversion electrons in coincidence with the 8.22-MeV alpha group. We plan to investigate this by changing the detector geometry in the future measurements. Because of this uncertainty, the intensity values and hence the hindrance factors in Table II are in parentheses.

We express our thanks to Dr. F. Asaro and Dr. S. Bjørnholm for helpful discussion and suggestions, and to Mrs. Helen V. Michel for permission to use her computer programs for hindrance-factor calculations. Thanks are also due to F. S. Grobelch and the Hilac crew for excellent machine operation.

One of the authors, P. Eskola, is indebted to the National Research Council for Sciences, Helsinki, Finland, for financial support.

Footnotes and References

†Guest Scientist supported by the National Research Council for Sciences, Helsinki, Finland.
*On leave of absence from Department of Physics, University of Helsinki, Finland.

1. A. Ghiorso, T. Sikkeland, and M. Nurmia, Phys. Rev. Letters 18, 401 (1967).
2. G. N. Flerov, G. N. Akap'ev, A. G. Demin, V. A. Druin, Yu. V. Lobanov, and B. V. Fefilov, Soviet J. Nucl. Phys. 7, 588 (1968).
3. A. Ghiorso, M. Nurmia, J. Harris, K. Eskola, and P. Eskola, Phys. Rev. Letters 22, 1317 (1969).
4. A. Ghiorso and T. Sikkeland, Phys. Today 20, 25 (1967).
5. J. T. Routti and S. G. Prussin, Nucl. Instr. Methods 72, 125 (1969).
6. I. Ahmad, A. M. Friedman, R. F. Barnes, R. K. Sjoblom, J. Milsted, and P. R. Fields, Phys. Rev. 164, 1537 (1967).
7. M. A. Preston, Phys. Rev. 71, 865 (1947).
8. C. M. Lederer, J. M. Hollander, and I. Perlman, Table of Isotopes (John Wiley & Sons, Inc., New York, 1967).

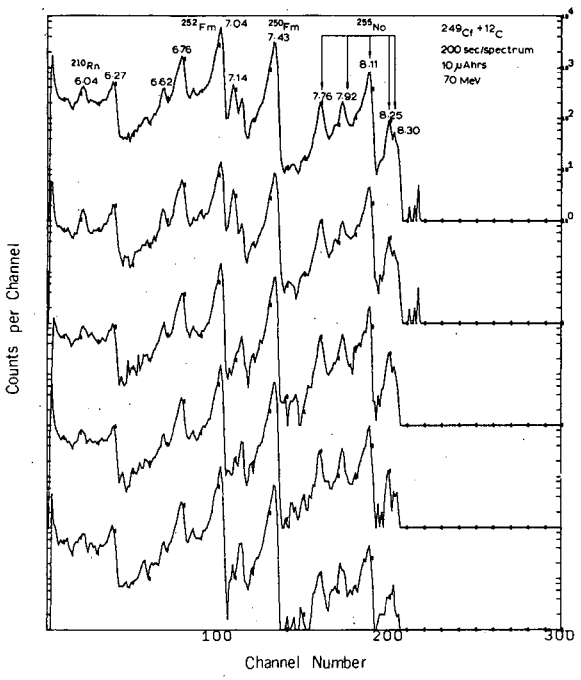

Fig. 1. A series of alpha spectra of the activities produced by bombardment of ^{249}Cf with 70-MeV ^{12}C ions. The top spectrum is the sum of the individual spectra from the four detectors.
(XBL698-4881)

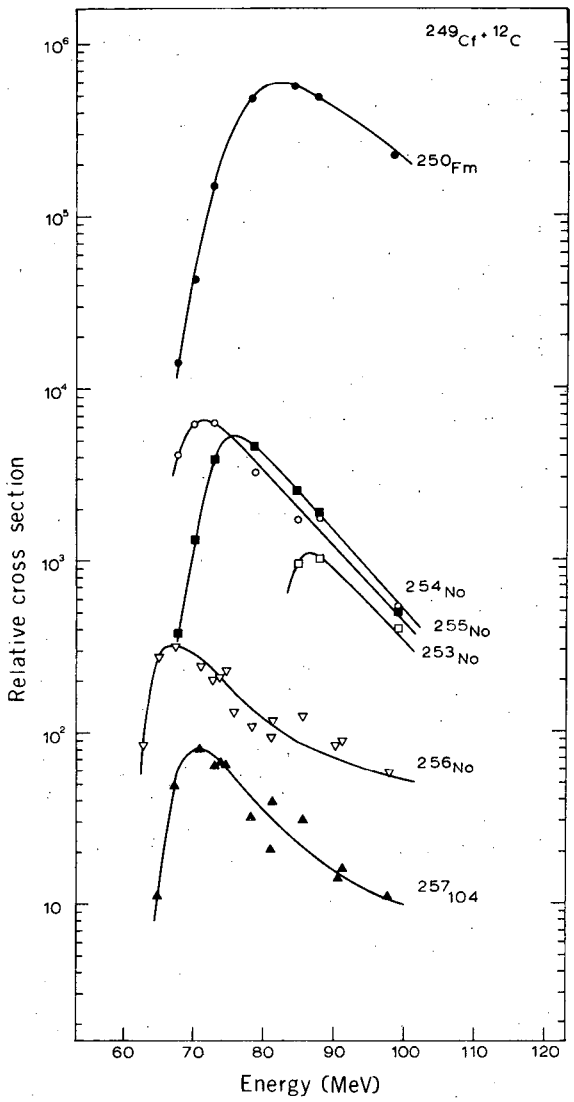

Fig. 2. Excitation curves of several activities produced by bombardment of ^{249}Cf with ^{12}C ions. (XBL694-4815)

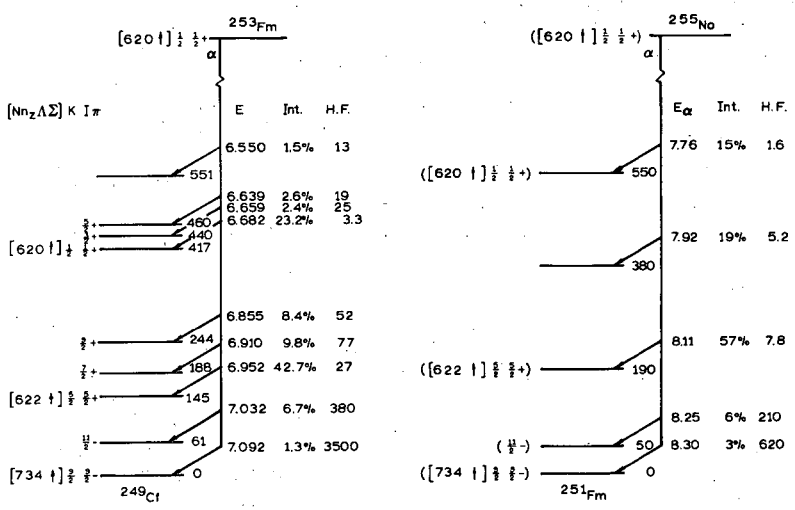

Fig. 3. Decay schemes of ^{253}Fm and ^{255}No. Numbers to the right of the levels give their energies in keV. Alpha energy E_α is in MeV.
(XBL701-6102)

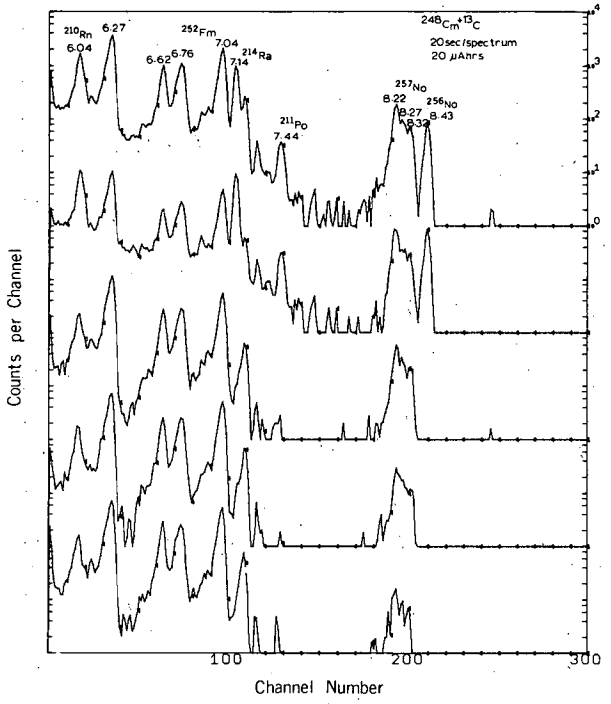

Fig. 4. A series of alpha spectra of the activities produced by bombardment of ^{248}Cm with ^{13}C ions. The series of spectra is a sum of four different experiments with energies ranging from 66 to 74 MeV. (XBL698-4880)

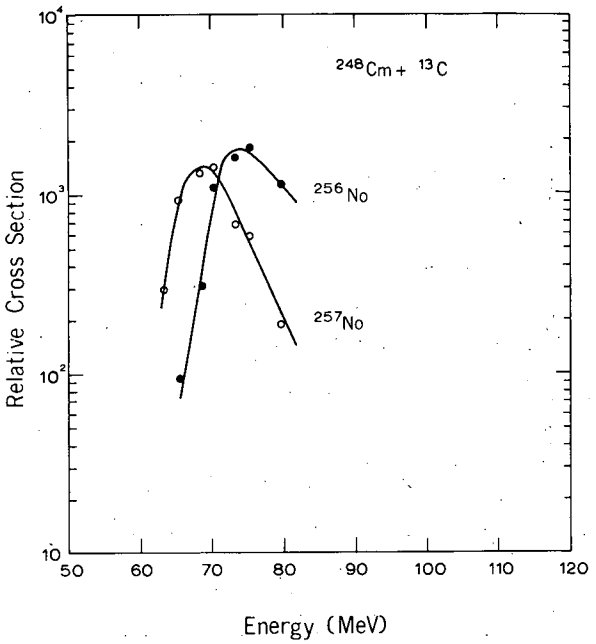

Fig. 5. Excitation curves of ^{256}No and ^{257}No produced by bombardment of ^{248}Cm with ^{13}C ions. (XBL698-4882)

PROPERTIES OF ^{258}Lr AND ^{259}Lr

Albert Ghiorso, Matti Nurmia, Kari Eskola, † and Pirkko Eskola*

An 8.6-MeV 8-sec alpha activity was discovered at Berkeley in 1961[1] and shown to be an isotope of element 103. In these experiments a target consisting of a mixture of californium isotopes with masses 249 to 252 was bombarded with ^{10}B and ^{11}B ions, and therefore an unambiguous isotopic assignment was difficult and not proposed. It appeared most likely at that time that the activity was due to ^{257}Lr. Subsequent studies in Dubna[2,3] seemed to conflict with this assignment and indicated that ^{257}Lr has a longer half-life of 35 sec, which is the same as that of ^{256}Lr.

In our experiments on element 104, rutherfordium, [4] we have observed an 8.6-MeV alpha activity with a half-life of about 5 sec. It was produced in bombardments of ^{249}Cf with ^{12}C and ^{13}C ions, and in both cases its excitation curve was different from those of the activities assigned to rutherfordium isotopes. The data was consistent with attributing the activity to ^{258}Lr produced by ^{249}Cf(^{12}C, p2n)^{258}Lr and ^{249}Cf(^{13}C, p3n)^{258}Lr reactions.

In a recent series of bombardments of a 47-μg target (350 μg/cm^2) of ^{248}Cm with ^{15}N ions we observed two distinct alpha activities that we believe to be due to the decay of lawrencium isotopes. One has the dominant alpha peak at 8.61 MeV and a half-life of 4 ± 1 sec, and the corresponding values for the other are 8.43 MeV and 6.5 ± 2 sec. The peak cross section of the 4-sec activity is twice that of the 6.5-sec activity, and the maxima occur at about 88 MeV for the former and at 80 MeV for the latter. The measured excitation functions for both the activities have the characteristic shape of a compound nuclear reaction. Neither one of the activities was observed in

bombardments of the ^{248}Cm target with ^{12}C or ^{13}C ions or a ^{246}Cm target with ^{15}N ions. The 4-sec activity was, however, produced in a bombardment of a ^{244}Pu target with ^{19}F ions. On the basis of the above evidence we propose that the 8.61-MeV 4-sec alpha activity is due to ^{258}Lr and the 8.43-MeV 6.5-sec alpha activity is due to ^{259}Lr.

It is plausible in the light of these new results that the 8.6-MeV 8-sec alpha activity discovered in 1961 was ^{258}Lr. The apparently too long half-life was probably due to comparatively poor statistics and possible interference from adjacent Lr isotopes.

We have made some preliminary alpha-decay studies of lighter Lr isotopes by bombarding ^{249}Cf with ^{10}B and ^{11}B ions. Because of the complexity of the alpha spectra and strong interference from known No activities through pxn reactions, the unfolding of the spectra has not been completed yet.

Footnotes and References

†On leave of absence from Department of Physics, University of Helsinki, Finland.
*Guest scientist supported by the National Research Council for Sciences, Helsinki, Finland.

1. A. Ghiorso, T. Sikkeland, A. E. Larsh, and R. M. Latimer, Phys. Rev. Letters 6, 473 (1961).
2. E. D. Donets, V. A. Shchegolev, and V. A. Ermakov, At. Energ. (USSR) 19, 109 (1965); Engl. Transl.: Soviet J. At. Energy 19, 995 (1965).
3. G. N. Flerov, Yu. S. Korotkin, V. L. Mikheev, M. B. Miller, S. M. Polikanov, and V. A. Shchegolev, Nucl. Phys. A106, 476 (1967).
4. A. Ghiorso, M. Nurmia, J. Harris, K. Eskola, and P. Eskola, Phys. Rev. Letters 22, 1317 (1969).

LIFETIMES OF GROUND-BAND STATES IN $^{148, 150, 152}$Sm†

R. M. Diamond, F. S. Stephens, K. Nakai,* and R. Nordhagen‡

The half-lives of the 4+, 6+, 8+ ground-band members in ^{152}Sm and of the 2+ and 4+ members of ^{150}Sm and ^{148}Sm have been measured, by use of a recoil-distance Doppler-shift method.[1-4] The levels studied in this work were Coulomb excited by ^{40}Ar projectiles from the Berkeley Hilac. The de-exciting transitions were observed with a Ge detector at 0 deg to the beam direction. This counter was operated in coincidence with a backscatter ring counter for particles, so that multiple excitation of the higher spin levels was emphasized and a collimated beam of ^{152}Sm recoils with a high velocity (v/c = 0.0340) was produced. These recoiling nuclei were stopped at various distances from the target by a lead stopper attached to a precision micrometer. Figure 1 shows some typical spectra for ^{152}Sm.

We have integrated the areas of the shifted and unshifted peaks (from moving and stopped nuclei, respectively) and corrected the results for (a) geometry, (b) absorption, (c) efficiency of the Ge counter, (d) change in solid angle due to the motion of the recoiling ^{152}Sm, and (e) angular distribution of the gamma transitions with the attenuation of the distribution by the very strong hyperfine field acting at the nucleus. This leads, for ^{152}Sm, to the experimental points plotted in Fig. 2. The smooth curves are least-square fits to the data (allowing for the feeding due to one prior transition) and give the half-lives listed in Table I. Also listed are the B(E2) values together with those predicted from B(E2; 2→0) by: the rigid rotor model, the harmonic oscillator, and the centrifugal stretching model of Davydov and Ovcharenko.[5]

It can be seen that the experimental B(E2)'s are significantly above the rigid rotor values. These deviations may be compared with those calculated from the results of other kinds of measurements on ^{152}Sm, i.e., from (a) the ground band energy-level spacings, (b) the electric monopole transition rates between the β band and ground band, (c) the branching ratios and B(E2) values connecting the β band and ground band, and (d) the μ-mesic and Mössbauer measurements

Table I. Lifetimes of ground-band states in $^{148, 150, 152}$Sm.

Nucleus	Transition	Energy (keV)	$T_{1/2}$ (psec)	α_T [a]	B(E2;I→I-2) in ($e^2 \times 10^{-48}$ cm^4) Experimental	Rotor	Vibrational	D–C [b]
^{152}Sm	2 → 0	121.8			0.686 ± 0.014 [c]	(0.686)	(0.686)	(0.686)
	4 → 2	244.6	57.3 ± 1.8	0.112	1.009 ± 0.033	0.981	1.372	1.036
	6 → 4	340.2	9.9 ± 0.5	0.038	1.20 ± 0.06	1.078	2.058	1.221
	8 → 6	418.7	3.0 ± 0.3	0.021	1.42 ± 0.14	1.133	2.744	1.406
^{150}Sm	2 → 0	334.0	46.8 ± 1.6	0.042	0.278 ± 0.010	(0.278)	(0.278)	
	4 → 2	439.4	6.3 ± 0.4	0.019	0.54 ± 0.04	0.398	0.556	
^{148}Sm	2 → 0	551	7.1 ± 0.4	0.010	0.156 ± 0.010	(0.156)	(0.156)	
	4 → 2	630	1.8 ± 0.5	0.0072	0.31 ± 0.08	0.223	0.312	

a. Calculated as $\alpha_K + \alpha_L + 1.33\ \alpha_M$ from the tables of Hager and Seltzer.
b. These values have been taken from the calculations by Davydov and Ovcharenko, Ref. 5, for $\mu = 0.3$, $\gamma = 10$ deg. See text.
c. Weighted average of literature values.

of the change in mean-square radius between the 2+ and 0+ levels. All these types of studies indicate deviations from rigid rotor B(E2) values in the same general range as observed. The measurements presented here are in quantitative agreement with (d) and parts of the data from (c). However, (a) indicates somewhat larger, and (b) somewhat smaller, deviations from the rotor model.

The B(E2) values for $^{148, 150}$Sm indicate nearly harmonic oscillator behavior, as is already suggested by their energy-level spacings, and are roughly in agreement with earlier measurements. We believe values from these measurements have fewer uncertainties associated with them than those from conventional heavy-ion multiple Coulomb-excitation yield measurements. In the latter case, a desired B(E2) value (lifetime) may depend upon (a) several other B(E2) values in the band, (b) higher multipole moments of the nucleus, (c) static moments, and (d) excitation of other coupled bands. In this method, none of these affects the result, apart from a small correction (which may be empirically made) due to feeding from higher states.

Footnotes and References

†Condensed from UCRL-19517; submitted to Phys. Rev. Letters.
*On leave from Osaka University, Osaka, Japan.
‡Present address: University of Oslo, Oslo, Norway.
1. S. Devons, G. Manning, and D. St. P. Bunbury, Proc. Phys. Soc. (London) A68, 18 (1955).
2. I. F. Wright, Bull. Am. Phys. Soc. 6, 285 (1961).
3. T. K. Alexander and K. W. Allen, Can. J. Phys. 43, 1563 (1965).
4. R. M. Diamond, F. S. Stephens, W. H. Kelley, and D. Ward, Phys. Rev. Letters 22, 546 (1969).
5. A. S. Davydov and V. I. Ovcharenko, Yadern. Fiz. 3, 1011 (1966) [Engl. transl.: Soviet J. Nucl. Phys. 3, 740 (1966)].

Fig. 1. Coulomb excitation spectra of ^{152}Sm by ^{40}Ar. The lead plunger is set at the indicated distances from the target. The positions of the unshifted lines are given at the top of the figure, those of the shifted lines at the bottom. (XBL6912-6333)

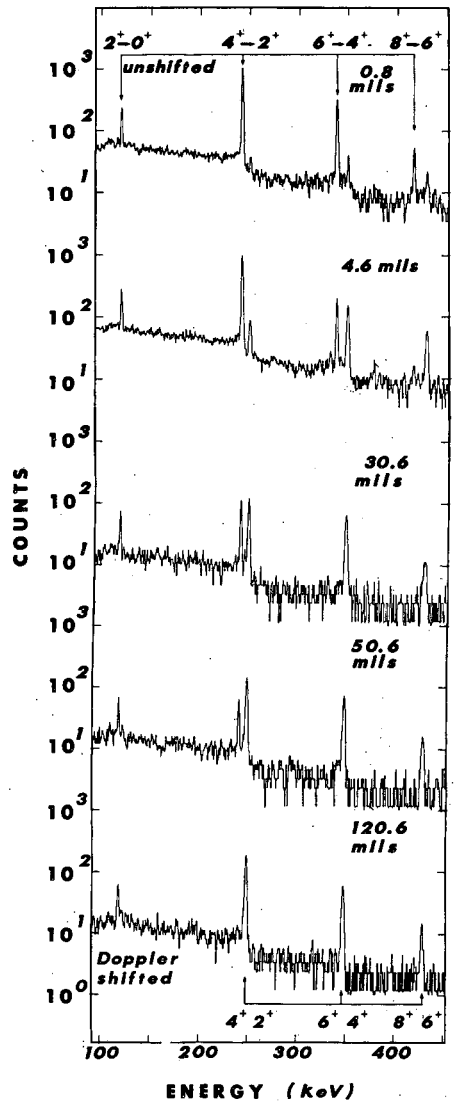

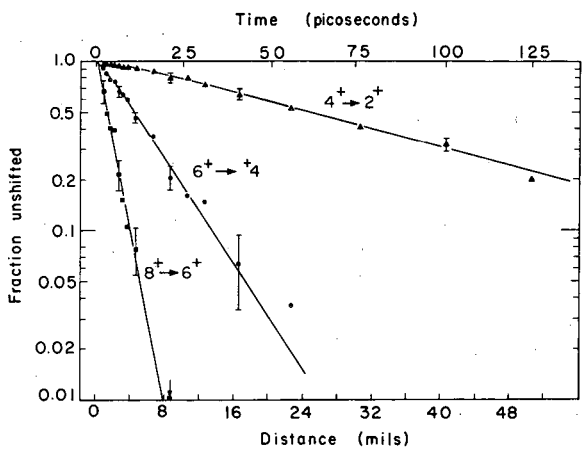

Fig. 2. The fraction of each transition in ^{152}Sm that is unshifted in energy vs the distance between target and plunger. The symbols are the experimental points; the lines are the computer-calculated best fits allowing for one stage of feeding. (XBL695-2814)

THE SPIN DEPENDENCE OF THE DEORIENTATION OF RECOILING FREE ATOMS

R. Nordhagen, † G. Goldring, * R. M. Diamond, K. Nakai, ‡ and F. S. Stephens

Among the strongest hyperfine fields encountered to date have been the magnetic fields found in highly excited, free atoms. Such atoms are produced in nuclear reactions when the bombarding energies are sufficient to let the products leave the target and recoil into vacuum or gas. Ben Zvi et al. [1] have recently shown the occurrence of strongly perturbed γ-ray angular distributions following Coulomb excitation of the first 2^+ level in thin targets of even-even nuclei. By studying recoils both into vacuum and into gas, the nature of the hyperfine fields was explored, and the feasibility of measuring magnetic moments of excited nuclear states by these methods was established. It was found that the time-integrated perturbation factors, G_k, in the angular distribution

$$W(\theta) = \sum_{k=0}^{k=2n} A_k G_k P_k(\cos\theta) \qquad (1)$$

followed the assumptions of a randomly oriented time-dependent magnetic hyperfine interaction. [1] These results, obtained with ^{16}O beams up to 40 MeV in energy, indicated fields of between 20 and 30 MG.

In the work reported here, strongly perturbed angular correlations have been studied following heavy-ion compound-nucleus reactions of the type (HI, xn). In the specific reactions chosen, $^{120, 122, 124}Sn(^{40}Ar, 4n)^{156, 158, 160}Er$, the recoil velocities of the product nuclei are of the order of 2% of the speed of light for a bombarding energy of 150 MeV. Thus large hyperfine fields are expected when the product nuclei recoil in vacuum. Ground-band transitions from states with spins I = 8 to I = 2 and mean lives from τ_m = 3.1 to 433 psec were observed. Assuming a time-dependent, randomly fluctuating hyperfine interaction, the time-integrated perturbation factor in the angular distribution is given by $G_k = 1/(1 + p_k \omega^2 \tau_c \tau_m)$. For the magnetic dipole case, $\omega = gH\,\mu_N/\hbar$, g being the nuclear g factor and H the field at the nucleus. It is assumed that the field randomly changes direction with J, the atomic spin, in an average correlation time τ_c.

If this simple time-dependent theory is assumed and the perturbation takes place during the entire decay cascade, the yrast region included, the fit shown in Fig. 1 is obtained. As can be seen, the fit is poor and χ^2 is large. Moreover, the average g factor obtained, g = 0.24, is considerably smaller than the value of g_R found in this mass region, $g_R \approx 0.3$. The fit is relatively sensitive to the value of g; taking g as 0.3, for example, gives a χ^2 of 11. Thus, it seems that the assumptions of a constant g factor or a full perturbation during the entire decay are not in accord with the observations.

The poor fit of Fig. 1 can be substantially improved by ignoring the perturbation in the time prior to entering the ground band. During this feeding stage the nuclei cascade through states of high spin, and we might expect a strongly reduced interaction for high nuclear spins. When a large nuclear spin I and a small atomic spin J couple to a resultant F, I is highly aligned with F. The precession of I around F, caused by the hyperfine field, will not cause appreciable reorientation of I under these circumstances. Only when I becomes comparable to J will large perturbations occur. A simple estimate of these effects is to assume that the perturbation disappears for I > J, and has the full value for I $\leq$ J. In this case we obtain a curve similar to that in Fig. 2 as the best fit, with J = 8. Having explored other simplified models in which the J distribution varies both in time and over the system, and also in which the correlation time depends on J, we find the expression for G_k modified to include a factor K(I, J); $G_k = 1/[1 + p_k \omega^2 \tau_c \tau_m K(I, J)]$. Essentially, K(I,J) was found to depend on the ratio I/J, and a best fit given in Fig. 2 was obtained with $\chi^2 \approx 1.6$.

The g factors obtained, as is apparent from the figure, indicate no variation among the three Er nuclei. An absolute value for the average g factor, $g = 0.37 \pm 0.03$, was derived with $H^2 \tau_c$ as above. Apparently, there is also no large variation of g factors with I, but as we have introduced an I-dependent correction, such a variation may be masked. However, since the mean life of a state with given spin varies considerably among the three nuclei, a dependence of the g factor on I would have to be correlated with the mean life to produce such a masking.

In conclusion, we have found evidence that a strong I and J dependence does occur in the perturbation of angular distributions from high-velocity free atoms, an effect which has not previously been observed. It is still, however, possible to obtain g-factor estimates when these effects are taken into account.

Footnotes and Reference

†Present address: University of Oslo, Oslo, Norway.
*Present address: Weizmann Institute, Rehovoth, Israel.
‡On leave from Osaka University, Osaka, Japan.

1. I. Ben Zvi, P. Gilad, M. Goldberg, G. Goldring, A. Schwartzschild, A. Sprinzak, and Z. Vager, Nucl. Phys. A121, 592 (1968).

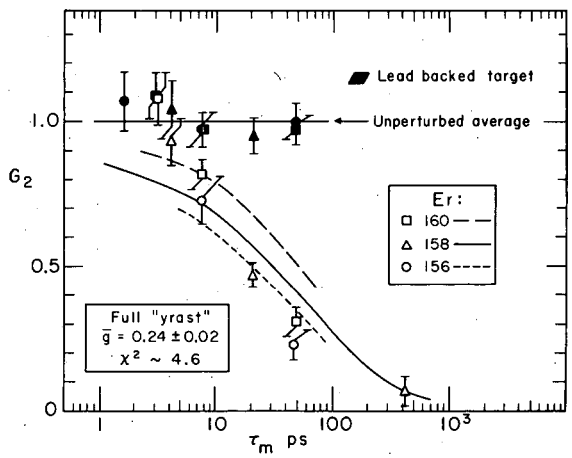

Fig. 1. Perturbation factors, G_2, for transitions in the ground bands of $^{156, 158, 160}$Er recoiling in lead and in vacuum, plotted against the mean life of the emitting level. The lines are drawn through the calculated points only, and do not give the variation of perturbation with mean life, as this depends on the mean lives of the previous transitions in the cascade. The fit is performed under the assumption of a full perturbation taking place during the entire decay cascade, including the yrast region. (XBL697-3195)

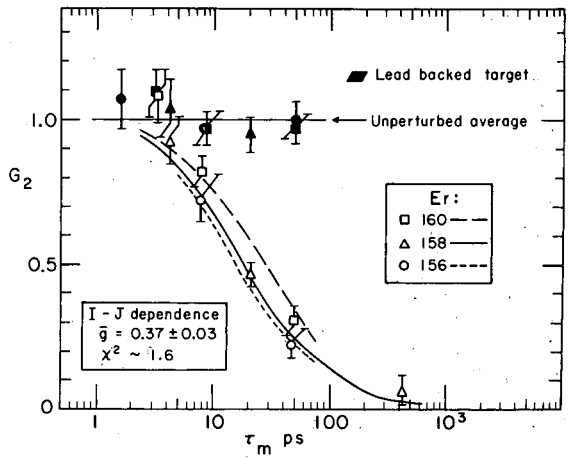

Fig. 2. Perturbation factors, G_2, for transitions in the ground bands of $^{156, 158, 160}$Er recoiling in lead and in vacuum, as in Fig. 1, but for the assumption of an I-J-dependent perturbation. The lines drawn through the calculated points have the same significance as in Fig. 1. (XBL697-3196)

ISOMERS IN ^{156}Gd, ^{172}Yb, AND ^{182}W

R. Nordhagen,† R. M. Diamond, and F. S. Stephens

With the increased use of pulsed-beam techniques and elaborate electronics the number of short-lived isomers found in nuclear reactions is rapidly increasing. Among the isomers of particular interest have been the low-lying, high-spin states found in the even-even rare earth nuclei. These are believed to be due generally to two-quasi-particle configurations. We have found three new microsecond isomers in the even-even rare earths which probably are additions to this general class of two-quasi-particle isomeric states. A more complete description of this work has been published elsewhere.[1]

The three isomers were produced with the α-particle beam of the Lawrence Radiation Laboratory Hilac. In addition to the overall pulsed nature of the beam (duty cycle $\approx$ 20%) an electrostatic beam-pulsing system was employed to produce short beam bursts (down to $\approx$ 1 μsec duration) at repetitive intervals during the $\approx$ 5-msec main pulse. For all isomers a beam energy of 27 MeV was used. For γ-ray studies, thick targets, mostly of natural composition, were bombarded. In a few cases targets of separated isotopes were also used. The spectra were obtained with Ge(Li) counters of about 6 cm^3 volume, situated at 90 deg to the beam direction and with front faces a few cm from the target position. Following each short beam burst, and after an adjustable delay, a gate unit would route the ADC addresses to consecutive subgroups of memory storage. In addition, the gate unit triggered the beam bursts and controlled their duration. Suitable care was taken to avoid subgroup overlap and to obtain uniformity in time, and the delay had to be adjusted to avoid contaminating the subgroup immediately following the beam burst with in-beam γ rays. The number of subgroups could be up to 7, one additional group always being reserved for the transitions being observed between the main beam pulses. These would be due to long-lived ($t_{1/2} \gtrsim$ msec activities. The number of subgroups and their length in time determined the repetition interval for the short beam pulses. The conversion-electron spectra were observed with a 3-mm-deep Si(Li) detector coupled to the same electronic system. A solenoidal field at 90 deg to the beam direction focused the electrons onto the detector. The targets employed in the electron-spectrum measurements were self-supporting or thin carbon-backed foils between 300 and 800 μg/cm^2 thick.

The information on ^{156m}Gd, produced via the ^{154}Sm(α, 2n)^{156m}Gd reaction, is less clear than for the other two. The half-life data are shown in Fig. 1; a half-life of 2.7 $\pm$ 0.1 μsec was obtained. The following relatively strong rays were found to follow the decay: 89.0, 128.6, 155.5, 199.2, 228.3, 296.3, 380.2, and possibly 450.8 keV. A partial decay scheme is given in Fig. 2, based on the previously known[2] states up to spin 6. The 8 $\rightarrow$ 6 and 10 $\rightarrow$ 8 ground-band transitions are assigned on evidence from the spectra observed in-beam, where both lines appear with the same intensity relative to the lower ground-band members, as do the corresponding known transitions in the other even-even Gd nuclei. They also follow the level systematics expected for the ^{156}Gd ground band. Electron spectra were observed, confirming the γ-ray information, but were not sufficiently good to add much to the decay scheme. The intensities of the ground-band transitions indicate feeding to the three highest states observed, but the decay sequence from the isomeric state could not be determined from the present data.

The isomer in ^{172m}Yb was studied by means of the ^{170}Er(α, 2n)^{172m}Yb reaction, mainly on targets of natural Er. For the final γ-ray spectrum the separated isotope, ^{170}Er, was used for target material. The transitions observed, with energies and intensities relative to the 78.7-keV transition (100%), are given in Table I. The half-life data are given in Fig. 1; the observed half-life was 3.6 $\pm$ 0.1 μsec. From the electron spectra it was possible to show that the 174.6-keV transition has an E1 character. The decay scheme is shown in Fig. 3. Most of this scheme is reasonably easy to establish, due to the substantial amount of information available[2] on ^{172}Yb, and by making use of the observed intensities. However, the assignment of a level at 1353.5 keV rests solely on transition energies, and is tentative. The E1 character of the 174.6-keV transition limits the spin of the isomeric state to I = 4, 5, or 6, all odd parity. However, it is hard to see why, if the spin were 4 or 5, the energetically favored transitions to the lower spin 3 or 4 states, rather than to the 5 and 6 states, would not occur. Thus, a spin assignment of $I^{\pi} = 6^-$ seems favored for the 1551.1-keV state.

Table I. Energies and intensities observed in the decay of the ^{172m}Yb 3.6-μsec isomeric state.

E_γ (keV)	I_γ [a]	Transition $I_i^\pi \rightarrow I_f^\pi$, $K_i \rightarrow K_f$
78.7 [b]	100	$2^+ \rightarrow 0^+$, $0 \rightarrow 0$
90.7 [b]	25	$4^+ \rightarrow 3^+$, $3 \rightarrow 3$
112.7 [b]	29	$5^+ \rightarrow 4^+$, $3 \rightarrow 3$
174.6 ± 0.2	70	$(6^-) \rightarrow 5^+$ $(6) \rightarrow 3$
181.6 [b]	50	$4^+ \rightarrow 2^+$, $0 \rightarrow 0$
197.6 ± 0.2	7	$(6^-) \rightarrow$ 1353.5 keV
203.4 [b]	38	$5^+ \rightarrow 3^+$, $3 \rightarrow 3$
279.7 [b]	25	$6^+ \rightarrow 4^+$, $0 \rightarrow 0$
813.5 ± 0.3	2	1353.5 keV $\rightarrow 6^+$
912.8 ± 0.3	13	$3^+ \rightarrow 4^+$, $3 \rightarrow 0$
1003.5 ± 0.3	3	$4^+ \rightarrow 4^+$, $3 \rightarrow 0$
1011.1 ± 0.3	23	$(6^-) \rightarrow 6^+$, $(6) \rightarrow 0$
1093.2 ± 0.4	5	1353.5 keV $\rightarrow 4^+$
1094.4 ± 0.3	49	$3^+ \rightarrow 2^+$, $3 \rightarrow 0$
1116.2 ± 0.4	3	$5^+ \rightarrow 4^+$, $3 \rightarrow 0$

a. Relative to $I_{78.7}$. Larger intensities have errors ≈ 10%, weak lines up to ≈ 50%.
b. Used as relative standards, taken from Ref. 2.

Table II. Energies of transitions observed in ^{182m}W.

Energy (keV)	Transition $I_i^\pi \rightarrow I_f^\pi$
100.1 [a]	$2^+ \rightarrow 0^+$
229.3 [a]	$4^+ \rightarrow 0^+$
351.0 [a]	$6^+ \rightarrow 4^+$
464.0 ± 0.2	$8^+ \rightarrow 6^+$
518.5 ± 0.2	isom $\rightarrow 10^+$
567.6 ± 0.2	$10^+ \rightarrow 8^+$
1086.1 ± 0.4	isom $\rightarrow 8^+$
511.0 [a]	β^+

a. Used as relative standards, taken from Ref. 2.

Among the nearest even-even nuclei, several two-quasi-particle states with $I^\pi = 6^+$ are known. These states generally decay to both the spin 6 and 4 states of the ground band, a fact which supports the different assignment of the isomer ^{172m}Yb, as in this isomer no direct transition to the spin 4 ground-band state is seen. Of the several possible combinations of the two-quasi-particle configurations found in this mass region, the Nilsson orbits due to the 5/2- [512] and 7/2+ [633] neutron configurations are most likely the ones giving rise to the isomeric state with $I^\pi = 6^-$. The same two orbits are the lowest two in the neighboring nucleus ^{173}Yb.

Natural targets of Hf were bombarded to produce ^{182m}W, mainly by the ^{180}Hf(α, 2n)^{182m}W reaction. Table II gives the energies of the gamma transitions assigned to ^{182m}W. Figure 4 gives the decay scheme with intensities for the primary transitions, and the half-life data are plotted in Fig. 1. The observed half-life was 1.4 ± 0.1 μsec. To establish the sequence of the two transitions of 518.5 and 567.6 keV we note that the 567.6-keV energy is close to the one expected for a 10 → 8 transition in ^{182}W. Moreover, this transition appears in the in-beam spectrum with approximately the same intensity relative to the other ground-band transitions in ^{182}W as shown by the 10 → 8 transition relative to the other ground-band ones in ^{180}W. The 518.5-keV transition is relatively weaker in-beam, as would be expected for an isomeric transition. From the measured conversion coefficient of the 518.5-keV transition and the lifetime of the 2230.5-keV level, it is very likely that this transition is M1. Since the 1086.1-keV transition cannot be M3 the spin of the isomeric state must be $I^\pi = 9^+$ or 10^+.

As with the other isomers we assume that the 2230.5-keV isomeric state in ^{182}W is probably based on a two-quasi-particle configuration. In the neighboring odd nucleus, ^{183}Re, Emmott et al.[3] observed an $I^\pi = 25/2^+$ isomer ($t_{1/2}$ = 1.0 msec, E = 1907.0 keV) and proposed that the properties of this isomer could be explained by the state's having a three-quasi-particle configuration, consisting of the single proton in the ground-state orbit 5/2+ [402] coupled to a two-quasi-particle $I^\pi = 10^+$ state. Possible configurations for this latter state are the two-neutron configuration based

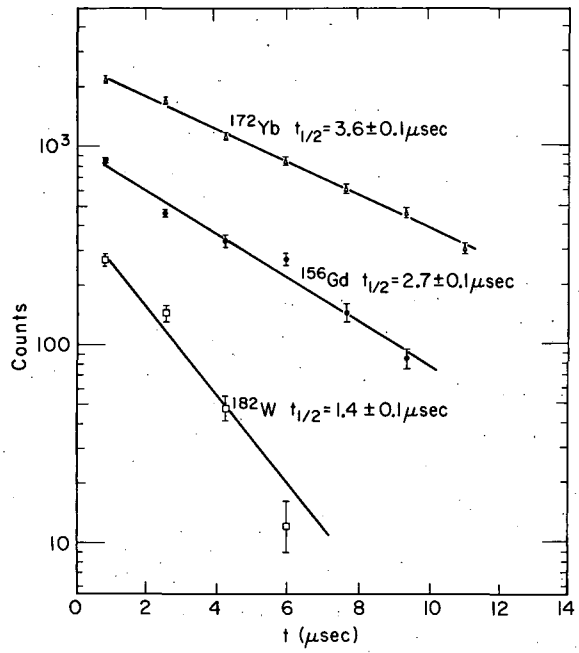

Fig. 1. Half-life measurements for the three isomers studied. (XBL697-3287)

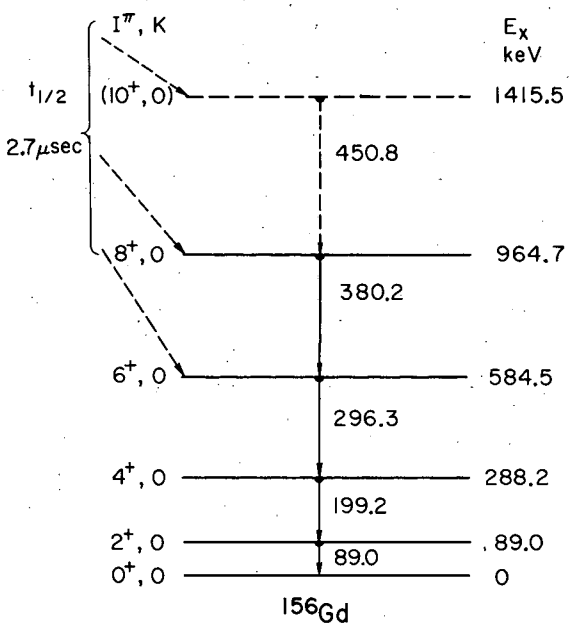

Fig. 2. Partial decay scheme for the 2.7-μsec isomer in 156 Gd. (XBL698-3368)

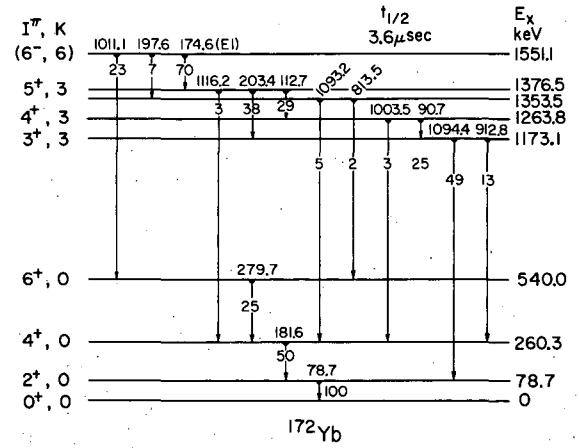

Fig. 3. Decay scheme for the 3.6-μsec isomer in ^{172}Yb. (XBL697-3285)

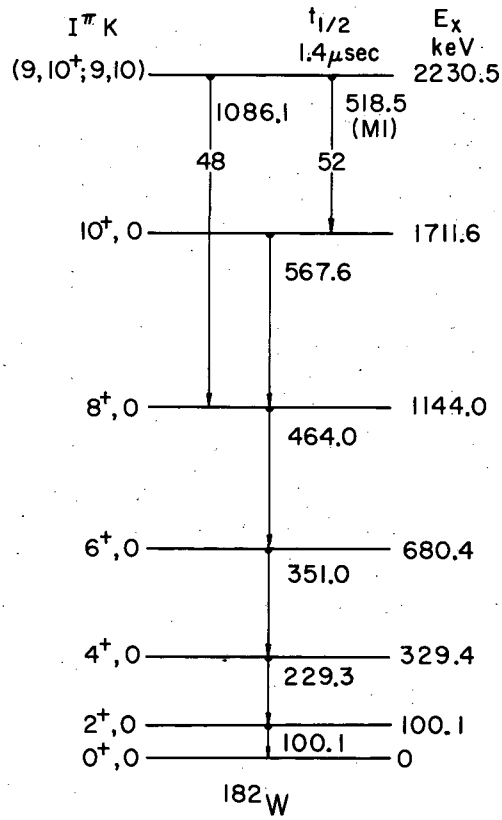

Fig. 4. Decay scheme for the 1.4-μsec isomer in ^{182}W. (XBL697-3286) →

on the orbits 9/2+ [624], 11/2+ [615] and the two-proton configuration 9/2- [514], 11/2- [505]. J. O. Newton[4] has pointed out that the state observed in ^{182}W is very likely this same I = 10 state. In this picture, the 1086.1-keV transition should be the same one as the 193-keV isomeric transition in ^{183}Re. In ^{182}W, this reduced transition probability is only 1/10 as fast as in ^{183}Re, presumably due to a smaller admixture into the isomeric state of the ground-band state with the same spin because of the greater energy separation of the corresponding levels of the two bands. Finally, it must be pointed out that other configurations producing reasonably low-lying $I^{\pi} = 9^{+}$ states are also possible. Without further information, such a spin cannot be excluded, although we prefer the assignment $I^{\pi} = 10^{+}$.

Footnote and References

†Present address: Institute of Physics, University of Oslo, Oslo, Norway.

1. R. Nordhagen, R. M. Diamond, and F. S. Stephens, Nucl. Phys. A138, 231 (1969).
2. C. M. Lederer, J. M. Hollander, and I. Perlman, Table of Isotopes, 6th Edition (John Wiley & Sons, New York, 1967), and references therein.
3. M. J. Emmott, J. R. Leigh, D. Ward, and J. O. Newton, Phys. Letters 20, 56 (1966).
4. J. O. Newton, private communication, 1969.

QUASI-ROTATIONAL STATES OF ^{172}Os, ^{174}Os, AND ^{176}Os

J. R. Leigh, F. S. Stephens, and R. M. Diamond

The reaction (^{28}Si, 4n) on $^{148, 150, 152}$Sm targets has been employed to study neutron-deficient osmium isotopes of mass 172, 174, and 176. The Berkeley Hilac was used to accelerate silicon ions to energies between 125 and 166 MeV. Angular distributions and excitation functions of the γ rays have been performed, using Ge(Li) detectors.

In the reactions with the ^{148}Sm and ^{150}Sm targets γ-ray spectra have also been recorded in coincidence with evaporated charged particles. Evaporated protons and α particles were detected in an annular phosphorus-diffused-silicon counter at 160 deg to the beam direction. The protons and alphas are distributed in energy about their respective Coulomb barriers, and their separation was further enhanced by adjusting the detector bias, and hence the depletion depth, so that the higher-energy protons were not completely stopped. Inelastically scattered Si ions were stopped by a 0.05-mm aluminum foil placed over the detector face. This allows the γ rays arising from charged-particle reactions to be identified, making assignments of γ rays associated with xn reactions more reliable, even when the charged-particle reactions are competing strongly. These assignments are based on excitation functions, angular distributions, relative intensities, and energy-level systematics.

The results for the Os isotopes are presented in Table I. The energies are expected to be accurate to 0.1% in all cases. The relative yields, corrected for internal conversion, detector efficiency, and absorbers, are generally accurate to within less than 20%. The assignment of transitions to the quasi-rotational band is better than 90% certain; where the confidence level is less than this, the transitions, possibly belonging to the ground-state band, are not assigned. The assignment of the transitions as having E2 character is consistent with the results of Newton et al.,[1] which indicate that the anisotropy, defined as $(I_0\text{-}I_{90})/I_{90}$, should lie in the range 0.33 to 0.75. New data on the ground-state rotational band of ^{170}W have been obtained from the α-γ coincidence work. Gamma rays from states up to the 10^{+} have been observed following the reaction ^{148}Sm(Si, α2n)^{170}W.

The variation in energy of the first 2^{+} level of some even-even nuclei for neutron numbers between 88 and 120 is displayed in Fig. 1. The lower-Z isotopes are characterized by the sudden onset of deformation at 88 to 90 neutrons, and then a region of relatively constant deformation. As Z is increased the change from the "vibrational" to the "rotational" isotopes is much more gradual and the deformed region covers fewer isotopes. The results presented here extend previous work on the Os isotopes[2, 3] through the region of maximum deformation (minimum 2^{+} energy) and are consistent with the trends presented above.

Table I. Transitions for osmium isotopes.

Assignment	^{172}Os E_γ	I	A	^{174}Os E_γ	I	A	^{176}Os E_γ	I	A
Ground-state-band transitions									
$2^+ \rightarrow 0^+$	227.7	100	0.30 ± 0.05	158.5	100	0.34 ± 0.03	135.2	100	0.36 ± 0.09
$4^+ \rightarrow 2^+$	378.4	94	0.37 ± 0.07	276.0	80	0.44 ± 0.03	260.2	100	0.33 ± 0.04
$6^+ \rightarrow 4^+$	448.4	80	0.25 ± 0.07	342.3	74	0.47 ± 0.04	346.9	102	0.30 ± 0.03
$8^+ \rightarrow 6^+$				393.9	59	0.45 ± 0.06	415.0	66	0.37 ± 0.10
$10^+ \rightarrow 8^+$				445.4	43	0.47 ± 0.09	476.3	48	0.40 ± 0.10
Other prominent transitions									
	470.6	64	0.47 ± 0.16	495.7	30	0.30 ± 0.12	533.9	29	0.19 ± 0.15
	487.9	25	0.30 ± 0.29	541.9	26	0.10 ± 0.14			
	499.0	39	0.41 ± 0.20	583.2	23	0.24 ± 0.16			

The lightest mercury isotopes observed[2] show little tendency for the first excited state to drop. It would be interesting to extend these to lower neutron number to establish that there is a qualitative difference between the Pt and Hg isotopes in this respect.

References

1. J. O. Newton, F. S. Stephens, R. M. Diamond, K. Kotajima, and E. Matthias, Nucl. Phys. A95, 357 (1967).
2. J. Burde, R. M. Diamond, and F. S. Stephens, Nucl. Phys. A92, 306 (1967).
3. J. O. Newton, F. S. Stephens, and R. M. Diamond, Nucl. Phys. A95, 377 (1967).

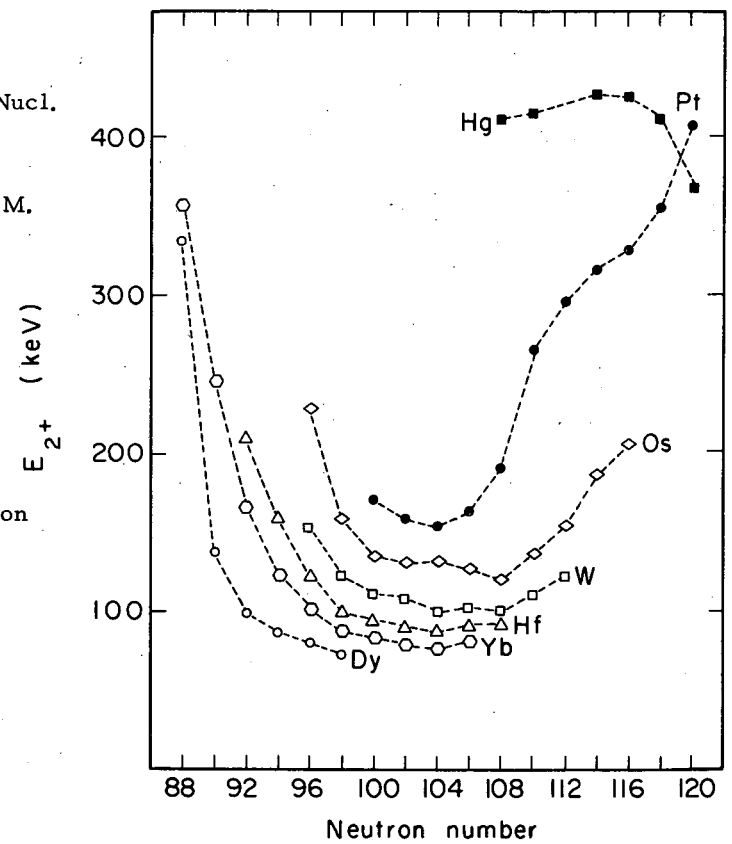

Fig. 1. Variation in energy of the first 2^+ level of some even-even nuclei, as a function of neutron number. (XBL701-2154)

EVIDENCE FOR AN OBLATE BAND BASED ON THE 9/2- ISOMER IN $^{199}Tl^{+}$

J. O. Newton,* S. D. Cirilov,* F. S. Stephens, and R. M. Diamond

Low-lying 9/2- isomeric states have been observed[1,2] in the neutron-deficient odd-mass thallium nuclei from mass 201 to 193 (Fig. 1), but there has as yet been no explanation for the existence of such states. We have studied the transitions and states feeding this isomer in ^{199}Tl by in-beam spectroscopic techniques, involving both conversion-electron and γ-ray singles spectra (Fig. 2), γ-γ coincidence measurements, excitation functions, and γ-ray angular anisotropy determinations. The decay scheme deduced is shown in Fig. 3. Among the most prominent states found are an 11/2-, a 13/2-, and possibly a 15/2- state. These are also observed in the other light odd-mass thallium nuclei, as will be described in a later paper, and are shown in Fig. 4.

Recently Blomqvist[3] has suggested that the simple shell model considerably overestimates the energy required to excite the odd proton to the $h_{9/2}$ state in thallium. The main reason is that in the ground states of the odd thallium nuclei very little energy can be obtained from pairing correlations, since the nearest unblocked level into which proton pairs can scatter is far above the Fermi surface. However, when a proton is excited to the $h_{9/2}$ orbit there should be an unblocked level close to the Fermi surface and the pairing energy should be correspondingly increased. The excitation energy to the $h_{9/2}$ orbit should therefore be reduced over the single-particle spacing by an amount equal to the gain in pairing energy. It was estimated empirically[3] (by comparing the proton binding energies in ^{203}Bi and in ^{201}Tl and then correcting for the Coulomb energy) that this type of effect might reduce the excitation energy of the $h_{9/2}$ state in ^{201}Tl from $\approx$ 4.2 MeV (the $s_{1/2}$-$h_{9/2}$ gap) to about 1.6 MeV, and it was suggested that interactions involving the neutron holes might lower this still further to the observed energy of 0.91 MeV. This idea seems valid; however, a difficulty that remains is that similar calculations for the lighter thalliums yield similar excitation energies for their 9/2- states, whereas experimentally these levels fall monotonically in energy to less than 390 keV in ^{193}Tl.

In addition, our measurements show the existence, not only of the low-lying 9/2- state, but also of the 11/2-, 13/2-, and possibly 15/2- states above it. In each nucleus the spacing between the 9/2- state and the other two states is strikingly similar, as shown in Fig. 4. This highly systematic behavior suggests strongly that these states are closely related to one another, possibly in some collective manner.

We wish to point out a possible explanation for these levels which at first sight looks implausible, but for which a reasonably strong case can be made, nevertheless. This is that the odd-parity states arise from a rotational band based on the 9/2- [505] Nilsson state. This state is derived from the $h_{9/2}$ shell-model orbit, and in order for it to be a low-lying level, the excited thallium nuclei must have oblate deformation. This last hypothesis can be supported by combining the calculations of Kumar and Baranger[4] on the potential energy of deformation of the light mercury nuclei with an estimate of the lowering of the 9/2- [505] state at the appropriate deformation. The results of this simple treatment are given in Table I, where column 5 shows that none of the Hg isotopes would be expected to be deformed, whereas the last column indicates that the 9/2- state in the light Tl nuclei would be expected to be oblate. The change in energy of the 9/2- states as a function of mass number is also given approximately correctly in the last column of Table I. Even the observed distortion of the band energies from the simple I(I+1) dependence supports the idea that this is a deformed rotational band, and in particular one based on the 9/2- [505] state. Such a band would be indirectly Coriolis-coupled to the 1/2- [541] state, which has a large decoupling parameter, a $\approx$ +4.7, and so would distort the 9/2- band in about the observed fashion. Branching ratios and E2/M1 mixing ratios also are in approximate agreement with such a picture.

We conclude that the pairing-energy correction suggested by Blomqvist,[3] together with the hypothesis that the 9/2- level in the odd-mass thalliums is the 9/2- [505] state in a nucleus with oblate deformation, is in satisfactory agreement with the data. To test this suggestion further, data on the lifetimes of the 11/2- and higher members of the proposed band would be especially valuable.

Table I. Energies for oblate shapes in the Tl nuclei.

Neutron Number N	A(Tl)	β(Hg)[a]	E_{def}[a] (MeV)	Zero-point energy	$E_{zp}+E_{def}$ (MeV)	$E_\beta(9/2-[505])$[c]	$E_{zp}+E_{def}+E_\beta$[d] (MeV)
112	193	-0.135	-0.93	1.42	0.49	-1.50	-1.01
114	195	-0.128	-0.77	1.49	0.72	-1.41	-0.69
116	197	-0.116	-0.61	1.56	0.95	-1.28	-0.33
118	199	-0.099	-0.38	1.00	0.62	-1.10	-0.48
120	201	-0.080	-0.15	1.10	0.95	-0.88	+0.07
122	203	0	0	1.42	1.42		
124	205	0	0	2.52	2.52		

a. β(Hg) is the deformation at the oblate minimum in the potential of the Hg nucleus.
b. E_{def} is the energy of the oblate potential minimum with respect to the potential energy for $\beta = 0$.
c. $E_\beta(9/2-[505])$ is the difference between the energy of this state at a deformation of β(Hg) and that at $\beta = 0$.
d. The deformation may be stable provided that $E_{zp}+E_{def}+E_\beta$ is < 0.

Footnotes and References

†. Condensed from UCRL-19527; submitted to Nucl. Phys.
*Present address: Department of Nuclear Physics, Research School of Physical Sciences, Australian National University, Canberra, Australia.

1. R. M. Diamond and F. S. Stephens, Nucl. Phys. 45, 632 (1963).
2. V. T. Gritsyna and H. H. Foster, Nucl. Phys. 61, 129 (1965).
3. J. Blomqvist, Nuclear Theory Group Progress Report, State University of New York at Stony Brook, April 1969, p. 29; and private communication, June 1969.
4. K. Kumar and M. Baranger, Nucl. Phys. A110, 529 (1968).

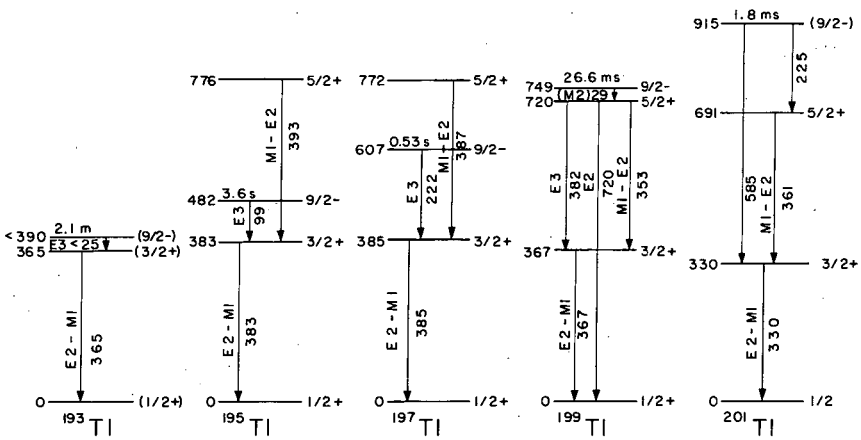

Fig. 1. Partial level schemes for the light odd-mass thallium isotopes possessing the 9/2- level. Data are taken from Refs. 1 and 2. (XBL701-2180)

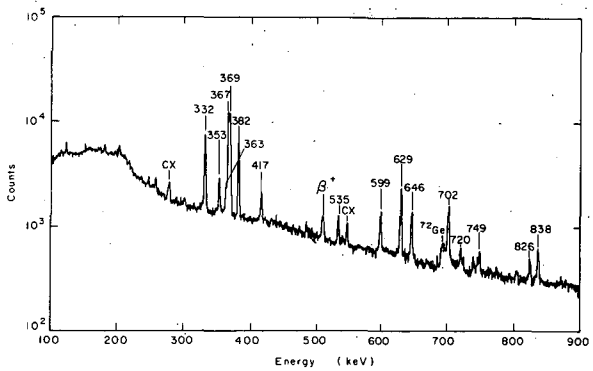

Fig. 2. Spectrum of the γ rays, taken in-beam, from the reaction of 27-MeV helium ions on gold. (XBL701-2045)

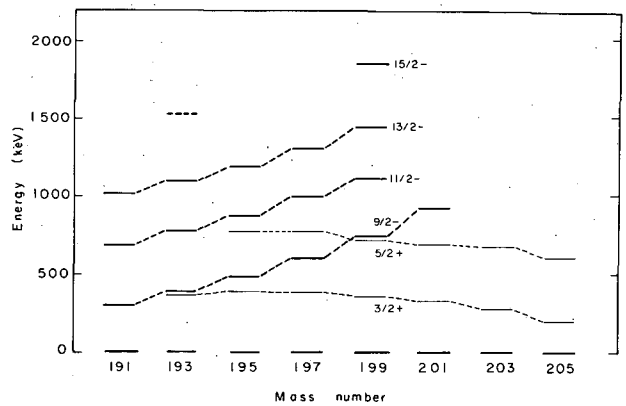

Fig. 4. Systematics for the 9/2-, 11/2-, 13/2-, and 15/2- states in the odd-thallium nuclei derived from(heavy ion, xn) experiments. (XBL701-2050)

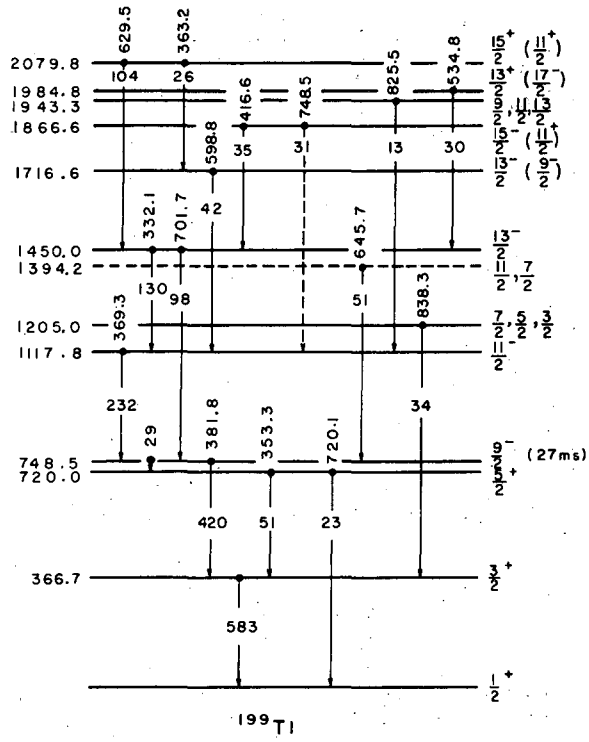

Fig. 3. Proposed decay scheme for ^{199}Tl. Uncertain levels and transitions not definitely placed are shown by broken lines. When more than one spin assignment is given, the less likely ones are placed in parentheses. Intensities are total transition intensities and include any component between beam pulses. (XBL701-2044)

LIFETIME MEASUREMENT OF THE FIRST EXCITED STATE IN ^{206}Pb

J. L. Quebert,† K. Nakai,* R. M. Diamond, and F. S. Stephens

The first excited state of ^{206}Pb (2^+, 803 keV) is expected to have a half-life of a few picoseconds. Production of this state by Coulomb excitation with 170-MeV ^{40}Ar projectiles on a thin target leads to a high recoil velocity of the excited nucleus. These conditions allow us to apply the recoil-distance Doppler-shift method[1,2] to determine the half-life rather accurately.

The experiment has been performed at the Hilac, using an argon beam of ≈ 2 nA intensity. The thin target of enriched ^{206}Pb (1.48 mg/cm^2) was evaporated onto a nickel foil 4 μin. thick. This was then stretched on a ring holder to get a surface as flat as possible. The γ rays were recorded by a 35-cm^3 Ge(Li) coaxial detector at 0 deg to the beam and operated in coincidence with the backscattered ^{40}Ar projectiles detected by a silicon ring counter. The recoiling nuclei

were stopped at different distances from the target with a flat bismuth plunger. Comparison of the relative intensities of the Doppler-shifted (s) and unshifted (u) transitions as a function of the distance between the target and the plunger allows determination of the half-life of the transition under study. This is most conveniently done by plotting the fraction $F = u/(u + s)$ against the distance, provided the recoil velocity is accurately known. This velocity has been evaluated from the energy shift between the shifted and unshifted lines. The effective velocity so measured was $v = (0.0265 \pm 0.0003) \times c$. Figure 1 shows a few of the spectra obtained as a function of the stopping distance, and the variation in the relative intensities of the shifted and unshifted peaks can be clearly seen.

A number of corrections and sources of error must be taken into account in the experimental data handling. These are: evaluation of the background; variations in the solid angle at the γ-ray counter for the two peaks (in fact, these corrections are very small because of the short distances between the target and stopper); variation in the counter efficiency for the shifted peak compared with the unshifted one; and correction of the shifted transition intensity for the change in the angular distribution due to the motion of the recoiling nucleus.

In the theoretical analysis the angular distribution of the γ rays in coincidence with back-scattered projectiles has been evaluated by use of the de Boer-Winther program.[3] Corrections must be applied to this angular distribution, for the finite geometry of the detector and for the deorientation caused by the large hyperfine field acting on the recoiling nucleus.[4]

The feeding of the 2^+ state coming from higher states has been assumed negligible because of the very small probability of exciting higher states in ^{206}Pb by the Coulomb excitation process with ^{40}Ar projectiles of the energy used.

A least-square fit to the data points has been made to obtain the best value of the half-life. Figure 2 shows the corrected experimental values of F as a function of the stopping distance, and the results for the best fit (straight line).

The results, corrected for internal conversion, are:

$$T_{1/2} = (9.17 \pm 0.57) \times 10^{-12} \text{ s},$$

$$B(E2,\ 0^+ \rightarrow 2^+) = (0.091 \pm 0.006)\ e^2b^2$$

This last value is smaller than the ones previously deduced by other methods, as is shown in Fig. 3.

Footnotes and References

†On leave of absence from C. E. N., Bordeaux-Gradignan, France.
*On leave of absence from Osaka University, Osaka University, Osaka, Japan.

1. S. Devons, G. Manning, and St. P. Bunbury, Proc. Phys. Soc. (London) A68, 18 (1955).
2. R. M. Diamond, F. S. Stephens, W. H. Kelly, and D. Ward, Phys. Rev. Letters 22, 546 (1969).
3. A. Winther and J. de Boer, A Computer Program for Multiple Coulomb Excitation, California Institute of Technology Report, Nov. 18, 1965.
4. I. Ben Zvi, P. Gilad, M. Goldberg, G. Goldring, A. Schwartzschild, A. Sprinzak, and Z. Vager, Nucl. Physics A121, 592 (1968).
5. P. H. Stelson and F. K. McGowan, Phys. Rev. 99, 112 (1955).
6. R. Barloutaud, Rapport C.E.A. 1531, 1960.
7. O. Nathan, Nucl. Phys. 30, 332 (1962).
8. A. Z. Hrynkiewicz, S. Kopta, S. Szymczyk, T. Walczak, and I. Zuzniecov, Nucl. Phys. 79, 495 (1966).

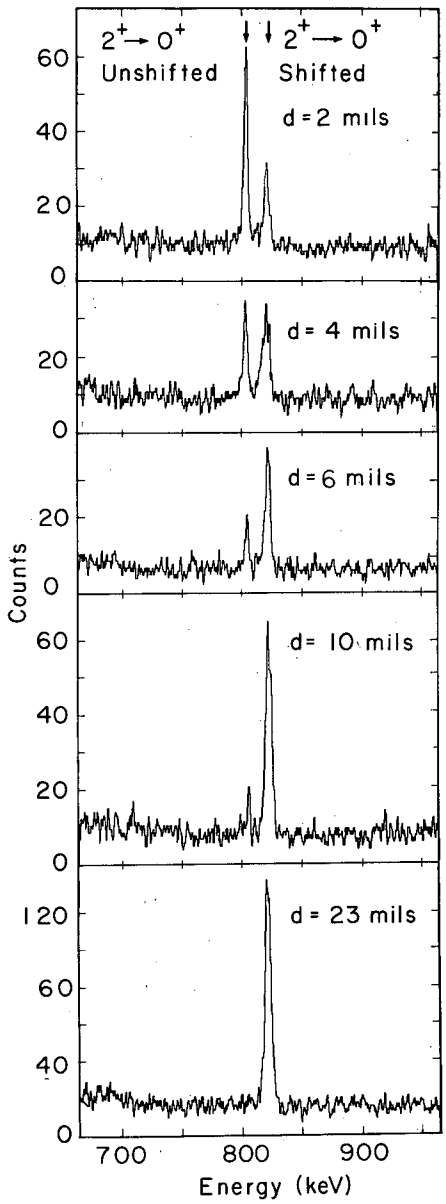

Fig. 1. Gamma spectra from the $2^+ \rightarrow 0^+$ transition (803 keV) in ^{206}Pb at different stopping distances. One can see the variation of the shifted and unshifted line intensities with the distance. (XBL701-2174)

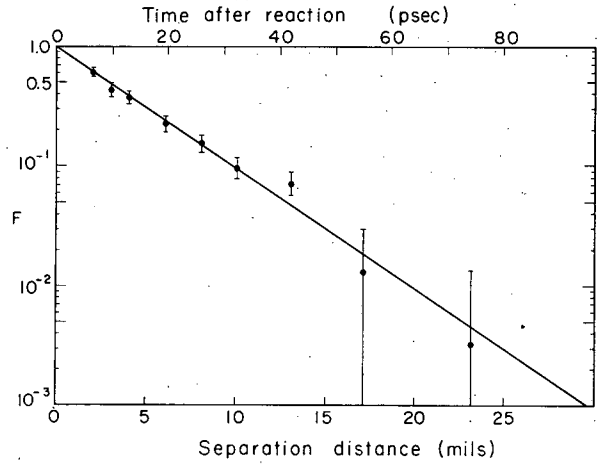

Fig. 2. Plot of log [u/(u + s)] vs the separation distance of the target and plunger. The symbols are the experimental points and the straight line is the best fit result. (XBL701-2176)

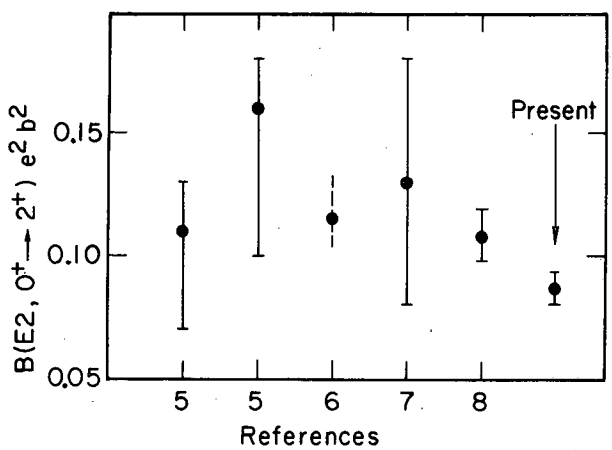

Fig. 3. Comparison of the result of this experiment with previous data. (XBL701-2175)

STROBOSCOPIC MEASUREMENT OF THE g FACTOR OF THE 7^- LEVEL IN ^{206}Pb

K. H. Maier,† K. Nakai,* R. M. Diamond, and F. S. Stephens

The 2 200-MeV 7^- level in ^{206}Pb of lifetime τ = 178 μsec and its decay are well known. Recently Quitmann and Jaklevic[1] measured the angular distributions of the deexciting γ rays and the g factor by a time integral method as g = 0.035 ± 0.020. They used the ^{204}Hg(α, 2n)^{206}Pb reaction on a thick liquid ^{204}Hg target to excite this level, and their results showed that the relaxation time in this case is at least comparable to the lifetime of the level. Thus all prerequisites were given for a more precise determination of the g factor by the stroboscopic method, which has recently been developed by the group at the Hahn-Meitner Institut, Berlin,[2] and independently by Nagamiya and Sugimoto,[3] and is especially suited for the lifetime encountered here.

In short, the principle is to excite the nuclei with many equidistant beam pulses during the lifetime of the level studied and to observe the resulting coherent superposition of the angular distributions of the de-exciting γ rays emitted by the nuclei rotating in an external magnetic field. In general this wipes out the angular distribution. But when the beam-repetition time is an integral multiple of half the Larmor period, a constructive interference results, and one gets an angular distribution at a time fixed relative to the beam pulse or a periodic distribution in time at a fixed angle. Therefore when the field B is being varied and the time T between beam pulses is kept fixed, the count rate at a fixed angle and corresponding time shows a resonance behavior at $B = (n\pi\hbar)/(Tg\mu_n)$.

The ^{206}Pb isomer was produced by a 26-MeV α beam from the LRL Hilac in a liquid mercury target enriched in ^{204}Hg to 84%. The target was about 4 mm in diameter and 0.4 mm thick. It was covered with a 0.0125-mm Mylar foil. The γ-ray spectra were very clean. By far the largest background line was the 511-keV annihilation radiation, which amounted to 15% of the isomeric transition at 516 keV and was quite well resolved from it. The two Ge detectors were placed at ± 45 deg to the beam and perpendicular to the magnetic field. This was produced by an electromagnet and measured with a rotating-coil gaussmeter. The timing shown in Fig. 1 was derived from a 200-kHz quartz oscillator, so that the only adjustments required were a delay compensating for the time of flight of the beam and the widths of the windows. Neither of these values was very critical. The necessary adjustments were made by using a time-to-height converter spectrum.

Figure 2 shows the double ratio of the intensity of the 516-keV line, namely $(Y_{11}/Y_{12})/(Y_{21}/Y_{22})$, where the first index stands for the counter and the second for the counting-time window. This double ratio multiplies the effect by about four and eliminates almost completely the influence of instabilities in the apparatus. The other lines from the decay of the isomer at 343, 538, 803, and 881 keV showed the same resonance, though less pronounced, due to smaller count rates and asymmetries.

The final analysis of the data involves a fitting procedure taking into account the finite time windows, detector angles, etc., which is not completed yet. It is known, however,[3,4] that only minor corrections have to be applied to the simple expression stated, yielding immediately g(uncorrected) = -0.0217 ± 0.0005. The error is partly due to the incomplete evaluation and will be reduced to about 1%, which is due mainly to the uncertainty of the field measurement. The width of the resonance is proportional to $(1/\tau+1/T_r)$, and at the present stage of the data analysis the relaxation time can be given as $T_r \geq 0.6$ msec.

Assuming a pure $(i_{13/2}, p_{1/2})_{7^-}$ neutron configuration results in g = 0.182 using the Schmidt values for the single particles and g = -0.063 using the measured moments of ^{197}Hg and ^{207}Pb. The discrepancy with the measured value can only be explained by assuming either a g factor for the $i_{13/2}$ orbit of only 40% of the Schmidt value, or complicated admixtures to the ^{206}Pb 7^- level, as the most likely admixed neutron configurations[5] tend to increase the g factor. For a more detailed analysis, a measurement of the magnetic moment of the $i_{13/2}$ level in ^{205}Pb or ^{207}Pb would be needed.

Footnotes and References

†On leave from Hahn-Meitner-Institut, Berlin, Germany.
*On leave from Osaka University, Osaka, Japan.

1. D. Quitman and J. Jaklevic, Measurement of the Magnetic Moments of the Microsecond Isomers in ^{73}As and ^{206}Pb, UCRL-18958, 1969.
2. J. Christiansen, H.-E. Mahnke, E. Recknagel, D. Riegel, G. Weyer, and W. Witthuhn, Phys. Rev. Letters 21, 554 (1968).
3. S. Nagamiya and K. Sugimoto, Osaka University Report OULNS 69-3, 1969.
4. H.-E. Mahnke, Diplomarbeit, Hahn-Meitner Institut, Berlin, 1968.
5. W. W. True, Phys. Rev. 168, 1388 (1968).

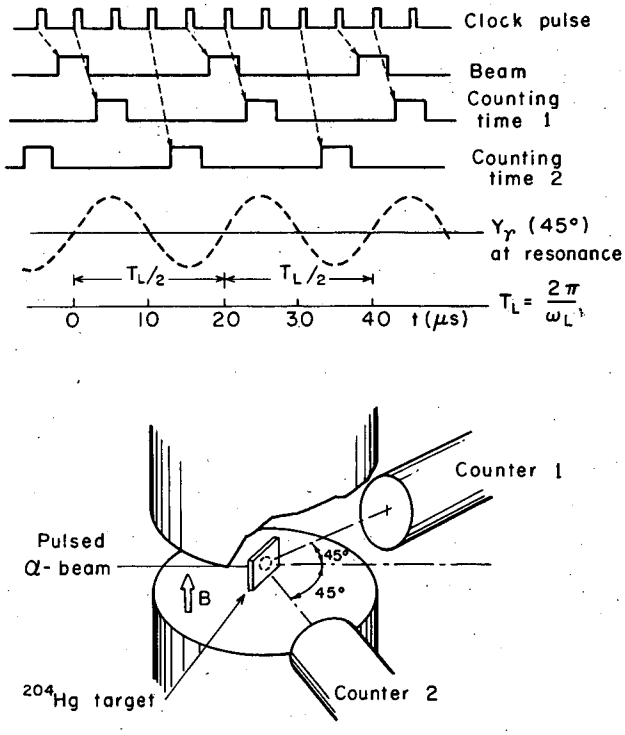

Fig. 1. Timing sequence and schematic counter arrangement. The broken arrows indicate how the timing pulses were derived.
(XBL701-2156)

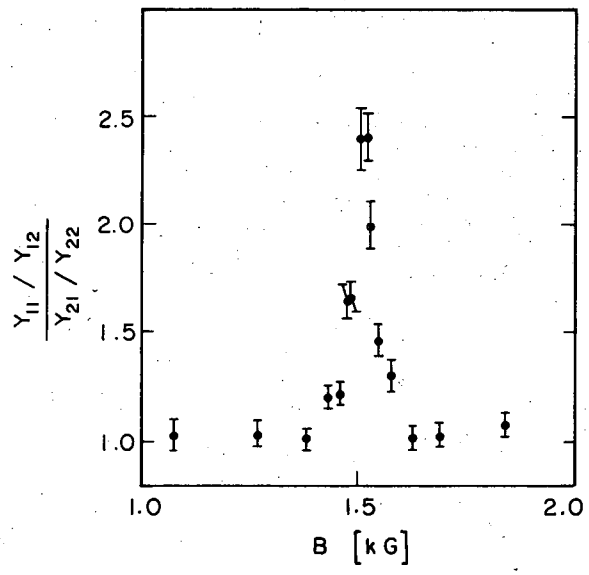

Fig. 2. Double ratio of the intensity of the 516-keV line $(Y_{11}/Y_{12})/(Y_{21}/Y_{22})$ vs magnetic field.
(XBL701-2155)

THE REORIENTATION EFFECT IN PROJECTILE EXCITATION. I. ^{20}Ne AND ^{22}Ne

K. Nakai,† F. S. Stephens, and R. M. Diamond

Determination of static quadrupole moments by the reorientation effect in Coulomb excitation[1] provides a sensitive test for nuclear models. The magnitude of the effect is roughly proportional to the mass (A_1) of the nucleus with which the nucleus of interest (A_2) is excited [$r \propto A_1/(1+A_1/A_2)$]. Thus Coulomb excitation of the projectile has the highest sensitivity for this effect when the nuclei are bombarded on heavy-mass targets. The Hilac provides heavy-ion beams suitable for this purpose, and more possibilities are expected with the proposed Super-Hilac.

Measurements of the static quadrupole moments of the 2^+ states in ^{20}Ne and ^{22}Ne have been performed by this method.[2] The Ne beam from the Hilac was used to bombard thin targets of ^{120}Sn, ^{130}Te, and ^{148}Sm ($\approx$ 1 mg/cm^2). Two coincidence γ-ray spectra, one between a NaI counter at 55 deg and a backscatter ring counter (at 160 deg) and another between the NaI counter and a particle counter at 90 deg, have been measured simultaneously. The ratio of the γ-ray intensities from the 2^+ state of Ne to that of the target nucleus at each angle (R^{160}, R^{90}) as well as the double ratio, R^{160}/R^{90}, were compared with values calculated by the deBoer-Winther Coulomb excitation program.[3] The single ratios are nearly independent of the efficiency of the particle detector except for small corrections which have been made. The double ratio also was independent of the efficiency calibration of the NaI counter. One of the main uncertainties in the final results is due to ambiguities in the excitation probabilities of the target nuclei (reorientation effect in target, etc.). However, by proper choice of the target, these ambiguities could be made small compared with the large reorientation effect in projectile excitation. Figures 1 and 2 show typical results of the experiment and of the analysis. The results are summarized in Table I. The values obtained for the quadrupole moments are consistent with a measurement[4] which came out during this work, and are more accurate. They are about 30% larger than the values calculated from the $B(E2, 0^+ \rightarrow 2^+)$ by use of the rigid-rotor model. A similar situation has been reported for the 2^+ state in ^{24}Mg.[5]

Footnote and References

†On leave from Osaka University, Osaka, Japan.

1. J. deBoer and J. Eichler, The Reorientation Effect, in Advances in Nuclear Physics, vol. 1 (Plenum Press, N. Y., 1968).
2. K. Nakai, F. S. Stephens, and R. M. Diamond, Quadrupole of the First Excited States in ^{20}Ne and ^{22}Ne, Nucl. Phys. (to be published).
3. A. Winther and J. deBoer, in Coulomb Excitation, a Collection of Reprints (Academic Press, N. Y., 1966).
4. D. Schwalm and P. Povh, Phys. Letters 29B, 103 (1969).

Table I. Summary of the experimental results.

Target	Basis of calculations: B(E2, ↑ target) (e^2b^2)	Basis of calculations: Q(target) (b)	Result: B(E2, ↑ Ne) (e^2b^2)	Result: Q(Ne) (b)
(a) ^{20}Ne				
^{120}Sn	0.23 ± 0.012[a]	$+0.5\|Q_r\|$	0.048 ± 0.0055	-0.22 ± 0.020
		0.0	0.048 ± 0.0055	-0.25 ± 0.020
		$-0.5\|Q_r\|$	0.048 ± 0.0055	-0.28 ± 0.020
	0.23 ± 0.012[a]	$(0.0 \pm 0.5)\|Q_r\|$[b]	0.048 ± 0.0055	-0.25 ± 0.036
^{130}Te	0.30 ± 0.03[c]	-0.15 ± 0.2[c]	0.048 ± 0.009	-0.24 ± 0.035
^{148}Sm	0.79 ± 0.07[d]	-0.5 ± 0.3[e]	0.048 ± 0.0086	-0.23 ± 0.035
Summary			0.048 ± 0.007[f]	-0.24 ± 0.03[f]
(b) ^{22}Ne				
^{130}Te	0.30 ± 0.03[c]	-0.15 ± 0.2[c]	0.031 ± 0.007	-0.21 ± 0.045
^{148}Sm	0.79 ± 0.07[d]	-0.5 ± 0.3[e]	0.034 ± 0.007	-0.205 ± 0.03
Summary			0.033 ± 0.006[f]	-0.21 ± 0.04[f]

a. P. H. Stelson, F. K. Mcgowan, R. L. Robinson, W. T. Milner, and R. O. Sayer, Phys. Rev. 170, 1172 (1968).
b. Assumption: Q_r is a value calculated from B(E2) using the rigid rotor model.
c. A. Christy, I. Hall, R. P. Harper, I. M. Nagib, and B. Wakefield, contribution to the International Conference on Properties of Nuclear States, Montreal, 1969.
d. R. M. Diamond, F. S. Stephens, K. Nakai, and R. Nordhagen, Lifetimes of Ground-Band States in $^{148, 150, 152}$Sm, to be submitted for publication.
e. H. S. Gertzman, D. Cline, H. E. Gove, P. M. S. Lesser, and J. J. Schwartz, Bull. Am. Phys. Soc. 13, 1471 (1968); J. J. Simpson, D. Eccleshall, M. J. L. Yates, and N. J. Freeman, Nucl. Phys. A94, 177 (1967).
f. Possible systematic errors of ±5% have been included.

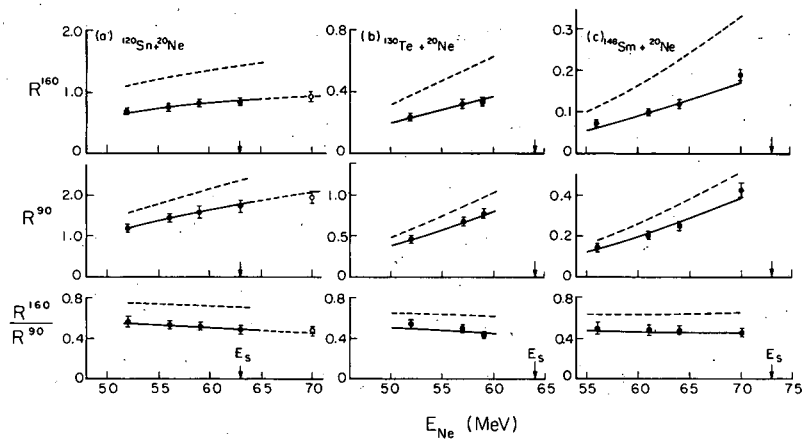

Fig. 1. Typical results of the experiments and analysis on ^{20}Ne. The solid lines show the best-fit curves for the experimental points, and the dashed lines show curves with Q = 0. (XBL697-3359)

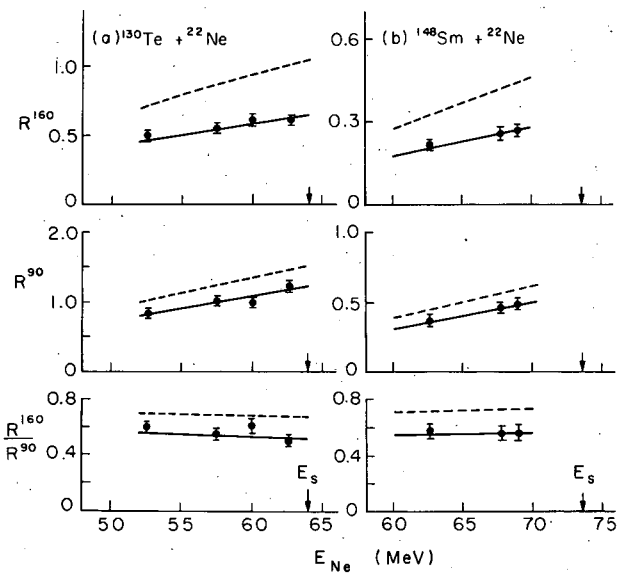

Fig. 2. Typical results of the experiments and analysis on ^{22}Ne. The solid lines show the best-fit curves for the experimental points, and the dashed lines show curves with Q = 0. (XBL697-3356)

THE REORIENTATION EFFECT IN PROJECTILE EXCITATION. II. ^{28}Si, ^{32}S, AND ^{40}Ar.

K. Nakai,† J. L. Quebert,* F. S. Stephens, and R. M. Diamond

The reorientation effects in projectile Coulomb excitation of ^{28}Si, ^{32}S, and ^{40}Ar were studied by the same method as described in the previous article on $^{20,22}Ne$.[1] Because of some difficulty in getting low energy beams from the Hilac and because of the low yields with lighter targets, the experiments have been carried out mainly with ^{206}Pb as the target. Only in the case of ^{40}Ar were ^{120}Sn and ^{130}Te targets used as well. In the analysis, the $B(E2, 0^+ \rightarrow 2^+)$ value of ^{206}Pb played an important role. So, we measured the lifetime of the 2^+ state in ^{206}Pb, using the "Doppler-shift recoil-distance method," which is described in another article.[2] The static quadrupole moment of the 2^+ state in ^{206}Pb was assumed to be $0.0 + 0.5\ Q_r$.[3]

The results are shown in Table I. Figure 1 illustrates the data for ^{28}Si and ^{32}S, and part of that for ^{40}Ar. The evidence indicates a positive quadrupole moment (oblate shape) for ^{28}Si, a negative moment (prolate shape) for ^{32}S, and a small value (nearly spherical) for ^{40}Ar. The result for ^{28}Si agrees well with a previous measurement,[4] and the ^{40}Ar result seems to us to be reasonable. But the change of shape from oblate to prolate between ^{28}Si and ^{32}S is rather unexpected. However, Hartree-Fock calculations have shown that the minimum Hartree-Fock energies are very close for both prolate and oblate shapes of nuclei in the region of ^{28}Si and ^{32}S,[5] and so it may not be surprising that the shapes of nuclei change from one to another.

The intrinsic quadrupole moments of the 2^+ states in s-d shell nuclei measured by the present projectile-excitation method are summarized in Fig. 2 together with values from other measurements.[4,6-8]

Footnotes and References

†On leave from Osaka University, Osaka, Japan.
*On leave from CEN, Bordeau-Gradignan, France.

1. Preceding paper, this report; submitted to Nucl. Phys.
2. This report, Lifetime Measurement of the First Excited State in ^{206}Pb.
3. Qr is a quadrupole moment calculated from $B(E2, 0^+ \rightarrow 2^+)$ by use of the rigid rotor model.
4. O. Häusser, T. K. Alexander, D. Pelte, B. W. Hooton, and H. C. Evans, Phys. Rev. Letters 23, 320 (1969).
5. G. Ripka, in Advances in Nuclear Physics, vol. 1 (Plenum Press, Inc., N. Y., 1968).
6. O. Häusser, B. W. Hooton, D. Pelte, T. K. Alexander, and H. C. Evans, Phys. Rev. Letters 22 359 (1969).
7. D. Schwalm and B. Povh, Phys. Letters 29B, 103 (1969).
8. V. S. Shirley, Table of Nuclear Moments, in Hyperfine Structure and Nuclear Radiations, ed. by E. Matthias and D. A. Shirley (North-Holland Publishing Co., Amsterdam, 1968).

Table I. Summary of the experimental results.

Target	Basis of calculations: B(E2, ↑ target) (e^2b^2)	Basis of calculations: Q(target) (b)	Result (projectile): B(E2, $0^+ \rightarrow 2^+$) (e^2b^2)	Result (projectile): Q(2^+) (b)
(a) ^{28}Si				
^{206}Pb	0.091 ± 0.006[a]	+0.5 $\lvert Q_r \rvert$	0.033 ± 0.004	0.126 ± 0.040
		0.0	0.033 ± 0.004	0.110 ± 0.040
		-0.5 $\lvert Q_r \rvert$	0.033 ± 0.004	0.098 ± 0.040
Summary	0.091 ± 0.006[a]	(0.0 ± 0.5 $\lvert Q_r \rvert$)[b]	0.033 ± 0.004	+0.11 ± 0.05
(b) ^{32}S				
^{206}Pb	0.091 ± 0.006[a]	+0.5 $\lvert Q_r \rvert$	0.033 ± 0.004	-0.192 ± 0.040
		0.0	0.033 ± 0.004	-0.202 ± 0.040
		-0.5 $\lvert Q_r \rvert$	0.033 ± 0.004	-0.215 ± 0.040
Summary	0.091 ± 0.006[a]	(0.0 ± 0.5 $\lvert Q_r \rvert$)[b]	0.033 ± 0.004	-0.20 ± 0.06
(c) ^{40}Ar				
^{120}Sn	0.23 ± 0.012[c]	+0.5 $\lvert Q_r \rvert$	0.034 ± 0.004	-0.032 ± 0.040
		0.0	0.034 ± 0.004	-0.021 ± 0.040
		-0.5 $\lvert Q_r \rvert$	0.034 ± 0.004	0.081 ± 0.040
	0.23 ± 0.012[c]	(0.0 ± 0.5 $\lvert Q_r \rvert$)[b]	0.034 ± 0.004	-0.021 ± 0.065
^{130}Te	0.30 ± 0.03[d]	-0.15 ± 0.20[d]	0.032 ± 0.006	0.019 ± 0.060
^{206}Pb	0.091 ± 0.006[a]	+0.5 $\lvert Q_r \rvert$	0.030 ± 0.005	0.052 ± 0.062
		0.0	0.030 ± 0.005	0.040 ± 0.062
		-0.5 $\lvert Q_r \rvert$	0.030 ± 0.005	0.022 ± 0.062
	0.091 ± 0.006[a]	(0.0 ± 0.5 $\lvert Q_r \rvert$)[b]	0.030 ± 0.005	0.040 ± 0.080
Summary	Average		0.032 ± 0.003	0.01 ± 0.04

a. Reference 2.
b. Assumption: Q_r is a value calculated from B(E2) by use of the rigid rotor model.
c. P. H. Stelson, F. K. McGowan, R. L. Robinson, W. T. Milner, and R. O. Sayer, Phys. Rev. 170, 1172 (1968).
d. A. Christy, I. Hall, R. P. Harper, I. M. Nagib, and B. Wakefield, Contribution to the International Conference on Properties of Nuclear States, Montreal, 1969.

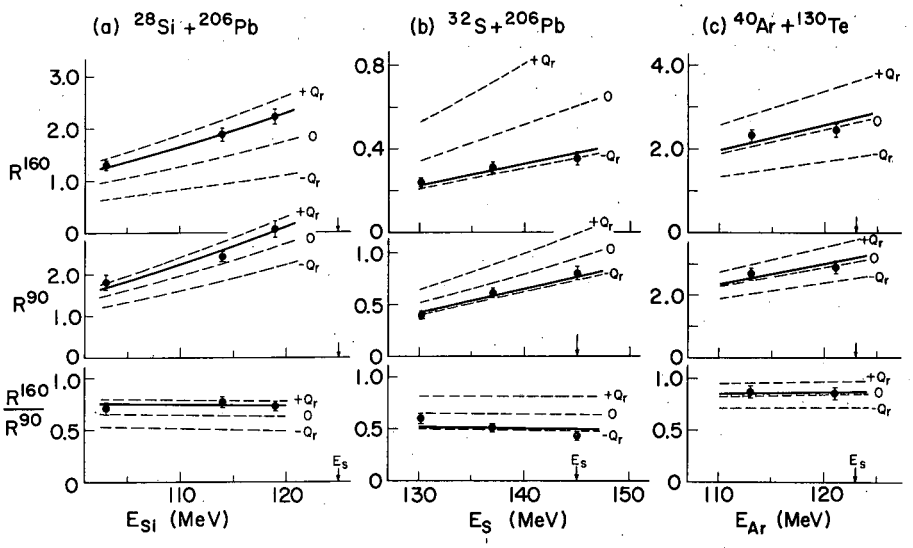

Fig. 1. Typical results of the experiments and analysis. The solid lines are the best fits and the dashed lines show the curves for $Q = 0$ or $\pm Q_r$. (XBL701-2138)

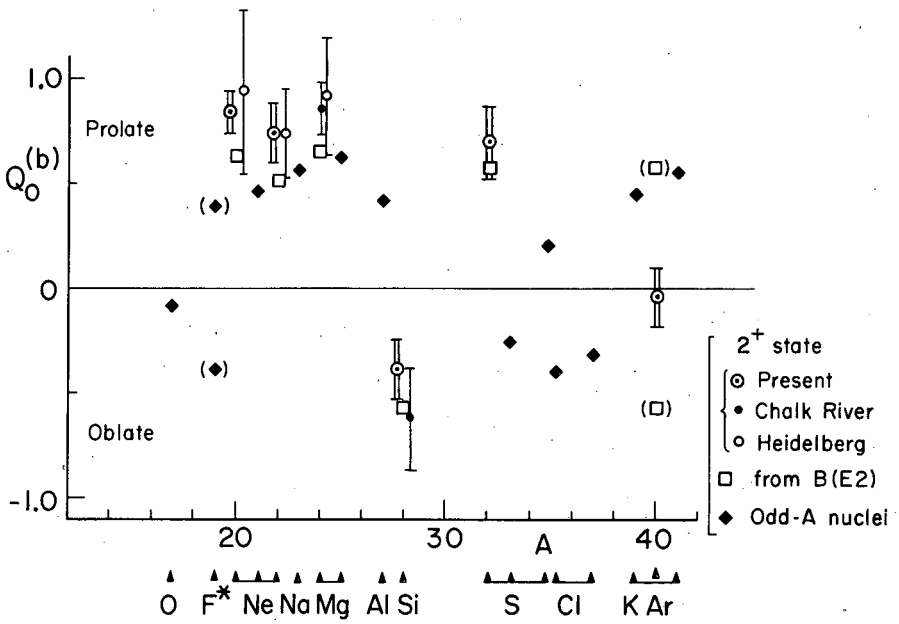

Fig. 2. Intrinsic quadrupole moments in s-d shell nuclei. The circles indicate the intrinsic moments of first-excited 2^+ states determined by this method (double circles), the method of the Chalk River group (closed circles), and that of the Heidelberg group (open circles). The squares indicate the values calculated from B(E2, $0^+ \rightarrow 2^+$). The intrinsic moments of odd-A nuclei [assuming K = I except for $^{19}F^*$(K = 1/2, I = 5/2)] are shown by the diamonds. (XBL701-2137)

STUDIES OF Mo AND Ru ISOTOPES WITH (α, xn) REACTIONS

J. M. Jaklevic, C. M. Lederer, and J. M. Hollander

Continuing a program of in-beam γ-ray spectroscopy at the 88-inch cyclotron, we have studied levels in nuclei produced by $(\alpha, xn\gamma)$ reactions on targets of separated Zr and Mo isotopes. Level schemes of ^{92}Mo and ^{94}Ru, as well as some preliminary results on ^{94,96,98}Mo and ^{96,98,100,102}Ru, have already been reported.[1-3] Of these latter nuclei, only ^{94}Mo was found to have an isomer with $t_{1/2} \gtrsim 3$ nsec.[3]

Recently we have used $\gamma\gamma$-coincidence measurements, employing two Ge(Li) spectrometers, in an effort to assign weaker transitions to the correct reaction products and to establish new levels. Some results for odd-mass ruthenium nuclei are given elsewhere.[4] Figures 1 and 2 show the level schemes of ^{96}Ru and ^{102}Ru as examples of these results. Usually, the placements of transitions were established from the coincidence measurements, and the isotopic assignments were made by observing the change of relative γ-ray intensities when the beam energy or target thickness was varied.

Spin and transition multipolarity assignments are based on measurements of angular distributions of the γ rays relative to the incident beam direction. Although these data alone do not determine spin uniquely, the interpretations are supported by observation of the occurrence or absence of crossover transitions, and also by the well-known general occurrence of stretched, downward transitions ($\Delta I = -\lambda$) following (α, xn) reactions. We feel, however, that caution must be used in the application of such spin-selection systematics to the weaker paths of de-excitation observed in these studies.

The analysis of similar results of ^{96,98}Mo and ^{98}Ru is in progress.

References

1. J. M. Jaklevic, C. M. Lederer, and J. M. Hollander, Phys. Letters 29B, 179 (1969); Nuclear Chemistry Annual Report, 1968, UCRL-18667, Jan. 1969 p. 12.
2. J. M. Jaklevic, C. M. Lederer, and J. M. Hollander, Nuclear Chemistry Annual Report, 1968 UCRL-1886, Jan. 1969, p. 15.
3. This report, An 86-Nanosecond Isomer in ^{94}Mo.
4. This report, Levels of ^{97,99,101}Ru Populated in (α, xn) Reactions.

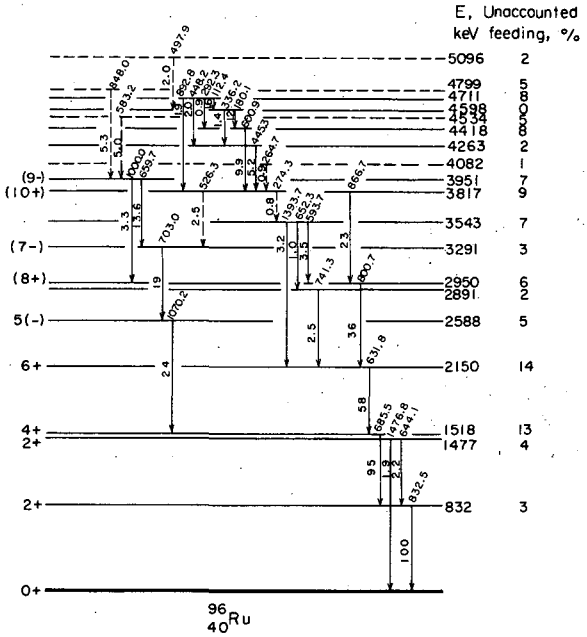

Fig. 1. Levels of ^{96}Ru populated in the ^{94}Mo(α, 2n) reaction. Relative intensities of the γ rays are shown on the transition arrows. (XBL702-2326)

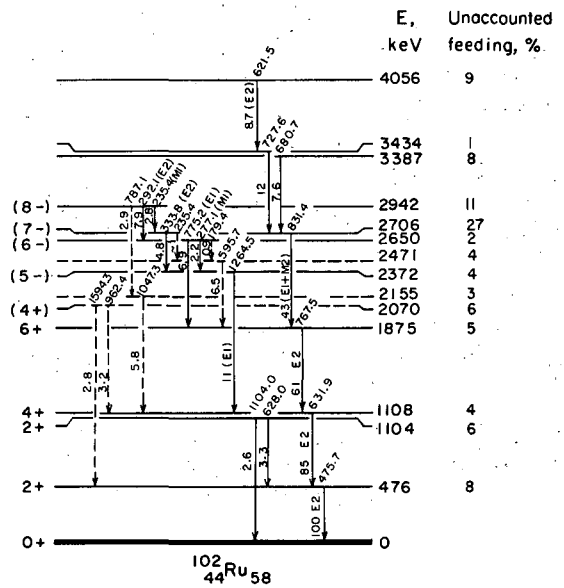

Fig. 2. Levels of ^{102}Ru populated in the ^{100}Mo (α, 2n) reaction. (XBL702-2327)

AN 86-NANOSECOND ISOMER IN ^{94}Mo

J. M. Jaklevic, C. M. Lederer, and J. M. Hollander

Levels of ^{94}Mo were studied in the reaction ^{92}Zr(α, 2nγ). Targets of separated ^{92}Zr were bombarded with 30-MeV α particles at the 88-inch cyclotron, and the resulting γ-ray spectra measured with Ge(Li) detectors, both during and between beam bursts.[1]

Gamma rays of 84, 449, 532, 702, 849, and 870 keV were observed to decay with a half-life of 86.5 ± 2.0 nsec. Of these, all but the 84- and 532-keV transitions have prompt components, indicating that these two transitions originate from the isomeric level. These data support the presence of a level in ^{94}Mo at 2953 keV with the above half-life, which decays as shown in Fig. 1. The cascade relationships were also confirmed by γ-γ coincidence measurements employing two Ge(Li) detectors.

The spin and parity of the isomeric state were deduced from the following considerations: Spins and parities of the levels at 870, 1572, and 2421 keV are well established by previous studies,[2] and these assignments are consistent with the angular distributions observed in our experiments. The 6+ state is fed directly from the isomer by the 532-keV transition, which has a partial half-life of 116 nsec. This value strongly suggests an M2 multipolarity and a corresponding transition probability of 0.10 single-particle unit (spu).[3] An E2 assignment would imply a strength of only 5×10^{-3} spu, which seems highly unlikely, and any other multipolarity can be virtually ruled out. The spin and parity of the isomer are thus 8-.

The 84-keV transition has a conversion coefficient $\alpha_T = 2.2 \pm 0.3$, which implies a pure E2 multipolarity and therefore a 6- assignment for the 2870-keV level. The partial lifetime for this transition corresponds to a strength of 0.21 spu.

It is interesting that all γ rays which follow decay of the isomer, except the 84-keV transition, are also observed in the EC + β^+ decay of ^{94}Tc.[4] However, in the ^{94}Tc decay study the 449- and 532-keV transitions were given different placements from energy sum considerations. It may nevertheless be worthwhile to search for both the 84-keV γ ray and a delayed component of the other transitions in the decay of ^{94}Tc.

The placement of most other transitions in the level scheme (Fig. 1) is derived from the coincidence measurements. Placement of the 292-, 306-, 365-, 484-, 598-, 911-, 941-, and 1052-keV γ rays above the isomeric level is supported by the observation of delayed γ-γ coincidences.

References

1. T. Yamazaki and G. T. Ewan, Phys. Letters 24B, 278 (1967).
2. C. M. Lederer, J. M. Hollander, and I. Perlman, Table of Isotopes (John Wiley & Sons, New York, 1967).
3. S. A. Moszkowski, in Alpha, Beta, and Gamma-ray Spectroscopy, ed. by K. Siegbahn (North Holland Publ. Co., Amsterdam, 1965), Ch. XV.
4. J. Barrette, A. Boutard, and S. Monaro, Can. J. Phys. 47, 995 (1969).

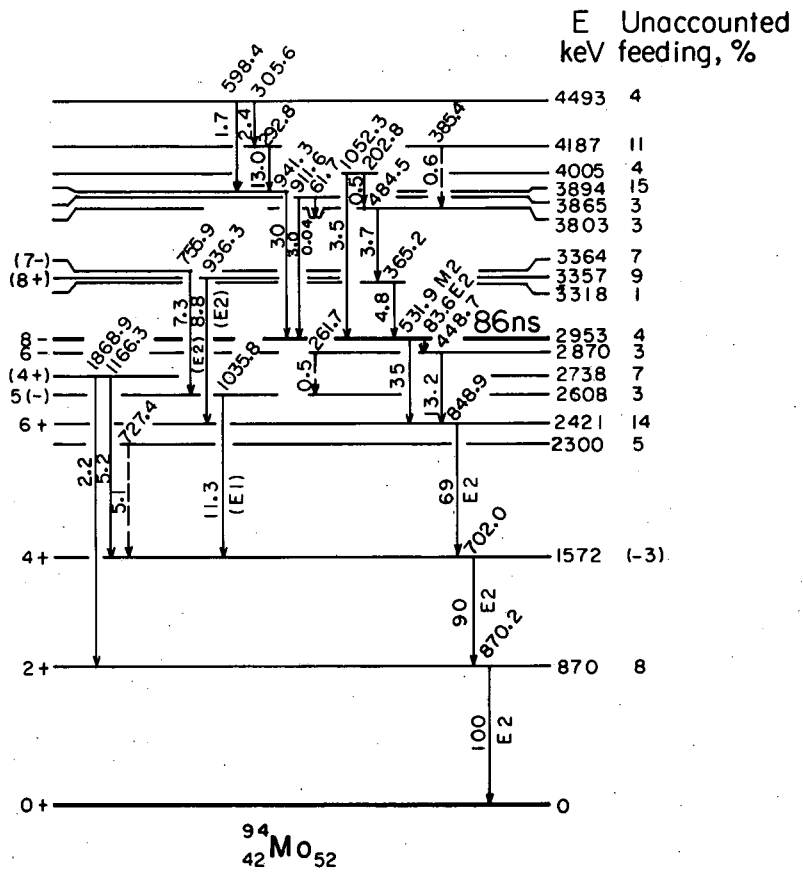

Fig. 1. Level scheme for ^{94}Mo. (XBL702-2387)

LEVELS OF ^{97,99,101}Ru POPULATED IN (α, xn) REACTIONS

C. M. Lederer, J. M. Jaklevic, and J. M. Hollander

Levels of odd-mass ruthenium isotopes were produced by the reactions ^{94}Mo(α, n)^{97}Ru, ^{98}Mo(α, 3n)^{99}Ru, and ^{100}Mo(α, 3n)^{101}Ru. Targets of separated Mo isotopes were irradiated with 30-MeV α particles in the 88-inch cyclotron, and the resulting γ rays were observed by techniques already described.[1] Assignment of the transitions to the appropriate Ru isotopes was made by observing the variation in γ-ray intensities relative to transitions in neighboring even-mass (α, 2n) products when the target thickness or beam energy was varied.

Level schemes are shown in Figs. 1 and 2. The spin assignments for most of the low-lying levels in ^{99}Ru and ^{101}Ru were derived or confirmed in recent Coulomb-excitation experiments.[2] Additional assignments have been made by us on the basis of angular distributions and decay patterns.

In ^{101}Ru we observe a strong cascade feeding the well-known 11/2- isomeric state:

$$2445(23/2-) \xrightarrow{(E2)} 1594(19/2-) \xrightarrow{(E2)} 959(15/2-) \xrightarrow{(E2)} 528(11/2-).$$

The energies and angular distributions of these transitions bear a strong resemblance to those of the dominant 6+ → 4+ → 2+ → 0+ cascade observed in the reaction ^{98}Mo(α, 2nγ)^{100}Ru (see Fig. 1). This suggests an interpretation of the 959-, 1594-, and 2445-keV states of ^{101}Ru as (maximum-spin) members of the multiplets formed from one- two-, and three-phonon excitations coupled to the $h_{11/2}$ neutron state.

By contrast, the Coulomb-excitation results on ^{101}Ru indicate that the low-lying positive-parity states are not well described by the weak coupling model as simple phonon excitations based on the ground state.[2] A possible explanation of this different is the likely dominance of the $(d_{5/2})^2_\nu$ 2+ configuration in the "phonon," which would result in positive-parity states whose character is intermediate between that of the weak coupling description and a multiparticle $(d_{5/2})^n_\nu$ configuration, subject to the exclusion principle. On the other hand, the $(h_{11/2})^2_\nu$ 2+, 4+. . . configurations are probably not a major component of the "phonon" structure, and thus the weak coupling model may be more appropriate to levels related to the 11/2- state.

A markedly different structure is seen in ^{97}Ru and ^{99}Ru (Fig. 2). Failure to observe an 11/2- isomer in either of these nuclei must indicate that it lies higher than in ^{101}Ru. In all three nuclei we observe some positive-parity states of higher spin (11/2+, 15/2+) which may possibly contain some characteristics of multiple-phonon states. However, the level populations and decay patterns are markedly different in the three cases. Other differences between the superficially similar structures of ^{99}Ru and ^{101}Ru have already been noted.[2] For example, the M1 transition 3/2+ → 5/2+ is 1000 times as fast in ^{101}Ru as in ^{99}Ru. We conclude that the structure of the states of these isotopes, particularly those of positive parity, is poorly understood, and further theoretical as well as experimental attention is required.

References

1. This report, Studies of Mo and Ru Isotopes With (α, xn) Reactions.
2. O. C. Kistner and A. Schwarzschild, Phys. Rev. 154, 1182 (1967).

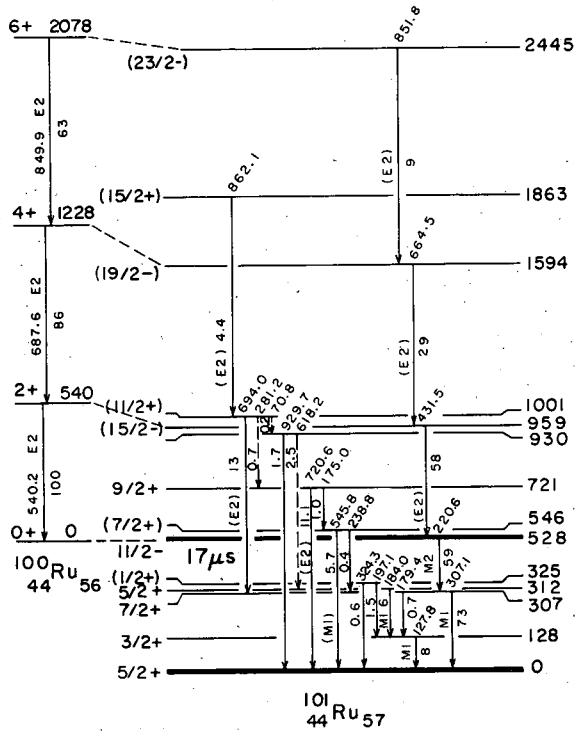

Fig. 1. Level structure of ^{101}Ru observed in the ^{100}Mo(α, 3n) reaction. Relative intensities of the transitions are indicated on the arrows. The dominant cascade observed in the reaction ^{98}Mo(α, 2n) is also shown for comparison. (XBL702-2324)

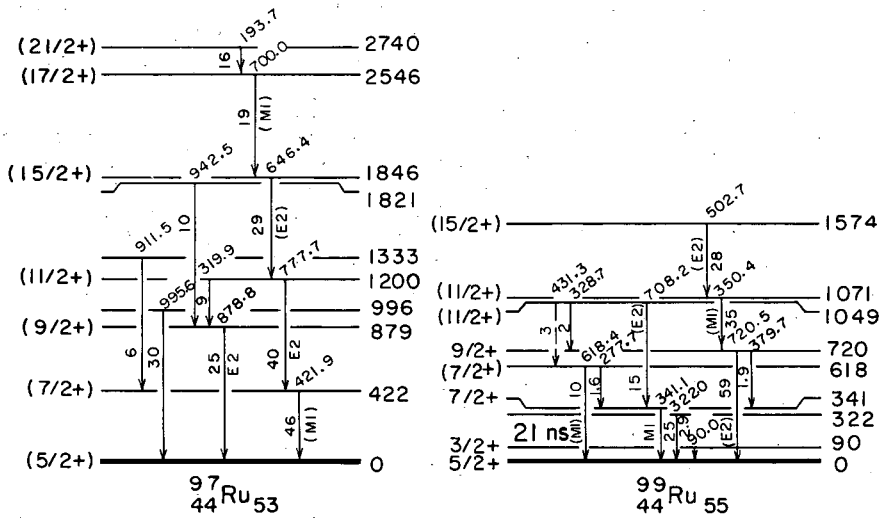

Fig. 2. Levels of ^{97}Ru and ^{99}Ru observed in the reactions ^{94}Mo(α, n) and ^{98}Mo(α, 3n). (XBL702-2323)

Nuclear Reactions and Scattering

RECOIL OF ^{48}Cr AND ^{49}Cr FROM $^{4}He + ^{46}Ti$ REACTIONS

M. K. Go and S. S. Markowitz

A thick-target method for nuclear recoil studies has been proposed.[1] We wish to extend that method for targets with thickness that is comparable to but less than the average range (R_0) of the recoiling nuclei.

By using a Gaussian distribution for the recoil nuclei, the recoiling behavior of any target thickness can be calculated. Figure 1 represents such a calculation for a 1-mg/cm^2 and a 200-μg/cm^2 target for an average recoil range of 300 μg/cm^2 in aluminum. From Fig. 1, we see that the relative amount of activity in equal catcher foils does not change whenever the target thickness is large compared with R_0. When the target thickness is less than R_0, the relative amount of activity in equal catcher foils not only depends on R_0 but also depends on the target thickness.

To test such a semi-thick-target method, we used TiO_2 targets and aluminum catcher foils. The TiO_2 used (enriched in ^{46}Ti), having the average atomic charge ($\bar{Z}$) 12.7 and the average mass per atom ($\bar{A}$) 26.2, can be considered to have the same stopping power as aluminum (A = 27, Z = 13).

The target is made by vacuum evaporation of ^{46}Ti-enriched TiO_2 onto 1-mil aluminum foils. The thickness is about 200 μg/cm^2 with good uniformity. Five to six aluminum foils (160 μg/cm^2) are stacked to form the catcher assembly. The target with aluminum degraders is bombarded with 45-MeV α particles in the 88-inch cyclotron at 1.5 μA for 10 to 30 min. After bombardment the target and catcher foils are counted with a Ge(Li) detector. The ^{48}Cr and ^{49}Cr activities are determined from the 0.116- and 0.09-MeV γ rays respectively. The relative amounts of activity in the catcher foils are determined and plotted on probability paper.[1] From these probability plots (Figs. 2 and 3), the experimental average range can be estimated.

With the compound-nucleus assumption, the recoil energy is given by[2]

$$E_r = \frac{A_p A_r}{(A_p + A_t)^2} E_p, \qquad (1)$$

where E and A are energy and mass number respectively. The subscripts r, p, and t refer to recoil, projectile, and target nucleus respectively. The average recoil ranges for different recoil energies are calculated by Steward[3] based on the theory of Lindhard et al.[4]

The actual α energy for the ^{48}Cr experiment is 27.8 MeV. Calculation with Eq. (1) and Steward's program gives a recoil range of 365 μg/cm^2 Al. From Fig. 2, the experimental range is estimated as 380 μg/cm^2 Al. For the ^{49}Cr experiment, the calculated range is 240 μg/cm^2 Al, whereas the recoil range from Fig. 3 is 250 μg/cm^2.

References

1. M. K. Go and S. S. Markowitz, Thick-Target Method for Nuclear Recoil Studies, in Nuclear Chemistry Annual Report, UCRL-18667, Jan. 1969, p. 29.
2. L. Winsberg and J. M. Alexander, Phys. Rev. 121, 518 (1961).
3. P. G. Steward, Stopping Power and Range for Any Nucleus in the Specific Energy Interval 0.01 to 500 MeV/amu in Any Nongaseous Material (Ph.D. Thesis), UCRL-18127, May 1968.
4. J. Lindhard, M. Scharff, and H. Schiøtt, Kgl. Danske Videnskab. Selskab Mat-Fys. Medd. 33, No. 14 (1963).

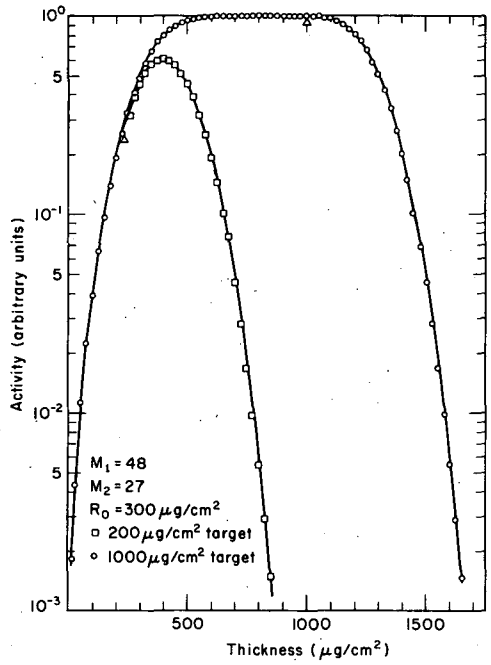

Fig. 1. Calculated distribution of recoil for targets of different thicknesses based on a stacking of thin (1 μg/cm^2) targets (Ref. 1). Target material and catcher foils are assumed to have equal stopping power for the recoiling nuclei. The triangles indicate the interferences of targets and catchers. (XBL 701-2032)

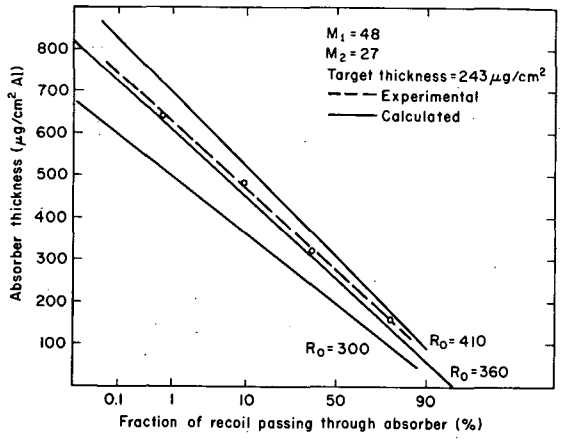

Fig. 2. Probability plot for ^{48}Cr recoil from ^{46}Ti(α, 2n)^{48}Cr. A straight line indicates Gaussian distribution. The experimental range is estimated to be 380 μg/cm^2 in aluminum. (XBL 701-2031)

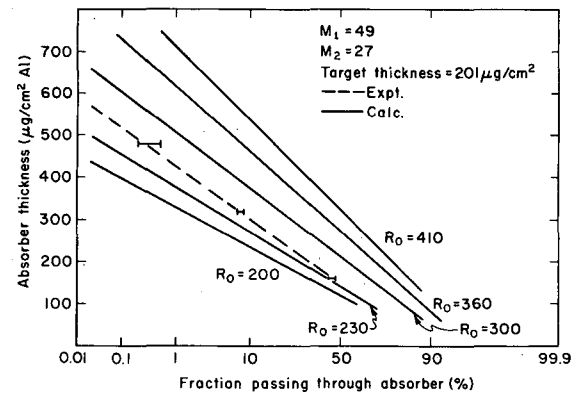

Fig. 3. Probability plot for ^{49}Cr recoil from ^{46}Ti(α, n)^{49}Cr. The large errors in experimental values are due to low counting rate. The experimental range is 250 μg/cm^2 Al. (XBL 701-2034)

COMPARISON OF EXCITATION FUNCTIONS FOR ^{48}Cr AND ^{48}V PRODUCTION FROM ^{3}He + ^{47}Ti AND ^{4}He + ^{46}Ti REACTIONS

M. K. Go and S. S. Markowitz

One of the main assumptions of the compound-statistical theory of nuclear reaction is that the decay of the compound nucleus is independent of the mode of its formation. Ghoshal[1] has verified this assumption with the ^{64}Zn* system.

When the projectile particle p fuses with the target nucleus t to form a compound nucleus C, the excitation energy (E*) of the compound system is

$$E^* = E_p - E_r + E_{BE} = E_p(A_p/A_c) + E_{BE}, \quad (1)$$

where E_p is the kinetic energy of the incident particle, E_r is the recoil energy of the compound nucleus, E_{BE} is the binding energy of particle p to the compound nucleus, A_p and A_c are the mass numbers of particle p and compound nucleus C.

If the independence postulate is correct, plots of the reaction cross sections versus excitation energy should be very similar for any one product from the same compound nucleus formed by different nuclear reactions. The difference in these excitation functions can be caused only by the difference in the formation of the compound nucleus.

We wish to test the independence postulate with the $^{50}Cr^*$ system. Titanium dioxide, enriched in either ^{46}Ti or ^{47}Ti, is vacuum evaporated onto thin (1.6 mg/cm^2) aluminum foils. The stacked target, with appropriate aluminum degrader foils, is bombarded at the 88-inch cyclotron with either ^3He or α particles. After bombardment the target foils are counted with a Ge(Li) γ-ray counter. The ^{48}Cr is determined from the 0.116-MeV γ ray. The ^{48}V is determined by using the 0.98-MeV γ ray and corrected for the decay from ^{48}Cr. $^{47}Ti(^3He, 2n)^{48}Cr$, $^{47}Ti(^3He, pn)^{48}V$, $^{46}Ti(\alpha, 2n)^{48}Cr$, and $^{46}Ti(\alpha, pn)^{48}V$ excitation functions are plotted in Fig. 1. Excitation energies are calculated from Eq. (1) and from the nuclear masses given by Harvey.[2] The growth and decay of ^{48}V are displayed in Fig. 2.

The excitation functions for ^{48}V are very similar. They have the same magnitude and peak at the same excitation energy. The ^3He excitation function above 40 MeV excitation energy may contain contributions from the $^{48}Ti(^3He, p2n)^{48}V$ reaction, since the target contains ^{48}Ti (16.5%). The agreement for the ^{48}Cr excitation functions is not so good. However, they do have the same shape and peak at the same excitation energy. If the $^{46}Ti(\alpha, 2n)^{48}Cr$ excitation function is multiplied by 0.8, the two excitation functions become almost identical.

References

1. S. N. Ghoshal, Phys. Rev. 80, 939 (1950).
2. B. G. Harvey, Introduction to Nuclear Physics and Chemistry (Prentice-Hall, Inc., Englewood Cliffs, New Jersey, 1962), p. 336.

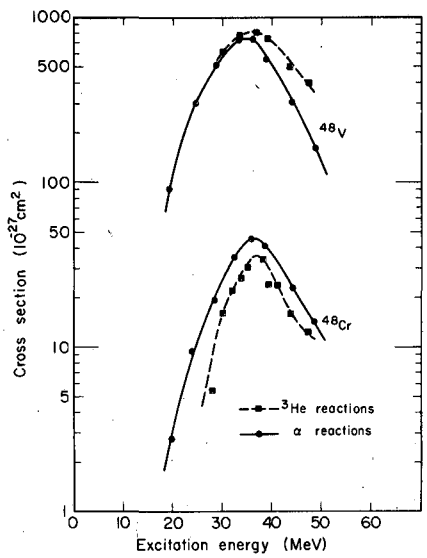

Fig. 1. Excitation functions for $^{46}Ti(\alpha, pn)^{48}V$, $^{46}Ti(\alpha, 2n)^{48}Cr$, $^{47}Ti(^3He, pn)^{48}V$, and $^{47}Ti(^3He, 2n)^{48}Cr$ reactions. The solid and dotted lines are drawn only to guide the eyes. (XBL 701-2147)

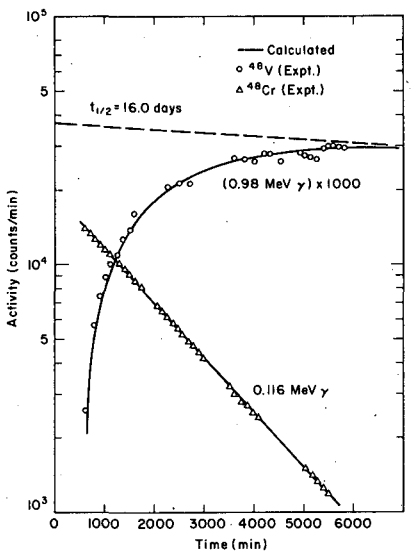

Fig. 2. Growth and decay of ^{48}V from the decay of ^{48}Cr. The solid lines are calculated from equations for simple and complex radioactive decay. The ^{48}V activity at later times (not shown) is extrapolated to t = 0 and is shown as the dotted line. (XBL 701-2033)

FRAGMENT PRODUCTION FROM THE INTERACTION OF 5.5-GeV PROTONS WITH URANIUM

Arthur M. Poskanzer, Gilbert W. Butler, and Earl K. Hyde

Fragments ejected from uranium targets inserted in the 5.5-GeV external proton beam of the Bevatron have been detected by a telescope of silicon semiconductor detectors incorporated in a power-law particle-identification system. Individual isotopes of the elements from hydrogen to carbon were resolved (see Fig. 1), and from nitrogen to argon the study was continued for the elements without isotopic separation. One counter telescope could cover only a limited energy region, so three sets of measurements were made with different telescopes in order to cover the entire energy spectrum above an instrumental cutoff. Some typical energy spectra showing curves derived from data taken at 90 deg to the proton beam are displayed in Fig. 2. Similar sets of data were taken at 20, 45, 135, and 160 deg. The energy spectra were extrapolated and integrated to obtain the angular distributions of the fragments, and the results are given in Fig. 3. The integration of these curves in turn resulted in the set of total cross sections for individual isotopes shown in Fig. 4.

This study has resulted in a detailed set of data on the energy and angular distribution characteristics of 21 nuclides from hydrogen to carbon. The data are being studied to obtain insight on the nature of nuclear reactions between GeV protons and complex nuclei. Many of the fragment characteristics are superficially like those expected from nuclear evaporation. The data are being examined to determine whether these fragments can be accounted for partially or completely as the products of evaporation during the second step of the cascade-evaporation mechanism conventionally used to describe high energy reactions.

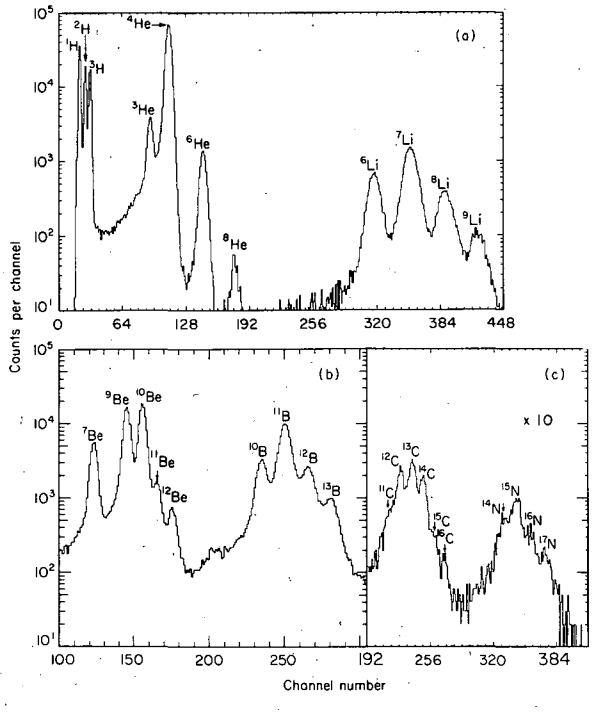

Fig. 1. Three typical particle spectra of fragments ejected from uranium targets. The detector telescope consisted of a 61μ ΔE detector an E detector, and a rejection detector. (XBL 6910-3939)

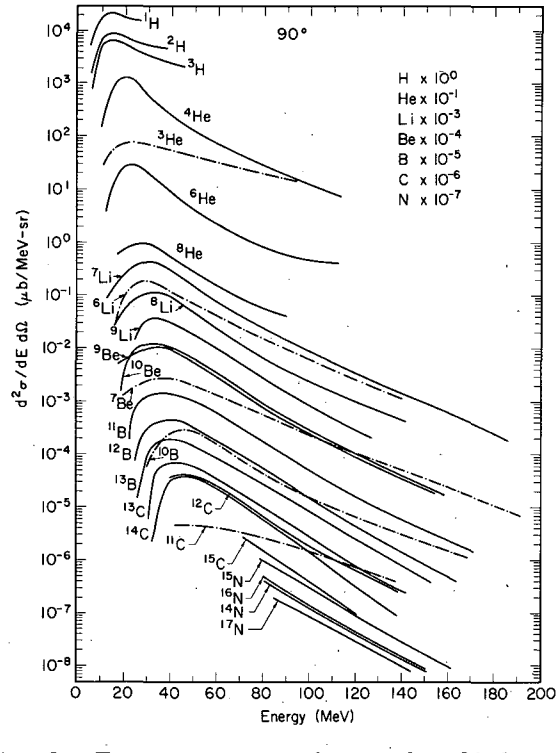

Fig. 2. Energy spectra observed at 90 deg to the beam for fragments ejected from uranium bombarded with 5.5-GeV protons. The curves for each element have been multiplied by a different factor which is indicated in the upper right part of the figure. (XBL 698-3385)

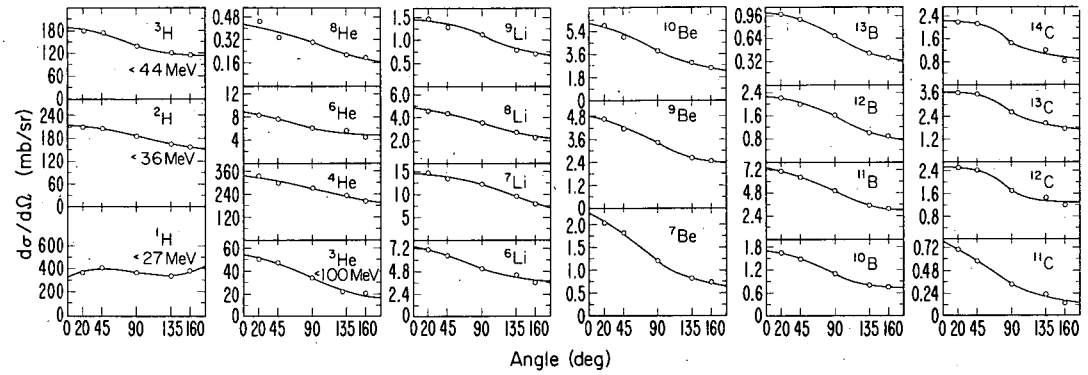

Fig. 3. Angular distributions of fragments ejected from uranium bombarded with 5.5-GeV protons. (XBL 698-3434)

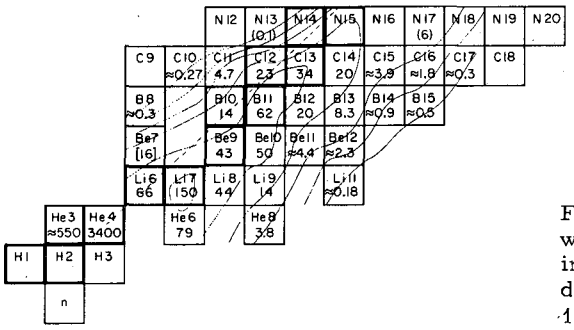

Fig. 4. A section of the chart of the nuclides with total production cross sections (expressed in mb) from uranium. The contour lines are drawn at yield levels of 0.3, 1, 3, 10, 30, and 100 mb. (XBL 698-3384A)

LIFETIME OF THE 3.19-MeV (6^+) STATE IN ^{42}Ca†

R. A. Mendelson and R. T. Carpenter *

The lifetime of the (6^+) 3.19-MeV state in ^{42}Ca has been measured by obtaining the time distribution of coincidences between positrons forming the state, from the decay of the (7^+) 615-keV state in ^{42}Sc, and 440-keV-decay γ rays. The metastable (61-sec) state in ^{42}Sc was generated by the ^{40}Ca(^{3}He, p)^{42}Sc reaction by use of a 6.10-MeV ^{3}He beam from the University of Iowa Van de Graaff. A 60-sec beam-on–off cycle was employed. Positrons were detected by a 2-in.-diam × 1-in.-high plastic scintillator, and γ rays by a 1-in. × 1-in. NaI(Tl) scintillator. Both scintillators were viewed by RCA-8575 photomultipliers whose dynodes were gated to avoid damage during the beam-on time. The value obtained for the mean lifetime was $(7.72 \pm 0.26) \times 10^{-9}$ sec, which corresponds to a $B(E2, 6_1^+ \rightarrow 4_1^+) = (6.40 \pm 0.22)\, e^2F^4$ (see Fig. 1).

The previously determined value[1] for the reduced-transition probability from the first excited state to the ground state is $B(E2, 2_1^+ \rightarrow 0_1^+) = (74 \pm 17)e^2F^4$. If all the states involved were pure j-j coupling shell-model states, the B(E2)'s would have a spin dependence of the form $(2J_f + 1)W^2(J_iJ_fjj, 2j)$, where J_i and J_f are the spins of the initial and final states and j is the spin of the orbital involved. Removing these factors from the reduced transition probabilities should give the same result for E2 transitions between any two states in the same configuration, whereas experimentally the $(6_1^+ \rightarrow 4_1^+)$ result is smaller than that for the $2_1^+ \rightarrow 0_1^+$ transition by a factor 5.3 ± 0.8. This indicates that the lower states have larger collective admixutres than the upper states.

This interpretation can be made more quantitative by comparing the experimental result with recent theoretical calculations by Gerace.[2] In this work, Gerace has found an upper limit to the

amplitude of the collective admixture in the 6^+ level at 3.19 MeV by extending the rotational band and assuming the interaction matrix element between the rotational 6^+ state and the $f_{7/2}{}^2 6^+$ state to be the same as between the corresponding 4^+ states, which was determined[3] by fitting the observed energy spectrum. In this way, Gerace obtains an upper limit for the collective amplitude of 0.2. He then calculates B(E2) values for the $6^+ \rightarrow 4^+$ transition and obtains 2.6, 7.0, and 14.0, all in e^2F^4, for amplitudes of 0, 0.1, and 0.2, respectively. For these results an effective charge of 0.5 e is assumed for the neutrons. It is seen that the experimental value of $(6.40 \pm 0.22)e^2F^4$ is explained exactly with a collective amplitude of about 0.1. Thus the present result is entirely consistent with the earlier picture of levels in the calcium isotopes that contain sizable collective admixtures.

Footnotes and References

†Condensed from Phys. Rev. 181, 1552-1555 (1969).
*University of Iowa, Iowa City, Iowa.

1. F. R. Metzger and G. K. Tandon, Phys. Rev. 148, 1733 (1966).
2. W. J. Gerace (private communication).
3. W. J. Gerace and A. M. Green, Nucl. Phys. A93, 110 (1967).

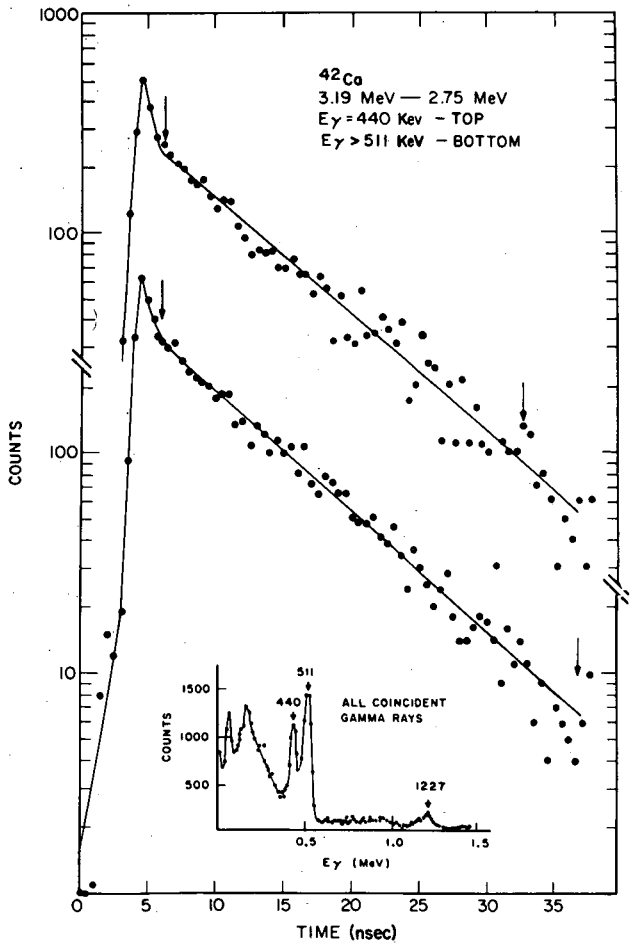

Fig. 1. Time distributions obtained for the decay of the (6^+) 3.19-MeV level in ^{42}Ca corresponding to indicated γ-ray energy intervals. (XBL 701-220)

THE STRUCTURE OF ^{16}O AND THE $^{17}O(p, d)^{16}O$ REACTION†

Robert Mendelson, J. C. Hardy, and Joseph Cerny

Recent shell-model calculations[1] have enjoyed considerable success in describing experimental properties of the oxygen isotopes ^{15}O, ^{16}O, and ^{17}O. Unlike previous structure calculations, both "collective" and "spherical" states were described in a unified, microscopic picture. By use of a spherical basis of $1d_{5/2}$, $1p_{1/2}$, and $2s_{1/2}$ orbitals, wave functions were calculated which reproduced the energy level schemes,[1] gave satisfactory values for electromagnetic transition rates,[1] and gave agreement with experimental single-nucleon stripping amplitudes.[2,3]

We have tested these wave functions, using the pickup reaction $^{17}O(p, d)^{16}O$. A 31-MeV proton beam from the 88-inch cyclotron was used to bombard oxygen gas enriched to 73% in ^{17}O. Particles were detected by using two (dE/dX)-E counter telescopes which fed Goulding-Landis identifiers. A detailed discussion of the experimental equipment has been presented elsewhere.[4]

Figure 1 shows a typical (p, d) spectrum. The resolution (FWHM) was 100 keV. The (6.05–6.13)-MeV doublet was determined at all angles to be dominated (i.e., >70%) by the 6.13-MeV state; this followed from consideration of the centroid positions and peak widths. No evidence of significant population of the 2^+, T = 0, 13.01-MeV or 1^-, T = 1, 13.08-MeV states was seen. Possible population of the 3^-, T = 0 state at 13.12 ± 0.010 MeV (Γ = 128 keV) was observed through the broadening of the high energy side of the 13.26-MeV state.

The (p, d) angular distributions were fitted with the distorted-wave Born approximations (DWBA) code DWUCK, using finite range correction and no cutoff on the radial integration. The shape of the predicted angular distributions was found to be sensitive to the deuteron parameters, so that parameter sets from several sources were used to obtain fits. (See Fig. 2.) A summary of our experimental spectroscopic factors (C^2S) and theoretical predictions using the complete shell-model wave functions obtained in Ref. 1 are presented in Table I.[5] Two prescriptions were used in calculating the Woods-Saxon form factors in the DWBA calculations: (i) the effective binding energy method (EBM), in which the bound-state well depth was determined by the binding energy of the $T_<$ state (for both $T_<$ and $T_>$ states), and (ii) the separation energy method (SEM), in which the well depth was dependent only on the binding energy of the final state. The experimental spectroscopic factors calculated by the EBM are shown in parentheses.

The agreement with theory is seen to be fair for the negative-parity states. However, a prominent feature of transitions to even-parity states is the large discrepancy between theory and experiment for the population of the 10.36-MeV state. The spectroscopic strength of this state is calculated to be 30% of that of the ground state, but is observed to be too weak by at least a factor of twenty. This is far outside the error attributable to the reaction theory, and represents a significant failure of the model. The theoretical spectroscopic strength for this "rotational" state is contributed to approximately equally by 2p-2h and 4p-4h terms, which overlap with a large 3p-2h and a smaller 5p-4h term (in ^{17}O), respectively. Since the transition should take place through major components in both initial and final wave functions, the disagreement indicates a gross inadequacy in the description of either or both wave functions.

The 2^- and (3^-) states at 15.22 and 15.42 MeV respectively were not seen in the $^{15}N(^3He, d)^{16}O$ and $^{14}N(\alpha, d)^{16}O$ reactions,[2,6] indicating that they do not contain significant $(1p_{1/2}^{-1}\ 1d_{5/2})$ amplitude; consequently these T = 0 states presumably contain some of the $(1p_{3/2}^{-1}\ 1d_{5/2})$ amplitude. The maximum strength for $1p_{1/2}$ pickup is 1.0 for $T_<$ states (and $T_>$ states), and 3.0 if we allow $1p_{1/2}$ and $1p_{3/2}$ pickup. The maximum experimentally observed strength for $\ell = 1$ T = 0 states is equal to 1.5, of which 0.5 comes from the presumed $1p_{3/2}$ strength. It thus appears that little of the total $1p_{3/2}$, T = 0 strength is expended below 18 MeV. The weak population of the 1^-, T = 0 state at 7.12 MeV is of particular interest, since it can be populated only by $1p_{3/2}$ pickup. Although the major components in the 2^-, 8.88-MeV and 3^-, 6.13-MeV states must be different from those in the 1^-, 7.12-MeV state, it is not expected that the 2^- and 3^- states should have significantly more $1p_{3/2}$ strength. Thus the population of the 7.12-MeV state sets a value on $(1p_{3/2}^{-1}\ 1d_{5/2})$ admixtures of $C^2S \approx 0.1$ for each state.

Thus, the weakness of $1p_{3/2}$ admixture, with its attendant high-lying strength, and the apparent high degree of concentration of the $1d_{3/2}$ strength (in the 12.53-MeV state)[5] suggests that the neglect of these orbitals in the shell-model calculation may not be responsible for the serious discrepancy found in the yield of the 4^+, 10.36-MeV state. It appears that the source of discrepancy may lie in the values of the matrix elements rather than in the approximations used. In fact, our data are consistent with less configuration mixing than the model indicates.

Footnote and References

†Condensed from UCRL-18950, submitted to Phys. Letters.

1. A. P. Zuker, B. Buck, and J. B. McGrory, Phys. Rev. Letters 21, 39 (1968).
2. H. W. Fulbright, J. A. Robbins, M. Blann, D. G. Fleming, and H. S. Plendl, Phys. Rev. 184, 1081 (1969).
3. W. Bohne, H. Homeyer, H. Lettau, H. Morgenstern, J. Scheer, and F. Sichelschmidt, Nucl. Phys. A128, 537 (1969).
4. G. W. Butler, J. Cerny, S. W. Cosper, and R. L. McGrath, Phys. Rev. 166, 1096 (1968).

5. We thank J. B. McGrory for calculating the spectroscopic factors, using the complete wave functions.

6. M. S. Zisman, E. A. McClatchie, and B. G. Harvey (Lawrence Radiation Laboratory), private communication.

Table I. Spectroscopic factors (C^2S) for major levels of interest in ^{16}O.

State (MeV)	J, T	Set I	Set III	Theory: ZBM (Ref. 1)
0.00	$0^+, 0$	0.985	1.00	0.88
6.05	$0^+, 0$	<0.16	<0.24	0.00014
6.13	$3^-, 0$	0.38–0.48	0.30–0.43	0.40
6.92	$2^+, 0$	<0.08	<0.07	0.028
7.12	$1^-, 0$	0.08	0.07	---
8.88	$2^-, 0$	0.36	0.27	0.26
9.85	$2^+, 0$	<0.004	<0.008	0.09[a]
10.36	$4^+, 0$	0.006 ±0.003	0.012 ±0.006	0.25
12.53	$2^-, 0$	<0.06	<0.04	---
12.97	$2^-, 1$	0.60–0.91 (0.20–0.32)	0.40–0.61 (0.13–0.20)	0.29
13 08	$1^-, 1$	<0.23 (<0.08)	<0.15 (<0.05)	---
13.12	$3^-, 0$	<0.36	<0.27	---
13.26	$3^-, 1$	0.54–0.90 (0.19–0.32)	0.37–0.64 (0.12–0.20)	0.39
15.22	$1^-, 0$	0.08 ±0.03	0.13 ±0.04	---
15.42	$(3^-), 0$	0.19 ±0.06	0.31 ±0.10	---

a. This spectroscopic strength may actually refer to the nearby 2^+ state at 11.53 MeV.

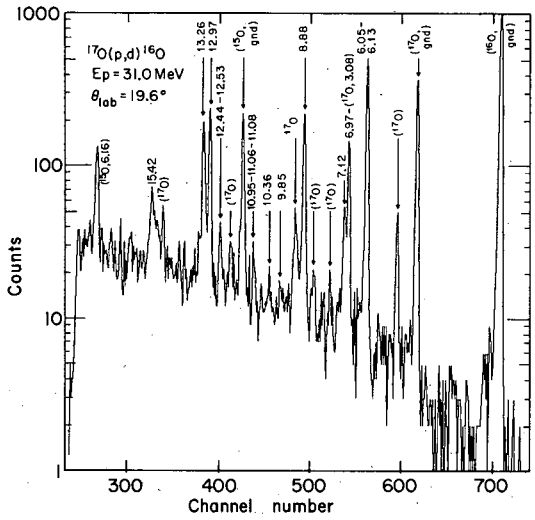

Fig. 1. A typical $^{17}O(p, d)^{16}O$ spectrum. (XBL 695-2761)

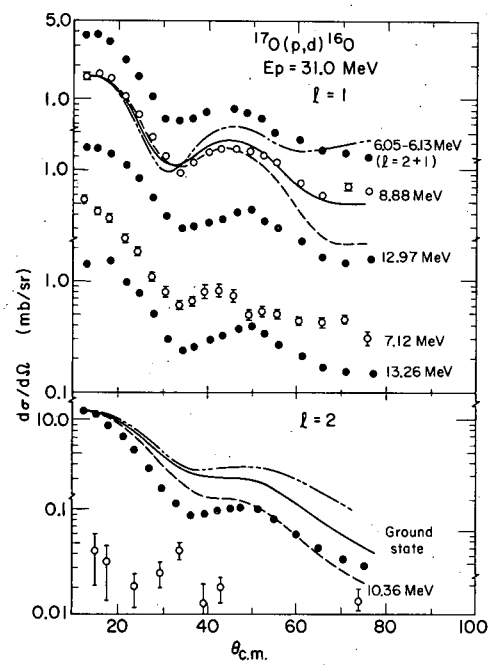

Fig. 2. Angular distributions and typical $\ell = 1$ and $\ell = 2$ DWBA fits. The dash-dot-dot line refers to Set I deuteron parameters, the solid line to Set II parameters, and the dashed line to Set III parameters. (XBL 695-2760)

THE NEW NUCLIDES ^{19}Na AND ^{23}Al OBSERVED VIA THE (p, ^{6}He) REACTION†

Joseph Cerny, R. A. Mendelson, Jr., G. J. Wozniak,
John E. Esterl, and J. C. Hardy

Although the masses and decay schemes of the A = 4n+1 series of T_Z = - 3/2 nuclei in the light elements are fairly well established, [1] almost nothing is known about the comparable 4n+3 nuclei. We have successfully utilized a new nuclear reaction tool--the (p, ^{6}He) reaction--capable of studying in general these 4n+3, T_Z = - 3/2 nuclei.

A 54.7-MeV proton beam from the 88-inch cyclotron was used to bombard thin targets of adenine ($C_5H_5N_5$), ^{24}Mg, and natural silicon. Figure 1 presents a diagram of one of the two similar counter-telescope and electronic systems which were simultaneously employed. Four silicon transmission detectors were used in each telescope. After a fast coincidence among the first three detectors restricted the origin of all allowed events to a single beam burst, two particle identifications (PI) were performed and compared, using the signals from the two successive differential-energy-loss detectors--denoted ΔE2 and ΔE1, respectively--and the third "E" detector. Any events traversing the first three counters were rejected by the fourth.

Even with the above electronics, pileup between events coincident within a single beam burst were found to create a substantial background (≈ 50 nb/sr at our typical counting rate) which interfered with reaction peaks (≈ 100 nb/sr). As a result, time-of-flight (TOF) measurements over the 51-cm flight path between the target and the ΔE2 counter have been added, and, in addition, a subnanosecond pileup-detection system (PUD) on the signal from the ΔE2 counter places a further requirement on each event. These improvements make feasible the study of highly endothermic nuclear reactions with cross sections as low as 10 nb/sr.

An outline of the added TOF and PUD electronics is also shown in Fig. 1. Signals from the (ΔE2) preamplifier were used in two ways. First, utilizing the leading edge of the pulse, they provided a start signal for the PUD system time-to-amplitude converter (TAC). Second, by clipping this tail pulse to form a bipolar pulse of 30 nsec total width, a timing signal was obtained from the zero-crossing point. This latter pulse provided the PUD stop pulse. Any deviation between the normal leading-edge time and the cross-over time was indicative of pileup.

The zero-crossing discriminator output was also used to start another TAC, which was stopped by a pulse derived from the arrival time of a beam burst in the fast Faraday cup shown in Fig. 1. The phase width provided by the cyclotron was restricted to about 6 deg (FWHM) by the use of internal collimators, and an overall time resolution of 1.4 nsec FWHM was measured.

Events in each system with acceptable identifications were sent via an analogue-to-digital converter multiplexer system to an on-line PDP-5 computer. Following the run, each ^{6}He event was analyzed in detail. The PUD was corrected for time walk of the leading-edge trigger, and mass information was obtained by calculating $E_T(TOF)^2$; the latter yielded an overall FWHM of 0.6 amu for mass 6. "Windows" were set on the PI, PUD, and mass data.

Figure 2 presents final energy spectra from the ^{12}C(p, ^{6}He)^{7}B, ^{14}N(p, ^{6}He)^{9}C, ^{24}Mg(p, ^{6}He)^{19}Na, and ^{28}Si(p, ^{6}He)^{23}Al reactions. The ^{14}N(p, ^{6}He)^{9}C data were used for calibration purposes. The spectra appear quite clean after the mass and pileup restrictions have been applied, with the slightly greater background at the higher energies in the silicon spectrum probably arising from reactions on ^{29}Si and ^{30}Si. If the adenine data were considered <u>without</u> these mass and pileup restrictions, for example, the energy region of interest would contain a continuous background of magnitude ≈ 1/3 the corrected ^{9}C ground-state peak extending from the ^{7}B ground state to ≈ 18 MeV, as well as scattered counts at higher energies.

The mass excess of ^{19}Na is determined to be 12.97 ± 0.070 MeV [^{12}C = 0]. Since the first excited state in the T = 3/2, $T_z = \frac{N-Z}{2}$ = 3/2 analogue nucleus ^{19}O lies at only 96 keV excitation (the next state is at 1.47 MeV) and since the mechanism of the (p, ^{6}He) reaction is uncertain, there is some ambiguity as to whether this mass excess applies to the ground state or to the first excited state of ^{19}Na (the experimental resolution was ≈ 200 keV), or both. We will take it to be the ground state, noting that in either event ^{19}Na is <u>proton unstable</u>; with this assumption, ^{19}Na is unbound to ^{18}Ne + p by 366 ± 70 keV.

The mass excess of ^{23}Al is determined to be 6.766 ± 0.080 MeV. Therefore, ^{23}Al is bound to ^{22}Mg + p by 146 ± 82 keV and is nucleon stable. It should be the lightest such isotope in the T_Z = - 3/2,

4n + 3 mass series, is expected to have half-life < 600 msec, and should emit β-delayed protons of ≈ 200 keV.

Both these nuclei complete isobaric quartets;[2,3] their masses have been predicted by the isobaric multiplet mass equation (IMME), as discussed in Ref. 1, and thus permit yet another check of its validity. Mass predictions for these nuclei from the IMME,[1] from a systematic study of Coulomb energies in the $1d_{5/2}$ shell,[3] and from the Kelson-Garvey nuclidic mass relationship[4] are given in Table I. Good agreement is to be seen among the various theoretical predictions and between them and experiment for both ^{19}Na and ^{23}Al.

Table I. Experimental and predicted mass excesses (in MeV ± keV).

Nuclide	Mass	Predictions		
		IMME	$d_{5/2}$ shell, Coulomb (Ref. 3)	Kelson-Garvey (Ref. 4)
^{19}Na	12.974 ± 70	12.90 ± 130	12.965 ± 25	12.87
^{23}Al	6.766 ± 80	6.684 ± 98	6.743 ± 25	6.71

Footnotes and References

†Condensed from Phys. Rev. Letters 22, 612 (1969).

1. J. Cerny, Ann. Rev. Nucl. Sci. 18, 27 (1968).
2. In fact, as is discussed in Refs. 1 and 3, the mass 19 isobaric multiplet for which three members are known comprises the first excited T = 3/2 states ($J^\pi = 3/2+$) in the T_Z = 3/2, 1/2, and -1/2 nuclei.
3. J. C. Hardy, H. Brunnader, J. Cerny, and J. Janecke, Phys. Rev. 183, 854 (1969).
4. I. Kelson and G. T. Garvey, Phys. Letters 23, 689 (1966).

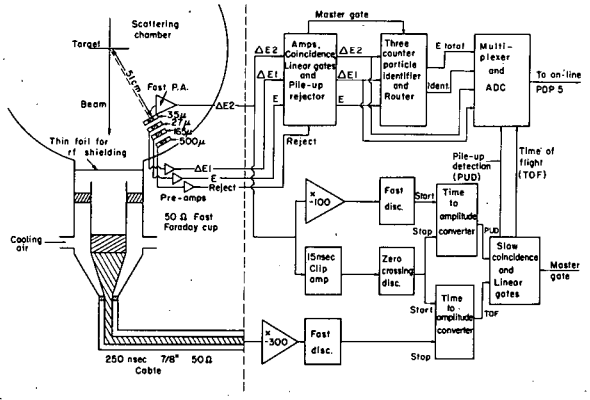

Fig. 1. An abbreviated diagram of the experimental layout and the electronic equipment for one of the two similar detection systems employed in these measurements. (XBL 691-1668)

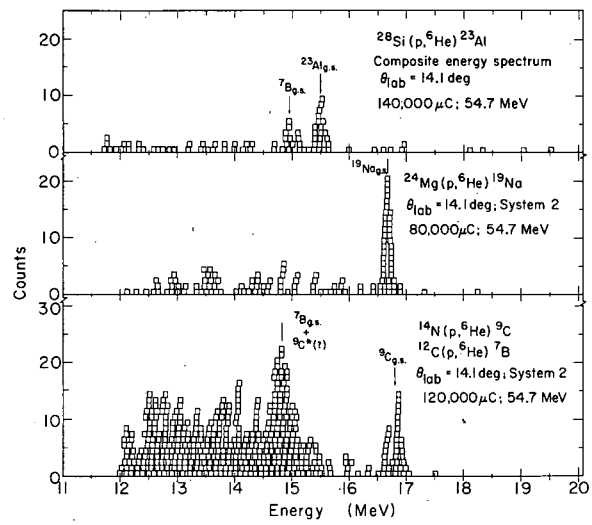

Fig. 2. The energy spectra from the (p, ^{6}He) reaction on adenine (bottom), ^{24}Mg (middle), and natural silicon (top). Data from detection system 2 only are shown for the first two targets; data from both systems are combined to produce the ^{28}Si(p, ^{6}He)^{23}Al spectrum. Each block is one count and the block width is 80 keV. Transitions to the first excited state of ^{9}C might be present, distorting the spectrum of the ^{7}B g. s. in the data from the adenine target. (XBL 691-1667)

A SIMPLE METHOD FOR INVESTIGATING THE PARENTAGE OF STATES USING TWO-NUCLEON TRANSFER REACTIONS†

J. C. Hardy, H. Brunnader,* and Joseph Cerny

The simultaneous observation of (p, t) and (p, ^{3}He) reactions on a target with isospin T_i has been used for some time to locate and identify analogue final states with isospin $T_f = T_i + 1$. The signature of a pair of such states is that the angular distributions of the corresponding tritons and ^{3}He particles have the same shape, and their magnitudes are related by a simple calculable factor. We have examined what is now a fairly large body of relevant experimental data, and used it as a means of establishing the validity of the approximations made in calculating the cross-section ratio. We have then used the same approximations to calculate ratios for analogue final states with $T_f = T_i$. In certain cases the same experimental techniques can be used not only to identify such states, but also to determine information regarding their structure. Experimental data presented on such states in sd-shell nuclei indicate a striking simplicity in their parentage. Evidently the experimental method described provides a new and useful spectroscopic tool for investigating the parentage of nuclear states.

When (p, t) and (p, ^{3}He) reactions on the same target produce analogue final states with $T_f = T_i + 1$, the ratio of their differential cross sections may then be written as

$$R \equiv \frac{\frac{d\sigma}{d\Omega}(p,t)}{\frac{d\sigma}{d\Omega}(p,{}^3\mathrm{He})} = \frac{k_t}{k_{^3\mathrm{He}}} \times \frac{2}{(2T_f-1)} \times \left\{ \frac{\sum_\Lambda^{LJ} \left| \sum^{N\rho_1\rho_2} A_{NLJ} \left[\Omega_n B_\Lambda^{LN} \right]_{(p,t)} \right|^2}{\sum_\Lambda^{LJ} \left| \sum^{N\rho_1\rho_2} A_{NLJ} \left[\Omega_n B_\Lambda^{LN} \right]_{(p,{}^3\mathrm{He})} \right|^2} \right\}, \quad (1)$$

where Ω_n is the overlap of the relative motion of the transferred particles as they appear in the target with their relative motion in the triton (or ^{3}He particle); and B_Λ^{LN} contains the distorted waves and the form factor of the transferred nucleons. The numerator and denominator of the bracketed factor on the right-hand side of Eq. (1) differ principally inasmuch as the mass-3 wave functions and the reaction Q values are different. The effects of both can be estimated to be $\lesssim 7\%$ for $A \leq 60$ and Ep = 45 MeV. Thus, to a good approximation, the bracketed factor may be assumed equal to unity.

Experimental cross-section ratios ($15 \text{ deg} \lesssim \theta_{cm} \lesssim 45 \text{ deg}$) to such analogue states for a number of nuclei with $14 \leq A \leq 40$ (and $1 \leq T_f \leq 3$) are listed in Table I together with the values of R calculated from the first two factors in Eq. (1). The agreement is uniformly excellent, and justifies neglecting the third factor in that equation.

What has not been recognized previously is that by making the same approximations for any 0^+ target a simple result can also be derived for the cross-section ratios corresponding to certain analogue final states with $T_f = T_i$. Then, only transitions to natural-parity levels [$\pi = (-)^J$] should be excited in both (p, t) and (p, ^{3}He) reactions, and each would be characterized by a single L value, namely that for which L = J. The angular distributions should be identical in shape and their relative magnitudes should acquire a maximum value [$R = (k_t/k_{^3\mathrm{He}})(2T_f)$] when the wave function of the final state differs from that of the target ground state by the removal of paired nucleons. This follows from the same approximation as was used to reduce Eq. (1). It should be emphasized that in principle any number of shells can be involved, and that there is no restriction on the complexity of the wave functions of the initial and final states. These transitions can be discerned, since any unpaired particles involved in the transfer would reduce the magnitude ratio.

To provide a preliminary experimental investigation of this theory, we have examined the (p, t) and (p, ^{3}He) reactions on the even-even T = 1 targets ^{22}Ne, ^{26}Mg, ^{30}Si, ^{34}S, and ^{38}Ar. The experiments were carried out using the external 45.0-MeV proton beam of the 88-inch cyclotron. Reaction products were detected and identified by using a solid-state counter telescope; spectra of tritons and ^{3}He particles were recorded simultaneously. The apparatus is described in detail elsewhere.[1] Angular distributions were extracted for all statistically significant peaks whose energies might correspond to pairs of T = 1 final states; if the angular distributions for two of these states had the same shape, then they were positively identified as being T = 1 analogues. A list of such states covering all targets investigated is given in Table II together with cross-section ratios extracted from the data and calculated values for the cross-section ratios, assuming the

Table I. Experimental and calculated relative cross sections $\frac{d\sigma}{d\Omega}(p,t)/\frac{d\sigma}{d\Omega}(p,{}^3He)$ for states with $T_f = T_i + 1$.

Final states J^π, T_f	Allowed L-values(s)	Target nucleus	Cross-section ratio R(exp)	R(calc)
$0^+, 1$	0	^{16}O	2.19±0.22	1.88
$0^+, 1$	0	^{36}Ar	1.92±0.19	1.80
$2^+, 1$	2	^{36}Ar	1.54±0.20	1.78
$3/2^+, 3/2$	0, 2	^{21}Ne	1.05±0.10	0.93
$5/2^+, 3/2$	0, 2, 4	^{25}Mg	0.85±0.09	0.92
$5/2^+, 3/2$	0, 2, 4	^{27}Al	0.89±0.09	0.90
$5/2^+, 3/2$	2	^{31}p	0.71±0.11	0.88
$0^+, 2$	0	^{22}Ne	0.70±0.09	0.62
$0^+, 2$	0	^{26}Mg	0.61±0.06	0.61
$0^+, 2$	0	^{30}Si	0.54±0.10	0.60
$0^+, 2$	0	^{34}S	0.66±0.06	0.60
$0^+, 2$	0	^{38}Ar	0.62±0.07	0.60
$0^+, 2$	0	^{42}Ca	0.60±0.05	0.60
$0^+, 3$	0	^{40}Ar	0.36±0.04	0.35

picked-up nucleons are "paired." Those cases for which the experimental ratio is significantly less than the calculated one must involve some "unpaired" pickup; then the calculated ratio in the table is bracketed. The two pairs of 0^+ levels, which could be produced only by paired pickup, do indeed show the maximum ratio, and the (3^-) levels, which could not involve paired pickup, give a reduced value as expected.

The most striking result, however, appears in the top half of the table. Here, three transitions are indicated as being dominated by the transfer of paired nucleons. These transitions are just the ones which would have been predicted from the simplest shell model interpretation as being $j^n \rightarrow j^{n-2}$; the remaining transitions would have been predicted as crossing subshells with unpaired transfer. There can be no doubt that the wave functions of the states involved in these reactions are vastly more complex than is indicated by such a simple model, so it is therefore interesting that at least in the case of paired transfer the parentage remains simple.

Footnotes and References

†Condensed from Phys. Rev. Letters 22, 1439 (1969).
*Present address: McMaster University, Hamilton, Ontario, Canada.

1. J. C. Hardy, H. Brunnader, J. Cerny, and J. Jänecke, Phys. Rev. 183, 854 (1969).

Table II. Experimental and calculated relative cross sections $\frac{d\sigma}{d\Omega}(p,t)/\frac{d\sigma}{d\Omega}(p,{}^3He)$ for states with $T_f = T_i$.

Final states Nucleus	E_x	J^π, T	Target nucleus	Cross-section ratio R(exp)	$R(j^2; calc)$
^{20}Ne ^{20}F	10.275 g.s.	$2^+, 1$	^{22}Ne	2.00±0.20	1.88
^{24}Mg ^{24}Na	9.517 g.s.	$4^+, 1$	^{26}Mg	2.50±0.30	1.86
^{28}Si ^{28}Al	9.379 0.031	$2^+, 1$	^{30}Si	1.15±0.10[a]	[1.84]
^{32}S ^{32}P	7.005 0.078	$2^+, 1$	^{34}S	1.20±0.30	[1.82]
^{36}Ar ^{36}Cl	6.612 g.s.	$2^+, 1$	^{38}Ar	1.90±0.20	1.81

(continued)

Table II. (continued)

Final states			Target nucleus	Cross-section ratio	
Nucleus	E_x	J^π, T		R(exp)	$R(j^2; calc)$
^{20}Ne ^{20}F	12.25 ± 0.03 1.851	} $(3^-), 1^b$	^{22}Ne	1.40 ± 0.15	c
^{28}Si ^{28}Al	10.70 ± 0.03 1.35 ± 0.03	} $0^+, 1^{b,d}$	^{30}Si	1.85 ± 0.20	1.84
^{28}Si ^{28}Al	10.909 1.633	} $(2^+), 1^b$	^{30}Si	1.80 ± 0.20	1.83
^{36}Ar ^{36}Cl	8.55 ± 0.03 1.949	} $2^+, 1$	^{38}Ar	1.45 ± 0.20	[1.81]
^{36}Ar ^{36}Cl	9.70 ± 0.03 3.12 ± 0.10	} $0^+, 1^b$	^{38}Ar	2.20 ± 0.70	1.80

a. The ground state of ^{28}Al was not resolved from its 2^+ state, so the quoted experimental ratio is a lower limit. For various reasons (e.g., pure L = 2 angular distribution) it seems unlikely that this ratio will approach the "paired" value.
b. These spin-parities were determined from this work by fitting experimental angular distributions with DWBA calculations.
c. As a simple example of an "unpaired" ratio for this transition, pickup from the $p_{1/2}$ and $d_{5/2}$ shells yields a value for R of 1.30.
d. A level is known in ^{28}Al at 1.372 MeV which is certainly 1^+; the strong 0^+ observed by us presumably indicates the presence of a doublet.

^{34}Ar AND T = 1 STATES IN ^{34}Cl FROM TWO-NUCLEON PICKUP REACTIONS†

H. Brunnader,* J. C. Hardy, and Joseph Cerny

Two-nucleon transfer reactions are characterized by selection rules which restrict the spin S and isospin T as well as the parity change $\Delta\pi$ which can be transferred during a reaction.[1,2] The most rigorous of these selection rules is that S + T = 1. For the (p, t) reaction the transferred particles are both neutrons and require T = 1 (and consequently S = 0); for (d, α), the zero isospin of the deuteron and α particle require T = 0 (and S = 1). A somewhat weaker selection rule is that $\Delta\pi = (-)^L$, where L is the total orbital angular momentum transferred by the reaction. Thus for the (p, t) reaction on 0^+ targets only those final states which have natural parity–i.e., $\pi_f = (-)^{J_f}$–can be produced. We have used these selection rules and by combining the results of the reactions (p, t), (p, ^{3}He), and (d, α) have determined spins and isospins of states in ^{34}Ar and ^{34}Cl.

Since the target nucleus ^{36}Ar has isospin $T_i = 0$, the differential cross sections for the (p, t) and (p, ^{3}He) reactions leading to analogue final states (in ^{34}Ar and ^{34}Cl) with isospin $T_f = 1$ must both proceed by S = 0, T = 1 transfer, and hence should have the same shape, the ratio of their magnitudes being given by $R = 2k_t/k_{^3He}$. Thus by comparing the angular distributions corresponding to states which, because of their excitation energies, are suspected of being analogues, it should be possible to uniquely determine the $T_f = 1$ final states. This is complicated in practice by the fact that the (p, ^{3}He) reaction can produce both $T_f = 0$ and $T_f = 1$ states in ^{34}Cl; consequently, where the possibility of unresolved doublets is significant, some ambiguity can arise. By use of the (d, α) reaction, which can produce only $T_f = 0$ states, this ambiguity can generally be resolved.

The experiments were carried out using the external 45-MeV proton and deuteron beams from the 88-inch cyclotron. The reaction products were detected by using two independent counter telescopes on opposite sides of the beam. Signals from each telescope were fed into a Goulding-Landis

particle identifier, and the total energy signal was routed according to particle type into one of the 1024-channel segments of a 4096-channel analyzer. An ^{16}O impurity in the ^{36}Ar-enriched (99.6%) target gas provided continuous energy calibration, and a carbon dioxide target, run immediately before and after the argon, established the exact energy scale.

The results on ^{34}Cl and ^{34}Ar are summarized in Fig. 1, where all J^{π}, T assigments (except the ground states and the 0.146-MeV level in ^{34}Cl) are entirely due to this work. The J^{π} values for ^{34}Ar levels were determined by comparing the results of DWBA calculations[4] with the experimental angular distributions. Several such experimental distributions are shown on the left side of Fig. 2. On the right side of the same figure are shown the (p, ^{3}He) angular distributions corresponding to their suspected T = 1 analogues in ^{34}Cl; the latter have been multiplied by $(2k_t/k_{^3He})$ to facilitate comparison. In this case, the dashed curves are not the results of calculations; their shapes were determined as providing the best fit to the triton data. The same curves, but renormalized, were then drawn through the corresponding (p, ^{3}He) angular distributions. Thus, if two states are analogues, the dashed curve should fit the (p, ^{3}He) data, and the magnitudes of the distributions as they appear in the figure should be the same. With the exception of the ^{34}Ar 3.30-MeV and ^{34}Cl 3.35-MeV states, the experimental and calculated ratios agree, and on this basis it is possible to assign $T_f = 1$ to the ground, 2.16-MeV, 3.94-MeV, and 4.67-MeV states of ^{34}Cl; the assignments are confirmed by the fact that none of these states is produced in the (d, α) reaction. Of course, once it is established that they are analogues, their spin-parities follow from the calculations already described for the (p, t) reaction.

Based on the intensity of the (p, t) reaction to the state in ^{34}Ar at 3.30 MeV, a $T_f = 1$ state should be observed in ^{34}Cl at approximately the same energy, but the peak observed at this energy with the (p, ^{3}He) reaction was produced too strongly. Furthermore, the same peak appears in the ^{36}Ar(d, α)^{34}Cl spectrum, for which $T_f = 1$ final states are forbidden. Thus an unresolved doublet of states must be involved: one is the 2+, $T_f = 1$ analogue to the 3.30-MeV level in ^{34}Ar; the other has $T_f = 0$. The peaks observed at 4.97 and 6.16 MeV in ^{34}Cl can also be shown, by similar arguments, to be $T_f = 0$ and 1 doublets.

Enough T = 1 states in ^{34}Cl have been identified as a result of this work that it is possible to examine the variation of Coulomb displacement energies over a greater range of excitation energies and configurations than is normally possible. In Fig. 1 the energy shifts for excited 0+ states are significantly less than those between 2^+ or 3^- states, and the energy shifts between states in the pair ^{34}Cl-^{34}S are in general less than those between the same states in the pair ^{34}Ar-^{34}Cl. These effects are both manifestations of the so-called Coulomb pairing energy and can be explained as the result of increased Coulomb energy due to the physical proximity of protons that are paired in a seniority-zero configuration. The observed effects can be described quite well by assuming simple configurations for which expressions have been derived[5] giving Coulomb displacement energies between states both with seniority zero and two. The agreement reflects the fact that the Coulomb force has a long range and consequently is relatively insensitive to details of the nuclear configurations.

Footnotes and References

†Condensed from Nuclear Physics A137, 487 (1969).
*Present address: McMaster University, Hamilton, Ontario, Canada.
1. N. K. Glendenning, Phys. Rev. 137, B102 (1965).
2. I. S. Towner and J. C. Hardy, Advan. Phys. 18, 401 (1969).
3. P. W. M. Glaudemans, G. Wiechers, and P. J. Brussaard, Nucl. Phys. 56, 529 and 548 (1964).
4. These calculations used the program DWUCK, written by D. Kuntz, whom we thank for making it available. A modification to take account of two-nucleon transfer reactions was made by us and follows the "zero range interaction" approximation (Ref. 1).
5. K. T. Hecht, Nucl. Phys. A102, 11 (1967); J. C. Hardy, H. Brunnader, J. Cerny, and J. Jänecke, Phys. Rev. 183, 854 (1969).

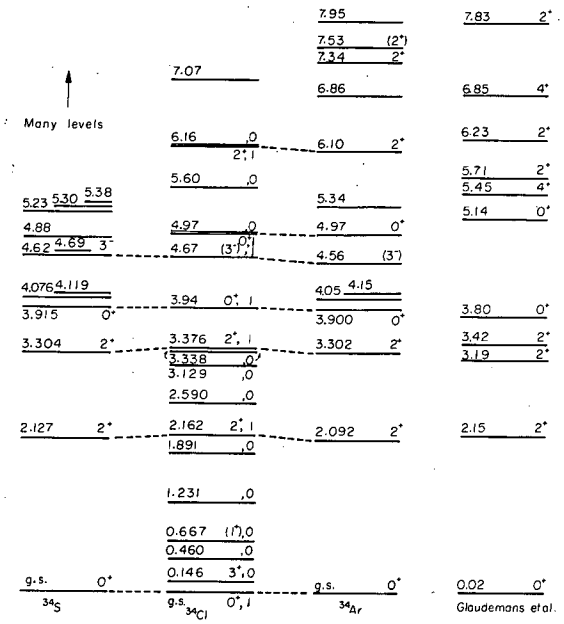

Fig. 1. Energy levels of the known mass-34 states. The ground states of ^{34}S and ^{34}Ar are normalized to the same energy as the ground state of ^{34}Cl. Some known levels in ^{34}S and ^{34}Cl at higher excitations that were not observed in these experiments have been deleted. Those doublets in ^{34}Cl marked with one energy and two (J^{π}, T) values were unresolved. At the right of the figure is shown the calculated spectrum (Ref. 3) of natural parity T = 1 states in mass 34. (XBL 692-2834)

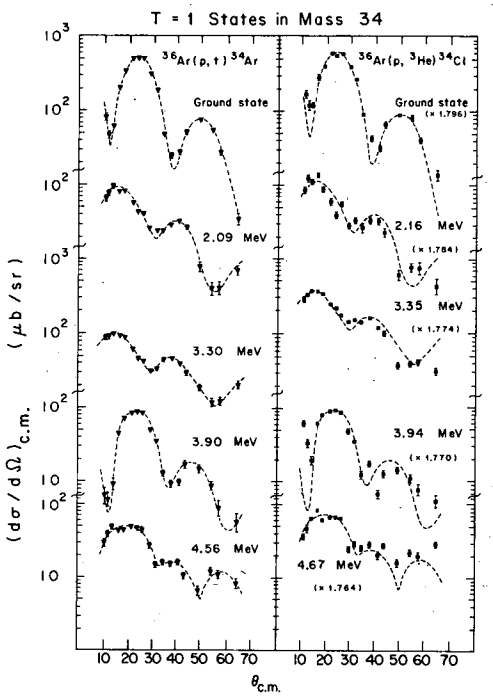

Fig. 2. Angular distributions for the reactions $^{36}Ar(p,t)^{34}Ar$ and $^{36}Ar(p,{}^{3}He)^{34}Cl$ leading to analogue T = 1 final states. The ^{3}He data points have been multiplied by $(2k_t/k_{^3He})$. (XBL 6810-7032A)

T = 2 AND T = 3 ANALOGUE STATES, $28 \leq A \leq 40$[†]

J. C. Hardy, H. Brunnader,[*] and Joseph Cerny

The advent of new experimental techniques for measuring the masses of neutron-deficient nuclei has led to recent interest in investigating the limits of stability in the lighter nuclides. As an aid to such measurements, accurate mass predictions are of great value, and for this purpose the isobaric-multiplet mass equation (IMME) is frequently used:

$$M(A, T, T_z) = a(A, T) + b(A, T)\, T_z + c(A, T)\, T_z^2 . \qquad (1)$$

To predict the mass of a particular state it is necessary to know the masses of three other members of the same multiplet, since the coefficients a, b, and c must be experimentally determined for each value of A and T. The masses of all $T_z = +2$ (A = 4n) nuclei are known to within less than ±10 keV in the region $28 \leq A \leq 40$ and consequently, for each value of A, measurement of the excitation energies of T = 2 analogue states in two other isobars permits use of the IMME for relatively accurate predictions of other members of the multiplet. Similarly, the measurement of two T = 3 states in mass 38 combined with the less accurately known mass (±150 keV) of ^{38}S yields rough predictions for that multiplet.

We have located and identified the lowest-energy (0^+), T = 2 states in ^{28}Al, ^{28}Si, ^{32}P, ^{32}S, ^{36}Cl, ^{36}Ar, ^{40}K, and ^{40}Ca, as well as the T = 3 states in ^{38}Cl and ^{38}Ar. The method used was to simultaneously observe the (p, t) and (p, ^{3}He) reactions. If the target nucleus has isospin T_i and

the reactions produce analogue final states with $T_f = T_i + 1$, then their angular distributions have the same shape and the ratio of their differential cross sections is given by $(k_t/k_{^3He}) \times 2/(2T_f - 1)$. This provides an unambiguous experimental method for identifying high-isospin analogue states.

The measurements were carried out using the 45-MeV proton beam from the 88-inch cyclotron. Both solid and gas targets were used, the reaction products being detected by using two independent counter telescopes mounted on opposite sides of the beam. The signals from each telescope were fed into a Goulding-Landis particle identifier, and the total-energy signal was routed according to particle type into the 1024-channel segments of a 4096-channel analyzer. Sample triton and ^{3}He spectra are shown in Fig. 1.

The excitation energies of observed states were determined by analyzing the data with the computer program LORNA.[1] This program corrects the energies of incoming and outgoing particles for kinematic effects and absorber losses, then determines the energies of unknown peaks, using an energy scale established from a least-squares fit to peaks whose Q values are known. For the experiments described here, contaminants were already present or introduced in the targets to provide calibration. The most useful calibration reactions[2] were $^{12}C(p,t)^{10}C$ and $^{12}C(p,{}^3He)^{10}B$. The results are listed in Table I.

Table I. Summary of experimental results for high T states.

Nucleus	Analogue state	Excitation energy: This work (MeV ± keV)	Other work (MeV ± keV)	Average (MeV ± keV)
^{28}Al	0^+; 2	5.983 ± 25	---	[5.983 ± 25]
^{28}Si	0^+; 2	15.206 ± 25	15.221 ± 5	15.221 ± 5
^{32}P	0^+; 2	5.071 ± 40	---	[5.071 ± 40]
^{32}S	0^+; 2	12.034 ± 40	11.984 ± 4	11.984 ± 4
^{36}Cl	0^+; 2	4.295 ± 30	4.333 ± 25	4.316 ± 19
^{36}Ar	0^+; 2	10.858 ± 35	---	[10.858 ± 35]
^{38}Cl	0^+; 3	8.216 ± 25	---	[8.216 ± 25]
^{38}Ar	0^+; 3	18.784 ± 30	---	[18.784 ± 30]
^{40}K	0^+; 2	4.375 ± 25	4.370 ± 70	4.374 ± 24
^{40}Ca	0^+; 2	11.978 ± 25	11.970 ± 25	11.977 ± 23

Table II. Predicted mass excesses of unmeasured neutron-deficient nuclei.

Nucleus	T_z	Estimated mass from IMME (MeV ± keV)	Kelson-Garvey mass predictions (MeV)
^{28}S	-2	4.31 ± 200	4.44
^{32}Ar	-2	-2.59 ± 320	-2.28
^{36}Ca	-2	-6.58 ± 210	-6.48
^{38}Sc	-2	-4.55 ± 1020	-4.70
^{38}Ti	-3	11.08 ± 1680	10.82
^{40}Ti	-2	-9.07 ± 265	-9.07

The J^π values shown in the table were determined by comparing the results of DWBA calculations[3] with the experimental angular distributions. In addition we investigated the strength of the (p, t) reaction leading to each analogue state (with $T_> = |T_z| + 2$) compared with the strength of the reaction to the ground state (which has $T_< = |T_z|$) of the same final nucleus. The comparison between the experimental results and calculations which assume the simplest shell-model configurations shows good agreement except for the reaction $^{34}S(p,t)^{32}S$. Obviously such simple configurations are unrealistic; however, the good overall agreement cannot be ignored, since the (p, t) reaction is generally very sensitive to details of the assumed wave functions. In addition, three more cases of similar agreement are known,[4] and together with the present data they span the region $20 \leq A \leq 52$. Presumably these results reflect the fact that the parentage of both the ground and analogue states are reasonably simple even if the wave functions themselves are not. This indication is similar to the more definite results recently obtained[5] for certain states in the same mass region with $T_f = T_i$.

Using the IMME (Eq. 1) and measured energies from Table I, one can predict masses for a number of neutron-deficient nuclei which are as yet unobserved. The results are given in Table II together with the predictions by Kelson and Garvey.[6] Both sets of predictions agree throughout. The observation and firm identification of T = 3 states in mass 38 indicate that analogue states with $T > 2$ can be adequately studied by the present methods. Consequently, it appears that they can be extended to heavier nuclei, particularly those in the $(1f_{7/2})$ shell.

Footnotes and References

†Condensed from UCRL-18942, June 1969; Phys. Rev., in press.
*Present address: McMaster University, Hamilton, Ontario, Canada.
1. The program LORNA was written by C. C. Maples, to whom we are grateful for making it available.
2. H. Brunnader, J. C. Hardy, and J. Cerny, Phys. Rev. 174, 1247 (1968); R. A. Paddock, S. M. Austin, W. Benenson, I. D. Proctor, and F. St. Ament, Phys. Rev. 182, 1104 (1969); F. Ajzenberg-Selove and T. Lauritzen, Nucl. Phys. A114, 1 (1968).
3. These calculations used the program DWUCK, which was written by D. Kuntz and modified by us for two-nucleon transfer reactions following the "zero-range interaction" approximation [see N. K. Glendenning, Phys. Rev. 137, B102 (1965)].
4. J. Cerny, Ann. Rev. Nucl. Sci. 18, 27 (1968).
5. J. C. Hardy, H. Brunnader and J. Cerny, Phys. Rev. Letters 22, 1439 (1969).
6. I. Kelson and G. T. Garvey, Phys. Letters 23, 689 (1966).

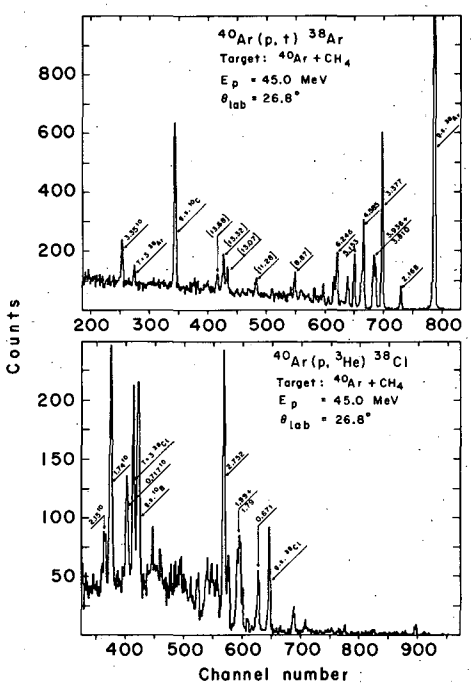

Fig. 1. Energy spectra of the reactions $^{40}Ar(p, t)^{38}Ar$ and $^{40}Ar(p, ^3He)^{38}Cl$. The states shown bracketed were determined in this work, the calibration having been established by using the other marked states. (XBL 684-2297)

ISOSPIN PURITY AND DECAY OF THE T = 3/2 ANALOGUE STATE IN ^{17}F†

J. C. Hardy, John E. Esterl, R. G. Sextro, and Joseph Cerny

The T_z = - 3/2 nucleus ^{17}Ne β^+-decays to levels in ^{17}F. With the exception of decay branches to the ground and first excited states--both first-forbidden--all branches lead to levels that are above the proton separation energy. From the relative intensities of the emitted proton groups, absolute log ft values can be determined for all significant ^{17}Ne decay branches with a precision not afforded by other methods. In particular, since the strength of the super-allowed decay to the T = 3/2 analogue state is determined predominantly by the Fermi matrix element, an accurate evaluation of its log ft value provides a sensitive measure of the state's isospin purity.

Stacked foils of TiO_2 were bombarded in the external 45-MeV ^3He beam of the 88-inch cyclotron, producing ^{17}Ne from the reaction $^{16}O(^3He, 2n)^{17}Ne$. At half-second intervals helium was swept through the target chamber, picking up the recoil nuclei and transporting them in 100 msec to a counting chamber 15 ft away. This chamber was conical, with a cooled ΔE-E counter telescope

mounted internally at the apex and a 2×2-in. NaI(Tl) crystal mounted externally at the base. The ΔE counters ranged in thickness from 14 to 50 μ, with a 1-mm E counter. Energy signals from these detectors were fed into a Goulding-Landis particle identifier and the total-energy signals corresponding to protons or alphas were then time-sorted into eight groups of a pulse-height analyzer to provide lifetime as well as energy data. Coincidences between identified protons and γ's were also recorded, and the energies of both were stored two-dimensionally. The energy resolution (FWHM) for identified particles was ≈ 40 keV.

Proton spectra from the decay of ^{17}Ne are shown in both halves of Fig. 1. Center-of-mass proton energies (± ≈ 20 keV) are shown for all observed peaks, the energy calibration having been determined from the peaks marked 10.60 and 4.88 MeV; the former is due to the decay of the analogue state[1] in ^{17}F, and the latter has been independently calibrated by comparison with known[1] decays of the analogue states in ^{33}Cl and ^{29}Al. The lifetimes for all peaks marked in the spectra were found to be compatible with 109.5 ± 1.0 msec.

In the bottom half of Fig. 1 is a singles proton spectrum and below it is a spectrum recorded simultaneously of those protons in coincidence with 511-keV γ rays. The chance rate was negligible. Most of the coincident γ rays result from the annihilation of the positrons feeding levels in ^{17}F, but note that the relative heights of the three peaks below channel 110 are approximately doubled in the coincidence spectrum. This indicates that they must correspond to proton decays to the first excited state (0^+) of ^{16}O, which itself decays by internal pair conversion. The proposed decay scheme is shown in Fig. 2; energies of levels in ^{17}F agree with Ref. 2 except for those at 4.609 and 5.480 MeV, which were apparently incorrect in the earlier work. The analogue state decays to the ^{16}O ground (0 ± 3%), second (22 ± 3%), third (24 ± 6%), and fourth (44 ± 7%) excited states. The upper limit for unobserved decay modes was determined to be ≲ 10% of the total proton decays observed. The log ft value thus determined for the superallowed β^+ decay is $3.28^{+.05}_{-.08}$.

Since the model-dependent Gamow-Teller matrix element is small ($\langle\sigma\rangle^2 \approx 0.1$) compared with the model-independent Fermi matrix element ($\langle 1\rangle^2 = 3$), any significant discrepancy of the measured log ft from its calculated value[3] of 3.29 should be interpreted as arising from admixtures of configurations with T = 1/2 into the analogue state wave function; such configurations would cause a reduction in the Fermi matrix element proportional to the percentage admixture. The experimental log ft value thus was used to determine the isospin purity of the analogue state to be ≥ 90%.

Detailed calculations for levels in ^{17}F and the β^+ decay feeding them have been reported,[4] and there is good qualitative agreement with our results. From these calculations, the wave function for the ground state of ^{17}Ne and its (T = 3/2) analogue in ^{17}F is well represented by a $(p_{1/2})$ hole coupled to the ^{18}O ground state. The same components coupled to T = 1/2 will be referred to as the "anti-analogue" configuration. It is expected to be split between two $1/2^-$ states in ^{17}F; one is the state at 3.1 MeV, the other is calculated to be at ≈ 6 MeV. The β^+ decay to the former is correctly predicted to be retarded, but for the latter a log ft value of 3.4 is expected. It seems likely that one of the states observed just above 8 MeV is the other state involving the anti-analogue configuration. Based on the experimental log ft values, the components of the anti-analogue configuration in the levels at 3.1 and ≈ 8 MeV are approximately 85% and 15% respectively.

Footnote and References

†Condensed and revised from a preliminary report appearing in Nuclear Isospin, ed. by J. D. Anderson, S. D. Bloom, J. Cerny, and W. W. True (Academic Press, New York, 1969), p. 725.

1. J. Cerny, Ann. Rev. Nucl. Sci. 18, 27 (1968).
2. S. R. Salisbury and H. T. Richards, Phys. Rev. 126, 2147 (1962); R. L. Dangle, L. D. Oppliger, and G. Hardie, Phys. Rev. 133B, 647 (1963).
3. J. C. Hardy and B. Margolis, Phys. Letters 15, 276 (1965).
4. B. Margolis and N. de Takacsy, Phys. Letters 15, 329 (1965); Can. J. Phys. 44, 1431 (1966).

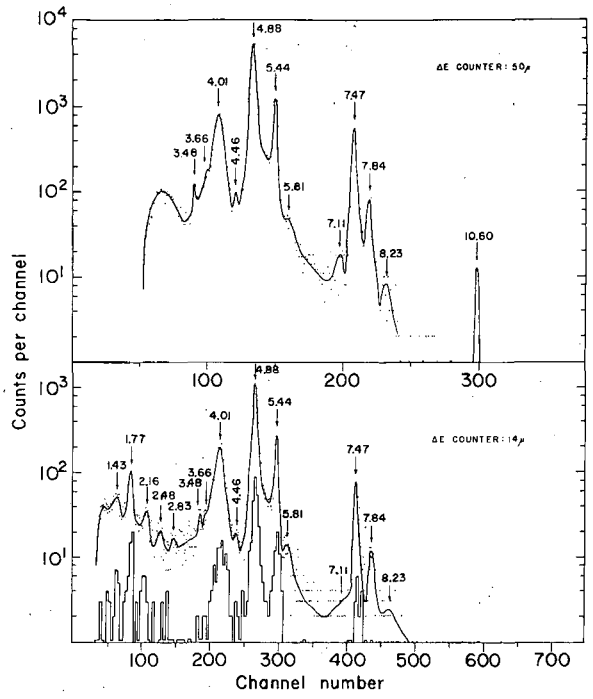

Fig. 1. Proton spectra from the decay of ^{17}Ne. The histogram shows protons in coincidence with 511-keV γ rays; it gives three-channel sums. (XBL 692-235)

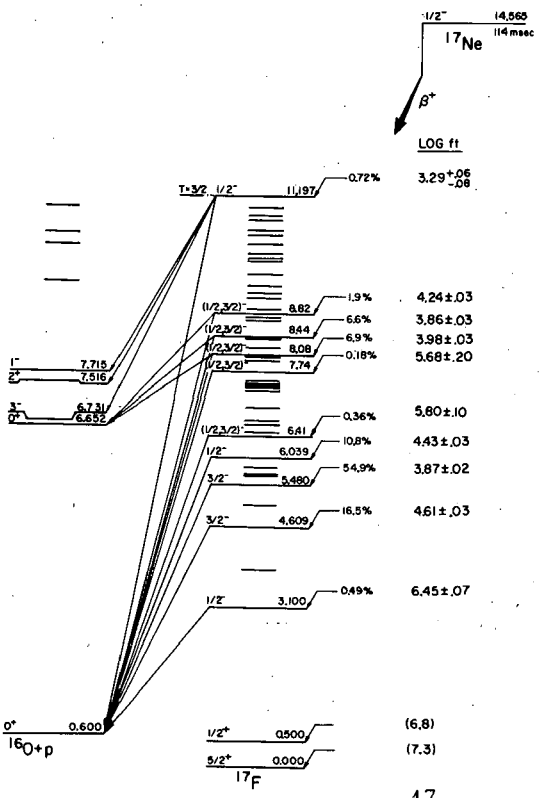

Fig. 2. Proposed decay scheme of ^{17}Ne. (701-2187)

ISOSPIN-FORBIDDEN DECAY PROPERTIES OF THE LOWEST T = 2 STATES OF ^{20}Ne, ^{24}Mg, ^{28}Si, ^{32}S, AND ^{40}Ca†

Robert L. McGrath,* Joseph Cerny, J. C. Hardy, G. Goth, and Akito Arima‡

In the past several years the lowest T = 2 isobaric analog states in a number of T_z = 0 light nuclides have been located.[1] These states were first observed by using two-nucleon transfer reactions, and, subsequently, as T-forbidden resonances. All available data are consistent with the expectation of relatively narrow widths for these states, sicne there are no T-allowed particle decay modes. These T = 2 states lie at least 3.5 MeV above the T-forbidden proton and alpha decay thresholds, and consequently the narrow widths imply a relatively high degree of isospin purity Study of both the particle and γ-decay modes can provide information as to the T = 0 and T = 1 admixtures and directly reflects upon the nature of the charge-dependent force itself.

We have studied the T-forbidden particle decay modes of the lowest-lying T = 2 states in ^{20}Ne, ^{24}Mg, ^{28}Si, ^{32}S, and ^{40}Ca by utilizing the (p, t) reaction to form these states and then observing the coincidences between the tritons forming the states and the protons and α particles from their decay. The data were obtained by using proton beams from the 88-inch cyclotron, the beam energy being adjusted between 42 and 46 MeV in order to maximize the (p, t) cross section. Self-supporting targets of ^{26}Mg (99.2% enriched), ^{30}Si (89%), Cd^{34}S (37.2%), ^{42}Ca (94.4%), ranging in thickness between 400 μg/cm^2 and 1 mg/cm^2, and a ^{22}Ne (91.3%) gas target were used. Tritons were detected in a dE-E counter telescope located at +22 deg (corresponding to the second maximum in the L = 0 angular distribution). With the exception of ^{22}Ne, where the gas target limited us to one decay telescope at -90 deg, two decay telescopes were positioned at -90 and -125 deg. Decay α particles from the analog states could not penetrate the dE detectors, but could be unambigously identified from the kinematics. If pulses from the decay dE and triton dE detectors were in coincidence (2τ = 50 nsec), the signals from each telescope were passed on to Goulding-Landis

particle identifiers. Provided the event corresponded to a triton in coincidence with either a proton or a particle stopping in the dE detector, total-energy signals and appropriate logic pulses were stored in the memory of an on-line PDP-5 computer and written on magnetic tape. Triton singles energy spectra were also accumulated.

The kinematics of reactions with three-particle final states are completely specified if the energies and angles of two of the particles are measured. A typical reaction, $^{42}Ca(p,t)^{40}Ca \rightarrow {}^{36}Ar + \alpha$, is exhibited in Fig. 1. The data lie along bands determined by the kinematics and experimental resolution, and these were projected onto the triton energy axis in order to find the decay properties. Figure 2 shows the projection for ^{40}Ca; the $^{36}Ar + \alpha$ projection exhibits a prominent peak at the triton energy corresponding to the T = 2 state, indicating the principal mode of decay.

Branching ratios were calculated by comparing the net number of coincidence events (after correction for "real" continuum and "chance" backgrounds) in a given decay mode to the number predicted from the net number of triton singles counts. Table I summarizes the branching ratios for all five T = 2 states, and it is apparent that the sums are close to 100%, indicating we have observed most of the particle decay modes. Although experimental cutoffs did not permit the examination of all allowed decay modes, barrier-penetration effects in general make transitions to higher-lying states unimportant.

The T = 2 states studied were found to decay by both proton ($\Delta T = 1, 2$) and alpha ($\Delta T = 2$) emission. With the exception of ^{20}Ne, these states have large branching ratios to the ground states of the residual nuclides, making it feasible to study them as compound nuclear resonances. Several such studies (Refs. 2-5) are in qualitative agreement with the results of this work.

An attempt to estimate the kinds of impurities that would be introduced by the Coulomb potential was undertaken in ^{40}Ca in order to ascertain whether large $\Delta T = 2$ admixtures might be expected. A first-order perturbation theory calculation included mixing with the zero-particle zero-hole ground state, the four-particle four-hole 3.35-MeV state, and the two-particle two-hole states of the same configuration as the T = 2 state (but recoupled to T = 0 and T = 1). Within the framework of this calculation it seems reasonable to ignore other states, since none are expected to produce large Coulomb matrix elements. However, the calculated admixtures do not appear to be large enough to explain the observed decays.

Footnotes and References

†Condensed from UCRL-18940, June 1969; Phys. Rev. (to be published).
*Present address: State University of New York, Stony Brook, New York 11790.
‡Department of Physics, University of Tokyo, Tokyo, Japan.
1. J. Cerny, Ann. Rev. Nucl. Sci. 18, 27 (1968).
2. R. Bloch, R. E. Pixley, and P. Truöl, Phys. Letters 25B, 215 (1967).
3. H. M. Kuan, D. W. Heikkinen, K. A. Snover, F. Riess, and S. S. Hanna, Phys. Letters 25B, 217 (1967).
4. F. Riess, W. J. O'Connell, D. W. Heikkinen, H. M. Kuan, and S. S. Hanna, Phys. Rev. Letters 19, 367 (1967); K. A. Snover, D. W. Heikkinen, F. Riess, H. M. Kuan, and S. S. Hanna, Phys. Rev. Letters 22, 239 (1969); D. W. Heikkinen, H. M. Kuan, K. A. Snover, F. Riess, and S. S. Hanna, Bull. Am. Phys. Soc. 13, 884 (1968).
5. H. M. Kuan, F. Riess, K. A. Snover, D. W. Heikkinen, D. C. Healey, and S. S. Hanna, Bull. Am. Phys. Soc. 13, 884 (1968).

Table I. Summary of T = 2 branching ratio data.

Mode	Net events	Branching ratios[a] (× 100)	Summed branching ratios[b]	Normalized branching ratios
$^{20}Ne \rightarrow {}^{16}O + \alpha_0$	-3 ± 2	-6 ± 5		≈0
$^{16}O + (\alpha_1 + \alpha_2)$	17 ± 6	35 ± 12		38
$^{16}O + (\alpha_3 + \alpha_4)$	15 ± 6	29 ± 12		32
$^{19}F + (p_0 + p_1 + p_2)$	7 ± 4	14 ± 9		16
$^{19}F + (p_3 + p_4 + p_5)$	6 ± 4	13 ± 8		14
			85 ± 29	
$^{24}Mg \rightarrow {}^{23}Na + p_0$	108 ± 11	71 ± 7		74
$^{23}Na + p_1$	1 ± 6	1 ± 4		1
$^{20}Ne + \alpha_0$	7 ± 6	3 ± 3		3
$^{20}Ne + \alpha_1$	48 ± 10	22 ± 4		22
			97 ± 16	
$^{28}Si \rightarrow {}^{24}Mg + \alpha_0$	93 ± 10	72 ± 8		81
$^{24}Mg + \alpha_1$	11 ± 5	8 ± 4		9
$^{27}Al + p_0$	4 ± 7	4 ± 8		5
$^{27}Al + (p_1 + p_2)$	4 ± 5	4 ± 5		5
			88 ± 16	
$^{32}S \rightarrow {}^{31}P + p_0$	32 ± 6	86 ± 17		75
$^{28}Si + \alpha_0$	9 ± 4	18 ± 7		16
$^{28}Si + \alpha_1$	6 ± 3	11 ± 5		9
			115 ± 24	
$^{40}Ca \rightarrow {}^{36}Ar + \alpha_0$	125 ± 12	116 ± 11		100
$^{36}Ar + \alpha_1$	-2 ± 2	-1 ± 2		≈0
$^{39}K + p_0$	-2 ± 7	-3 ± 9		≈0
			112 ± 19	

a. Standard deviation includes only counting statistics.
b. Standard deviation also includes uncertainties in the number of triton counts and in decay telescope solid angles.

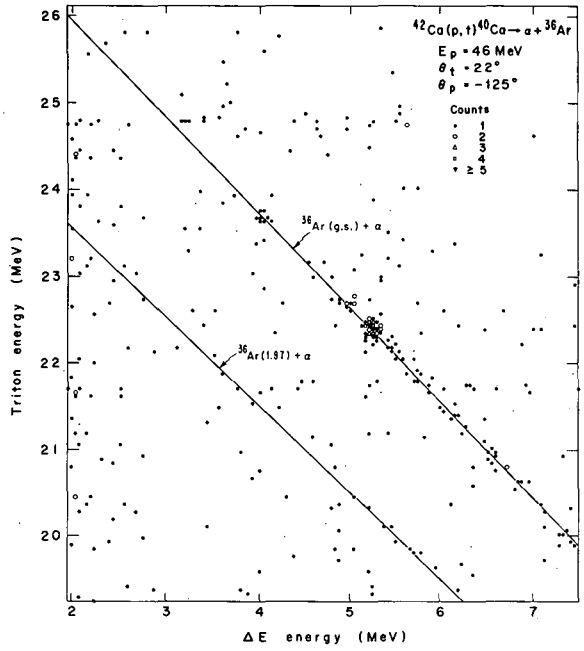

Fig. 1. A two-dimensional energy spectrum of events consisting of tritons in coincidence with particles which stopped in the ΔE detector of telescope #3. From the ΔE energy losses, these particles are known to be α particles and, consequently, the data correspond to the ^{42}Ca(p, t)^{40}Ca → α + ^{36}Ar reaction. The diagonal lines were calculated from the kinematics. The cluster of events along the ^{36}Ar ground-state line at 22.4 MeV triton energy is associated with the decay of the 0^+ T = 2 state located at 11.98 MeV in ^{40}Ca. (XBL 687-3281)

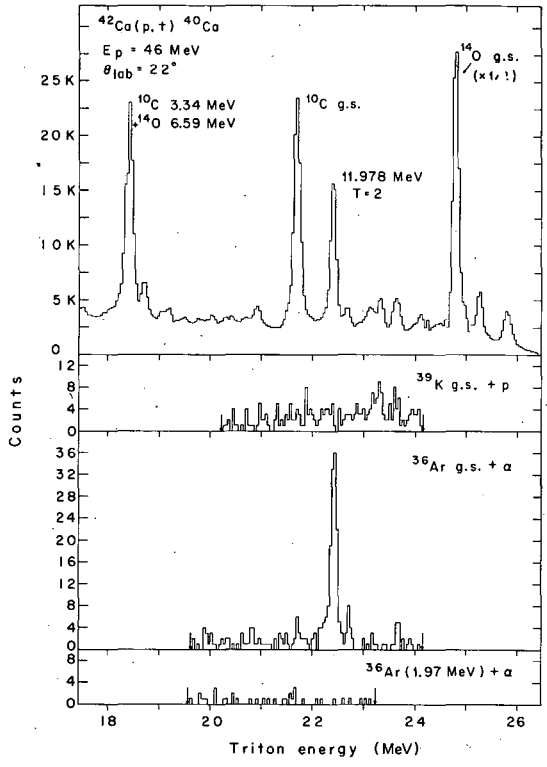

Fig. 2. The top spectrum shows the triton singles data containing the ^{40}Ca T = 2 state. The lower-lying excited states are not observed because of the relatively thin detectors used in the triton telescope. The lower spectra are summed projections from both decay telescopes of events lying along kinematics bands in the coincidence data onto the triton energy axis; the arrows in these spectra mark the energy cutoffs determined by kinematics and detector thickness.
(XBL 687-3279)

THE (^{3}He, ^{6}He) REACTION ON ^{6}Li AND ^{7}Li†

A. D. Bacher, R. L. McGrath,* J. Cerny, R. de Swiniarski,‡
J. C. Hardy, and R. J. Slobodrian‡‡

Current interest in the level structure of three-nucleon[1] and four-nucleon[2] nuclei has prompted an investigation of the systems (3p) and ^{4}Li by means of the (^{3}He, ^{6}He) reaction on ^{6}Li and ^{7}Li. In spite of its low yield [$d\sigma/d\Omega \approx$ (1-4) μb/sr at forward angles], the (^{3}He, ^{6}He) reaction has been used previously[3] to determine the masses of several proton-rich nuclei (e.g., ^{7}B and ^{9}C). To the extent that the (^{3}He, ^{6}He) reaction on ^{6}Li can be considered a direct three-neutron transfer, it should selectively populate the lowest state in the (3p) system, since the protons in the target already have the appropriate shell-model configuration. A similar argument applies to the formation of the lowest T = 2 state in ^{4}Li.

Previous investigations of the (3p) system have been made with the ^{3}He(^{3}He, t)3p and ^{3}He(p, n)3p reactions. Measurements of triton spectra from the ^{3}He(^{3}He, t)3p reaction at 18 to 20 MeV[4] suggest a sequential decay through the 20-MeV level in ^{4}He. At 44 MeV[5] departures of the triton

spectra from four-body phase space can be accounted for by including the Coulomb interaction between the triton and the (3p) system. Neutron spectra from the ^{3}He(p, n)3p reaction at 25 MeV[6] indicate a slight deviation from four-body phase space. This has been tentatively explained as due to a $^1S_0$ final-state interaction between two of the three protons. At 50 MeV[7] the departure from phase space is considerably more pronounced and has been interpreted in terms of a T = 3/2 state in the (3p) system at Ex(3p) = (9 ± 1) MeV with a width Γ = (10.5 ± 1) MeV.

There have been several previous attempts to locate the T = 2 state in ^{4}Li. A careful search[8] of the π^- decay modes of the hypernucleus ^{4}He (e.g., $^4\text{He} \rightarrow \pi^- + p + {}^3\text{He}$) shows no evidence for sharp resonances in ^{4}Li. In a high-resolution measurement of the excitation function for p + ^{3}He elastic scattering at backward angles,[9] there is no indication of a narrow level in ^{4}Li for excitations above the p + ^{3}He threshold between 9.5 and 11.6 MeV. Finally, in a recent study of the ^{7}Li(^{3}He, ^{6}He)^{4}Li reaction at 37 MeV and 20 deg[10] no evidence was found for a sharp state in ^{4}Li up to an excitation of about 12 MeV.

In the experiment reported here a 53.2-MeV ^{3}He beam from the 88-inch cyclotron was used to bombard self-supporting enriched ^{6}Li and ^{7}Li targets (≈200 μg/cm^2). The resultant ^{6}He nuclei were identified by using a three-counter particle identification system that has been described previously.[3, 11] A typical particle-identifier spectrum is shown in Fig. 1.

The ^{6}He energy spectrum at 14.1 deg from the reaction ^{6}Li(^{3}He, ^{6}He)3p is shown in Fig. 2(a). The spectrum covers ^{6}He energies between 26 and 40 MeV, and allows an investigation of the residual (3p) system from the threshold (Q = -10.45 MeV) to an excitation of about 12 MeV. The spectrum shape is remarkably smooth, and is quite similar to the solid curve which gives the phase-space distribution for the four-particle final state, ^{6}He + 3p, modified to include the Coulomb interaction between the ^{6}He and the (3p) system.[12]

The ^{6}He energy spectrum at 14.1 deg from the reaction ^{7}Li(^{3}He, ^{6}He)^{4}Li is shown in Fig. 2(b). The spectrum covers an excitation in ^{4}Li of 15 MeV relative to the p + ^{3}He threshold (Q = -9.98 MeV). In this range no evidence is seen for a narrow state in ^{4}Li. It is clear, however, that if the order-of-magnitude estimates of a width of 10 keV for a T = 2 level in ^{4}Li at 10.6 MeV[9] are correct, its presence could be washed out by the resolution in this experiment, in view of the apparently large contributions to the cross section from the three-, four-, and five-body continuum states. The relatively sharp rise of the spectrum between 0 and 3.5 MeV excitation in the (p + ^{3}He) system is similar to that seen at forward angles in the ^{6}Li(p, t)^{4}Li reaction,[13] and is presumably due to a p-wave p-^{3}He final-state interaction corresponding to the low-lying, broad T = 1 states in ^{4}Li.[2] A more detailed comparison indicates that this feature is considerably less prominent in the ^{7}Li(^{3}He, ^{6}He)^{4}Li reaction. This raises the question of whether the (^{3}He, ^{6}He) reaction mechanism is selective of the simple configurations corresponding to higher isospin states, particularly in the very light nuclei for which contributions from the multiparticle continuum states are known to be large. At present there is insufficient data in the form of angular distributions for (^{3}He, ^{6}He) reactions to test the three-neutron transfer mechanism.

Footnotes and References

†Condensed from UCRL-19521, Dec. 1969.
*Present address: State University of New York, Stony Brook, New York 11790.
‡Present address: Institut des Sciences Nucléaires, Grenoble, France.
‡‡Present address: Université Laval, Quebec, Canada.

1. G. C. Phillips, in Proceedings of International Nuclear Physics Conference, Gatlinburg (Academic Press, New York, 1967), p. 949.
2. W. E. Meyerhof and T. A. Tombrello, Nucl. Phys. A109, 1 (1968).
3. R. L. McGrath, J. Cerny, and E. Norbeck, Phys. Rev. Letters 19, 1442 (1967); G. W. Butler, J. Cerny, S. W. Cosper, and R. L. McGrath, Phys. Rev. 166, 1096 (1968).
4. A. D. Bacher and T. A. Tombrello, Bull. Am. Phys. Soc. 10, 693 (1965).
5. T. A. Tombrello and R. J. Slobodrian, Nucl. Phys. A111, 236 (1968).
6. A. D. Bacher, F. G. Resmini, R. J. Slobodrian, R. de Swiniarski, H. Meiner, and W. M. Tivol, Phys. Letters 29B, 573 (1969), and references therein.
7. L. E. Williams, C. J. Batty, B. E. Bonner, C. Tschalär, H. C. Benöhr, and A. S. Clough, Phys. Rev. Letters 23, 1181 (1969).
8. W. Gajewski, J. Sacton, P. Vilain, G. Wilquet, D. Stanley, D. H. Davis, E. R. Fletcher, J. E. Allen, V. A. Bull, A. P. Conway, and P. V. March, Phys. Letters 21, 673 (1966).
9. P. F. Donovan, J. V. Kane, J. F. Mollenauer, D. Boyd, P. D. Parker, and Č. Zupančič, Phys. Rev. 158, 973 (1967).

10. V. Z. Gol'dberg, A. A. Ogloblin, and V. P. Rudakov, Soviet J. Nucl. Phys. 9, 10 (1969).
11. F. S. Goulding, D. A. Landis, J. Cerny, and R. H. Pehl, IEEE Trans. Nucl. Sci. NS-13[3], 514 (1966).
12. T. A. Tombrello and A. D. Bacher, Phys. Letters 17, 37 (1965).
13. J. Cerny, C. Detraz, and R. H. Pehl, Phys. Rev. Letters 15, 300 (1965).

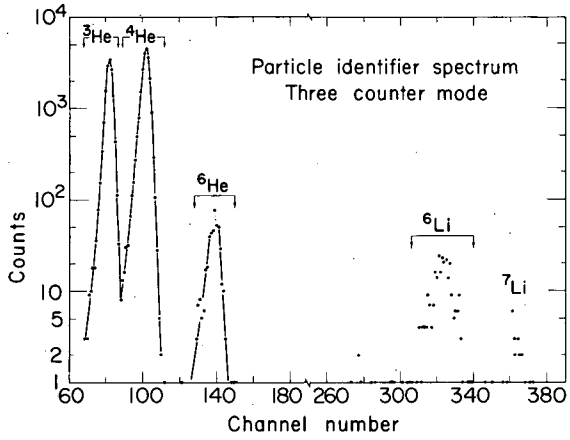

Fig. 1. A typical three-counter particle-identification spectrum for one of the counter telescopes, showing the window for accepted ^{6}He events. Note the break in the horizontal scale between the Z = 2 and Z = 3 nuclei. The Z = 3 events are for calibration purposes and represent a smaller total charge. (XBL 701-2261)

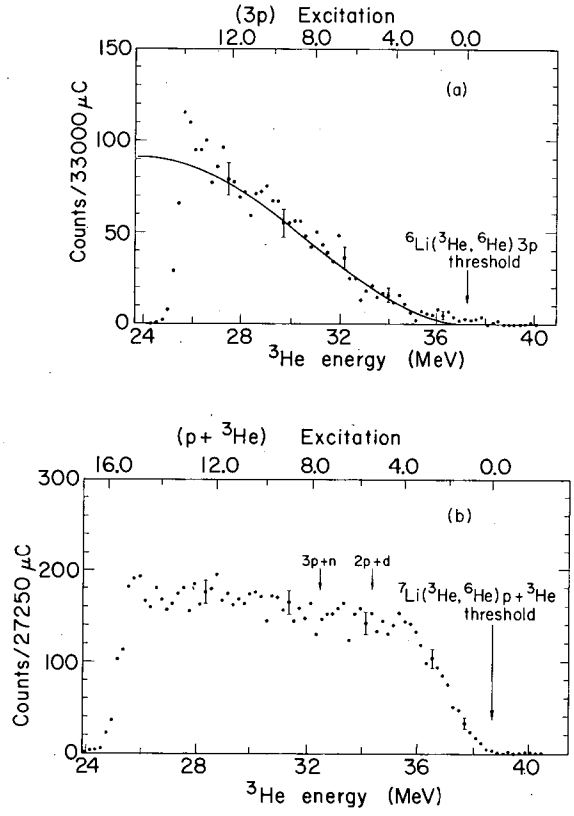

Fig. 2. The ^{6}He energy spectrum for one of the telescopes at 14.1 deg (lab). (a) From the ^{6}Li(^{3}He, ^{6}He)3p reaction. The scale at the top of the figure gives the excitation in the residual (3p) system. The solid curve represents the four-body phase-space distribution described in the text. (b) From the ^{7}Li(^{3}He, ^{6}He)^{4}Li reaction. Arrows mark the thresholds for the p + ^{3}He, 2p + d, and ^{3}p + n final states. The scale at the top gives the excitation in ^{4}Li relative to the p + ^{3}He threshold. (XBL 701-2262)

ANALYSIS OF P-^{4}He CROSS SECTION AND POLARIZATION DATA FROM 20 TO 60 MeV

E. T. Boschitz,† M. Chabre,* H. E. Conzett,
R. J. Slobodrian,‡ and W. F. Tivol

In 1949 Critchfield and Dodder[1] carried out a phase-shift analysis of proton-^{4}He cross-section data between 1 and 3.6 MeV. They found two acceptable solutions, one corresponding to the ordering $p_{1/2}$, $p_{3/2}$ of the ground and first excited state doublet of ^{5}Li, and the other predicting the inverted ordering. The two solutions predicted different polarizations in p-^{4}He scattering, so a single polarization measurement by Heusinkveld and Freier[2] in 1952 determined the ordering of the states. (In fact, it was necessary only to determine that the sign of the polarization changed between 2 and 3 MeV.)

Since that time a very considerable effort, both experimental and theoretical, has gone into the study of this system—for two reasons. First, large polarizations persist over a considerable energy range, so that ^{4}He has been most useful and popular as an analyzer of proton polarization—

which, of course, stimulated experimental determinations of its analyzing, hence polarizing, power. The second and more basic reason is that the p-^{4}He system is the simplest nuclear system involving spin–a spin 1/2, spin-zero system with the spin-zero "particle" quite tightly bound. Thus, scattering states of a given total angular momentum and parity cannot be mixtures of different orbital angular momenta, as is the case in nucleon-nucleon scattering, in which the attendant introduction of mixing parameters necessarily complicates phase-shift analyses. Hence, below the first inelastic threshold, the d + ^{3}He channel, which sits at 22.9 MeV, there is only one parameter, the real phase shift, to determine for each angular momentum state. On the other hand, the system is not so simple as to be uninteresting. The resonance behavior corresponding to states in ^{5}Li and the effects of the inelastic channels provide the elements of interest. One would expect, then, that a description of the proton-alpha interaction in terms of a unique set of phase shifts would be more easily arrived at than has been the case, for example, with the nucleon-nucleon interaction.

The sources of data used in our analysis are the following: cross section data from 20 to 28 MeV are from Allison and Smyth,[3] at 31 MeV from Bunch et al.,[4] at 40 MeV from Brussel and Williams,[5] at 49 MeV from Davies et al.,[6] and at 55 MeV from Hayakawa et al.[7] Polarization data at 29, 40, and 49 MeV are from Craddock et al.,[8] at 38 MeV from Hwang et al.,[9] and those at 20, 27, 34, 44, 55, and 63 MeV are our measurements.

Figure 1 shows our fits. Although only polarization data are compared with calculated curves from our phase-shift analyses, it should be noted that differential cross-section data were included at each energy at which they were available, and interpolated values were used otherwise. At 63 MeV only the polarization data were analyzed. One can see the smooth change with energy of the polarizations. The scales are displaced by the value 0.6; the back-angle maximum polarization stays near or above 80%.

The results of our analysis are summarized in Fig. 2. Here we show the phase shifts and inelastic parameters as functions of energy. The (real) phase shifts $\delta_\ell^{\pm}$ and inelastic parameters $\eta_\ell^{\pm}$ for the ℓth partial wave, with total angular momentum $j = \ell \pm 1/2$, appear as follows in the expression for the partial-wave scattering amplitude,

$$f_\ell^{\pm}(\theta) \propto \frac{\eta_\ell^{\pm} \exp(2i\delta_\ell^{\pm}) - 1}{2ik} ,$$

where k is the momentum in units of $\hbar$. The phase shifts up to 20 MeV are those of Weitkamp and Haeberli,[10] and the narrow resonance effect near 25 MeV is <u>not</u> shown here. Above 20 MeV the dashed curves show the trends of the phase shifts, with their actual values showing some scatter about these curves. The least scatter is shown by the δ_0 values and the most by the δ_1^- values as shown. The 29-MeV s- and p-phase shifts stand off the curves by as much as 5 or 10 deg. Two possible explanations exist. The cross-section data were interpolated between 27.5 and 31 MeV, so they may be in error. The other possibility is the tentative 3/2+ or 5/2+ ^{5}Li level at 20 MeV suggested by Tombrello et al.[11] in interpreting their d + ^{3}He excitation function through that energy region. Such a state would have an effect near 27.5 MeV proton energy. This could affect only the $d_{3/2}(\delta_2^-)$ or $d_{5/2}(\delta_2^+$ phase shift, but an appreciable change in one of those and the corresponding inelastic parameter might allow the s- and p-phase shifts to move back to the curves.

In summary, the general pattern is clear. The s-wave interaction is repulsive (we have plotted <u>minus</u> δ_0 here), consistent with the closed s-shell α particle. The interaction is attractive in the p, d, f, and g states and stronger in the $j = \ell + 1/2$ states, again consistent with the shell-model ordering. The $g_{7/2}$ phase shift, δ_4^-, is consistent with zero up to 60 MeV. The inelastic parameters, which can deviate from unity only above 23 MeV, show that there is relatively little s-wave absorption, and absorption in the higher partial waves comes in smoothly with increasing energy. No g-wave absorption was necessary.

Footnotes and References

†Present address: NASA Lewis Research Center, Cleveland, Ohio.
*Present address: CNRS Institut Fourier, Grenoble, France.
‡Present address: Université Laval, Quebec 10, Canada.

1. C. L. Critchfield and D. C. Dodder, Phys. Rev. 76, 602 (1949).
2. M. Heusinkveld and G. Freier, Phys. Rev. 85, 80 (1952).

3. P. W. Allison and R. Smythe, Nucl. Phys. A121, 97 (1968).
4. S. M. Bunch, H. H. Forster, and C. C. Kim, Nucl. Phys. 53, 241 (1964).
5. M. K. Brussel and J. H. Williams, Phys. Rev. 106, 286 (1957).
6. B. W. Davies, M. K. Craddock, R. C. Hanna, Z. J. Maroz, and L. P. Robertson, Nucl. Phys. A97, 241 (1967).
7. S. Hayakawa, N. Horikawa, R. Kajikawa, K. Kikuchi, H. Kobayashi, K. Matsuda, S. Nagata, and Y. Sumi, J. Phys. Soc. Japan 19, 2004 (1964).
8. M. K. Craddock, R. C. Hanna, L. P. Robertson, and B. W. Davies, Phys. Letters 5, 335 (1963).
9. C. F. Hwang, D. H. Norby, S. Suwa, and J. H. Williams, Phys. Rev. Letters 9, 104 (1962).
10. W. G. Weitkamp and W. Haeberli, in Proceedings 2nd International Conference on Polarization Phenomena of Nucleons, Edited by P. Huber and H. Schopper (Birkhäuser Verlag, Basel, 1966); Nucl. Phys. 83, 65 (1966); and private communication.
11. T. A. Tombrello, A. D. Bacher, and R. J. Spiger, Bull. Am. Phys. Soc. 10, 423 (1965); Phys. Rev. 154, 935 (1967).

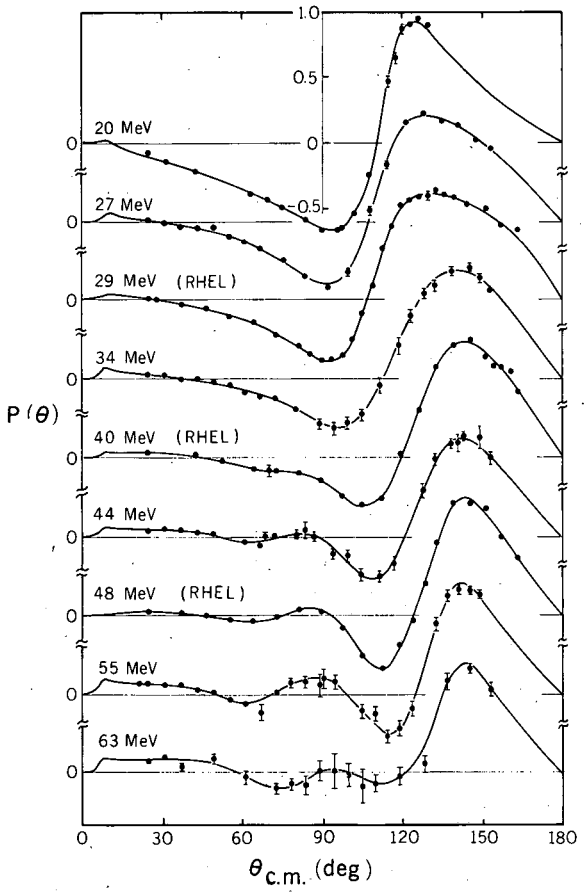

Fig. 1. Experimental and calculated results of p-^{4}He polarizations between 21 and 63 MeV. (MUB-7490)

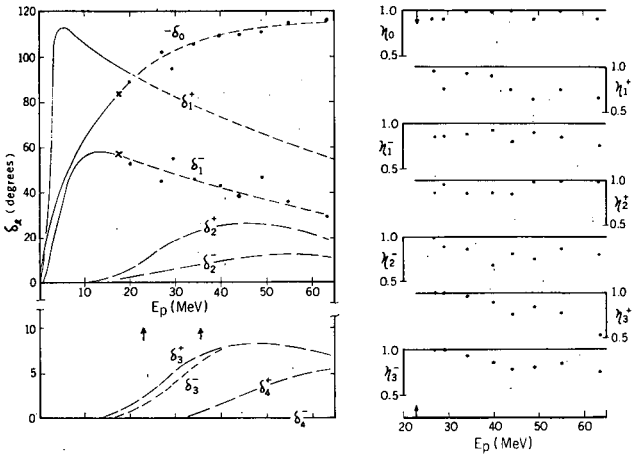

Fig. 2. Energy dependence of the phase shifts $\delta_\ell^{\pm}$ and inelastic parameters $\eta_\ell^{\pm}$ determined by this analysis. The phase-shift curves below 20 MeV are from Ref. 10. The arrow at 22.9 MeV marks the first inelastic threshold, that at 35.4 MeV marks the energy at which all reaction channels are open. (MUB-7491)

ALPHA-^{4}He ELASTIC SCATTERING FROM 30 TO 70 MeV†

A. D. Bacher, F. G. Resmini,* H. E. Conzett,
R. de Swiniarski,‡ and H. Meiner††

For excitation energies below 16 MeV the level structure in ^{8}Be is well understood in terms of states with a configuration of two α particles. However, it is apparent from the level diagram[1] for ^{8}Be shown in Fig. 1 that the level structure above 16 MeV rapidly becomes more complex as the p + ^{7}Li, n + ^{7}Be, and d + ^{6}Li reaction channels open and other configurations for the states become more important. The even-spin, positive-parity states in this region, which are the only states formed in ^{4}He-^{4}He elastic scattering, are shown in the expanded diagram on the right half of Fig. 1. Detailed measurements of the ^{4}He-^{4}He elastic scattering across this region of excitation in ^{8}Be were undertaken in order to resolve some ambiguities in earlier work.[2,3] In this work angular distributions have been obtained at 125 energies between 30 and 70 MeV using a ^{4}He beam from the 88-inch cyclotron, magnetically analyzed to 0.02% in energy. The measurements cover a region of excitation in ^{8}Be between 14.9 and 34.9 MeV.

Figure 2 shows the behavior of the excitation functions at center-of-mass angles of 56 and 72 deg. In the lower curve at 72 deg (a zero of P_4), the 2^+ doublet near 17 MeV excitation in ^{8}Be is clearly seen. Anomalies due to higher 2^+ states at 20.2, 22.2, and 25.2 MeV are also evident. The gradual rise of the cross section above a ^{4}He energy of 55 MeV is due primarily to a broad anomaly in the $\ell = 6$ partial wave. In the upper curve at 56 deg (a zero of P_2), 4^+ states near 20 and 26 MeV excitation are also apparent.

Figure 3 compares the behavior of the excitation functions at center-of-mass angles of 32 deg (a zero of P_4) and 76 deg (a zero of P_6). The anomalies due the 2^+ and 4^+ states are most conspicuous, but a comparison of the two excitation functions above 55 MeV clearly shows the importance of the $\ell = 6$ partial wave.

A phase-shift analysis of these data including partial waves up through $\ell = 8$ is in progress, and some preliminary conclusions can be drawn. The $\ell = 0$ phase shift follows a curve close to a hard-sphere behavior between 30 and 39 MeV ^{4}He energy. Close to 40.5 MeV there is evidence for a broad 0^+ level with an elasticity (Γ_α/Γ) less than 1/2. This is in agreement with a prediction by Barker[4] from an intermediate-coupling shell-model calculation. Measurements between 32 and 35 MeV enable us to clearly resolve the 2^+ levels at 16.6 and 16.9 MeV and to determine their parameters. Double-level fits to the $\ell = 2$ phase shift indicate that the level positions are shifted slightly from those previously determined from measurements of the ^{7}Li(^{3}He, d) and ^{10}B(d, α) reactions. The excitations of the 2^+ and 4^+ levels near 20 MeV lie about 300 keV higher in excitation than previously reported,[3] namely, at 20.2 and 19.9 MeV respectively.

Footnotes and References

†Condensed from papers contributed to APS meetings, Bull. Am. Phys. Soc. 14, 534 and 1218 (1969).
*Present address: University of Milano, Milan, Italy.
‡Present address: Institut des Sciences Nucléaires, Grenoble, France.
††Present address: University of Basel, Basel, Switzerland.
1. T. Lauritsen and F. Ajzenberg-Selove, Nucl. Phys. 78, 1 (1966).
2. M. W. Kermode, Phys. Letters 25B, 183 (1967).
3. H. E. Conzett and R. J. Slobodrian, Bull. Am. Phys. Soc. 13, 1388 (1968).
4. F. C. Barker, Nucl. Phys. 83, 418 (1966).

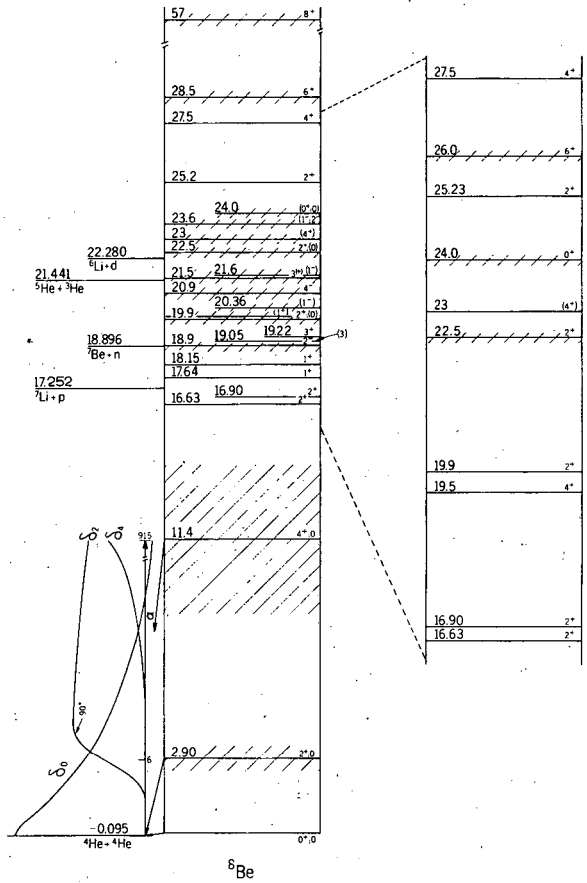

Fig. 1. The level diagram for ^{8}Be as taken from Ref. 1. The even-spin, positive-parity levels above 16 MeV excitation are shown in the expanded level diagram at the right. (XBL 694-423)

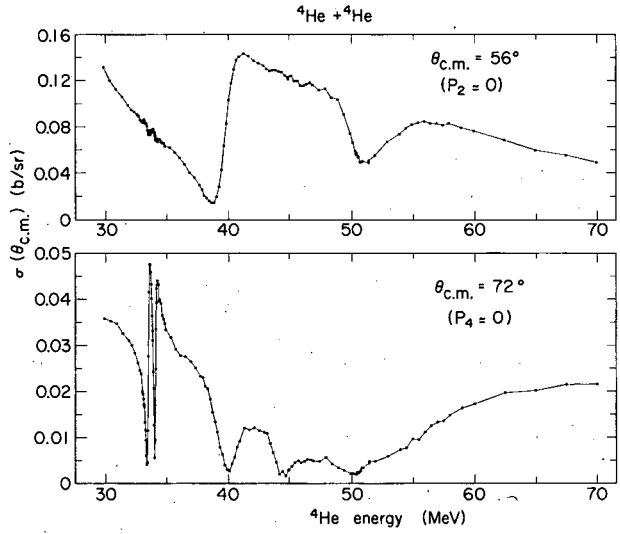

Fig. 2. Excitation functions for the ^{4}He-^{4}He elastic scattering at c.m. angles of 56 deg ($p_2 \approx 0$) and 72 deg ($P_4 \approx 0$). (XBL 694-2493)

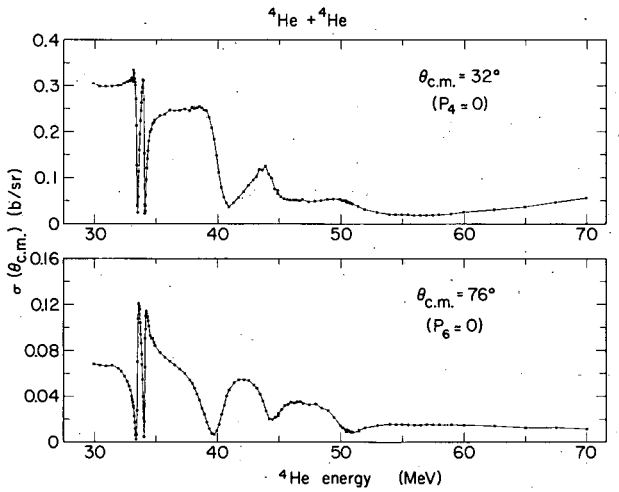

Fig. 3. Excitation functions for the ^{4}He-^{4}He elastic scattering at c.m. angles of 32 deg ($P_4 \approx 0$) and 76 deg ($P_6 \approx 0$). (XBL 694-2494)

OBSERVATION OF THE ^{3}He(p, n)3p REACTION AT 25 MeV †

A. D. Bacher, F. G. Resmini, * R. J. Slobodrian, ‡ R. de Swiniarski, ††
H. Meiner, ** and W. M. Tivol

Recent studies[1-4] of the mirror reactions ^{3}He(p, n)3p and ^{3}He(n, p)3n have sought evidence for an enhancement near the four-body end point due to a three-proton or three-neutron interaction. These studies have been motivated by an intrinsic interest in the reaction mechanism leading to a four-body final state and by the possibility, admittedly remote, of detecting effects due to three-body forces.

Previous work has set limits on the production of a triproton[2] or trineutron[4] system and provides rough values of the cross section for the formation of the four-body final state. Measurements of the ^{3}He(p, n)3p reaction have been made by Anderson et al.[1] at 14.1 MeV and 3 deg, and by Cookson[2] at 13.1 MeV and 20 deg. There is no evidence for a neutron group, below the four-body end point, corresponding to a triproton system which Anderson estimates would be unbound by 1.2 MeV on the basis of previous[3] but unconfirmed[4] work on the trineutron. Due to the extremely low neutron yield, no distinct neutron spectrum was observed, and there is disagreement between the cross sections reported.

In experiment reported here we have measured the neutron spectrum from the ^{3}He(p, n)3p reaction at a proton energy of 24.9 MeV. In contrast to previous work this energy is considerably above the reaction threshold (10.3 MeV). One expects a higher neutron yield if the cross section is essentially determined by the energy dependence of four-body phase space. The experimental setup is sketched in Fig. 1. The proton beam from the 88-inch cyclotron was focused at the center of a 15.2-cm-long gas target held at a ^{3}He pressure of 1 atm by 6.2-mg/cm^2 Al entrance and exit windows. The neutrons were detected at a lab angle of 8 deg by means of a proton-recoil spectrometer. Protons recoiling from the polyethylene radiator were detected and identified by a telescope consisting of three counters of thickness 140 μ, 300 μ, and 3 mm. A triple-coincidence requirement was used to reduce the number of random events caused by the neutron background and by (n, α) processes in the Si detectors. The sum of the pulses from counters ΔE_1 and ΔE_2 was used as the ΔE signal for particle identification[5] of the protons. The particle-identifier spectrum shown in Fig. 1 represents a considerable improvement over previous experience[6] in this energy range with a two-counter system.

The neutron background was measured by running the beam, for the same integrated charge, through a ^{4}He gas target, chosen because of the high threshold for neutron production (25.7 MeV) and the similar multiple scattering effect on the beam. The detection efficiency of the recoil spectrometer was measured with the ^{2}H(d, n)^{3}He reaction, at deuteron beam energies of 13.5 MeV and 11.6 MeV. The cross section was calculated from the Legendre coefficients given by Brolley et al.[7]

The neutron spectrum from the ^{3}He(p, n)3p reaction at 8 deg is presented in Fig. 2 for a total integrated charge of 43 000 μC. The measured spectrum (not shown) was corrected for the background contribution and the 1/E dependence of the spectrometer efficiency. The error bars include the statistical errors for both the ^{3}He target spectrum and the ^{4}He target background. The spectrum covers a neutron energy range down to 8.5 MeV, corresponding to a 3p excitation of 7 MeV. The total number of counts beyond the four-body end point (16.7 MeV) is consistent with zero. There is no evidence for a distinct neutron group corresponding to a strong interaction in the three-proton system. The four-body phase-space prediction, indicated by the dashed curve in Fig. 2, does not appear to account for the observed rise of the spectrum below the end point. A more satisfactory fit is obtained by considering the sequential reaction mechanism $p + {}^3He \rightarrow n + p + (2p)$, in which the three-body phase space is weighted by a $^1S_0$ interaction between two protons in the final state.[8] The result, shown by the solid curve of Fig. 2, has a shape more consistent with the trend of the experimental spectrum.

In summary, the neutron energy spectrum from the reaction ^{3}He(p, n)3p has been observed at a proton energy of 24.9 MeV and 8 deg. The departure of the spectrum from four-body phase space is tentatively explained as due to a $^1S_0$ final-state interaction between two protons. In view of these results it is clearly of interest to study this reaction at higher energies,[9] with particular attention to the forward angles. It is clear that the nature of the reaction mechanism leading to the four-body final state must be understood before departures from phase space can be attributed unambiguously to an interaction in the three-nucleon system.

Footnotes and References

†Condensed from Phys. Letters 29B, 573 (1969).
*Present address: University of Milano, Milan, Italy.
‡Present address: Université Laval, Québec, Canada
††Present address: Institut des Sciences Nucléaires, Grenoble, France.
**Present address: University of Basel, Basel, Switzerland.

1. J. D. Anderson, C. Wong, J. W. McClure, and B. A. Pohl, Phys. Rev. Letters 15, 66 (1965).
2. J. A. Cookson, Phys. Letters 22, 612 (1966).
3. V. Ajdačič, M. Cerineo, B. Lalović, G. Paić, I. Šlaus, and P. Tomaš, Phys. Rev. Letters 14, 666 (1965).
4. S. T. Thornton, J. N. Bair, C. M. Jones, and H. B. Willard, Phys. Rev. Letters 17, 201 (1966), and references therein.
5. F. S. Goulding, D. A. Landis, J. Cerny, and R. H. Pehl, Nucl. Instr. Methods 31, 1 (1964).
6. R. J. Slobodrian, H. Bichsel, J. S. C. McKee, and W. F. Tivol, Phys. Rev. Letters 19, 595 (1967).
7. J. E. Brolley, T. M. Putman, and L. Rosen, Phys. Rev. 107, 820 (1957).
8. In this calculation the neutron energy spectrum is expressed by

$$d^2\sigma/dE_n d\Omega \propto \int_0^{E_{max}} \rho(E_n, E_{2p}) \left[\frac{C k_{2p}}{(-\frac{1}{a} + \frac{1}{2} r_0 k_{2p}^2 - \frac{h(n)}{R} - P r_0^3 k_{2p}^4)^2 + C^2 k_{2p}^2} \right] dE_{2p},$$

where E_{2p} is the excitation in the 2p system, $\rho(E_n, E_{2p})$ is the three-body phase-space term, the second term is the expression for the $^1S_0$ interaction in effective range theory, and E_{max}, the upper limit of the integral, is a function of E_n and E_{2p}.
9. At the time of writing this paper preliminary reports (see C. J. Batty et al., Rutherford Laboratory Report RHEL/R170, 1968, p. 78) of measurements at a proton energy of 50 MeV indicate a significant departure from phase space of the neutron spectrum at forward angles.

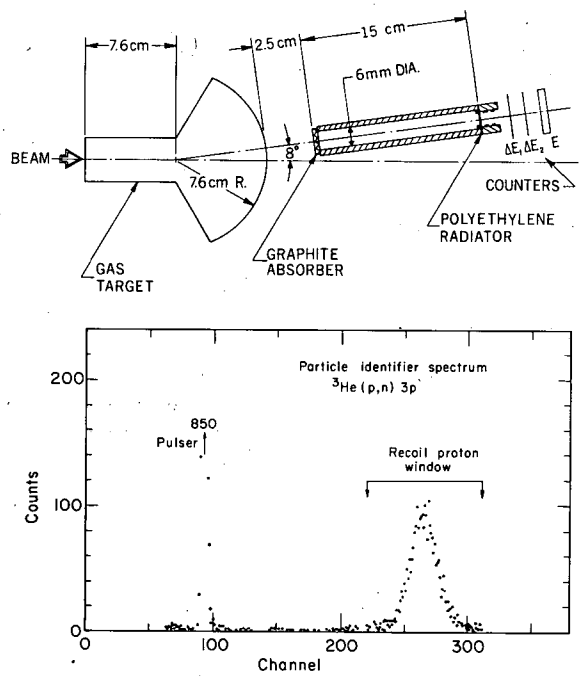

Fig. 1. (top) The experimental setup, showing the gas target and the proton-recoil spectrometer at 8 deg. The diameter of the brass collimator is shown enlarged by a factor of 3.
(bottom) The particle-identifier spectrum for the recoil protons, showing the window for accepted events. (XBL 696-2961)

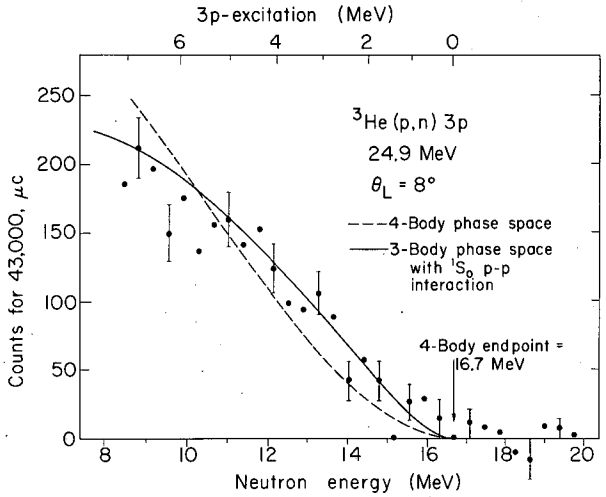

Fig. 2. The neutron energy spectrum from the ^{3}He(p, n)3p reaction at 24.9 MeV and 8 deg. The dashed curve corresponds to the four-body phase-space prediction. The solid curve corresponds to three-body phase space weighted by a $^1S_0$ interaction between two protons. The vertical scale is proportional to $d^2\sigma/dEd\Omega$. (XBL 694-2431)

INELASTIC SCATTERING OF 24.5-MeV POLARIZED PROTONS ON ^{20}Ne

A. D. Bacher, R. de Swiniarski,† D. L. Hendrie, A. U. Luccio,*
G. R. Plattner, F. G. Resmini,* and J. Sherman

A recent experiment on the inelastic scattering of 24.5-MeV protons on ^{20}Ne has shown that a large hexadecapole (β_4) deformation is needed to reproduce the shape and the magnitude of the cross sections leading to the 2^+, 4^+, and 6^+ excited states of the ground-state rotational band.[1] The optical-model parameters used in the analysis were determined by a search on the elastic cross section only, since no polarization measurements were available at the time. In order to improve the optical-model parameters and to test the sensitivity to the β_4 deformation, of the analyzing power for the first few excited states of the rotational band, we have measured the asymmetries for the low-lying states in ^{20}Ne with the polarized proton beam[2] from the 88-inch cyclotron. The measurements were made with eight cooled Si(Li) detectors (5 mm thick), located symmetrically on opposite sides of the beam. Up to 40 nA of polarized protons was delivered on target by the cyclotron with a polarization near 80%. The sign of the polarization was periodically changed at the source in order to cancel intrumental asymmetries. The overall energy resolution was about 150 keV, and therefore only asymmetries for the well-separated low-lying states in ^{20}Ne could be obtained, namely for the 0^+(g. s.), 2^+(1.63 MeV), 4^+(4.25 MeV), and 2^-(4.97 MeV) states.

Coupled-channels calculations with the parameters given in Ref. 1 are shown in Figs. 1-3 together with the experimental analyzing powers. As can be seen from these figures, the coupled-channels calculations with the β_2 and β_4 deformations taken from Ref. 1 essentially fail to reproduce the polarization data, the agreement being progressively worse for higher energy states. Similar effects have already been seen in recent polarization experiments on other nuclei in the s-d shell.[3] Further collective-model calculations are being made to investigate the behavior of the analyzing power with varying quadrupole and hexadecapole deformations and with a more realistic form[4] of the deformed spin-orbit potential.

Footnotes and References

†Present address: Institut des Sciences Nucléaires, Grenoble, France.
*Present address: University of Milano, Milan, Italy.

1. R. de Swiniarski, C. Glashausser, D. L. Hendrie, J. Sherman, A. D. Bacher, and E. A. McClatchie, Phys. Rev. Letters 23, 317 (1969).
2. D. J. Clark, A. U. Luccio, F. Resmini, and H. Meiner, Operation of the Polarized-Ion Source and Axial Injection System for the Berkeley 88-Inch Cyclotron, UCRL-18934, Oct. 1969.
3. A. G. Blair, C. Glashausser, R. de Swiniarski, J. Goudergues, R. Lombard, B. Mayer, J. Thirion, and P. Vaganov, Excitation of Collective States in Light Nuclei by Inelastic Scattering of 20.3-MeV Polarized Protons (UCRL-18927, Aug. 1969), Phys. Rev. (to be published).

4. H. Sherif and J. S. Blair, Phys. Letters 26B, 489 (1968).

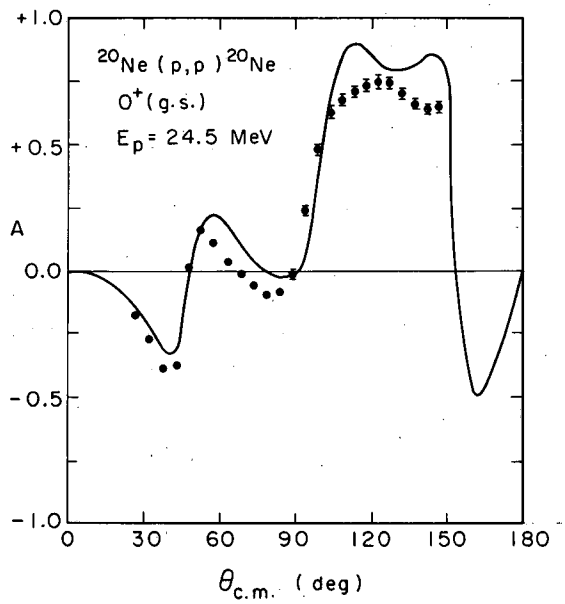

Fig. 1. The experimental analyzing power for the elastic scattering of 24.5-MeV polarized protons on ^{20}Ne. The error bars indicate the relative uncertainties in the measurements. The uncertainty in the absolute normalization is ±7%. The solid curve is the result of a coupled-channels calculation using values for the β_2 and β_4 deformations from Ref. 1. (XBL 701-2251)

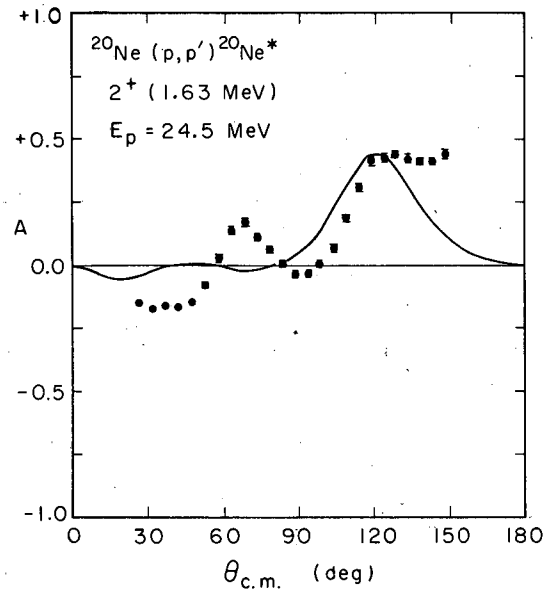

Fig. 2. The experimental analyzing power for inelastic scattering to the 2$^+$ first excited state of ^{20}Ne at 1.63 MeV. See caption for Fig. 1. (XBL701-2252)

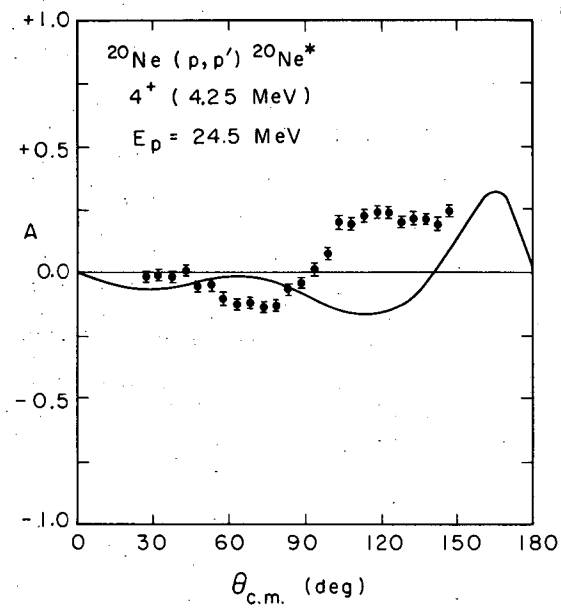

Fig. 3. The experimental analyzing power for inelastic scattering to the 4$^+$ second excited state of ^{20}Ne at 4.25 MeV. See caption for Fig. 1. (XBL 701-2253)

EVIDENCE FOR Y_4 DEFORMATION IN ^{20}Ne AND OTHER s-d SHELL NUCLEI†

R. de Swiniarski,* C. Glashausser,‡ D. L. Hendrie, J. Sherman,
A. D. Bacher, and E. A. McClatchie††

Accurate measurements of the large intrinsic quadrupole deformation of the first excited 2^+ states in ^{20}Ne, ^{24}Mg, ^{28}Si, and ^{32}S have recently been performed.[1] Such data are a critical test of the detailed microscopic calculations of nuclear properties now being carried out by methods such as deformed Hartree-Fock. Some of these calculations suggest that nuclei of the 2s-1d shell should also have a ground-state hexadecapole deformation which changes both in size and in sign through the shell. Previous inelastic scattering results analyzed with DWBA, Austern-Blair, and other less sophisticated models indicate that large direct transition strengths are needed in order to explain the magnitude of the cross sections for the first 4^+ states in ^{20}Ne and ^{28}Si, but not ^{24}Mg.

We have measured the inelastic scattering of 24.5-MeV protons from ^{20}Ne, using a proton beam from the Berkeley 88-inch cyclotron. The cross sections for the lowest 0^+, 2^+, 4^+, and 6^+ states are analyzed with the same coupled-channels method used for rare-earth nuclei.[2] The same model is then used to analyze the data of Crawley and Garvey[3] for inelastic scattering of 17.5-MeV protons from ^{24}Mg, ^{28}Si, and ^{32}S.

In the coupled-channels calculations the states explicitly coupled are assumed to be the lowest members of a pure K = 0 rotational band. The intrinsic deformation of these states is parameterized according to the following definition of the nuclear radius:

$$R(\theta) = R_0 \left[1 + \beta_2 Y_{20}(\theta) + \beta_4 Y_{40}(\theta)\right].$$

The interaction potential arises from the deformation of both the real and imaginary central terms of the optical potential and is calculated correctly to all orders. Thus, all possible multiple excitation paths between the coupled states are explicitly included. Coulomb excitation and deformed spin-orbit terms are included in many of the calculations but are found to have no significant effect. The coupled-channels code of A. D. Hill, which includes a spin-orbit term in the optical potential, is used for most of the calculations. The predictions for the 6^+ state in ^{20}Ne are made with the program of N. K. Glendenning, which, however, does not include a spin-orbit term. The 2^+ and 4^+ curves are insensitive to the spin-orbit potential.

Starting optical-model parameters were obtained by fitting only the elastic cross sections, using the search code MERCY. These parameters were then adjusted to preserve the fits to the elastic scattering in the coupled-channels calculations. Usually it was sufficient to adjust only W_D, a_I, and V_0. The parameters used for the curves shown in Figs. 1 and 2 are given in Table I.

The experimental cross sections and theoretical curves for the 0^+, 2^+, 4^+, and 6^+ states in ^{20}Ne are shown in Fig. 1. With values of +0.47 for β_2 and +0.28 for β_4, good fits are obtained to the shape and magnitude of the 0^+, 2^+, and 4^+ cross sections; the 6^+ cross section is underestimated by a factor of about 2. The sensitivity of the predictions for the 4^+ and 6^+ states to the value of β_4 is also illustrated in this figure. When β_4 is omitted, the predicted 4^+ and 6^+ cross sections are too small by one or two orders of magnitude. If β_4 is negative, the predicted shape of the 4^+ angular distribution does not match the experimental curve.

The coupled-channels predictions for the 0^+, 2^+, and 4^+ states in ^{24}Mg, ^{28}Si, and ^{32}S are shown in Fig. 2; no 6^+ data were available. The values of β_2 and β_4 are given in Table I. The signs of the β_2 deformations in ^{24}Mg and ^{28}Si were chosen to agree with the results of Ref. 1. Hartree-Fock calculations predict an oblate deformation for ^{32}S, but this has not yet been verified experimentally and is not determined by the present analysis. The sign and magnitude of β_4 for ^{32}S are not very sensitive to the sign of β_2. The fits to the elastic scattering are good for all three nuclei; the striking difference in the shapes of the 4^+ angular distributions for ^{24}Mg and ^{28}Si-^{32}S is also qualitatively explained. However, the general quality of the fits shown in Fig. 2 is inferior to that obtained for the 0^+, 2^+, and 4^+ states in ^{20}Ne.

Nondirect processes may be responsible for some of the discrepancies, especially for the 6^+ state in ^{20}Ne and for the 4^+ state in ^{24}Mg. However, there is evidence that such processes are not important at forward angles for the 4^+ states with larger cross sections. Excitation functions for the 0^+, 2^+, and 4^+ states in ^{20}Ne were smooth for proton energies between 23 and 26 MeV.

Table I.

	Nuclide			
	^{20}Ne	^{24}Mg	^{28}Si	^{32}S
V_0(MeV)	54.4	46.0	46.0	47.0
r_0(f)	1.05	1.22	1.24	1.21
a_0(F)	0.73	0.60	0.62	0.62
W_D(MeV)	6.30	3.60	8.0	9.5
r_I(F)	1.26	1.27	1.19	1.26
a_I(F)	0.55	0.64	0.40	0.28
V_s(MeV)	3.57	7.26	6.0	6.0
r_s(F)	0.95	1.22	1.24	1.21
a_s(F)	0.33	0.60	0.62	0.62
β_2(exp)	+0.49	+0.47	-0.34	-0.30
β_4(exp)	+0.28	-0.05	+0.25	+0.25

In addition, the 4^+ cross section decreases by more than an order of magnitude between forward and backward angles. An additional source of ambiguity is the known imperfection in the rotational description of these nuclei. The energy levels, particularly in ^{32}S, already show considerable deviation from the strict rotational-model pattern.

In terms of the rotational model, nonzero values of β_4 imply a hexadecapole moment in the ground state and in all the states of the rotational band built upon it. However, the inelastic scattering data alone might be equally well described by a vibrational model, with some modifications of the values of β_2 and β_4. Thus, the interpretation of β_4 as describing the static Y_4 deformation of the ground-state band relies upon measurements of a nonzero quadrupole moment; such a measurement[4] has not yet been made for ^{32}S. The quadrupole moments of the 2^+ states of ^{20}Ne and ^{24}Mg are about 30% larger than expected[1] on the basis of the rotational model from the electromagnetic values of $[B(E2)2^+ \rightarrow 0^+]$. Since the analysis of the inelastic scattering depends upon the evaluation of matrix elements between the ground state and excited states, the present results should be interpreted in terms of a transition probability instead of a static moment when the two are not consistent.

To summarize, the coupled-channels analysis of the present ^{20}Ne data show clearly the existence of a large hexadecapole deformation. A similar analysis of available data suggests a large hexadecapole deformation also in ^{28}Si and ^{32}S, whereas ^{24}Mg is found to have a very small Y_4 deformation.

Footnotes and References

†Condensed from Phys. Rev. Letters 23, 317 (1969).

‡Present address: Rutgers—The State University, New Brunswick, New Jersey.

††Present address: Arkon Scientific Laboratories, Berkeley, California.

1. A complete list of references can be found in the paper from which this is condensed.
2. D. L. Hendrie, N. K. Glendenning, B. G. Harvey, O. N. Jarvis, H. H. Duhm, J. Saudinos, and J. Mahoney, Phys. Letters 26B, 127 (1968).
3. G. M. Crawley and G. T. Garvey, Phys. Rev. 160, 981 (1967); G. M. Crawley (thesis), Princeton University, 1965.
4. Very recent results by K. Nakai, F. Stephens, and R. Diamond yield a positive quadrupole moment for ^{32}S (private communication).

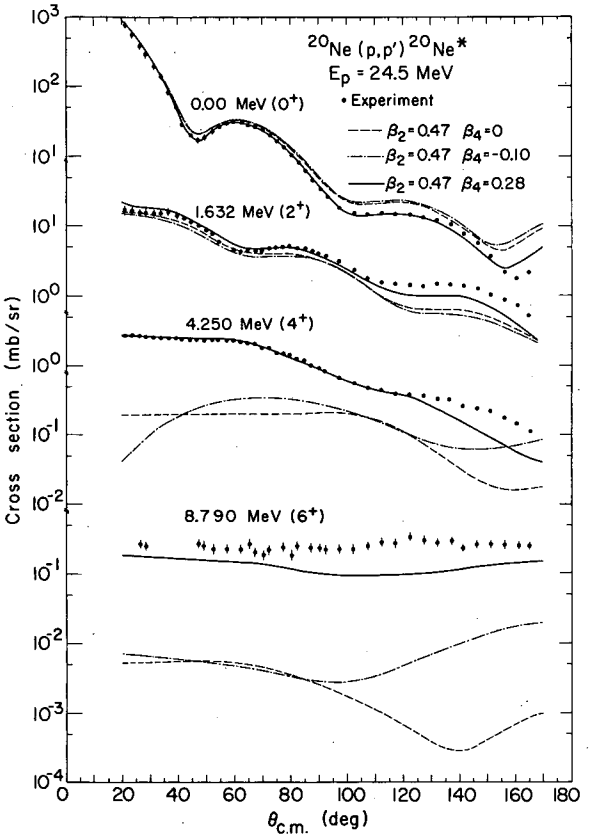

Fig. 1. Measured cross sections and theoretical predictions for the inelastic scattering of 24.5-MeV protons from ^{20}Ne. The curves were calculated with a coupled-channels program; a rotational model was used with the values of β_2 and β_4 indicated. (XBL696-2984)

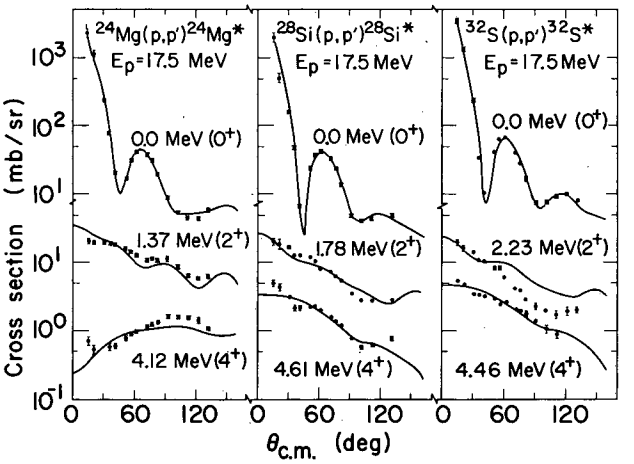

Fig. 2. Experimental cross sections of Crawley and Garvey (Ref. 3) for the inelastic scattering of 17.5-MeV protons from ^{24}Mg, ^{28}Si, and ^{32}S. The curves are coupled-channels predictions with the values of β_2 and β_4 indicated in Table I. (XBL696-2985)

INELASTIC SCATTERING OF 30.3-MeV PROTONS FROM ^{10}B†

R. de Swiniarski,* F. G. Resmini,‡ A. D. Bacher, C. Glashausser,††
E. A. McClatchie,** and J. Sherman

The cross sections for inelastic proton scattering can in general be reasonably well reproduced by using either the DWBA or the coupled-channels method, together with collective-model wave functions for the nuclear states. However, if shell-model wave functions are used with a microscopic model for the interaction between the incident proton and the target nucleons, the calculations have been generally unsuccessful in explaining most of the inelastic scattering data.[1] This suggests that the present microscopic models are incomplete, and that the neglect of tensor and spin-orbit forces as well as knockout-exchange terms in the effective interaction is too restrictive.

A program for a more sophisticated microscopic calculation has recently been written at Berkeley,[2] and one of the aims of the experiment reported here was to obtain inelastic scattering data for a nucleus in the p shell (in this case, ^{10}B) to test the new microscopic calculations. Since this work is still in progress, only some preliminary collective-model coupled-channels calculations are presented here.

The measurements for this work were made with magnetically analyzed 30.3-MeV protons from the 88-inch cyclotron. Protons scattered from an enriched ^{10}B target were detected by an array of four cooled Si(Li) detectors (5 mm thick) with an overall resolution between 25 and 40 keV. This allowed cross sections to be extracted for all the known states up to 7 MeV excitation, with the exception of the 5.17–5.18-MeV doublet. The experimental spectrum at θ_{lab} = 135 deg is shown in Fig. 1. The 4^+ state at 6.03 MeV is the most strongly excited state at this and all other angles.

The differential cross sections for the inelastic excitation of the 6.03-MeV state and of several others are indicated in Fig. 2. These other states are approximately equally excited with the exception of the weak (0^+, T = 1) state at 1.74 MeV, which can be made only by a combined spin- and isospin-flip mechanism from the (3^+, T = 0) ground state. It is worth noting the differences in the shapes of the angular distributions for excitations leading to states having the same spin and parity. Such differences cannot be explained by the usual collective-model description of the excitation.

Optical-model fits to the elastic cross section have been performed using the search code MERCY. Figure 3 indicates the fit obtained with these parameters: V = 51.75 MeV, W_D = 5.17 MeV, V_{so} = 9.79 MeV, r_0 = 1.10 F, a_0 = 0.553 F, r_I = 1.30 F, a_I = 0.685 F, r_{so} = 1.01 F, a_{so} = 0.57 F, χ^2/N = 1.29, N = 0.99. Preliminary coupled-channel or DWBA calculations have been performed for several of the more strongly excited states, using collective-model wave functions. The results are presented in Fig. 4. These 1^+, 2^+, and 4^+ states can be excited via either an ℓ = 2 or ℓ = 4 transfer. The forward-angle behavior appears to favor the ℓ = 2 calculations. Similar results have also been obtained from an analysis of the inelastic scattering of 32-MeV ^{3}He particles on ^{10}B.[3] The results of the microscopic model calculations will be reported in a forthcoming paper.

Footnotes and References

†Presented as a contributed paper to the APS Summer Meeting, Hawaii, September 1969; Bull. Am. Phys. Soc. 14, 851 (1969).

*Present address: Institut des Sciences Nucléaires, Grenoble, France.

‡Present address: University of Milano, Milan, Italy.

††Present address: Rutgers–The State University, New Brunswick, New Jersey.

**Present address: Arkon Scientific Laboratories, Berkeley, California.

1. See, for example, G. R. Satchler, Nucl. Phys. A95, 1 (1967).
2. R. Ascuitto and J. C. Hocquenghem (Lawrence Radiation Laboratory), private communication.
3. G. T. Squier et al., Nucl. Phys. A119, 369 (1968).

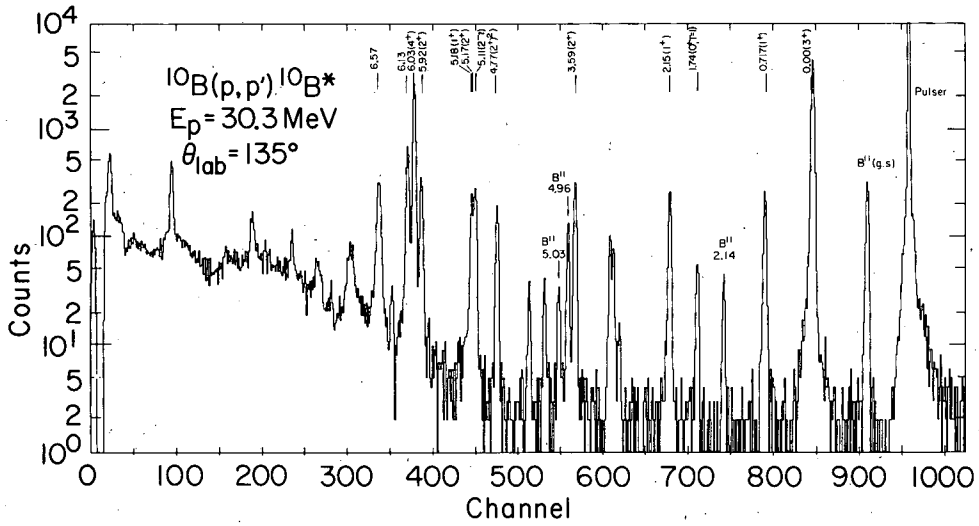

Fig. 1. The experimental spectrum for the inelastic scattering of 30.3-MeV protons from ^{10}B at a lab angle of 135 deg. The self-supporting boron targets were enriched to about 90% ^{10}B. (XBL698-3538)

Date of request:

Call-No.

General Electric Company
Energy Systems & Technology Div.
FBRD Library
310 DeGuigne Dr.
Sunnyvale, CA 94086

For use of | Status | Dept. S-36

Author (or periodical title, vol. and year)

Title (with author & pages for periodical articles) (Incl. edition, place & date) ☐ This edition only

Verified in (or source of reference)

If non-circulating, please supply ☐ Microfilm ☐ Hard copy if cost does not exceed $_____

Note: *The receiving library assumes responsibility for*

AUTHORIZED BY:_____
(FULL NAME)

C

INTERIM REPORT

INTERLIBRARY LOAN REQUEST

According to the A.L.A. Interlibrary Loan Code

REPORTS: Checked by

SENT BY: ☐ Library rate ☐ _____

Charges $_____ Insured for $_____

Date sent_____

DUE_____

RESTRICTIONS: ☐ For use in library only

☐ Copying not permitted ☐ _____

NOT SENT BECAUSE: ☐ In use ☐ Non circulating ☐ Not owned ☐ _____

Estimated Cost of: Microfilm_____

Hard copy_____

BORROWING LIBRARY RECORD:

Date received_____

Date returned_____

By ☐ Library rate ☐ _____

Postage enclosed $_____ Insured for $_____

RENEWALS: *(Request and report on sheet C)*

Requested on_____

Renewed to_____
(or period of renewal)

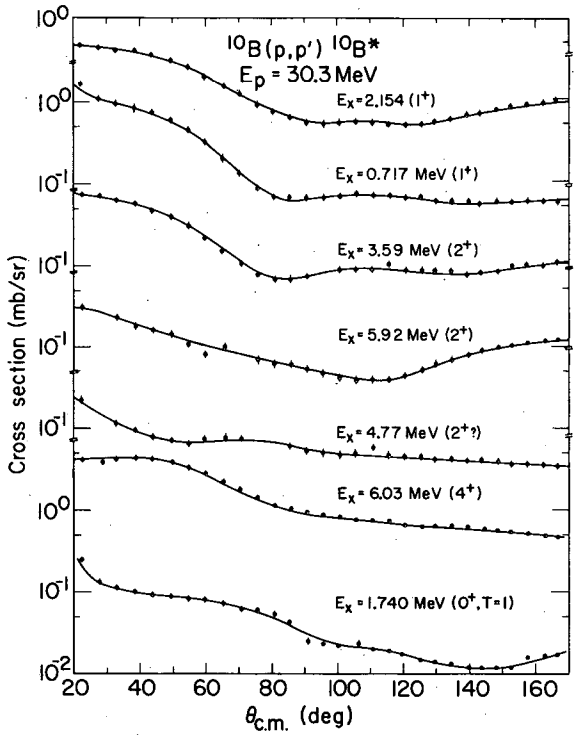

Fig. 2. Center-of-mass cross sections for inelastic excitation of several of the states observed in ^{10}B. The smooth curves serve only to connect the points, and the error bars shown are the relative errors for each state. (XBL698-3537)

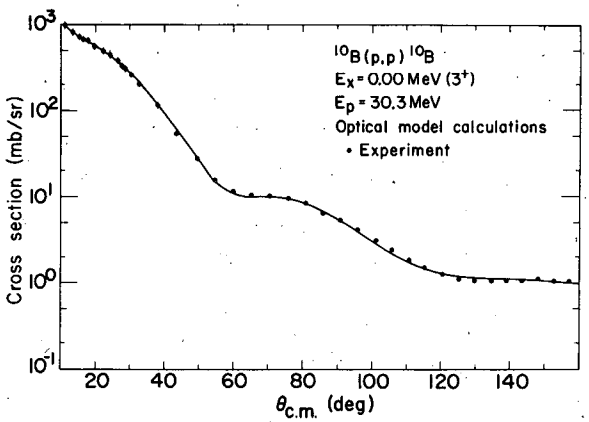

Fig. 3. The c. m. cross section for the elastic scattering of 30.3-MeV protons from ^{10}B. The solid curve represents the optical-model calculations using the parameters listed in the text. (XBL698-3536)

Fig. 4. The c. m. cross sections for the inelastic excitation of the 1^+ (0.717 MeV), 1^+ (2.154 MeV), 2^+ (3.53 MeV), and 4^+ (6.03 MeV) states. The solid and dashed curves are the results of the collective-model coupled-channels calculations with the indicated values for β and ℓ.
(XBL698-3535)

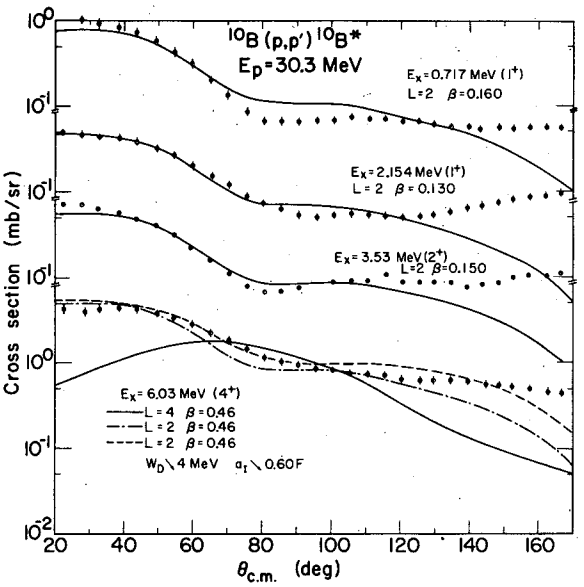

THE $^{205}Tl(p, p')^{205}Tl$ REACTION†

C. Glashausser,* D. L. Hendrie, J.-M. Loiseaux,‡
and E. A. McClatchie††

The existence of at least five octupole transitions in ^{205}Tl, suggested in work reported earlier,[1] has been confirmed. In addition, a spin ($7/2^+$, $9/2^+$) has been assigned to a state at 0.924 MeV and values of B(EL) have been extracted for many levels. The new measurements, at 19.64 MeV, were taken with 25 keV energy resolution and high statistical accuracy; they extend forward to 27 deg (lab) to insure proper identification of the angular momentum transfer (L). Similar measurements were performed for ^{206}Pb at the same time, so that the ratios of the absolute cross sections for ^{205}Tl and ^{206}Pb are accurate to about ±7%, although the individual absolute cross sections have errors of about ±15%.

Angular distributions for the 0.80-MeV (2^+), 2.65-MeV (3^-), 1.69-MeV (4^+), and 3.77-MeV (5^-) states in ^{206}Pb are shown in Fig. 1. The curves are macroscopic-model DWBA predictions with optical parameters determined from the elastic scattering cross section and strengths determined by normalization to the experimental data.

Angular distributions for five states at excitation energies of 2.48, 2.62, 2.71, 3.21, and 3.26 MeV in ^{205}Tl are illustrated in Fig. 2. The solid line has the shape of a smooth curve drawn through the data points for the 2.65-MeV (3^-) state in ^{206}Pb. This curve matches the ^{205}Tl angular distributions very well in every case, and allows the assignment of L = 3 (spin $5/2^-$ or $7/2^-$) to each of these levels.

The existence of so many L = 3 transitions appears to contradict the description of the 2.62- and 2.71-MeV doublet in ^{205}Tl as a pure $3s_{1/2}$ hole coupled weakly to the 3^- state in ^{206}Pb. This description has been suggested by Solf et al.,[2] based on its excitation energy, resonant structure, and absolute cross section measurement in the study of isobaric analog resonances in $^{205}Tl(p, p')^{205}Tl$. If the ground state of ^{205}Tl were simply $[3s_{1/2}^{-1}, {}^{206}Pb\ 0^+]$, the present measurements would certainly rule out the simple description proposed by Solf et al.[2] However, it is possible that the extra transitions observed here are transitions from other configurations in the ^{205}Tl ground state to relatively pure weak-coupling excited states. Such an explanation appears plausible for the 3.21- and 3.26-MeV states, based on the position and strength of these states. However, the 2.48-MeV level is less likely to be a pure weak-coupling state, since the only nearby configuration, $[1h_{11/2}^{-1}, {}^{206}Pb\ 2^+]_{7/2^-}$, is expected to be very weakly excited.

Another explanation for these strong L = 3 transitions, of course, is the possible admixture of the $[3s_{1/2}^{-1}, {}^{206}Pb\ 3^-]$ component in $5/2^-$ or $7/2^-$ states whose dominant structure may be unrelated to the 3^- state in ^{206}Pb. This is especially likely for the 2.48-MeV state, which lies close to the 2.62–2.71-MeV doublet. The summed cross section for the doublet is 55±5% of the cross section for the 3^- state in ^{206}Pb. The ratio of the cross sections for the two states of the doublet is 0.85±0.06. Both these values are in disagreement with the simple weak-coupling predictions of about 75% and 0.75, respectively.

A summary of the positions and strengths of all levels observed in $^{205}Tl(p, p')^{205}Tl$ and of the principal levels in ^{206}Pb is presented in Table I. The single-particle strength parameter G_L was determined from the formula

$$G_L = \left[\frac{2J_0+1}{2J+1}\right]\frac{(L+3)^2}{4\pi} Z^2 \beta_L^2,$$

where J_0 and J are the spins of the ground state and final state, respectively, Z is the atomic number of the target, and β_L is the deformation parameter. This last was determined by adjusting the normalization of the appropriate DWBA curve (shown in Fig. 1) to give the best fit to the experimental angular distributions. The underlined values of J in Table I have been assumed in the calculation of G_L.

Of special interest is the level at 0.924 MeV, which has been assigned L = 4 (spin $7/2^+$ or $9/2^+$). This state was observed also in the $^{208}Pb(p, \alpha)^{205}Tl$ reaction, but not in the (t, α) or (d, He^3) reactions[1,3] on Pb^{206} or the $^{205}Tl(\gamma, \gamma')^{205}Tl$ reaction.[4] A spin of $3/2^+$ had previously been proposed for this state,[2] but such an assignment is ruled out by the present measurements. This state may correspond to the lowest $7/2^+$ state predicted by Covello and Sartoris[5] to lie very

Table I. Energies, spins, and strengths of states observed in the $^{205}Tl(p, p')^{205}Tl$ and $^{206}Pb(p, p')^{206}Pb$ reactions at 19.64 MeV. Values in parentheses indicate tentative assignments. The underlined value of J has been assumed in the calculation of G_L.

A. ^{205}Tl

E_x	L	J^π	G_L
0.297	2	$3/2^+$	8.5
0.622	2	$5/2^+$	8.6
0.924	4	$7/2^+$, $9/2^+$	2.7
1.14	(2)	($\underline{3/2^+}$, $5/2^+$)	0.96
1.340	(2)	($\underline{3/2^+}$, $5/2^+$)	0.8
1.431	(4)	($7/2^+$, $\underline{9/2^+}$)	4.2
1.484	(5)	($9/2^-$, $\underline{11/2^-}$)	2.5
2.487	3	$\underline{5/2^-}$, $7/2^-$	5.7
2.625	3	$\underline{5/2^-}$, $7/2^-$	14.7
2.716	3	$\underline{5/2^-}$, $7/2^-$	13.0
2.971	(3)	($5/2^-$, $\underline{7/2^-}$)	0.75
3.18	(3)	($5/2^-$, $\underline{7/2^-}$)	1.5
3.213	3	$\underline{5/2^-}$, $7/2^-$	3.3
3.256	3	$\underline{5/2^-}$, $7/2^-$	5.2
3.414	(5)	($9/2^-$, $\underline{11/2^-}$)	2.2
3.537	(5)	($9/2^-$, $\underline{11/2^-}$)	6.9

B. ^{206}Pb

E_x	L	J^π	G_L
0.803	2	2^+	6.3
1.684	4	4^+	2.5
2.648	3	3^-	25.5
3.776	5	5^-	6.9

close to 0.9 MeV. Its strength, 2.7 single-particle units, corresponds very closely to the strength of the 1.69-MeV level in ^{206}Pb.

The values of G_L determined for the first $3/2^+$ and $5/2^+$ excited states are very similar to each other, a fact which might be taken as an indication of weak coupling. However, such a description has been shown[5] to be inappropriate for these states; evidence for this view is found in the smaller value of G_L for the 2^+ state in ^{206}Pb. The present value for ^{206}Pb agrees well with that determined by Saudinos.[6]

The 1.431-MeV level is an unresolved doublet;[7] its angular distribution is fitted very well, however, with L = 4. This may mean that both states are ($7/2^+$, $9/2^+$), or that one of the two states is weakly excited.

The 1.484-MeV state probably corresponds to the single-hole $1h_{11/2}$ state observed in $^{206}Pb(t, \alpha)^{205}Tl$ and $^{206}Pb(d, He^3)^{205}Tl$. The assignment of L = 5 here agrees with this description, but it can be only a tentative assignment, since it is difficult to distinguish L = 5 distributions from distributions for states of higher spin. The absolute cross section for this state corresponds closely to the cross section for the 1.6-MeV $(i_{13/2})^{-1}$ single neutron hole state observed[8] in $^{207}Pb(p, p')^{207}Pb$. Tentative L = 5 assignments have also been made for several states around 3.5 MeV. The peak at 3.537 MeV appears somewhat wider than the other peaks in the spectrum, and is likely to consist of two or more states. Many states in this region have been observed to resonate strongly in the $^{205}Tl(p, p')^{205}Tl$ work performed at the University of Washington.[9]

Footnotes and References

†Condensed in part from UCRL-19528, Jan. 1970.

*Present address: Rutgers–The State University, New Brunswick, New Jersey.

‡Present address: Institut de Physique Nucléaire, Orsay, France.

††Present address: Arkon Scientific Laboratories, Berkeley, California.

1. Nuclear Chemistry Annual Report, 1968, UCRL-18667, Jan. 1969, p. 121.
2. J. Solf, W. R. Hering, J. P. Wurm, and E. Grosse, Phys. Letters 28B, 413 (1969).
3. S. Hinds, R. Middleton, J. H. Bjerregaard, Ole Hansen, and O. Nathan, Nucl. Phys. 83, 17 (1966).
4. R. Moreh and A. Wolf, Phys. Rev. 182, 1236 (1969).
5. A. Covello and G. Sartoris, Nucl. Phys. A93, 481 (1967).
6. G. Vallois, J. Saudinos, and O. Beer, Phys. Letters 24B, 512 (1967).
7. R. Diamond (Lawrence Radiation Laboratory) and P. O. Tjøm, private communication.
8. C. Glashausser, B. G. Harvey, D. L. Hendrie, J. Mahoney, E. A. McClatchie, and J. Saudinos, Phys. Rev. Letters 21, 918 (1968).
9. W. R. Wharton, W. J. Courtney, and P. Richard, Phys. Rev. (to be published).

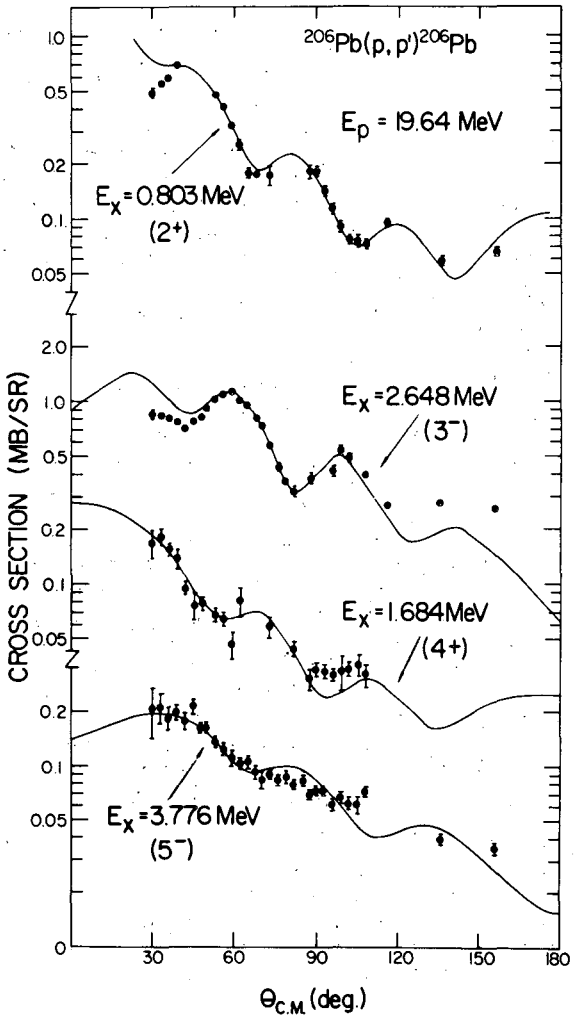

Fig. 1. Experimental differential cross sections for states of spin 2^+, 3^-, 4^+, and 5^- observed in the ^{206}Pb(p, p')^{206}Pb reaction. The solid curves are DWBA predictions.
(XBL701-221)

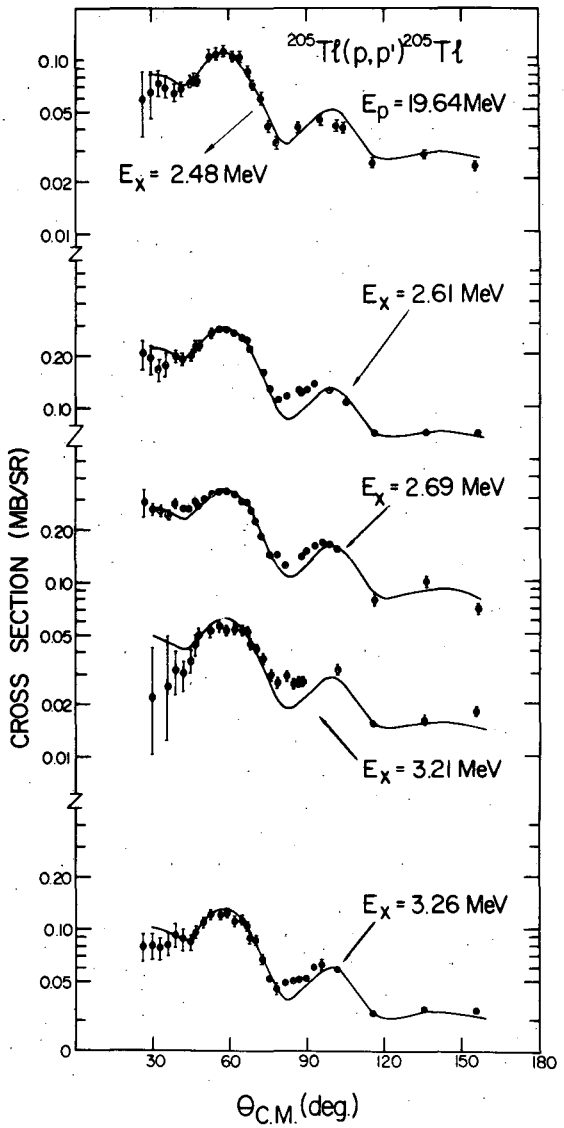

Fig. 2. Experimental differential cross sections for states in ^{205}Tℓ with L = 3 angular distributions. The solid curve has the shape of a smooth curve drawn through the data points for the 2.65-MeV (3^-) state in ^{206}Pb.
(XBL701-222)

A STUDY OF THE LOW-LYING STATES OF ^{207}Bi

E. A. McClatchie,† C. Glashausser,* and D. L. Hendrie

We have studied the (^{3}He, d) reaction at 35 MeV on both ^{206}Pb and ^{208}Pb over the angular range 13 to 40 deg lab. This reaction should populate the single proton states in ^{207}Bi and ^{209}Bi of the type ($n\ell j$), where ($n\ell j$) represents a proton in the Z = 82–126 shell. Also populated will be particle-core coupled states of appropriate spin and parity that might mix appreciably with the single-particle states. Since there are many more low-lying collective states in ^{206}Pb than in ^{208}Pb, one should certainly expect the (^{3}He, d) reaction on these nuclei to yield a much richer spectrum of states in ^{207}Bi than in ^{209}Bi. This was indeed found to be the case.

^{209}Bi Results

The (^{3}He, d) reaction predominantly populates only six states up to an excitation energy of 4 MeV, as shown in Fig. 1. These are the expected single-proton states $1h_{9/2}$, $2f_{7/2}$, $1i_{13/2}$, $2f_{5/2}$, $3p_{3/2}$, and $3p_{1/2}$, and lie at excitation energies of 0.0, 0.89, 1.60, 2.81, 3.10, and 3.61 MeV. Each state is populated with essentially the full spectroscopic strength, with the exceptions noted below.

(a) A state at 2.59 MeV, which is the $13/2^+$ member of the $h_{9/2}(3^-)$ septuplet, is weakly populated by the (^{3}He, d) reaction. This is no doubt due to a small admixture of $i_{13/2}$ single-particle component in the $13/2^+$ member of the collective multiplet.

(b) The $3p_{1/2}$ state at 3.61 MeV is now thought[1] to contain not all of the expected $p_{1/2}$ strength. A state at 4.4 MeV, some 50% as strong as the 3.61-MeV, is believed to account for the remainder of the $p_{1/2}$ strength.

^{207}Bi Results

The (^{3}He, d) spectrum on ^{206}Pb at 38 deg lab is shown in Fig. 1. Some 18 states are populated with significant cross sections up to an excitation energy of 3.5 MeV. This indicates that, as expected, the single-proton states are considerably more fragmented in ^{207}Bi than in ^{209}Bi. In a preliminary analysis of the ^{207}Bi data, we have used the ^{208}Pb(^{3}He, d)^{209}Bi angular distributions to assign spins and strengths to the stronger states in ^{207}Bi. The results are as follows:

(a) 0.9 ± 0.1 of the $h_{9/2}$ strength goes to the ^{207}Bi ground state.

(b) The $f_{7/2}$ strength goes to at least two states in ^{207}Bi. The fits to these states (0.99 and 0.75 MeV) are shown in Fig. 2. Together they account for 0.9 ± 0.1 of the $f_{7/2}$ strength.

(c) 0.9 ± 0.1 of the $i_{13/2}$ strength goes to the state at 1.6 MeV in ^{207}Bi.

(d) The $f_{5/2}$ strength goes to two or more states. Fits to the 2.78- and 2.93-MeV states are shown in Fig. 3. Together these account for 0.85 ± 0.1 of the $f_{5/2}$ strength.

(e) The states at 3.03, 3.13, 3.32, and 3.45 MeV all appear to have p-type angular distribution. No distinction can be made between $p_{3/2}$ and $p_{1/2}$. Together these four groups account for 0.7 ± 0.1 of the total p strength, indicating that some p strength is probably present in states at higher energy than 3.5 MeV.

Footnotes and Reference

†Present address: Arkon Scientific Laboratories, Berkeley, California.

*Present address: Rutgers–The State University, New Brunswick, New Jersey.

1. B. H. Wildenthal, B. M. Preedom, E. Newman, and M. R. Eates, Phys. Rev. Letters 19, 960 (1967).

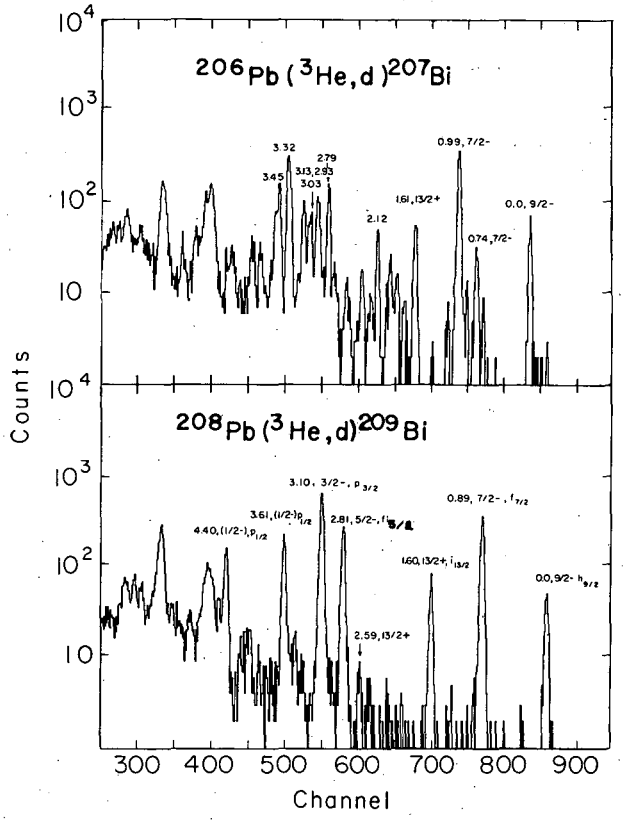

Fig. 1. (^{3}He, d) spectra from ^{206}Pb and ^{208}Pb at 38 deg lab. (XBL701-2263)

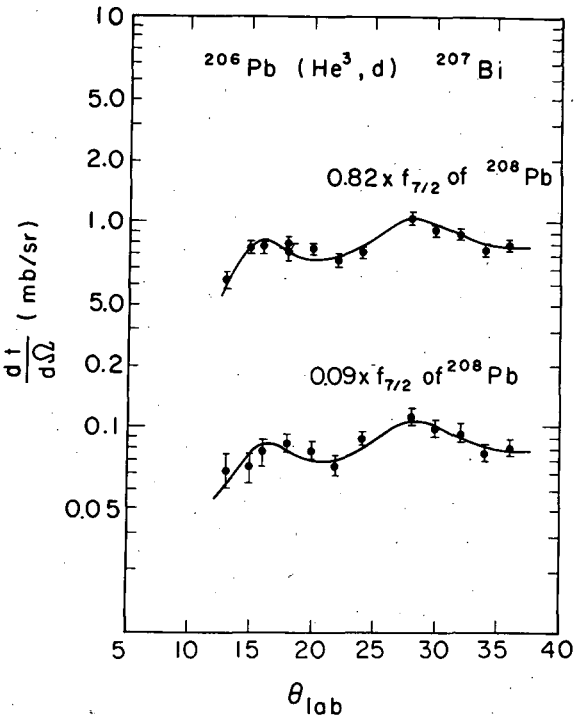

Fig. 2. Angular distributions of the ^{206}Pb (^{3}He, d) ^{207}Bi reaction to the 0.99- (upper points) and 0.75-MeV states. Curves are the ^{208}Pb(^{3}He, d) ^{209}Bi angular distribution to the $f_{7/2}$ single-particle state at 0.89 MeV. (XBL702-2328)

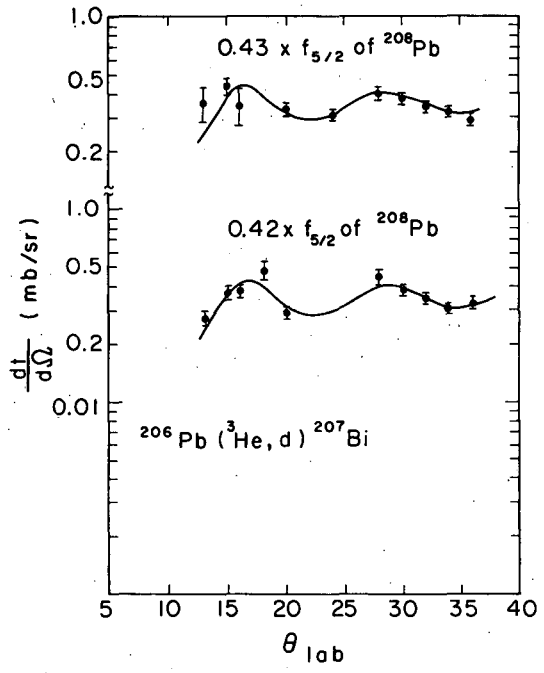

Fig. 3. Angular distributions of the ^{206}Pb(^{3}He, d) ^{207}Bi reaction to the 2.78- (upper points) and 2.93-MeV states. Curves are the ^{208}Pb(^{3}He, d)^{209}Bi angular distributions to the $f_{5/2}$ single-particle state at 2.81 MeV. (XBL702-2321)

STUDY OF THE $^{58}Ni(p, ^3He)^{56}Co$ REACTION AT 45 MeV

G. L. Bruge,† R. F. Leonard,* and M. S. Zisman

Among the odd-odd nuclei ^{56}Co is particularly interesting because it can be described in terms of a proton hole in the closed $f_{7/2}$ (Z = 28) shell and a single neutron outside the closed N = 28 shell. Although it cannot be studied by means of single-nucleon transfer experiments, it has been studied by more complex two-nucleon transfer reactions, $^{54}Fe(He^3, p)^{56}Co$ and $^{58}Ni(d,\alpha)^{56}Co$ (Refs. 1, 2) and the (^{3}He, t) (Refs. 3-6) charge-exchange reaction on ^{56}Fe. In these experiments the low-lying states were identified as nearly pure one-particle–one-hole states of the configuration $(1f_{7/2}^{-1})_p (2p_{3/2})_n$. Higher excited states [1.452 (0^+), 1.721 (1^+), 1.924 (3^+), 2.296 (2^+), 3.613 (0^+), and 4.450 (2^+)] are considered to be two-particle–two-hole states of the configuration $[(1f_{7/2}^{-2})_0 + (2p_{3/2})]_p (2p_{3/2})_n$. Of these latter six states, the lower four have been interpreted[2] as T = 1 antianalog levels and the upper two as T = 2 analogs of the ground and first excited state of ^{56}Fe. The previous work has also reported an unexpectedly large number of L = 2 transitions.

Observation of another 0^+ level at about 3.52 MeV has been reported,[1,3,4] and, more recently, in a paper by Dzubay et al.,[5] who studied the $^{56}Fe(^3He, t)^{56}Co$ reaction and discussed this level in terms of isospin mixing with the ground-state analog at 3.61 MeV. Moreover, $^{56}Fe(^3He, t)$ experiments done at Saclay[6] showed that, although some of the low-lying states in ^{56}Co gave angular distributions with expected shapes,[7] some also showed unexplainable patterns. The (p, ^{3}He) experiment reported here was done to obtain better knowledge of most of the levels of ^{56}Co, especially the low spin states.

The energy-analyzed 45-MeV proton beam of the 88-inch cyclotron has been used for this experiment. The outgoing particles were identified by an E-ΔE telescope followed by a Goulding-Landis identifier circuit. Angular distributions have been measured for 26 levels at excitation energies up to 5.2 MeV, at scattering angles between 14.5 and 76.8 deg c.m. A typical ^{3}He energy spectrum is shown in Fig. 1. The overall energy resolution (FWHM) is approximately 50 keV.

Some preliminary estimates of the angular momentum transfers have been made by comparing angular distributions with those of previously identified levels. In addition, DWBA calculations have been carried out, using Glendenning's table of structure amplitudes[9] and a modified DWUCK computer code.[10] For these calculations the ^{58}Ni ground state was described by Auerbach's wave function[11] and some of the ^{56}Co levels by the wave functions of Vervier.[12] Some of the results are shown in Fig. 2. The energies predicted by Vervier and the normalization factors N indicate the quality of the wave functions. The calculations are consistent with our preliminary L determinations and, in several cases, give the probable spin. Table I shows a summary of these results.

The first four excited states are not badly described, but there are many other problems. We have observed four L = 0 transitions at 1.444, 2.456, 3.501, and 3.587 MeV and two possible 1^+ transitions at 1.714 and 3.137 MeV. This is more than any simple model can explain.[13] The 3.501- and 3.587-MeV levels were extensively discussed when they were observed through the (^{3}He, t) reaction.[3,5] We can confirm that the 1.444-MeV level is a 0^+, but nothing is known about the level at 2.456 MeV. The nature of these levels requires further study. The 1.714-MeV level (a known 1^+ state)[2,8] is strongly excited in the $^{56}Fe(^3He, t)^{56}Co$ experiment,[6] but its angular distribution does not correspond to the usual 1^+ assignment. A similar behavior is observed in this work, where the 1.714- and 3.137-MeV states have similar angular distributions not characteristic of any single L value. Both are therefore considered possible 1^+ states.

In addition to the 3.587-MeV level, which is the T = 2 isobaric analog of the ^{56}Fe ground state, and L = 2 level has been observed at 4.432 MeV which is probably the analog of the first 2^+ level in ^{56}Fe. As expected, a large number of 2^+, 3^+, 4^+, and 5^+ levels have been observed. The cross section for the strongly excited 6^+ level observed at 2.271 MeV is reasonably well described[12] by a DWBA calculation using the simple configuration $(f_{7/2}^{-1})_p (f_{5/2})_n$. In addition, two strong levels are populated at 5.09 and 5.17 MeV, the latter being a possible 2^+. There is no indication of the nature of these two states.

The experimental results show that analysis of the ^{56}Co levels requires more detailed wave functions than are available at present. Further analysis is planned when such wave functions become available.

Table I. Energy levels observed in the $^{58}Ni(p, ^3He)^{56}Co$ reaction at 45 MeV. The cross sections have been integrated between 12.5 and 62.5 deg c. m. The L and J^π values as suggested in our work are given. The quoted J^π values marked by asterisks have been confirmed by DWBA calculation. The known J^π values are taken from Refs. 1, 2, 3, 5, 6, and 8. Also listed are the energies and J^π values predicted by Vervier and the corresponding normalization factors N.

Energy (MeV)	Integrated cross section (μb)	Probable L value	Suggested spin	Already known or suggested spin	Predicted energy(MeV) (Ref. 9)	Normalization factor N
0.0	9.79±1.68	4	4^{+*}	4^+	0.	11
0.166±0.010	15.8 ±1.9	2+4	3^{+*}	3^+	0.089	37
0.578±0.010	23.4 ±2.8	4+6	5^{+*}	5^+	0.531	24
0.84 ±0.015	3.75±1.25		5^{+*}		1.017	14
0.961±0.015	10.9 ±2.2	2	2^{+*}	2^+	0.784	16
1.001±0.015	14.4 ±2.9	2	3^{+*}		1.031	690
1.106±0.015	4.06±1.		4^{+*}		1.155	303
1.444±0.015	11.9 ±1.8	0	0^+	0^+		
1.714±0.015	5.67±1.56	0+2	1^+	1^+		
1.924±0.015	15.2 ±2.3	2	$2^+, 3^{+*}$	3^+	2.036	32
2.050±0.015	22.6 ±2.3	2	2^{+*}	2^+	2.063	143
2.220±0.015	4.49±1.12	3+4	3^+			
2.271±0.010	41.2 ±4.1	6	6^{+*}		2.383	56
2.371±0.015	7.61±2.3	4	4^+		2.342	23
2.456±0.015	12.8 ±2.2	0	$0^+, 1^+$			
2.626±0.015	11.8 ±2.		$2^+, 3^+$			
2.734±0.015	9.54±1.68		$1^+, 3^+$			
2.946±0.020	2.2 ±0.94					
3.048±0.020	9.8 ±1.7					
3.137±0.015	14.3 ±2.3	0+2?	1^+?		3.154	730
3.396±0.015	9.42±1.9	2+4	3^+			
3.501±0.015	15.7 ±3.4	0	$0^+, 1^+$	$0^+, 1^+$		
3.587±0.015	19.5 ±3.7	0	0^+	0^+		
4.432±0.020	15.8 ±2.4	2	2^+	2^+		
5.090±0.020	51.4 ±6.4					
5.187±0.020	15.4 ±6.2	2	2^+?			

Footnotes and References

†NATO Fellow on leave from CEN, Saclay, France.

*On leave from NASA Lewis Research Center, Cleveland, Ohio.

1. T. A. Belote et al., Nucl. Phys. A109, 666 (1968).
2. J. M. Laget and J. Gastebois, Nucl. Phys. A122, 431 (1968).
3. P. G. Roos and C. D. Goodman, in Proceedings of the Second Conference on Nuclear Isospin, Asilomar, 1969 (Academic Press, New York, 1969, p. 297.
4. F. D. Bechetti et al., ibid, p. 171.
5. T. G. Dzubay et al., Isospin Mixing for Bound States in ^{56}Co and ^{58}Co, Princeton University Report PUC 937-361.
6. G. Bruge et al., Bull. Am. Phys. Soc. 14, 1208, AE7 (1969).
7. G. Bruge et al., Nucl. Phys. A129, 417 (1969).
8. C. M. Lederer et al., Table of Isotopes (Sixth Edition) (John Wiley & Sons, New York, 1967).
9. N. K. Glendenning, Table of Structure Amplitudes for the (p, ^{3}He) Reactions, UCRL-18269, Aug. 1968.
10. We are indebted to J. C. Hardy for providing us the DWUCK code that he has adapted for the two-nucleon transfer, and for his help in the calculations. We also thank P. D. Kunz for making the code available.
11. N. Auerbach, Nucl. Phys. 76, 321 (1966).
12. J. Vervier, Nucl. Phys. 78, 497 (1966), and private communications.
13. See G. Bruge et al., Study of the $^{58}Ni(p,t)^{56}Ni$ Reaction, following report.

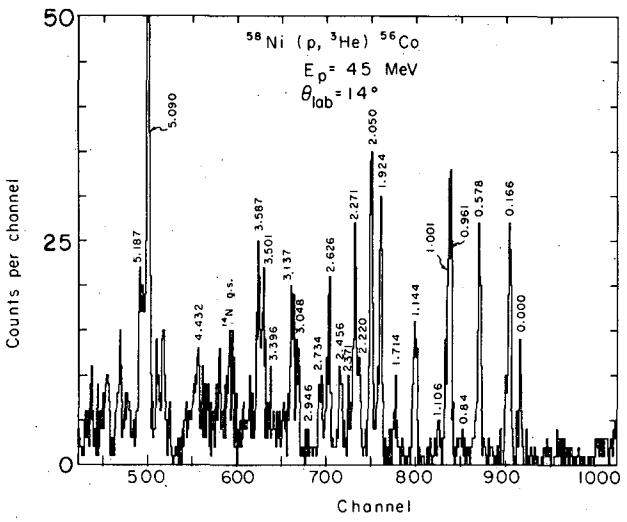

Fig. 1. Experimental spectrum observed for the ^{58}Ni(p, ^{3}He)^{56}Co reaction at 14 deg E_p = 45 MeV. (XBL701-2179)

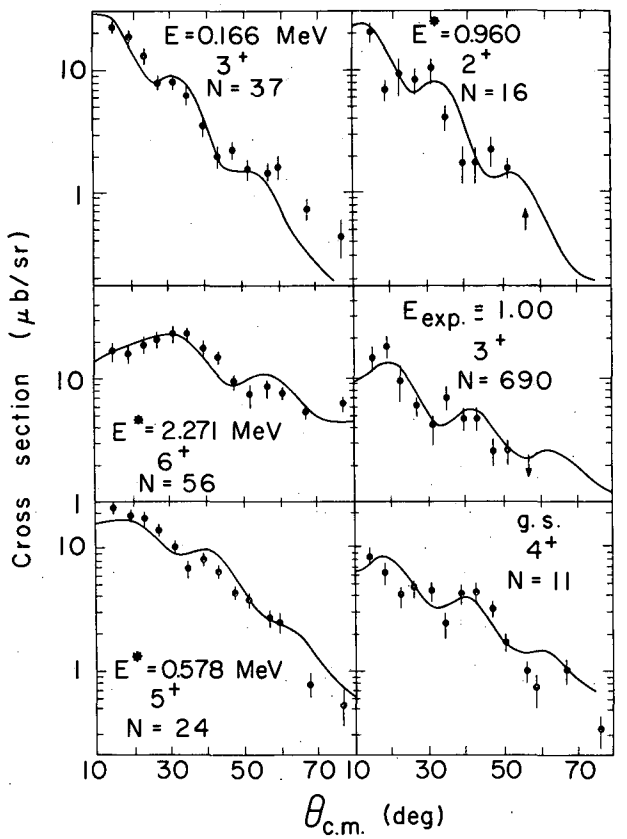

Fig. 2. Some examples of fits obtained as explained in the text. N is the normalization factor of the calculated curve (full line) to the experimental points. (XBL701-2178)

THE ^{58}Ni(p, t)^{56}Ni REACTION AT 45 MeV, COMPARISON WITH THE ^{58}Ni(p, ^{3}He)^{56}Co REACTION

G. L. Bruge,† R. F. Leonard,* and M. S. Zisman

The ^{58}Ni(p, t)^{56}Ni reaction was studied with the 45-MeV proton beam from the 88-inch cyclotron. The triton spectra were obtained simultaneously with the ^{3}He spectra discussed in the preceding paper in this report.[1] Figure 1 shows a typical triton spectrum. The energy resolution (FWHM) is about 40 keV. We have observed 25 levels in a 9-MeV energy range, and we have measured angular distributions for 21 of them.

In Table I we give, as for the (p, ^{3}He) experiment, a summary of our results. It should be noted that most of the energies we give in Table I differ systematically from these determined in Ref. 2 by about 50 keV. Our calibration, which includes the contaminant peak from the ^{16}O(p, t)^{14}O reaction, gives good agreement with the previous energy determinations[3,4] for the first few states in ^{56}Ni, and is also consistent with our (p, ^{3}He) calibration.[1] In the same way as for the (p, ^{3}He) experiment, a preliminary determination of the angular momentum of the transferred neutron pair has been made, using a set of "typical curves" corresponding to several levels previously identified by Davies et al.[2] These empirical assignments have been further confirmed by a set of rough calculations involving simple configurations for several excited states,[5] using Glendenning's tables of structure amplitudes.[6]

Table I. Energies, cross sections (integrated from 12.5 to 62.5 deg c.m.), and suggested spins for excited states of ^{56}Ni. For comparison the results of Davies et al. (Ref. 2) are given.

Energy (MeV)	Possible L	Suggested J^{π}	Integrated cross sections (μb)	Levels observed in Ref. 2: Energy (MeV)	Levels observed in Ref. 2: J^{π}
0.0	0	0^+	192±19	0	0^+
2.697±0.014	2	2^+	23.6 ±2.8	2.64	2^+
3.956±0.014	4	4^+	37.1 ±4.1	3.90	4^+
5.000±0.020	0	0^+	6.49±1.50	4.95	0^+
5.339±0.019	2	2^+	12.7 ±1.7	3.33	(2^+)
5.483±0.024	(3)	(3^-)	4.80±1.12		
5.989±0.020	4	4^+	7.48±1.37	5.90	4^+
6.222±0.026	2, 1	$2^+, 1^-$	2.24±0.74		
6.318±0.028	4	4^+	5.80±1.25	6.38	4^+
6.419±0.015	4	4^+	17.5 ±1.93		
6.554±0.018			21.4 ±2.55	6.58	0^+
6.644±0.019	0	0^+	16.8 ±2.12		
7.021±0.026	2	2^+	4.36±1.0	7.00	
7.170±0.027	1	1^-	6.99±1.37	7.12	1^-
7.289±0.025			7.55±1.50		
7.455±0.017	2	2^+	43.4 ±4.3	7.42	2^+
7.567±0.018	3	3^-	25.7 ±2.55	7.56	3^-
7.653±0.031			6.99±1.37		
7.788±0.024			5.86±1.75		
7.912±0.040	0	0^+	2.52± .27	7.92	0^+
8.082±0.100				(8.09)	
8.654±0.020				8.48	2^+
8.771±0.026					
8.896±0.020					

Our results can be compared to those of Davies et al.[2] We can confirm most of their strongly excited levels; however, our better resolution allowed us to split some of them. In addition, four new levels have been observed at 5.483, 6.222, 7.289, and 7.788 MeV. All of them are weakly excited. The 5.483-MeV level has an angular distribution which suggests a 3^- assignment. A study of (α,α') systematics[7] in the Ni isotopes indicates that the first 3^- state in ^{56}Ni should be at about 5 MeV excitation. If this tentative assignment is correct it will be necessary to find another interpretation for the 3^- state observed previously at 7.56 MeV[2] and found at 7.567 MeV in this work. The level at 6.222 MeV is either 1^- or 2^+. The last two do not display classifiable angular distributions.

A 6.38-MeV level has been identified by Davies et al. as the isobaric analog state of the T = 1 ^{56}Co ground state.[2] In this work two levels have been observed, at 6.318 and 6.419 MeV, both displaying L = 4 angular distributions. The analog state is expected at 6.424 MeV,[8] and can be identified with the stronger 6.419-MeV state within the limits of the various errors.

Davies's 6.58-MeV level is split into the 6.552- and 6.641-MeV states. The angular distribution for the 6.641-MeV state is compatible with an L = 0 transition. Taking into account the experimental errors, the 6.552-MeV level could be the isobaric analog of the 0.166-MeV level of ^{56}Co, whose spin (3^+) is reasonably well established.[1] This seems unlikely, however, since excitation of a 3^+ level is forbidden by the selection rules for (p, t) reactions, and the 6.641-MeV state is relatively strongly excited.

We have tried to study the parentage of possible pairs of analog states, using the method of J. C. Hardy et al.[9] Table II gives the values of the ratio $R = (d\sigma/d\Omega)(p,t)/(d\sigma/d\Omega)(p,{}^3He)$, taken at the first measured maximum of the angular distributions. The calculated ratio is $R_{cal} = (k_t/k_{^3He})\,(2/T_f)$, where $T_f = 1$. This relationship is valid only if all the transferred nucleons are picked up from the same orbit.

The experimental and calculated values agree for the first and third cases. The 2^+ levels are not easily compared, since the angular distributions are somewhat different, suggesting that they are not analog states. The experimental ratio for the 0^+ pair agrees very well with the calculated ratio. This would be expected for a 0^+ T = 1 two-particle–two-hole state, the description suggested for the 1.444-MeV state in ^{56}Co. However, a more detailed calculation is necessary to determine the exact nature of the T = 1 state in ^{56}Ni. Such calculations are planned for this as well as for the other levels in ^{56}Ni.

Table II. Ratio of (p, t) to (p, ^{3}He) cross sections for the three possible pairs of analog states observed in this work.

Level energy (MeV)				
^{56}Ni	^{56}Co	J^π	R	R_{cal}
6.419	0.	4^+	1.55	1.73
7.445	0.96	2^+	2.5	1.70
7.908	1.444	0^+	1.72	1.67

Footnotes and References

†NATO Fellow, on leave from CEN, Saclay, France.

‡On leave from NASA Lewis Research Center, Cleveland, Ohio.

1. G. L. Bruge et al., Study of the ^{58}Ni(p, ^{3}He)^{56}Co reaction at 45 MeV, preceding report.
2. W. G. Davies et al., Phys. Letters 27B, 363 (1968), and included experimental references.
3. C. G. Root et al., Nucl. Phys. 71, 449 (1965).
4. R. G. Miller and R. W. Kavanagh, Nucl. Phys. A94, 261 (1967).
5. J. C. Hardy's modified version of the code DWUCK has been used. We are grateful to him for helping in the calculation and to P. D. Kunz for furnishing the code originally.
6. N. K. Glendenning, Tables of Structure Amplitudes for (p, t) Reactions, UCRL-18268, June 1968.
7. G. Bruge et al., 44-MeV α-Particle Scattering on Even-Even Spherical Nuclei Near Closed Shells and Nuclear Structure of Collective States, Nucl. Phys. (to be published).
8. R. Sherr, Phys. Letters 24B, 321 (1967).
9. J. C. Hardy et al., Phys. Rev. Letters 22, 1939 (1969).

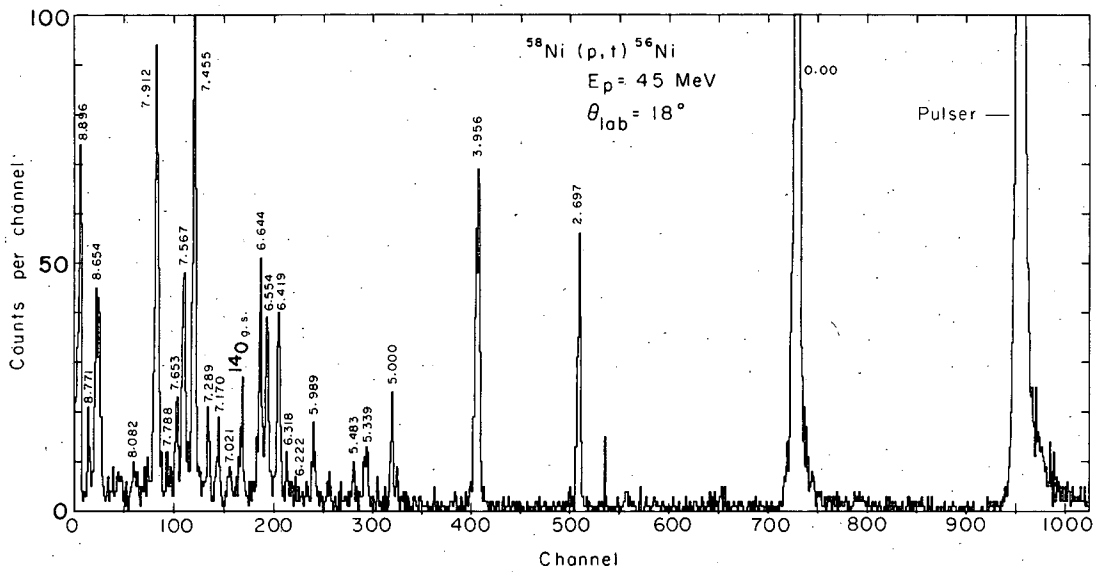

Fig. 1. Observed experimental spectrum for the ^{58}Ni(p, t)^{56}Ni reaction at 18 deg. (XBL701-2177)

A SEARCH FOR HIGH-SPIN STATES IN THE A = 90 REGION

M. S. Zisman, E. A. McClatchie,† and B. G. Harvey

In recent years a search for high-spin levels has been carried out at the 88-inch cyclotron.[1-3] The technique used is to observe the states which are strongly populated in the (α, d) reaction at α-particle energies in the range of 40 to 50 MeV. This reaction has previously proven its usefulness in selectively populating high-spin states in light nuclei,[1,3] and the trend has been shown to continue in the medium-mass ($54 \leq A \leq 70$) region.[2,3]

Up to this point, the high-spin states were always of the same type, namely

$$\left[(\vec{J}_i, \vec{T}_i) + (\vec{j}, \vec{t})^2_{J=2j,\, T=0}\right]_{\vec{J}_f,\, \vec{T}_f = \vec{T}_i},$$

where J_i, T_i are the spin and isospin of the target, j, t are the spin and isospin of the shell-model state into which the stripped nucleons are captured, and J_f, T_f are the spin and isospin of the final state. When $J_i \neq 0$, more than one state of this structure can be formed (due to the vector coupling $\vec{J}_f = \vec{J}_i + \vec{J}$) and multiplets have been observed.[1,3] However, as the target mass increases the proton-neutron configurations for low-lying states are no longer of the $(j)^2$ type, since the particles are filling different shell-model states. Thus, the most likely high-spin levels will now be of the $(j_1, j_2)_{J=j_1+j_2}$ type.

It is worthwhile to mention again the reasons for the strong population of such high-spin states with the (α, d) reaction. First of all, the cross section for a high-spin state is enhanced relative to that for a lower-spin state by the statistical factor $2J + 1$. Second, the kinematics of the (α, d) reaction favors a large angular momentum transfer. By this we mean that $\vec{Q} \times \vec{R}\,[= |\vec{k}_i - \vec{k}_f| \times \vec{R}]$, the "classical" angular momentum transfer at the nuclear surface, is large. For the ^{90}Zr(α, d)-^{92}Nb (g. s.) reaction at $\theta = 0$ deg and $E_\alpha = 40$ MeV, $\vec{Q} = 1.1$ and $\vec{Q} \times \vec{R} \approx 8$. This indicates a preference for populating states which require an $L \approx 8$ transfer. The third reason concerns the general tendency of all two-nucleon transfer reactions to exhibit a selectivity based on the degree to which the transferred nucleons are correlated in the nucleus. In particular, the (α, d) reaction shows a preference for populating states which look very much like a deuteron coupled to an

unperturbed target core. This implies a wave function for the two transferred particles which has large amounts of triplet spin orientation and $\ell = 0$ (i.e., no relative angular momentum of the particles about their center of mass). This selectivity has been treated quantitatively by Glendenning.[4] In his notation, the preferred states are those which have a large "structure factor," G_{NLSJT}. This factor too can be seen to favor high-spin states of the type mentioned above (see Ref. 5).

The A = 90 mass region was selected for this study because it is near the N = 50 closed shell, where the shell-model concept is useful. The two targets used in the initial experiment (at $E_\alpha = 40$ MeV) were ^{88}Sr and ^{90}Zr. In this region the high-spin shell-model configurations which might be expected to be preferentially populated are (suppressing radial quantum numbers) $(g^{\pi}_{9/2}, d^{\nu}_{5/2})_{7+}$, $(g^{\pi}_{9/2}, g^{\nu}_{7/2})_{8+}$, $(g_{7/2})^2_{7+}$, and $(d_{5/2})^2_{5+}$. The picture is simplified somewhat by the fact that the state of configuration $(g^{\pi}_{9/2}, d^{\nu}_{5/2})_{7+}$ is known[6,7] in both final nuclei. This gives an immediate test of whether the (α, d) reaction will still selectively populate such high-spin states in this mass region. As can be seen in Figs. 1 and 2, the 7+ member of the $(g^{\pi}_{9/2}, d^{\nu}_{5/2})$ multiplet is selected in both cases. Also, in each spectrum there is one other level [$E^*(^{90}Y) = 3.11$ MeV, $E^*(^{92}Nb) = 2.58$ MeV] whose cross section is comparable to that of the $(g^{\pi}_{9/2}, d^{\nu}_{5/2})_{7+}$ state.

The problem of discriminating among the various possible configurations for these higher excited states is a difficult one. We hope to be able to observe this state in other nuclei in this mass region and establish systematic trends in its population. This should give some insight into the correct configuration involved, as it has in other regions of the periodic chart.[1-3]

Footnote and References

†Present address: Arkon Scientific Laboratories, Berkeley, California.

1. E. Rivet, R. H. Pehl, J. Cerny, and B. G. Harvey, Phys. Rev. 141, 1021 (1966).
2. C. C. Lu, M. S. Zisman, and B. G. Harvey, Phys. Letters 27B, 217 (1968).
3. C. C. Lu, M. S. Zisman, and B. G. Harvey, Phys. Rev. 186, 1086 (1969).
4. N. K. Glendenning, Phys. Rev. 137, B102 (1965).
5. N. K. Glendenning, Tables of Structure Amplitudes for (α, d) Reactions, UCRL-18270, Aug. 1968.
6. J. B. Ball and M. R. Cates, Phys. Letters 25B, 126 (1967).
7. W. L. Alford, D. R. Koehler, and C. E. Mandeville, Phys. Rev. 123, 1365 (1961).

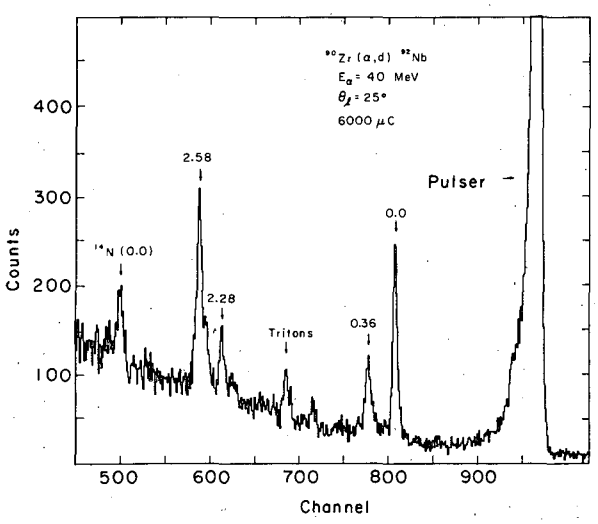

Fig. 1. Deuteron energy spectrum from the $^{90}Zr(\alpha, d)^{92}Nb$ reaction at $E_\alpha = 40$ MeV and a scattering angle of 25 deg (lab). Excitation energies are given in MeV. (XBL6912-6379)

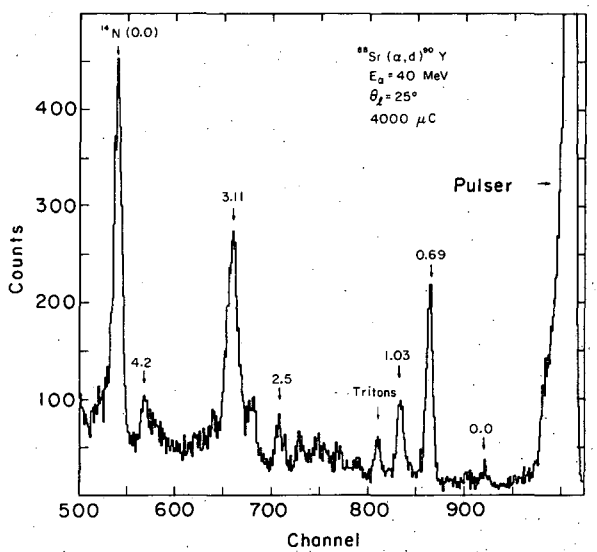

Fig. 2. Deuteron energy spectrum from the $^{88}Sr(\alpha, d)^{90}Y$ reaction at $E_\alpha = 40$ MeV and a scattering angle of 25 deg (lab). Excitation energies are given in MeV. (XBL6912-6378)

EXCITED STATES OF ^{54}Fe †

J. M. Moss,* C. Glashausser,‡ D. L. Hendrie, and J. Thirion*

Among the large amount of theoretical and experimental effort to determine the range of validity of the nuclear shell model, considerable recent interest has been aroused[1] in the purity of shell closure at ^{56}Ni (Z = 28, N = 28). The solution to problems like this lies in large measure in determination of the properties of excited states in nuclei 1 or 2 nucleons removed from the proposed closed shell, such as ^{54}Fe in this case (Z = 26, N = 28). The absence of suitable targets prevents single-nucleon transfer reactions leading to ^{54}Fe. Attempts to investigate the states of ^{54}Fe by inelastic scattering have been partially foiled by the large number of close-lying, and hence unresolvable, multiplets in the spectrum. We have avoided these problems by investigating the states of ^{54}Fe by means of an $^{54}Fe(p, p'\gamma)$ prompt coincidence experiment in the standard collinear geometry,[2] using the resolving power of Ge(Li) gamma detectors to separate the multiplets. Crucial to success of the experiment was the manufacture of a large-volume Ge(Li) detector of high efficiency by the Nuclear Instrumentation Group.

Previous to the coincidence experiment, a (p, p') excitation function was measured; from this we ascertained that a beam energy of 10 MeV best avoided experimental problems due to compound nuclear resonances. For coincidence counting, the scattered protons were detected in an annular Si(Li) counter which subtended an angular range of 168 to 172 deg. The beam was prepared by accelerating 20-MeV H_2^+ ions in the 88-inch cyclotron and energy-analyzing them with a bending magnet and a slit of small aperture. Ions scattered from the slit would be degraded to H^+ ions, and were removed from the beam by a second magnet well removed from the target area. The beam was then focused through the annular counter onto a self-supporting isotopically enriched ^{54}Fe metal foil and then collected and measured in a well-shielded Faraday cup. Deexcitation γ rays were measured in a movable 40-cm^3 cylindrical drifted Ge(Li) counter with experimental resolution of 6 keV. Data were taken at five angles from 25 to 90 deg. The gamma detector was calibrated for energy and efficiency with standard γ-ray sources from IAEA and a ^{56}Co source.

Signals from the counters were prepared by Goulding-Landis high-rate amplifier-pileup rejector systems.[3] Fast coincidences were determined by a time-to-amplitude conversion technique; the apparatus was arranged to provide four additional time peaks for analysis of chance events. Time resolution was 23 nsec, well within the cyclotron repetition time of 142 nsec. Coincident proton and gamma signals were analyzed by a multiplexed Robinson 4000-channel ADC[4] into an on-line PDP-5 computer, and then onto magnetic tape for later data extraction. Calibrated and synchronized pairs of pulses were fed into the preamplifiers and continued through the remaining system exactly as real events; from these we could detect gain shifts (none were found), monitor electronic efficiency, and measure dead-time effects. A proton monitor counter was used throughout to check beam energy shifts and Faraday cup normalization. The gamma counter position was moved hourly to reduce possible systematic errors; a total of 10 hours of data was taken at each of the five positions.

Contributions of chance events in the spectra were analyzed by evaluating four "chance" peaks in the time spectrum. This result was checked by comparison with the gamma spectrum produced by coincidences (necessarily chance) with elastically scattered protons; the two methods gave statistically identical results. A gamma spectrum corresponding to each proton group was then produced; a typical spectrum is shown in Fig. 1. The angular distribution for each gamma decay from each excited state of ^{54}Fe was then generated; the full-energy peaks and escape peaks from the spectra were used. The decay scheme and branching ratios obtained for states up to 5 MeV are shown in Fig. 2.

Because of the simplifications in nuclear alignment resulting from the standard collinear geometry, parameters involving the excitation mechanism can be removed from the analysis of the angular distributions. Each decay can then be analyzed for spectroscopic content, viz, spin of initial and final states and the mixing ratio between the two lowest multipolarities (usually M1 and E2) in the gamma decay. Warburton et al. have provided a program that statistically analyzes each decay in terms of these parameters.[5] A typical analysis, showing χ^2 as a function of the mixing ratio for several choices of initial spin, is shown in Fig. 3, along with the predicted gamma angular distributions plotted with the data. Table I gives a summary of the results of this analysis.

Further, we could measure the lifetimes of many of the states by the Doppler-shift attenuation method, the stopping medium for the recoiling nucleus being the target itself. Estimates of the

stopping power of Fe in Fe are taken from the literature.[6] Figure 4 shows a sample datum; the results for all states are given in Table II.

The sum total of these data are ample to provide severe restrictions on possible descriptions of the levels. Only a qualitative discussion will be given here in terms of states expected if one assumes that ^{56}Ni is a good doubly magic core. First one expects a 0+ 2+ 4+ 6+ multiplet due to recoupling of the two $f_{7/2}$ proton holes: the 0.0-, 1.409-, 2.540-, and 2.948-MeV states are obvious choices. Secondly, the excitation of an $f_{7/2}$ nucleon to the next highest $p_{3/2}$ orbital should yield four states; based on levels in ^{56}Co they should be from the lowest, 4+, 3+, 5+, and 2+, and spread over about 1 MeV. Likely candidates are the 3.296-, 3.345-, 4.029-, and possibly the 4.700-MeV levels, based both on energy systematics and on the decay data. The two-particle–two-hole band of ^{56}Ni can be estimated from a model of Bansal and Franch[7] to start about 2.5 MeV; candidates for the 0+, 2+, and 4+ members are the 2.564-, 2.959-, and 3.838-MeV states. On the other hand, Auerbach[8] calculates an $[(f_{7/2})^3_{3/2}, p_{3/2}]_{0+}$ state at 2.53 MeV, providing an alternative explanation for the 2.564-MeV state. However, decay rates indicate that in no case can the configurations be as pure as the above discussion would indicate, nor does this scheme explain other known states, such as the 2+ level at 3.164 MeV.

Footnotes and References

†Condensed in part from Joel M. Moss, In-Beam Proton-Gamma Ray Coincidence Studies Using a Large Coaxial Ge(Li) Detector (Ph. D. Thesis), UCRL-18902, April 1969.

*Present address: CEN, Saclay, France.

‡Present address: Rutgers–The State University, New Brunswick, New Jersey.

1. For example, L. Zamick, Is Ni^{56} a Good Closed Shell?, UCRL-18406, Aug. 1968; P. Goode and L. Zamick, Phys. Rev. Letters 22, 958 (1969).
2. A. E. Litherland and A. J. Ferguson, Can. J. Phys. 39, 788 (1961).
3. F. S. Goulding, D. A. Landis, and R. H. Pehl, The Design and Performance of a High-Resolution High-Rate Amplifier System for Nuclear Spectrometry, UCRL-17560, May 1967.
4. L. B. Robinson, F. Gin, and F. S. Goulding, A High-Speed 4096-Channel Analogue-Digital Converter for Pulse-Height Analysis, UCRL-17419, Jan. 1968.
5. A. R. Poletti and E. K. Warburton, Phys. Rev. 137B, 595 (1965).
6. J. Linhard, M. Scharff, and H. E. Schiott, Kgl. Danske Videnskab. Selskab Mat.-Fys. Medd. 33, No. 14 (1963); P. G. Steward and R. Wallace, Calculations of Stopping Power and Range-Energy Values for Any Heavy Ion in Nongaseous Media, UCRL-17314, Dec. 1966.
7. R. K. Bansal and J. B. French, Phys. Letters 11, 145 (1964); L. Zamick, Phys. Letters 19, 580 (1965).
8. N. Auerbach, Phys. Letters 24B, 260 (1967).

Table I. Multipole mixing ratios for transitions in ^{54}Fe.

Level	E_γ (MeV)	$J_i \rightarrow J_f$	(E2/M1)
2.959	1.550	2 → 2	$0.105 \pm^{0.040}_{0.042}$
3.164	1.755	2 → 2	$0.63 \pm^{0.57}_{0.25}, \delta \geq 2.4$
			$\delta \leq -10$
3.296	0.756	4 → 4	$-1.1 \leq \delta \leq -0.67$, $-0.24 \leq \delta \leq 0.18$
	0.756	3 → 4	$0.38 \leq \delta \leq 1.66$
	1.887	3 → 2	$-12 \leq \delta \leq -0.25$
3.345	0.806	3 → 4	$0 \pm 0.14, \delta \geq 3.5$
	1.936	3 → 2	$-0.65 \pm^{0.18}_{2.25}$
4.029	0.733	5 → 4	0.27 ± 0.07
	0.733	3 → 4	$-1.2 \pm^{0.82}_{1.5}$
	0.733	4 → 3	0.27 ± 0.09
	0.733	2 → 3	$-9 \leq \delta \leq -0.43$
4.048	0.703	2 → 3	$-2.75 \leq \delta \leq -0.38$
	0.703	4 → 3	0.23 ± 0.09
4.074	2.665	3 → 2	$1.88 \pm^{0.50}_{0.44}$
4.265	1.725	3 → 4	$0.81 \pm^{0.73}_{0.39}$
	1.725	4 → 4	-0.53 ± 0.24
4.287	2.879	1 → 2	All values of δ
	2.879	2 → 2	$0.40 \pm^{0.07}_{0.04}, \delta \leq -14$
	2.879	3 → 2	$-0.16 \pm^{0.05}_{0.01}$
4.579	3.170	2 → 2	$-0.105 \pm 0.09, -1.8 \pm 0.5$
4.781[a]	3.372	3 → 2	-0.018 ± 0.026
4.949	2.409	4 → 4	$-0.36 \pm^{0.2}_{0.3}$

a. This state is known to have negative parity, thus the mixing ratio is δ(M2/E1).

Table II. Mean lifetimes for states in ^{54}Fe from the Doppler-shift attenuation analysis.

Level	E_γ (MeV)	τ (psec)
1.409	1.409	$1.1 \pm^{0.50}_{0.32}$
2.540	1.131	≥ 3
2.564	1.155	≥ 2
2.948	0.408	≥ 0.8
2.959	1.550	0.075 ± 0.012
	2.959	
3.164	3.164	$0.23 \pm^{0.05}_{0.04}$
3.296	1.887	≥ 3
3.345	1.936	≥ 3
3.838	2.429	0.091 ± 0.02
4.029	0.733	≥ 1
4.048	2.639	$0.44 \pm^{0.34}_{0.15}$
4.074	2.665	0.084 ± 0.025
4.265	1.725	$0.119 \pm^{0.033}_{0.025}$
4.287	2.878	$0.080 \pm^{0.024}_{0.020}$
4.579	3.170	≤ 0.01
4.656	1.360	-
4.700	1.355	-
4.781	3.372	0.048 ± 0.016
4.949	2.409	0.042 ± 0.015

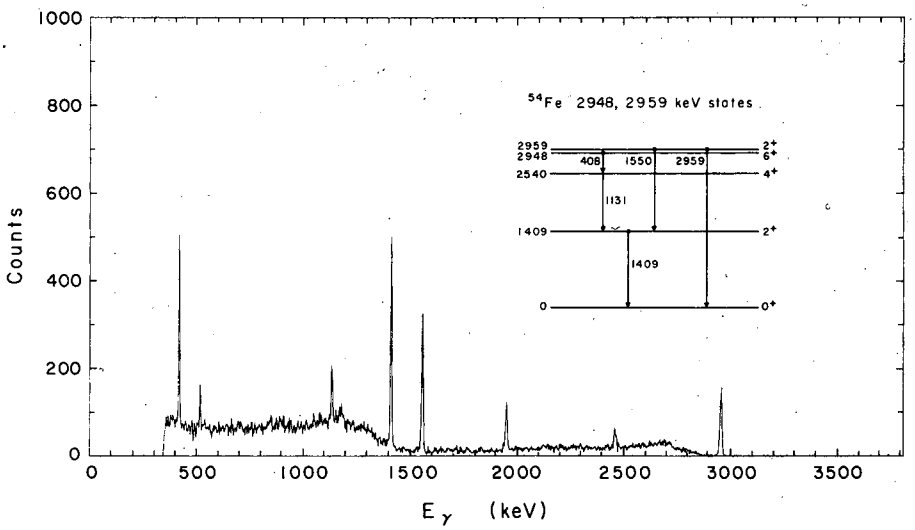

Fig. 1. γ-Ray coincidence spectrum for the 2.948- and 2.959-MeV states of ^{54}Fe (unresolved in the proton spectrum) at θ_γ = 55 deg. (XBL691-1763)

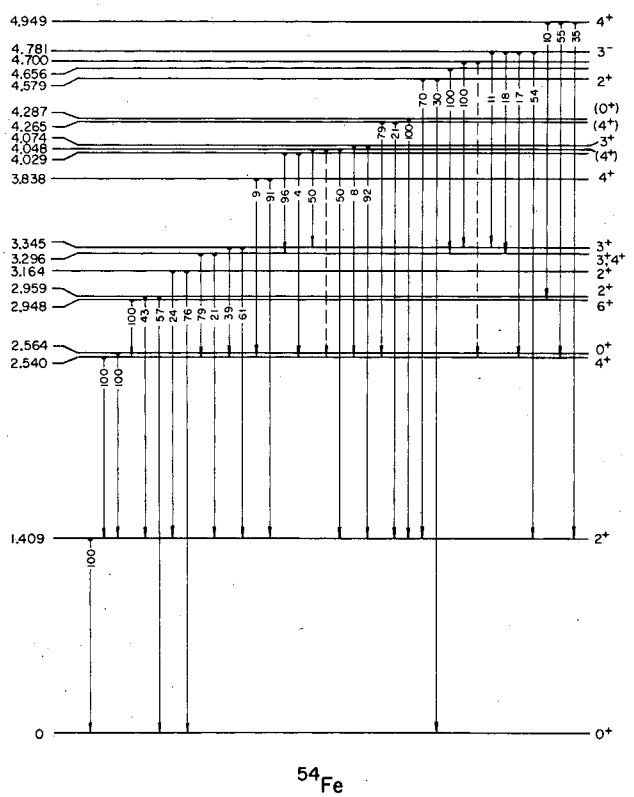

Fig. 2. Levels of ^{54}Fe below 5 MeV. The branching ratios were derived in this experiment. The spin assignments include those from previous work and from this experiment. (XBL693-2241)

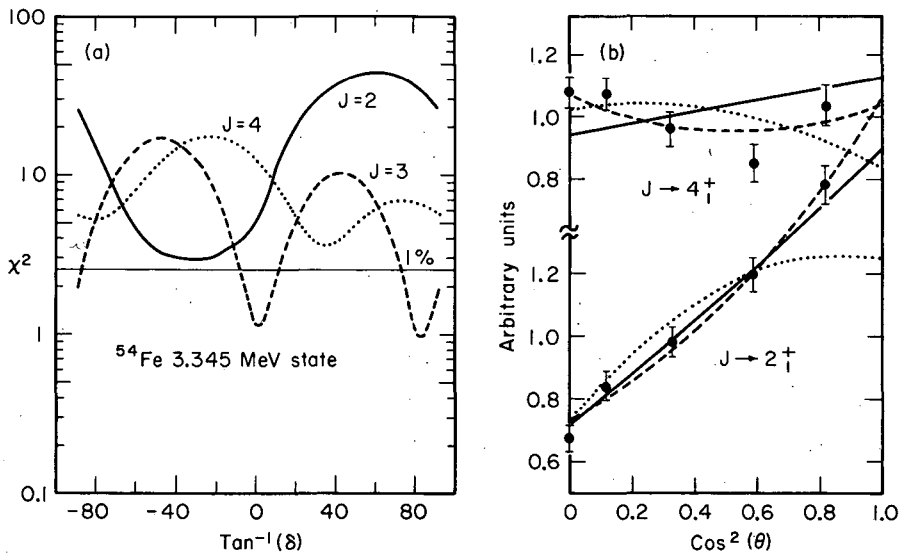

Fig. 3. χ^2 analysis for the 3.345-MeV state of ^{54}Fe and best fits to the angular correlations for each initial spin. The $J_i \rightarrow 4_1^+$ and $J_i \rightarrow 2_1^+$ angular correlations were analyzed simultaneously. The variables displayed explicitly are as follows: for $J_i = 4$, $\delta(4 \rightarrow 2)$ is chosen to be zero and $\delta(4 \rightarrow 4)$ is shown; for $J_i = 3$, $\delta(3 \rightarrow 2)$ is chosen to be zero and $\delta(3 \rightarrow 4)$ is shown; for $J_i = 2$, $\delta(2 \rightarrow 4)$ is chosen to be zero and $\delta(2 \rightarrow 2)$ is shown. (XBL692-2106)

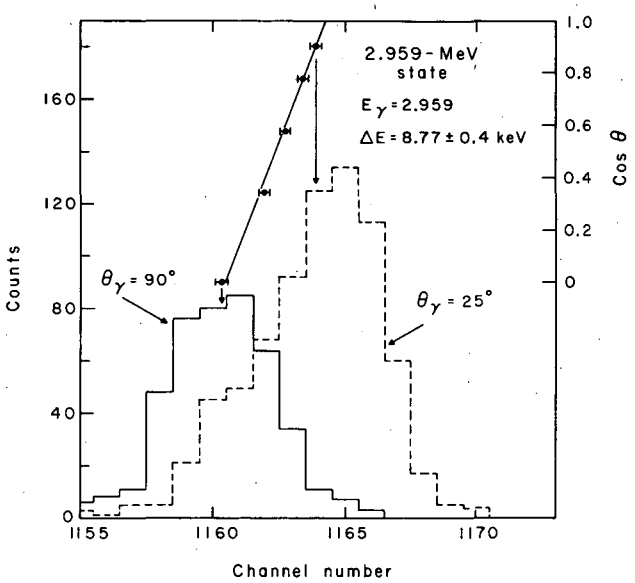

Fig. 4. Summary of the Doppler-shift analysis for the 2.959-MeV state (2.959-MeV γ ray). The FE γ-ray peaks at θ_γ = 90 deg and θ_γ = 25 deg are shown. Shown on the same channel scale is the best-fit line to the centroids of all five gamma angles. The form of the line was $E_0 + \Delta E_{obs} \times \cos\theta_\gamma$. (XBL693-2235)

Nuclear Theory

GENERALIZATION OF THE THEORY OF STRIPPING REACTIONS TO INCLUDE INELASTIC PROCESSES†

R. J. Ascuitto* and Norman K. Glendenning

The usual distorted-wave Born approximation (DWBA) for transfer reactions makes three basic assumptions. First, it assumes that the transfer takes place directly from the elastic entrance channel to the residual channel. Only the transferred particles are treated explicitly, while all the others, which we shall refer to collectively as the core, are regarded as passive. The reaction is assumed to proceed only to the extent that the core state is unchanged. Second, it assumes that the elastic optical potential provides wave functions for the relative motion that are good inside the nucleus, or at least in the surface region, since this is where the transfer process is concentrated. Third, it assumes that the transfer process itself is weak, so that it can be treated in first order. With these assumptions the transition amplitude can be computed for (d, p) reactions from

$$T_{p,d} = \int \psi_p^{(-)*} \langle \phi_p(A+1) | V_{np} | \phi_d(A) \rangle \, \psi_d^{(+)} \, d\underset{\sim}{r}_n \, d\underset{\sim}{r}_p , \tag{1}$$

where ψ_d and ψ_p are distorted waves describing only the elastic scattering in the channels d and p, and ϕ_p and ϕ_d describe the nuclear states between which the reaction takes place.[1]

There are certainly situations in which one or both of the first two assumptions are false, although the third assumption is probably usually valid for particle transfer reactions. As concerns the first assumption, the theory fails to the extent that the reaction of interest does take place between states, one of which is not the parent of the other.

However, if there are strongly enhanced inelastic transitions, the usual DWBA fails in all cases because of the second assumption. This can be understood as follows. The (one-channel) optical potential is chosen so as to reproduce the elastic cross section. This assures that the wave function for the relative motion is correct in the external region. However, for the purpose of calculating the reaction, it is needed in the interior region, or at least in the neighborhood of the nuclear surface. It is here that the one-channel optical model breaks down due to de-excitation of other channels back to the elastic channel, if their coupling is sufficiently strong.

In this paper[2] we present a generalization of the usual treatment of stripping reactions, which includes higher-order processes that proceed through intermediate states of the nuclei involved. Our method is more amenable to numerical calculation than an equivalent generalization proposed by other authors.[3,4]

Let the target nucleus (A) be governed by the Hamiltonian $\mathcal{H}_A$, whose eigenfunctions are denoted by $\phi_{\alpha J}(\underset{\sim}{A})$. For the total system we have

$$\mathcal{H} = \mathcal{H}_A + T + V(\underset{\sim}{d}, \underset{\sim}{A}),$$

where T is the energy of relative motion and V is the deuteron-nucleus interaction. With the eigenfunction of total angular momentum

$$\underset{\sim}{I} = j_d + \underset{\sim}{J}_d \text{ and parity } \pi = (-)^{\ell_d} \pi_{\alpha_d} ,$$

$$\phi^M_{d\pi I}(\hat{\underset{\sim}{R}}, \underset{\sim}{A}) = \left[\mathcal{Y}_d(\hat{\underset{\sim}{R}}) \, \Phi_{\alpha_d J_d}(\underset{\sim}{A}) \right]^M_I , \tag{3}$$

where $\mathcal{Y}$ is a spin-orbit function, we expand a solution ψ of $\mathcal{H}$, corresponding to incident particles in the channel d as

$$\psi^{M}_{d\pi I} = \frac{1}{R} \sum_{d'} u^{d\pi I}_{d'}(R)\ \phi^{M}_{d'\pi I}(\hat{\underset{\sim}{R}}, \underset{\sim}{A}), \tag{4}$$

where we use d to denote the whole collection of quantum numbers in a deuteron target channel, $d \equiv \alpha_d\ J_d\ \ell_d\ j_d$, and by d' some other state of intrinsic motion $\alpha'_d\ J'_d$ or relative motion ℓ'_d, or both. In the usual way[5, 6] we get a system of coupled equations for the radial functions u(r). They have the form, for each channel d',

$$[T_{d'} + V^{\pi I}_{d'd'}(R) - E_{d'}]\ u^{d\pi I}_{d'}(R) = -\sum_{d'' \neq d'} V^{\pi I}_{d'd''}(R)\ u^{d\pi I}_{d''}(R). \tag{5}$$

These are to be solved subject to the boundary conditions that there are incoming waves (I) only in the channels containing the nucleus in its ground state, whereas all channels may have outgoing waves (O):

$$u^{d\pi I}_{d'}(R) \to \delta_{d'd}\ I_{\ell_d}(k_d R) - \left(\frac{v_d}{v_{d'}}\right)^{1/2} S^{\pi I}_{d',d}\ O_{\ell_{d'}}(k_{d'} R). \tag{6}$$

For the proton system we could obtain an analogous system of equations, except that we recognize that the stripping reaction acts like a source of protons in the various proton channels. We must instead solve the inhomogeneous system

$$[T_p + V^{\pi I}_{pp}(r_p) - E_p]\ w^{d\pi I}_{p}(r_p) = -\sum_{p' \neq p} V^{\pi I}_{pp'}(r_p)\ w^{d\pi I}_{p'}(r_p) - \rho^{d\pi I}_{p}(r_p), \tag{7}$$

where ρ denotes the proton source. We calculate this from

$$\rho^{d\pi I}_{p}(r_p) = r_p \sum_{d'} \langle \phi^{M}_{p\pi I}(\underset{\sim}{r}_p, \underset{\sim}{A+1}) |V_{np}(r)|\ \phi_0(r)\ \phi^{M}_{d'\pi I}(\hat{\underset{\sim}{R}}, \underset{\sim}{A})\ u^{d\pi I}_{d'}(R)/R \rangle. \tag{8}$$

Here $\underset{\sim}{r} = \underset{\sim}{r}_n - \underset{\sim}{r}_p$ and $2\underset{\sim}{R} = \underset{\sim}{r}_n + \underset{\sim}{r}_p$, and ϕ_0 is the deuteron wave function. In this matrix element all coordinates, including $\hat{\underset{\sim}{r}}_p$, are integrated except r_p. The terms in this sum represent the various transitions, both the direct and the many indirect ones that proceed through excited states of the deuteron system to the channel p. Of course the strength with which the various levels d' contribute depends on the extent to which each of them is a parent of the level p.

Equation (8) is to be solved with the physical boundary conditions that proton channels of this reaction have only outgoing waves,

$$w^{d\pi I}_{p} \to -\left(\frac{v_d}{v_p}\right)^{1/2} S^{\pi I}_{p,d}\ O_{\ell_p}(k_p r_p). \tag{9}$$

The cross section can be written now in terms of these S-matrix elements.[2]

The source term can be explicitly evaluated under the usual zero-range approximation,

$$V_{np}(r)\,\phi_0(r) = D_0\,\delta(\underset{\sim}{r}).$$

To carry out the integration of the coordinates A we make a parentage expansion

$$\Phi^{M_p}_{J_p}(A+1) = \sum_{j_n \ell_n \alpha_d J_d} \beta_{\ell_n j_n}(J_d, J_p)\left[\Phi_{\alpha_d J_d}(\underset{\sim}{A})\,\mathcal{Y}_{j_n}(\hat{\underset{\sim}{r}}_n)\right]^{M_p}\chi_{\ell_n j_n}(r_n),$$

where χ is a single-particle radial function for the neutron in the nucleus (A + 1). We obtain, eventually,

$$\rho_p^{d\pi I}(r) = D_0 \sum_{d'\ell_n j_n} \beta_{\ell_n j_n}(J_{d'}, J_p)\,(-)^{\ell_{d'} + J_p + j_p + I}$$

$$\times \left(\frac{\hat{j}_p\,\hat{j}_{d'}\,\hat{\ell}_p\hat{\ell}_n}{4\pi}\right)^{1/2} \begin{pmatrix} \ell_p & \ell_n & \ell_{d'} \\ 0 & 0 & 0 \end{pmatrix} \begin{Bmatrix} j_p & j_n & j_{d'} \\ J_{d'} & I & J_p \end{Bmatrix} \begin{bmatrix} \ell_p & 1/2 & j_p \\ \ell_n & 1/2 & j_n \\ \ell_{d'} & 1 & j_{d'} \end{bmatrix}$$

$$\times \chi_{\ell_n j_n}(r)\,u^{d\pi I}_{d'}(r).$$

Here we see explicitly the radial form of the source, which contains the product of the neutron bound state and the deuteron scattering state, as expected. That they have the same coordinate r follows of course from the zero-range approximation. For simplicity we have omitted the usual center-of-mass correction.

To summarize, we have shown how to go beyond the usual DWBA treatment of transfer reactions to include the effects of inelastic scattering in both entrance and exit channels. Our basic equations cannot be rigorously derived from the Schrödinger equation for the system. However, we can say that they embody no approximations beyond those made in the usual distorted-wave method, whereas they do carry the effects of inelastic processes on the transfer reaction. These effects are carried to all orders among the retained channels so that both causes of failure of the usual DWBA are covered. However, like the DWBA, the transfer reaction is treated as a weak process, in first order only.

Footnotes and References

†Condensed from UCRL-18529; Ref. 2.

*Present address: Yale University, New Haven, Connecticut.

1. See, for example, the review by N. K. Glendenning, Ann. Rev. Nucl. Sci. 13, 191 (1963) and references cited therein to the original literature.
2. R. J. Ascuitto and N. K. Glendenning, Phys. Rev. 181, 1396 (1969).
3. S. K. Penny and G. R. Satchler, Nucl. Phys. 53, 145 (1964).
4. P. J. Iano and N. Austern, Phys. Rev. 151, 853 (1966).
5. N. K. Glendenning, in Proceedings of the International School of Physics "Enrico Fermi" Course XL (1967), edited by M. Jean (Academic Press, New York, 1969).
6. N. K. Glendenning, Nucl. Phys. A117, 49 (1968).

STUDY OF INELASTIC PROCESSES ON (d, p) REACTIONS IN DEFORMED NUCLEI

Norman K. Glendenning and Raymond S. Mackintosh

It was pointed out by Satchler[1] some years ago that the intensity of the (d, p) reaction, as then treated, could be used to measure directly the decomposition of the single-particle wave functions in deformed nuclei. The Nilsson wave function is expressed as a superposition of components having various angular momenta

$$\chi_\Omega = \sum_{N\ell j} C_{N\ell j\Omega}\, \chi_{N\ell j\Omega} .$$

The cross section to a member of the rotational band with spin I, based on this single-particle state, is proportional to $C^2_{N\ell I\Omega}$, and thus the reaction can be used as an experimental test of the Nilsson functions. This technique has been extensively investigated, particularly by Sheline and collaborators[2] and Elbek and Tjøm.[3] However, the above proportionality holds strictly only if the reaction proceeds directly from the ground state of the even target nucleus to the state in question on the odd nucleus. If either the target or final nuclei is set into rotation by the free particle, this no longer is true, because the transferred neutron, in this case, is not obliged to carry all the angular momentum into the final state. Since the cross sections for inelastic scattering by deformed nuclei are large, we undertook to compute the effect of inelastic processes on the (d, p) reaction by use of the source term technique.[4]

In ^{24}Mg(d, p) at 10.1 MeV leading to the states of the [211] 1/2+ band, we not only see in Fig. 1 the relative strengths of the 3/2+ and 5/2+ levels greatly altered by the inelastic processes, but also we find substantially different angular distributions for these two $\ell = 2$ states emerging from the calculation. In this figure we have multiplied the arbitrarily normalized data[5] for the four states by 0.29, 0.57, 0.4, and 0.4 respectively. Other calculations[6] have been performed which include inelastic effects but with "better" intrinsic wave functions. In this case it was possible to fit the data with a much smaller range of normalization factors--except, that is, for the 7/2+ state. This state, which is forbidden in a DWBA calculation using the usual intrinsic wave functions (which have no $j = 7/2+$ component), cannot be fitted. The same is true for the 7/2+ state in the ground band of ^{25}Mg (see Fig. 2). However, we have achieved a considerable improvement to the angular distribution of the ground state. In Fig. 3 we illustrate the effect of inelastic processes on the polarization. In these cases we have found that coupling among the outgoing channels contributes an amplitude to the weak 7/2+ states comparable to that arising from the excited 2+ state of the target, and also substantially alters the 3/2+ and 5/2+ angular distributions near 60 deg.

Among the calculations performed[6] in the rare earth region is that for stripping to the three states of the 5/2- band in ^{167}Er with 12.1-MeV deuterons. The results are shown in Fig. 4, where we also find that, as is not the case for magnesium, the 4+ state of the target is also important for some states. A calculation in which the 7/2-, 9/2-, and 11/2- levels are included is also illustrated in this figure. Here again we see large modifications for the weaker states introduced by inelastic effects.

In summary, our calculations show that the usual method of analysis, which neglects the effect of inelastic processes on the (d, p) reaction, leads to large errors (factor of 7 or so) for the weaker members of a band and small but significant errors ($\approx$ 20%) for the strongest states.

References

1. G. R. Satchler, Ann. Phys. (N. Y.) 3, 275 (1958).
2. M. N. Vergnes and R. K. Sheline, Phys. Rev. 132, 1736 (1963) and other contributions listed in Ref. 3.
3. B. Elbek and P. O. Tjøm, Advances in Nuclear Physics, III, edited by Baranger and Vogt (Plenum Press, New York, 1969).

4. R. J. Ascuitto and N. K. Glendenning, Phys. Rev. 181, 1396 (1969), and preceding paper in this Annual Report.
5. R. Middleton and S. Hinds, Nucl. Phys. 34, 404 (1962).
6. Raymond S. Mackintosh, The Theoretical Analysis of Nuclear Reactions Involving Strongly Deformed Nuclei Using Phenomenological Models (Ph. D. Thesis), UCRL-19529, in preparation.

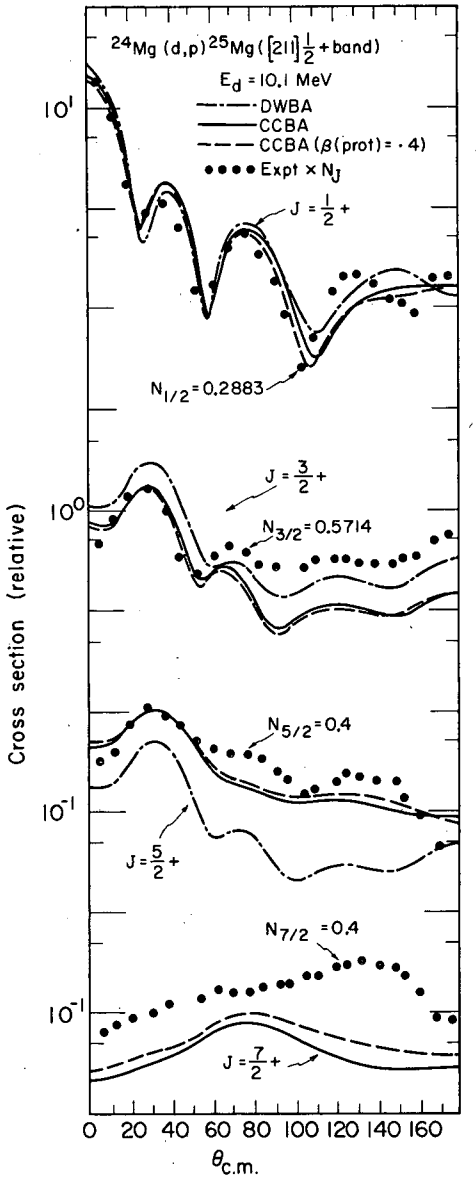

Fig. 1. The effect of inelastic scattering processes in the reaction ^{24}Mg(d, p) at 10.1 MeV is illustrated by comparing the complete calculation CCBA with the usual DWBA, which omits these processes. This calculation includes the four lowest states of the [211] 1/2+ band. Also shown is a CCBA calculation in which the nuclear deformation in the ^{25}Mg channels is increased from 0.3 to 0.4. (XBL 701-2086)

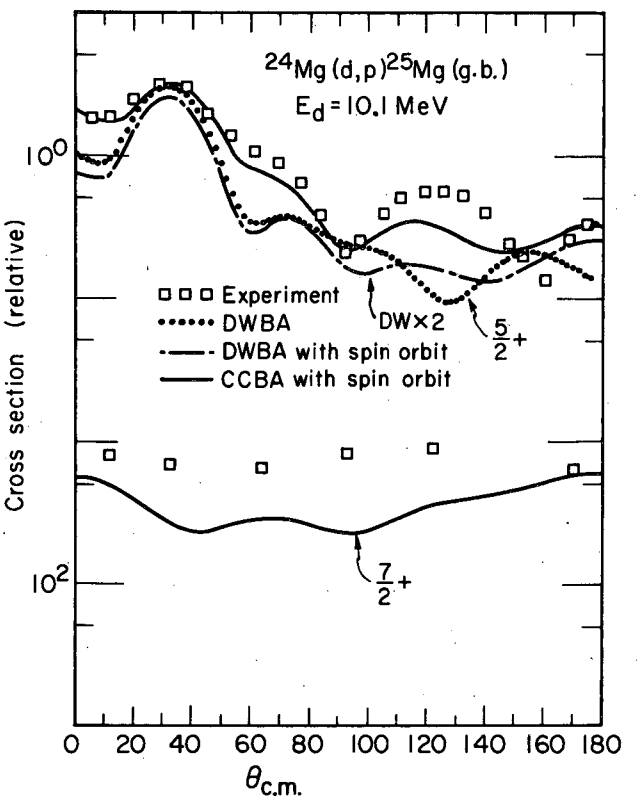

Fig. 2. As for Fig. 1, but the ground band of ^{25}Mg. With the particular wave functions used, the 7/2+ state is forbidden without indirect transitions; in this case scattering in the entrance and exit channels contributes about equal amplitudes. The data are normalized to the stripping peak of the CCBA 5/2+ state calculation. Also shown is a DWBA calculation of the g. s. without spin orbit interactions in the optical potential. (XBL 701-2088)

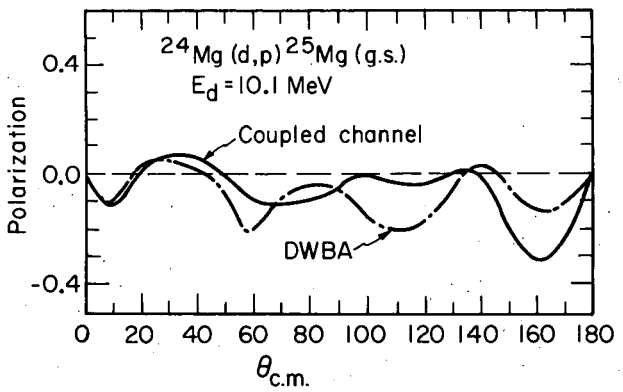

Fig. 3. The influence of inelastic processes on the polarization of protons from the g. s. of ^{25}Mg for 10.1-MeV deuterons. (XBL 701-2087)

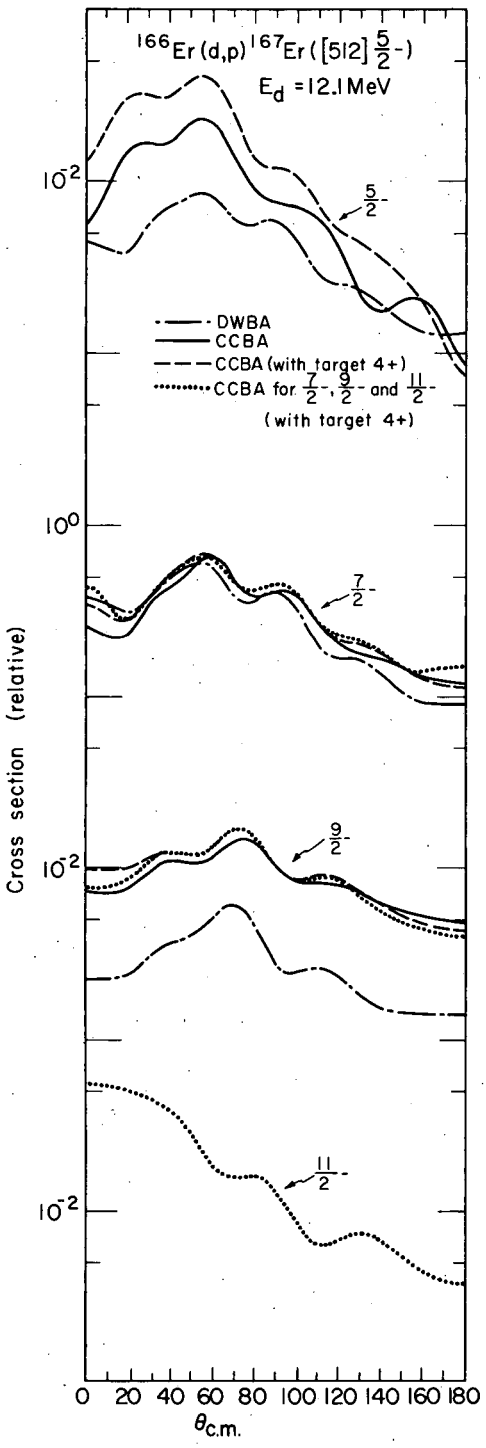

Fig. 4. The effect of inelastic processes on the stripping of 12.1-MeV deuterons leading to the [512] 5/2- band in ^{164}Er. We compare calculations in which transitions through the target 4+ state are included with those with the 2+ state alone. We also give the result of a calculation in which the 7/2-, 9/2-, and 11/2- levels of this band are coupled together. (XBL 701-2085)

SPACE EXCHANGE EFFECTS FOR COMPOSITE PROJECTILES

Richard Schaeffer

Microscopic calculations of inelastic scattering on charge exchange with light projectiles are usually performed by using[1] an effective interaction between the excited nucleus of the target and the center of mass of the projectile, but neglecting exchange effects arising from antisymmetrization of the projectile and target wave functions and from the exchange nature of nuclear forces. However, analysis[2] of (^{3}He, t) data[3] on N = 28 targets, where states with spins up to 7 was excited, showed serious discrepancies. In order to fit experimental results, the strength of the effective force, which should be the same for any final state, had to be strongly increased for transfer of high angular momentum. Such discrepancies appeared also for (pp') scattering,[4] but were removed[5-9] by introducing a knock-on term that takes account of the antisymmetrization of the incident particle and target nucleons and of the exchange nature of nuclear forces. It was not possible to draw definite conclusions about the importance of exchange for composite particles from an earlier attempt[2] to introduce these exchange effects because of the approximations made; i. e., we assumed[2] that the nucleus in the ^{3}He and ^{3}H were concentrated at the center of mass of the projectile. We here take account of the space extension of the projectiles as suggested in Ref. 2. The formalism we propose is simple, but accurate enough to give a definitive answer about the size of the exchange effects. They are still treated approximately, but the approximation we use, introduced by Petrovich et al.[7] for (p, p') scattering, was seen to be a good one, especially for transfer of high spin.

The lowest states of ^{48}Sc, excited by ^{48}Ca(^{3}He, t)^{48*}Sc, at 30 MeV can reasonably be assumed to be due to a recoupling of a $f_{7/2}$ neutron hole and a $f_{7/2}$ proton particle, which makes this reaction especially interesting when compared with others such as inelastic scattering of ^{3}He and nucleons. We shall study only the natural parity states (0^+ to 6^+), since the excitation of the unnatural parity states occurs through a strong tensor force, as preliminary calculations indicated in Ref. 2 and as was shown in Ref. 10. The exchange term for unnatural parity states requires therefore the introduction of a tensor term built with $\vec{k}$ instead of with $\vec{r}$, and we have not included such an interaction. We have taken the range of 1F for the n-n force, generally used for these reactions since it leads to better angular distributions. With such a force, the ratio V_6/V_0 is[2] about 4 when exchange effects are neglected. These effects, when a Serber mixture is used, increase the 6^+ cross section by a factor of 2.2 at the first maximum. They are slightly larger at backward angles. The 0^+ cross section on the contrary is not modified. These contributions increase regularly with increasing spin transfer (Table I) and therefore the discrepancy between theory and experiment due to the relative strengths of 6^+ and 0^+ cross sections is partly removed.

With a Rosenfeld mixture, exchange effects are even more important (a factor 4 for the 6^+ cross section). Such a force, however, gives very poor results for (p, p') scattering calculations.[5] The relative magnitude of direct and exchange contributions at the first maximum of the cross section does not depend strongly on the shape of the interaction used, as shown in Table I. For the Gaussian and the 1.37-F range Yukawa, the direct contribution decreases very rapidly at large angles and becomes comparable in size to the exchange term.

Even if the effects due to exchange processes are quite important, they are not strong enough to explain the discrepancy seen in Ref. 2. The ratio V_6/V_0 is still about 2.6 in the most favorable case, i. e., with a Rosenfeld mixture and a 1-F range Yukawa radial shape.

At lower energy, the ratio $(\sigma_{[D+E]})/\sigma_{[D]})$ at the first maximum is slightly larger, and at 75 MeV it is only about 1.9 for the 6^+ cross section (Table I), compared with 2.2 at 37 MeV.

The exchange effects have about the same magnitude for inelastic α, ^{3}He, and ^{3}H scattering. We have taken the ^{3}He and ^{3}H potentials from Ref. 2 and computed the ratio $(\sigma_{[D+E]})/(\sigma_{[D]})$ of the cross sections at their first maximum for a $f_{7/2} \rightarrow f7/2$ transition with various spin transfers (Table II). The optical potential for α particles is taken from Ref. 11. The two-body interaction is taken to have a Serber mixture, and a Yukawa-type radial form of range 1 F. The small differences have their origin in the projectile size, but they may not be really significant when the uncertainties in the optical parameters are considered. The magnitude of the exchange effects, as studied for the (^{3}He, t) reaction, are therefore typical for inelastic scattering of composite particles with masses up to 4.

In particular, their energy and range dependence are approximately the same for α, ^{3}He, and

^{3}H. They have also the same qualitative features as for (p, p') or (p, n) scattering,[6, 12] but are considerably smaller, mainly because of the strong absorption which does not allow the nucleons of the projectile to penetrate very far into the target nucleus.

Table I. Ratio $\sigma_{[D+E]}/\sigma_{[D]}$ of the cross section including exchange effects ($\sigma_{[D+E]}$ to the one neglecting them ($\sigma_{[D]}$) at the first maximum for various spin transfers. Column 1 gives the energy of the incident ^{3}He particles and column 2 gives the type of radial shape used for the nucleon-nucleon interaction, that is, before averaging over the projectile. This average has been performed in the calculation The mixtures used are the Serber (S) and Rosenfeld (R) ones.

Energy (MeV)	Radial shape of N-N force	Mixture	0^+	2^+	4^+	6^+
30	Yukawa, 1F	S	1.3	1.5	1.8	2.2
30	Yukawa, 1F	R	1.6	2.1	2.8	3.9
30	Yukawa, 1.37F	S	1.1	1.3	1.7	2.4
30	Gauss 1.78F (2.32F)	S	1.4	1.6	1.9	2.5
18	Yukawa, 1F	S	1.3	1.5	1.8	2.3
75	Yukawa, 1F	S	1.2	1.4	1.6	1.9

Table II. Ratio $\sigma_{[D+E]}/\sigma_{[D]}$ of the cross section including exchange effects ($\sigma_{[D+E]}$) to the one neglecting them ($\sigma_{[D]}$) at their first maximum for various spin transfers and various projectiles. λ is the range of the Gaussian used for the projectile mass distribution. The transition is assumed to be $(f_{7/2}\ f^{-1}_{7/2})^{0^+} \rightarrow (f_{7/2}\ f^{-1}_{7/2})^{J^+}$, J = 0, 2, 4, and 6.

	λ (F)	0^+	2^+	4^+	6^+
^{3}He, t	1.48	1.3	1.5	1.8	2.2
^{3}He, ^{3}He'	1.61	1.3	1.5	1.8	2.1
t, t'	1.37	1.3	1.5	1.8	2.3
α, α'	1.31	1.2	1.4	1.7	2.3

References

1. V. A. Madsen, Nucl. Phys. 80, 177 (1966); N. K. Glendenning and M. Veneroni, Phys. Rev. 144, 839 (1966).
2. P. Kossanyi-Demay, P. Roussel, M. Faraggi, and R. Schaeffer, to be published.
3. G. Bruge, A. Bussiere, H. Faraggi, P. Kossanyi-Demay, J. M. Loiseaux, P. Roussel, and L. Valentin, Nucl. Phys. A129, 417 (1969); Proceedings of the Dubna International Symposium on Nuclear Structure, July 1968.
4. G. R. Satchler, Nucl. Phys. A95, 1 (1967).
5. D. Agassi and R. Schaeffer, Phys. Letters 26B, 703 (1968).
6. J. Atkinson and V. A. Madsen, Phys. Rev. Letters 21, 295 (1968); W. G. Love, L. W. Owen, R. M. Drisko, G. R. Satchler, R. Stafford, R. J. Philpott, and W. T. Pinkston, Phys. Letters 29B, 478 (1969).
7. F. Petrovich, H. McManus, V. A. Madsen, and J. Atkinson, Phys. Rev. Letters 22, 895 (1969).
8. R. Schaeffer, Nucl. Phys. A132, 186 (1969).
9. J. Picard, O. Beer, A. El Behay, P. Lopato, Y. Terrien, G. Vallois, and R. Schaeffer, Nucl. Phys. A128, 481 (1969).
10. E. Rost and P. D. Kunz, to be published.
11. E. P. Lippincott and A. M. Bernstein, Phys. Rev. 163, 1170 (1967).
12. R. Schaeffer (Thesis), Orsay, 1969 (unpublished), and Proceedings of the Symposium on Nuclear Reactions and Polarizations, Quebec, 1969 (to be published).

IMPORTANCE OF TWICE-DOUBLE TRANSFER IN INELASTIC SCATTERING TO PAIR VIBRATIONAL STATES

R. Ascuitto† and B. Sørensen*

In this note a novel mechanism for inelastic proton scattering leading to a pair vibrational state is studied. A microscopic calculation of ^{48}Ca(p, p'), elastic and inelastic scattering, is made which includes exchange effects and two-step (p, t) plus (t, p) reactions through the ground state of ^{40}Ca. The method used to do this is the source-term approximation of Ascuitto and Glendenning.[1] The inclusion of exchange effects in the inelastic processes were made by the method of Ascuitto and Hocquenghem.[2] The nuclear structure wave functions were taken from Sorensen.[3]

In order to treat the strong coupling of reaction channels involving the strongly pair-correlated 0^+ states into the weak inelastic channels involving such states, a symmetric set of coupled equations including the source terms was solved:

$$(T_t + V_{tt} - E_t)\, w_t(R_t) = -\sum_{t'} V_{tt'}\, w_{t'}(R_t) - \sum_{t'} \rho^{\mathrm{exc}}_{tt'}(R_t) - \sum_{p} \rho^{\mathrm{reac}}_{tp}(R_t),$$

$$(T_p + V_{pp} - E_p)\, u_p(r_p) = -\sum_{p'} V_{pp'}\, u_{p'}(r_p) - \sum_{p'} \rho^{\mathrm{exc}}_{pp'}(r_p) - \sum \rho^{\mathrm{reac}}_{pt}(r_p).$$

The expressions for the individual terms are given in Refs. 1 and 2. The center-of-mass motion of the transferred pair was matched to a Hankel function of the correct asymptotical behavior in order to lessen the influence of the harmonic oscillator wave functions used for the two transferred neutrons. The optical parameters of the proton were obtained from a fit to the elastic scattering data, those of the triton from the (p, t) angular distribution for the ground-state transition.

The scattering potentials were taken to be of Gaussian form,

$$V_{pi} = (-33.12 - 3.39\, \bar{\sigma}_p \cdot \bar{\sigma}_i)\, e^{-0.46\, r^2}\ \mathrm{MeV},$$

$$V_{ti} = -51.35\, e^{-0.296\, r^2}\ \mathrm{MeV}.$$

The proton potential is taken from a phase-shift analysis,[4] and the triton potential is obtained from it by averaging over the triton wave function, assumed to be Gaussian.

The stripping interaction is assumed to be of zero range with a strength determined from the (p, t) data.

Two 0^+ excited states in ^{48}Ca are excited in (p, p'), which has been studied at $E_p = 12$ MeV.[5, 6] The main fragment of the pair vibration is believed to be the level at 5.45 MeV, to which we confine the analysis. This state is mainly of 2p-2h character and gets only direct excitation by admixture with the ground state. In comparison with conventional shell-model calculations, the boson calculation is believed to give an upper limit for the direct matrix element between the ground state and this excited state. On the other hand, no renormalization for three-body effects was introduced in the potentials. Such effects lead to direct excitation of a pair of neutrons by the collision with the incident proton, but they may be compensated by the amount of 2p2h configurations removed from the 5.45-MeV level by admixture with the other 0^+ level at 4.3 MeV. Thereby one also explains the similarity in the inelastic excitation of these two levels.

Our computer codes do not allow a simultaneous consideration of exchange and transfer-source terms, so we first determined effective potentials that simulated the effect of exchange (which turns out to imply a factor of 2 in the proton interaction depth) and used these potentials for the calculation including transfer processes. At the incident energy considered here only the ^{46}Ca ground state serves as intermediate state. Virtual reactions through excited 0^+ states in ^{46}Ca are neglected in the first-order treatment of the source terms.[1] Calculations have also been performed at higher

E_p, including now the pair vibrational state in ^{46}Ca.

The 12-MeV results are presented in Figs. 1 and 2. It can be seen that the direct inelastic transition is too weak by more than an order of magnitude. With exchange effects the situation is improved, but only by a factor of about four. On the other hand, when the indirect transition through the ground state of ^{46}Ca by means of a (p, t) followed by a (t, p) reaction is included, the observed cross section is accounted for very well.

Footnotes and References

†Present address: Yale University, Department of Physics, New Haven, Connecticut 06250.
*Present address: Niels Bohr Institute, Blegdamsvej 17, Copenhagen, Denmark.

1. R. Ascuitto and N. Glendenning, in Nuclear Chemistry Annual Report, 1968, UCRL-18667, Jan. 1969, p. 133, and The Role of Inelastic Processes in Two-Nucleon Transfer Reactions, UCRL-18874, April 1969.
2. R. Ascuitto and C. Hocquenghem, private communication, 1969.
3. B. Sørensen, Nucl. Phys. A134, 1 (1969).
4. Y. Tang et al., Phys. Rev. 131, 2631 (1963).
5. A. Marinov and J. Erskine, Phys. Rev. 147, 826 (1966).
6. A. Tellez et al., Nucl. Phys. A127, 438 (1969).

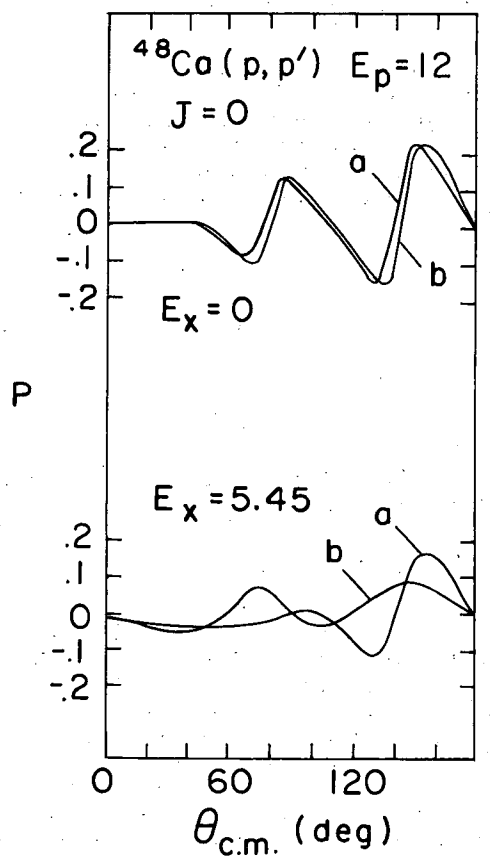

Fig. 1. Angular distribution of protons elastically and inelastically scattered on ^{48}Ca ground state and pair vibration. Dots and circles: Measured values from Refs. 5 and 6 respectively. Calculation a: direct inelastic transition without exchange; b: everything included (exchange and indirect excitation through the ground state of ^{46}Ca). XBL 701-2169)

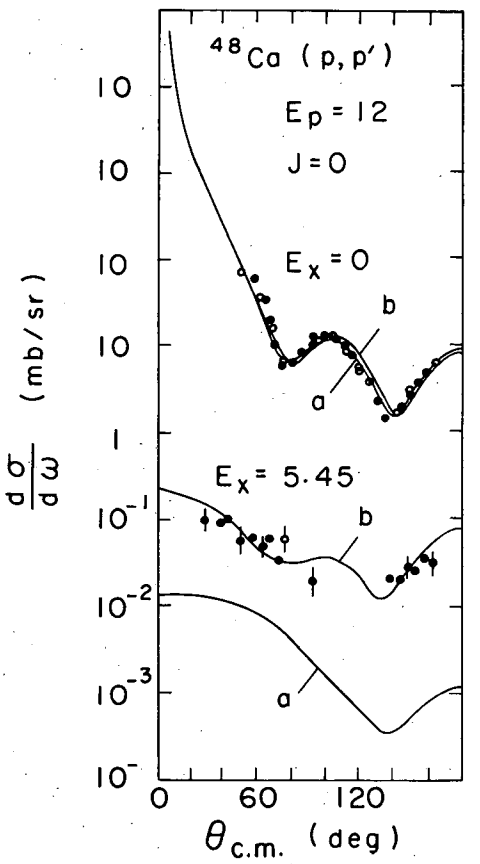

Fig. 2. Polarization of protons elastically and inelastically scattered on ^{48}Ca, cf. caption to Fig. 1. (XBL 701-2168)

COUPLING OF TWO-NUCLEON TRANSFER AND INELASTIC SCATTERING PROCESSES IN THE LEAD REGION

R. Ascuitto† and B. Sorensen*

A number of low-lying excited states in ^{208}Pb may be well described as either 1p1h or 2p2h configurations based on a closed core. Since the particle and hole configurations belong to different major shells, one may even to a first approximation neglect their interaction and thus construct 2p2h states in ^{208}Pb by simply combining the low-lying 2p states of ^{210}Pb with the low-lying 2h states of ^{206}Pb, and construct the 1p1h states similarly by combining ^{207}Pb and ^{209}Pb states. The energies of levels obtained in this way agree surprisingly well in a large number of cases with observed levels of the same spin and parity, but of course there are exception such as the strongly collective 3^- state. In any case the uncorrelated combinations provide a basis that is useful for studying transfer and scattering processes on the same footing. In particular their couplings, which require knowledge of matrix elements between excited states, may be related, in the combination picture with equal matrix elements in neighboring nuclei, to a ground state, and hence in some cases have been measured. In Fig. 1 we illustrate schematically a number of levels and transitions between them that we can include in a coupled-channel treatment of the processes mentioned, such as the source term calculations first performed by Ascuitto and Glendenning.[1]

Let us first consider the pair vibration $0_-\,0_+$, for which we have used a notation which suggests that this state has two holes distributed as in the $(A_0\text{-}2)$ ground state 0_- and has two particles distributed as in the (A_0+2) ground state, 0_+. This now implies that the transition matrix element between 0_- and $0_-\,0_+$ equals the one between the (A_0) ground state 0 and 0_+. Similarly the matrix element between 0_+ and $0_-\,0_+$ equals the one between 0 and 0_-. We can play the same game to relate matrix elements between others of these special 2p2h states and the 2p or 2h state on which they are built to matrix elements between the A_0 core and a 2p or 2h state. For example,

$$\langle 2_+ \| A^+_{abj} \| (2_-2_+)_I \rangle = \sqrt{2I+1}\ \delta_{J,2}\ \langle O \| A^+_{ab2} \| 2_- \rangle,$$

where

$$A^+_{abJM} = (1+\delta_{ab})^{-1/2} (a^+_a a^+_b)_{JM}.$$

In some cases we are forced to consider residual admixture. For example the states $2_-\,0_+$ and $0_-\,2_+$, which have unperturbed energies only 8 keV apart, therefore mix strongly even with a modest matrix element. We have calculated their admixture, which is found to be nearly 50%, and the energy difference is increased to 230 keV, compared with the experimental one of 253 keV. A residual quadrupole interaction was used to calculate the splitting, corresponding to the fact that we obtained wave functions for the 2h and 2p states in a BCS + TDA calculation with a pairing plus quadrupole interaction.[2] The two states on the figure are denoted

$$|2_1\rangle \approx \frac{1}{\sqrt{2}} \left(|0_-2_+\rangle + |2_-0_+\rangle\right)$$

and

$$|2_2\rangle \approx \frac{1}{\sqrt{2}} \left(|0_-2_+\rangle - |2_-0_+\rangle\right).$$

Similarly one can calculate the mixing between $(2_-2_+)_0$ and $0_-\,0_+$ or between $(2_-2_+)_2$ and 2_1 or 2_2. It is clear that the quintuplet $(2_-2_+)_J$ will appear nondegenerate.

Considering now a (p, t) reaction on ^{210}Pb, one may reach the state 2_1 by three main routes, either directly, $0_+ \to 2_1$ (which really goes via the $2_-\,0_+$ component only), or by either of the two-step routes $0_+ \to 2_+ \to 2_1$ (which uses only the 0_-2_+ component) and $0_+ \to 0_-0_+ \to 2_1$ (which can use both components). It is clear from the difference in relative phase in the wave function that the three possible routes for reaching 2_1 and 2_2 will not interfere in the same way. In Fig. 2 the cross sections are shown for the (p, t) reaction at 20 MeV, which has been studied by the Los Alamos group.[3] The form of the interactions causing the inelastic processes is similar to the ones described in our other contribution to this report (preceding paper), except that the scalar strength

V^0_{pi} was adjusted to reproduce the inelastic cross section for ^{206}Pb(p, p') $0_- \rightarrow 2_-$. Optical parameters were fitted to elastic scattering of protons and tritons. The strength of the stripping interaction does not affect the relative cross sections, since the reaction was considered weak enough to be treated only in first order (i.e., source term in the triton channels, not in the proton channels; cf. the coupled equations of the other contribution to this report). Here also the effect of the exchange source term is considered to be incorporated in the renormalized V^0_{pi} and V^0_{ti}.

Figure 2 shows that although the inelastic processes are themselves weak (corresponding BE2 values are about 5 spu) the two-step routes do still contribute significantly to the total cross sections. Inelastic scattering in the final nucleus adds to both the 2_1 and 2_2 cross sections, but considerably more in 2_1, in which the two components in the wave function then must be excited coherently. The routes via inelastic excitation in the target interfere at forward angles largely in a destructive way, but at backward angles in a constructive way. The opposite is the case for 2_2.

In Fig. 3 we show the reaction cross section for the states $(2_- 2_+)_J$, which could not be reached by a direct process, but has to go through either 2_+ or 2_1 or 2_2. One may note that the unnatural-parity states have zero differential cross section at $\theta_{c.m.} = 0$ or 180 deg.

There are a large number of experimental levels in this region, but poor angular distributions make it difficult to establish a correspondence. The 20-MeV (t, p) data from the same group, leading from ^{206}Pb to states in ^{208}Pb, is of limited help because of the lack of J dependence of the (t, p) angular distributions in the region of Q values in question. Yet some progress may be achieved in pursuing the comparison of the (t, p) and (p, t) data, since the $(2_- 2_+)_J$ states should be characterized by equally probable excitation in the two reactions, a property not shared by states such as $0_- 4_+$, $4_- 0_+$, $2'_- 0_+$, and $0'_- 0_+$, which are in the same region (cf. Fig. 1), but unfortunately shared by several 1p1h states.

The angular distributions of 1p1h states does not generally distinguish them from the 2p2h states excited by direct reaction. However, if the 2p2h state is excited by a two-step mechanism its angular distribution may be changed. As an example of this, one may compare the J = 2 level in Fig. 3 with the ones in Fig. 2. Such behavior has not been found earlier. In the study of vibrational nuclei[1] the harmonic two-phonon J = 2 state built of two identical J = 2 quanta had the same angular distribution as the direct transition to the one-phonon state. It is thus encouraging that we have found an example in which the two-step process can be distinguished from the mere admixture of states that can be reached directly. The reason may be related to the fact that the state $(2_- 2_+)_J$ is not built of identical quanta. Looking at the particular routes included in cases a, b, and c of the cross sections for the levels 2_1 and 2_2 shown in Fig. 2, one also sees that the interference between different two-step processes of different nature may change the angular distribution. An example of a 1p1h level of angular momentum J = 2, reached by a direct process, is shown at the bottom of Fig. 4.

Figure 4 also shows the transition leading to the collective 3^- state and a harmonic 0^+ two-phonon state built on it. Here the calculation used wave functions of Gillet et al.,[4] and the inelastic matrix element between the ground state and the 3^- as well as the one between the 3^- and the $(3^2)_0$ were included (cf. Fig. 1). The main route for the process leading to the 0^+ state is in this picture $0_+ \rightarrow 3^- \rightarrow (3^2)_0$, but it is seen to give an order-of-magnitude too small a cross section. We therefore calculated the mixture of the state $(3^2)_0$ with the nearby pair vibration $0_- 0_+$ and with the ground state, both of which, to first order, can be expressed by an overlap, and we found that the state $(3^2)_0$ contained respectively 5 and 4% of the two other states. Including the direct cross section to these components, we obtained the solid curve shown in Fig. 4, in excellent agreement with experiment.

It is the aim of this investigation to consider a large number of additional states of nature similar to the few discussed here, and to compare the (t, p) and (p, t) data leading to these states.

Footnotes and References

†Present address: Yale University, Department of Physics, New Haven, Connecticut 06250.
*Present address: Niels Bohr Institute, Blegdamsvej 17, Copenhagen, Denmark.

1. R. Ascuitto and N. Glendenning, in Nuclear Chemistry Annual Report, 1968, UCRL-18667, Jan. 1969, p. 133, and The Role of Inelastic Processes in Two-Nucleon Transfer Reactions, UCRL-18874, April 1969.
2. B. Sørensen, On the Description of Fermion Systems in Boson Representations. IV. Numerical Calculation of Quadrupole Excitations in Cd, Sn, Te, Sm, and Pb (UCRL-18903, April 1969),

Nucl. Phys. (to be published).
3. E. Flynn, G. Igo, and P. Barnes, private communication.
4. V. Gillet et al., Nucl. Phys. 88, 321 (1966).

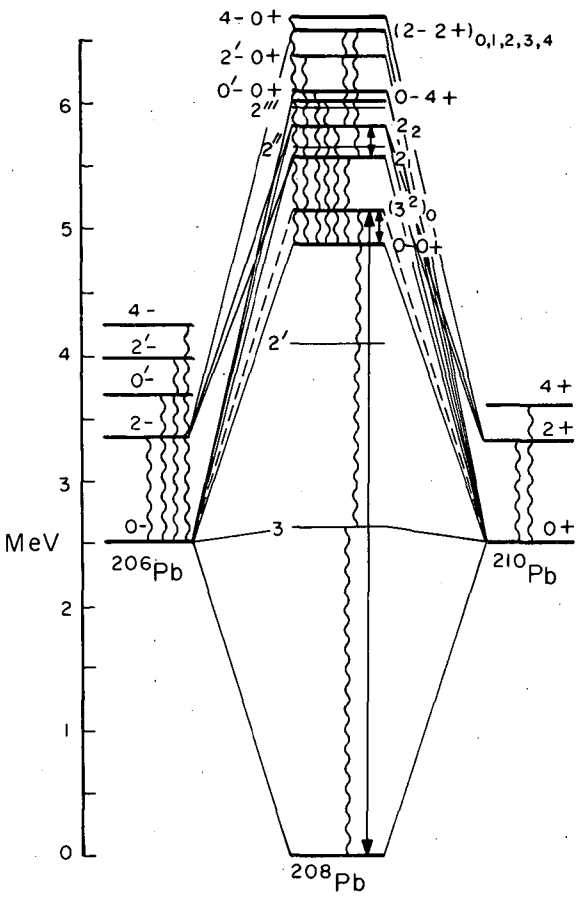

Fig. 1. Schematic display of some levels and transitions included in the calculations. Two-hole levels are denoted by a minus suffix on the spin quantum number, two-particle levels by a plus suffix. This indexing is also used to show the main structure of 2p2h states. The levels 2_1 and 2_2 are described in the text. Wiggly lines indicate inelastic transitions, full lines transfer. Level interaction discussed in the text is indicated by full lines with arrows.
(XBL 701-2170)

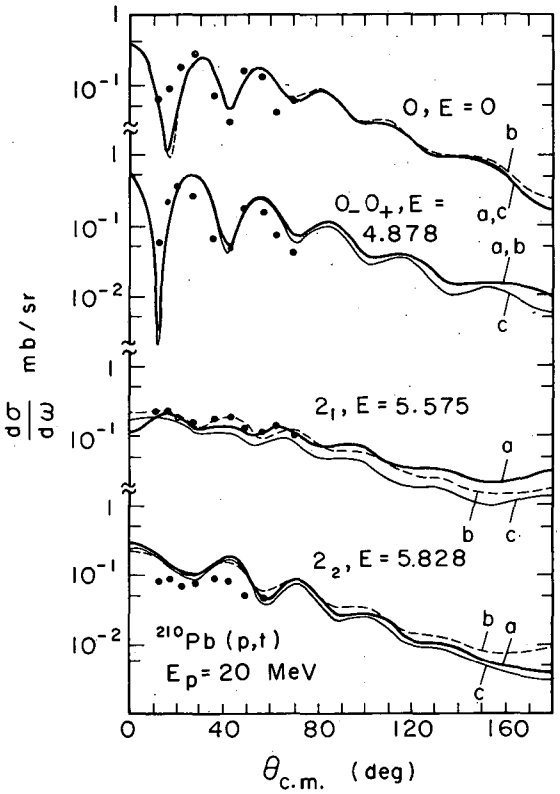

Fig. 2. Calculated (lines) and experimental (dots) reaction cross sections:
(a) all routes included;
(b) no inelastic excitation in target;
(c) no inelastic excitation in final product.
(XBL 701-2171)

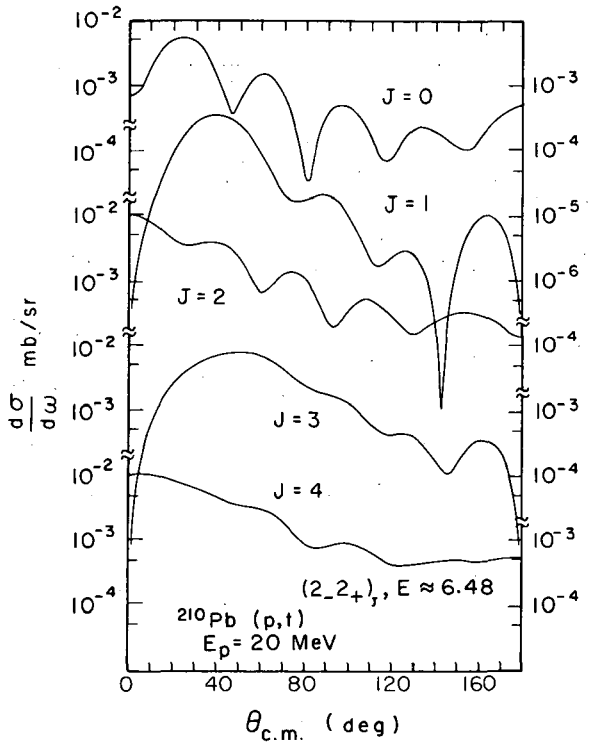

Fig. 3. Calculated reaction cross sections including all routes. (XBL 701-2172)

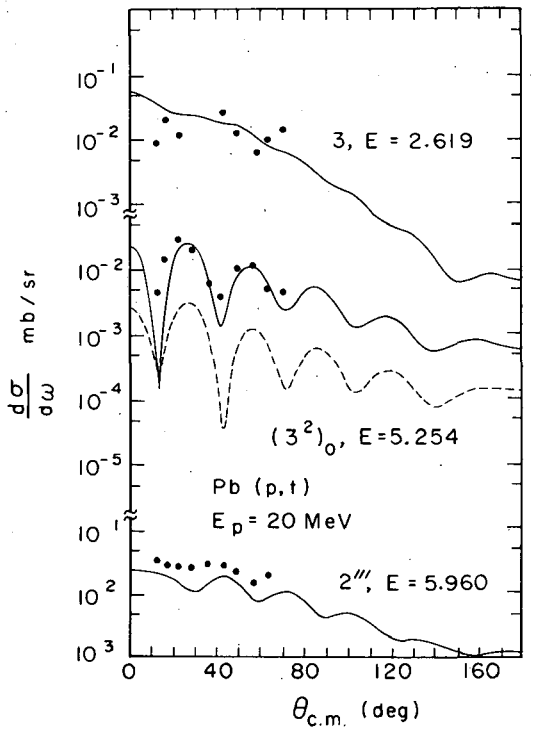

Fig. 4. Reaction cross sections for levels based on 1p1h configurations. The dashed line for the J = 0 state includes only two-step processes, the full line includes in addition direct excitation via admixtures in the state.
(XBL 701-2173)

DIRECT TWO-NUCLEON TRANSFER REACTIONS AND THEIR INTERPRETATION IN TERMS OF THE NUCLEAR SHELL MODEL †

I. S. Towner* and J. C. Hardy

The distorted-wave Born approximation (DWBA) treatment for direct two-nucleon transfer reactions has been derived following the formalism of Satchler, spin-orbit coupling being included in the distorted-wave expansions. Methods for the evaluation of the integrals involved are described, and in particular a discussion is given of two different "zero-range" approximations, one involving an assumption that the heaviest projectile has zero extent, the other assuming the interaction to have zero range. These two approaches are compared. The main emphasis, however, is directed towards extracting reliable spectroscopic information from experimental two-nucleon transfer reactions, and to this end, shell-model expressions for the spectroscopic amplitude have been derived, together with closed formulae for two-particle coefficients of fractional parentage (cfp). The JT representation is used principally throughout, but expressions are given for the LSJT representation as well as for the separate treatment of neutrons and protons. Examples illustrating (i) excitation of analogue states, (ii) comparison of (p,t) and (p, ^{3}He) reactions to mirror states, and (iii) coherence effects between different shell model orbitals indicate the usefulness of two-nucleon transfer reactions in determining nuclear structure information such as spins, parities, two-body matrix elements, etc. As a further aid to the analysis of experimental data, numerical tables of two-particle cfp's in the isospin formalism for j = 1/2, 3/2, and 5/2 are given for states of low seniority, and in the non-isospin formalism for j = 3/2, 5/2, 7/2, and 9/2 shells.

Footnotes

†Abstract from Advan. Phys. 18, 401 (1969)
*Nuclear Physics Laboratory, Oxford, England.

TABLES OF FRACTIONAL PARENTAGE COEFFICIENTS IN THE ISOSPIN FORMALISM FOR THE j = 3/2 AND 5/2 SHELLS†

I. S. Towner* and J. C. Hardy

Values of one- and two-particle coefficients of fractional parentage in the isospin formalism have been computed for the j = 3/2 and 5/2 shells. These values are tabulated for the first half of each shell. For the second half particle-hole formulae are quoted by which the coefficients of fractional parentage may be readily obtained.

Footnotes

†Abstract from Nucl. Data A6, 153 (1969).
*Nuclear Physics Laboratory, Oxford, England.

TABLES OF CLEBSCH-GORDAN COEFFICIENTS FOR ODD- AND EVEN-MASS DEFORMED NUCLEI†

David J. Gorman and Frank Asaro

A set of tables has been prepared as a convenient source of the Clebsch-Gordan coefficients commonly used in the calculation of nuclear transition probabilities for deformed nuclei.

The coefficients are written in the form

$$C^{II,\,L,\,IF}_{KI,\,KF-KI,\,KF} = \langle\, II\ L\ KI\ KF-KI \,|\, II\ L\ IF\ KF \,\rangle,$$

where II and IF are the spins of the initial and final states; KI and KF are the projections of the nuclear angular momentum on the nuclear symmetry axis for the initial and final states; L is the angular momentum carried off by the radiation emitted during the transition between the initial and final states.

The compilation is arranged into four tables applicable to both odd- and even-mass nuclei. In all cases the maximum value of L was 6.

Four tables, produced on the CDC 6600 computers at Lawrence Radiation Laboratory–Berkeley, are included in the article from which this is condensed. Table I gives the coefficients for values of KI and KF from 1/2 to 31/2. Table II gives the coefficients for KI from 1/2 to 11/2 and negative half-integral values of KF. Table III gives the coefficients for integral values of KI from 0 to 16. Table IV gives the coefficients for KI from 0 to 5 and negative integral values of KF.

Footnote

†Condensed from David J. Gorman and Frank Asaro, Tables of Clebsch-Gordan Coefficients for Odd- and Even-Mass Deformed Nuclei, UCRL-18975, Sept. 1969.

A CALCULATION OF THE MAGNETIC MOMENTS OF THE 86.5- AND 105.3-keV STATES IN ^{155}Gd

E. Browne† and D. J. Gorman

The magnetic moments of the 86.5- and 105.3-keV levels of ^{155}Gd were calculated by taking into account the coupling of the even-parity rotational bands due to the Coriolis and $\Delta N = 2$ interactions.

The expectation value $\langle \psi_J | \mu_z | \psi_J \rangle$ of the "z" component of the magnetic moment was evaluated by using the "mixed" wave functions given by Borggreen et al. [1] and the gyromagnetic factors $g_R = 0.3$, $g_s = 0.6\, g_{s\ free} = -2.3$, and $g_\ell = 0$. The magnetic moment of a state with spin J, (M = J) mixed by the Coriolis interaction with other states of the same spin and parity but differing in their value of K is given by the relation

$$\mu = g_R J + \langle J1\ J0 | JJ \rangle \sum_{K,K'} C_K C_{K'} \times \left\{ \langle J1\ K\ K'-K | J\ K' \rangle \langle K' | G'_{K'-K} | K \rangle \right.$$

$$\left. + \delta_{K,\frac{1}{2}}\, \delta_{K',\frac{1}{2}}\, (-)^{J-\frac{1}{2}}\, \Pi_K \langle J1 -\tfrac{1}{2}\ 1 | J\ \tfrac{1}{2} \rangle \langle \tfrac{1}{2} | G'_1 | -\tfrac{1}{2} \rangle \right\},$$

where C_K and $C_{K'}$ are the Coriolis admixtures, Π_K is the parity of the state (+ or -), and the summation is over all values of K and K' such that K' = K, K ± 1; $\langle J1\ J0 | JJ \rangle$ is a Clebsch-Gordan coefficient.

When Nilsson wave functions are used the single-particle matrix elements can be written explicitly:

$$\langle K | G'_0 | K \rangle = K(g_\ell - g_R) + \tfrac{1}{2}(g_s - g_\ell) \sum_\ell \left(a^2_{\ell, K-\frac{1}{2}} - a^2_{\ell, K+\frac{1}{2}} \right),$$

$$\langle K' | G'_{\pm 1} | K \rangle = \mp \frac{1}{\sqrt{2}} \left\{ (g_\ell - g_R) \sum_\ell \left(a_{\ell, K'+\frac{1}{2}}\, a_{\ell, K+\frac{1}{2}} \right.\right.$$

$$\times \sqrt{[\ell \mp (K+\tfrac{1}{2})][\ell \pm (K+\tfrac{1}{2}) + 1]} + a_{\ell, K'-\frac{1}{2}}\, a_{\ell, K-\frac{1}{2}}$$

$$\left.\left. \times \sqrt{[\ell \mp (K-\tfrac{1}{2})][\ell \pm (K-\tfrac{1}{2}) + 1]} \right) \right\}$$

$$\mp \frac{1}{\sqrt{2}} (g_s - g_R) \sum_\ell a_{\ell, K' \mp \frac{1}{2}}\, a_{\ell, K \pm \frac{1}{2}}.$$

The calculation was performed on the CDC 6600 computer, using Nilsson wave functions for a deformation of $\eta = 6$ in the L-S representation. Our results are given in Table I together with those of Ref. 1 and the experimental values. [3] The calculated magnetic moment of the 86.5-keV state agrees with the corrected one of Borggreen et al.; [2] however, it does not agree with the experimental value. [3]

Footnote and References

†Present address: Care of Gloria Lando, P. O. Box 760, Asuncion, Paraguay.

1. J. Borggreen, G. Loevhoeiden, and J. C. Waddington, Nucl. Phys. A131, 241 (1969).
2. J. C. Waddington, private communication, 1969.
3. H. Blumberg, B. Persson, and M. Bent, Phys. Rev. 170, 1076 (1968).

Table I. Comparison of values obtained in various works.

Excited-state energy (keV)	Magnetic moment, μ (nm)		
	Borggreen et al., Ref. 1	This work	Experimental value
86.5	-0.5 -1.3[2]	-1.31	-0.53 ± 0.05
105.3	-0.33	-0.28	-0.38 ± 0.06 or 0.13 ± 0.04

MICROSCOPIC DESCRIPTIONS OF γ-VIBRATIONAL BANDS IN THE RARE EARTH REGION

S. Cheng, G. L. Struble, and J. Wong

We have performed a calculation to describe γ-vibrational bands in deformed nuclei in the framework of Migdal's finite Fermi system theory.[1] According to this theory, the role of the nuclear structure in the interaction of nuclei with the external field can be treated exactly on the basis of phenomenological constants. One set of constants determines the self-consistent field in which the independent particles move. There are also introduced two phenomenological amplitudes Γ^{ω} and Γ^{ξ} characterizing the interaction in the particle-hole and particle-particle channels, respectively. Migdal's theory is a generalization of the random-phase approximation (RPA), since the two-particle interaction is replaced by the amplitudes Γ^{ω} and Γ^{ξ}, which include the effects of multiple collisions. From general arguments[1] the amplitudes are taken to be of the form

$$\Gamma(x_1 x_2) = \pi^{3/2} r_0^3 [f + f' \underset{\sim}{\tau}_1 \cdot \underset{\sim}{\tau}_2) + (g + g' \underset{\sim}{\tau}_1 \cdot \underset{\sim}{\tau}_2) \underset{\sim}{\sigma}_1 \cdot \underset{\sim}{\sigma}_2] \delta(\underset{\sim}{r}_1 - \underset{\sim}{r}_2).$$

The constants are chosen to fit the experimental data. The collective excitation energies are given by the poles of the quasi-particle density matrix. The system of equations for determining these poles reduces to

$$(E_1 + E_2) Z^{\pm}_{12}(\omega) - Z^{\pm}_{12}(\omega) = - \sum_{34} \{(u_1 v_2 \pm v_1 u_2) \Gamma^{\omega}_{1423} (u_3 v_4 \pm v_3 u_4 + (u_1 u_2 \mp v_1 v_2) \Gamma^{\xi}_{1234} (u_3 u_4 \mp v_3 v_4)\} Z_{24 \pm}(\omega).$$

Here the E's are the quasi-particle energies, $Z^{\pm}_{12}$ are simply related to the density matrices,[2] the u's and v's are occupation amplitudes for the single-particle states and are obtained by solving the well-known BCS equations, and ω is the collective excitation energy.

The most recent attempts at a microscopic description of the γ-vibrational bands were by Faessler and Plastino.[3] These authors used the RPA and a spin-independent surface-δ interaction. In fact the amplitudes Γ are density dependent, and so the surface-δ interaction may be a reasonable approximation. However, in order to solve the RPA equations, the authors made a

number of approximations in order to solve these complex matrix equations by a relatively simple dispersion relation. It is our purpose here to numerically examine the implications of these approximations.

There are five different approximations to make the equations separable: (i) only the k = 2 multipole of the amplitude is kept. (ii) the particle-particle amplitudes are discarded, (iii) the exchange particle-hole amplitude is neglected, (iv) terms with factors (uv-vu) are ignored, and (v) an arbitrary truncation in the number of single-particle states is made. In Table I we isolate the effect of these approximations on six nuclei by removing them individually from the Faessler-Plastino calculation. The calculation was performed by use of a set of 13 proton orbitals and 16 neutron orbitals. The coupling constant was chosen to be -120/A MeV. In column I we give the TDA result with all approximations. In column II we lift the restriction of approximation 1, in column III we lift restriction 2, in column IV we lift restriction 3, and in column V we lift restriction 4. Comparing the results in column I with those in II–V, we observe that the inclusion of all multipoles has a marked effect on the results, not accounted for by a simple renormalization of the coupling constant. The inclusion of particle-particle matrix elements also has a large effect. In the degenerate model the inclusion of the particle-particle matrix elements merely renormalizes the strength of the interaction. In this nondegenerate sample the effect is similar. The neglect of the exchange particle-hole elements is a relatively small effect, nevertheless it is not systematic and can yield 16% changes, usually in the direction to improve agreement with experiment.

Table I. Results obtained for various approximations to the exact TDA. See text for discussion.

Nucleus	Experimental energy	Column number I	II	III	IV	V
^{168}Er	0.83	0.84	0.28	0.40	0.88	0.15
^{170}Er	0.93	0.93	0.52	0.48	0.98	0.27
^{168}Dy	1.00	1.02	0.47	0.49	1.07	0.36
^{172}Dy	1.48	1.30	1.10	0.66	1.29	0.68
^{174}Dy	1.67	1.07	0.80	0.51	1.16	0.78
^{176}Dy	1.29	0.61	0.22	0.14	0.73	0.27

We conclude that the gross qualitative features of energy systematics can be deduced from simple separable models, but for a quantitative interpretation other effects--in particular the inclusion of all multipoles in the interaction--and the possibility of a spin dependence in the interaction amplitude must be considered.

References

1. A. B. Migdal, Theory of Finite Fermi Systems and Properties of Atomic Nuclei (Nauka, Moscow, 1965).
2. S. T. Belyaev, in Selected Topics in Nuclear Theory, edited by F. Janouch (IAEA, Vienna, 1963).
3. A. Faessler and A. Plastino, Nucl. Phys. A94, 580 (1967).

ON THE VALIDITY OF QUASI-PARTICLE DESCRIPTIONS FOR N = 83 ODD-ODD ISOTOPES†

Jean Kern* and Gordon L. Struble

Recently several groups[1-4] have obtained new and precise results on the low-energy structure of ^{140}La and ^{142}Pr using (d, p) and (n, γ) reaction spectroscopy. We wish to present a very simple phenomenological picture that can explain these experimental data.

We assume that the system of neutrons can be described by one particle in the $2f_{7/2}$ shell-model orbital plus the inert core of 82 neutrons. The protons, however, are described by a system of independent quasi particles.[5] Experimental systematics on neighboring even- and odd-mass nuclei suggest that only configurations with one quasi proton in either the $1g_{7/2}$ or $2d_{5/2}$ states are important in the description of the lowest excitations. For a given spin J, we may write the ^{142}Pr wave functions as

$$|JM\rangle_1 = \alpha_{1J} \mid 2d^0_{5/2}\ 2f_{7/2};\ JM\rangle + \beta_{1J} \mid 1g^0_{7/2}\ 2f_{7/2};\ JM\rangle$$

$$|JM\rangle_2 = \alpha_{2j} \mid 2d^0_{5/2}\ 2f_{7/2};\ JM\rangle + \beta_{2J} \mid 1g^0_{7/2}\ 2f_{7/2};\ JM\rangle.$$

Because of the orthonormality constraints, only one of these four parameters and the relative phase are independent.[6]

Analysis of (d, p) cross sections allows a simple determination of the absolute values of the amplitudes. But gamma branching ratios depend on the sign as well as the magnitude of the amplitude, and, because all the relevant transitions have M1 multipolarity, the branching ratios are sensitive to the effective dipole moments of the neutron and the quasi protons.

In the table we list the levels observed[1, 3, 4] in ^{142}Pr and ^{140}La and their properties insofar as the experiment data are uniquely determined by the model wave function.[7] The measured (d, p) intensities are entirely consistent with the amplitude assignments (see columns 4 and 5) within the experimental error. Similarly, when experimental values are used for the magnetic moments, the amplitudes given in columns 6 and 7 fit all the branching ratios within the experimental error. Both these agreements suggest that our physical picture is reasonable.

The x-ray transition probabilities are more sensitive than the (d, p) spectroscopic factors to small admixtures in the wave function. Thus the amplitudes determined by the two experiments might not be expected to agree. However, in comparing the amplitudes, we see impressive agreement with few exceptions. But we should point out that the assignment of the amplitudes from the branching-ratio calculation might not be unique and that the (d, p) results were considered in choosing the initial guesses for the least-squares fit to the experimental data.

Footnotes and References

†Submitted to International Conference on Properties of Nuclear States, Montreal, August 25-30, (1969).

*University of Fribourg, Fribourg, Switzerland.

1. J. Kern, G. L. Struble, and R. K. Sheline, Phys. Rev. 153, 1331 (1967).
2. L. B. Hughes, T. J. Kennett, and W. V. Prestwich, Nucl. Phys. 89, 241 (1966).
3. J. Kern, G. L. Struble, R. K. Sheline, E. T. Jurney, R. Koch, B. P. Maier, U. Gruber, and O. W. B. Schult, Nuclear Levels in ^{142}Pr, submitted to Phys. Rev.
4. E. T. Jurney, R. K. Sheline, E. B. Shera, O. W. B. Schult, B. P. Maier, R. Koch, U. Gruber, J. Kern, and G. L. Struble, A Study of the Levels in ^{140}La Using the ^{139}La(n, γ)^{140}La Reaction, Phys. Rev. (to be published).

5. A. M. Lane, Nuclear Theory (W. A. Benjamin, Inc., New York, 1964).
6. In using this description for ^{140}La, the roles of α and β must be interchanged.
7. The ^{140}La γ-branching analysis must be considered as preliminary, since it will be redone, using recent experimental data from Ref. 4. We include this calculation as additional proof for the validity of the quasi-particle picture.

Table I.

Nucleus	Level energy [keV]	Spin	State vectors: From the (d, p) analysis α	From the (d, p) analysis $\lvert\beta\rvert$	From γ-branching α	From γ-branching β
^{142}Pr	0.0	2	0.87	0.49	0.96	-0.28
	3.683	5	0.64	0.77	0.63	-0.78
	17.740	3	0.59	0.81	0.60	-0.80
	63.746	6	1.00	~0	0.997	0.07
	72.294	4	0.34	0.94	0.22	-0.975
	84.998	1	0.93	0.37	0.995	0.10
	128.251	5	0.77	0.64	0.78	0.63
	144.587	4	0.94	0.34	0.975	0.22
	176.863	3	0.81	0.59	0.80	0.60
	200.525	2	0.49	0.87	0.28	0.96
^{140}La	0.0	3	0.90	0.43	0.99	0.11
	29.956	2	0.69	0.72	0.72	-0.69
	34.659	5	1.0	~0	0.99	0.11
	43.806	1	0.81	0.59	0.89	-0.46
	48.81	6	0.98	0.2	---	---
	63.171	4	1.0	~0	0.97	0.25
	103.75	6	0.2	0.98	---	---
	162.656	2	0.72	0.69	0.69	0.72
	272.318	4	~0	1.0	0.25	-0.97
	284.64	7	1.0	0.0	---	---
	318.201	3	0.43	0.90	0.11	-0.99
	321.95	5	~0	1.0	0.11	-0.99
	467.8	1	0.59	0.81	0.46	0.89
	581.1	0	1.0	0.0	1.00	0.00

PAIRING CORRELATIONS IN THE TIN ISOTOPES IN THE FRAMEWORK OF THE HFB METHOD

J. Bar-Touv† and G. L. Struble

A common feature of many nuclear structure calculations for the tin isotopes [1] is the assumption that the spherical shell model single-particle field is the canonical basis to be used in the study of pairing correlations. The implication of this choice, as various calculations (including the one discussed here) show, is that for tin isotopes even with an open core (e.g., letting all nucleons above an inert ^{56}Ni core participate in the production of the self-consistent field), all pairing correlations are due to the valence neutrons. With a reasonable choice of single-particle energies and a big enough model space (e.g., 12 orbitals above the ^{56}Ni core), Baranger and Clement [1] were able to get quite satisfactory results for the odd-even mass differences and somewhat reasonable agreement between the low-lying states of the odd-mass isotopes and the one-quasi-particle states of the spherical Hartree-Fock-Bogoliubov (HFB) solution.

Our purpose is to reexamine the various assumptions commonly employed in the study of pairing correlations in the tin isotopes. Specifically we examine whether the spherical Hartree-Fock

(HF) solution is the lowest solution in all the tin even-mass isotopes. Then, by using both the lowest spherical and lowest deformed HF solutions for constructing the trial wave function for solving the HFB equations, we examine which HFB solution is lower in energy. It is commonly argued that even if one starts with a deformed basis, pairing correlations restore spherical symmetry for these nuclei. In doing so there is no need to consider proton-proton pairing, since this kind of pairing is excluded by the relatively big single-particle gap of the protons (e.g., for ^{116}Sn this gap for a reasonable set of parameters is of the order of 5 MeV, compared with 0.65 MeV for the neutrons).

In order to be able to make comparisons with other recent calculations we choose our single-particle parameters in such a way that our spherical HF field for ^{116}Sn is close to the corresponding one used in Ref. 1. We also employ the Tabakin interaction with an oscillator length b = 2.22 F. In order to test our single-particle parameters, we first calculate the spherical HFB solutions for the even-mass isotopes between ^{112}Sn and ^{124}Sn. We find the single-particle gap in the proton HF field is preserved to the extent that all pairing correlations result from the pairing of neutrons. Due to this result and the fact that these spherical HFB solutions give a somewhat improved description of the odd-even mass differences, we believe we have a reasonable set of parameters for extending the HFB calculations.

Our extended calculations reveal that as soon as deformation in the underlying HF field is allowed, the proton single-particle gap disappears (e.g., for ^{116}Sn the proton gap reduces to 0.1 MeV while the neutron gap stays at its initial value). This reduction makes the proton Fermi surface vulnerable to dispersion, and indeed the corresponding HFB solutions have strong pairing between protons. The results for the pairing energy, the HF energy, and the HFB energy of the lowest deformed and spherical solutions are presented in Table I. The quadrupole deformation parameter β for the deformed HFB solution is also given. The HF and HFB energies of each isotope are defined up to a constant E_0 that varies with each isotope. In all the spherical HFB solutions pairing is due only to the neutrons, whereas in all the deformed solutions both the protons and neutrons pair. Up to and including ^{118}Sn the deformed HFB solutions are lower in energy. The differences between the two solutions start with 3.94 MeV at ^{112}Sn and decrease (almost linearly with a constant slope of 0.54 MeV per particle) with mass number to the point where the spherical solutions become lower. It is also observed that the deformation of the HFB solution is rather large, i.e., the deformation of the underlying HF field does not vanish due to pairing although some reduction does occur. Another observation one can make from this table is the reduction of β with mass. This is accompanied by a lower gain for the deformed HF and HFB solutions.

To summarize briefly, it is shown here that the self-consistent HFB field is not necessarily spherical, and that for deformed HFB solutions proton pairing is not excluded. Unfortunately the utilization of the deformed quasi-particle field for calculating the properties of the low-energy spectrum (e.g., by the RPA approximation) would be quite tedious. However, from the point of view of relating the intrinsic structure of Sn isotopes to the solutions of the HFB equations, one cannot ignore the fact that for some cases the commonly used approximations may not be valid.

Footnote and Reference

†Case Western Reserve University, Cleveland, Ohio.

1. David L. Clement and E. W. Baranger, Nucl. Phys. A120, 25 (1968).

Table I. Properties of the HFB solutions for the Sn isotopes. All energies are in MeV.

Isotope	B	E_{HF}	E_{PAIR}	E_{HFB}
^{112}Sn	0	276.25	-9.89	266.36
^{112}Sn	0.421	269.78	-7.36	262.42
^{114}Sn	0	277.95	-8.41	269.54
^{114}Sn	0.391	274.06	-7.07	266.99
^{116}Sn	0	280.96	-8.18	272.78
^{116}Sn	0.373	276.23	-5.04	271.19
^{118}Sn	0	285.27	-8.73	276.54
^{118}Sn	0.366	278.90	-2.76	276.14
^{120}Sn	0	290.49	-9.54	280.95
^{122}Sn	0	295.79	-10.45	285.34
^{122}Sn	0.249	297.33	-9.83	287.50
^{124}Sn	0	300.68	-10.91	289.77
^{124}Sn	0.191	302.79	-10.49	292.30

GENERALIZED PAIRING CORRELATIONS IN THE s-d SHELL†

A. Goodman, G. L. Struble, J. Bar-Touv,* and A. Goswami*

An investigation of pairing correlations in light nuclei must consider the possibility that neutron-proton pairing may be present. In particular, isospin pairing[1] might occur as a result of the importance of the T = 0 component in the force.[1] In this paper, only N = Z even-even nuclei are discussed. Experimentally these nuclei appear to possess deformed equilibrium shapes. Hartree-Fock (HF) calculations[2] confirm this, but a serious difficulty arises since they give many different self-consistent solutions, some of which differ only slightly in energy.[3] The usual choice for the physical state is the solution for which $\langle H \rangle$ is a minimum. However, this criterion may not be meaningful, since higher correlations--e.g., pairing--could lower the energy of other solutions relative to the lowest HF solution, which itself often shows large fluctuations. Therefore we examine Hartree-Fock-Bogoliubov (HFB) solutions.

We start with the Hamiltonian

$$\mathcal{H} = \Sigma \epsilon_\alpha c_\alpha^\dagger c_\alpha + \frac{1}{2} \Sigma \langle \alpha\beta | V | \gamma\delta \rangle c_\alpha^\dagger c_\beta^\dagger c_\delta c_\gamma ,$$

$$|\alpha\rangle \equiv |n \ell j m \tau\rangle ,$$

and look for self-consistent solutions to the HFB matrix

$$\begin{pmatrix} \Gamma & \Delta \\ \Delta^+ & -\tilde{\Gamma} \end{pmatrix}.$$

In the $|\alpha\rangle$ representation,

$$\Gamma_{\alpha\beta} = \epsilon_\alpha \delta_{\alpha\beta} + \Sigma \langle \alpha\gamma | V | \beta\delta \rangle_a \langle c_\gamma^\dagger c_\delta \rangle, \qquad \Delta_{\alpha\beta} = \tfrac{1}{2} \Sigma \langle \alpha\beta | V | \gamma\delta \rangle_a \langle c_\delta c_\gamma \rangle .$$

By assuming that Δ is diagonal in the space-spin part of the underlying HF representation and $\langle T \rangle = 0$[1], one can simplify equations for N = Z even-even nuclei.

The HFB equations are solved by using experimental ϵ's and the force taken from the work of Bar-Touv and Kelson.[2] The solutions exhibit two systematic features: first, that T = 0 and T = 1 pairing are mutually exclusive, and second, that a large HF gap excludes pairing (in the BCS sense).

^{24}Mg and ^{32}S are of special interest, since HF calculations give two solutions which differ in energy by only $\approx$ 3 MeV. The lower solution is axially asymmetric, with an HF gap of $\approx$3 MeV. The energy gain due to pairing in the higher solution makes $\langle \mathcal{H} \rangle$ comparable for both solutions. However, the axially asymmetric solution has one crucial defect, since the spacings between the K = 0 and the K = 2 bands are underestimated by a factor of almost two.[4] In the paired solution, the two-quasi-particle state with K = 2 has an unperturbed energy of 5.6 MeV in ^{24}Mg and 6.7 MeV in ^{32}S. Preliminary calculations suggest that the quasi-particle interaction will bring this state to the experimental energy. Also, by using HFB solutions, the cranking moment of inertia is lowered. In addition, the Thouless-Valatin correction is expected to be less important for the paired state, since a larger part of the residual interaction has been considered. A comparison of theoretical and experimental moments of inertia is shown in Fig. 1. The experimental values for ^{32}S and ^{28}Si are the result of an extrapolation subtracting out the effect of the interaction of the I = 0+ member of the ground band with the spherical 0+ state observed at 3.78 MeV and 4.97 MeV respectively. For ^{20}Ne and ^{28}Si, the moment of inertia elected corresponds to the HF states. The HFB solutions for ^{32}S are listed in the table. The ground-state energy is -179.41; the pairing energy is -5.4 MeV.

In conclusion, it should be noted that the axially symmetric solution with pairing may result in an intrinsic basis for ^{24}Mg and ^{32}S that is closer to the physical state than the axially asymmetric HF solution.

Table I. Best axially symmetric solution for ^{32}S.

E_α (MeV)	6.04	5.60	3.83	3.28	2.85	5.17
Ω_α (MeV)	1/2	3/2	1/2	5/2	3/2	1/2
v_α^2	0.984	0.980	0.968	0.838	0.210	0.020
u_α^2	0.016	0.020	0.032	0.162	0.790	0.980
$\Delta_{np}^{T=0}(\alpha)$	-1.53	1.57	1.36	-2.41	-2.33	-1.44

Footnotes and References

†Submitted to International Conference on Properties of Nuclear States, Montreal, August 25-30, 1969.

*Case Western Reserve University, Cleveland, Ohio.

1. A. Goodman, G. Struble, and A. Goswami, Phys. Letters 26B, 260 (1968).
2. J. Bar-Touv and I. Kelson, Phys. Rev. 138, B1035 (1965); for earlier work see this reference.
3. M. K. Pal and A. P. Stamp, Phys. Rev. 158, 924 (1967).
4. J. Bar-Touv and I. Kelson, Phys. Rev. 142, 599 (1966).

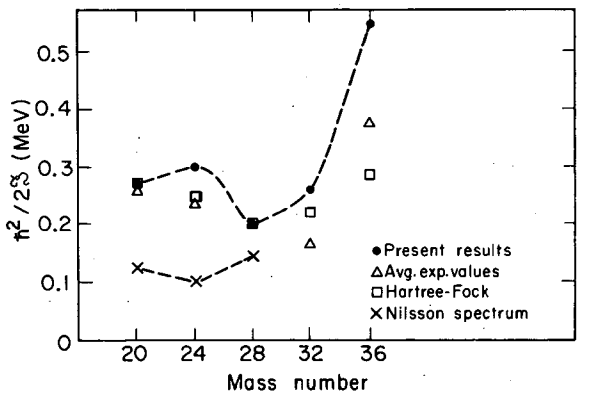

Fig. 1. Comparison of theoretical and experimental moments of inertia. (XBL 701-2102)

HARTREE-FOCK-BOGOLIUBOV CALCULATIONS IN THE s-d SHELL

A. L. Goodman, G. L. Struble, J. Bar-Touv,† and A. Goswami†

Attempts to describe the N = Z even-even nuclei in the s-d shell in terms of simple intrinsic state models have in general been unsuccessful. Although the low-energy structure of ^{20}Ne is very well described by Hartree-Fock (HF), there are serious problems in the description of ^{24}Mg, ^{32}S, and ^{36}Ar.[1] Still, the concept of an intrinsic state is very attractive, and so we tried to generalize HF by including pairing correlations.[2] In this paper we approximate the Hartree-Fock-Bogoliubov (HFB) equations in such a way as not to allow the pairing degrees of freedom to influence the underlying single-particle structure. Further, we use a simple phenomenological force and work in a rather restricted shell-model space. We have now solved the complete HFB problem[3] in a completely parameter-free manner in order to check the validity of our previous results and to better understood the nature of both T = 0 and T = 1 pairing in light nuclei.

The HFB equations may be written in matrix form as

$$\begin{bmatrix} (\mathcal{H} - \lambda) & \Delta \\ \Delta^{+} & (\lambda - \tilde{\mathcal{H}}) \end{bmatrix} \begin{bmatrix} u \\ v \end{bmatrix} = E \begin{bmatrix} u \\ v \end{bmatrix},$$

where $\mathcal{H}$ is the matrix representation of the HF Hamiltonian, λ is a Lagrange multiplier which fixes the number of protons and neutrons, and Δ is called the pairing potential.[3] The E's are quasi-particle energies and the vectors u and v are the complex coefficients of the quasi-particle transformation

$$a^{+}_{\alpha u} = \sum_{i\nu} [u_{\alpha\mu,\, i\nu}\, c^{+}_{i\nu} + v_{\alpha\mu,\, i\nu}\, c_{i\nu}].$$

Here α and i denote space-spin indices, and μ and ν are isospin indices. We assume generalized time reversal as our only self-consistent symmetry and solve these equations by iteration until self-consistency is achieved.

The HFB transformation matrix (B_{gen}) can be written as the product of three separate transformations,[3]

$$B_{gen} = R\, B_{sp}\, D,$$

where D is a transformation among the particle basis states and defines the canonical basis, B_{sp} represents a special Bogoliubov transformation (BCS) between particle and hole states in the canonical basis, and R is a transformation among the quasi particles defined in the first two trans-

formations. The essential approximation we made in Refs. 1 and 2 is to assume that the canonical basis is given by HF and that $\mathcal{H}$ and Δ are diagonal in this basis.

We carried out the calculations, using the Yale t matrix.[4] In Table I we give the pairing potential in the canonical basis. As can be seen, Δ is far from diagonal. In Table II we list HF energies, pairing energies, and the total binding energies for ^{24}Mg, ^{32}S, and ^{36}Ar as predicted by the theories used in Refs. 1 and 2 and the complete HFB. It is concluded that the diagonal Δ approximation may lead to serious discrepancies.

Table I. The pairing potential Δ expressed in the canonical basis for the nuclei ^{24}Mg, ^{32}S, and ^{36}Ar.

$\Omega\pi$	^{24}Mg	^{32}S	^{36}Ar
5/2+	1.372	-1.934	-1.372
-3/2+	1.428 0.678	3.355 0.466	2.508 0.425
	0.678 -2.604	0.466 -2.166	0.425 -1.526
1/2+	1.189 0.378 -0.116 1.058	-3.707 -0.365 -0.530 -0.402	-3.862 -0.553 -0.264 -0.610
	0.378 -2.589 0.845 -0.458	-0.365 3.561 -0.103 0.019	-0.553 2.755 -0.256 0.030
	-0.116 0.845 2.547 0.367	-0.530 -0.103 -1.940 -0.989	-0.264 -0.256 -1.360 -0.310
	1.058 -0.458 0.367 1.656	-0.402 0.019 -0.989 -4.104	-0.610 0.030 -0.310 -4.016
-3/2-	-2.178	3.411	2.620
1/2-	-2.264 -0.022	-4.153 -0.015	-4.003 -0.034
	-0.022 2.537	-0.015 3.524	-0.034 2.707

Table II. Energies given for several pairing approximations. HF + BCS refer to the approximation of Ref. 2. Approx. HFB refers to the approximation of Ref. 1.

	Method	E_{HF}	E_{pair}	E_{total}
^{24}Mg				
	HF + BCS	-126.02	-6.31	-132.33
	Approx. HFB	-126.53	-5.58	-132.11
	HFB	-124.73	-7.80	-132.53
^{32}S				
	HF + BCS	-219.01	-4.75	-223.76
	Approx. HFB	-218.94	-4.88	-223.83
	HFB	-215.32	-9.21	-224.53
^{36}Ar				
	HF + BCS	-283.71	-3.39	-287.10
	Approx. HFB	-282.76	-3.92	-286.68
	HFB	-282.24	-9.52	-291.76

The validity of the number nonconservation approximation has been tested by calculating the mass discontinuity in the canonical basis, and it is found that there is no significant difference between the theory of Ref. 1 and the HFB results. Numerical calculations also show that T = 1 pairing and T = 0 pairing between particles in the same single-particle state are suppressed and that only T = 0 pairing between particles in time-conjugate states occurs.

The inclusion of pairing correlations has very significant effects on the intrinsic states. In the first place it restores axial symmetry to ^{24}Mg and ^{32}S, bringing them into qualitative agreement with experiment. Further, the pairing always reduces the α-clustering effect and reduces the overall deformation. This is illustrated by comparing Figs. 1 and 2, where we have plotted the equidensity contours for the ^{36}Ar HF and HFB solutions. Both solutions are oblate, but the HFB solution is much less deformed. This is reflected in the moment of inertia, which is only half as large for the HFB solution. These results suggest that ^{36}Ar is more properly described as a vibrator. This is again qualitatively borne out by experiment.

Footnote and References

†Case Western Reserve University, Cleveland, Ohio.

1. J. Bar-Touv, A. Goswami, A. L. Goodman, and G. L. Struble, Phys. Rev. 178, 1670 (1969).
2. A. L. Goodman, G. L. Struble, and A. Goswami, Phys. Letters 26B, 260 (1968).
3. A. L. Goodman, G. L. Struble, J. Bar-Touv, and A. Goswami, Generalized Pairing in Light Nuclei. II (UCRL-19506, Jan. 1970), submitted to Phys. Rev.
4. C. M. Shakin, Y. R. Waghmare, and M. H. Hull, Phys. Rev. 161, 1006 (1967).

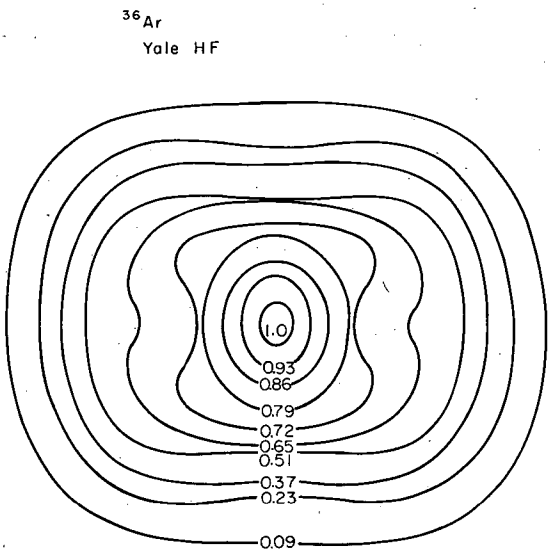

Fig. 1. Equidensity contours for the ^{36}Ar Hartree-Fock solution using the Yale potential. The densities are given in the units of 0.302 F^{-3}. (XBL 6912-6351)

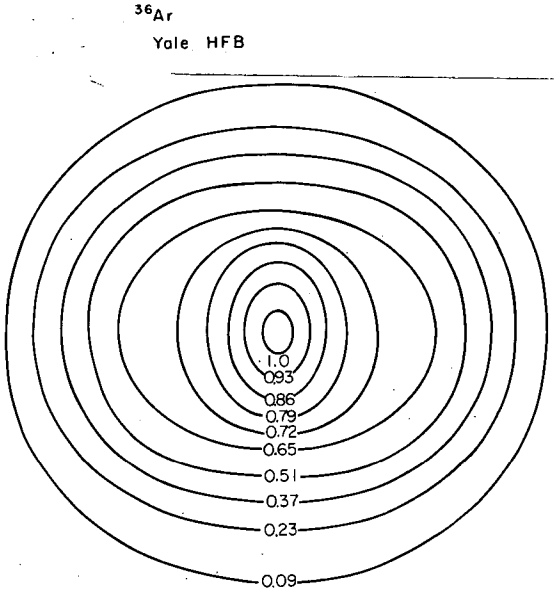

Fig. 2. Equidensity contours for ^{36}Ar Hartree-Fock-Boholiubov solution using the Yale potential. The densities are given in units of 0.300 F^{-3}. (XBL 6912-6347)

THE ANALOGUES OF A FOUR-PARTICLE–FOUR-HOLE STATE OF ^{16}O IN 2s, 1d SHELL NUCLEI†

G. L. Struble and S. N. Tewari

It is well known that the 0^+ state at 6.06 MeV in ^{16}O is the beginning of a rotational band. Banerjee et al. [Phys. Letters 24B, 209 (1967)] have successfully explained this state on the basis of the Hartree-Fock (HF) theory. It is identified as the lowest member of a triaxial four-particle-four-hole HF state. Further, one of the 0^+ states around 7 MeV in ^{20}Ne cannot be explained by using the space of 2s, 1d shell alone. In the opinion of several authors it may be an eight-particle-four-hole state, the analogue of a four-particle–four-hole state in ^{16}O. In view of these results, we have been prompted to calculate the analogous n-particle–four-hole states in N = Z even-even nuclei of the 2s, 1d shell. For the Hamiltonian we have used the two-body Rosenfeld force and assumed a ^4He core. The single-particle energies relative to this core were chosen to fit the experimental energies of ^{17}O and ^{15}O. It has been shown by Banerjee (Maryland University Technical Report No. 875) that the invariance of HF densities under the operations T, $Pe^{-i\pi J_y}$ and $e^{i\pi J_z}$ allows one to predict the shapes of the HF state (T and P refer to the time-reversal and parity operations). Our calculations confirm these predictions and give the following energies for the band head relative to the ground state: ^{16}O (triaxial) 2.4 MeV, ^{20}Ne (triaxial) 4.23 MeV, ^{24}Mg (oblate) 9.1 MeV, ^{32}S (oblate) 47.90 MeV, ^{36}Ar (oblate) 73.64 MeV.

The positions of the band head were determined by subtracting an appropriate value of $A J^2$ from the ground-state and n-particle–four-hole HF energies. The moment of inertia parameter A was computed by the second-order cranking model. Despite the simple nature of our Hamiltonian and the crudeness of our approach it is clear from our results that the n-particle–four-hole states will not be observed beyond ^{24}Mg. In the upper half of the 2s,1d shell hole-particle degrees of freedom from the ^{40}Ca core should become increasingly important.

It is observed that in both ^{16}O and ^{20}Ne the energy of the n-particle–four-hole state falls considerably below the experimental energies. In view of the fact that the n-particle–four-hole HF states in both nuclei have a large value of $\langle J^2 \rangle$, a slight overestimate of A by the cranking model could easily account for the discrepancy. For example, in ^{20}Ne the value of $\langle J^2 \rangle$ for the eight-particle–four-hole state is 30 units, compared with 15 units for the ground state. If the cranking-model value of A for the eight-particle–four-hole state is decreased by only ≈ 0.08, the state is placed close to the experimental energy.

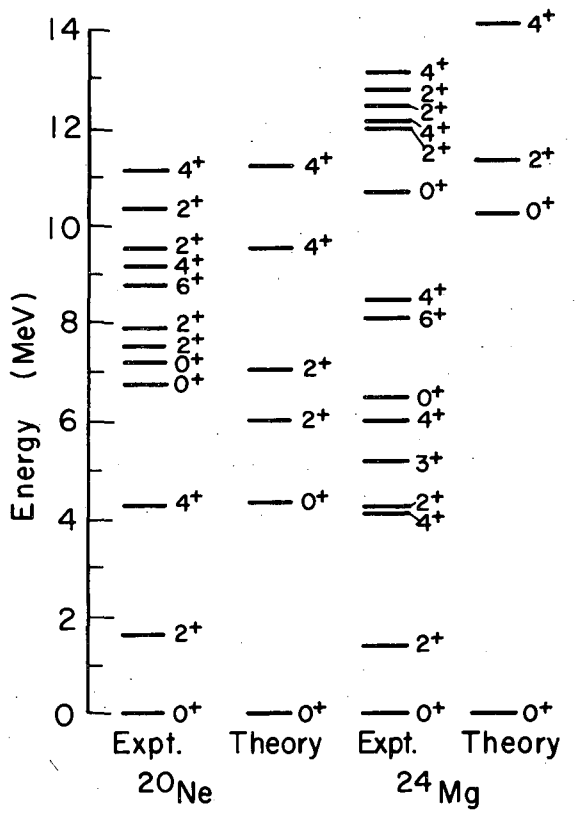

Fig. 1. Comparison between experimental and calculated energies. (XBL 701-2103)

The n-particle–four-hole HF intrinsic states exhibit very large energy gaps, 10.29 MeV in ^{20}Ne and 9.2 MeV in ^{24}Mg. This suggests that they will be stable to two-particle–two-hole and higher admixtures and that the projected angular momentum states may yield good approximations to the physical states. In ^{24}Mg the energy spectrum has been calculated by using the projected states. The accuracy of the projected states has also been tested in this case by calculating the energy fluctuation $\langle P^J H^2 \rangle - \langle P^J H \rangle^2$. The fluctuation turns out to be between 4 and 5 MeV^2 for the J = 0, 2, 4 states. The smallness of the fluctuation suggests that the projected states in ^{24}Mg are approximately good eigenstates. The energies from the eight-particle–four-hole state in ^{20}Ne were calculated by the Davidov-Filipov model because of the complexities of the nonaxial projection calculation. The comparison between theory and experiment is shown in Fig. 1.

Footnote

†Submitted to International Conference on Properties for Nuclear States, Montreal, August 25-30, 1969.

A CALCULATION OF ODD-PARITY STATES IN ^{16}O AND ^{40}Ca FROM THE NUCLEON-NUCLEON INTERACTION†

P. K. Haug* and M. Weigel‡

It is well known that the excitation energies $\omega_A^k = E_k(A) - E_0(A)$ are given by the poles of reduced renormalized response function. [1] Near the pole one can express the response function by

$$\tilde{L}_{\mu\nu\alpha\beta}(\omega) \approx - \frac{\tilde{\rho}_{\mu\alpha,k}\tilde{\rho}_{\beta\nu,k}}{\omega - \omega_A^k + i\sigma} ,$$

where $\tilde{\rho}_{\mu\alpha,k}$ is the renormalized particle-hole amplitude corresponding to the quantum number sets μ and α. If one neglects retardation effects the equation for $\tilde{\rho}$ is[1,2]

$$(\epsilon_\alpha - \epsilon_\mu - \omega_A^k)\tilde{\rho}_{\alpha\mu,k} = (n_\alpha - n_\mu)\sum_{\beta\lambda} F_{\alpha\lambda\mu\beta}(\omega_A^k)\,\tilde{\rho}_{\mu\lambda,k} .$$

It can be shown[3] that the ladder approximation should be appropriate for dealing with the short-range nucleon-nucleon interaction V^N ($\equiv K^L$), which reduces the equation for the unrenormalized particle-hole force K^L to

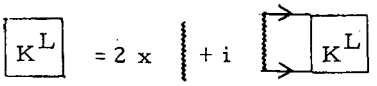

We used the solutions for this equation in the so-called Λ^{00}-approximation[4] for the nuclear matter problem. For the nucleon-nucleon potential we took the hard-shell Puff potential[4] fitted to the S-wave phase shifts up to 320 MeV. The solutions are density-dependent. The density dependence of the particle-hole force was interpolated with the help of a Thomas-Fermi distribution from the values inside the nucleus and the vacuum values (local density approximation). Furthermore we assumed all renormalization factors to be equal. Nuclear matter calculations suggested a value of $0.8 + 0.05$ for z at the Fermi level.[5] We obtained best agreement with the experimental situation with $z = 0.795$ for ^{16}O and $z = 0.81$ for ^{40}Ca. Therefore in order to avoid additional parameters we set $z = 0.8$ for all cited calculations, so making our model practically free of adjustable parameters. The results are shown in Figs. 1 and 2. For comparison with other calculations we calculated the weighted mean quadratic deviation for ^{16}O. We obtained the value 0.27. Without renormalization one gets for the comparably simple Kallio-Kolltveit potential the value 0.36.[6]

Footnotes and References

†Condensed from Ref. 2.

*Address: Project Symphonie, Bonn, Germany.

‡On leave from Sektion Physik der Universität München, Munich, Germany.

1. For instance: M. Weigel, Nucl. Phys. A137, 629 (1969).
2. P. K. Haug and M. Weigel, Nuovo Cimento Letters 2, 17, 799 (1969).
3. David A. Kirzhnits, Field-Theoretical Methods in Many-Body Systems (Pergamon Press, New York, 1967).
4. R. D. Puff, Ann. Phys. 13, 317 (1961).
5. G. Wegmann, Z. Physik 211, 235 (1968).
6. H. A. Mavromatis, W. Markiewicz, and A. M. Green, Nucl. Phys. A90, 101 (1967).

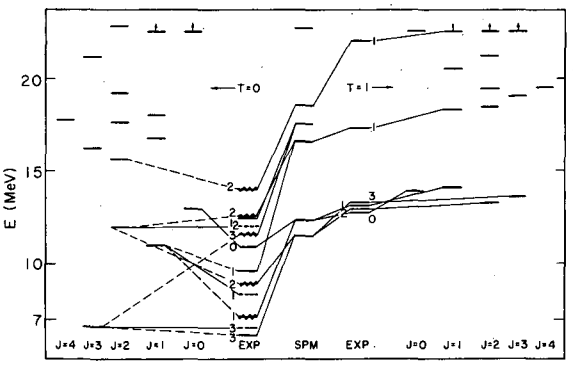

Fig. 1. Calculated and experimental levels for ^{16}O. (XBL 701-2101)

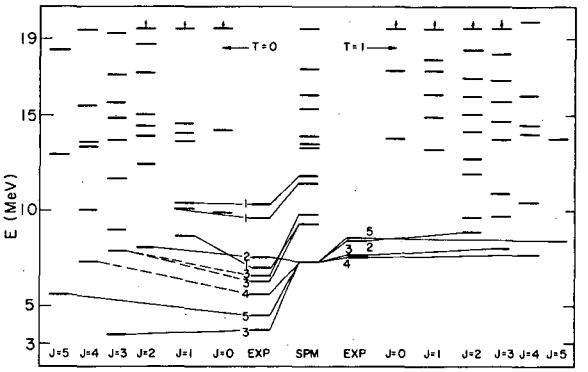

Fig. 2. Calculated and experimental levels for ^{40}Ca. (XBL 701-2100)

SINGLE-PARTICLE RESONANCES IN THE RPA TREATMENT OF NUCLEON-NUCLEUS SCATTERING

L. Garside and M. Weigel†

In an earlier work it was shown how one can treat the nucleon-nucleus scattering in the framework of RPA.[1,2] In order to achieve a practicable treatment we assumed that the so-called bound-state problem is solved with the full particle-hole force. The coupling to the continuum was done by approximating the particle-hole matrix elements containing single-particle continuum states by a schematic force. The model was so designed that one assumes the solutions of the bound-state problem to be already a good first approximation to the experimental situation. But it is well known that in many cases one has to include in the bound-state problem certain single-particle resonances in order to obtain good agreement. A famous example is, for instance, the $1d_{3/2}$ resonance of ^{16}O necessary for the calculation of the excited negative parity states of ^{16}O.[3] We overcome this difficulty by using a method of Garside and MacDonald,[4] in which one shifts the single-particle resonance into a bound state by adding a small single-particle potential to the original one. Due to this shift one can now apply the original formalism but with a different coupling to the continuum, since one has to compensate the additional potential. We are able to give the explicit formulas for the scattering problem and the modified bound-state problem containing only the separable particle-hole force, the additional single-particle potential, and the bound-state solutions.

Footnotes and References

†On leave from Sektion Physik der Universität München, Munich, Germany.

1. M. Weigel, Nucl. Phys. A137, 629 (1969); Linear Response Theory in Nucleon-Nucleus Scattering, UCRL-18907, May 1969.
2. M. Weigel, Inclusion of Nuclear-Structure Calculations in Nucleon-Nucleus Scattering (UCRL-18994, Sept. 1969), submitted to Phys. Rev.
3. V. Gillet, in Proceedings of the International School of Physics "Enrico Fermi," Course XXXVI (1966) (Academic Press, New York, 1966).
4. L. Garside and W. M. MacDonald, Phys. Rev. 138, B582 (1965).

LINEAR RESPONSE THEORY IN NUCLEON-NUCLEUS SCATTERING†

Manfred Weigel*

The general theory for scattering of nucleons on a hole nucleus was investigated in the framework of Green's functions. [1] We have been able to express the scattering amplitude T^R due to the effective particle-hole interaction in terms of the effective particle-hole interaction and the reduced renormalized linear response function. In this treatment ground-state correlations of the nucleus are included. Furthermore we took into account Migdal's quasi-particle description of nuclei, thus dealing only with renormalized quantities. [2] We also give the method of obtaining the particle-hole force starting from the real nucleon-nucleon force. Assuming pure quasi-particle propagation in the intermediate states we obtain a formalism similar to the RPA treatment, [3] but in contradiction to the RPA method we have been able to show that one has to use the experimental single-particle energies instead of the Hartree-Fock single-particle energies, and the effective particle-hole force instead of the true nucleon-nucleon force. [4] If we neglect ground-state correlations we obtain the results of MacDonald. [5]

The resonances of the scattering are determined by the zero points of the Fredholm determinant. The expansion of the Fredholm determinant contains only the effective particle-hole interaction and the shell-model single-quasi-particle propagator. In principle one could obtain the resonances by summing up terms in the Fredholm expansion until convergence is achieved. The main problems are the multidimensional integrations involved in this approach. In order to avoid this difficulty we treated only the extended schematic model. [4] Due to the degeneracy of the Fredholm determinant only the first two terms of the expansion are nonzero. In this model the T matrix can be given explicitly. Furthermore one obtains the energy shift caused by the continuum and the width.

Footnotes and References

†Condensed from Ref. 1.

*On leave from Sektion Physik der Universität München, Munich, Germany.

1. M. Weigel, Nucl. Phys. A137, 629 (1969).
2. A. B. Migdal, Theory of Finite Fermi Systems and Applications to Atomic Nuclei (Interscience, New York, 1967).
3. K. Dietrich and K. Hara, Nucl. Phys. A111, 392 (1968).
R. H. Lemmer and M. Veneroni, Phys. Rev. 170, 883 (1968).
4. G. E. Brown, Unified Theory of Nuclear Models and Forces (John Wiley & Sons, New York, 1967).
5. W. M. MacDonald, Nucl. Phys. 54, 393 (1964); 56, 636 (1964).

INCLUSION OF NUCLEAR-STRUCTURE CALCULATIONS IN NUCLEON-NUCLEUS SCATTERING†

M. Weigel

The goal of this investigation is the inclusion of a normal shell-model structure calculation in the treatment of the nucleon-nucleus scattering. The microscopic approach to the scattering problem with inclusion of ground-state correlations usually leads to a very complicated system of equations for the particle-hole amplitudes which is hardly solvable for a general particle-hole force. The reason is the necessary inclusion of continuum single-particle states, so that one is no longer able to solve a problem in a finite vector space only, as in the case of a nuclear-structure calculation. [1,2] Therefore one usually treats the whole problem in the framework of a schematic model. [1] But it is well known that a schematic approach is poor in the bound-state problem. For this reason the model designed splits the problem into two parts: First, one has to solve the usual nuclear structure problem with the full particle-hole force (or to take it from the literature), taking into account only bound one-particle wave functions. It is known that this approach is already a good first approximation to the physical situation. Then we use the solutions of the nuclear-structure problem in the scattering problem and in the extended bound-state problem. The deviations from the nuclear structure calculations--caused by the matrix elements of the interaction between continuum-bound and continuum-continuum single-particle states--are treated by a schematic approach. This implies that these special matrix elements can be approximately

represented by a separable particle-hole force. We have given the explicit expressions for particle-hole amplitudes and the scattering amplitude in terms of the solutions of the nuclear-structure problem and the separable force alone. Furthermore we derived the energy-dispersion relation for the energy eigenvalues for "bound" states, which may be complex. The scattering amplitude has resonances for these complex energy values—as expected. [2]

In several cases one has to include a single-particle resonance in the nuclear-structure calculation in order to obtain a good first approximation (for example the $1d_{3/2}$ state in ^{16}O). Since our formalism does not directly apply to this situation, we will have to treat this problem in a forthcoming paper.

Footnotes and References

†Condensed from Ref. 2.
*On leave from Sektion Physik der Universität München, Munich, Germany.
1. K. Dietrich and K. Hara, Nucl. Phys. A111, 392 (1968); R. H. Lemmer and M. Veneroni, Phys. Rev. 170, 883 (1968); and M. Weigel, Nucl. Phys. A137, 629 (1969).
2. M. Weigel, Inclusion of Nuclear-Structure Calculations in Nucleon-Nucleus Scattering (UCRL-18994, Sept. 1969), submitted to Phys. Rev.

PROPERTIES OF NUCLEAR MATTER IN THE Λ^{00} APPROXIMATION WITH LOCAL NUCLEON-NUCLEON FORCES†

H. Gall,* G. Wegmann,* and M. Weigel‡

It is well known that the Brueckner approach to the nuclear matter problem consists mainly in summing up the ladder-graphs in the effective two-body scattering amplitude. Furthermore one neglects all terms in the K matrix that lead to an imaginary contribution for the effective one-particle potential. If one includes some (or all) of these terms several new approximations can be created. They are denoted by the type of intermediate particle-particle-propagation used[1] (Λ^{00}, Λ^{01}, Λ^{HF1}, and Λ^{11} approximation). Since these approximations do not lead to a single-particle description of nuclear matter a priori as the Brueckner approach does, the nuclear matter problem in these approximations has been studied only with simple separable nucleon-nucleon-interactions. [1] But it is known that velocity-dependent potentials fitted to the nucleon-nucleon scattering data without a hard-core behavior give too much binding energy. [2] Therefore we tested the relatively simple Λ^{00} approximation in a model calculation to show the decrease of binding energy in comparison with a separable interaction. We restricted ourselves to a local S-wave potential. [3] In the case of a local potential one cannot solve the T-matrix equation directly, as in the separable case. We overcame this difficulty by using a method designed by Laughlin and Scott. [4] Our results show the decrease of the binding energy (see Fig. 1, for instance: $E/N = -34.5$ MeV for the separable Foster potential in the Λ^{00} approximation). One can see, furthermore, that the equilibrium data are not uniquely determined in the Λ^{00} approximation (Figs. 1 and 2).

The condition should be $E/N = \mu = d\epsilon/d\rho$ (pressure = 0, μ denotes the chemical potential). This condition can be fulfilled a priori in the Hartree-Fock and Λ^{11} approximation only. [5] Since we have used an S-wave potential our results seem to be reasonable. Furthermore, we did not obtain the momentum distribution of the shell model (see Fig. 3, $\rho_{s.p.}(P/PF) = 1$ for $P \leq P_F$).

Footnotes and References

†Condensed from paper submitted to Phys. Rev.
*Address: Sektion Physik der Universität München, Munich, Germany.
‡On leave from Sektion Physik der Universität München, Munich, Germany.
1. J. C. Reynolds and R. D. Puff, Phys. Rev. 130, 1877 (1963); D. S. Falk and L. Wilets, Phys. Rev. 124, 1887 (1961); T. C. Foster, Phys. Rev. 149, 784 (1966); D. E. Beck and A. M. Sessler, Phys. Rev. 146, 161 (1966); G. Wegmann, Z. Physik 211, 235 (1968); M. Weigel, Nuovo Cimento 54B, 326 (1968).
2. B. S. Bhakar and R. J. McCarthy, Nucl. Phys. A104, 283 (1967).
3. M. Weigel, Z. Physik 216, 307 (1968).
4. R. Laughlin and L. Scott, Phys. Rev. 171, 1196 (1968).

5. G. Baym, Phys. Rev. 127, 1391 (1962).

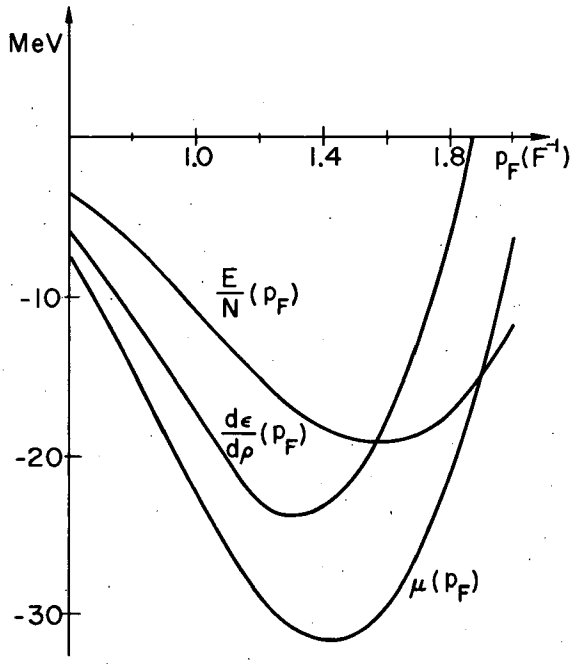

Fig. 1. Energy per nucleon as a function of Fermi momentum. (XBL701-2097)

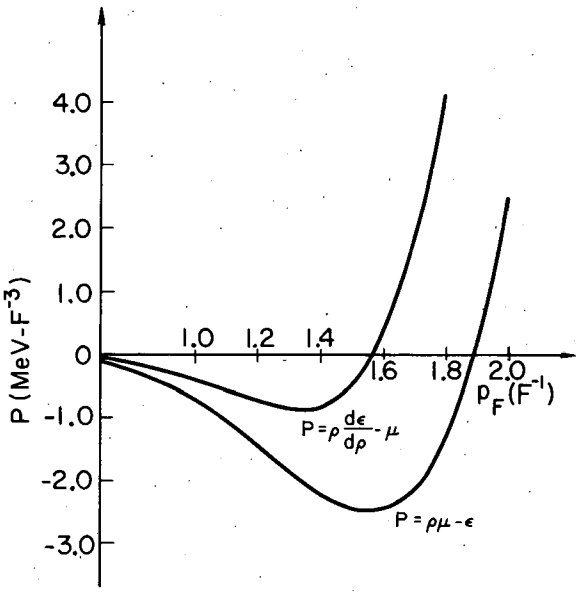

Fig. 2. Pressure according to different equilibrium conditions. (XBL701-2098)

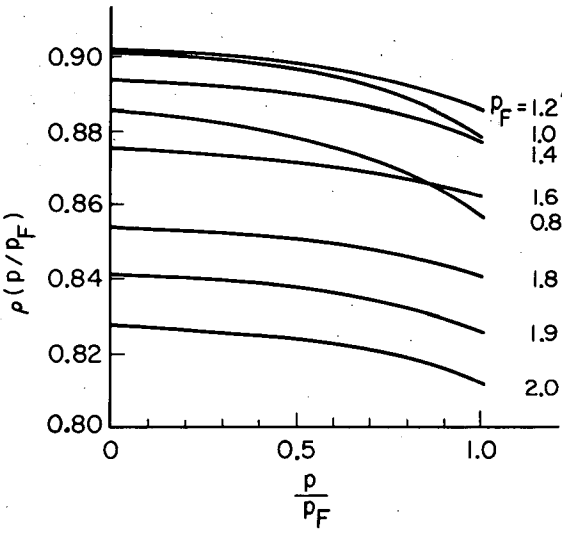

Fig. 3. Momentum distribution as a function Fermi momentum. (XBL701-2099)

TRITON CALCULATIONS WITH REALISTIC POTENTIALS

A. D. Jackson,† A. Lande,* and P. U. Sauer‡

Usual calculations of the triton binding energy follow a variational approach, and their success depends in large measure on the insight employed in the choice of a trial wave function. An alternative approach is to generate a complete set of three-body states and to diagonalize the Hamiltonian matrix in a truncated basis of such states. The nature of the nucleon-nucleon interaction suggests that only states having particle permutation symmetry [3] S, [21] D, and [21] S play an important role in determining the properties of the triton ground state. It is thus desirable to construct a complete set of states so that they will have well-defined orbital permutation symmetry. Moshinsky et al.[1] have shown that it is a relatively simple matter to generate just such a set of states.

The most convenient coordinate system for the three-body calculation may be written in terms of single-particle coordinates as

$$\begin{aligned} \underset{\sim}{\dot{x}}_1 &= (1/\sqrt{2})\,(\underset{\sim}{x}_1 - \underset{\sim}{x}_2), \\ \underset{\sim}{\dot{x}}_2 &= (1/\sqrt{6})\,(\underset{\sim}{x}_1 + \underset{\sim}{x}_2 - 2\,\underset{\sim}{x}_3), \\ \underset{\sim}{\dot{x}}_3 &= (1/\sqrt{3})\,(\underset{\sim}{x}_1 + \underset{\sim}{x}_2 + \underset{\sim}{x}_3)\,. \end{aligned} \tag{1}$$

The harmonic oscillator Hamiltonian is invariant under this coordinate change, and we may write a complete set of orbital states for the three-body system as

$$\left|\phi_{n_1\ell_1}(\underset{\sim}{\dot{x}}_1)\,\phi_{n_2\ell_2}(\underset{\sim}{\dot{x}}_2)\,LM\right\rangle \tag{2}$$

(The coordinate $\underset{\sim}{\dot{x}}_3$ may be ignored because of the translational invariance of the nucleon-nucleon potential.) Moshinsky et al.[1] define a second coordinate transformation

$$\begin{aligned} \underset{\sim}{r}_1 &= (1/\sqrt{2})\,(-i\,\underset{\sim}{\dot{x}}_1 + \underset{\sim}{\dot{x}}_2)\,, \\ \underset{\sim}{r}_2 &= (1/\sqrt{2})\,(+i\,\underset{\sim}{\dot{x}}_1 + \underset{\sim}{\dot{x}}_2)\,, \end{aligned} \tag{3}$$

and demonstrate that the states

$$\left\{\left|\phi_{n_1\ell_1}(r_1)\,\phi_{n_2\ell_2}(r_2)\,LM\right\rangle + (-)^{\ell_1+\ell_6-L+I}\left|\phi_{n_2\ell_2}(r_1)\phi_{n_1\ell_1}(r_2)\,LM\right\rangle\right\} \tag{4}$$

are states of well-defined particle permutation symmetry. Moreover, states having the form (4) may be expanded as a sum of states of the form (3) in such a way that the expansion coefficients are trivially related to the ordinary harmonic oscillator transformation brackets.[2] Totally antisymmetric states of the three-nucleon system may be obtained by combination of the orbital states (4) with spin-isospin states of adjoint symmetry.

We can now construct and diagonalize the Hamiltonian matrix including all states for which $Q = (2n_1 + \ell_1) + (2n_2 + \ell_2)$ is less than some Q_0. It remains to be demonstrated that a value of Q_0 small enough to permit calculation will provide a good basis for describing the triton wave function for realistic nucleon-nucleon interactions.

As a simple example we consider a Yamaguchi potential, which is the average of the singlet- and triplet-S potentials and has the form

$$\langle P\,|V|\,P'\rangle = \frac{\lambda}{M}\,\frac{1}{P^2+\beta^2}\,\frac{1}{P'^2+\beta^2}\,, \tag{5}$$

where $\lambda = 0.35249\ F^{-3}$ and $\beta = 1.4487\ F^{-1}$. Since this potential is separable, our results may be compared with the binding energy of 12.49 MeV obtained from a solution of the Faddeev equations.[3] By design, this potential contains only [3]S states. For $Q_0 = 28$ and $\hbar\omega = 64.79$ the Hamiltonian matrix contained 147 [3]S states and gave a binding energy for the triton of 12.19 MeV, in satisfactory agreement with the exact result. It is of interest to note that a similar shell-model calculation of the deuteron binding energy displayed very similar convergence as a function of Q_0. It would appear that the deuteron might provide a simple and sensible way to estimate a value of Q_0 satisfactory for a triton calculation.

The Reid potential[4] is a soft-core potential which provides a quantitative fit to scattering data for laboratory energies less than 350 MeV. It should provide a more rigorous test of the applicability of this method. A deuteron calculation suggests that $Q_0 = 28$ and $\hbar\omega = 51.19$ will provide sufficient freedom for the triton calculation. Due to the large number of [21]D states at $Q_0 = 28$ (i.e., 560) the calculation was performed with $Q_S = 28$ and $Q_D = 16$. Only [3]S and [21]D states were included in the calculation. The resulting triton binding energy was 3.86 MeV. This estimate of the binding energy would surely be improved by the addition of more [21]D states. This result is roughly comparable to the value of 6.8 MeV obtained by Delves et al.[5] for the hard-cord Hamada-Johnston potential.

Calculations are in progress to increase the number of [21]D states and to include the effects of other permutation symmetries. It is already clear, however, that this straightforward approach to the three-body problem is a practical one and is capable of providing meaningful results even for realistically hard nucleon-nucleon potentials.

Footnotes and References

†Present address: State University of New York at Stony Brook, Stony Brook, Long Island, New York.
*Present address: Niels Bohr Institute, Blegdamsvej 17, Copenhagen, Denmark.
‡Present address: Center for Theoretical Physics, Massachusetts Institute of Technology, Cambridge, Massachusetts.

1. V. C. Aguilera-Navarro, M. Moshinsky, and W. W. Yeh, Rev. Mex. Fis. 17, 241 (1968).
2. T. A. Brody and M. Moshinsky, Tables of Transformation Brackets (Gordon & Breach, New York, 1967).
3. K. Hartt, private communication.
4. R. Reid, Ann. Phys. 50, 411 (1968).
5. L. M. Delves, J. M. Blatt, I. Pask, and B. Davies, Phys. Letters 25B, 472 (1969).

MATRIX ELEMENTS OF THE LAMBDA-NUCLEON POTENTIAL FROM PHASE SHIFTS

A. D. Jackson,† A. Lande,* and P. U. Sauer‡

Elliott et al.[1] have described a technique for deducing matrix elements of the nucleon-nucleon potential directly from phase shifts. This technique can be used to relate the limited ΛN scattering data to the separation energy B_Λ in hypernuclei.

Following Ref. 1, we construct an auxiliary potential of the form

$$V_0 = (1/2)\mu\omega^2 r^2 - (\hbar^2/2\mu)\alpha \quad \text{for } r < a,$$
$$= 0 \quad \text{for } r > a,$$

where μ is the reduced mass of the system. When $(\hbar^2/2\mu)(k^2 + \alpha) = (2n + \ell + 3/2)\hbar\omega$, the solution to the Schrödinger equation for V_0 has the form $B R_{n\ell}$ for $r < a$, where R_n is the ordinary harmonic oscillator wave function. By matching this solution to the plane wave at $r = a$ we obtain an auxiliary phase shift δ_0. Provided that the difference between the true potential V and V_0 is sufficiently small to be treated in Born approximation, we find

$$\langle n\ell | V | n\ell \rangle = \langle n\ell | V_0 | n\ell \rangle - (\hbar^2 k/2\mu B^2) \tan(\delta - \delta_0).$$

The parameters a and α, chosen separately for each n, ℓ, and $\hbar\omega$, are such that $\delta - \delta_0$ is small. The resulting values of $\langle n\ell | V | n\ell \rangle$ are found to be insensitive to the choice of α and a, which leads Elliott et al. to conclude that they are, in some sense, model-independent.

The ΛN scattering data for laboratory energies less than 45 MeV can be described in terms of scattering lengths and effective ranges[2-4] under the assumption that low-energy cross sections are dominated by the $^1S_0$ and $^3S_1$ channels. Oscillator matrix elements in these channels deduced according to the Elliott procedure for several sets of scattering parameters were found to be in substantial agreement with one another. Matrix elements were also deduced from the effective ranges and scattering lengths of a variety of potential constructed to reproduce Λ separation energies of s-shell hypernuclei.[2] We note that in the vicinity of $\hbar\omega \approx 17$ MeV, a value appropriate for the calculation of Λ separation energies in light hypernuclei, the matrix elements deduced from phenomenological interaction are approximately 25% smaller than those deduced from phase shifts. Thus, we would expect that the matrix elements deduced from scattering data would seriously overestimate Λ separation energies.

In calculating separation energies for $\Lambda\,^5$He, $\Lambda\,^9$Be, and $\Lambda\,^{13}$C, we assume that the nucleons lie in their lowest shell-model states. The values of the single-particle oscillator parameter b were picked to reproduce the mean square charge radii of ^{4}He, ^{8}Be, and ^{12}C. (The effects of a finite proton charge distribution were included.) The Λ was assumed to occupy the 0S oscillator state with the same value of $\hbar\omega$. The p-shell nucleons in ^{8}Be and ^{12}C are assumed to be in an LS-coupled state with L = 0 and S = 0. Matrix elements of the ΛN interaction were evaluated with the aid of an unequal-mass Moshinsky transformation.[5] The results of this calculation are summarized in Table I. The errors on b reflect the experimental error in the determination of charge radii. The errors quoted for separation energy include the effects of the uncertainty of b and the spread of values obtained for the relative oscillator matrix elements.

Our expectation that the matrix elements deduced from scattering data would overestimate Λ separation energies is confirmed. This disagreement may be due to the importance of higher partial waves in low-energy scattering or the importance of tensor forces in the $^3S_1$ channel. The latter explanation is appealing, since nucleon-nucleon matrix elements derived from scattering length and effective range data are about 30% more attractive than matrix elements deduced from a proper coupled-channel calculation as described in Ref. 1.

Footnotes and References

†Present address: State University of New York at Stony Brook, Stony Brook, Long Island, New York.
*Present address: Niels Bohr Institute, Blegdamsvej 17, Copenhagen, Denmark.
‡Present address: Center for Theoretical Physics, Massachusetts Institute of Technology, Massachusetts.

1. J. P. Elliott, A. D. Jackson, H. A. Mavromatis, E. A. Sanderson, and B. Singh, Nucl. Phys. A121, 241 (1968).
2. G. Alexander and U. Karshon, in High Energy Physics and Nuclear Structure (North-Holland Publishing Co., Amsterdam, 1967), p. 36.
3. G. Alexander, U. Karshon, A. Shapira, G. Yekutieli, R. Englemann, H. Filthuth, and W. Lughofer, Phys. Rev. 173, 1452 (1968).
4. G. Fast, J. C. Helder, and J. J. deSwart, Phys. Rev. Letters 22, 1453 (1969).
5. D. H. Davis and J. Sacton, in High Energy Physics and Nuclear Structure (North-Holland Publishing Co., Amsterdam, 1967), p. 21.
6. M. M. Bakri, Nucl. Phys. A96, 115 (1967).

Table I. Comparison of calculated and experimental Λ separation energies.

	b (F)	Scattering data (MeV)	Phenomenological potentials	Experiment[5] (MeV)
^{5}He	1.34±0.03	9.1±1.8	3.5±1.5	3.00±0.02
^{9}Be	1.66±0.05	10.5±0.9	4.6±0.6	6.52±0.05
^{13}C	1.66±0.05	19.5±1.2	11.5±0.8	10.51±0.51

REARRANGEMENT EFFECTS AND THE PARAMETERIZATION OF THE EFFECTIVE FIELD IN NUCLEI†

H. Meldner* and C. M. Shakin‡

In this work we provide a simple parameterization of the nonlocal effective field in nuclei. The parameters as determined by fitting the properties of nuclear matter are quite similar to those which have been shown to yield good results for the size and binding energies of finite nuclei throughout the periodic table.[1] The computed self-consistent single-particle energies are significantly different from the separation energies due to rearrangement effects. This fact has important consequences for structure calculations and the analysis of particle knock-out experiments.

Avoiding the introduction of an explicit form for the two-body force, we simply assumed that the nonlocal potential for a single particle in nuclear matter is given by

$$V(\vec{r}-\vec{r}') = v \frac{\exp[-|\vec{r}-\vec{r}'|/a]}{|\vec{r}-\vec{r}'|/a} \frac{\rho}{2}\left[1-\left(\frac{\rho}{2\rho_1}\right)^{2/3}\right], \tag{1}$$

where ρ is the density, v is a strength parameter ($v < 0$), a is a nonlocality parameter, and ρ_1 we term the saturation parameter. The nonlocal single-particle potential due to an effective nonlocal two-body interaction could have the above form.

The single-particle energy for the infinite system is

$$\epsilon(k) = t(k) + V(k) = \frac{\hbar^2 k^2}{2m} + \frac{4\pi v a^3}{1+a^2k^2}\left(\frac{\rho}{2}\right)\left[1-\left(\frac{\rho}{2\rho_1}\right)^{2/3}\right], \tag{2}$$

where the second term is the Fourier transform of $V(\vec{r}-\vec{r}')$. We maintain the distinction between the single-particle energy ϵ as defined in (2) and the separation energy S which differs from ϵ by rearrangement effects,[2,3]

$$S(k) = -\epsilon(k) - \Delta_R(k) . \tag{3}$$

(Examples of Δ_R for finite nuclei are presented in Table I.)

Note that for a saturating system, $S(k_F) = E_{av} = E_B/A$,[4] where E_B is the binding energy. The relation given in Eq. (3), as well as the conjecture that Δ_R will not always be small in the atomic case, is due to Koopmans.[2]

For our model, the binding energy per particle is E_{av}, where

$$-E_{av} = \frac{1}{2}\frac{3}{\rho}\int_0^{k_F}\left(\frac{\hbar^2k^2}{2m}+\epsilon(k)\right)\left(\frac{2k^2}{3\pi^2}\right)dk = \frac{3}{5}\frac{\hbar^2k_F^2}{2m}+\frac{2}{\pi}v\left[1-\left(\frac{\rho}{2\rho_1}\right)^{2/3}\right][ak_F-\tan^{-1}(ak_F)] , \tag{4}$$

with $\rho = (2k_F^3/3\pi^2)$. We require that $E_{av} = +15.6$ MeV and $(\partial E_{av}/\partial k_F) = 0$ at an appropriate $k_F \approx 1.3$ F^{-1}. The values of v and ρ_1 satisfying these conditions are plotted as function of a for various k_F in Fig. 1. The small circles and squares of Fig. 1 correspond to the values for v, ρ_1, and a determined independently from a fit to various data for finite nuclei.[1] Optimum values of the parameters are being determined by making a more careful study of the shape of the charge density than that performed in Ref. 1.

Table I contains the single-particle energies (i. e., eigenvalues, ϵ) of protons in a self-consistent solution for ^{16}O. The parameters ρ_1, v, a, and τ are those of Set A of Ref. 1, which were chosen there to give good results for ^{208}Pb. The separation energies are obtained by comparing the self-consistent solution for ^{15}N with that for $^{16}O[E_{av} = + 7.76$ MeV, $(E_{av})_{expt} = + 7.98$ MeV]. Particularly remarkable is the very large rearrangement effect for the more deeply bound orbitals, a systematic feature for all nuclei. For ^{40}Ca, $\epsilon(1s) = - 79.6$ MeV and $S(1s) = + 45.8$ MeV, etc. Roughly, $S(1s) \approx \frac{1}{2} |\epsilon(1s)|$. Although the magnitude of Δ_R decreases as one considers more weakly bound orbits, the rearrangement energy remains a significant fraction of ϵ and may not be neglected. Here we face a general inconsistency of the so-called shell-model calculations which is, in fact, an old topic.[3,4] As a quantitative example, we have calculated the energies of the configuration $(1f_{7/2})^n(1d_{3/2}^{-1})^n$ for neutron or proton excitations in ^{40}Ca. The energies of these configurations including the rearrangement effects (self-consistency of the field) are roughly one-half of that assigned by using the eigenvalue difference $\epsilon(1f_{7/2})-\epsilon(1d_{3/2})$.

Summary

1. In the calculation of energy differences, as in the case of particle-hole excitations and separation energies, rearrangement must be included. The eigenvalues ϵ obtained from self-consistent calculation should not be compared with experimental separation energies, except possibly in the case of high-energy knock-out experiments such as (e, e'p).

2. Rearrangement effects are relatively less important for absolute quantities. For example, when a particle is added or subtracted, the changes in the eigenvalues ϵ are such that $\delta\epsilon$ rarely exceeds 0.5 MeV for light nuclei, and is usually smaller. The change in the self-consistent single-particle wave functions is very small. For example, if we remove a column (1s proton) from the self-consistent Slater determinant for ^{40}Ca, and take the overlap integral with a self-consistent solution for ^{39}K with a 1s proton hole, we find a spectroscopic factor ≈ 0.999.

Table I. Single-particle, rearrangement, and separation energies (in MeV) for proton orbitals in a self-consistent solution for ^{16}O. The parameters are those of Set A of Ref. 1, except that the spin-orbit parameter has been changed to $\sigma = 0.45$.

$n\ell j$	ϵ	Δ_R	S	S^{expt}
$1p_{1/2}$	-14.6	2.3	12.3	12.1
$1p_{3/2}$	-29.2	9.5	19.7	18.4
1s	-64.3	26.2	38.1	

Footnotes and References

†Condensed from Phys. Rev. Letters 23, 1302 (1969).
*Present address: University of California–San Diego, LaJolla.
‡Present address: Massachusetts Institute of Technology, Cambridge, Massachusetts.
1. H. Meldner, Phys. Rev. 178, 1815 (1969), and Nuovo Cimento 53B, 195 (1968).
2. T. Koopmans, Physica 1, 104 (1934).
3. K. A. Brueckner, Phys. Rev. 110, 597 (1958).
4. N. M. Hugenholtz and L. Van Hove, Physica 24, 363 (1958).

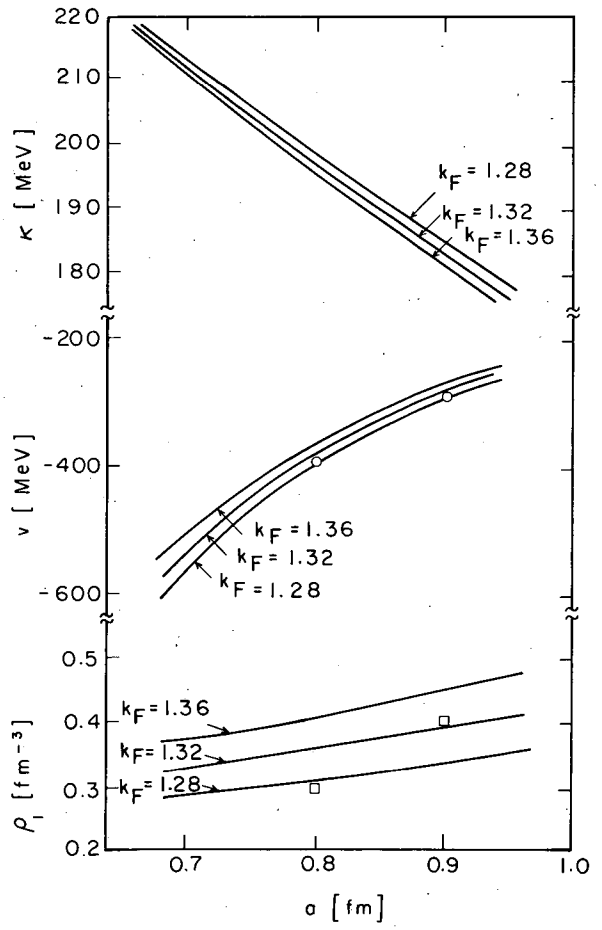

Fig. 1. Parameters v and ρ_1 for nuclear matter as a function of the nonlocality parameter a for various values of k_F. Values of v (circles) and ρ_1 (squares) independently determined from a study of finite nuclei (Ref. 1) are indicated. The compressibility κ is also shown. (XBL702-2322)

THE OCCURRENCE OF SHAPE ISOMERS OVER THE PERIODIC TABLE

Chin Fu Tsang

Shape isomers may be classified into different types. Three types are shown in Fig. 1, which shows the potential energy of a nucleus as a function of a deformation parameter[1] ϵ leading to fission. For each curve, the lowest minimum corresponds to the ground state and the secondary minimum corresponds to the shape isomeric state between two potential barrier peaks. In the Type I nuclei, the ground state is spherical ($\epsilon = 0$) and the isomeric state is at $\epsilon \approx 0.4$. In the Type II nuclei, the ground state is deformed ($\epsilon \approx 0.2$) and the isomeric state is at $\epsilon \approx 0.6$. In the Type III nuclei, the ground state is again spherical and the isomeric state corresponds to a third minimum at $\epsilon \approx 0.8$. The deformations of the ground states and secondary minima are due to single-particle shell effects and stay about the same for all nuclei. This can be understood on a schematic study of the Nilsson level diagram due to Myers and Swiatecki[2] and Strutinski.[3] This can also be seen from the calculated barriers of Nilsson et al.[4] Thus the first point to note is that the secondary minimum due to the shell effect occurs at $\epsilon \approx 0.4$, 0.6, and 0.8 for Type I, II, and III shape isomers respectively.

The second point to note is that these potential energy curves are obtained by imposing shell effects on a smooth liquid-drop barrier shape. When the secondary minimum falls on one side of the liquid drop saddle point, one finds a small peak on this side and a large peak on the other. But when it falls on top of the liquid drop saddle point, a most prominent two-peak structure is found (i. e., the two peaks are of about equal height). This provides a necessary condition for the occurrence of the shape isomeric states.

Therefore the shape isomer may occur when its liquid drop saddle points are at deformations $\epsilon \approx 0.4, 0.6, 0.8$. Once we know the liquid drop saddle-point deformation the fissibility parameter may be found,[5] which, in turn, gives the particular nucleus, based on a mass formula. We use the Myers-Swiatecki mass formula[2] and find bands on the Z, N plane where Type I, II, and III isomers may be found (Fig. 2). Type I and III isomers occur when the ground state is spherical, i. e., when their Z's or N's are close to magic numbers, and Type II isomers occur when the ground state is deformed, i. e., when their Z and N are away from magic numbers.

Based on this simple picture it is found that the observed fission isomer in the actinide region falls very nicely on the Type II band, which appears in our figure to be the only shape isomer that is on the beta-stability line. Ruddy and Alexander have recently found fission isomers in other regions. Their fission isomers in the Rn region may, perhaps, be our Type III isomers, but their lighter fission isomers cannot be explained in our picture.

References

1. S. G. Nilsson, Kgl. Danske Videnskab. Selskab Mat. -Fys. Medd. 29, No. 16 (1955).
2. W. D. Myers and W. J. Swiatecki, Arkiv Fysik 36, 593 (1967).
3. V. M. Strutinsky, Nucl. Phys. A122, 1 (1968).
4. S. G. Nilsson, C. F. Tsang, A. Sobiczewski, Z. Szymanski, S. Wycech, C. Gustafson, I. L. Lamm, P. Möller, and B. Nilsson, Nucl. Phys. A131, 1 (1969).
5. S. Cohen and W. J. Swiatecki, Ann. Phys. 22, 406 (1963).

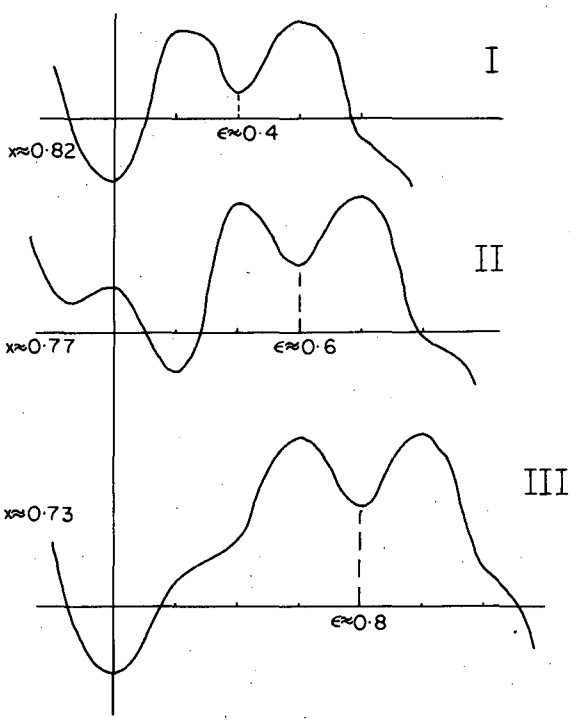

Fig. 1. Classification of shape isomers. Potential energy is plotted as a function of deformation ϵ for three types of shape isomers. (XBL701-154)

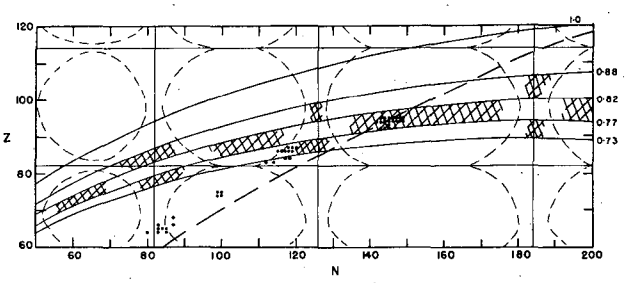

Fig. 2. The occurrence of shape isomers of Types I, II, and III over the Z, N plane, indicated by shaded areas in bands. The broken line indicates the approximate line of beta stability. The vertical and horizontal lines indicate neutron and proton magic numbers. Experimentally found fission isomers are indicated by dots. (XBL701-82)

SHAPE ISOMERIC STATES IN HEAVY NUCLEI[†]

C. F. Tsang and S. G. Nilsson[*]

When the total potential energy of a nucleus is plotted as a function of deformations, there may exist a secondary minimum, in addition to the lowest minimum. The lowest minimum represents the ground state; the secondary minimum represents an isomeric state with a different nuclear shape from the ground-state deformation. This state is prevented from decaying into the ground

state by an inner potential barrier peak, and from fissioning by an outer potential barrier peak.

The isomeric state is studied for nuclei in (a) the actinide region, (b) the neutron-deficient region about Pb, and (c) the superheavy region. The method of calculation is described in Ref. 1, which gives nuclear potential energy surfaces as a function of deformations.

For the actinide region the results are displayed in Fig. 1, which shows the potential energy of all even-even nuclei between U (Z = 92) and Fm (Z = 100) as a function of the Nilsson deformation parameter[1] ϵ. By assuming an empirical inertial parameter associated with fission,[1] the half-life of penetration through the outer peak from the isomeric state is calculated. The results can be compared with the observed spontaneous fission half-lives of the actinide fission isomers with very good agreement, as shown in Fig. 2.

We have also calculated the potential energy barrier for the neutron-deficient isotopes of Th, Ra, Rn, Po, Pb, and Hg. A typical result is shown in Fig. 3. In this region the outer peak is usually much larger than the first peak, and also the isomeric state is at a much higher energy than the ground state. Hence the isomer is more likely to penetrate through the inner peak and γ-decay to the ground state than to penetrate through the outer peak and fission.

Similar results are obtained for shape isomers along the beta-stability line with $70 < Z < 90$, and also in the superheavy region. In the former case the outer peak is very large, so that no fission of the isomeric state is expected to be observable. In the latter region, however, a fissioning shape isomer may perhaps be found.

Footnotes and Reference

†Condensed from UCRL-18963, to be published in Nucl. Phys.
*Present address: Department of Mathematical Physics, Lund Institute of Technology, Lund, Sweden.

1. S. G. Nilsson, C. F. Tsang, A. Sobiczewski, Z. Szymanski, S. Wycech, C. Gustafson, I. L. Lamm, P. Möller, and B. Nilsson, Nucl. Phys. A131, 1 (1969).

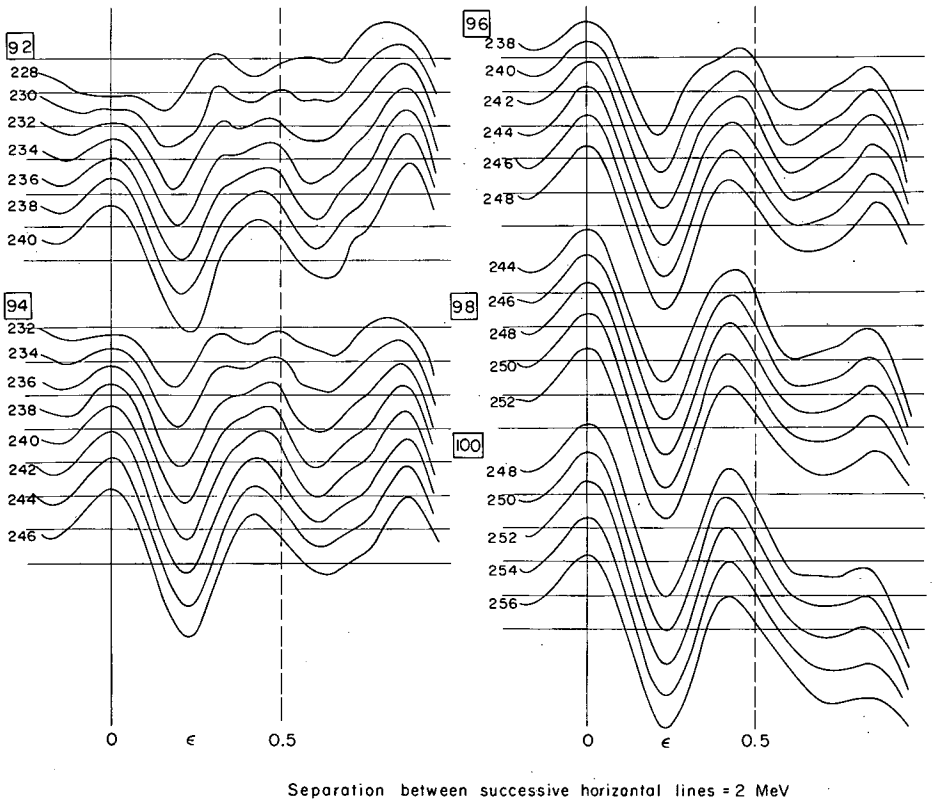

Fig. 1. The two-peak barrier shapes for isotopes of elements Z=92 to 100. (XBL691-1638)

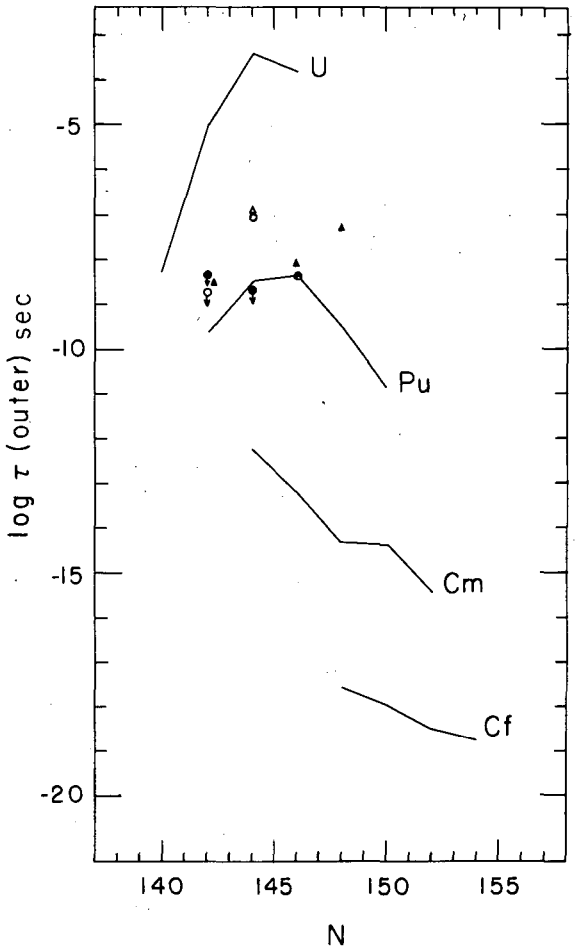

Fig. 2. Theoretical half-lives (solid curves) for fission barrier penetration of the outer peak. Experimental spontaneous fission half-lives of U isomers are shown as open triangles and circles, and those of Pu are shown as filled triangles and circles. (XBL698-1387)

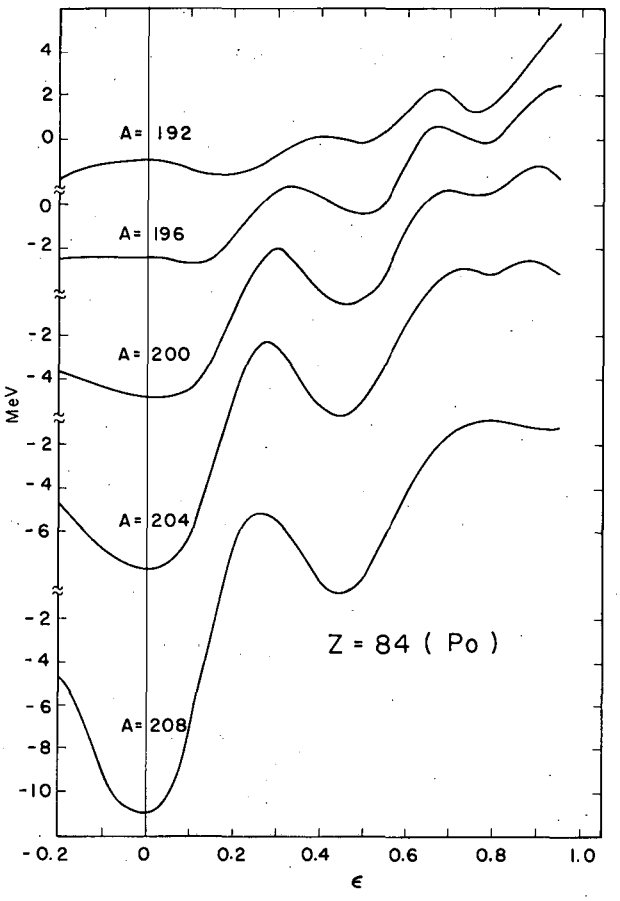

Fig. 3. Total potential energy minimized with respect to ϵ_4 for each ϵ as a function of ϵ for neutron-deficient isotopes of $_{84}$Po. (XBL694-2443)

FURTHER THEORETICAL RESULTS ON THE STABILITY OF SUPERHEAVY NUCLEI†

Chin Fu Tsang and Sven Gösta Nilsson*

In a recent work[1] we have calculated the stability properties of superheavy nuclei near the proton closed shell 114 and neutron closed shell 184. We have found in the same calculation that N = 196 is also a neutron closed shell. This latter result is not confirmed by other calculations and its physical validity is not assured. However, we have taken the approach of assuming our model and deriving all possible results on this basis. Therefore we have studied the stability of superheavy nuclei over an extended region, i. e., $106 \leq Z \leq 128$ and $176 \leq N \leq 204$.

In Fig. 1 are shown the estimated half-lives of alpha decay and spontaneous fission in contour plots. Some of the beta-stable nuclei are also indicated. It is clear that any stability against spontaneous fission in this region is due to the extra binding resulting from the shell effect centered

around Z = 114 and N = 184 to 196. On the other hand, the trends of alpha half-lives are essentially determined by the liquid drop model with modifications caused by the extra shell effect. Thus the kinks in the curves occur when either the parent or the daughter nucleus is associated with a nucleon closed shell. One has to point out here that the numbers represented by these curves are uncertain by a factor as large as 10^6 due to various uncertainties in the calculations discussed in Ref. 1.

Assuming the face values of this figure, one can make use of it to indicate possibilities of production of superheavy nuclei. An example is to study the possibilities when a $^{86}_{36}$Kr ion beam becomes available. In Table I we show the compound nuclei that might be formed by bombarding various neutron-rich targets from Pb to Cm with ^{86}Kr. It is still very much an open question whether such a compound nucleus would be formed in the first place. At the moment let us assume that through emission of four neutrons a cold compound nucleus is obtained in the ground state. From Fig. 1, it is apparent that for ^{208}Pb and ^{210}Po targets, the compound nucleus undergoes spontaneous fission instantaneously and one may not expect to produce any superheavy nuclei. With targets heavier than ^{226}Ra, it turns out that the alpha half-life is less than the spontaneous-fission half-life at each step (Fig. 1). If the compound nucleus decays by emitting α particles all the way, in each case we end up with a long-lived superheavy nucleus. Any β decay on the way, if competitive, will always help in reaching even longer-lived nuclei.

It is here appropriate again to emphasize that Fig. 1 and the conclusions based thereon depend strongly on the magnitude of the N = 196 shell spacing, which, as stated earlier, is a controversial result obtained on the basis of our specific potential model.

Table I. Production of superheavy nuclei by $^{86}_{36}Kr_{50}$ beam. The first column identifies the target nucleus. The second column indicates the compound nucleus that is formed by the fusion of the target and the projectile. If all the excitation energy were carried away by the emission of four neutrons, one would get the nucleus shown in the third column. Now assuming that beta decays were extremely slow compared with spontaneous fission and alpha decay, one finds the longest-lived superheavy nucleus that can be reached, as indicated in the fourth column with its major mode of decay. If the nucleus in column 4 undergoes beta decay one gets the superheavy nucleus shown in the fifth column with its major mode of decay.

	Target			Compound Nucleus		After emitting 4n		Longest-lived nuclei reached after competition between s.f. and successive α-decay			After β decay		
	A	Z	N	Z	N	Z	N	Z	N	Major decay	Z	N	Major decay
Pb	208	82	126	118	176	118	172		(s.f)				
Po	210	84	126	120	176	120	172		(s.f)				
Rn													
Ra	226	88	138	124	188	124	183	118	178	$\alpha(10^{-3}s)$	112	184	$\alpha(10^{4}y)$
Th	232	90	142	126	192	126	188	116	178	$\alpha(10^{-1}s)$	112	182	$\alpha(10^{2}y)$
U	238	92	146	128	196	128	192	114	178	$\alpha(10^{3}s)$	110	182	$\alpha(10^{2}y)$
Pu	244	94	150	130	200	130	196	114	180	$\alpha(10^{4}s)$	112	182	$\alpha(10^{2}y)$
Cm	248	96	152	132	202	132	198	114	180	$\alpha(10^{4}s)$	112	182	$\alpha(10^{2}y)$

Footnotes and References

†Condensed from UCRL-18966, to be published in Nucl. Phys.

*Department of Mathematical Physics, Lund Institute of Technology, Lund, Sweden.

1. S. G. Nilsson, C. F. Tsang, A. Sobiczewski, Z. Szymanski, S. Wycech, C. Gustafson, I. L. Lamm, P. Möller, and B. Nilsson, Nucl. Phys. A131, 1 (1969).

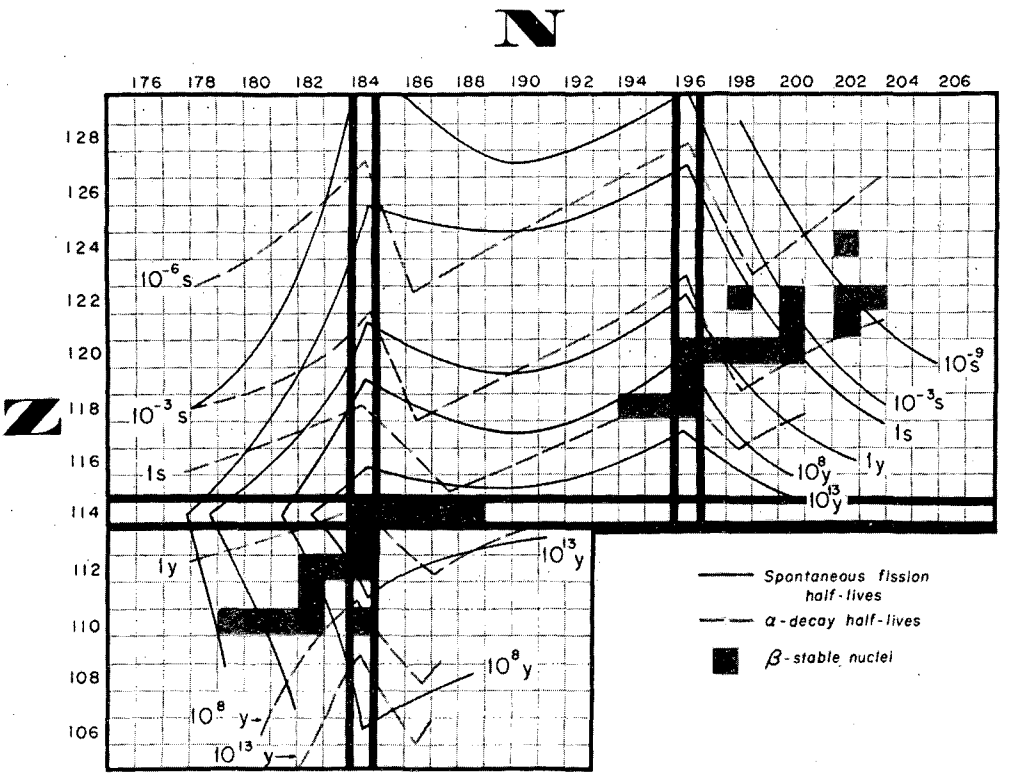

Fig. 1. Contours of theoretical half-lives for $106 \leq Z \leq 128$, and $176 \leq N \leq 204$. The thick dark lines are contours of spontaneous-fission half-lives. The broken lines are contours of alpha half-lives. Some of the beta-stable nuclei are shaded. (XBC692-1535)

THE NUCLEAR STRUCTURE AND STABILITY OF HEAVY AND SUPERHEAVY NUCLEI†

S. G. Nilsson,* C. F. Tsang, A. Sobiczewski,‡
Z. Szymanski,‡ S. Wycech,‡ C. Gustafson,* I. L. Lamm,*
P. Möller,* and B. Nilsson*

To describe a deformable heavy nucleus, we have employed a generalized harmonic oscillator potential with distortion coordinates ϵ, ϵ_4 representing essentially P_2 and P_4 distortion in shape. In addition to a spin-orbit force, a shape-correction term is used to flatten the bottom of the well. The strengths of the terms added to the oscillator potential represent two adjustable parameters for protons and two for neutrons, which are fitted to reproduce optimally the observed level order in the actinide ($A \approx 242$) and rare earth ($A \approx 165$) regions. A linear A dependence is assumed for these parameters for extrapolations to the superheavy region ($A \approx 300$). Pairing energy contributions are calculated on the basis of the single-particle levels obtained. The pairing matrix element G is assumed to be isospin dependent and proportional to the surface area of the nucleus. The conservation of the volume of equipotential surfaces usually employed is complemented by the Strutinsky method of liquid-drop normalization.[1] This method ensures that on the average the behavior of deformation energy is that given by a charged liquid drop. If correction terms in the normalization function are employed up to sixth order, the final results are stable with respect to the range parameter employed in the normalization.[2] The liquid-drop parameters are taken, without readjustment, from those of the semi-empirical mass formula of Myers and Swiatecki.[3]

Two major types of results are obtained from the calculation. The first type is the single-particle level diagrams for the heavy and superheavy nuclei. An example is shown in Fig. 1. We

find, in addition to the known magic numbers, a proton magic number at Z = 114 and a neutron magic number at N = 184, confirming previous studies by various authors. The second type is potential energy surfaces of these nuclei. Examples are shown in Fig. 2, where we plot the energy minimized with respect to ϵ_4 as a function of ϵ. The lowest minimum of the curves gives the ground-state binding energy and its deformation. The secondary minimum gives the energy and deformation of a shape isomeric state. The level diagrams at the secondary minimum for the actinide nuclei are also obtained.

The stability of the nucleus is understood by its alpha-decay, beta-decay, and spontaneous-fission half-lives. From the ground-state masses, alpha half-lives have been calculated and beta stability is also studied. The beta-stable nuclei in the region A ≈ 300 are found to lie on the beta-stability line extrapolated from the region of known nuclei. The alpha half-lives in this region range from 10^{-6} sec to 10^{13} years.

The estimation of spontaneous fission half-lives depends very strongly on the estimation of inertial parameter associated with the fission process. In Fig. 3 are plotted the spontaneous fission half-lives as functions of the inertial parameter B. Three methods of estimating B are shown. The first is an empirical estimate obtained by using the barriers we calculated for the actinides and requiring these to give the correct experimental half-lives. The second estimate is also empirical and is due to Moretto and Swiatecki.[4] They used, instead of our calculated barriers, liquid-drop barriers modified by a Myers-Swiatecki shell-correction term, with the ground-state masses and fission barriers adjusted to experimental values. The third is a microscopic calculation based on the assumption of adiabatic collective motion in the fission degree of freedom. The estimated initial parameter is a sensitive function of the pairing-force strength as well as of the coupling between quadrupole and hexadecapole modes. Each of the three estimates involves uncertainties as large as 30% of its value, and they are within 30% of each other. In lieu of anything definitely better we have used the lowest of the three estimates to give the spontaneous fission half-lives.

By these calculations, half-lives of the superheavy nuclei around Z = 114 and N = 184 are calculated. The even-even nucleus with the longest spontaneous fission half-life is $^{298}114$ with a value of 10^{16} years, but the even-even nucleus with the longest total half-life is found to be $^{294}110$ with a value of 10^{8} years. These numbers are found to have an uncertainty as large as a factor of 10^{6}.

Footnotes and References

†Condensed from Nucl. Phys. A131, 1,61 (1969), and Izv. Akad. Nauk SSSR, Ser. Fiz., to be published.

*Department of Mathematical Physics, Lund Institute of Technology, Lund, Sweden.
‡Institute for Nuclear Research and University of Warsaw, Warsaw, Poland.

1. V. M. Strutinsky, Nucl. Phys. A95, 420 (1967); V. M. Strutinsky, Nucl. Phys. A122, 1 (1968).
2. C. F. Tsang, On the Microscopic and Macroscopic Aspects of Nuclear Structure with Applications to Superheavy Nuclei (Ph. D. Thesis), UCRL-18899, May 1969.
3. W. D. Myers and W. J. Swiatecki, Arkiv Fysik 36, 593 (1967).
4. L. G. Moretto and W. J. Swiatecki, private communication, 1967.

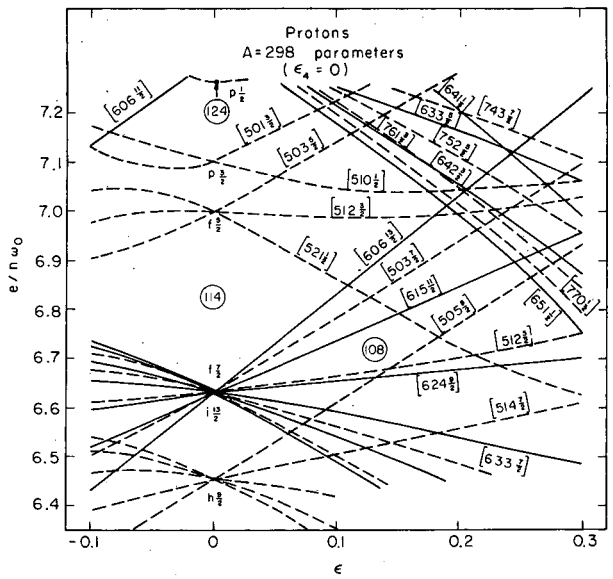

Fig. 1. Single-particle proton levels A ≈ 298; κ = 0.0534; μ = 0.686; ϵ_4 = 0. (XBL687-3434)

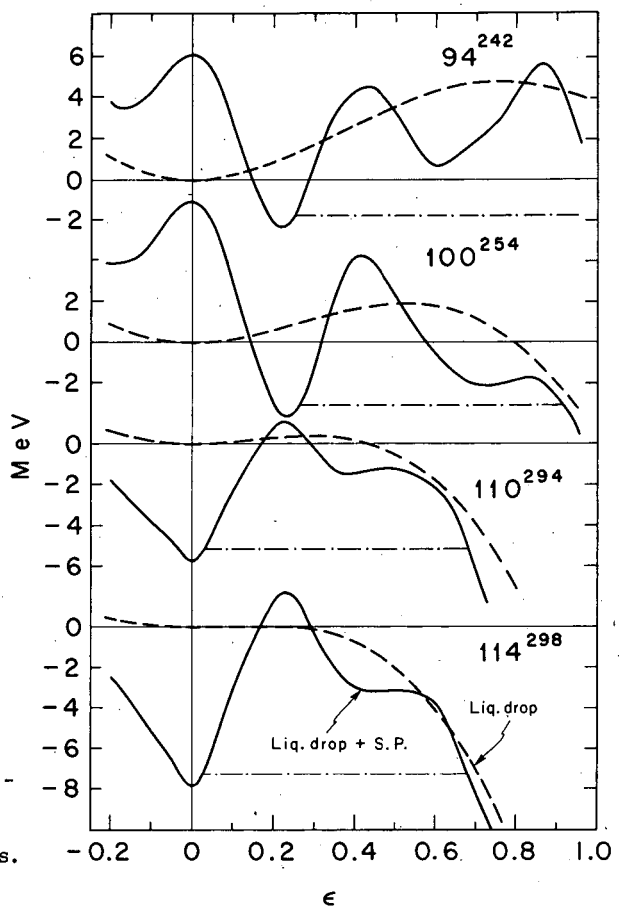

Fig. 2. Potential energy minimized with respect to ϵ_4 as a function of ϵ for various nuclei. The broken curves correspond to liquid drop fission barriers. The solid curves are the barriers after the inclusion of shell and pairing effects. (XBL688-3679)

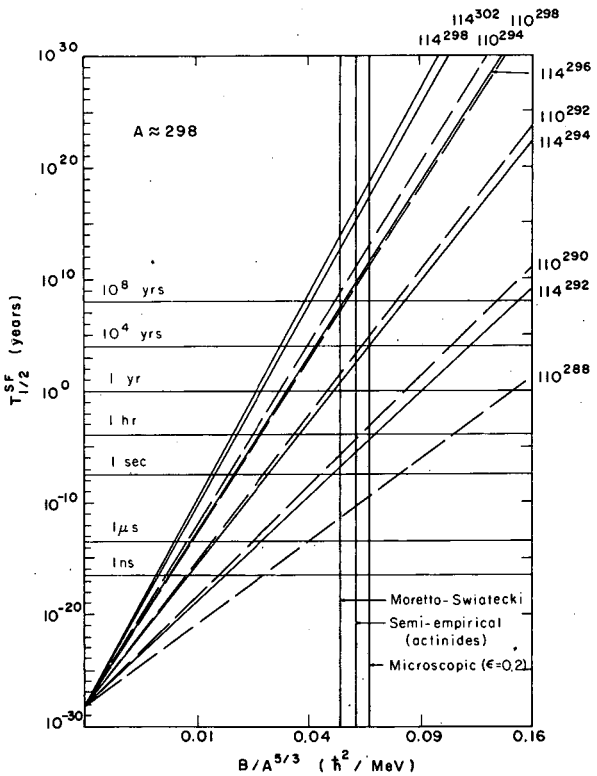

Fig. 3. Spontaneous fission half-lives of Z = 114 and 110 isotopes as functions of the inertial parameter B for barrier penetration. Three estimates of B are given. Further explanations in text. (XBL691-1640)

THE POTENTIAL ENERGY OF A LEPTODERMOUS SYSTEM

W. J. Swiatecki† and C. F. Tsang

A leptodermous system is a system with a bulk region and a thin surface region. Examples of leptodermous systems are:

- A drop of water (consisting of strongly interacting molecules).
- A classical gas of noninteracting point particles in a container.
- A degenerate gas of noninteracting fermions in an external potential well.
- A system of particles interacting by short-ranged saturating forces treated in the statistical Thomas-Fermi approximation. Electrostatic forces can also be present.
- Amorphous solids.
- Nuclei.

By studying, in general, such a system, one derives an expression for its energy as an expansion

$$E' = aV + bS + cL + \cdots , \tag{1}$$

where the volume V, surface area S, and integrated curvature over the surface L are defined with reference to "the equivalent system" with the same volume but zero skin thickness. The coefficients a, b, c are expressed in terms of the particle-density and energy-density functions of the system. The orders of successive terms differ by a factor corresponding to the ratio of the skin thickness to the dimension of the system. The first two terms of Eq. 1 are the energy terms given by the well-known liquid-drop model, which is a specialized case of this general type of system.

In order to test the validity of the leptodermous approach in the case of systems resembling nuclei, the analysis is applied to noninteracting fermions in an orthorhombic box (of nuclear dimensions) with infinite potential outside and zero potential inside. The energy of such a system is found exactly by summing the single-particle eigenvalues. This sum is investigated as a function of both particle number and shape. This (exact) sum E is then compared with the energy expression given by Eq. 1. It is found, on comparison, that the exact result is very well represented. Examples of the comparison are shown in Figs. 1 and 2. The convergence of the terms in the expansion is good, and is illustrated by listing below the contributions from terms of successive orders, for N = 60 eigenvalues (corresponding to 240 nucleons).

The 14 MeV represents the difference between the exact result and the expression 1 with the first three orders. It consists of higher-order terms as well as single-particle effects (shell effects), which are recognized as wiggles in Fig. 2.

Term $\propto N$	4830 MeV
Terms $\propto N^{2/3}$	1845 MeV
Terms $\propto N^{1/3}$	225 MeV
Rest	14 MeV
Exact result	6914 MeV

The conclusion is that the leptodermous expansion (a liquid-drop type of expression) is a good approximation for a system of noninteracting fermions in a potential well, i. e., for a nuclear shell model. The condition for the validity of a leptodermous expansion is not that the system should resemble a liquid drop, but that it should have a reasonably thin surface region.

Footnote

†Theoretical Physics Group, Lawrence Radiation Laboratory, Berkeley.

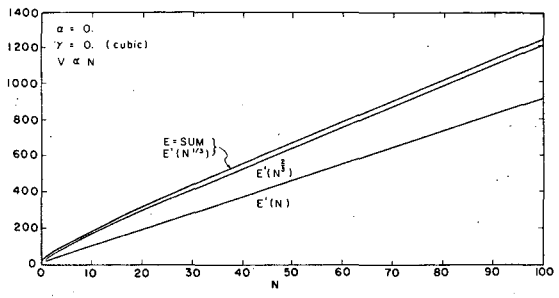

Fig. 1. The energy of particles in a cubic potential box as a function of eigenvalue number calculated in four different ways: (a) using the approximate expression E' with only the N term, E' (N); (b) E' with the N term and the $N^{2/3}$ term, E'($N^{2/3}$); (c) E' up to the $N^{1/3}$ term, E'($N^{1/3}$); (d) the exact calculation E. The volume of the box is assumed proportional to N. The unit of the ordinate is in $\pi^2\hbar^2/2M\beta^2$, where β is given by $V = \beta^3 N$. (XBL693-2256)

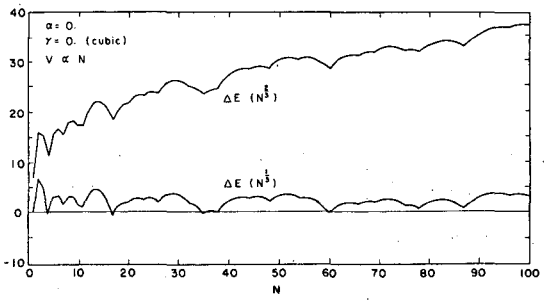

Fig. 2. The energy differences between E and E' ($N^{2/3}$) and between E and E' ($N^{1/3}$) as a function of the eigenvalue number N for a cubic Hill-Wheeler box. See Fig. 1. (XBL694-2445)

DROPLET MODEL ISOTOPE SHIFTS AND THE NEUTRON SKIN†

William D. Myers

A refinement of the liquid-drop model--called the "Droplet Model"--has recently been formulated.[1] One of the consequences of this approach is a nuclear mass formula that gives new insights into the relationships between various nuclear properties. For example, it provides us with a means for calculating both the isotope and isotone shifts in the nuclear charge radius and relating them to the existence and thickness of the neutron skin.

The droplet model is based on an expansion of nuclear properties about their liquid-drop-model values in terms of the two small quantities ϵ and δ, which are related to the neutron and proton densities ρ_n and ρ_z ($\rho = \rho_n + \rho_z$ and ρ_0 is the density of nuclear matter) by the expressions

$$\epsilon = -\frac{1}{3}(\rho-\rho_0)/\rho_0 , \tag{1}$$

$$\delta = (\rho_n - \rho_z)/\rho . \tag{2}$$

If the average values of the quantities ϵ and δ over the central region of the nucleus are specified by $\bar{\epsilon}$ and $\bar{\delta}$, then the radii of the spheres corresponding to the proton and neutron density distributions are given by

$$R_z = r_0 \left[\frac{2Z}{(1-3\bar{\epsilon})(1-\bar{\delta})}\right]^{1/3} \quad \text{and} \quad R_n = r_0 \left[\frac{2N}{(1-3\bar{\epsilon})(1+\bar{\delta})}\right]^{1/3} . \tag{3}$$

For a nucleus with N neutrons, Z protons, and a total of A particles we can define the quantity I by the expression

$$I = (N-Z)/A , \tag{4}$$

and then the neutron skin thickness t (equal to $R_n - R_z$) is given approximately by

$$t = \frac{2}{3} r_0 A^{1/3}(I-\bar{\delta}) . \tag{5}$$

The above relations are discussed in more detail in Sec. II of Ref. 1.

In order to calculate the charge radius R_z or the neutron skin thickness t we must know the values of $\bar{\epsilon}$ and $\bar{\delta}$ as functions of N and Z. The appropriate expressions, which are derived in Ref. 1, are

$$\bar{\epsilon} = (-2a_2 A^{-1/3} + L\bar{\delta}^2 + c_1 Z^2 A^{-4/3})/K , \tag{6}$$

$$\bar{\delta} = [I + (3c_1/8Q)Z^2 A^{-5/3}] \; / \; [1 + (9J/4Q)A^{-1/3}] . \tag{7}$$

The various coefficients appearing in these expressions are listed below with estimates of their values:

a_1 = 15.677 MeV, volume energy coefficient,
a_2 = 22.0 MeV, surface energy coefficient,
J = 35 MeV, symmetry energy coefficient,
K = 300 MeV, compressibility coefficient,
L = 99 MeV, density-symmetry coefficient,
M = 4.5 MeV, symmetry anharmonicity coefficient,
Q = 25 MeV, effective surface stiffness, and
c_1 = 0.745 MeV, Coulomb energy coefficient,
where
$c_1 = 3e^2/5r_0$ and
r_0 = 1.16 F, the nuclear radius constant. (8)

Figure 1 is a plot of the neutron skin thickness t as a function of the particle number A for nuclei along beta stability. It shows, for example, that in the mass region $A \approx 200$ the radius of the neutron distribution is expected to be, on the average, 0.3 F larger than that of the proton distribution. The neutron skin predicted in this work is relatively small compared with the spatial extent of the surface itself. In the mass region of $A \approx 200$ we find that the neutron skin is only 0.3 F thick, as compared with the 2.4-F thickness of the diffuse surface region. However, this 0.3-F neutron skin thickness is by no means negligible in comparison with the 1.0-F skin thickness that would result if the entire neutron excess of these nuclei were in the surface (thus making the neutron and proton bulk densities equal). It should be stressed that the droplet model predicts the neutron skin thickness to be expected on the basis of statistical considerations alone. One expects the skin thickness of any particular nucleus to depend also on the particular single-particle states that are occupied.

The anomalous behavior of the isotope and isotone shifts in the nuclear charge radius is related to the existence of a neutron skin. The quantity usually considered in these discussions is

$$\delta\langle r_z^2\rangle / \delta\langle r_z^2\rangle_{\text{standard}} . \tag{9}$$

The quantity $\delta\langle r_z^2\rangle$ is the change in the expectation value of r^2 for the proton distribution when a neutron or proton is added. In our case

$$\delta\langle r_z^2\rangle = \frac{3}{5}\left[R_z^2(N+1) - R_z^2(N)\right] . \tag{10}$$

The quantity $\delta\langle r_z^2\rangle_{\text{standard}}$ is defined in exactly the same way except that one uses for R_z the standard expression

$$R_z = 1.2\, A^{1/3} F\,. \tag{11}$$

The quantity of interest, expression 9, is plotted in Fig. 2 as a function of the mass number A. The dashed line in the lower part of the figure is the droplet-model prediction for nuclei along beta stability for the case in which $\Delta N = 1$. It is seen to be almost constant at a value of about 1/2. The circles are experimental points referring to atomic isotope shifts from the compilation of Brix and Kopfermann,[2] and the triangles refer to experimental points given in Elton's compilation[3] of isotope shifts in μ-mesic atoms. The upper part of Fig. 2 is again a plot of the quantity 9, but this time for the case $\Delta Z = 1$. The dashed line, which is approximately constant at a value of about 1.5, is the droplet-model prediction for nuclei along beta stability, and the experimental points are from a review paper by Quitmann.[4] The experimental points show considerable scatter, which is presumably due to single-particle and deformation effects. An extensive discussion of the microscopic origin of the isotope and isotone shift anomalies is contained in a paper by Uher and Sorensen,[5] and a related work by Brueckner et al. has recently appeared.[6]

One of the most interesting aspects of treating isotope shifts by means of the droplet model was the discovery that previous explanations[2,7] of this effect in terms of the nuclear compressibility are probably incorrect. In fact, in the calculations shown here nuclear compressibility tends to reduce the size of the isotope-shift anomaly rather than be the cause of it. This is shown in Fig. 3, where the quantity 9 is plotted as a function of A for nuclei along beta stability.

It seems useful to point out that so far as the isotope and isotone shifts calculated here agree with the experimental results they provide indirect support for the validity of the neutron-skin thickness calculations plotted in Fig. 1. The accumulating evidence in support of the results shown here makes more accurate experimental determination of the neutron skin thickness itself more important than ever before.

The author wishes to acknowledge the hospitality of the Niels Bohr Institute in Copenhagen, where most of this work was performed.

Footnotes and References

†Condensed from Phys. Letters 30B, 451 (1969).

1. William D. Myers, Average Nuclear Properties (Ph. D. thesis), UCRL-18214, May 1, 1968; William D. Myers and W. J. Swiatecki, Ann. Phys. (N. Y.) 55, 395 (1969).
2. Peter Brix and Hans Kopfermann, Rev. Mod. Phys. 30, 517 (1958).
3. H. R. Collard, L. R. B. Elton, and R. Hofstadter, Nuclear Radii, Vol. 2, New Series, Numerical Data and Functional Relationships in Science and Technology (Springer-Verlag, New York, 1967).
4. D. Quitmann, Z. Physik 206, 113 (1967).
5. Richard A. Uher and Raymond A. Sorensen, Nucl. Phys. 86, 1 (1966).
6. K. A. Brueckner et al., Phys. Rev. 181, 1506 (1969).
7. L. Wilets, Encyclopedia of Physics, Vol. 38, Pt. 1 (Springer, Berlin, 1958).

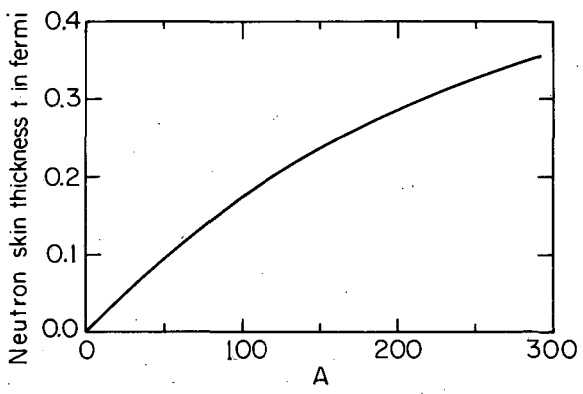

Fig. 1. Neutron-skin thickness t in fermis, plotted as a function of the mass number A for nuclei along beta stability. (XBL699-3828)

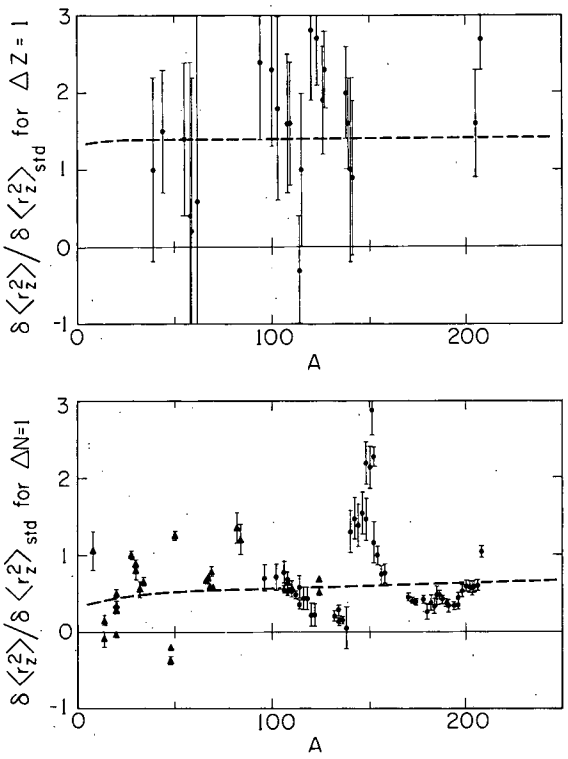

Fig. 2. The ratio of the change in $\langle r_z^2 \rangle$ to the change expected from the liquid drop model plotted against the mass number A. The upper part of the figure is for $\Delta Z = 1$ and the lower part is for $\Delta N = 1$. In both cases experimental points are shown as well as dashed lines representing the predictions of the droplet model for nuclei along beta stability. (XBL699-3830)

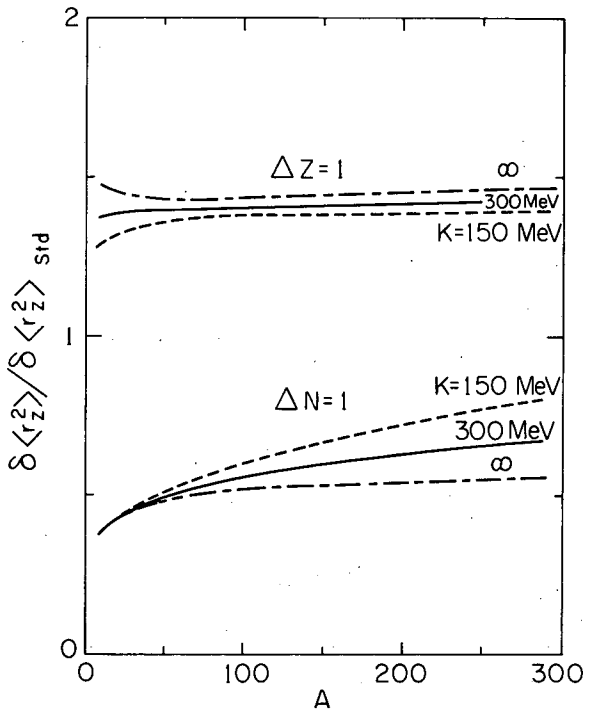

Fig. 3. The ratio of the change in $\langle r_z^2 \rangle$ to the change expected from the liquid drop model, plotted against the mass number A for nuclei along beta stability. Curves for $\Delta Z = 1$ and $\Delta N = 1$ are shown for three different values of the compressibility coefficient K. (XBL699-3829)

DROPLET-MODEL NUCLEAR DENSITY DISTRIBUTIONS AND SINGLE-PARTICLE POTENTIAL WELLS†

William D. Myers

The primary purpose of this work is to present a method for determining the single-particle potential wells appropriate for use in shell-model calculations. The study is based on a calculation (in terms of the Thomas-Fermi statistical method) of average nuclear properties using a phenomenological velocity-dependent force.

In Ref. 1 we found that the Thomas-Fermi method of Seyler and Blanchard[2] could be applied with profit to the calculation of nuclear binding energies and density distributions. It also predicts velocity-dependent neutron and proton single-particle potential wells, and the potentials obtained in this way for particles at the Fermi surface may be compared with the static wells normally employed for investigation energy levels in that region.

In this work the Thomas-Fermi method is applied to infinite and semi-infinite nuclear matter respectively. The properties of the neutron and proton potential wells which are deduced are then combined with previously determined droplet-model expressions in order to provide a description of the potential wells to be expected for finite nuclei.

As the first step in our formulation of a macroscopic theory of single-particle potential wells we used the Thomas-Fermi model to estimate the numerical values of the potentials felt by neutrons and protons in infinite nuclear matter.

We find that the potential well depths (N for neutrons and Z for protons) are given by

$$V\binom{N}{Z} = -51.4\ (\pm)\ 46.2\,\delta - 28.3\,\epsilon + 1.9\,\delta^2\ \text{MeV} \tag{1}$$

(+ for neutrons, - for protons), where the quantities ϵ and δ are given in terms of the neutron and proton densities, ρ_n and ρ_z ($\rho = \rho_n + \rho_z$, and ρ_0 is the density of nuclear matter), by the expressions

$$\epsilon = -(1/3)\,(\rho - \rho_0)/\rho_0 \tag{2}$$

$$\delta = (\rho_N - \rho_Z)/\rho\ . \tag{3}$$

The surface properties to be expected for the single-particle potential may be determined by solving the nuclear matter problem in the semi-infinite case. Using the same Thomas-Fermi method, we can find the surface density distributions of the neutrons and protons as a function of $\overline{\delta}$ (the bulk value of δ, which describes the system away from the surface region). The potential wells, which are self-consistent with these density distributions and are appropriate for particles at the neutron or proton Fermi surfaces, can also be calculated. Figures 1 and 2 are examples of such semi-infinite density and potential well distributions.

In order to make use of these results for predicting the properties of finite nuclei we must first calculate the radius of an equivalent sphere of constant density which represents the density distribution. This radius is given by the droplet-model expression

$$R_\rho = r_0 A^{1/3}(1 + \overline{\epsilon})\ . \tag{4}$$

The quantities $\overline{\epsilon}$ (which appears above) and $\overline{\delta}$ (which finds application in the following discussion) are the average values over the central region of the nucleus of the quantities ϵ and δ defined in Eqs. 2 and 3. The values of these quantities appropriate for a nucleus with N neutrons and Z protons, where $A = N + Z$ and $I = (N - Z)/A$, are given by the droplet-model expressions

$$\overline{\epsilon} = (-2a_2\,A^{-1/3} + L\overline{\delta}^2 + c_1\,Z^2\,A^{-4/3})/K\ , \tag{5}$$

$$\overline{\delta} = [I + (3c_1/8Q)Z^2\,A^{-5/3}]\,/[1 + (9J/4Q)\,A^{-1/3}]\ . \tag{6}$$

These expressions (discussed in detail in Sec. 2 of Ref. 1) make use of coefficients which describe various properties of infinite and semi-infinite nuclear matter.

In Table I the most useful relationships based on Figs. 1 and 2 and the droplet model are summarized. The numerical values of the various parameters which enter have been inserted so as to make the expressions convenient to use.

In order to facilitate comparison with experiment the droplet-model predictions (calculated according to the expressions in Table I) for various nuclear properties of interest are plotted in Fig. 3. That the predicted proton radii correspond closely to the experimental results is not surprising, since the parameters of the theory were chosen partly to insure this agreement. No parameters were adjusted to give the agreement seen to exist between the predicted potential well radii and depths and the values of these quantities determined by fitting single-particle energy levels.

The droplet-model approach has found application in an improved semi-empirical nuclear mass formula,[1] and in the prediction of isotope shifts and the neutron skin thickness.[9] In this

paper it has been successfully applied to predicting single-particle potential wells, and work is in progress to apply it to the calculation of fission barriers.[10] It seems as if it may be possible to encompass most macroscopic nuclear properties within a single algebraic theory which has at its heart the droplet model and which makes use of statistical methods such as the Thomas-Fermi model for extending the theory to new applications.

Footnote and References

†Condensed from UCRL-18997.

1. William Don Myers, Average Nuclear Properties (Ph. D. Thesis), UCRL-18214, May 1, 1968; William D. Myers and W. J. Swiatecki, Ann. Phys. (N. Y.) 55, 395 (1969).
2. R. G. Seyler and C. H. Blanchard, Phys. Rev. 124, 277 (1961); Phys. Rev. 131, 355 (1963).
3. A. E. S. Green, Nuclear Physics (McGraw-Hill Book Company, Inc., New York, 1955).
4. H. R. Collard, L. R. B. Elton, and R. Hofstadter, Nuclear Radii, Volume 2, Group I, Landolt-Börnstein, Numerical Data and Functional Relationships in Science and Technology (Springer-Verlag, Berlin, 1967).
5. K. Takeuchi and P. Moldauer, Phys. Letters 28B (1969) 384.
6. V. A. Chepurnov, Yadern. Fiz. (U. S. S. R.) 5, 955 (1967) [Engl. Transl.: Sov. J. Nucl. Phys. 6, 696 (1968).
7. J. Blomqvist and S. Wahlborn, Arkiv Fysik 16, 545 (1960).
8. E. Rost, Phys. Letters 26B, 184 (1968).
9. William D. Myers, Phys. Letters 30B, 451 (1969).
10. Rainer W. Hasse (Oak Ridge National Laboratory), private communication, 1969.

Table I. Droplet-model formulae (all distances in F).

N = neutron number, Z = proton number,

$A = N + Z$ $I = (N + Z)/A$,

$\bar{\delta} = (I + 0.0112\ Z^2\ A^{-5/3})/(1 + 3.15\ A^{-1/3})$,

$\bar{\epsilon} = -0.147\ A^{-1/3} + 0.330\ \bar{\delta}^2 + 0.00248\ Z^2\ A^{-4/3}$.

Density

$R_\rho = 1.16\ A^{1/3}\ (1 + \bar{\epsilon})$,

$t = 0.773\ A^{1/3}\ (I - \bar{\delta})$,

$R_\rho(^N_Z) = R_\rho\ (\pm)\ \frac{1}{2}\ t$.

For a Fermi function,

$R_{\rho,1/2} = R_\rho[1 - (0.99/R_\rho)^2]$,

$a_\rho = 0.55$.

Potential

$R_V = R_\rho + 0.82 - 0.56/R_\rho$,

$R_V(^N_Z) = R_V(\mp)\ 0.22\ \bar{\delta}$.

For a Fermi function,

$R_{V,1/2} = R_V[1 - (1.19/R_V)^2]$,

$a_V = 0.66$,

$V(^N_Z) = -51.4\ (\mp)\ 46.2\ \bar{\delta}$ MeV.

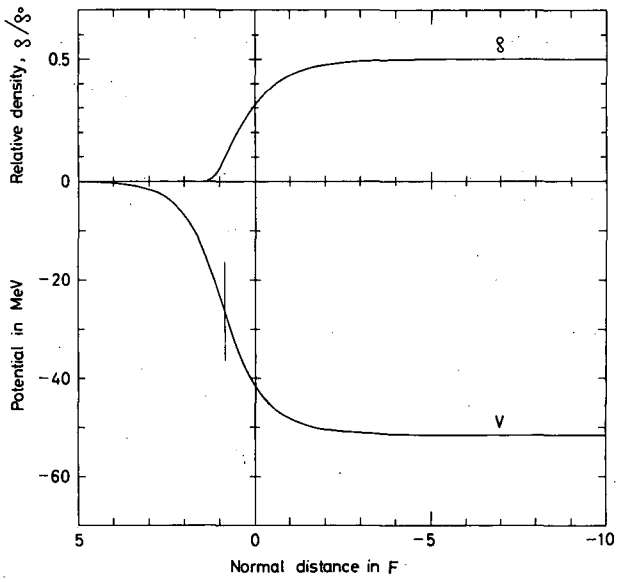

Fig. 1. The Thomas-Fermi density distribution ρ plotted relative to the "effective location of the surface" as defined in the UCRL-18797. In this case (the case of particle number symmetry, where $\bar{\delta} = 0$) the neutron and proton density distributions are equal and are both represented by the curve labeled ρ. The potential felt by particles at the Fermi surface is also plotted. This curve, which is labeled V, has the effective location of its surface outside that of the density, at a point that is indicated by a vertical bar. (XBL6911-6084)

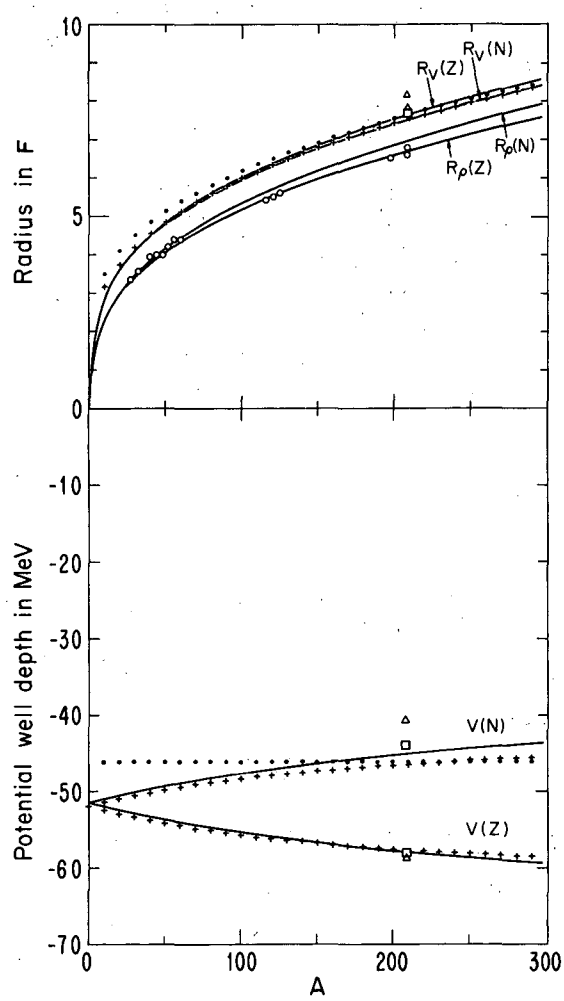

Fig. 3. The predictions of the algebraic theory (as summarized in Table I) plotted as solid lines against the mass number A for nuclei along Green's approximation to beta stability (Ref. 3), which is $I = 0.4\ A/(200 + A)$. The various symbols represent values of these same quantities experimentally determined in Refs. 4 through 8. (XBL6911-6087)

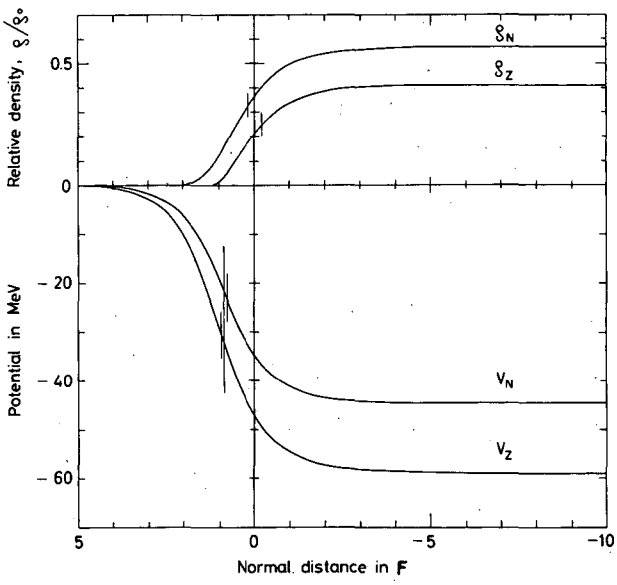

Fig. 2. The Thomas-Fermi density distributions and single-particle potential wells for a case of nonvanishing asymmetry $\bar{\delta}$. As in Fig. 1, the curves are plotted relative to the effective location of the surface of the total density. In addition, the locations of the neutron and proton surfaces are indicated by small vertical bars. The separate locations of the neutron and proton potential surfaces are given by the smaller bars on either side of the long vertical bar that indicates their average position. (XBL6911-6085)

CALCULATED FRACTIONAL INDEPENDENT YIELDS OF PRODUCTS FORMED IN THE SPONTANEOUS FISSION OF ^{252}Cf

R. L. Watson† and J. B. Wilhelmy

The independent yields of all isotopes produced in the spontaneous fission of ^{252}Cf have been calculated using the simple Gaussian distribution formalism of Wahl et al.[1] The assumption in this approach is that for each mass chain there is a Gaussian distribution of product yields having a fixed standard deviation, σ, and a mean corresponding to a most probable charge, Z_p, for that mass chain. Since the charge and mass values are discrete for individual isotopes we can mathematically evaluate the yield as

$$Y_M^I(Z_i) = \frac{Y_M}{\sqrt{2\pi}\,\sigma} \int_{Z_i-\frac{1}{2}}^{Z_i+\frac{1}{2}} \exp\left[-\frac{(Z_i-Z_p)^2}{2\sigma^2}\right] dz, \qquad (1)$$

where

$Y_M^I(Z_i)$ is the independent yield of any specific isotope,

Y_M is the total chain yield for a specific mass,

σ is the standard deviation of the Gaussian for all mass chains,

Z_p is the centroid of the distribution for a specific mass chain.

Equation (1) can be more conveniently expressed by changing variables so that

$$t = (Z_i - Z_p)/\sigma ;$$

substituting this in Eq. 1 gives

$$Y_M^I(Z_i) = \frac{Y_M}{\sqrt{2\pi}} \int_{t_1}^{t_2} e^{-t^2/2}\, dt. \qquad (2)$$

The limits are found to be

$$t_2 = \frac{Z_i - Z_p + \frac{1}{2}}{\sigma}, \qquad t_1 = \frac{Z_i - Z_p - \frac{1}{2}}{\sigma}$$

The independent yields can thus be calculated as the difference between two normal probability integrals:

$$Y_M^I(Z_i) = \frac{Y_M}{2}\left[\frac{1}{\sqrt{2\pi}} \int_{-t_2}^{t_2} e^{-t^2/2}\, dt - \frac{1}{\sqrt{2\pi}} \int_{-t_1}^{t_1} e^{-t^2/2}\, dt\right]. \qquad (3)$$

Values of these integrals are given in Ref. 2.

In order to quantitatively evaluate these equations it is necessary to know for each mass chain the values of σ, Z_p, and Y_M. Norris and Wahl report[3] that the standard deviation of the charge distribution is approximately constant for all mass chains and has a value of $\sigma = 0.59 \pm 0.06$. This value was obtained as an average of the individual determinations of σ for ten mass chains. The studies were done primarily with the $^{235}U(n_{th}, F)$ reaction, but were also correlated with data on other fission reactions, $^{233}U(n_{th}, F)$, $^{239}Pu(n_{th}, F)$ and $^{252}Cf(SF)$. The most probable charge values (Z_p) were taken from Fig. 1. This curve was constructed on the basis of empirical Z_p values given by Wahl et al.[1] and Z_p values determined by x-ray measurements by Kapoor, Bowman, and Thompson.[4] The values of the chain yields (Y_M) were taken from the radiochemical work of Nervik.[5] The results of these calculations for all isotopes that have prompt fission fields and have masses between 86 and 162 and charges between 36 and 62 are presented in Ref. 6.

By evaluating the elemental yields of all fission products a simple consistency check can be made on the calculations. The elemental yield is given as the sum of the independent yields of all products having the same atomic number:

$$Y_Z = \sum_{M=1}^{n} Y_M^I(Z) . \qquad (4)$$

Since there are usually only two products formed in the fission process, the requirement is that the sum of the two charge values add to give the atomic number of the fissioning nucleus. For the fission of ^{252}Cf this implies that

$$Y_Z = Y_{(98-Z)} .$$

The comparison of the calculated complementary elemental yields is presented in Fig. 2. It is seen that the deviations are reasonably small (10–15%) for the majority of the cases. However, for regions around symmetric fission (Z = 47–53), the deviations are larger, and in the worst case (Z = 48, 50) differ by a factor of 2. These deviations are not completely understood, but probably represent a breakdown in the simple assumptions, especially with regard to a constant σ value for all mass chains.

Footnote and References

†Present address: Cyclotron Institute, Texas A & M University, College Station, Texas 77840.

1. A. C. Wahl, R. L. Ferguson, D. R. Nethaway, D. E. Troutner, and K. Wolfsberg, Phys. Rev. 126, 1112 (1962).
2. Tables of Normal Probability Functions, National Bureau of Standards Applied Mathematics Series 23 (U. S. Government Printing Office, Washington, D. C. 1953).
3. Andrew E. Norris and Arthur C. Wahl, Phys. Rev. 146, 926 (1966).
4. S. S. Kapoor, H. R. Bowman, and S. G. Thompson, Phys. Rev. 140, B1310 (1965).
5. W. E. Nervik, Phys. Rev. 119, 1685 (1960).
6. R. L. Watson and J. B. Wilhelmy, Calculated Fractional Independent Yields of Products Formed in the Spontaneous Fission of ^{252}Cf, UCRL-18632, Feb. 1969.

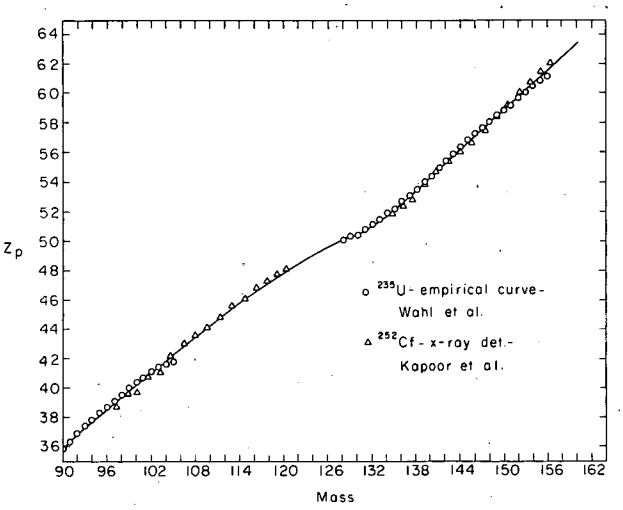

Fig. 1. A curve presenting the empirical most probable charge values as a function of atomic number. (XBL6812-7302)

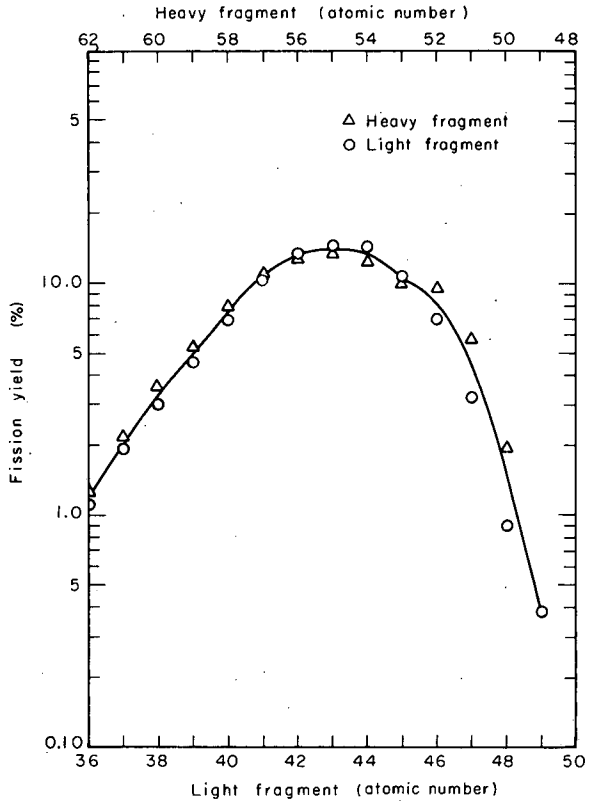

Fig. 2. A plot of the calculated elemental yields for the elements produced in the fission of ^{252}Cf. At each abscissa point the yield of the light and heavy fragments should coincide. Their deviations represent the inconsistencies in the calculations.
(XBL6812-7303)

Fission

SEARCH FOR CALIFORNIUM AND BERKELIUM FISSION ISOMERS

E. Cheifetz,† R. C. Gatti, and H. R. Bowman

The isotope ^{244}Cm was bombarded by alpha particles in an attempt to produce the fission isomer ^{246}Cf in an (α, 2n) reaction. The discovery of a ^{246}Cf fission isomer in a ^{238}U (^{12}C, 4n) reaction with a lifetime of ≈ 50 nsec and $\sigma_{isomer}/\sigma_{g.s.} \approx 10^{-2}$ was reported.[1] This reported ratio of $\sigma_{isomer}/\sigma_{g.s.}$ was the highest of any of the known fission isomers.

A target of 50 $\mu g/cm^2$ ^{244}Cm was placed in the experimental system which was used for detecting delayed fission in mica. A schematic diagram of this equipment is shown in Fig. 1. The products that did not undergo fission were collected on a silicon catcher of 100 μ thickness and counted for alpha activity after the bombardment. The target was also bombarded with protons and deuterons of several energies. No significant delayed fission activity was detected.

The results for the cases in which a definite alpha-emitting product was isolated are presented in Table I and are given directly in terms of the ratio $\sigma_{isomer}/\sigma_{g.s.}$. In the three cases presented

Table I. $\sigma_{isomer}/\sigma_{g.s.}$ upper limits in cases where an alpha-emitting product was formed.

Product	Reaction	Projectile Energy (MeV)	Detected alphas	Atoms of g.s.	Tracks	$\sigma_l/\sigma_{g.s.}$
^{246}Cf	$^{244}Cm(\alpha, 2n)$	29	Large	2.8×10^{6}	5	$\leq 2\times10^{-6}$
^{243}Bk	$^{244}Cm(p, 2n)$	12	62	7.9×10^{5}	15	$\leq 2\times10^{-5}$
^{243}Bk	$^{244}Cm(p, 2n)$	18	183	4.3×10^{6}	10	$\leq 2\times10^{-6}$

in Table I the number of tracks was consistent with the background measured with a beryllium target. In Table II we present the results obtained in the cases where no alpha emitters were isolated. Again only upper limits were found. For the higher bombarding energy the background increased, presumably because of lead and bismuth contamination in the silicon catcher. The value of the upper limits in Table II is based on the monitored beam current, the target thickness, and the efficiency for detecting a recoil product. The last value was obtained from the ^{246}Cf

Table II. σ_{isomer} upper limits for various reactions. (E_p = projectile energy, I = total beam current. When X4 appears in the track number, only 1/4 of the mica was scanned. BG = background target).

Reaction	E_p (MeV)	I (μAh)	Tracks	Product	$\sigma_{is}(\mu b)$
$^{244}Cf + \alpha$	43	0.31	58×4	^{244}Cf, ^{245}Cf	≤ 1.0
BG + α	43	0.30	47×4		
^{244}Cm + p	18	0.42	10	^{243}Bk, ^{242}Bk	≤ 0.5
BG + p	18	0.37	20		
^{244}Cm + p	28	0.39	45	^{242}Bk, ^{241}Bk	≤ 1.1
BG + p	28	0.30	28×4		
^{244}Cm + d	12	0.5	4	^{244}Bk, ^{245}Bk, ^{245}Cm	≤ 0.1

alpha activity detected in the catcher in the 30-MeV alpha bombardment. All the factors mentioned may, however, introduce an uncertainty of a factor of 2 in the results of Table II.

Since no isomer was detected in any of the reactions, the upper limits of the cross sections depend on the lifetimes of the unobserved isomers. In Fig. 2 we show the correction factor that must multiply the upper limits as a function of the lifetime, the projectile mass, and its energy.

Our limits on the production of a 50-nsec fission isomer in ^{246}Cf is 5×10^3 smaller than the reported ratio $\sigma_{isomer}/\sigma_{g.s.}$ for the ^{238}U (^{12}C, 4n) reaction. Such a large effect cannot be due to angular momentum effects only; in fact, among the known fission isomers, angular momentum has little effect on the $\sigma_{isomer}/\sigma_{g.s.}$ ratio. We therefore suggest that the assignment of ^{246}Cf identity to the fission isomer observed in the $^{238}U + {}^{12}C$ reactions is in error and that no isomer of 50-nsec half-life exists in berkelium or californium within the limits in cross section given in Table I or II.

The general observation that the isomer lifetimes or their production cross sections are very low for berkelium and californium isotopes is consistent with the detailed description of the double-peaked barrier in this region. The calculations indicate that the height of the second barrier is decreased by ≈ 2 MeV as compared with plutonium isotopes.[2] The calculated lifetime for the ^{246}Cf isomer is 10^{-15} sec. Such a short lifetime would be undetectable in our experiments.

Footnote and References

†On leave from the Weizmann Institute, Rehovoth, Israel.

1. Yu. F. Gangrskii, B. N. Markov, S. M. Polikanov, I. F. Kharisov, and Kh. Yungklaussen, Bull. Acad. Sci. USSR 32, 1644 (1968) (English Transl., p. 1525).
2. Chin Fu Tsang and Sven Gösta Nilsson, UCRL-18963, Aug. 1969 (submitted to Nucl. Phys.).

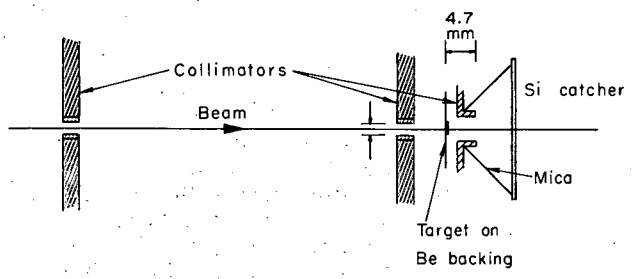

Fig. 1. Experimental arrangement. (XBL696-2930)

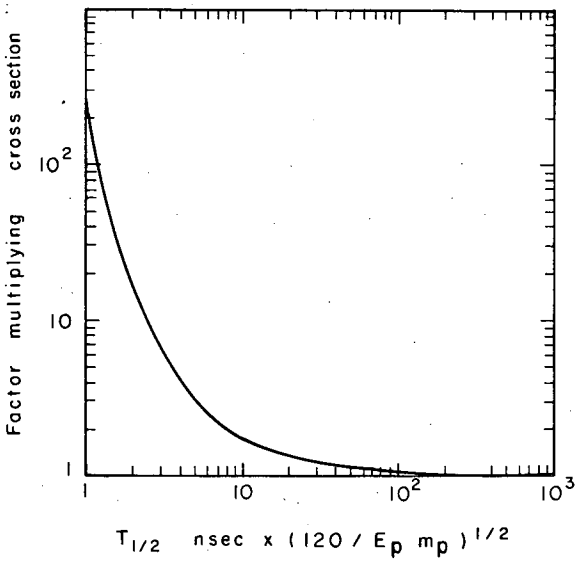

Fig. 2. Factor for correcting the lower limit cross sections as a function of $T_{1/2} \times [120/(E_p m_p)]^{1/2}$. ($T_{1/2}$ = isomer lifetime in nsec, E_p = projectile energy in MeV, m_p = projectile mass in amu.) This factor reduces conveniently to $T_{1/2}$ for 30-MeV alphas. (XBL696-2931)

THE DISTRIBUTION OF K x RAYS AS A FUNCTION OF MASS AND ATOMIC NUMBER IN THE SPONTANEOUS FISSION OF ^{252}Cf†*

R. L. Watson,‡ R. C. Jared, and S. G. Thompson

Measurements of the intensities of K x rays in coincidence with fission fragments were carried out in an experiment in which the energies of complementary fission-fragment pairs and K x rays were recorded event by event by using silicon semiconductor detectors and a multiparameter analyzer. The purpose of this study was to further examine the applicability of high resolution x-ray measurements as a means of defining features of the primary charge distribution and to investigate the effect of fragment total kinetic energy on the K x-ray spectra.

In processing the data the fission-fragment pulse heights were transformed into fragment masses, the x-ray pulse heights were sorted according to the mass of the fragment detected in fragment 2 detector and the total kinetic energy of the fission event into separate x-ray energy spectra for each 2-amu interval of mass and 15-MeV interval of total kinetic energy, and these "mass and energy sorted" x-ray spectra were plotted by a CalComp plotter.

The spectra of K x rays summed over all mass intervals are shown in Fig. 1 for the three intervals of total kinetic energy: (a) 190 to 205 MeV, (b) 175 to 190 MeV, (c) 160 to 175 MeV, and in (d) the K x-ray spectrum is summed over all mass and total kinetic energy intervals (160 to 205 MeV). The marked changes of x-ray intensities exhibited by the spectra compared in Fig. 1 clearly illustrate the variation of fragment atomic number as a function of total kinetic energy. It can be seen that sorting the total x-ray spectrum (d) with respect to total kinetic energy has the effect of accentuating the contributions of spectrum (a) of the light fragment–high Z and heavy fragment–low Z elements, to spectrum (b) of the light and heavy fragment–intermediate Z elements, and to spectrum (c) of the light fragment–low Z and heavy fragment–high Z elements. This behavior is a reflection of the fact that the average total kinetic energy increases as the atomic numbers of the light and heavy fragments approach Z=49 and is in accord with the well-known variation of the average total kinetic energy with fragment mass.

Each of the mass-sorted x-ray spectra was analyzed by using a computerized least-squares peak-fitting procedure to separate the individual x-ray distributions of each element from those of the other elements contributing to the same spectrum. In this way the intensities of x rays associated with every mass and total kinetic energy interval were determined for each element. The x-ray intensities are presented in a contour plot as a function of atomic number and neutron number in Fig. 2. In this figure, large variations are observed in x-ray intensities from one Z to the next and it is interesting to note the occurrence of the intense peaks centered at the odd-odd nuclei $^{108}_{43}Tc_{65}$, $^{136}_{53}I_{83}$, $^{140}_{55}Cs_{85}$, and $^{146}_{57}La_{89}$. In the work described in Ref. 1, it was found that these x-ray intensity peaks are accounted for by highly converted transitions occurring at 69, 59, 78, and 64 keV respectively.

The absolute x-ray intensities summed over the whole range of total kinetic energy (160 to 205 MeV) are listed in Table I as a function of mass interval and atomic number. These absolute intensities are estimated to be accurate on the average to within less than 20% and the relative intensities to within approximately 10%.

Pursuing now the question of how best to relate the K x-ray yield distribution to the nuclear charge distribution, we begin by noting that the yield of K x rays from a fission fragment of atomic number Z and mass number A may be expressed as the product of a K x-ray emission probability [C(Z, A)] and the fragment yield

$$Y^{x}_{(Z,A)} = C_{(Z,A)} Y_{(Z,A)} \qquad (1)$$

The K x-ray yields measured in the present experiment are not the yields of K x rays from fragments of specific mass and atomic numbers, but rather the yield of K x rays from fragments of specific atomic numbers averaged over a range of mass numbers. Hence Eq. 1 must be reformulated slightly to take into account the large dispersion associated with the mass determinations. In terms of the mass dispersion function, $d_A(M)$, which describes the yield distribution of

Table I. K x-ray intensity as a function of fragment mass interval and atomic number.

Light fragment post-neutron-emission mass interval	Light fragment atomic numbers										Total x rays[a] per fission	Total x rays per fragment
	38[a]	39[a]	40[a]	41[a]	42[a]	43[a]	44[a]	45[a]	46[a]	47[a]		
91-93	0.31	0.39	0.27								1.05	0.063
93-95	0.33	0.50	0.58	0.26	0.11						1.86	0.081
95-97	0.37	0.67	0.95	0.52	0.36	0.18					3.05	0.106
97-99	0.38	0.83	2.04	1.18	0.82	0.39					5.72	0.132
99-101	0.40	0.64	2.96	2.53	1.90	1.07	0.36				9.85	0.156
101-103	0.54	0.72	2.69	3.82	4.24	2.72	0.97	0.16			15.9	0.178
103-105	0.38	0.70	1.71	3.85	6.81	7.03	1.90	0.46			22.9	0.203
105-107	0.24	0.50	0.65	2.21	6.87	12.5	4.79	0.71	0.10		28.6	0.221
107-109	0.38	0.50	0.56	1.16	4.36	15.1	8.56	2.46	0.51		33.6	0.264
109-111		0.36	0.34	0.59	1.47	9.31	10.6	3.70	1.47		28.0	0.243
111-113				0.13	0.55	3.61	7.08	4.16	2.63	0.56	18.8	0.191
113-115				0.10	0.21	1.04	2.45	2.56	4.71	1.37	12.4	0.164
115-117						0.27	0.69	0.95	4.17	2.16	8.35	0.169
117-119							0.17	0.13	1.14	1.02	2.52	0.119
119-121									0.20	0.20	0.43	0.074
121-123												
Total light fragment intensities	3.39	5.90	12.8	16.5	27.8	53.4	37.7	15.3	15.0	5.44	193.2	

Heavy fragment post-neutron-emission mass interval	Heavy fragment atomic numbers												Total x rays[a] per fission	Total x rays per fragment
	51[a]	52[a]	53[a]	54[a]	55[a]	56[a]	57[a]	58[a]	59[a]	60[a]	61[a]	62[a]		
131-133	0.91	0.54	2.03		0.30								3.83	0.084
133-135	0.89	0.42	7.14	0.53	1.39								10.4	0.135
135-137	0.76	0.24	9.94	1.80	5.44	0.74		0.12					19.0	0.213
137-139	0.72	0.48	8.19	3.67	13.5	2.60	1.00	0.26					30.5	0.290
139-141	0.88	0.55	4.29	3.53	20.5	5.89	3.64	1.17					40.4	0.350
141-143	0.69	0.61	2.19	2.40	17.2	10.7	8.58	1.67	0.25				44.4	0.374
143-145	0.31	0.41	0.88	0.97	10.1	11.9	16.3	4.08	1.45				46.4	0.396
145-147		0.10	0.57	0.82	3.74	7.50	18.6	9.32	4.15	0.41			45.2	0.386
147-149			0.34	0.50	1.20	2.69	11.5	12.5	8.32	2.36	0.59		40.1	0.570
149-151			0.26	0.44	0.46	1.16	4.43	9.62	10.5	4.81	1.67	0.66	34.0	0.742
151-153				0.30	0.37	0.71	1.68	4.60	8.48	7.67	2.89	1.04	27.8	0.909
153-155				0.21	0.21	0.52	0.81	1.84	4.36	8.00	4.48	1.75	22.2	0.974
155-157					0.11	0.13	0.31	0.67	1.28	3.84	3.70	2.13	12.2	0.884
157-159								0.18	0.25	0.88	1.28	1.30	3.89	0.549
159-161										0.14	0.26	0.38	0.78	0.23
161-163										0.13	0.13	0.13	0.33	0.22
Total heavy fragment intensities	5.16	3.34	36.0	15.3	74.5	44.5	66.9	46.0	39.1	28.3	15.0	7.47	381.4	

[a]Numbers in this column have units of 10^{-3} x rays per fission.

fragments having mass number A as a function of mass interval, the measured yield of K x rays arising from fragments of atomic number Z and sorted into mass interval M is given by

$$Y^{x}_{(Z,M)} = \sum_{A} Y^{x}_{(Z,A)} d_{A}(M)$$

$$= \sum_{A} C_{(Z,A)} Y_{(Z,A)} d_{A}(M). \qquad (2)$$

It was pointed out by Glendenin et al.[2] that if the function $d_A(M)$ is broad compared with the width of a mass interval, then the detailed structural features of the yield of K x rays as a function of mass interval will be washed out and $Y^{x}_{(Z,A)}$ will be averaged over a large number of isotopes. It is likely that, in general, the K x-ray emission probability, $C_{(Z,A)}$, does not vary rapidly from one isotope of a given nuclear type to the next (such as from one even-odd nucleus to the next even-odd nucleus of the same Z), and even though a large difference in the magnitude of $C_{(Z,A)}$ may be expected in going from a nucleus of one nuclear type to the nuclear type of the immediately adjacent nuclei (such as from an even-odd nucleus to the two adjacent even-even nuclei), if the fluctuation from one isotope to the next is fairly constant and the dispersion function $d_A(M)$ sufficiently broad, then it is quite possible that the measured K x-ray distribution can be satisfactorily represented by replacing $C_{(Z,A)}$ in Eq. 2 with an average K x-ray emission probability $\bar{C}_Z$ such that

$$Y^{x}_{(Z,M)} = \bar{C}_Z \sum_{A} Y_{(Z,A)} d_{A}(M) \quad . \qquad (3)$$

The yield distribution of fission fragments as a function of atomic number can similarly be formulated in terms of a smoothly varying distribution function $P_Z(A)$ defined by the relation

$$Y_{(Z,A)} = Y_{(Z)} P_Z(A) \quad , \qquad (4)$$

where $Y_{(Z)}$ is the total yield of fragments of atomic number Z. Although the function $P_Z(A)$ may deviate very slightly from a Gaussian due to small variations which occur in σ_Z from one mass chain to another, the most probable mass number A_p defined by the distribution function $P_Z(A)$ will correspond to the mass number of the most probable atomic number, Z_p. The total yield of K x rays from fragments of atomic number Z is obtained by summing over all mass intervals as follows:

$$Y^{x}_{(Z)} = \sum_{M} Y^{x}_{(Z,M)} = C_Z \sum_{M} \sum_{A} Y_{(Z,A)} d_{A}(M) \quad ,$$

but

$$\sum_{M} \sum_{A} Y_{(Z,A)} d_{A}(M) = Y_{(Z)} \quad ,$$

hence

$$Y^{x}_{(Z)} = \bar{C}_Z Y_{(Z)} \qquad (5)$$

or

$$\bar{C}_Z = \frac{Y^{x}_{(Z)}}{Y_{(Z)}} \quad . \qquad (6)$$

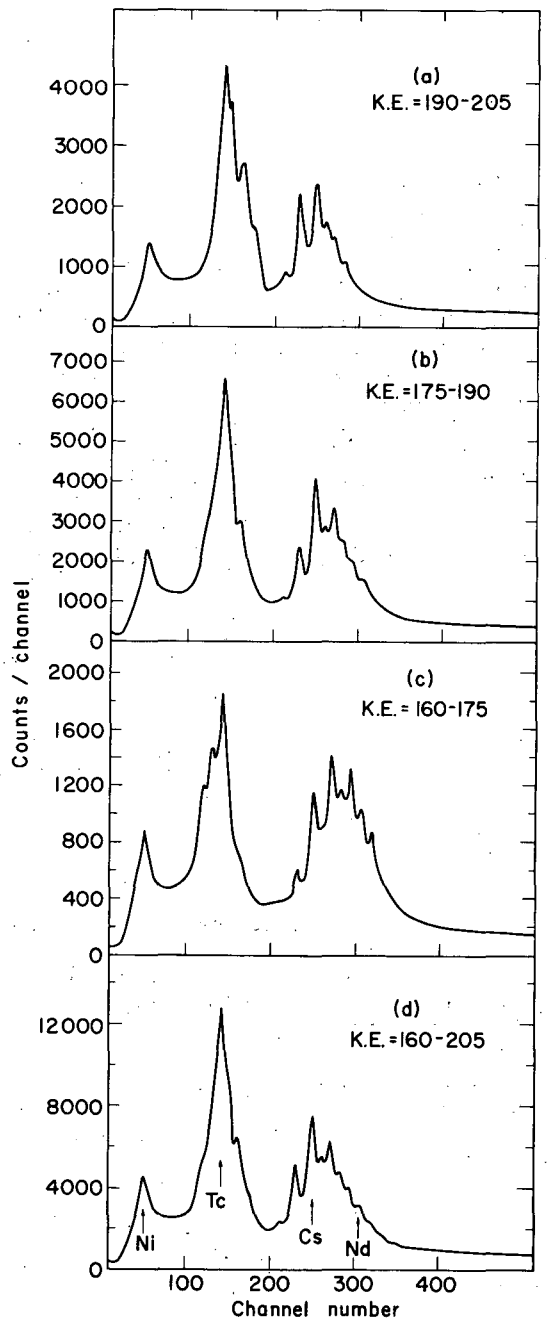

Fig. 1. K x-ray spectra (unsorted with respect to mass) for three intervals of total kinetic energy (a, b, and c) and for the full range of total kinetic energy (d). (XBL698-3464)

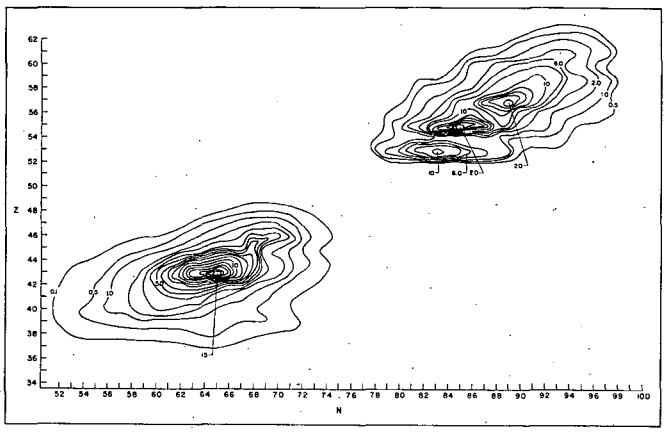

Fig. 2. A contour plot of the intensity of K x rays arising from fission fragments as a function of atomic number and neutron number (in units of 5×10^{-4} K x rays per fission). (XBL701-227)

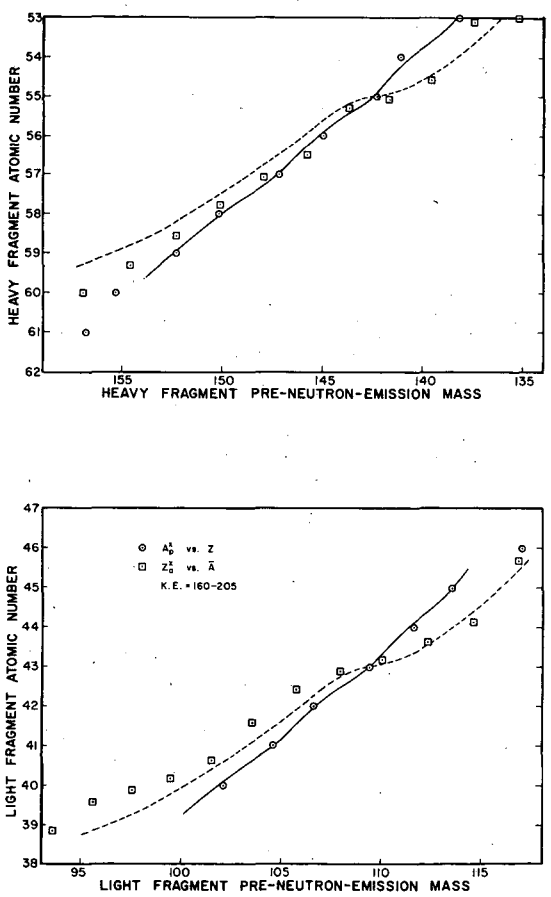

Fig. 3. The most probable pre-neutron-emission masses associated with the emission of K x rays (A_p^x) as a function of atomic number, and the average atomic numbers associated with the emission of K x rays (Z_a^x) as a function of pre-neutron-emission mass. The solid and dashed lines represent averages of the respective complementary light and heavy fragment data points. (XBL701-225)

Substituting Eqs. 4 and 6 into Eq. 3, we obtain

$$Y^{x}_{(Z,\,M)} = Y^{x}_{(Z)} \sum_{A} P_{Z}(A) d_{A}(M). \qquad (7)$$

The dispersion function was determined experimentally and found to be Gaussian. Since the dispersion function is symmetrical about the average mass of a given mass interval, its overall effect will be to broaden the distribution of $Y^{x}_{(Z,\,M)}$ without changing the position of its most probable value. Hence, within the limits of error imposed by the assumption that the K x-ray distribution can be represented by the average K x-ray emission probability $\bar{C}_{Z}$, the most probable mass associated with the emission of K x rays, A^{x}_{p}, may be taken as the centroid, A_{p}, of the P_{Z} distribution defined in Eq. 4. The most probable mass, A_{p}, plotted as a function of Z should correspond identically to the curve obtained by plotting the most probable charge, Z_{p}, as a function of A.

All of the $Y^{x}_{(Z,\,M)}$ distributions were fitted with Gaussian functions and in this way the centroids, A^{x}_{p}, and widths were obtained. The average atomic numbers, Z^{x}_{a}, associated with the emission of K x rays from fragments of a given mass interval were also determined as a function of the average fragment mass.

The acceptability of the A^{x}_{p} values for representing the Z_{p} curve can be tested by checking to see how well they fulfill the requirement of charge and mass conservation. If the values of A^{x}_{p} are taken as corresponding to the values of A_{p}, then these most probable post-neutron-emission numbers, when transformed to pre-neutron-emission mass numbers, for complementary atomic number pairs (i.e., Z_{L} and Z_{H} pairs that fulfill the relationship $Z_{L} + Z_{H} = 98$) should sum to the mass number of the fissioning nucleus, 252. The average deviation from this sum for the pre-neutron-emission values of A^{x}_{p} was 0.3 amu. The deviation is in all cases except one (for the pair Z_{L}=44, Z_{H}=54) within experimental error, and since it is highly unlikely that such consistency could be obtained if substantial biasing of the A^{x}_{p} values due to details of nuclear structure were occurring, we conclude that they must accurately represent the true values of A_{p}. Thus it appears that the Z_{p} curve can in this way be adequately defined by K x-ray measurements.

The degree of consistency of the present data in fulfilling the requirements of charge and mass conservation is shown graphically in Fig. 3. In this figure are plotted the experimental values of pre-neutron-emission A^{x}_{p} versus Z separately for light and heavy fragments. The atomic number and mass number scales have been arranged such that complementary Z and A combinations intersect at the same relative positions on the two graphs. The solid line is an average of the light-fragment and heavy-fragment points obtained by superimposing the complementary Z and A points of the two graphs and drawing a curve passing equidistant between adjacent data points. The fact that the curve passes very close to all of the experimental points indicates that the charge and mass conservation requirements are fulfilled extremely well. Also shown in Fig. 3 are the experimental values of Z^{x}_{a} plotted versus pre-neutron-emission $\bar{A}$. The dashed line is the average curve passing through complementary pairs of these points. It is seen that very poor fulfillment of the requirement of charge and mass conservation is obtained for this set of data points. The apparent reason for this is that the atomic number resolution is one Z unit, and hence there is no effective averaging of $C_{(Z,\,A)}$ over Z in the determination of Z^{x}_{a}, which would tend to average out the effects of specific features of nuclear structure.

Table II. Values of the most probable nuclear charge (Z_{p}).

Post-neutron-emission mass number	Z_{p}	Post-neutron-emission mass number	Z_{p}
100	39.2 ± 0.3	137	53.0 ± 0.2
101	40.2 ± 0.3	138	53.3 ± 0.2
102	40.6 ± 0.3	139	53.8 ± 0.2
103	41.1 ± 0.2	140	54.4 ± 0.2
104	41.6 ± 0.2	141	55.0 ± 0.1
105	42.0 ± 0.2	142	55.4 ± 0.1
106	42.5 ± 0.1	143	55.9 ± 0.1
107	43.0 ± 0.1	144	56.3 ± 0.1
108	43.4 ± 0.1	145	56.8 ± 0.1
109	43.9 ± 0.1	146	57.2 ± 0.1
110	44.4 ± 0.2	147	57.6 ± 0.1
111	45.0 ± 0.2	148	58.1 ± 0.1
112	45.4 ± 0.2	149	58.5 ± 0.2
113	45.7 ± 0.2	150	59.0 ± 0.2
114	46.0 ± 0.3	151	59.4 ± 0.2
115	46.7 ± 0.5	152	59.8 ± 0.2
		153	60.3 ± 0.3

Using the post-neutron-emission values of A_p^x, a curve was constructed from which the Z_p value for each mass chain could be read. These values of Z_p are listed in Table II. The errors quoted for these numbers were determined graphically from the errors in the values of A_p^x.

Footnotes and References

†Condensed from a paper submitted for publication in Phys. Rev., December 1969.
*Par. of this work was carried out at Texas A & M University, College Station, Texas, and was supported by the U. S. Atomic Energy Commission and the Robert A. Welch Foundation.
‡Present address: Texas A & M University, College Station, Texas 77840
1. R. L. Watson, J. B. Wihelmy, R. C. Jared, C. Rugge, H. R. Bowman, S. G. Thompson, and J. O. Rasmussen, UCRL-19510, Nov. 1969 (to be published in Nucl. Phys.).
2. L. E. Glendenin, H. C. Griffin, W. Reisdorf, and J. P. Unik, in Proceedings of the International Atomic Energy Agency Symposium on Nuclear Fission, Vienna, July 1966, Paper No. SM-122/114.

A STUDY OF THE LOW ENERGY TRANSITIONS ARISING FROM THE PROMPT DE-EXCITATION OF FISSION FRAGMENTS†*

R. L. Watson,‡ J. B. Wilhelmy, R. C. Jared, C. Rugge,
H. R. Bowman, S. G. Thompson, and J. O. Rasmussen††

A four-dimensional experiment in which the energies of coincident complementary fragment pairs, internal conversion electrons, and K x rays emitted as a result of the spontaneous fission of ^{252}Cf were recorded event by event by using a multiparameter analyzer has previously been described.[1] Here we report the major results of this investigation.

The fourfold coincidence data were used to make "x-ray window sorts" for the purpose of determining the atomic number of the nuclide responsible for any given electron peak appearing in the internal conversion electron spectra. This was accomplished in the computer processing of the fourfold coincidence events by placing "windows" on each observed electron peak and sorting out only those fourfold coincidence x-ray events in the electron "window." These sorts were carried out for each mass interval in which the electron peak appeared.

Examples of the results of this analysis of an electron spectrum for the light fragment mass interval 107 to 109 are shown in Fig. 1. The energy intervals labeled alphabetically in the electron spectrum delineate the "windows" used in the "x-ray window sorts." The x-ray spectra shown in Fig. 1 were obtained by sorting out of the fourfold coincidence x-ray data only those events that were in coincidence with fourfold coincidence electron events falling in the electron window corresponding to the appropriate alphabetic label. The mass intervals associated with the x-ray spectra in this figure are those in which the x rays appeared in their highest intensity. It is clearly seen from the K_α x-ray components in Fig. 1 that electron peaks A, B, C, D, and E arise from isotopes of Tc, Mo, Mo, Mo, and Ru respectively.

Determinations of the masses of the fragments responsible for the various electron peaks were made by plotting the intensities of x rays derived from the "x-ray window sorts" as a function of mass. These plots for any given single electron peak uniquely establish the mass resolution, and the first moment of the distribution identifies the true mass of the fission fragment.

The results of the analysis of the data obtained in this experiment combined with those obtained by Watson[2] in earlier experiments are tabulated in Table I. Explanatory information pertaining to the various headings is as follows:

1. Mass number: Determined from the centroid of a plot of electron peak intensities or coincident K x-ray intensities as a function of mass.

Table I. Interpretation of data.[a]

Mass number	Atomic number	K line energy (keV)	I_{rel}	$t_{1/2}$ (nsec)	I_{abs}	γ-ray energy (keV)	Confidence level	Observations
98	40(Zr)	194	1.2			213	B	
101	40(Zr)	80	13			99	C	
102	40(Zr)	134	4.9	1.7	1.6	153	B	
	40(Zr)	189	2.5			(208)	A	
106	42(Mo)	74	27	1.1	6.2	95	A	K to L ratio (4.8) consistent with E2
	42(Mo)	130				(151)	B	
	42(Mo)	151				172	A	
	42(Mo)	171	11	1.2	8.1	192	A	
107	43(Tc)	44	25	1.0	6.0	(66)	C	
108	43(Tc)	47	47	1.0	11	69	A	
	43(Tc)	76	12	0.9	2.7	98	B	
109	43(Tc)	101	4.3			123	A	
110	44(Ru)	49	18	2.2	7.5	72	B	
	44(Ru)	127				150	C	
	44(Ru)	218	4.7	<0.5		241	A	K to L ratio (4.0) consistent with E2
113	45(Rh)	38	8.7			(62)	C	
116	46(Rh)	24	4.3	0.6	0.82	49	A	K to L ratio (2.4) consistent with E2
136	53(I)	25	10			59	B	
	53(I)	54	2.5	0.4	0.56	(88)	B	
139	54	251	0.38			283		
140	55(Cs)	24				(61)	B	
	55(Cs)	41	44	1.0	11	78	A	
	55(Cs)	81	18	2.6	8.8	118	B	K to L ratio (5.3) consistent with M1
143	55(Cs)	75				112	C	
144	56(Ba)	75	30	1.2	9.4	113	B	
	56(Ba)	145				183	A	
	56(Ba)	161	9.4	1.0	2.5	199	A	K to L ratio (4.1) consistent with E2
	56	245	0.27			283		
145	57(La)	60	15	1.7	7.3	100	C	
146	57(La)	24	39	0.6	9.4	64	A	K to L ratio (2.5) consistent with E2
	57(La)	91	7.2	2.7	2.0	131	A	
	57	256	0.17			296		
148	58(Ce)	117	11	1.3	3.4	158	A	K to L ratio (3.7) consistent with E2
149	59(Pr)	100	8.4	1.8	3.2	143	A	K to L ratio (3.6) consistent with E2
	58	204	0.36			(245)		
150	59(Pr)	23				66	C	
	59(Pr)	31	30	1.4	9.9	74	A	
152	58(Ce)	122				163	B	
156	62(Sm)	24	4.8	2.9	2.6	72	C	K to L ratio (1.7) consistent with E2
	62	43	2.7	1.9	1.1	91		
158	62	66	7.9	1.9	3.2	(114)		
	62	70				(118)		

[a]See text for explanatory remarks.

2. Atomic number: Determined from the "x-ray window sorts" for those cases in which the chemical symbol (in parentheses) follows the atomic number. For those cases in which only the atomic number is listed no determination was possible, and the numbers listed are the atomic numbers of the most probable charge elements.

3. K line energy: These energies were determined from the least-squares analysis of the triple coincidence electron spectra. They have been corrected for momentum shift but not for binding energy shift (i.e., the same K line from stopped fission fragments would appear 0.9 keV higher than the listed energy).

4. I_{rel}: Under this heading are listed the intensities of the peaks as they appear in the 1-nsec electron spectra of Watson.[2] These intensities are listed in units of 10^{-4} electron/fission and the relative values are estimated to be accurate to ± 10% for peaks above 50 keV and to ± 20% for peaks below 50 keV.

5. $t_{\frac{1}{2}}$: The listed transition half-lives were determined from the relative intensities of peaks appearing in the 1- and 2-nsec electron spectra of Watson.[2] These numbers are estimated to be accurate to better than ± 20%. Transitions for which relative intensities appear but no half-lives are given decay with half-lives less than 0.5 nsec.

6. I_{abs}: The absolute intensities listed here were corrected for decay and are listed in units of 10^{-3} electron/fission. The decay corrections were based upon the half-life determinations listed in the preceding column. These intensities are estimated to be uncertain by ± 25% for peaks above 50 keV and ± 35% for peaks below 50 keV.

7. γ-ray energy: Gamma-ray energies not enclosed in parentheses were determined from the γ-ray spectra of Bowman[3] and of Cheifetz.[4] They are the energies of prominent gamma rays appearing in these spectra at positions predicted by the conversion electron energies and are estimated to be accurate to ± 1 keV. Energies that are enclosed in parentheses are γ-ray transition energies estimated solely on the basis of the conversion electron energies and are given only for those cases in which clearly visible gamma rays could not be seen in the γ-ray spectra.

8. Confidence Level: Three levels of confidence were used to grade the degree of certainty in the various assignments. Level A distinguishes those cases that were clearly enough resolved to allow relatively unambiguous determinations in mass, atomic number, and peak energy. For these cases the mass assignments are believed to be accurate to ± 1 amu, the atomic number assignments are believed to be exact, and the energy assignments are believed to be good to ± 1 keV. Level B denotes cases in which interfering structure caused larger uncertainties in the mass and energy assignments (± 2 amu and ± 5 keV respectively). Level C was assigned to those cases in which interfering structure or low statistics gave rise to an uncertainty of ± 1 in the atomic number assignments as well as to uncertainties in the mass and energy assignments. No confidence level was assigned to cases in which an atomic number determination was not possible.

9. Observations: Listed in this column are K to L electron intensity ratios (numbers in parentheses) for those cases where such a determination was possible. These ratios are to be taken as rough estimates since interfering structure in most cases prevented the accurate determination of L line intensities.

Footnotes and References

†Condensed from UCRL-19510, Nov. 1969 (to be published in Nucl. Phys.).
*Part of this work was carried out at Texas A & M University, College Station, Texas, and was supported by the U. S. Atomic Energy Commission and the Robert A. Welch Foundation.
‡Present address: Texas A & M University, College Station, Texas 77840
††Present address: Yale University, 225 Prospect Street, New Haven, Connecticut 06520.
1. R. L. Watson, R. C. Jared, S. G. Thompson, and J. O. Rasmussen, in Nuclear Chemistry Division Annual Report, 1967, UCRL-17989, January 1968, p. 139.

2. R. L. Watson (Ph. D. Thesis), UCRL-16798, July 1966.
3. H. R. Bowman, Lawrence Radiation Laboratory, Berkeley, California, unpublished data.
4. E. Cheifetz, Lawrence Radiation Laboratory, Berkeley, California, unpublished data.

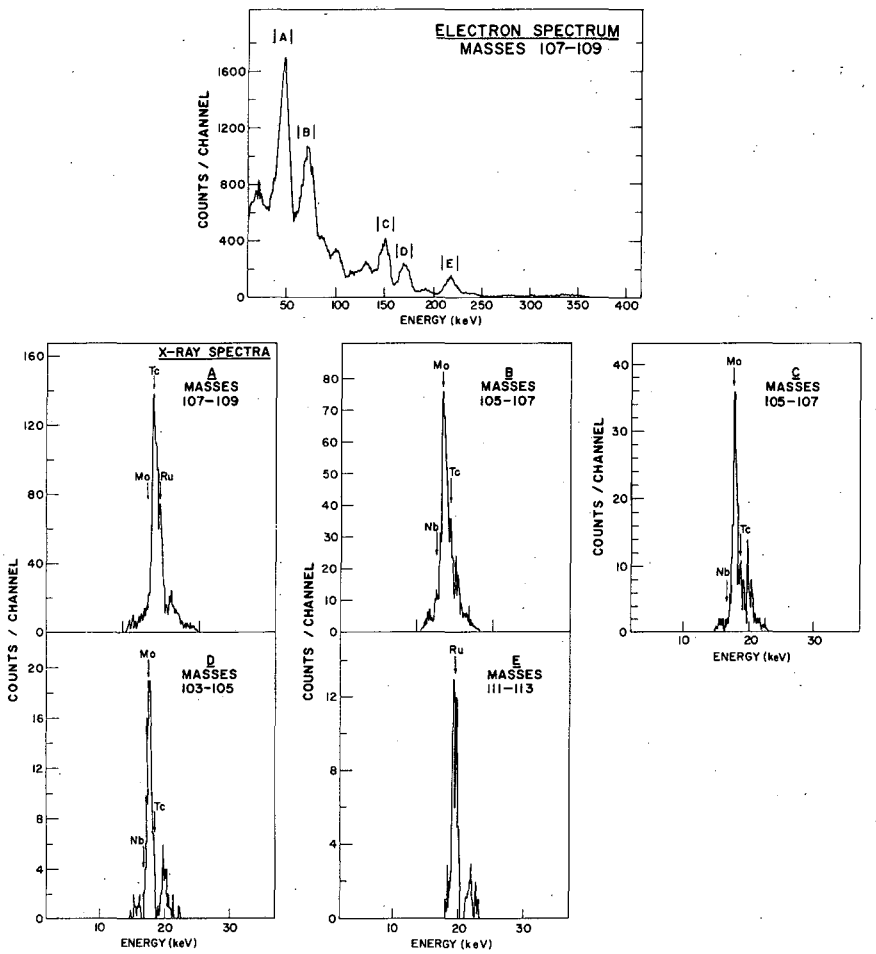

Fig. 1. An electron spectrum for the light fragment mass interval 107 to 109 and the K x-ray spectra resulting from x-ray "window" sorts on the alphabetically labeled electron peaks. The x-ray spectra shown are for the mass intervals in which the x rays appeared in their highest intensities.
(XBL701-226)

BETA-DECAY STUDIES ON THE SHORTEST-LIVED FISSION PRODUCTS

J. B. Wilhelmy, S. G. Thompson, and J. O. Rasmussen†

The fission process produces isotopes with large neutron excesses and therefore gives a unique opportunity for the study of high-Q-value β-decay systematics. As part of a detailed study on radiations emitted by short-lived fission products, [1] information has been gained on the total gross β-decay rates of all fission products. In addition, significant new data has been obtained on lifetimes of several specific short-lived isotopes.

The fission fragments from a 10-μg source of ^{252}Cf (3.7×10^8 f/min) were collected on a continuously moving belt and transported past a detection point located ≈ 50 cm from the source. At the detection point a Ge(Li) detector was used to measure the gamma rays emitted after the beta decay of the products. To a good approximation the physical dimensions of the detector could be considered to give a window of fixed geometry at which the radiations could be detected. By varying the velocity of the belt, then, the time spent within the detection window could be altered. It is easy to show that for a single component decay, the number of decays observed in the detection window can be expressed as [1]

$$\Delta N = \text{const}\,(\lambda t)\, e^{-\lambda t} \quad , \tag{1}$$

where λ is the decay constant and t is the transit time from the source to the detector. For any specific half-life this function will have a maximum which, through differentiation, can be shown to occur at

$$t = \frac{t_{1/2}}{\ln(2)} \quad .$$

Therefore the observed counting rate for a single transition will have a maximum that is related to the half-life of its beta-decaying parent. Thus the gross observed counting rate as a function of time should reflect the weighted yield of the half-life distribution of the fission products. Figure 1 presents the experimentally measured counting rates as a function of the transit from the source to the detectors. Experimental measurements were made with transit times from as short as 0.27 sec to as long as 4.8 hr. At the longest transit times the recorded rates are decreasing, indicating a reduction in the specific activity of the products. This occurs because the decays are feeding long-lived or stable isotopes. Moving to shorter times, there is an increase in counting rates, reflecting a higher yield of products with shorter half-lives. There is a broad maximum at around 10 to 100 sec and then the curve decreases quite rapidly. At the shortest measured time the rate is down by a factor of ≈ 8 below the maximum. This decrease indicates the absence of a substantial yield of fission products having half-lives shorter than ≈ 1 sec. We have attempted to interpret these experimental observations from the known β-decay properties.

Using the standard reduced transition probability description of Moszkowski[2] the β-decay log(ft) value can be given by the familiar relation

$$\log(ft) = \log(f_0 t) + \log(c) \quad . \tag{2}$$

Moszkowski presents a nomogram relating $\log(f_0 t)$ to the decay energy and half-life of the transition. This coupled with a presentation of graphs for log(c) versus energy gives a very rapid method for determining the log(ft) value. Rearranging Eq. 2 , the half-life can be expressed as

$$t_{1/2} = \frac{10^{[\log(ft) - \log(c)]}}{f_0} \quad . \tag{3}$$

To give an analytic method for the calculation of half-lives we have approximated the value of log(c) in the fission fragment region as

$$\log(c) = [-0.19 + (Z - 20)(-0.095/20)] \log(E)$$

$$+ [0.35 + (Z - 20)(0.36/20)] \quad ,$$

where E is the β-decay energy. The quantitative relationship for f_0 is[2]

$$f_0 = \left(\frac{W_0^4}{30} - \frac{3}{20} W_0^2 - \frac{2}{15}\right) \left(W_0^2 - 1\right)^{1/2}$$

$$+ \frac{2.302}{4} W_0 \log_{10} \left[W_0 + \left(W_0^2 - 1\right)^{1/2}\right],$$

where W_0 is the total decay energy expressed in units of the rest mass of the electron (m_0c^2). Therefore, the half-life to a specific state can be calculated if the decay energy is known and an assumption is made about the total log(ft) value. To determine the total decay lifetime it is necessary to couple the above prescription, which is for the decay to a single level, with a composite level density formula.

The level density formalism we have chosen is that developed by Gilbert and Cameron.[3] This was done primarily because they present a complete prescription for explicity evaluating the nuclear level densities without any a priori knowledge of resonances, pairing, or shell corrections in the desired isotopes. At high energies they represent the level density for spin state J as

$$\rho(U, J) = \frac{\sqrt{\pi}}{12} \frac{e^{2\sqrt{aU}}}{aU^{5/4}} \frac{(2J + 1)\, e^{-(J+\frac{1}{2})^2/2\sigma^2}}{2\sqrt{2\pi}\, \sigma^3} \quad , \tag{4}$$

where U is the effective excitation energy given by

$$U = E - U_0 = E - P(Z) - P(N) \, ,$$

with P(Z) and P(N) being the proton and neutron pairing energies tabulated by Cameron and Elkin.[4] The level density parameter a is given by

$$\frac{a}{A} = 0.00917\, S + 0.142,$$

where A is the mass of the isotope and S is the shell effect given by

$$S = S(Z) + S(N) \, ,$$

with S(Z) and S(N) also being presented by Cameron and Elkin.[4] The spin cutoff parameter σ can be evaluated through an empirical relationship of Jensen and Luttinger:[5]

$$\sigma^2 = 0.0888 \cdot a \cdot t \cdot A^{2/3},$$

where t is the thermodynamic temperature of the nucleus given by

$$t = \sqrt{\frac{U}{a}} \quad .$$

At energies below a specific tangency point given by

$$U_x = 2.5 + \frac{150}{A} \quad ,$$

the level density formula is taken to be

$$\rho(E, J) = \frac{1}{T} e^{(E-E_o)/T} \frac{(2J+1)\, e^{-(J+\frac{1}{2})^2/2\sigma^2}}{2\sigma^2} \quad .$$

The values of T and E_0 are determined by requiring that Eqs. 4 and 5 and their first derivatives be continuous at $E = E_x$.

Combining the level density formalism with Eq. 3 , we can express the total decay constant as an integral over the allowed energy:

$$\lambda = \int_0^{Q_\beta} \frac{\ln(2)\, f_0}{10^{[\log(ft) - \log(c)]}} \rho\,[(Q_\beta - E), J] \; dE \qquad (6)$$

To integrate this expression a value has to be assumed for log(ft) and for the spin state J. To obtain the half-life of a specific isotope we assume that the decay will occur through a Gamow-Teller allowed transition ($\Delta I = 0, 1, \Delta\pi = 0$). This gives a total decay constant of

$$\lambda_{tot,\,J} = \frac{\ln(2)}{t_{1/2}} = 0.5(\lambda_{J-1} + \lambda_J + \lambda_{J+1}) \quad , \qquad (7)$$

where the individual λ_J terms are evaluated by Eq. 6 . The factor of 0.5 comes from the parity requirements and assumes that states of spin J have equal chance of positive or negative parity.

Figure 2 presents the results of the calculations for the half-lives of ^{110}Tc as a function of β-decay energy for various assumed ground-state spins. There are two abscissa scales shown. One is for the half-life obtained by assuming a log(ft) value of 5 and the other is a reduced half-life independent of the log(ft) value where

$$t_{1/2} = (t_{1/2\,\text{red.}}) \left[10^{\log(ft)}\right]$$

There is a spread of ≈ 3 to 4 in the calculated half-life, depending on the value of J assumed. A change of 1 MeV in the β-decay energy yields a change in half-life between a factor of 5 and 8. The half-life is exponentially dependent on the value of log(ft), but a value of 5 for this constant appears to be reasonable, since only Gamow-Teller allowed transitions are considered. Using the Q_β^- value of 8.59 MeV given in the mass table of Myers and Swiatecki[6] and assuming the ground-

state spin to be 5+ we calculate a half-life of 0.0134 sec for the β^- decay of ^{110}Tc. The experimental value is believed to be 0.83 sec,[1] which is a factor of 60 longer than the calculated number. Deviations of this order of magnitude were typically found for the calculations of the highest known Q-value beta decays. For these cases the calculated values were always much shorter than the experimental data. Such observations imply that the assumptions of simply including all allowed spin states tend to overestimate the number of decay channels. This is, of course, seen most clearly for the highest Q-value beta decays where the number of apparent allowed channels is drastically affected by the exponential dependence of the level density formulas. The fact that the half-lives do not experimentally become this short supports the speculations of recent years regarding a total radiative strength in beta decay. The theoretical development has followed the experimental discovery that medium and heavy nuclei have sharp isobaric analog states with well-defined isospins.[7]

In β^- decay a neutron is effectively changed into a proton and the ground state isospin is lowered by one unit. In the Fermi-allowed beta decay the interaction potential is assumed to be constant, which implies that the only change in β^- decay is that a neutron is changed into a proton with the total nuclear configurations remaining the same. The state which meets the requirement is in fact the isobaric analog state of the parent. It would be degenerate in energy with the parent except for the Coulomb energy, which is added by placing an additional positive charge in the nucleus. This Coulomb displacement energy is always positive (for β^- decay) and therefore this isobaric analog state lies higher in energy than the parent, and transitions to it are energetically forbidden. Fermi transitions can thus only occur to the extent that the isospin representation is not valid (i.e., to the extent of the mixing between the states of various isospin). These considerations qualitatively explain the large hindrance factors that are experimentally found for Fermi transitions.

For Gamow-Teller transitions, the interaction potential is not a constant but includes the Pauli spin flip operator, ($\vec{\sigma}$), which reverses the intrinsic spin of the particle relative to its orbital angular momentum. Such an operator gives the familiar Gamow-Teller selection rules $\Delta I = 0, \pm 1$ (except $0 \rightarrow 0$ is forbidden). Since isobaric analog states appear to explain the hindrances for Fermi transitions, there has been conjecture that there may be giant resonance effects that concentrate the Gamow-Teller radiative strength. Fujita and Ikeda[8] state that if the nuclear forces were spin independent as well as isospin independent, then the locations of the isospin resonance (the isobaric analog state) and the Gamow-Teller resonance would coincide. They conclude that the Gamow-Teller resonance would be appreciably wider since the nuclear forces are not spin independent. However, since the predominant part of the transition operator is still the isospin lowering operator, $\vec{T}_-$, the Gamow-Teller resonance should be located in energy near the isobaric analog state.

The existence of such a resonance has several experimental consequences. For fission products the isobaric analog state lies in energy $\approx$ 10 MeV above the ground state of the parent. Therefore, the majority of the theoretical Gamow-Teller decay strength is not obtainable, since it is energetically forbidden. The increase in β-decay energy associated with the very neutron-rich isotopes does not exhaust the total strength of the Gamow-Teller resonance, since the resonance is correlated with the parent, not the daughter. The higher Q_{β^-} values only imply that the resonance has a higher energy relative to the daughter's ground state. This theory gives a total radiative strength for beta decay and is independent of the nuclear level density. It thus avoids the very short half-lives which are calculated for regions with high level densities.

To quantitatively study the predictions of the theory it would be necessary to represent the extent of the mixing of the resonance state with states that are energetically allowed. The high Q-value beta decays associated with the short-lived fission products should enable sampling of portions of the tail of the resonance distribution and could be most helpful in testing the quantitative aspects of the theoretical predictions. We hope to proceed with these studies as more specific isotopic half-lives become known in this region through correlations with information on prompt fission radiations.[9]

Footnote and References

†Present address: Yale University, 225 Prospect Street, New Haven, Connecticut 06520.

1. Jerry Barnard Wilhelmy, High-Resolution Gamma and X-Ray Spectroscopy on Unseparated Fission Products (Ph. D. Thesis), UCRL-18978, August 1969.
2. S. A. Moszkowski, Phys. Rev. 82, 35 (1951).

3. A. Gilbert and A. G. W. Cameron, Can. J. Phys. 43, 1446 (1965).
4. A. G. W. Cameron and R. M. Elkin, Can. J. Phys. 43, 1288 (1965).
5. J. H. D. Jensen and J. M. Luttinger, Phys. Rev. 86, 907 (1952).
6. William D. Myers and Wladyslaw J. Swiatecki, Nucl. Phys. 81, 1 (1966).
7. J. D. Anderson, C. Wong, and J. W. McClure, Phys. Rev. 126, 2170 (1962); Phys. Rev. 129, 2178 (1963).
8. Jun-Ichi Fujita and Kiyomi Ikeda, Nucl. Phys. 67, 145 (1965).
9. Gamma-Ray Studies on Short-Lived Fission Products, J. B. Wilhelmy et al., following paper in this Report.

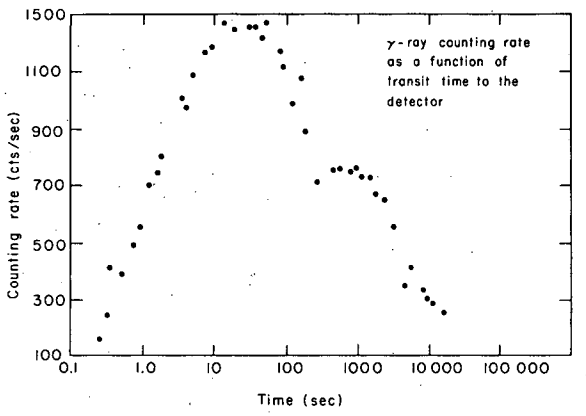

Fig. 1. The observed γ-ray counting rate as a function of transit time to the detector.
(XBL683-2228)

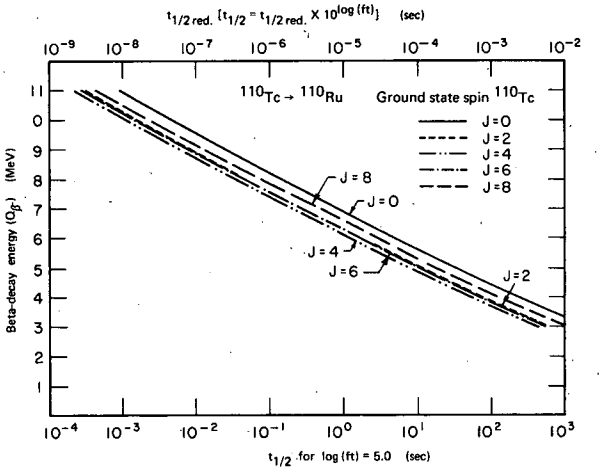

Fig. 2. The calculated half-life for the decay of $^{110}Tc \rightarrow {}^{110}Ru$ as a function of the β-decay energy, evaluated for five assumed ground-state spins of ^{110}Tc. The bottom abscissa is obtained assuming a log(ft) = 5.0. The upper abscissa is for a reduced half-life which is related to the true half-life by $t_{1/2} = (t_{1/2\,red.}) \left[10^{log(ft)}\right]$.
(XBL698-3457)

GAMMA-RAY STUDIES ON SHORT-LIVED FISSION PRODUCTS

J. B. Wilhelmy, S. G. Thompson, J. O. Rasmussen, †
J. T. Routti, and J. E. Phillips

Long-term experiments have recently been completed on the study of radiations emitted following beta decay of short-lived fission products.[1] The primary objective of these studies was to obtain information in a region which, due to the very short half-lives, was inaccessible by standard radiochemical techniques. The shortest-lived fission products generally are those isotopes that have appreciable yield as prompt fission products. It was therefore hoped that many of the transitions observed following beta decay would also be observed as prompt radiations arising in the de-excitation of the primary fission products. Correlations are now being attempted between the beta-decay transitions and transitions observed in various experimental studies of prompt radiations.[2-5] This includes a very recent experiment, which is still in the process of being analyzed, where measured in coincidence with the kinetic energies of the prompt products were: (a) gamma rays of energies up to 2 MeV, (b) gamma rays in coincidence with K x rays, and (c) gamma rays in coincidence with other prompt gamma rays.[6]

For the study of the post-beta-decay transitions the fission fragments from an ≈ 10-μg source of ^{252}Cf (3.7×10^8 f/min) were embedded into a continuously moving belt system and transported past a detection point some 50 cm from the source. By varying the velocity of the belt, measurements were made with transit times from the source to the detection point from as short as 0.27 sec to as long as 4.8 hr. Three individual experiments were performed: (a) K x-ray, γ-ray coincidence studies; (b) high resolution γ-ray singles studies; (c) high resolution K x-ray singles studies. The coincidence studies were used to obtain information on the atomic number of the decaying isotope, and the K x-ray and γ-ray singles measurements were used to give high resolution information on the quantitative yields of the individual radiations. The complexity of the spectra required sophisticated computer processing codes for both the x rays[7] and γ rays.[8] A typical γ-ray spectrum is shown in Fig. 1. This spectrum was taken with a transit time from source to detector of 57.7 sec and covers an energy range from 10 to 730 keV. From such spectra, absolute intensities of the transitions were extracted as a function of transit time, thus enabling information to be obtained on their decay characteristics. In the course of the analysis ≈ 20,000 γ-ray photopeaks were processed in the various spectra. The determined intensities of the lines at the specifc transit times were fitted to decay equations, thus obtaining information on half-lives and total yields per fission for the individual transitions. Results listing energies, half-lives, and intensities for approximately 750 transitions have been tabulated.[1] Of these about one-third have been assigned to specific isotopes. The majority of the assignements have been based on information presented in the literature and these correlations have, in general, been good. Figure 2 presents the experimental data and computer fits for six transitions assigned to the decay of ^{139}Xe → ^{139}Cs. This decay has been studied by Alväger et al.[9] by use of mass-separated xenon fission products. The results of their analysis and our current results are shown in Table I. It is seen that, with the exception of the 613-keV transition, which is quite weak in our determinations, the agreement is quite satisfactory. The energies of the transitions and the overall half-life are very good and the relative intensities are reasonable in light of the uncertainties in the efficiency calibrations.

Of special interest in these studies have been the beta decays leading to the population of states in even-even nuclei. The systematics of the first excited levels of these nuclei are of use in determining characteristics of the nuclear potential energies and in particular for studying regions of proposed deformation. Many of the very neutron-rich isotopes can only be produced in the fission process, and some of these in both the light and heavy regions are in areas of proposed deformation. In the light fission products the isotopes in the regions near ^{110}Ru have been predicted to be deformed[10] and in the heavy products those isotopes having around 90 neutrons are also believed to be good candidates for permanent deformation. We have attempted to correlate the β-decay transitions with transitions observed from prompt radiations which appear as possible assignments as the first excited states of neutron-rich even-even isotopes. Since many of the prompt data are still under analysis, many of the assignments have to be regarded as tentative. Listed in Table II are the energies of the first 2+ states of even-even nuclei observed as β-decay products. The energy values are the arithmetic means of the energy determination for the transition of the various experimental transit times, and the error estimates are the standard deviations obtained in calculating these means. The lines are classified A, B, C according to a subjective confidence level in the assignment. Also, for comparison, are listed the literature values of the transitions that are known. The agreement is, in general, quite good. The authenticity of many of the assignments to the most neutron-rich isotope will be determined upon further analysis of the prompt fission data.

From the β-decay studies information has been obtained on previously unreported short-lived fission products. Table III contains the new assignments and includes: the beta-decaying isotope, the subjective confidence level classification, the half-life, the energies of any observed transitions, the absolute yields of these transitions per fission, and the calculated transition yields per β^- decay. For five of the isotopes, half-life information has been presented in the literature, but since major transitions have now been assigned they are included in this tabulation. Again many of the assignments have to be regarded as tentative until verification is possible from the prompt radiation studies. It is also hoped that the analysis will yield substantially more isotopic assignments for the β-decay transitions that have already been tabulated in Ref. 1.

Footnote and References

†Present address: Yale University, 225 Prospect Street, New Haven, Connecticut 06520.

1. Jerry Barnard Wilhelmy, High-Resolution Gamma and X-Ray Spectroscopy on Unseparated Fission Products, UCRL-18978, Aug. 1969.

2. H. R. Bowman, S. G. Thompson, R. L. Watson, S. S. Kapoor, and J. O. Rasmussen, in Physics and Chemistry of Fission (IAEA, Vienna, 1965), p. 1639.
3. R. L. Watson, A Study of the Internal Conversion Electrons Emitted Within Three Nanoseconds After the Spontaneous Fission of ^{252}Cf (Ph. D. Thesis), UCRL-16798, July 1966.
4. W. John and J. J. Wesolowski, Lawrence Radiation Laboratory, Livermore, unpublished data, Dec. 1969.
5. R. L. Watson, J. B. Wilhelmy, R. C. Jared, C. Rugge, H. R. Bowman, S. G. Thompson, and J. O. Rasmussen, A Study of the Low Energy Transitions Arising from the Prompt Deexcitation of Fission Fragments, UCRL-19510, Nov. 1969 (submitted to Nucl. Phys.).
6. E. Cheifetz et al., Lawrence Radiation Laboratory, Berkeley, unpublished data, Jan. 1970.
7. C. Rugge, R. L. Watson, and J. B. Wilhelmy, UCRL-18771 (in preparation).
8. J. T. Routti and S. G. Prussin, Nucl. Instr. Methods 72, 125 (1969).
9. T. Alväger, R. A. Naumann, R. F. Petry, G. Sidenius, and T. Darrah Thomas, Phys. Rev. 167, 1105 (1968).
10. I. Ragnarsson and S. G. Nilsson, Lund Institute of Technology, P. O. Box 725, Lund 7, Sweden, private communication.
11. Karheinz Hübenthal, Edouard Mannand, and André Mousses, Compt. Rend. 265 (Series B), 579 (1967).
12. Arlen R. Zander, Peter R. Gray, and Thomas G. Ebrey, Nucl. Phys. 75, 209 (1966).
13. C. M. Lederer, J. M. Hollander, and I. Perlman, Table of Isotopes (John Wiley & Sons, Inc. New York, 1967).
14. A. v. Baeckmann and H. Feuerstein, Radiochim. Acta 5, 234 (1966).
15. J. Von Klinken and L. M. Taff, Nucl. Phys. A99, 473 (1967).
16. Greenberg, Sie, and Stokstad, Yale University, New Haven, Connecticut, private communication, Sept. 1969.
17. R. L. Watson and J. B. Wilhelmy, UCRL-18632, Feb. 1969.
18. A. C. Wahl, R. L. Ferguson, D. R. Nethaway, D. E. Troutner, and K. Wolfsberg, Phys. Rev. 126, 1112 (1962).
19. I. Amarel, R. Bernas, R. Foucher, J. Jastrzebski, A. Johnson, J. Teillac, and H. Gauvin, Phys. Letters 24B, 402 (1967).

Table I. Measured properties for some of the transitions in the decay of ^{139}Xe.

Alväger et al.[9]		Current experiment					
Energy (keV)	Relative intensity (per cent)	Energy (keV)	Number of points used in calculations	Half-life (sec)	Absolute intensity[a] (per cent per fission)	γ/β^-[b] (per cent)	Relative intensity[c] (per cent)
175.0 ± 1.5	33.4	175.0 ± 0.3	9	41.7 ± 0.8	0.627	13.0	26.3 ± 0.4
218.8 ± 1.0	100.	218.7 ± 0.2	22	41.7 ± 0.8	2.360	49.4	100. ± 1.4
289.9 ± 1.5	18.7	289.7 ± 0.3	8	38.1 ± 1.2	0.565	11.8	23.9 ± 0.6
296.6 ± 1.5	42.2	296.5 ± 0.3	9	34.9 ± 0.9	0.855	17.9	36.2 ± 0.6
393.5 ± 1.5	14.4	393.6 ± 0.3	5	39.1 ± 6.7	0.277	5.7	11.6 ± 0.9
612.6 ± 1.5	9.4	613.4 ± 0.5	3	78.0 ± 29.2	0.496	10.3	20.8 ± 5.0
$t_{\frac{1}{2}}$ = 39.3 ± 0.7 sec				$t_{\frac{1}{2}}$ = 39.5 ± 1.1 sec			

[a] Absolute intensities were determined using a calculated rate for the fission source (see Ref. 1, page 90).

[b] The branching ratios were calculated using the absolute intensities and a value of 4.83% per fission for the cumulative yield of ^{139}Xe as calculated in Ref. 17.

[c] Errors quoted for the relative intensities are the statistical uncertainties found upon performing a weighted least-squares fit through the data points. They do not reflect the errors in the efficiency determination (≈ 10%) and are presented only to indicate the relative accuracy within the determinations.

Table II. Current experimental values of the energies of the observed first 2+ states in fission product nuclei.

Element	Mass	2+(keV)	Class	Lit.(Ref.)
Mo	100	535.77 ± 0.41	A	533 (11)
	102	296.01 ± 0.16	C	
	104	192.02 ± 0.15	B	
Ru	102	475.09 ± 0.49	A	474.8 (12)
	104	357.96 ± 0.96	A	357.7 (13)
	106	269.83 ± 0.40	A	280 (14)
	108	242.27 ± 0.16	B	
	110	240.67 ± 0.11	A	
Pd	108	433.70 ± 0.36	A	433.8 (13)
	110	373.93 ± 0.56	A	373.8 (13)
	112	348.88 ± 0.17	C	
	114	332.86 ± 0.19	C	
Cd	114	558.46 ± 0.44	A	558.1 (13)
	116	513.70 ± 0.55	B	573.1 (13)
Xe	138	589.64 ± 0.84	B	
	140	372.35 ± 0.19	C	
Ba	140	602.22 ± 0.71	A	602.2 (9)
	142	359.70 ± 0.18	A	361.0 (9)
	144	199.31 ± 0.17	A	
Ce	142	641.21 ± 0.54	A	641.6 (9)
	144	397.49 ± 0.53	A	
	146	258.53 ± 0.15	C	
	148	158.45 ± 0.08	B	
Nd	146	454.15 ± 0.26	A	455 (13)
	148	301.72 ± 0.34	A	302 (15)
	150	130.12 ± 0.06	A	130.1 (16)
Sm	152	121.20 ± 0.14	B	121.78(13)
	154	81.89 ± 0.07	B	81.99 (13)

Table III. Isotopic assignments for new results on the short-lived fission products.

Decaying isotope	Class	Half-life[a] (sec)	Gamma transitions: Energy[b] (keV)	Yield/fission[b] (percent)	Yield/β^- [c] (percent)
^{102}Nb	C	2.97 ± 0.09	296.01 ± 0.16	2.57 ± 0.30	76
^{104}Nb	B	1.02 ± 0.08	192.02 ± 0.15	1.21 ± 0.53	74
			(2 → 0 in ^{104}Mo)		
			368.69 ± 0.22	0.408 ± 0.017	25
			(4 → 2 in ^{104}Mo)		
^{105}Mo[d]	B	58.1 ± 1.4	68.71 ± 0.10	2.37 ± 0.57	50
			376.03 ± 0.32	0.294 ± 0.008	6
			423.91 ± 0.37	0.492 ± 0.028	10
			[a][93.12 ± 0.10	0.319 ± 0.006	7]
^{106}Mo	A	7.89 ± 1.18			
^{108}Mo	B	0.860 ± 0.389			
^{108}Tc	B	5.17 ± 0.07	242.27 ± 0.16	2.55 ± 0.26	83
			(2 → 0 in ^{108}Ru)		
^{109}Ru	B	34.5 ± 2.9	116.39 ± 0.13	0.411 ± 0.010	9
			358.78 ± 0.33	0.805 ± 0.040	17
^{109}Rh	B	90.1 ± 3.6	151.44 ± 0.48	0.124 ± 0.027	2
			177.92 ± 0.19	0.675 ± 0.016	12
			215.09 ± 0.32	0.102 ± 0.002	2
			326.81 ± 0.31	3.42 ± 0.50	62
^{110}Tc	A	0.825 ± 0.039	240.67 ± 0.11	0.599 ± 0.016	77
			(2 → 0 in ^{110}Ru)		
^{110}Ru	A	15.9 ± 0.5			
$^{111}_{(109)}$Rh	B	62.7 ± 2.1	249.46 ± 0.26	0.767 ± 0.020	16
			291.33 ± 0.33	1.22 ± 0.29	25
^{112}Ru	C	0.686 ± 0.545			
^{112}Rh	C	4.65 ± 0.14	348.88 ± 0.17	3.39 ± 0.66	100
			(2 → 0 in ^{112}Pd)		
$^{113}_{(111)}$Rh	B	0.910 ± 0.081	128.51 ± 0.10	0.167 ± 0.009	7

Table III. (Continued)

Decaying isotope	Class	Half-life[a] (sec)	Gamma transitions Energy[b] (keV)	Yield/fission[b] (percent)	Yield/β^- [c] (percent)
^{114}Rh	C	1.68 ± 0.07	332.86 ± 0.19	0.782 ± 0.20	83
			(2 → 0 in ^{114}Pd)		
^{138}I	B	6.30 ± 0.29	589.64 ± 0.084	1.01 ± 0.03	41
			(2 → 0 in ^{138}Xe)		
^{140}I	C	0.880 ± 0.120	372.35 ± 0.19	0.240 ± 0.017	60
^{143}Ba[e]	B	13.7 ± 0.6	81.37 ± 0.10	0.221 ± 0.019	4
			156.55 ± 0.13	0.492 ± 0.166	9
			172.75 ± 0.12	0.758 ± 0.013	14
			289.81 ± 0.13	0.490 ± 0.018	9
			515.50 ± 0.31	0.673 ± 0.030	13
			[103.78 ± 0.06	0.849 ± 0.011	16]
			[228.83 ± 0.11	0.389 ± 0.306	7]
^{144}Cs[f]	A	1.01 ± 0.05	199.31 ± 0.17	0.302 ± 0.010	44
			(2 → 0 in ^{144}Ba)		
^{144}Ba[e]	B	9.02 ± 0.45	388.47 ± 0.23	1.63 ± 0.05	41
			430.38 ± 0.40	1.23 ± 0.04	31
			[418.02 ± 0.32	0.33 ± 0.03	8]
^{144}La[g]	A	39.8 ± 0.6	397.49 ± 0.53	5.51 ± 0.47	98
			(2 → 0 in ^{144}Ce)		
^{145}Ba	B	5.60 ± 0.59	297.82 ± 0.38	0.232 ± 0.009	10
			544.88 ± 0.48	0.383 ± 0.047	16
			571.10 ± 0.29	0.330 ± 0.039	14
^{145}La	A	29.2 ± 0.8	160.33 ± 0.25	0.397 ± 0.072	8
^{146}Ba	C	2.18 ± 0.18	327.00 ± 0.26	0.259 ± 0.013	38
			[64.44 ± 0.04	0.125 ± 0.004	16]
			[251.29 ± 0.18	0.233 ± 0.015	30]
^{146}La	C	8.34 ± 0.28	258.53 ± 0.15	2.49 ± 0.24	65
			(2 → 0 in ^{146}Ce)		

Table III. (Continued)

Decaying isotope	Class	Half-life[a] (sec)	Gamma transitions Energy[b] (keV)	Yield/fission[b] (percent	Yield/β^- [c] (percent)
^{148}La	B	1.29 ± 0.08	158.45 ± 0.08 ($2 \rightarrow 0$ in ^{148}Ce)	0.452 ± 0.171	65
(149) (150) (151)Ce	B	1.02 ± 0.06	84.79 ± 0.09 118.57 ± 0.09	0.068 ± 0.005 0.182 ± 0.005	
^{150}Pr	A	12.4 ± 0.4	130.12 ± 0.06 ($2 \rightarrow 0$ in ^{150}Nd)	0.788 ± 0.014	40
^{151}Pr	B	4.04 ± 0.73	164.00 ± 0.10	0.195 ± 0.045	14

[a]The value is calculated as a weighted average of the individual half-life determinations for the listed transitions and, where applicable, from genetically determined half-lives. Transitions listed in brackets are taken to be less certain in assignment and are not used in the half-life calculations.

[b]These values are taken from Table VI-5 of Ref. 1.

[c]Determined by using the calculated fission yield of ^{252}Cf by Watson and Wilhelmy.[17] These values should be regarded as only approximate.

[d]The Table of Isotopes[13] lists half-life as 42 sec.

[e]Wahl et al.[18] list half-life of ^{143}Ba as 12 ± 2 sec. Amarel et al.[19] list half-life of ^{144}Ba as 11.4 ± 2.5 sec. Because of the very similar half-lives, some of the specific transition assignments may be to the wrong isotope.

[f]Amarel et al.[19] list half-life as 1.06 ± 0.10 sec.

[g]Amarel et al.[19] list half-life as 41 ± 2 sec.

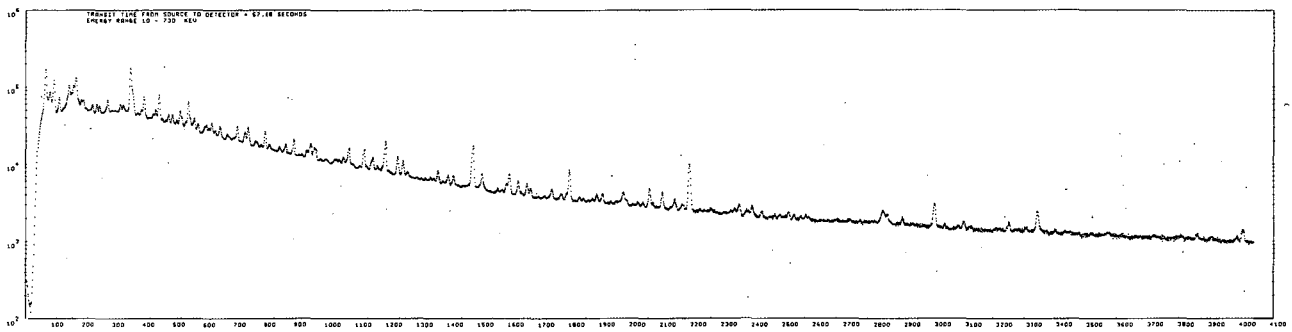

Fig. 1. A typical γ-ray spectrum. This spectrum was recorded with a transit time from the source to the detector of 57.7 sec. (XBL697-971)

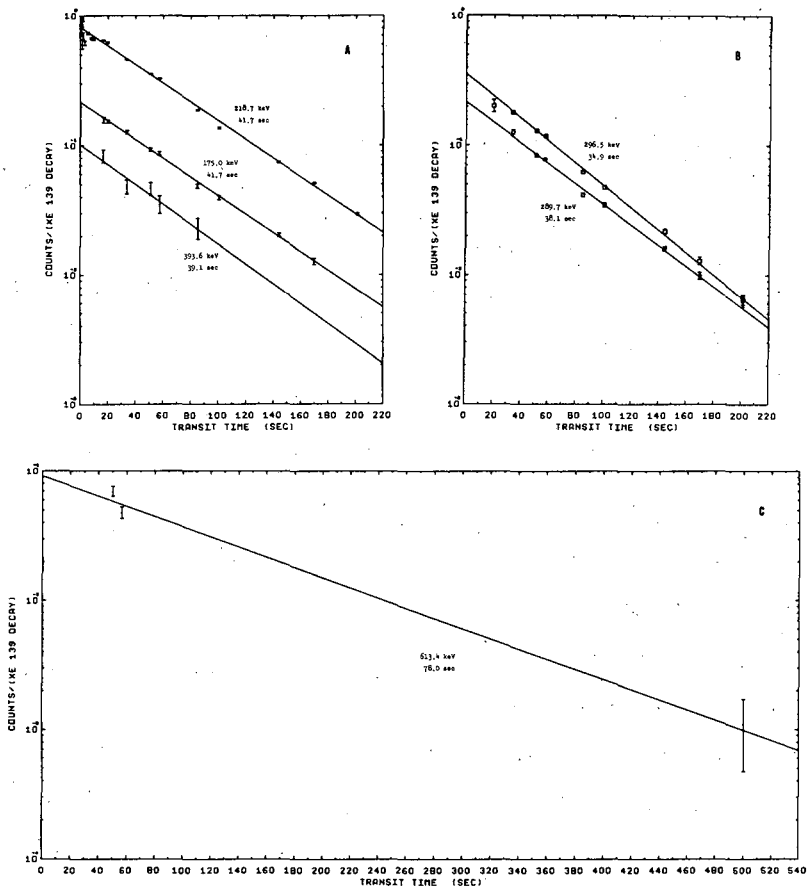

Fig. 2. (A), (B), and (C). The experimental data and computer fits for six transitions assigned to the decay $^{139}Xe \rightarrow {}^{139}Cs$.
(XBL698-1264)

EFFECTS OF ANGULAR MOMENTUM ON KINETIC ENERGY RELEASE IN FISSION†

Torbjorn Sikkeland*

Values for the most probable kinetic energy release in fission following compound-nucleus reactions between various targets and ions are reproduced, with a standard deviation of 1.5 MeV, by the expression

$$\bar{E}_K^0\,(\mathrm{MeV}) = 0.0042\, Z_0^2/A_0^{1/3} + 0.075\, E_0, \tag{1}$$

where Z_0, A_0, and E_0 are respectively the atomic number, mass number, and the excitation energy of the compound nucleus.

The total kinetic energy, E_K, of the fission fragments at infinite separation depends primarily on their mutual Coulomb potential, V_C, at the scission configuration, and hence on the nucleonic composition and shape at that configuration. This dependence has been studied both theoretically[1] and experimentally.[2] It has been deduced that the scission shape is approximately equal to two spheroids connected with a neck.[1, 2]

As will be described below, values for $\bar{E}_K$ can be evaluated from the experimentally determined most probable laboratory-frame (lab) angles between coincident fragment pairs.

The technique used in measuring the angular correlation functions has been described in detail elsewhere.[3, 4] The ion beams at an energy of 10.4 MeV/nucleon were furnished by the Berkeley Hilac. Lower energies were obtained by degradation with Al foils. The ion energy spectra were measured with a silicon diode detector. The two silicon diode detectors, in the coincidence experiments, were in the plane with and at opposite sides of the beam axis. In general one was kept at an angle $\psi_2 = 90$ deg to that axis, and the correlation function was then obtained by measuring the fragment-fragment coincidence rate as a function of the lab angular position ψ_1 of the other. For the system $^{20}Ne + {}^{nat}Pd$ this rate was measured as a function of the position ψ, where $\psi = \psi_1 + \psi_2$.

The correlation functions have been shown in general to consist of two peaks.[3, 4] The fragments recorded at the narrower one come from fissioning nuclides produced in compound-nucleus reactions, and those arriving at the most probable angles, $\bar{\psi}_1$, for this peak represent the most probable fission event in those reactions. We now assume for this event that (a) the coincident primary fragments have the same nucleonic composition and excitation energy, and (b) nucleons are emitted symmetrically around 90 deg in the center-of-mass system of the emitters, e.g., the compound nucleus and the fragments. Then, throughout the acceleration, the fragments have the same velocity and mass. Let us denote by v and v_0 the respective velocities of the fragments at infinite separation when nucleon emission does or does not occur before full acceleration. Let us furthermore denote by $\bar{E}_K$ and $\bar{E}_K^0$ the total kinetic energies of the fragments when their mass is $A_0/2$ and their velocities are v and v_0, respectively. The quantity $\bar{E}_K^0$ is of primary interest, since it represents the kinetic energy release of a nucleus for which the composition (Z_0, A_0), excitation energy, E_0, and angular momentum distribution can be estimated.

From the law of conservation of linear momentum we obtain for $\bar{E}_K^0$ the expression

$$\bar{E}_K^0 = (1-F)\bar{E}_K\,, \tag{2}$$

where

$$\bar{E}_K = (A_I E_I/A_0)\,(1+4\tan^2\bar{\psi}) \quad \text{for } \bar{\psi}_2 = 90 \text{ deg}\ ; \tag{3a}$$

$$= (A_I E_I/A_0)\ \tan^2\bar{\psi} \qquad \text{for } \bar{\psi}_1 = \bar{\psi}_2 = \bar{\psi}\ , \tag{3b}$$

and

$$F = (4/3)\, N_N/A_0 - (2N_p/Z_0) + (2R_0/A_0)\left[\sum_{i=1} (1/r_{ni}) + (1-2A_0/Z_0) \sum_{j=1} (1/r_{pj})\right]. \quad (4)$$

Here, Z_0 and A_0 have been defined before; A_I and E_I are the mass number and lab energy of the ion respectively; N_N and N_P represent respectively the number of nucleons and of protons emitted before scission; and r_{ni} and r_{pj} are the distances between the centra of the fragments at which, respectively, the ith neutron and jth proton are emitted. These distances are given in units of the distance, R_0, between the centra at scission.

For our systems, first-chance fission was estimated to be the most probable event, hence $N_N = N_P = 0$. The distance, r_{xi}, is related to the level width, Γ_{xi}, for the emission of the ith particle x by the expression

$$\hbar/\Gamma_{xi} = \left[R_0/v\,(r_{xi}^2 - r_{xi})^{1/2}\right] + 1/2 \ln 2\,(r_{xi}^2 - r_{xi})^{1/2} + 2\, r_{xi}^{-1}, \quad (5)$$

where $\hbar$ is Planck's constant divided by 2π.

Approximate values for R_0 and v were obtained from the expressions $Z_0^2\, e^2/(4R_0) = \bar{E}_K$ and $1/2\, m_0 A_0 v^2 = \bar{E}_K$, where m_0 is the nucleonic mass.

In the estimation of Γ_{xi} we used the equation based on the level density expression $\rho = \rho_0 \exp(aE)^{1/2}$ (Ref. 5). Here, E is the excitation energy of the nucleus following particle emission, and a is the level density parameter, which was set equal to A/10. In the cascade we assumed the kinetic energy carried off by a neutron to be 4 MeV, and that carried off by a charged particle to be equal to its Coulomb barrier with respect to the residual nucleus.

Values for $\bar{E}_K$ and $\bar{E}_K^0$ are given in columns 4 and 5 of Table I. The errors in $\bar{E}_K^0$ given in column 6 represent one standard deviation and are estimated from the uncertainties of 1% in E_I and 0.22 in $\bar{\psi}_i$, and the error of 1% introduced by the uncertainty in the values for Γ_{xi}.

The accuracy of $\bar{E}_K^0$ also depends on the validity of assumptions (a) and (b) given above. Assumption (a) has been shown to be valid for products in (I, xn) reactions.[6] Furthermore, the mass and kinetic energy distributions of the final fragments in heavy-ion ion-induced fission have been shown to be symmetric.[2, 7] These experimental facts strongly suggest that assumptions (a) and (b) are indeed correct.

Included in Table I are many systems for which $\bar{E}_K^0$ was measured only at full ion energy. These experiments were performed in order to test also the dependence of $\bar{E}_K^0$ on (Z_0, A_0) and to compare directly values for $\bar{E}_K$ with those obtained previously from the measured most probable lab kinetic energy.[2] The agreement is satisfactory.

It is apparent from Table I that $\bar{E}_K^0$ increases slightly with increasing E_I. However, only for the system $^{197}Au + {}^{40}Ar$ is this increase outside experimental errors. Using a simple model, we can show in the following that this variation in $\bar{E}_K^0$ is mainly due to angular momentum effects. This model is based on these six assumptions: (a) the Coulomb potential, V_c, at scission is converted solely into kinetic energy; (b) the scission shape is characterized by two touching collinear spheroids of uniform density; (c) the ratio, C, of the major to the minor axis is the same for both fragments and independent of bombarding energy; (d) the nuclear matter is incompressible and the moments of inertia of the spheroids are those of a rigid body; (f) the fragments are emitted along the symmetry axis, i.e., the major axis; and (f) the most probable value of the projection of the total angular momentum, I, on the symmetry axis is zero.

It follows from these assumptions that experimental values for V_c should be given by

$$V_c = \bar{E}_K^0 - BI_p^2, \quad (6)$$

and that they should be independent of bombarding energy. Here, I_p is the most probable value of I and

$$B = \frac{25C^{8/3}\hbar^2}{2^{1/3}(1+6C^2)^2 m_0 r_0^2 A_0^{5/3}} , \tag{7}$$

where for r_0, the nuclear radius parameter, we used the value 1.2×10^{-13} cm, and values for C were taken from the liquid-drop model calculations by Cohen and Swiatecki.[1] Estimated values for B are given in column 7 of Table I.

Since essentially no nucleons are emitted before fission, the I-distribution at scission is equal to that of the compound nucleus. Assuming a sharp cutoff at $I = I_{CN}$, the average value, $\langle I^2 \rangle$, of the square of I can be estimated for such a distribution.[8] A realistic I-distribution is probably rounded near the top in such a way that the value of I_p^2 is somewhere between those of $\langle I^2 \rangle$ and I_{CN}^2. We shall therefore set

$$I_p^2 = (1/2)(\langle I^2 \rangle + I_{CN}^2) = 3/2 \langle I^2 \rangle , \tag{8}$$

and assign an error of 30% to the values for I_p^2.

Values for V_c are given in column 8 of Table I, and we see that they are, within errors, independent of bombarding energy. A least-squares analysis of the data gives for V_c the expression

$$V_c = 0.1187\ Z_0^2/A_0^{1/3} . \tag{9}$$

It is interesting to note that V_c is proportional to the quantity $Z_0^2/A_0^{1/3}$, which is what one should expect for point charges. Values for V_c, as estimated from Eq. 9, can be compared directly with those estimated on the basis of the liquid-drop model. Such a comparison, based on data similar to those obtained here, has been performed previously,[2] and we shall therefore not discuss this aspect of the results.

Values for $\bar{E}_K^0$ calculated according to Eqs. 6 through 8 fit our experimental data with a standard deviation of about 1.5 MeV. They also fit fairly well experimental values for low-energy fission. This, however, is to be regarded as fortuitous, since at low energy asymmetric division is the most probable event, and effects of shells and structure in the mass surface of the fission products play an important role.[9]

The value of the quantity I_p^2 increases almost linearly with that of the excitation energy, E_0, of the compound nucleus. Then, if we assume, to a first approximation, the parameter B in Eq. 6 to have a constant value, $\bar{E}_K^0$ will vary linearly with E_0. This is the basis for the empirical expression, Eq. 1, given at the beginning, which is easier to use than Eq. 6, which contains an angular momentum term.

I thank Professor Marc Lefort for hospitality during my stay at the Institute of Nuclear Physics, Orsay, France; the Norwegian Research Council for Science and the Humanities, Oslo, for a research grant; and the Hilac crew for excellent operation.

Footnotes and References

†Condensed from UCRL-18991, Dec. 1969.

*Present address: Institute of Physics, University of Trondheim, Trondheim, Norway.

1. S. Cohen and W. J. Swiatecki, Am. J. Phys. 22, 406 (1963).
2. V. E. Viola, Jr. and T. Sikkeland, Phys. Rev. 130, 2044 (1963).
3. T. Sikkeland, Phys. Letters 27B, 277 (1968).
4. T. Sikkeland and V. E. Viola, Jr., in Proceedings of the Third Conference on Reactions Between Complex Nuclei (University of California Press, Berkeley, 1963).
5. J. R. Huizenga and R. Vandenbosch, in Nuclear Reactions, edited by P. M. Endt and P. B. Smith (North-Holland Publishing Co., Amsterdam, 1962).

6. M. Kaplan and R. D. Fink, in Proceedings of the Third Conference on Reactions Between Complex Nuclei (University of California Press, Berkeley, 1963).
7. F. Plasil (Ph. D. Thesis) UCRL-11193, Dec. 1963.
8. T. Sikkeland, Arkiv Fysik 36, 539 (1967).
9. E. K. Hyde, The Nuclear Properties of the Heavy Elements, III: Fission Phenomena (Prentice-Hall, Inc., Englewood Cliffs, N.J., 1964).

Table I. Values for various quantities connected with kinetic energy release in fission following compound nucleus reactions between complex nuclei. The quantities in the table have been defined in the text.

System	$Z_0^2/A_0^{1/3}$	E_I (MeV)	$\bar{E}_K$ (MeV)	$\bar{E}_K^0$ (MeV)	Std. dev. (MeV)	B (keV)	V_C (MeV)	Std. dev. (MeV)
$^{238}U + ^{40}Ar$	1854	414	231	227	3.8	0.45	219	4.6
$^{238}U + ^{40}Ar$	1854	348	226	224	3.8	0.45	219	4.2
$^{238}U + ^{40}Ar$	1854	272	220	220	4.0	0.45	218	4.1
$^{197}Au + ^{40}Ar$	1520	415	195	191	3.2	0.67	180	4.7
$^{197}Au + ^{40}Ar$	1520	352	189	187	3.2	0.67	180	4.1
$^{197}Au + ^{40}Ar$	1520	278	185	185	3.2	0.67	181	3.5
$^{197}Au + ^{40}Ar$	1520	187	177	177	2.9	0.67	176	3.2
$^{197}Au + ^{20}Ne$	1318	207	160	160	2.8	0.87	156	3.3
$^{197}Au + ^{20}Ne$	1318	160	157	157	2.8	0.87	155	2.9
$^{197}Au + ^{20}Ne$	1318	132	154	154	2.8	0.87	153	2.8
$^{197}Au + ^{16}O$	1267	165	154	154	2.8	0.93	150	3.0
$^{197}Au + ^{16}O$	1267	108	148	148	2.7	0.93	147	2.7
$^{165}Ho + ^{16}O$	994	154	123	123	2.2	1.40	117	2.8
$^{165}Ho + ^{16}O$	994	122	121	121	2.2	1.40	118	2.4
$^{238}U + ^{20}Ne$	1634	207	196	196	3.5	0.58	193	3.6
$^{238}U + ^{16}O$	1579	165	191	191	3.4	0.62	188	3.5
$^{209}Bi + ^{20}Ne$	1414	207	171	171	3.7	0.76	167	3.9
$^{209}Bi + ^{16}O$	1362	165	165	166	3.0	0.82	163	3.2
$^{175}Lu + ^{16}O$	1084	165	134	134	2.4	1.22	129	2.9
$^{159}Tb + ^{16}O$	953	154	120	120	2.2	1.51	114	3.0
$^{nat}Sb + ^{20}Ne$	714	207	95.2	95.2	2.4	2.50	82	4.9
$^{nat}Ag + ^{16}O$	607	165	84.0	84.0	2.2	3.2	72	5.0

II. Chemical and Atomic Physics

Atomic and Molecular Spectroscopy

ATOMIC POLARIZABILITIES FOR THE FIRST EXCITED ^2D STATE OF ALUMINUM, GALLIUM, INDIUM, AND THALLIUM

Joseph Yellin

One of the reasons for measuring the Stark effect is that polarizabilities deduced from such measurements serve as a useful test for oscillator strength calculations.[1,2] The atomic polarizability can be simply related to oscillator strengths. For example, it has been found that the Bates-Damgaard (B-D) Coulomb approximation[3] predicts correctly alkali polarizabilities. Measurements of polarizabilities by the atomic beam and level-crossing technique have helped to clarify the range of applicability of the B-D theory. Recently we have begun measurements of polarizabilities in the group IIIa elements.[4] It is known that the single-configuration B-D theory does not predict correctly the oscillator strengths of the diffuse series of these elements, and this failure may be due to configuration mixing.[5] Thus, the group IIIa elements are interesting from the viewpoint of multiconfigurational Coulomb approximations. It is of particular interest to measure the polarizabilities of the $s^2d\ ^2D$ states, since there is evidence that they are perturbed by the ^2D states arising from sp^2 configuration.[6]

We have calculated the polarizabilities of the first excited ^2D states of the group IIIa elements in the single configuration approximation. The polarizabilities were calculated from a general formula that is valid for alkali-like states.[4] The radial integrals were calculated directly from the B-D theory. The results are summarized in Table I, and their comparison with experimental results should prove interesting.

References

1. R. Marrus, D. McColm, and J. Yellin, Phys. Rev. 147, 556 (1966).
2. R. Marrus and J. Yellin, Phys. Rev. 177, 127 (1969).
3. D. R. Bates and A. Damgaard, Phil. Trans. Roy. Soc. London A242, 101 (1949).
4. T. R. Fowler and J. Yellin, Electric Field Effect in the Resonance Lines of Indium and Thallium, Phys. Rev. (to be published).
5. A. Dalgarno, Lecture notes, in Proceedings of the First International Conference on Atomic Physics, June 3-7, 1968, New York City (Plenum Press, New York, 1969).
6. P. F. Gruzdev, Opt. i Spectroskopiya 20, 377 (1966) [Engl. Transl: Opt. Spectr. USSR 20, 209 (1966)].

Table I. Atomic polarizabilities[a] $\times 10^{24}$ cm^{-3}.

Element	$\alpha(D_{3/2 \pm 3/2})$	$\alpha(D_{3/2 \pm 1/2})$	$\alpha(D_{5/2 \pm 5/2})$	$(\alpha(D_{5/2 \pm 3/2})$	$\alpha(D_{5/2 \pm 1/2})$	n[b]
Aluminum	-259.1	-1282.4	-47.7	-895.5	-1319.3	3
Gallium	103.0	604.0	-15.6	454.0	480.0	4
Indium	113.4	808.8	-113.4	772.4	1215.0	5
Thallium	67.6	385.2	-146.6	632.0	1021.0	6

a. Bates-Damgaard; α is defined by $\Delta W = 1/2\ \alpha E^2$.
b. Principal quantum number.

ATOMIC BEAM MEASUREMENT OF THE POTASSIUM-39-41-42 ISOTOPE SHIFT

Richard Marrus, Edmond C. Wang, and Joseph Yellin

The isotope shifts of ^{41}K and 12.4-hour ^{42}K relative to ^{39}K were studied in the D_1 line (7699 Å). An important preliminary to this experiment, the measurement of the Stark shift in the D_1 line of ^{39}K, was reported previously.[1] The measurements were made by the atomic beam method, in which electric fields are used to tune the hyperfine absorption lines of beam atoms (^{41}K or ^{42}K) into coincidence with the emission lines of the lamp (^{39}K). The resulting resonance absorption leads to a spin-flip which alters the trajectories of beam atoms, causing them to focus at the detector. The relevant energy-level diagram and the possible overlaps or coincidences for the ^{39}K- ^{41}K and ^{39}K- ^{42}K systems are shown in Fig. 1. The atomic beam apparatus was tuned to pass only atoms with $m_J = -1/2$ for ^{41}K and $m_J = +1/2$ for ^{42}K ($\mu_I < 0$), so that most of the beam atoms are in the lower hyperfine state.

A similar experimental arrangement was previously used to study isotope shifts in cesium and rubidium.[2,3] A dense beam of potassium interposed between the lamp and C region acts as a hyperfine filter, removing the hyperfine components of the lamp line. Thus the light emerging from the absorption beam has a spectral distribution showing intensity minima at the centers of the hyperfine lines. The width of the intensity minima is determined by the collimation of the absorption beam, and was about 200 MHz in this experiment. The use of a hyperfine filter is crucial, since the isotope shift is determined from the Stark shift and the latter is calibrated on the ground-state hyperfine structure [$\Delta\nu_{hf}(4^2S_{1/2}) = 462$ MHz], which must be present in the exciting light. Since the hyperfine structure is not resolved in the ^{39}K lamp line a hyperfine filter is essential.

In Fig. 2 are shown the results of Stark-scanning the filtered ^{39}K lamp line with a ^{41}K (99.18%) atomic beam. We find for the ^{41}-^{39}K isotope shift 7.4 ± 0.3 mK (1 millikayser = 10^{-3} cm^{-1}). This result is in agreement with an earlier spectroscopic measurement by Jackson and Kuhn, who found 7.6 ± 0.5 mK for the isotope shift.[4]

^{42}K was produced by the reaction $^{41}K(n,\gamma)^{42}K$. The target sample consisted of 1g KCl encapsulated in quartz under a helium atmosphere (100 mm of Hg). The sample was irradiated for 24 hours at the G. E. Reactor Facility at Vallecitos, which provided a neutron flux of $\approx 2\times10^{14}$/cm^2-sec. Approximately 2.5 Ci of ^{42}K was produced in each sample. In a typical experimental run 100 to 200 mg of KCl was consumed. The potassium was collected at the detector on a quartz surface for 5 min at each value of the applied voltage. The amount collected (signal) was measured through the β^- activity. Typical results for ^{42}K are shown in Fig. 3. We find for the ^{39}-^{42}K isotope shift 16 ± 4 mK.

The ^{39}-^{41}K isotope shift is based on 10 measurements, of which Fig. 2 is a typical example. The line width in each case is 7 mK, and the center of the line can be determined easily to ±2 mK or less. Systematic effects due to isotopic impurity were investigated by making several measurements with a lamp containing potassium in natural abundance. These measurements yielded a value for the isotope shift which is 0.2 mK higher and with the same accuracy as measurements made with the enriched ^{39}K lamp; though this increase is within the experimental error, it can be shown that an isotopic impurity of ^{41}K produces a systematic error in the same direction as the isotope shift.

Table I. Comparison of measured and calculated isotope shifts.

Isotopes	$\delta(\Delta E)_{ex}$	$\delta(\Delta E_B)$	$\delta(\Delta E_f)$
^{39}K	0	0	0
^{41}K	7.4 ± 0.3	8.9	-1.2
^{42}K	16 ± 4	13.0	-1.8

The measurements are summarized in Table I and compared with the normal mass effect (Bohr) and the field-effect isotope shift,[5] assuming a uniform charge-distribution model for the nucleus.

References

1. Richard Marrus and Joseph Yellin, Phys. Rev. 177, 127 (1969).
2. Richard Marrus, Edmond C. Wang, and Joseph Yellin, Phys. Rev. 117, 122 (1969).

3. T. H. Duong, R. Marrus, and J. Yellin, Phys. Letters 27B, 565 (1968).
4. D. A. Jackson and H. Kuhn, Proc. Roy. Soc. (London) A165, 303 (1938).
5. A. R. Bodmer, Nucl. Phys. 9, 371 (1958 59).

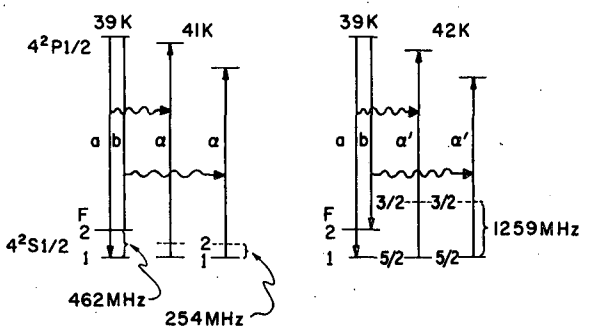

Fig. 1. Possible resonances for the ^{39}K - ^{41}K and ^{39}K - ^{42}K systems. (XBL 6912-6360)

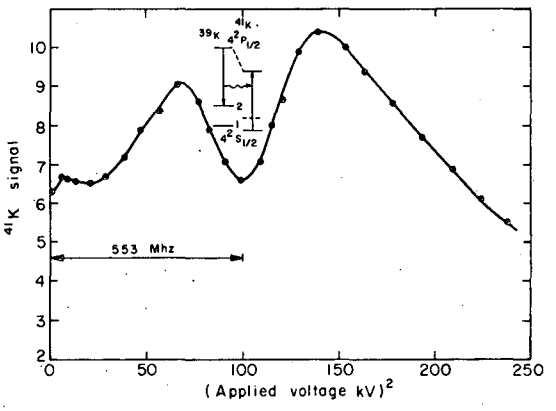

Fig. 2. Signal observed when a ^{39}K lamp filtered by a potassium absorption beam is scanned by a ^{41}K atomic beam. The D_2 line is removed by an interference filter.
(XBL 6812-7545)

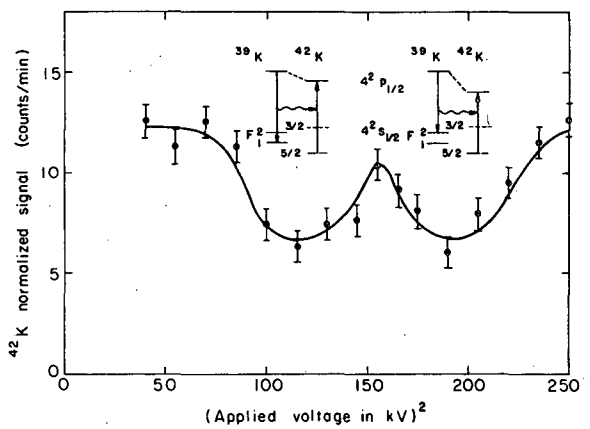

Fig. 3. Signal observed when a ^{39}K lamp filtered by a potassium absorption beam is scanned by a ^{42}K atomic beam. (XBL 6812-7548)

ELECTRIC FIELD EFFECT IN THE RESONANCE LINES OF INDIUM AND THALLIUM†

Thomas R. Fowler and Joseph Yellin

The atomic beam isotope-shift method depends on the possibility of tuning atomic energy levels by the application of electric fields (Stark tuning).[1] Although Stark tuning does not represent a fundamental limitation to the method, it is the most practicable technique at present. For the technique to be useful it must be calibrated; this is accomplished by measuring the Stark shift in terms of the hyperfine structure (hfs) present in the exciting radiation. Therefore, it is important to ascertain that the frequency of the transition under investigation can be changed by an amount equal to some hfs present in the transition (otherwise calibration is not possible). For this reason a determination of the relative (to hfs) Stark shift must precede the measurement of isotope shifts. By combining the relative Stark shift with a determination of the electric field, one can determine the absolute magnitude of the Stark shift, and hence the difference between the atomic polarizabilities of the levels involved in the transition. The polarizability difference is useful in checking methods for calculating f values. In this experiment the Stark shifts in the resonance lines of indium (4102 Å) and thallium (3776 Å) have been studied as a preliminary to measurement of isotope shifts as well as for its own sake.

The experimental technique is similar to that previously applied to cesium and rubidium.[2] The relevant energy-level diagrams are shown in Fig. 1, and in Fig. 2 are shown, as an example, the possible coincidences or overlaps between the emission lines of the thallium lamp and the absorption lines of the thallium beam atoms. Table I summarizes the frequencies at which overlaps occur, the corresponding electric fields (approximate), and the theoretical signal intensities. Typical experimental results for thallium are shown in Fig. 3. Table II summarizes the experimental results for indium and thallium and compares the atomic polarizabilities with calculations based on the Coulomb approximation.[3] It is concluded that the Stark effect is sufficiently large for both indium and thallium to permit the measurement of isotope shift.

Footnote and References

†Condensed from UCRL-19337; submitted to Phys. Rev.

1. R. Marrus, E. Wang, and J. Yellin, Phys. Rev. Letters 19, 1 (1967).
2. R. Marrus, D. McColm, and J. Yellin, Phys. Rev. 147, 556 (1966).
3. D. R. Bates and A. Damgaard, Phil. Trans. Roy. Soc. London A242, 101 (1949).

Table I. Frequency shifts, electric fields, and signal intensities associated with thallium (no state selection).

Overlapping lines	$\alpha' = \alpha$ $\gamma' = \gamma$, $\delta' = \delta$	$\gamma' = \delta$	$\alpha' = \gamma$	$\alpha' = \delta$
$\Delta\nu_s$(MHz)	0	12 090	21 311	33 401
Approx. kV/cm	0	366	485	610
Signal intensity	1.50	0.50	0.50	0.25

Table II. Summary of calculated and experimental polarizabilities.

	Theoretical polarizabilities* $\times 10^{24}$ cm^{-3}					Experimental
	$\alpha(^2P_{1/2})$	$\alpha(^2P_{3/2} \pm 3/2)$	$\alpha(^2P_{3/2} \pm 1/2)$	$\alpha(^2S_{1/2})$	$\Delta\alpha(^2S_{1/2}, {}^2P_{1/2})$	$\Delta\alpha(^2S_{1/2}, {}^2P_{1/2})$
Indium	4.7	4.5	7.4	150.8	146.1	138(11)
Thallium	2.7	4.4	9.0	125.0	122.3	115(12)

*Bates-Damgaard.

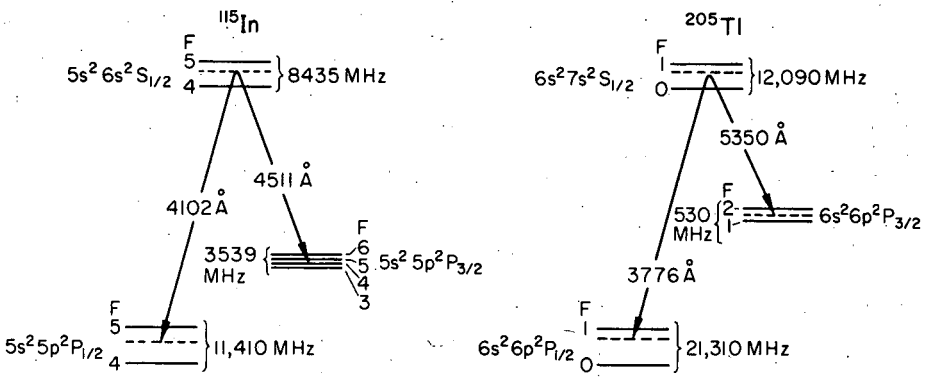

Fig. 1. Indium and thallium energy levels. (XBL 699-3811)

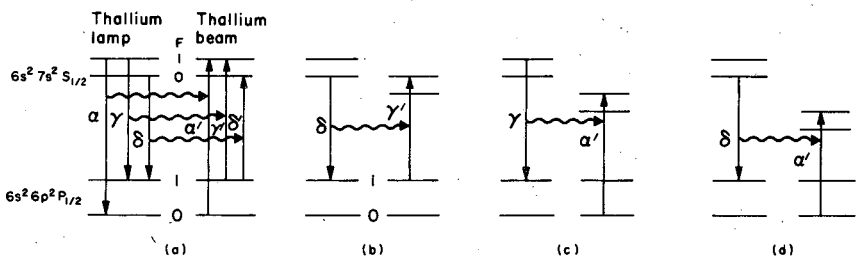

Fig. 2. Possible overlaps between absorption lines of thallium beam atoms (primed) and thallium lamp lines (unprimed).
(XBL 699-3810)

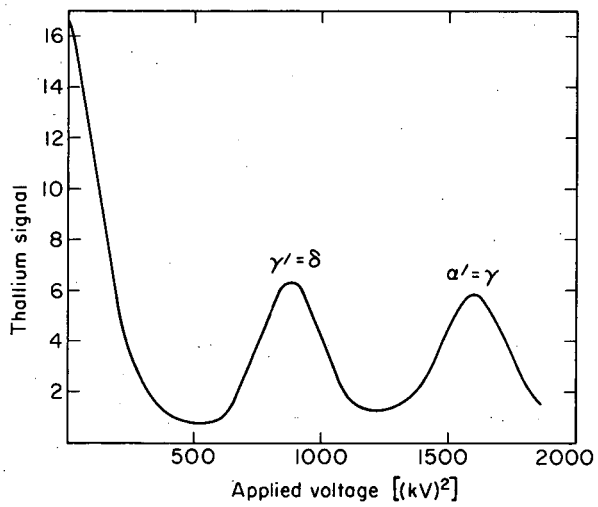

Fig. 3. Thallium Stark-shift data. Overlapping lines are indicated above the resonances.
(XBL 699-3812)

HYPERFINE STRUCTURE OF THE 4102-Å LINE OF INDIUM, AN INVESTIGATION BY AN ATOMIC BEAM SPECTROMETER

Richard Marrus and Joseph Yellin

It has been shown that an atomic beam apparatus may be used as a spectrometer of very high resolving power.[1] If the resolving power is defined as usual by $R = \lambda/\Delta\lambda$, then for the atomic beam spectrometer $R \approx 2\pi c\tau/\lambda$, where τ is the lifetime of the upper state of the transition which gives rise to λ. This follows from the fact that the absorption width of the atomic beam is the natural width $\Delta\nu_N = 1/2\pi\tau$. As an example, we have for the resonance line of cesium $R \approx 6\times 10^7$, a considerable improvement over the best interferometers. It is for this reason that the atomic beam technique can be used to obtain extremely fine detail of optical lines.[1,2]

In its present form the atomic beam spectrometer relies on Stark tuning for its operation. The spectral line under investigation is sampled by beam atoms moving perpendicularly to the light, and the application of electric field to the beam atoms causes a displacement of their absorption lines so that different portions of the spectral line can be sampled. The signal output of the spectrometer is simply related to the intensity of the spectral line at the frequency that is resonant with the absorption lines of the sampling beam.

A question arises whether the absorption width of the beam atom is $\Delta\nu_N$ and whether systematic line shifts occur at high electric fields. There are two reasons to suppose that both broadening and line shifts can occur. First, there is the purely technical problem of achieving uniform electric fields. Electric field gradient causes the line width to broaden and such broadening has been observed when the field plates are not parallel. The broadening increases with the applied electric field and can amount to many MHz. Secondly, hyperfine Stark effects[3] may become significant at high electric fields, causing a relative shift of the hyperfine absorption lines. The latter may result from a large tensor polarizability. In order to investigate these effects an analysis of the hyperfine structure present in the 4102-Å line of indium was undertaken by the atomic beam method. The large hyperfine splitting of both the $5^2P_{1/2}$ and $6^2S_{1/2}$ states, the large polarizability of the $6^2S_{1/2}$ state, and the possibility of completely resolving the hyperfine structure in a suitably made radio-frequency discharge lamp make indium particularly attractive. In addition the isotope shifts of indium are being investigated by the atomic beam method, so it is imperative to understand any systematic effects associated with the electric field.[4]

In indium the possibility exists for comparing hyperfine lines separated by $\approx 0.6\ \mathrm{cm}^{-1}$ corresponding to an electric field greater than 400 kV/cm. Furthermore, the separations of the various hyperfine components of the 4102-Å line can be accurately predicted from the known hyperfine-structure splitting of the $5^2P_{1/2}$ and $6^2S_{1/2}$ states. Thus hyperfine line shifts can be easily detected.

Preliminary results are shown in Fig. 1. No significant broadening or line shifts have thus far been observed. Note that the signal is plotted against the applied voltage $V \propto E$ and not V^2.

References

1. R. Marrus, E. Wang, and J. Yellin, Phys. Rev. Letters 19, 1 (1967).
2. T. H. Duong, R. Marrus, and J. Yellin, Phys. Letters 27B, 565 (1968).
3. J. R. P. Angel and P. G. H. Sandars, Proc. Roy. Soc. (London) A305, 125 (1968).
4. Relative hyperfine shifts can occur only if $J > 1/2$, hence it is planned to extend this work to other lines.

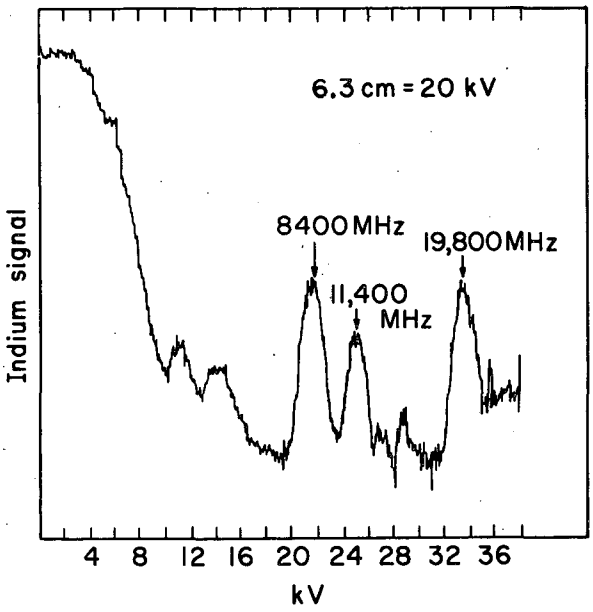

Fig. 1. Hyperfine structure of the 4102-Å line of indium. (XBL 6912-6359)

A SIMPLE METHOD FOR OBTAINING ATOMIC BASIS FUNCTIONS

Rolf J. Mehlhorn†

Radial wave functions are usually obtained by means of the Hartree-Fock method or one of its relativistic extensions. Experience with spectroscopic data has shown that these wave functions are rather inaccurate, particularly in view of the labor required to achieve convergence.

Klapisch[1] has shown that a simple alternative to these methods produces wave functions of comparable, or better, accuracy for the alkali metals. In essence the method uses an analytic function of the radius, depending on a few parameters, to describe the potential function seen by a given electron. The parameters are determined by comparison with spectroscopic data.

Schwartz[2] used a parametric potential function suggested by Tietz[3] to deduce relativistic wave functions for hyperfine-structure calculations. The advantage of the Tietz potential is its simplicity; it depends on a single parameter which can be estimated from a physical model. We have calculated nonrelativistic wave functions of complex atoms, using various modifications of the Tietz potential. The most useful form proved to be the function

$$U(r) = - Ne^2/r - (Z-N)e^2/r(1+\beta_\ell r^2),$$

where the parameter β_ℓ can be adjusted for each configuration, if necessary. N refers to the spectroscopic state of ionization; Z is the nuclear charge number. The radius r is expressed in atomic units. This function is easily seen to have the correct asymptotic behavior for small and large values of r.

To illustrate the accuracy of wave functions obtained with this potential we compare calculated and experimental Slater parameters of Pu II. The experimental values were deduced by Fred,[4] using the usual least-squares energy fitting method.[5] In Table I we have set out these values together with available Hartree-Fock values.[6] The removal of a 7s electron from the Pu I spectrum is not expected to change the Slater parameters appreciably. The parameters of U I should not deviate by more than 10% in going to Pu II.

Calculations for other spectra, e.g., rhenium I, indicate that the wave functions in general are not sufficiently accurate to serve for energy-level identification in a complex electronic

configuration. Probably this shortcoming is inherent in any procedure which assumes one set of radial wave functions to describe all the energy levels of a configuration, be it Hartree-Fock, Dirac-Slater, or the parametric potential.

The principal advantage of using a simple parameterized potential function to deduce the radial wave functions of a spectrum is the high efficiency of the method. Given values of the β_ℓ parameters, we were able to compute wave functions for 18 single electron states and 32 Slater parameters of Pu II in about 11 seconds on the CDC 6600 computer. It is suggested for future work that wave functions deduced with the aid of the parametric potential be used as basis functions for perturbation calculations involving a large number of excited configurations. Such calculations have been quite successful for simple spectra.[7] It will be of considerable interest to extend these studies to the heavier atoms.

Footnote and References

†Present address: Genetics Department, University of California–Berkeley.

1. M. Klapisch, Le Potentiel Parametrique: Une nouvelle méthode pour le calcule des fonctions d'onde atomique (Thèse), University of Paris, Orsay, June 1969.
2. C. Schwartz, Phys. Rev. 105, 173 (1957).
3. T. Tietz, J. Chem. Phys. 22, 2094 (1954).
4. M. Fred, private communication, 1969.
5. R. Mehlhorn, Energy Level Calculations for Singly Ionized Hafnium (Ph. D. Thesis), UCRL-18040, Jan. 1968.
6. J. B. Mann, Atomic Structure Calculations, Los Alamos Report LA-3691, 1968.
7. R. Zare, J. Chem. Phys. 45, 1966 (1966).

Table I. Theoretical and experimental Slater parameters for PuII.

	Parametric potential	Least squares	Hartree-Fock
ζ_f	2130	2341	---
F^2_{ff}	70119	67326	82182 (PuI)
F^4_{ff}	45244	56067	52822 (PuI)
F^6_{ff}	32956	29962	39555 (PuI)
ζ_d	1130	1150	---
G^1_f	7210	8000	13984 (UI)
F^2_{fd}	18003	17300	10792 (UI)
G^3_{fd}	6124	5600	27122 (UI)
F^4_{fd}	8662	7790	14064 (UI)
G^5_{fd}	4756	4800	8218 (UI)
G^3_{fs}	3105	2445	---

AB INITIO CALCULATIONS OF THE ELECTRONIC STRUCTURE OF DIATOMIC MOLECULES

Henry F. Schaefer III, Timothy G. Heil, and Stephen V. O'Niel

During the past 6 months we have developed methods[1,2] for the calculation of configuration interaction (CI) wave functions for diatomic molecules. In addition we have applied these methods to the calculation of potential curves for F_2 and Cl_2.[2,3]

It is possible to carry out CI calculation for diatomic molecules directly in terms of single Slater determinants. However, the size of the secular equation to be solved can be greatly reduced by performing the calculation in terms of symmetry-adapted functions, fixed linear combinations of determinants. Thus a significant problem to be solved is that of obtaining symmetry-adapted functions for diatomic molecules. This problem has been solved[1] in a practical manner by direct diagonalization of the operator $S^2 \pm (1/2)\sigma_v$, where σ_v is the operator that determines the + or - character of a Σ state. The other diatomic symmetries (Λ, M_s, and g or u) are readily satisfied by discarding all inappropriate Slater determinants arising from a given orbital occupancy.

Perhaps the most difficult technical problem involved in theoretical studies of diatomic molecules is the computation of large numbers of one- and two-electron molecular integrals. We have developed methods and computer programs[2] for the direct numerical calculation of two-center integrals over arbitrary molecular orbitals. This approach differs radically from other presently used two-center integral techniques, which are performed at least in part analytically and require the use of standard analytical functions, usually Slater-type orbitals. The basic approach used is to expand $1/r_{12}$ in ellipsoidal coordinates[4] and to use crossed Gauss-Legendre quadratures[5] for the two-dimensional (ξ, n) integrations.

Using the above methods for the computation of integrals, it is possible, for example, to make calculations directly in terms of atomic Hartree-Fock orbitals. Therefore the first application of the above techniques was to the calculation of valence-bond wave functions for the F_2 and Cl_2 molecules. In these calculations[2,3] all $^1\Sigma_g^+$ configurations were included that arose from the atomic Hartree-Fock orbitals. For F_2 this complete and literal application of the VB method yielded a dissociation energy of 0.32 eV, much better than the molecular Hartree-Fock D_e (Ref. 6), -1.4, but much less than the experimental value,[7] 1.65 eV. For Cl_2 the computed dissociation energy[3] was 0.71 eV, compared with the experimental value[7] 2.48 eV. We hasten to point out that the F_2 and Cl_2 molecules are among the most difficult to describe theoretically. More extensive calculations, including up to 318 configurations, were carried out for F_2, and a dissociation energy of 0.80 eV was obtained.

References

1. H. F. Schaefer, Diatomic Molecule Symmetry Eigenfunctions by Direct Diagonalization, J. Comput. Phys. (in press).
2. H. F. Schaefer, New Approach to Electronic Structure Calculations for Diatomic Molecules, J. Chem. Phys. (in press).
3. T. G. Heil, S. V. O'Neil, and H. F. Schaefer, High-Precision Valence-Bond Potential Curve for the Cl_2 Molecule, Chem. Phys. Letters (in press).
4. K. Ruedenberg, J. Chem. Phys. 19, 1459 (1951).
5. A. D. McLean and M. Yoshimine, IBM J. Res. Develop. 9, 203 (1965).
6. A. C. Wahl, J. Chem. Phys. 41, 2600 (1964).
7. A. G. Gaydon, Dissociation Energies and Spectra of Diatomic Molecules (Chapman and Hill, Ltd., London, 1968).

THE SPECTRUM OF DyI

J. G. Conway and E. F. Worden†

The term analysis of atomic energy levels of dysprosium is nearing completion. The spectrum of a single isotope of Dy has been photographed in the region of 2500 to 9800 Å, by use of DyI_3 sealed into a quartz tube and excited by microwaves of 2450 MHz. The spectrum has been completely measured and some 2200 lines recorded. Energy levels of both DyI, the neutral atom, and DyII, the first ion, have been found.

In the spectrum of DyI we have had two separate groups of levels of different parity. One configuration we knew was the $4f^96s^2$. Attempts to connect these groups have failed until recently. It was suspected that the second group belonged to the $4f^95d6s^2$ configuration, but the spacing of the levels did not seem right for what one expected from L-S type coupling. To carry the problem further the matrix elements of the f^9d configuration were generated, reasonable parameters were used, and the matrices were diagonalized. This calculation placed the S = 8 lowest and the S = 7 about 935 cm^{-1} away. Hund's Rule would put J =10 lowest. J = 7 from the calculations was at 2201 cm^{-1}. The levels we had known and were trying to understand were at 0, 953.39, and 2425.35 cm^{-1}. With the J values known, a search was made going from the low even level of $f^{10}s^2$ to low odd levels, then to very high even levels, and finally searching for low odd levels. By this route we located the second configuration at 7565.62 cm^{-1}. This is the $^7H_8$ of the $4f^95d6s^2$, which is 7565.62 cm^{-1} above the DyI ground state of $^5I_8(4f^{10}6s^2)$.

Footnote

†Present address: Lawrence Radiation Laboratory–Livermore.

ATOMIC ENERGY LEVELS OF SOME HEAVY ACTINIDES

John G. Conway and Earl F. Worden†

In the last two years sufficient quantities of Bk, Cf, and Es have become available that we have been able to prepare electrodeless discharge tubes of the iodides. These lamps are excited in a microwave cavity at a frequency of 2450 MHz. For Bk about 150 μg were available, for Cf about 35 μg, and for Es about 10 μg. In all cases lamps were prepared and spectra observed with less than this amount of material, since yields of 80 to 90% are common. Some spectra of Es were observed with 0.1 μg added to 100 μg of GdI_3. The work on these spectra is continuing, and will in fact take several years before the presently available plates are completely analyzed and an extensive list of energy levels is prepared. However, as the work has progressed we have been able to obtain certain information about the lowest levels of these elements.

Knowing the two lowest levels and having accurate hyperfine-structure measurements of these levels, we can calculate a nuclear moment and quadrupole moment. Such information is available for ^{249}Bk and ^{253}Es, and calculations of these moments have been made and reported.[1] The moments are the same for ^{249}Bk and ^{253}Es, and are 5.1±0.7 nm. The measurements of the hyperfine structure give values for a_{7s} which are accurate to a few percent. However, certain assumptions are made in using the Goudsmit-Fermi-Segrè formula that increase the final error to between 10 and 20%. The value of a_{7s} for ^{249}Bk is 1.424 cm^{-1} and for ^{253}Es is 1.526 cm^{-1}.

The hyperfine structure is wide enough and can be measured with sufficient accuracy that information about the quadrupole moment can be obtained. The quadrupole moment for ^{249}Bk is 4.7±1 barns and for ^{253}Es it is 5.1±1 barns.

There are four levels known for BkI and 8 levels for BkII. The electron configuration that is lowest in BkI is the $5f^97s^2$, the lowest configuration in BkII is $5f^97s$.

Table I. Atomic energy levels of berkelium.

Level (cm^{-1})	J value	g value	SL
BkI ($5f^9 7s^2$)			
0	7.5	1.288	^6H
5416.69	5.5	1.333	^6H
6530.71	6.5	1.263	^6H
9535.12	5.5		^6H
BkII($5f^9 7s$)			
0	8		^7H
1487.56	7		^5H
5598.11	6		^7H
6051.19	5		^7H
6809.52	7		^5H
6906.07	5		^5H
7038.48	4		^5H
7786.75	6		^5H

Table II. Atomic energy level for EsII($5f^{11}7s$).

Level (cm^{-1})	J	SL
0	8	^5I
938.66	7	^3I

Table III. Atomic energy levels of californium.

Level (cm^{-1})	J	g value	SL
CfI($5f^{10}7s^2$)			
0	8	1.213	^5I
CfII($5f^{10}7s$)			
0	8.5		^6I
1180.55	7.5		^4I

There are no new levels for Es. Those known are for EsII.

When the levels in BkII and EsII were known, a calculation to determine the G^3 value for these ions was made and compared with the values of G^3 for other actinides. It was found that G^3 is fairly constant across the actinide series. (The same is true for the rare earths.) By using an interpolated value of G^3, the position of the two lowest levels in CfII was calculated. At the same time a search was made for these two levels. The level was found at 1180.55 cm^{-1}; the calculation had predicted 1155 cm^{-1}.

The examination of several resolved Zeeman lines of Cf yields J and g information which makes it possible to identify the ground state of CfI as a J = 8, g = 1.213, which makes the ground state a $^5I_8$ of the $5f^{10}7s^2$ configuration.

Footnote and Reference

†Present address: Lawrence Radiation Laboratory–Livermore.

1. E. F. Worden, R. G. Gutmacher, J. G. Conway, and R. J. Melhorn, J. Opt. Soc. Am. 59, 1526 (1969).

FORMATION AND CHARACTERIZATION OF DIVALENT EINSTEINIUM IN A CaF_2 CRYSTAL

N. Edelstein, D. Fujita, W. Kolbe, and R. McLaughlin

Although no compounds of divalent actinides have been isolated, tracer chemistry experiments[1] and interpretation of charge-transfer bands in the visible and uv spectral range[2] indicate that actinide elements with Z > 97 might form a chemically stable dipositive oxidation state. Dipositive states of the entire lanthanide series have been stabilized in crystals of CAF_2.[3] However, the only dipositive actinide ion positively identified as being stabilized in CaF_2 has been Am^{2+}.[4] We report in this paper the identification by electron paramagnetic resonance of Es^{2+} in CaF_2.

Dipositive Es has the electronic configuration outside closed shells of $5f^{11}$. The lanthanide analog Ho^{2+} has the configuration $4f^{11}$. Both nuclei ^{253}Es and ^{165}Ho have I = 7/2, so the spectra

should be very similar. The EPR spectrum of Ho^{2+} in CaF_2 was studied by Sabisky[5] and the optical spectrum by Weakliem and Kiss.[6] The ground term of the f^{11} configuration is primarily $^4I_{15/2}$. Spin orbit coupling will mix other L-S states and, in the case of f^{11}, lower the Lande g value from that expected for a pure $^4I_{15/2}$, but J will remain a good quantum number. For the purposes of this discussion we assume the crystalline field does not mix in other J levels. A cubic crystalline field will split a J = 15/2 state into three Γ_8 quartets and two doublets, a Γ_6 and Γ_7. For the likely values of the crystalline field parameters, B_4 and B_6, either the Γ_6 or Γ_7 doublet should be the ground crystalline field state. If we assume $E_1 >> g\beta H$, where E_1 is the energy of the first excited crystalline field state relative to the ground state, we may then predict the g values of the possible ground doublets.

Powdered CaF_2 ($\approx$ 3 mg) to which had been added 2 wt % PbF_2 was placed in the center of a spectroscopic-grade carbon rod in which a small hole had been drilled. Approximately 6 μg of purified $^{253}Es^{3+}$ ($t_{1/2}$ = 20.5 days) in a volume of $\approx$ 1 λ HCl was pipeted onto the powder.[7] The carbon rod was attached to two electrodes, the apparatus was evacuated, and current was passed through the rod until the CaF_2 powder was observed visually to coalesce. The current was immediately turned off, and after cooling for approximately 10 min the CaF_2 crystal, now $\approx$ a 1 mm sphere, was removed. The crystal was colorless after annealing, but in approximately 1 hour turned medium red, and in about 3 to 4 hr was dark red or black due to radiation damage. The amount of Es that was incorporated in the crystal is unknown, but from radiation surveys of the carbon rod and crystal it was estimated that not more than 3 μg was contained in the crystal, and the actual amount might be much less. The radiation-induced emission of this crystal will be reported separately.[8]

The EPR spectrum of this crystal was taken at a frequency of $\approx$ 35 GHz and T = 4.2°K. An isotropic eight-line spectrum was found which can be fitted to the parameters of a spin Hamiltonian $\mathcal{H} = g\beta \vec{H}\cdot\vec{S}' + A\vec{I}\cdot\vec{S}'$, with I = 7/2 and S' = 1/2. Because of the large hyperfine interaction, spin levels were mixed and the energy expression given by Sabisky[5] was used to determine the parameters; the values obtained were $|g| = 5.809 \pm 0.005$ and $|A| = (0.1216 \pm 0.0001)$ cm^{-1}. The line widths were initially about 20 gauss peak to peak (the first spectrum was obtained about 1 hour after annealing the crystal), but continually broadened due to radiation damage of the crystal, and 8 h after annealing the spectrum was too broad to observe. The calculated g value for the Γ_6 state is -6.0, which is in reasonable agreement with the experimental value when effects of spin-orbit coupling and covalency are considered. An analysis of the hyperfine-coupling constant is now under way in order to evaluate the nuclear moment of ^{253}Es.

The results of this investigation show that dipositive Es is more readily stabilized in CaF_2 than the earlier actinides (excepting Am). This evidence supports the earlier work, which predicted that the heavier actinides should have chemically stable dipositive oxidation states.

References

1. J. Malý, J. Inorg. Nucl. Chem. 31, 1007 (1969).
2. L. Nugent, R. Baybarz, and J. Burnett, J. Phys. Chem. 73, 1177 (1969).
3. D. S. McClure and Z. J. Kiss, J. Chem. Phys. 39, 325 (1963).
4. N. Edelstein, W. Easley, and R. McLaughlin, J. Chem. Phys. 44, 3130 (1966).
5. H. R. Lewis and E. S. Sabisky, Phys. Rev. 130, 1370 (1963); E. S. Sabisky, Phys. Rev. 141, 352 (1966).
6. H. A. Weakliem and Z. J. Kiss, Phys. Rev. 157, 277 (1967).
7. Purification procedures for Es are discussed in a note by B. B. Cunningham, J. R. Peterson, R. D. Baybarz, and T. C. Parsons, Inorg. Nucl. Chem. Letters 3, 519 (1967).
8. J. G. Conway, B. B. Cunningham, N. Edelstein, D. Fujita, and R. McLaughlin, this report (following paper).

SPECTRA OF Es IN CaF_2

John G. Conway, N. Edelstein, D. K. Fujita, and R. McLaughlin

A crystal of CaF_2 containing about 0.1 wt% Es was prepared by melting the materials together in a carbon resistance furnace. Three mg of a mixture of optical-grade CaF_2 and 2 wt% PbF_2 were used, which produced a spherical crystal of about 1 mm diam. The Es was added to the mixture in hydrocholoric acid solution after being purified by a series of cation-exchange columns.

The spectra were recorded by use of a Jarrell-Ash 3/4-meter model 75-000 spectrograph.

The crystal was radioluminescent, and was definitely more reddish in appearance at liquid nitrogen temperature than at room temperature. The spectral difference between liquid nitrogen and room temperatures was very pronounced. At low temperature the spectrum consists of a few relatively sharp lines superimposed upon a continuum which extends from 590 to 670 nm. At room temperature the lines disappear and the continuum extends from 560 to 700 nm. The sharpening of the broad-band continuum is responsible for the color change observed when the temperature of the crystal is lowered. A tracing of the low-temperature spectrum is contained in Fig. 1.

With the crystal at liquid nitrogen temperature a search was made for sharp absorption lines, but none were found. Intense continuous absorption was observed which started at 410 nm.

These spectral results are consistent with the finding from EPR measurements[1] that Es is present in the divalent state in this crystal. The intense absorption at 410 nm represents a transition to a f^{10} d or charge-transfer state. The broad-band emission results from a transition from this state to an excited state of the f^{11} configuration. The relatively sharp f^{11} transitions become more intense at low temperature. The wavelengths of these lines are given in Table I. Similar effects have been observed in CaF_2 crystals that contained divalent Sm^{2+}.[2]

^{253}Es decays with a half-life of 20 d into 314-d ^{249}Bk. It is to be expected that the radioluminescence spectrum will be affected by this transformation of Es atoms into Bk atoms. Figure 1 compares the spectrum taken 10 days after Es purification with the spectrum taken 73 days after purification. The most reasonable explanation of these data is that the spectral features which grow in at 680 nm represent transitions associated with the Bk ion. The wavelengths of these lines are given in Table II. The decay of the spectral features associated with Es is also apparent. In order to verify these results the investigation of a more concentrated CaF_2:Bk crystal is planned.

Table I. Es radioluminescent lines; wavelength in Å.

5877.4	6200.6
5902.2S	6244.2S
5927.8	6255.2
5958.4	6364.4
6022.0	6381.0

S, = sharp

Table II. Bk radioluminescent lines; wavelength in Å.

6630.6	6668.8
6637.0	6723.3
6645.7	6760.5
6655.9	6770.6
6662.4	6782.8

References

1. N. Edelstein, unpublished work.
2. W. Kaiser, C. G. B. Garrett, and D. L. Wood, Phys. Rev. 123, 766 (1961).
3. N. Edelstein, W. Easley, and R. McLaughlin, Advances in Chemistry Series, No. 71 (American Chemical Society, Washington, D. C., 1967), p.203.
4. R. G. Gutmacher, E. K. Hulet, R. Loughheed, J. G. Conway, W. T. Carnall, D. Cohen, T. K. Keenan, and R. D. Baybarz, J. Inorg. Nucl. Chem. 29, 2341 (1967).

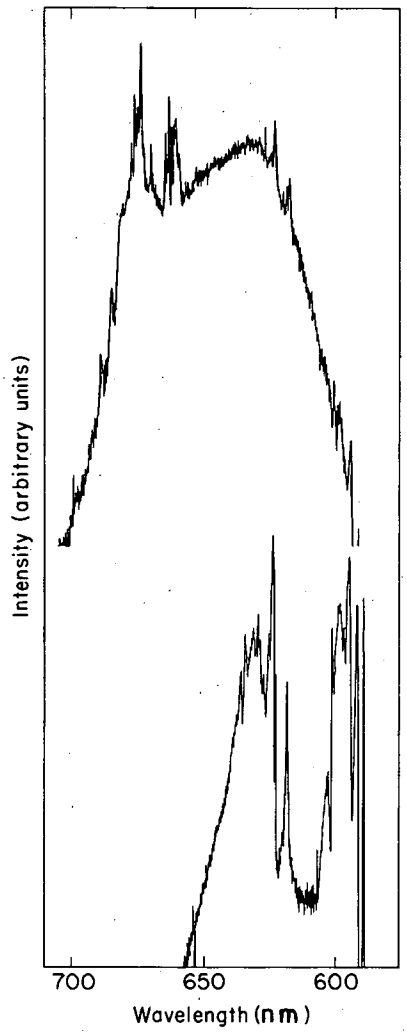

Fig. 1. Radioluminescence of CaF_2:Es. Upper curve displays the emission spectrum 73 days after purification of the Es; lower curve displays the spectrum 10 days after purification.
(XBL 701-2250)

THERMOLUMINESCENCE OF ACTINIDE IONS IN CaF_2

J. J. Stacy, R. McLaughlin, N. Edelstein, and John G. Conway

The thermoluminescence of lanthanide ions incorporated in CaF_2 has been studied by Merz and Pershan.[1] Each of the crystals was irradiated at 77° C and its temperature subsequently raised to above room temperature. During the heating process the crystal emits the characteristic spectrum of the trivalent ion. The intensity of the thermoluminescence changes with temperature, and all the lanthanides have peaks at the same temperature. Thus the thermoluminescence spectrum is a function of the host lattice and not of the dopant ion. Irradiation of the crystal causes divalent ions and holes (electron-deficient centers) to form in the lattice. As the crystal is warmed these holes recombine with the divalent ions and form an excited trivalent ion which then fluoresces. The temperatures at which different peaks occur are characteristic of different types of holes that can exist in CaF_2.

We have performed a similar set of experiments on actinide ions incorporated in CaF_2. Am in CaF_2 is similar to the lanthanides in that it forms the divalent state upon γ irradiation;[2] however, Np(3), Pu, and Cm(4) form the tetravalent state upon γ irradiation. Thus the irradiated lattice containing the tetravalent ion should contain electron traps rather than holes.

CaF_2 crystals containing from 0.05 to 0.30 wt % of dopant ion were γ-irradiated in liquid nitrogen and slowly warmed to room temperature by means of an adjustable flow of nitrogen gas. The light emitted was recorded by a photomultiplier and plotted as a function of temperature. The results are given in Table I. The temperature peaks are affected slightly (±3°) by differences in concentration, method of crystal growth, and heating rate (within the range 0.5 to 5.0 C°/min). The emitted light in all cases is characteristic of the trivalent ion. We had difficulty detecting the weak infrared thermoluminescence of Np, hence it is not included in the table; however, in the following discussion we assume that it behaves the same as Pu and Cm.

From Table I it is apparent that the thermoluminescence peaks occur at the same temperature for all the dopant ions. The most obvious explanation is that the divalent actinide is formed upon γ irradiation, and the mechanism for thermoluminescence is the same as that proposed by Merz and Pershan;[1] however, this is not true for the actinides. When Np, Pu, and Cm are irradiated at 77° C, broad absorptions occur in the visible and near-infrared regions. Since these absorptions occur at approximately the same wavelength for all three ions (as shown in Table II), they could not be the intense f-d transitions expected for divalent actinides, and must instead be due to color centers. Hence it is unlikely that the divalent actinide is formed upon γ irradiation. We are currently investigating other explanations for the thermoluminescence of these actinides.

Table I. Temperature peaks in the thermoluminescence spectra of some lanthanides and actinides in CaF_2.

Dopant ion	Temperatures of peaks (°K)				
	#1	#2	#3	#4	#5
Tm	136	178	---	241	263
Er	140	183	206	246	272
Ho	139	176	205	243	271
Am	141	192	---	248	---
Cm	145	---	216	242	267
Pu	141	190	213	238	261

Table II. Absorption maxima in trivalent actinides upon γ irradiation.

	Dopant Ion		
	Np	Pu	Cm
λ (Å)	5800	5800	5300
λ (Å)		8100	7800
λ (μ)	1.05	1.07	1.06

References

1. J. L. Merz and P. S. Pershan, Phys. Rev. 162, 217 (1967).
2. N. Edelstein, W. Easley, and R. McLaughlin, J. Chem. Phys. 44, 3130 (1966).
3. J. J. Stacy, R. D. McLaughlin, N. M. Edelstein, and J. G. Conway, in Nuclear Chemistry Annual Report 1967, UCRL-17989, Jan. 1968, p. 185.
4. N. Edelstein, W. Easley, and R. McLaughlin, Advances in Chemistry Series, No. 71 (American Chemical Society, Washington, D. C., 1967), p. 203.

A STUDY OF PROTACTINIUM OXIDE WITH THE MÖSSBAUER EFFECT

D. Quitmann,† R. Dod, and N. Edelstein

The 84.2-keV state in $^{231}_{91}Pa$ has a half-life of 41 nsec and is therefore well suited for Mössbauer studies, with the limitation that they require milligram amounts of the compounds of ^{231}Pa ($t_{1/2}$ = 32 500 yr). Protactinium is of particular interest since it occurs as $Pa^{5+}(5f^0)$, $Pa^{4+}(5f^1)$, and possibly Pa^{3+}. Croft, Stone, and Pillinger[1] have observed the Mössbauer resonance in both Pa_2O_5 and PaO_2, as a broad unresolved line with $^{231}ThO_2$ as the source. The $3/2^- - 5/2^+$ E1 transition has 12 components if totally split, and five for axial quadrupole splitting (intensities 10:9:6:4:1). We decided to repeat the experiments by Croft et al. with well-characterized absorbers and sources. The Mössbauer spectrometer used has been described by Faltens.[2]

From samples of $^{230}_{90}Th$ (about 1 mg, purity 92%), ^{231}Th was produced by irradiation at 2×10^{14} n/cm^2 sec. Count rates of 10^4/sec were obtained for the 84-keV line when a Ge(Li) detector, was used, with a peak-to-background ratio of about 10. We used $^{230}ThO_2$ and ^{230}Th metal

as sources. The latter was expected to result in an unsplit source. It was produced by reduction of ThF_4 with Ba metal. The x-ray-diffraction powder patterns of both sources agreed with that of standard samples. The ^{231}Pa was separated from its decay products by standard procedures.[3,4] Protactinium forms a series of oxides with different structures and with composition $PaO_{2.0 \ldots 2.5}$.[5] A Pa hydroxide precipitate was fired at 750–800° C in air to produce Pa_2O_5. This sample gave an x-ray diffraction pattern from which 40 lines were measured. Of these measured lines, 25 were indexed on the basis of a tetragonal structure with $a_0 = 5.434 \pm 0.001$ Å and $c_0 = 5.496 \pm 0.002$ Å. Six of the remaining lines were too diffuse to be measured accurately, but could be indexed on the basis of the assigned structure. There were nine low-angle, low-intensity lines which were not indexed. The lower oxide, PaO_2, was obtained by treatment of Pa_2O_5 in H_2 at 1540° C for 1 hr. Of the 26 lines measured from the x-ray diffraction pattern of this oxide, 22 were indexed on the basis of a cubic structure with $a_0 = 5.490 \pm 0.001$ Å. The other four lines were again low-angle and low-intensity lines and could not be indexed.

A small pill of the oxides was pressed (33 mg, 3 mm diameter) and measured in a close geometry (angular spread about 6 deg, absorber moving) at 4.2° K.

One of the spectra is reproduced in Fig. 1. The effect observed is increased by a factor of five, and a broad double-line structure is very clear; otherwise the spectrum agrees with the results of Croft, Stone, and Pillinger. No spectrum showed more structure. A fit with two Lorentz curves was made; the results are presented in Table I. The Th metal source seemed to yield a smaller line width. No isomer shift was detected between Pa in ThO_2 and Pa in the metal (≤ 0.05 cm/sec).

We feel that radiation damage within the absorber is of little or no significance. However, the lattice parameter for our sample of PaO_2 is slightly smaller than for the stoichiometric PaO_2. This indicates the presence of interstitial oxygen,[5] which might cause the spectrum to broaden and become unresolvable. Further work should be done with other Pa compounds and Pa metal.

Table I. Summary of the averaged parameters obtained by fitting two Lorentz lines to the Pa_2O_5 spectra. The errors quoted include an estimate of the uncertainty of the fitting procedure.

Source	Counts/Channel	Effect (%)	Position (cm/sec)	FWHM (cm/sec)	Effect (%)	Position (cm/sec)	FWHM (cm/sec)
Pa in the ThO_2	1.4×10^6	0.52	-0.83	1.6	0.52	+0.84	1.6
		(3)	(10)	(4)	(3)	(9)	(6)
Pa in Th metal	1.1×10^6	0.25	-0.93	1.1	0.27	+0.89	1.1
		(2)	(11)	(4)	(2)	(4)	(3)

Footnote and References

†On leave from Institut für Technische Kernphysik, Technische Hochschule, Darmstadt. Present address: IV. Physikalisches Institut, Freie Universität Berlin.

1. W. L. Croft, J. A. Stone, and W. L. Pillinger, J. Inorg. Nucl. Chem. 30, 3203 (1968).
2. M. O. Faltens, Mössbauer Resonance Studies of Gold Compounds (Ph. D. thesis), UCRL-18706, Feb. 1969.
3. H. W. Kirby, The Radiochemistry of Protactinium, National Academy of Sciences, Nuclear Science Series, NAS-NS 3016, 1959.
4. A. Chetham-Strode and O. L. Keller, Coll. Internat. du C. N. R. S., Orsay, July 1965, p. 189.
5. L. E. J. Roberts and A. J. Walker, Coll. Internat. du C. N. R. S., Orsay, July 1965, p. 51.

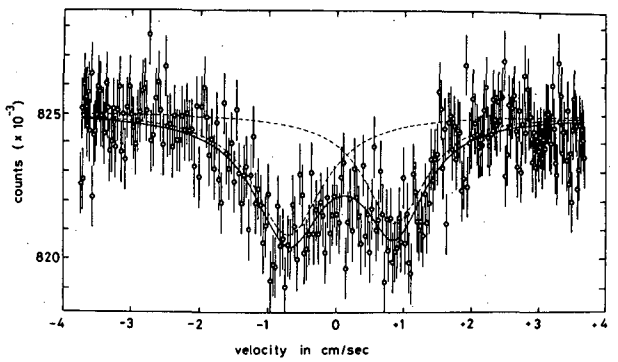

Fig. 1. Mössbauer absorption spectrum of $^{231}Pa_2O_5$; the source was ThO_2; temperature 4.2° K. (XBL 701-223)

DIFFUSION OF LITHIUM IN TUNGSTEN

F. L. Reynolds

The use of a mass spectrometer for investigation of diffusion phenomena was first suggested by McCracken and Love.[1] A second paper by the same authors appeared two years later.[2] Both papers were on the diffusion of lithium through tungsten. In their experiment a deposit of lithium about 100 atoms thick, 0.3 mm in diameter, was made on the backside of a tungsten ribbon filament. The filament was 1.0 mm wide and 0.03 mm thick. After the sample was deposited, the lithium diffused through the filament, evaporating from the front side as ions, and was detected with a mass spectrometer.

Both these papers left some doubts concerning the conclusion that diffusion through the bulk filament was the only transport mechanism. Two questions did concern the authors: 1. Did lithium remain for a finite lifetime on the filament? 2. What was the possibility that surface migration affected the results? They concluded that the resident lifetime of lithium on tungsten could affect the results below 1400° K, and that surface migration was not a problem in their experiment.

Surface migration rates are certainly several orders higher than volume diffusion through the metal. Also, the edge of the ribbon filament is no barrier to this migration. In Refs. 1 and 2 the experimental description leads one to believe that data were taken immediately after shutting off, or turning on, the sample beam. In Ref. 1, data were obtained from the rate of rise in the lithium emission; in the later paper data were taken after a steady state had been reached and the primary beam switched off. The subsequent decay current was measured against time. The authors were certainly aware of the possible migration on the surface, for they increased the filament width by a factor of two, which did not change the experimental results. To be conclusive, the filament width would have to be orders of magnitude larger, which of course would be impractical.

Interest in the diffusion of small samples through refractory metals was prompted by the possibility of the method as a surface ionization source for mass spectrometers. The sample might, for example, be added to a sealed capsule and heated to surface ionizing temperatures. The rate of lithium diffusion through tungsten looked remarkably good from the data given in Refs. 1 and 2. Recently Schwegler and White have used this method to study the diffusion of uranium in tungsten,[3] and Cuderman[4] made an ion source for potassium by diffusing potassium metal through a tantalum foil membrane. The very large diffusion constants given by Love and McCracken for lithium through tungsten seemed worth while redoing by perhaps modified techniques, which is the purpose of this report.

Numerous experimental attempts were made to incapsulate trace amounts of lithium metal in tantalum tubes sealed off by a helium arc. The lithium metal in the quantities used would attack the thin-wall tubing (0.001-in. wall, 0.040-in. diam). This evidence of attack made the data inconclusive. Tungsten tubing was also tried, but small cracks developed in the vapor-deposited tungsten tubing. For these experiments the detection mass spectrometer was a quadrupole type, which was not very sensitive to small beams. When a higher-sensitivity magnetic mass spectrometer was employed it was found that sufficient lithium existed as an impurity in the tungsten. This method eliminated the possibility of surface migration, since all the lithium had to come from the

bulk metal.

Several tungsten filaments were run, and the decay of ^{7}Li beam with time at various filament temperatures was followed. The temperature range studied was from 1200 to 1700 °K. Since the amount of Li in the tungsten is small, the measured diffusion coefficients were not influenced by the Li concentration. From emission spectrographic assay, there was less than 1 part of Li to 10^7 W, which was the limit of detection. The emission of ^{7}Li was followed in four tungsten filaments, starting at the lower temperatures and increasing the filament temperatures by arbitrary steps. No attempt was made to compare ^{6}Li with ^{7}Li in these determinations.

The diffusion constant was calculated from the slope of a plot of the natural logarithm of the ^{7}Li ion current against time. As pointed out, when the solute concentration of Li as impurity in the W is small, the diffusion can be described according to Schwegler and White[3] by Fick's laws,

$$J_{(x,t)} = -D\, dC_{(x,t)}/dx \qquad \text{(1st law)} \quad \text{and} \quad dC_{(x,t)} = -D\, d^2C_{(x,t)}/dx^2 \qquad \text{(2nd law)},$$

where $J_{(x,t)}$ is the solute flux, $C_{(x,t)}$ the solute concentration, and D the diffusion coefficient. Their solution to Fick's second law for impurity evaporation from a thin plate gives the solute concentration as a function of position in the filament and evaporation time:

$$C_{(x,t)} = \frac{2}{h} \sum_{n=1}^{\infty} \sin \frac{n\pi x}{h} \exp\left(\frac{-D\pi^2 n^\pi t}{h^2}\right) \int_0^h f(x') \sin \frac{n\pi x'}{h}\, dx,$$

where x = distance through the filament, t = evaporation time, h = total thickness of the filament, n = any positive integer. In deriving this equation they assumed that the initial solute concentration, f(x), is expandable in terms of a Fourier series

$$f(x) = \sum_{n=1}^{\infty} a_n \sin \frac{n\pi x}{h} \quad \text{and} \quad a_n = \frac{2}{h} \int_0^h f(x') \sin \frac{n\pi x'}{h}\, dx = \text{constant}.$$

The solute atom flux at the filament surface becomes (e.g., at x = 0)

$$J_{(0,t)} = \frac{2}{h} \sum_{n=1}^{\infty} \exp - \frac{D\pi^2 n^\pi t}{h^2} \int_0^h f(x') \sin \frac{n\pi x'}{h}\, dx,$$

which is reduced to

$$J_{(0,t)} = A \sum_{n=1}^{\infty} \exp - \frac{D\pi^2 n^2 t}{h^2}, \qquad A \text{ being a constant.}$$

This is for a thin slab, such as a filament whose thickness is less than 16 Dt.[5] By combining the above equation with the Saha-Langmuir equation, a portion of the flux is ionized according to

$$I^+/I_0 = (g^+/g_0) \exp[(\phi - Ip)/kT],$$

where ϕ = the work function, Ip = ionization potential, k = Boltzmann's constant, g^+/g_0 = constant, and T = °K. The detected solute ion current becomes

$$I^+ = A' \exp(-\pi^2 Dt/h^2).$$

Thus a plot of $\ln I^+$ against time gives a slope = $d \ln I^+/dt = -\pi^2 D/h^2$, or the diffusion coefficient $D = -(\text{slope} \times h^2)/\pi^2$.

By determining D for various temperatures the relation between D and the temperature can be obtained. Shewmon[6] gives this relation as

$$D = D_0 \exp(-Q/RT),$$

and experimentally D_0 and Q are obtained by plotting ln D against 1/T, the slope $d \ln D/d(1/T) = -Q/R$, and $\ln D_0$ is given by the intercept at $1/T = 0$; Q is the activation energy.

The results presented here differ from those obtained by Love and McCracken. As shown in Table I, the values for the diffusion coefficient, especially above 1400 °K, are in some determinations smaller by three orders of magnitude. About the only way to account for this difference is if surface migration is one of the transport mechanisms in their experiments.

Table I.

Mass spectrometrically determined diffusion coefficients of Li in polycrystalline W. A comparison with data from Love and McCracken is given.

Filament (°K)	D. Coefficient (cm^2 sec^{-1})		Filament (°K)	D. Coefficient (cm^2 sec^{-1})		
1193	4.90	E-10	1111	9.0	E-9	Ref. 1
			1176	3.9	E-8	
1215	3.33	E-10				
1220	3.41	E-10	1250	1.5	E-7	
1251	8.17	E-10				
1251	5.41	E-10				
1274	4.30	E-10				
1276	3.99	E-10	1333	5.8	E-7	
1425	1.36	E-9	1428	2.5	E-6	
1483	3.0	E-9	1400	1.2	E-6	Ref. 2
1582	5.8	E-9	1450	2.0	E-6	
1591	2.0	E-9	1500	3.0	E-6	
			1475	2.8	E-6	

The results shown in Fig. 1 have considerable scatter, and only an estimate of the activation energy can be obtained from this plot. The best-fit line gives a value of 0.8 eV, which is again not in accord with Ref. 2, their value being 1.8 eV. However, in calculating data from Ref. 2, a value of 2.86 eV was obtained from their Fig. 5, which compares to 2.42 obtained in Ref. 1.

From these data it would seem that the diffusion of Li through W is indeed slower than indicated by the work of Love and McCracken. From a practical viewpoint the method may not be so attractive for a surface ion source based on the diffusion of the sample through a thin metal membrane. It is still of considerable interest and will require further experimental investigation.

References

1. G. M. McCracken and H. M. Love, Phys. Rev. Letters 5, 201 (1960).
2. H. M. Love and G. M. McCracken, Can. J. Phys. 41, 83 (1962).
3. E. C. Schwegler, Jr., and F. A. White, Intern. J. Mass Spectr. Ion Phys. 1, 191 (1968).
4. J. F. Cuderman, Rev. Sci. Instr. 40, 1475 (1969).
5. J. Cranck, Mathematics of Diffusion (Oxford University Press, London, 1956).
6. P. G. Shewmon, Diffusion in Solids (McGraw-Hill Book Co., Inc., New York, 1963).

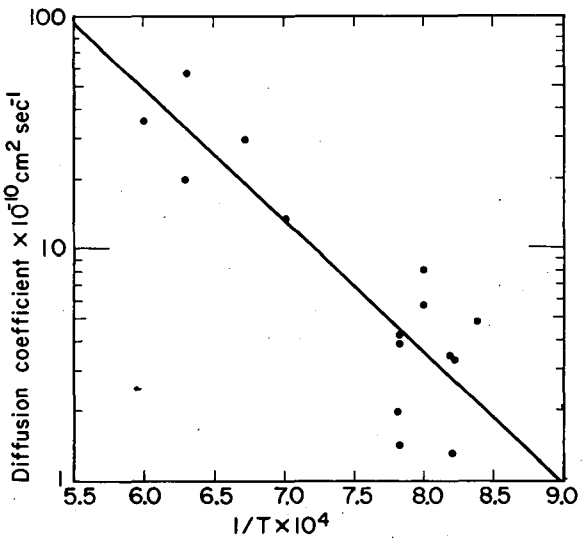

Fig. 1. The diffusion coefficient of ^{7}Li in polycrystalline tungsten as a function of temperature. (XBL 701-2096)

A SURVEY OF METASTABLE PEAKS IN SOME COMPOUNDS CONTAINING N-N AND NO GROUPS†

Amos S. Newton, A. F. Sciamanna, and Thomas Starr

The formation from N_2O and NO_2 of metastable states of the ions $(N_2^+)^*$ and $(NO^+)^*$, [1] which dissociated with the same half-life as the same metastable ions formed from N_2 and NO gas respectively but with differing kinetic energy release, suggested that other sources might yield data that would contribute to understanding the nature of the crossing states responsible for the metastability of these diatomic ions.

Compounds surveyed that contained N-N bonds were hydrazoic acid, diazomethane, and azomethane. The mass spectra of HN_3 and CH_2N_2 contained metastable peaks at $(M/q)^* = 7.00$ that were identical in shape to the peak observed in the mass spectrum of N_2. Appearance potentials and the shapes of the excitation curves of the $(M/q)^* = 7.00$ peak in HN_3 and CH_2N_2 showed the metastable ion to arise from N_2 gas in each case. These labile compounds decompose in the mass spectrometer ion source to yield N_2, which is then excited by the electron beam.

Azomethane, CH_3NNCH_3, showed no metastable peak at $(M/q)^* = 7.00$, so this molecule ion does not fragment to the metastable state of $(N_2^+)^*$. Metastable ions were observed at the apparent masses 7.33, 9.59, 10.33, 11.27 (intense peak), 16.7, and 31.9 (intense peak).

Dimethyl nitrosamine, $(CH_3)_2NNO$, was surveyed for occurrence of $(M/q)^* = 8.53$ from the metastable dissociation of $(NO^+)^*$. Only a very small peak at $(M/q)^* = 8.53$ was observed, and the intensity was too low to investigate. The compound is, however, extremely rich in metastable peaks, and such peaks were observed at the apparent masses 4.66, 4.78, 5.38, 5.96, 7.38 (very intense), 8.03, 9.57, 10.32, 11.25, 16.8, 17.9, and 36.7. Some of these peaks are explainable only as the result of very unusual rearrangements, and need further study.

Footnote and Reference

†A summary of some survey work performed with Thomas Starr, a summer student, 1969.

1. A. S. Newton and A. F. Sciamanna, J. Chem. Phys. 52, 327 (1970).

METASTABLE PEAKS IN THE MASS SPECTRA OF N_2O AND NO_2. II.[†]

Amos S. Newton and A. F. Sciamanna

A recent study[1] has shown both N_2^+ and NO^+ formed by electron impact on N_2 and NO respectively to possess metastable states which dissociate by delayed unimolecular processes. Previous studies on N_2O and NO_2[2,3] showed these molecules to be excited to metastable ionic states by electron impact. The product ion of their respective metastable dissociations was NO^+.

With increased sensitivity of detection, and other modifications[1] of our mass spectrometer (CEC Model 21-103B), a reinvestigation of these molecules has shown the presence of other metastable peaks as represented in Figs. 1 and 2. The metastable transitions now identified in the mass spectrum of these molecules are shown in Table I, together with the energetic data and half-life data which were determined for each of these transitions.

The transitions were shown to be unimolecular, since a plot of peak sensitivity vs pressure showed a large nonzero intercept for each, as shown in Figs. 3 and 4.

The appearance potentials (AP) and the values of kinetic energy release in each of the metastable transitions were determined as described previously.[1] The half-lives were determined by comparing discrimination curves for the ion-accelerating voltage with calculated curves for each respective transition. This method is applicable to transitions of very short half-life (<0.3 μsec). The results for the apparent mass $(M/q)^* = 20.45$ from N_2O, as shown in Fig. 5, indicate the presence of two half-lives of ≈0.09 and >0.3 μsec. A value of <0.2 μsec was previously cited for this transition,[2] and Coleman et al.[3] found $t_{1/2} = 0.54$ μsec, but did not observe the short-lived component. This same method was also used to determine the half-lives for the metastable dissociation of $(NO^+)^*$ from NO, N_2O, and NO_2 sources, as shown in Fig. 6, and for the dissociation of $(N_2^+)^*$ from N_2 and N_2O sources, as shown in Fig. 7. By the method of Berry,[4] corrections were made (when necessary) for initial kinetic energy arising from fast fragmentation processes in the ion source. The half-lives of the respective metastable ions are shown to be constant regardless of source. The kinetic energy release in the metastable transition, as shown in Table I, is a function of the source of the metastable ion.

The half-life for the metastable dissociation of N_2O^{+2} was determined by the disappearance of the parent M/q = 22 peak with increasing transit time from formation in the ion source to the collector (proportional to $V_A^{-1/2}$), as was done previously for CO_2^{+2}.[5] Experiments using a high-resolution mass spectrometer with a long transit time (≈ 6.7 μsec) showed no N_2O^{+2} ions to exist. The M/q = 22 peak under these conditions consisted solely of CO_2^{+2} ions.[6] We conclude that no stable N_2O^{+2} ions exist and that the background of the long-lived M/q = 22 in Fig. 8 is due to CO_2^{+2}.

For each transition the appearance potential was calculated by summing the bond energy, the ionization potentials to the respective charged fragments, and the kinetic energy release, T, in the dissociation. The agreement was within experimental error except in those cases in which the metastable species arose via a fast dissociation process in the original molecule, e.g., $(N_2^+)^*$ from N_2O, where the difference between observed and calculated appearance potential is 1.3 eV. This difference is attributed to initial kinetic energy release in the fast fragmentation process. This assumption was proven by studying the negative-repeller cutoff potentials of the metastable ions from each source. For $(N_2^+)^*$ and $(NO^+)^*$ from N_2O the values found for the initial kinetic energy release were 1.4 and 2.2 eV, respectively, compared to the energy deficits of 1.3 and 2.3 eV shown in Table I. For $(NO^+)^*$ from NO_2, the observed value was 3.4 eV of initial kinetic energy release, much higher than the expected value of 1.3 eV in Table I. No explanation of this lack of agreement was found.

In N_2O^{+2} no initial kinetic energy is possible, so the difference between the observed and calculated appearance potentials must be in radiative energy loss. An allowed radiative transition of 1.3 eV would have approximately the 0.46-μsec half-life observed for the metastable transition. It is therefore postulated that the ground state of N_2O^{+2} is a dissociative state, and the metastable lifetime is the radiative lifetime to this state by cascade processes from higher states.

The metastable dissociations of $(N_2^+)^*$ and $(NO^+)^*$ were previously ascribed to forbidden intersystem crossings to dissociative states of the respective molecule ions (predissociation). The energy balance precludes slow radiative processes to dissociative states, and the equality of half-lives from the various respective sources precludes tunneling mechanisms. The equality of

Table I. Energetics of formation of various ionic species and half-lives of metastable transitions in the mass spectra of N_2O, NO_2, NO, and N_2.

Molecule	(M/q)*	Transition	AP (eV)	Breaks (eV)	Standard	T (eV)	$t_{1/2}$ (μsec)	Calculated[a] AP (eV)	ΔAP(eV) (obs-calc)
N_2O	20.45	$N_2O^+ \rightarrow NO^+ + N$	15.7 ± 0.5	19.5	H_2^+	1.05 ± 0.05[b]	≈ 0.09 ≥ 0.03	15.23	0.5
	8.53	$NO^+ \rightarrow O^+ + N$	27.5 ± 0.5		He^+	0.13 ± 0.03	≥ 0.18	25.16[c]	2.3
	7.00	$N_2^+ \rightarrow N^+ + N$	27.5 ± 0.5	32 ± 1 37 ± 1	He^+	0.20 ± 0.05	≥ 0.15	26.18[c]	1.3
	8.91	$N_2O^{++} \rightarrow NO^+ + N^+$	36.5 ± 0.5		Ar^{++}	6.5 $^{+0.2}_{-0.5}$	0.46 ± 0.05	35.20	1.3
	22.00	N_2O^{++}	36.4 ± 0.5		Ar^{++}				
	7.00	N^{++}	57.1 ± 1.0	64.4 72.6	Ne^{++}			49.08(+NO) 55.56(+N+O)	
	8.00	O^{++}	60.5 ± 1.0	74.8	Ne^{++}			50.44(+N_2) 60.19(+N+N)	
NO_2	19.57	$NO_2^+ \rightarrow NO^+ + O$	12.6 ± 0.3(w)	14.1 ± 0.3(s) 15.6 ± 0.3	H_2^+	(1.1)[b] (0.5)[b]	(0.7)[b] (2.5)	12.86(T=0.5)	
	8.53	$NO^+ \rightarrow O^+ + N$	24.6 ± 0.5	30 ± 1	He^+	0.13 ± 0.03	≥ 0.18	23.35[c]	1.3
	7.00	N^{++}	51.5 ± 1(w)	65.0 71.0	Ne^{++}			48.65(+O_2) 53.73(+O+O)	
	8.00	O^{++}	52.1 ± 1(w)	69.3 75.5	Ne^{++}			51.88(+NO) 58.35(+N+O)	
N_2	7.00	$N_2^+ \rightarrow N^+ + N$	(24.9 ± 0.3)[d]		He^+	(0.55 ± 0.10)[d]	≥ 0.15	24.85	0.0
NO	8.35	$NO^+ \rightarrow O^+ + N$	(20.2 ± 0.2)[d]		He^+	(0.04 ± 0.02)[d]	≥ 0.18	20.14	0.0

a. AP calculated to the lowest dissociation limit. Figure includes measured kinetic energy release of the metastable transition.
b. Data taken from Reference 1.
c. Figure does not include any initial kinetic energy of the fast fragmentation process.
d. Data taken from Ref. 2.
s = strong onset.
w = weak onset.

half-lives of each respective species with change in T from various sources also puts severe restraints on predissociation mechanisms, especially for $(N_2^+)^*$ from N_2 and from N_2O. Here the gross inequality in T (0.55 and 0.20 eV respectively from the two sources) precludes the normal intersystem crossing on the right side of the potential energy diagram. A difference in energy of this amount would cause a marked change in transition probability with energy above the crossing point. A crossing on the left side is possible, and in this case, owing to the parallel nature of the two curves, little change in transition probability with change in potential energy is expected.[7] A second possibility is that only a small portion of the $(N_2^+)^*$ undergoes predissociation, and this is in competition with radiation to a lower state. The radiative transition probability from the excited level would then be the rate-determining step. The data do not allow one to eliminate this possibility.

Footnote and References

†Condensed from J. Chem. Phys. 52, 327 (1970).

1. A. S. Newton and A. F. Sciamanna, J. Chem. Phys. 50, 4868 (1969).
2. A. S. Newton and A. F. Sciamanna, J. Chem. Phys. 44, 4327 (1966).
3. R. J. Coleman, J. S. Delderfield, and B. G. Reuben, J. Mass Spectry. Ion Phys. 2, 25 (1969).
4. C. E. Berry, Phys. Rev. 78, 597 (1950).
5. A. S. Newton and A. F. Sciamanna, J. Chem. Phys. 40, 718 (1964).
6. The authors thank Dr. R. M. Teeter of the Chevron Research Company for these measurements.
7. J. Calvert and J. N. Pitts, Photochemistry (John Wiley and Sons, Inc., New York, 1966), pp. 185-89.

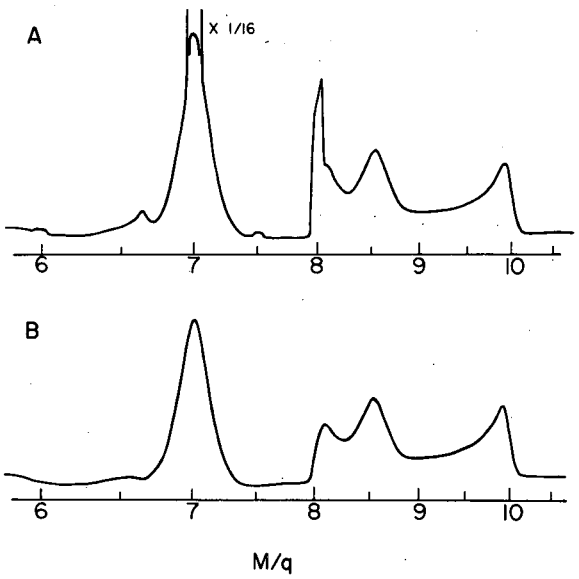

Fig. 1. Mass spectrum of N_2O in the mass range of M/q = 6 to M/q = 10.5. $MV_A = 22\,200$; inlet pressure = 400 μ. Curve A: $V_{e^-} = 100 + 0.0058\ V_A$; curve B: M/q = 6–7.7, $V_{e^-} = 31 + 0.0058\ V_A$; M/q = 7.7–10.5, $V_{e^-} = 51 + 0.0058\ V_A$. (XBL 695-522)

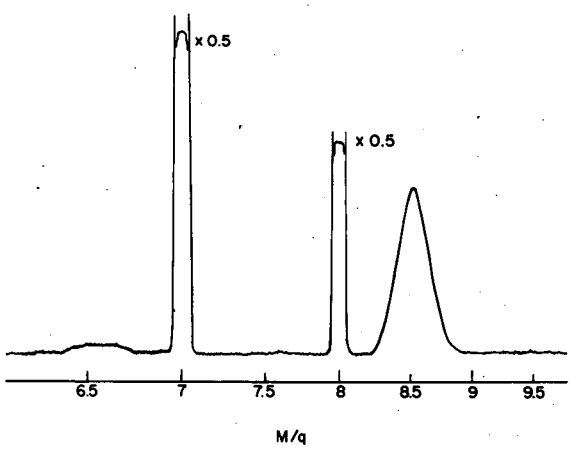

Fig. 2. Mass spectrum of NO_2 in the mass range M/q = 6.5 to M/q = 9.5. $MV_A = 22\,620$, $V_{e^-} = 100 + 0.0058\ V_A$, inlet pressure = 100 μ. (XBL 695-517)

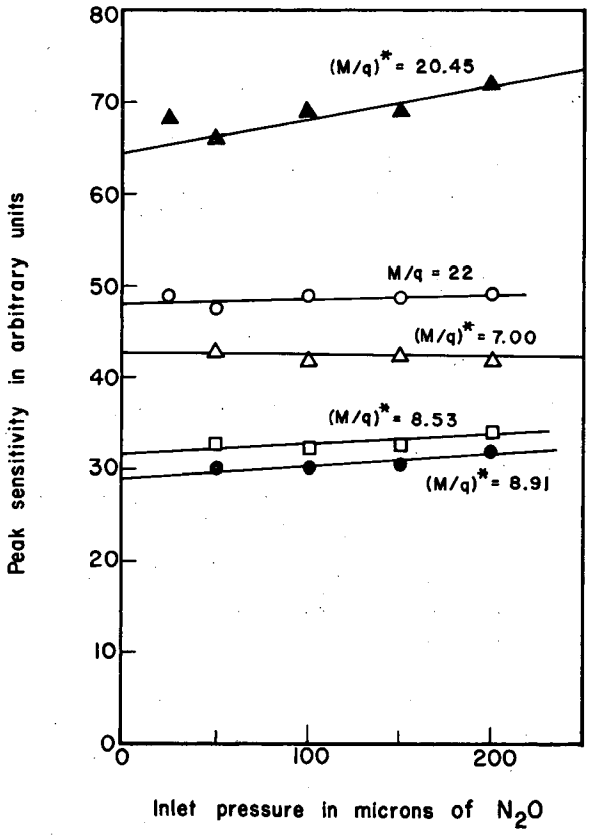

Fig. 3. Variation of peak sensitivity with inlet system pressure for various peaks in the mass spectrum of N_2O. Conditions: $(M/q)^* = 20.45$ and $M/q = 22$, $MV_A = 63\,000$, $V_{e^-} = 100$ eV; $(M/q)^* = 7.00$, $MV_A = 21\,000$, $V_{e^-} = 46.7$ eV; $(M/q)^* = 8.53$ and $(M/q^* = 8.91$ [measured at 8.10], $MV_A = 25\,600$, $V_{e^-} = 100$ eV. (XBL 695-518)

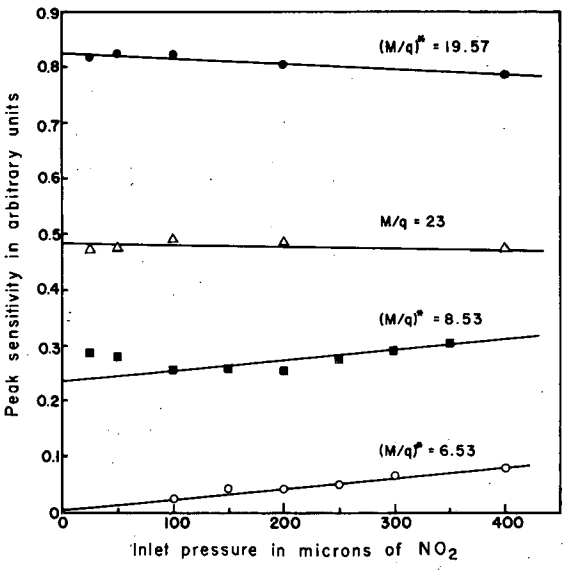

Fig. 4. Variation of peak sensitivity with inlet system pressure for various peaks in the mass spectrum of NO_2. $MV_A = 22\,600$, $V_{e^-} = 100$ eV. (XBL 695-521)

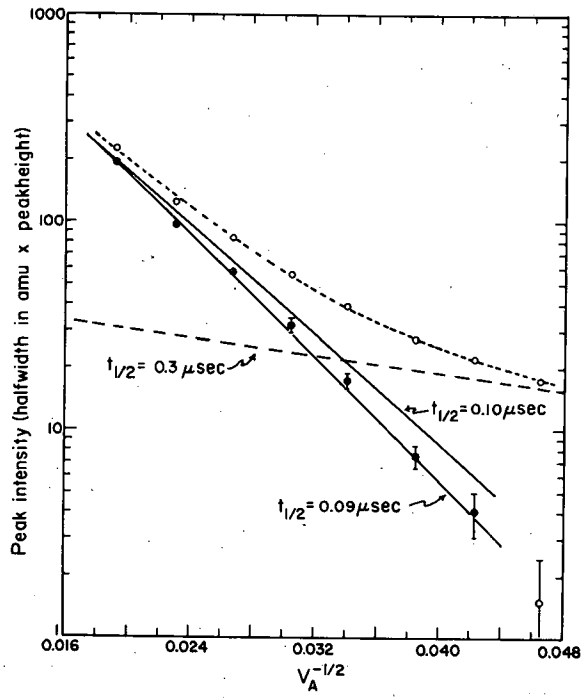

Fig. 5. Accelerating voltage discrimination curve of $(M/q)^* = 20.45$ peak in mass spectrum of N_2O. Open circles, dotted line: experimental points. Lines are of slope calculated for the transition, $N_2O^+ \rightarrow NO^+ + N$, for half-lives of 0.3, 0.10, and 0.09 μsec, respectively. Lower points are subtraction of the 0.3-μsec line from the observed points. (XBL 695-513)

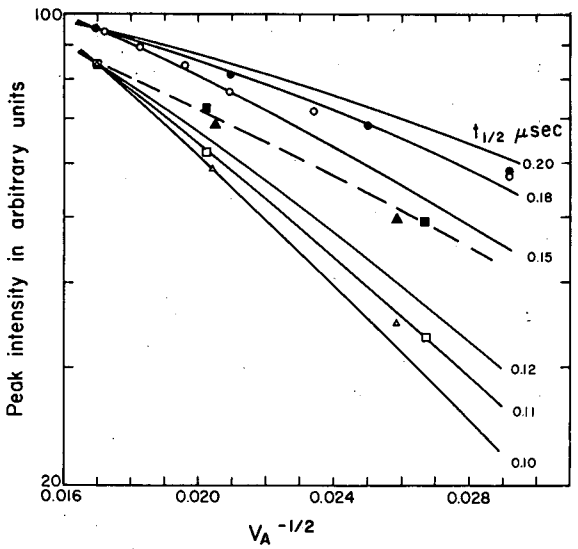

Fig. 6. Accelerating voltage discrimination curves of $(M/q)^* = 8.53$ from various sources. Points are experimental; lines are calculated for the transition $NO^+ \rightarrow O^+ + N$ at the assumed half-lives shown. Open circles: NO source; closed circles: NO source corrected for collision-induced component. Open squares: N_2O source; open triangles: NO_2 source; closed squares: N_2O source corrected for initial kinetic energy of NO^+; closed triangles: NO_2 source corrected for initial kinetic energy of NO^+. (XBL 695-519)

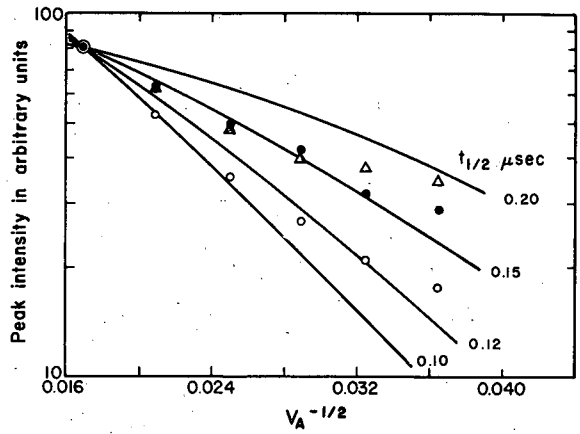

Fig. 7. Accelerating voltage discrimination curves of $(M/q)^* = 7.00$ peak from various sources. Points are experimental. Lines are calculated for the transition $N_2^+ \rightarrow N^+ + N$, with the assumed half-lives shown. Peak intensity expressed as product of peak height and half width in atomic mass units. Closed circles: N_2 source; open circles: N_2O source; triangles: N_2O source corrected for initial kinetic energy of N_2^+. (XBL 695-514)

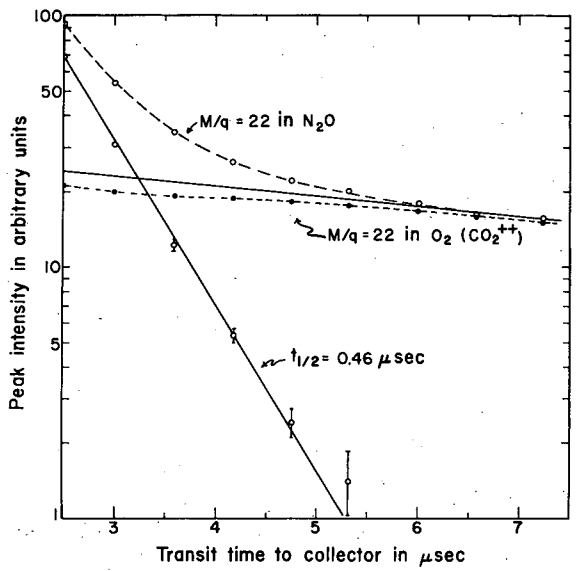

Fig. 8. Dependence of intensity of peak at M/q = 22 in the mass spectrum of N_2O with total transit time from formation in the ion source to the collector. Open circles, dashed line: observed intensity of M/q = 22 in N_2O; solid line, no points: line subtracted to yield an exponential decay; open circles, solid line: resolved decay of N_2O^{2+}; closed circles, dotted line: M/q = 22 peak of CO_2^{2+} (from O_2) normalized to N_2O curve at long transit times. (XBL 695-520)

THE METASTABLE DISSOCIATION OF THE DOUBLY CHARGED CARBON MONOXIDE ION†

Amos S. Newton and A. F. Sciamanna

In 1932 Friedlander, Kallmann, Lasareff, and Rosen[1] observed peaks at apparent mass $(M/q)^* = 10.3$ and $(M/q)^* = 18.3$ in the mass spectrum of CO, and attributed their occurrence to C^+ and O^+ ions respectively from the metastable dissociation of CO^{+2}. The mechanism was postulated to be a tunneling process. Hipple[2] failed to observe the metastable dissociation of CO^{+2}, but Kupriyanov[3] observed the metastable process while studying the collision-induced dissociation of CO^{+2}. Kupriyanov concurred that tunneling was the probable mechanism, and set limits of $400 > t_{1/2} > 2$ μsec for the half-life.

Metastable ions in the mass spectrum of CO have again been investigated by use of a Dempster-type mass spectrometer, CEC-Model 21-103B, that had previously been modified to increase the pumping speed, amplifier sensitivity, and other operational factors.[4,5] In this study one further modification was made, to increase the range of voltage that could be applied to the metastable supressor to a value of V_{mss} (the metastable supressor voltage) as high as 1.35 V_A (the ion-accelerating voltage).

In Fig. 1 is shown the mass spectrum of CO in the mass region M/q = 9 to M/q = 22. Included are the only two metastable peaks observed in the mass spectrum of CO, the broad peak at $(M/q)^* = 10.3$ and a broad peak at $(M/q)^* = 18.3$. These are the expected apparent masses for the product ions of the transition,

$$CO^{+2} \xrightarrow{(m)} C^+ + O^+, \quad \begin{matrix}(M/q)^*(C^+) = 10.287,\\ (M/q)^*(O^+) = 18.287.\end{matrix} \tag{1}$$

In addition there are a broad front and back on the M/q = 14 peak. In Fig. 2 the mass region from M/q = 13 to M/q = 20 is shown with a metastable supressor voltage at the collector of $V_{mss} = 1.065\ V_A$. Here all normal peaks are reversed (due to secondary negative particles produced in the collector); the front rise on M/q = 14 is eliminated but the back rise and the peak at $(M/q)^* = 18.3$ are still present.

In Fig. 3 these peaks are shown to be essentially linear with pressure, hence to arise from unimolecular processes. In Fig. 4 the appearance potentials (AP) of these peaks and of M/q = 14 are shown to be equal and of identical shape. The AP compared with that of $Ar^{+2} = 43.39$ eV[6] are all in the range 41.5 ± 0.4 eV, in agreement with the previous value from Dorman and Morrison[7] of 41.7 ± 0.3 eV and with the range of values calculated by Hurley[8] (41.2 to 42.8 eV).

In Fig. 5 are shown the metastable supressor cutoff curves of the peaks at $(M/q)^* = 10.3$ and 18.3. From these curves the kinetic energy release in the dissociation was found to be 5.7_3 and 5.7_6 eV respectively. A value 5.75 ± 0.2 eV is consistent with the precision of the method.

The half-life of the metastable dissociation was estimated by two methods. First, was that used to estimate the half-lives of CO_2^{+2} (Ref. 9) and N_2O^{+2} (Ref. 10), in which what was measured was the disappearance of the parent ion with time of transit between formation in the ion source and the collector. This is accomplished by comparing the ion-accelerating voltage discrimination curve of the parent CO^{+2} ion with that of a stable doubly charged ion of about the same M/q value. The parent CO^{+2} at M/q = 14 was compared with Ne^{+2} at M/q = 10. This gave a half-life for CO^{+2} of 20 ± 10 μsec. A second method used was to integrate the total ion current in the M/q = 10.3 peak, correct this for kinetic energy discrimination at the collector slit by the method of Berry,[11] and use this figure to calculate the decay rate in the equation

$$\frac{\Delta N}{\Delta t} \approx \frac{dN}{dt} = \lambda N. \tag{2}$$

In Eq. 2, N was taken as the ion current in the M/q = 14 peak and the time Δt was taken as the transit time for 8 cm path length beyond the collector in which C^+ ions from the decay are formed in collectible orbits.[12] This yielded a value $t_{1/2} = 18.3$ μsec. A reasonable evaluation of these respective values is 20 ± 10 μsec for the half-life for dissociation of CO^{+2}. Both these values assume that all CO^{+2} formed and accelerated out of the ion source dissociate with this half-life.

There is no evidence from our studies that any CO^{+2} ions are appreciably more stable than indicated by the 20-μsec half-life.

This long half-life and the near equality in M/q of C^+, O^+, and CO^{+2} lead to the side bands on M/q = 14 in Fig. 1. After traversing approximately 90 deg of the 180-deg trajectory in the analyzer tube, C^+ ions from the dissociation are collectable at masses < M/q = 14, and O^+ ions at masses > M/q = 14. Metastables with half-lives < 1 μsec do not exhibit this behavior.

When a dissociation energy of CO of 11.108 eV and ionization potentials of C and O atoms of 11.264 and 13.614 eV respectively are assumed, the reaction

$$CO(^1\Sigma^+) + e^- \longrightarrow C^+(^2P^0_{1/2}) + O^+(^4S^0) + 3e^- \qquad (3)$$

requires 35.986 eV at the dissociation limit. Adding the kinetic energy of 5.75 eV yields an expected AP of 41.74 eV, in essential agreement with the observed value of 41.5 ± 0.4 eV. No radiative process can be involved. Hurley's correlations[8] allow no crossing states of the $^3\Pi$ ground state of CO^{+2}. Hence these data are in agreement with the previous conclusions[1, 3] that CO^{+2} dissociates by a tunneling process. Further it is concluded that this tunneling is from the $\nu = 0$ vibrational level of CO^{+2}, since no longer-lived states are observed. In Fig. 6 is shown a provisional potential energy diagram of the lowest state of CO^{+2} consistent with the data. The barrier was calculated for a half-life of 20 μsec by the method given by Herzberg.[13]

Footnote and References

†Condensed from UCRL-19531; submitted to J. Chem. Phys.

1. E. Friedlander, H. Kallmann, W. Lasareff, and B. Rosen, Z. Physik 76, 60, 70 (1932).
2. J. A. Hipple, J. Phys. Coll. Chem. 52, 456 (1948).
3. S. E. Kupriyanov, Zh. Tekhn. Fiz. 34, 861 (1964) [Engl. Transl.: Soviet Phys.–Technical Phys. 9, 659 (1964)].
4. A. S. Newton, A. F. Sciamanna, and R. Clampitt, J. Chem. Phys. 47, 4843 (1967); 46, 1779 (1967).
5. A. S. Newton and A. F. Sciamanna, J. Chem. Phys. 50, 4868 (1969).
6. J. L. Franklin, J. G. Dillard, H. M. Rosenstock, J. T. Herron, and K. Draxl, Ionization Potentials, Appearance Potentials, and Heats of Formation of Gaseous Positive Ions, U. S. Department of Commerce, National Bureau of Standards NSRDS-NBS 26 (U. S. Government Printing Office, Washington, 1969).
7. F. H. Dorman and J. D. Morrison, J. Chem. Phys. 35, 575 (1961).
8. A. C. Hurley and V. W. Maslen, J. Chem. Phys. 34, 1919 (1961).
9. A. S. Newton and A. F. Sciamanna, J. Chem. Phys. 40, 718 (1964).
10. A. S. Newton and A. F. Sciamanna, J. Chem. Phys. 52, 327 (1970).
11. C. E. Berry, Phys. Rev. 78, 597 (1950).
12. A. S. Newton, J. Chem. Phys. 44, 4015 (1965).
13. G. Herzberg, Molecular Spectra and Molecular Structure. I. Spectra of Diatomic Molecules (D. Van Nostrand Company, Inc., Princeton, N. J., 1950), p. 409.

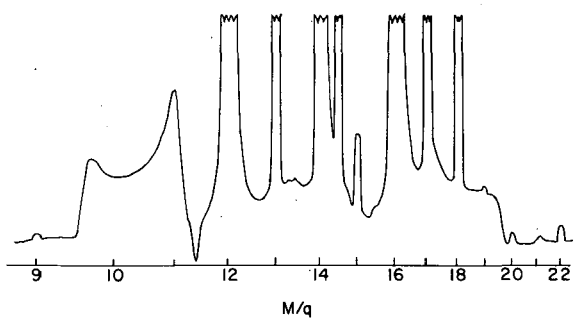

Fig. 1. Mass spectrum of CO in the mass region M/q = 9 to M/q = 22. Inlet pressure = 200 μ; focus maximized for the $(M/q)^*$ = 10.3 peak. (XBL 701-12)

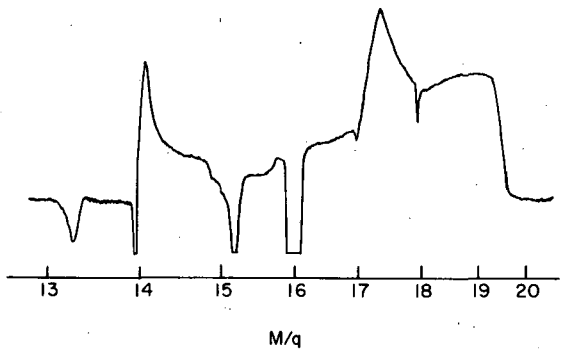

Fig. 2. Mass spectrum of CO in the mass region M/q = 13 to M/q = 20. Inlet pressure = 200 μ; V_{mss} = 1.065 V_A; focus maximized for the $(M/q)^*$ = 18.3 peak. (XBL 701-14)

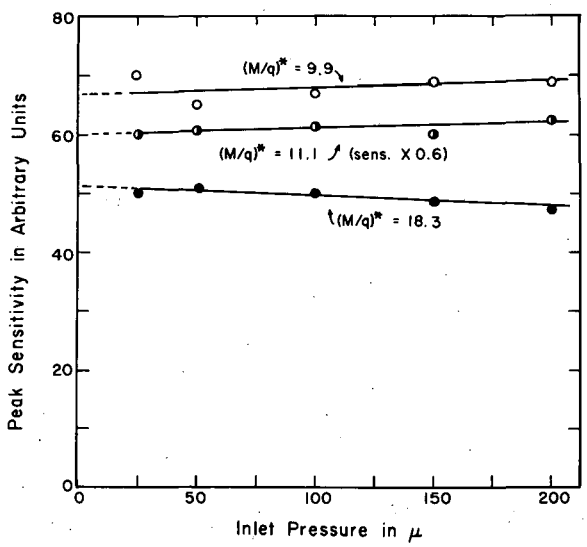

Fig. 3. Linearity with pressure of the $(M/q)^*$ = 10.3 and $(M/q)^*$ = 18.3 peaks in the mass spectrum of CO. Focus maximized for each peak measured. $(M/q)^*$ = 10.3 peak measured at the shoulder peaks at $(M/q)^*$ = 9.9 and 11.1. (XBL 701-16)

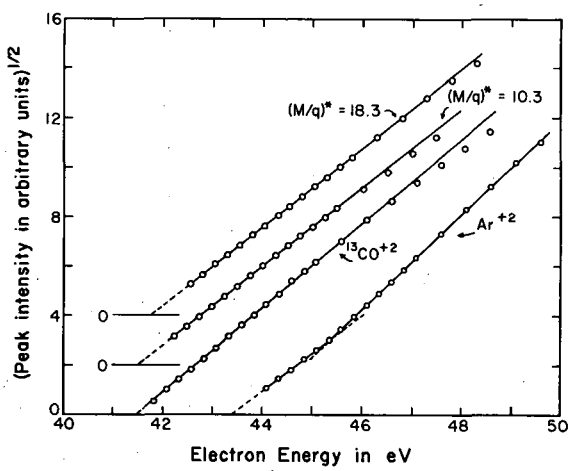

Fig. 4. Appearance potential curves of CO^{+2}, $(M/q)^*$ = 10.3, and $(M/q)^*$ = 18.3 peaks in the mass spectrum of CO. The energy scale is normalized to the ionization potential of Ar^{+2}. The CO^{+2} curve was measured with enriched ^{13}CO at M/q = 14.5. (XBL 701-17)

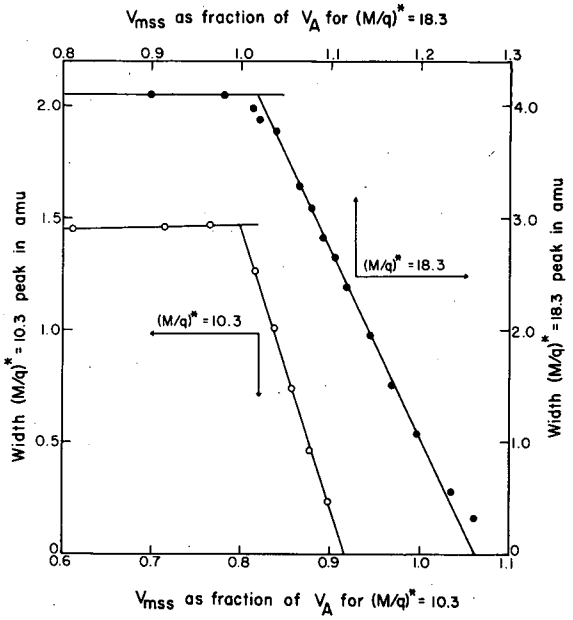

Fig. 5. Metastable suppressor cutoff curves of the $(M/q)^* = 10.3$ and $(M/q)^* = 18.3$ peaks in the mass spectrum of CO. (XBL 701-15)

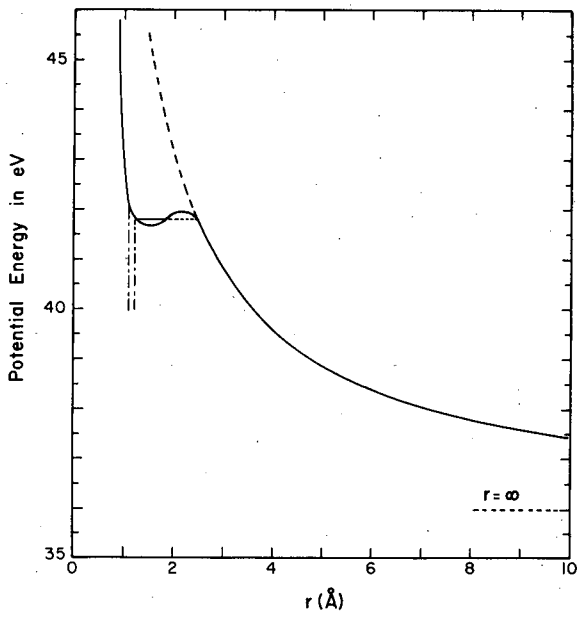

Fig. 6. Proposed potential energy diagram of the ground state of the CO^{+2} ion. (XBL 701-13)

L x-RAY EMISSION FROM FISSION FRAGMENTS SLOWING DOWN IN COPPER†

H. R. Bowman and Zeev Fraenkel*

The purpose of this experiment was to measure the number of fission-fragment inner-electron-shell vacancies that are produced during the slowing down of fragments emitted from the spontaneous fission of ^{252}Cf. A thin (50 μin.) copper foil was used as the slowing-down material, and the characteristic fission-fragment L x rays were measured by using a high-resolution (180 eV) silicon x-ray detector. Previous measurements by Armbruster,[1] using gas-filled proportional counters to detect the gross L x-ray radiations from ^{235}U fission fragments stopped in various materials, revealed rather high inner-shell ionization cross sections, and indicated that by using a high-resolution-type x-ray detector one might be able to identify individual fragments and hence the fission-fragment chemical yields in a manner that is dependent only on the atomic characteristics of the fragments.

Figure 1 shows the apparatus used in our experiment. The fission source, copper foil, and fission-fragment detector were mounted on movable arms in a vacuum chamber. The lead shield protected the x-ray detector from prompt fission x rays and γ rays as well as from radiations emitted in the first 2 cm of the fragment flight path. The fragment-detector holder was constructed to shield the x-ray detector from radiation emitted from the fragments after they were stopped in the fission detector. The latter shielding was not complete, and resulted in detection of a number of silicon x rays in both the copper-in and copper-out (background) measurements.

Copper K x rays were detected with the copper target in place and were used along with the silicon K x rays to calibrate the system during the runs. The x rays were detected in coincidence with fission fragments and stored in 256 channels of a 4096-channel pulse-height analyzer.

Figure 2 shows the L x-ray energy distribution emitted from ^{252}Cf fission fragments as they pass through 50 μin. of copper, Background has been subtracted and the data have been corrected for absorption[2] in the x-ray detector window (1 mil beryllium), the copper foil, and the gold on the surface of the x-ray detector (500 $\mu g/cm^2$). Also shown are the L x rays from natural molybdenum and barium, which were excited by use of an ^{55}Fe radioactive source.

The average number of light fragment L x rays observed was about 0.3 per fragment, and about 1/3 this number were from heavy fission fragments. Using average values for L x-ray fluorescence yields[2] indicates that more than three L-shell vacancies are created per fragment when light fragments pass through the foil, and about 1/5 as many are produced by slowing down heavy fragments.

The lack of structure in Fig. 2 results from the complexity of the individual L x-ray spectra and points out the general need for higher-resolution x-ray-detection systems. The inner-shell ionization cross section appears to vary smoothly but rapidly with the fission-fragment energy or velocity.

Probably the next step should be to measure the L x-ray spectra along with the fission-fragment masses in a two-dimensional experiment. These data might then be used to determine the prompt nuclear charge distributions for different masses in a manner that is independent of the nuclear properties of the fission products.

Footnotes and References

†Work done at the Weizmann Institute of Science, Rehovoth, Israel.
*Physics Department, Weizmann Institute of Science, Rehovoth, Israel.

1. P. Armbruster, Z. Physik 166, 341 (1962).
2. Ellery Storm and Harvey I. Israel, Photon Cross Sections from 0.001 to 100 MeV for Elements 1 through 100, Los Alamos Scientific Laboratory Report LA-3753, June 1967.

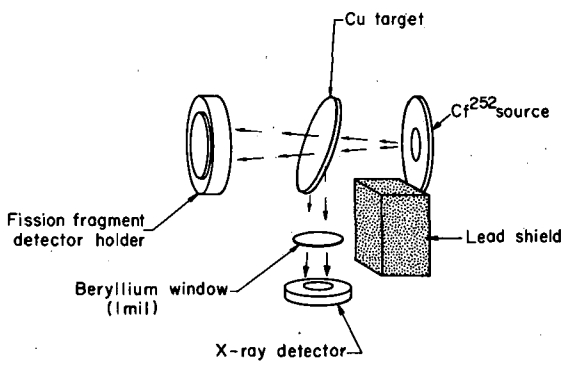

Fig. 1. Schematic diagram of the apparatus used in measuring the L x rays emitted from ^{252}Cf fission fragments as they pass through a thin copper foil. (XBL 6912-6397)

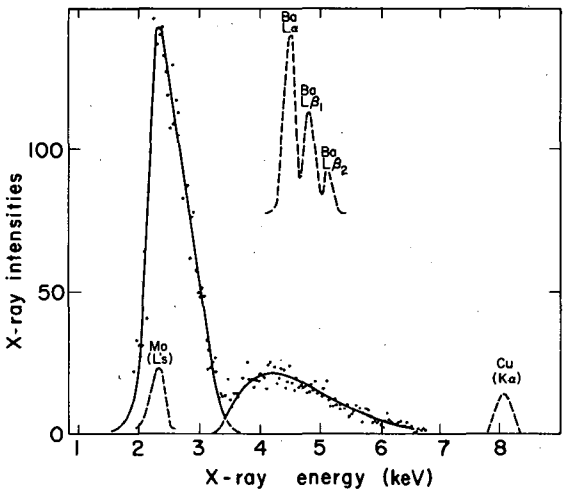

Fig. 2. The L x-ray energy distribution emitted from ^{252}Cf fission fragments while passing through a 50-μin. copper foil. (XBL 6912-6396)

Hyperfine Interactions

BETA-PARTICLE AND GAMMA-RAY ANGULAR DISTRIBUTIONS FROM POLARIZED ^{186}Re, ^{188}Re, and ^{194}Ir

W. D. Brewer† and D. A. Shirley

The conserved vector current theory of weak interactions (CVC)[1] predicts, among other things, the ratios of certain nuclear matrix elements in first-forbidden beta decays.[2] This prediction is embodied in the Fujita-Eichler relation,[3] which relates the matrix elements $\int \underline{\alpha}$ and $\int \underline{r}$. Thus the measurement of these matrix elements is of interest not only for nuclear structure theory but also as a possible test of CVC. The matrix elements contributing to a given decay may be determined by the analysis of certain observable quantities connected with the decay. These observables include: ft values, spectrum shapes, electron polarizations, beta-gamma directional and circular-polarization correlations, and the angular distributions of beta particles from polarized nuclei.

However, many first-forbidden decays obey the ξ approximation, and their observable properties therefore all have the characteristics of an allowed decay; hence, these decays are not useful for the measurement of first-forbidden matrix elements. Another large class of decays obeys the unique approximation and the matrix element $\int B_{ij}$ predominates, so these decays are also of no interest in this connection. Two isotopes whose decays obey neither of these approximations are ^{186}Re and ^{188}Re.[4] These decays have been studied by most of the above methods.[5] Unfortunately, the spectrum shape is not too sensitive to small variations in the matrix elements, and beta-gamma correlations can be used only if the beta decay is followed by a gamma ray. Thus observation of beta-particle asymmetries from polarized nuclei is the most sensitive and generally applicable method for study of the matrix elements.

Accordingly, we have measured the beta-particle angular distributions from ^{186}Re and ^{188}Re polarized in iron lattices at low temperatures. Similar measurements were made on the decays of ^{194}Ir, which has a decay scheme like those of the two Re isotopes but has not been so well studied previously. Each of these isotopes has a 1^- ground state which decays primarily to the 0^+ ground state in the daughter, but also to the 2^+ first excited state, which then emits a gamma ray. The decay schemes are shown in Fig. 1.

The stable isotopes ^{185}Re, ^{187}Re, and ^{193}Ir were each put into alloys with iron by melting. The alloys were formed into thin foils (2 mg/cm^2) and irradiated with thermal neutrons to make the desired activities. The foils were then cooled in a nuclear polarization cryostat like that described by Barclay[6] and the angular distributions of the beta particles were observed by using Ge(Li) detectors inside the cryostat to detect the high-energy electrons. The anisotropies of the $2^+ \rightarrow 0^+$ gamma rays were simultaneously observed. The latter give information about the relative admixture of the $\int B_{ij}$ matrix element in the $1^- \rightarrow 2^+$ beta decays, which is needed for the matrix-element analysis. The results are shown in Tables I and II. The observed beta-particle asymmetries are plotted against particle energy in Fig. 2. The angular distribution coefficients $A_1(r)$ and $A_2(r)$ are defined by

$$W(\theta) = 1 + A_1(r)B_1P_1(\cos\theta) + A_2(r)B_2P_2(\cos\theta),$$

where $W(\theta)$ is the relative counting rate (cold/warm) at angle θ to the quantization axis (in this case the magnetic field used to polarize the iron source foils), B_1 and B_2 are orientation parameters which describe the degree of nuclear polarization, and P_1 and P_2 are Legendre polynomials. The variable r is the ratio of the intensities of the two beta branches at a given energy: $r = I(1^- \rightarrow 2^+)/I(1^- \rightarrow 0^+)$.

The quantity R shown in Table II is the intensity ratio of the two beta multipolarities occurring in the $1^- \rightarrow 2^+$ decays: $R = I(L = 2)/I(L = 1)$. R is given by $1 - R/1 + R = \bar{U}_2/0.5916$, where $\bar{U}_2$ is obtained by comparing the observed gamma-ray anisotropy with the anisotropy calculated for pure $L = 1$ beta decays and shown in Table II.

Table I. Beta angular distribution coefficients $A_1(r)$ and $A_2(r)$. Particle energies are in keV.

^{186}Re			^{188}Re			^{194}Ir		
Energy	$A_1(r)$	$A_2(r)$	Energy	$A_1(r)$	$A_2(r)$	Energy	$A_1(r)$	$A_2(r)$
567 ±5	.5318 ±.0033	.0115 ±.0016	1199 ±10	.6318 ±.0049	.0518 ±.0070	1235 ±10	.6958 ±.0111	.1058 ±.0223
619 ±5	.5544 ±.0034	.0122 ±.0020	1295 ±10	.6498 ±.0050	.0436 ±.0115	1340 ±10	.7142 ±.0114	.1229 ±.0283
672 ±5	.5805 ±.0035	.0187 ±.0022	1391 ±10	.6658 ±.0052	.0559 ±.0120	1446 ±10	.7369 ±.0118	.1257 ±.0295
724 ±5	.6074 ±.0036	.0227 ±.0027	1487 ±10	.6807 ±.0055	.0700 ±.0070	1551 ±10	.7516 ±.0120	.1082 ±.0265
777 ±5	.6437 ±.0040	.0362 ±.0030	1583 ±10	.7028 ±.0056	.0730 ±.0088	1656 ±10	.7749 ±.0124	.1168 ±.0292
830 ±5	.6809 ±.0042	.0371 ±.0035	1679 ±10	.7180 ±.0058	.0722 ±.0145	1761 ±10	.7964 ±.0128	.1076 ±.0377
882 ±5	.7228 ±.0046	.0284 ±.0080	1775 ±10	.7525 ±.0058	.1008 ±.0130	1867 ±10	.8518 ±.0136	.1570 ±.0565
935 ±5	.7804 ±.0048	.0364 ±.0130	1871 ±10	.7906 ±.0065	.0738 ±.0280	1972 ±10	.9015 ±.0162	.1433 ±.0745
987 ±5	.8351 ±.0053	-.0075 ±.0175	1967 ±10	.8376 ±.0075	.0570 ±.0400	2077 ±10	.9505 ±.0210	.1971 ±.1200
1040 ±5	.9473 ±.0064	-.0714 ±.0200	2063 ±10	.9237 ±.0097	-.0350 ±.0250	2182 ±10	1.1419 ±.0330	.1952 ±.1500

Table II

	^{186}Re	^{188}Re	^{194}Ir
W(axial, obs.)	0.828±.005	0.902±.016	0.822±.047
W(axial, calc.)	$1 - .3963\ \bar{U}_2$ ± .0005	$1.0011 - .3725\ \bar{U}_2$ ± .0005	$1^{-.0103}_{+.0285} - .2282\ \bar{U}_2$
R	0.158±.015	0.380±.071	≤.04

The errors shown in the tables include statistical errors and estimated uncertainties in the experimental geometries and scattering corrections. The results are in general agreement with earlier work,[7-11] although a smaller A_2 term was found for ^{188}Re than in Ref. 9. The experimental accuracy is substantially better than in previous work except for the ^{194}Ir gamma-ray anisotropy results,[11] whose large errors are due to the presence of two unresolved gamma rays in the spectrum whose mixing ratios and intensities affect the observed anisotropy of the 328-keV gamma. No previous observations of the beta-particle angular distributions from polarized ^{194}Ir have been reported.

The conclusions that may be drawn are as follows: the gamma-ray data from the two Re isotopes indicate a finite admixture of $\int B_{ij}$ in the $1^- \rightarrow 2^+$ decays in both cases. The beta-particle data confirm the fact that the ξ approximation is not obeyed in these decays (the A_2 term is nonzero). The A_2 term in both cases appears to reverse sign at high energies, suggesting that it has the opposite sign in the $1^- \rightarrow 0^+$ transitions than in the $1^- \rightarrow 2^+$ transitions. This could be brought about by the $\int B_{ij}$ term in the latter transitions.[2]

The gamma-ray data from ^{194}Ir indicate that the $\int B_{ij}$ matrix element does not contribute to the $1^- \rightarrow 2^+$ decay in this case. This is in agreement with the A_2 term in the beta-particle angular

distribution, which increases monotonically with energy and thus must be the same in both beta decay branches. The large A_2 term in this case indicates that the decays do not follow the ξ approximation, in contradiction to an early spectrum shape measurement that gave allowed shapes.[12] Further analysis of the data presented here will allow determination of the nuclear matrix elements (or ratios of matrix elements) $\int \underline{\alpha}$, $\int \underline{r}$, $\int \underline{\alpha} \times \underline{r}$, and $\int B_{ij}$ and a test of the Fujita-Eichler relation for these decays.

Footnote and References

†NSF Graduate Fellow, 1968-69. Present address: I. Physikalisches Institut, Freie Universität, Berlin, W. Germany.

1. R. P. Feynman and M. Gell-Mann, Phys. Rev. 109, 193 (1958).
2. For a general review of first-forbidden beta decay, see H. A. Weidenmüller, Rev. Mod. Phys. 33, 574 (1961).
3. J. -I. Fujita, Phys. Rev. 126, 202 (1962); J. Eichler, Z. Physik 171, 463 (1962).
4. J. P. Deutsch, Brussels Colloquium for Low Energy Nuclear Physics (Sept. 1962), Report WI/62/II; P. Lipnik, ibid.
5. For a list of earlier experimental studies of ^{186,188}Re see W. D. Brewer, Weak Interaction Studies by Nuclear Orientation (Ph. D. Thesis), UCRL-19533, 1970.
6. J. A. Barclay, Spin-Lattice Relaxation by Nuclear Magnetic Resonance on Oriented Nuclei (Ph. D. Thesis), UCRL-18986, 1969.
7. A. V. Kogan, V. D. Kul'kov, L. P. Nikitin, N. M. Reinov, M. S. Stel'makh, and M. Šott, Soviet Phys. —JETP 16, 586 (1963).
8. M. Šott and M. Vinduška, Nucl. Phys. 66, 144 (1965).
9. M. Šott, N. J. Stone, J. E. Templeton, and M. Vinduška, Phys. Letters (to be published); see also J. E. Templeton, Applications of Nuclear Orientation (Ph. D. Thesis), Oxford, 1967.
10. A. V. Kogan, V. D. Kul'kov, L. P. Nikitin, I. A. Solokov, and M. S. Stel'makh, Soviet Phys. —JETP 13, 78 (1961).
11. P. G. E. Reid, M. Šott, and N. J. Stone, Nucl. Phys. A129, 273 (1969).
12. M. W. Johns and S. V. Nablo, Phys. Rev. 96, 1599 (1954).

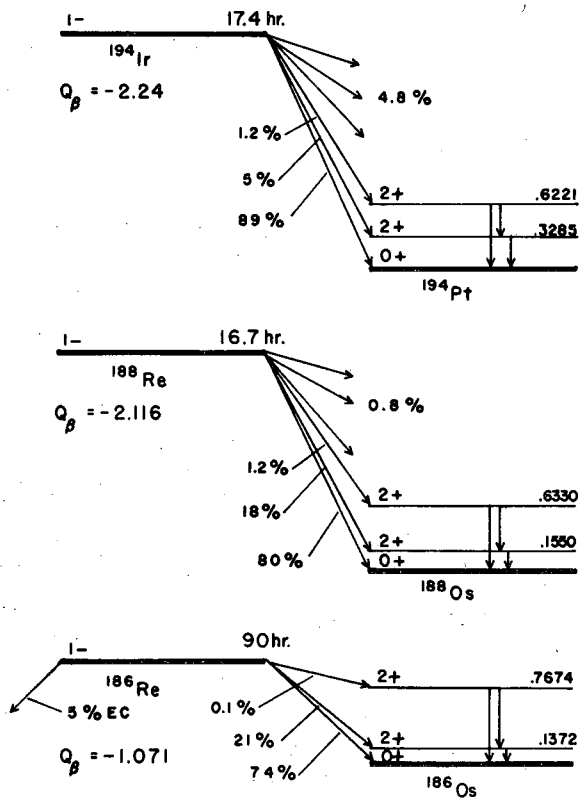

Fig. 1. Decay schemes of the isotopes used in this work. (XBL6912-6720)

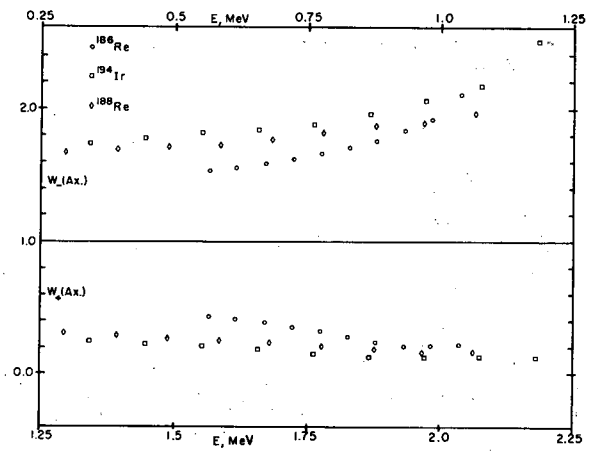

Fig. 2. Axial beta asymmetries for two signs of the polarizing field. $W_+(Ax.) = W(\pi)$ and $W_-(Ax.) = W(0)$. The upper energy scale is for the ^{186}Re data and the lower scale is for ^{188}Re and ^{194}Ir. Statistical errors are smaller than the symbols used for the data points. (XBL6912-6726)

MEASUREMENT OF THE MAGNETIC MOMENTS OF THE MICROSECOND ISOMERS IN ^{73}As AND ^{206}Pb†

D. Quitmann* and J. M. Jaklevic

Considerable alignment is given to the low-energy high-spin states populated by (α, xn) reactions. Without perturbation, the time-integrated angular distribution of gamma radiation emitted is described as $W(\theta) = 1 + \sum_k A_k P_k (\cos\theta)$, $k = 2, 4, \cdots$. The coefficients A_k depend on the spins involved, on the multipole character of the transition, and on the degree of alignment. If one applies a variable static magnetic field $H_\perp$ perpendicular to the beam-detector plane, the angular distribution becomes[1]

$$W(\theta) = 1 + \sum_k \frac{b_k/b_0}{1 + (k\omega_\perp \tau)^2} (\cos k\theta - k\omega_\perp \tau \sin k\theta), \qquad k = 2, 4 \cdots , \tag{1}$$

where $b_0 = 1 + 1/2\, A_2 + 9/16\, A_4 \cdots$, $b_2 = 3/4\, A_2 + 5/16\, A_4 \cdots$, $b_4 = 35/64\, A_4 \cdots$, and

$$\omega_\perp = g\, \mu_N\, H_\perp/\hbar , \qquad g = \mu/I\mu_N . \tag{2}$$

We have measured this change for the γ rays occurring in the decay of the $9/2^+$ isomer in ^{73}As and the 7^- isomer in ^{206}Pb, and derived the g factors, including their signs. It is to be noted that (a) no static interaction other than the one given by $H_\perp$ must be acting during the time of measurement, and (b) the time constant τ with which the anisotropic emission of the γ rays decays has to be known.

The experiments were performed at the 88-inch cyclotron by using the reactions ^{71}Ga$(\alpha, 2n)$-^{73}As or ^{204}Hg$(\alpha, 2n)^{206}$Pb and liquid metal[2] targets. The Ge(Li) detectors and the electronics were very similar to the setup described in Ref. 3. The variable field $H_\perp$ was known to within about 2%.

For ^{73}As, we derive from an angular distribution measurement ($H_\perp = 0$) and from a measurement described by Eq. (1)

$$A_2(360) = +0.34(4);\ A_4(360) = -0.05(5);\ A_2(66) = -0.20(5). \tag{3}$$

Figure 1 shows the change of the γ intensities with $H_\perp$. From this measurement and one with one of the detectors at 54 deg, we obtain

$$g = +1.03(11) \qquad \text{using } T_{1/2} = 5.8(5)\ \mu\text{sec}. \tag{4}$$

This agrees with the value $|g| = 1.146(7)$ obtained later.[4]

Given the observed coefficients A_2 and A_4 of a particular γ transition and the absence of perturbations in the isomeric level, one can derive estimates of the values of A_2 and A_4 valid for maximum alignment by using the tables and calculations of Yamazaki.[5] With these results for the 360- and 66-keV γ rays, and with the results of Refs. 6 and 7, we obtain a region of possible mixing ratios $\delta(360)$ and $\delta(66)$.[8] It amounts to the limit $\delta^2 < 10^{-2}$ for the admixture in either transition.

For the isomeric state in ^{206}Pb, the change of the γ-ray intensities with $H_\perp$ is displayed in Fig. 2. A least-squares fit of Eq. (1) to these data, neglecting the A_4 and higher terms, gave

$$g\,\tau = -(3.0 \pm 1.0) \times 10^{-6}\ \text{sec}. \tag{5}$$

Neglecting possible quadrupole relaxation and using a value for the nuclear half-life of

$T_{1/2}$ = 123 μsec, we obtain

$$g = -0.035(20). \quad (6)$$

The g factor was calculated for a $p_{1/2}\, i_{13/2}$ neutron hole configuration as g = - 0.06, using the g factors of the ^{207}Pb and ^{197}Hg moments (-0.20 with the Schmidt values). The use of more accurate wave functions[9] does not improve the agreement with experiment, giving g = 0.08.

Footnotes and References

†Condensed from UCRL-18958.
*On leave of absence from Institut für Technische Kernphysik, Technische Hochschule, Darmstadt. Present address: IV. Physikalisches Institut, Freie Universität, Berlin, W. Germany.

1. R. M. Steffen, Advan. Phys. 4, 293 (1955).
2. The experiment described failed to work for the 11/2- state in ^{101}Ru (17 μsec) which was produced by ^{100}Mo(α, 3n) in solid Mo metal; see UCRL-18958.
3. J. M. Jaklevic, C. M. Lederer, and J. M. Hollander (to be published).

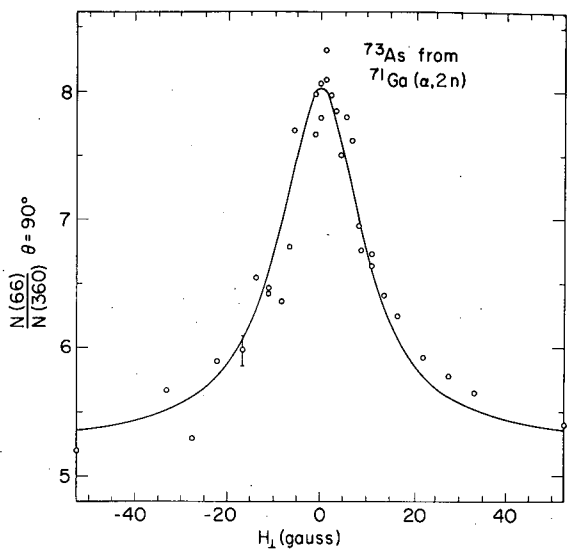

Fig. 1. Ratio of γ-ray intensities vs magnetic field $H_\perp$ for the ^{73}As 6-μsec isomer. The curve is from the least-squares fit. (XBL692-2015)

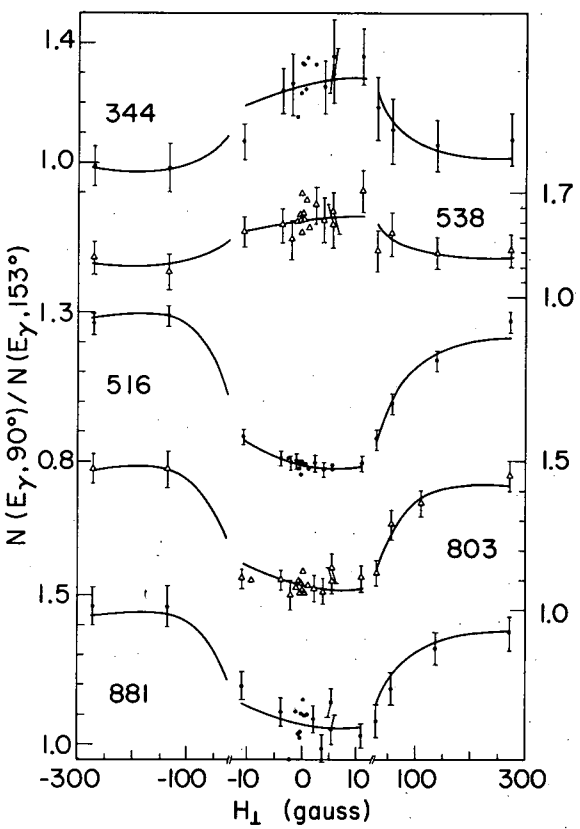

Fig. 2. Ratio of γ-ray intensities vs magnetic field for the ^{206}Pb 123-μsec isomer. The energies of the γ lines (in keV) are given between each set of points and the ordinate scale applicable. Note the changes in abscissa scale. The points in the region $H_\perp \approx 0$ have nearly the same errors as the points farther out. The curve is from the least-squares fit. (XBL698-3446)

4. D. Quitmann, J. M. Jaklevic, and D. A. Shirley, Phys. Letters 30B, 329 (1969); see also this Annual Report.
5. T. Yamazaki, Nucl. Data A3, 1 (1967).
6. E. Bodenstedt, G. Strube, W. Engels, H. Blumberg, R. -M. Lieder, and E. Gerdau, Phys. Letters 6, 290 (1963).
7. R. W. Hayward and D. D. Hoppes, Phys. Rev. 101, 93 (1956).
8. See Fig. 6 in UCRL-18958.
9. W. W. True, Phys. Rev. 109, 1675 (1958); ibid. 168, 1388 (1968).

NUCLEAR MAGNETIC RESONANCE IN A 6-μsec ISOMER PRODUCED BY A NUCLEAR REACTION†

D. Quitmann,* J. M. Jaklevic, and D. A. Shirley

The hyperfine interaction of an unstable nuclear state can be observed by the perturbation exerted on the anisotropy of the decay radiation. With the introduction of new techniques, this field of study has much expanded in recent years (see, e. g., Ref. 1). We have been able to observe nuclear magnetic resonance transitions in a γ-decaying isomer. Quite a number of isomers are amenable to this technique as they have lifetimes of 10^{-6} to 10^{-2} sec and are aligned by the producing nuclear reaction.

The isomeric state of ^{73}As at 426 keV ($I^{\pi} = 9/2^{+}$, $T_{1/2} = 5.8\,\mu$sec) was produced by the reaction ^{71}Ga(α, 2n) in a liquid gallium metal target. Due to the resulting alignment the 360- and 66-keV γ rays that de-excite the state in cascade ($9/2^{+} \rightarrow 5/2^{-} \rightarrow 3/2^{-}$) are emitted anisotropically. Since we can neglect higher-order terms, the time-integrated angular distrubions may be written $W(\theta) = 1 + A_2 \overline{G_2} P_2(\cos\theta)$. These were measured by using two Ge(Li) detectors and accepting only those pulses that occurred in the intervals between beam bursts. With no external perturbation ($\overline{G_2} = 1$), $A_2(360) = +0.34 \pm 0.05$ and $A_2(66) = -0.20 \pm 0.05$ were observed. A dc magnetic field H_0 is then added along the beam axis ($\vec{k}_1$ in the insert of Fig. 1), and an rf magnetic field $2H_1 \cos\omega t$ is applied perpendicular to it. NMR transitions occurring in the isomeric state result in an attenuation of the anisotropies of the γ rays as observed in the direction $\vec{k}_2$. This is described by the attenuation factor $\overline{G_2}$.[2] For a sizeable reduction in $\overline{G_2}$, one needs $g\mu_n H_1 T_{1/2}/\hbar \approx 1$ (e. g., 0.7 for $\overline{G_2} = 0.5$). The necessary H_1 field was produced in a very compact resonating coil system by a fixed-frequency oscillator delivering 150 watts.

Data were taken at two frequencies and four values of H_1 by sweeping H_0. Some results are presented in Fig. 1 as ratios of counts. H_1 and $\omega/2\pi$ are quoted near the curves. The experi-

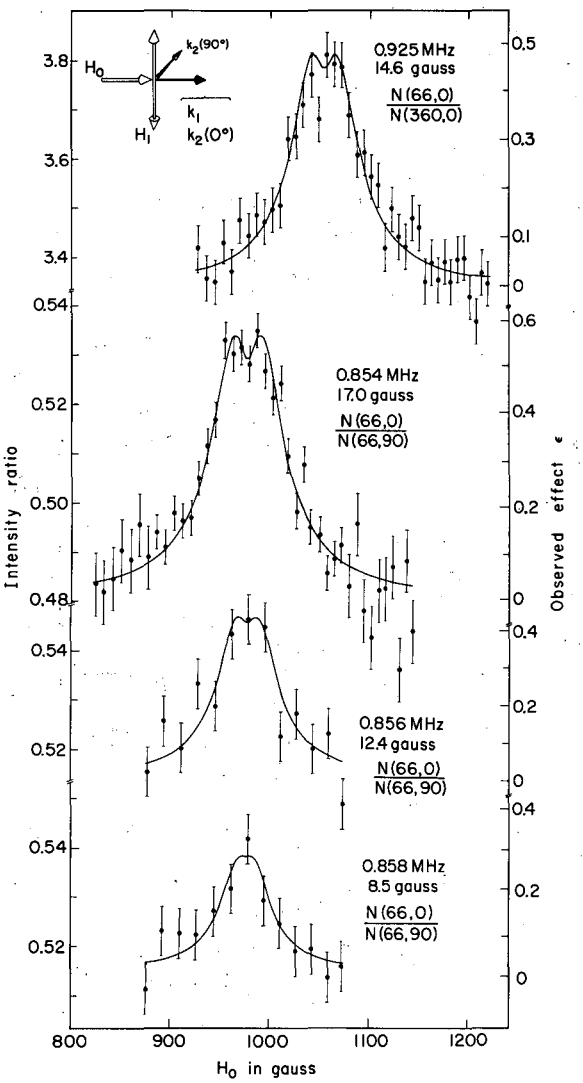

Fig. 1. Effect of NMR on the γ-ray intensities. Left scale: observed ratios. The right scales give $1-\overline{G_2}$ to within a few percent. The curves drawn are from the least-squares fits. (XBL694-2477)

mental points exhibit a non-Lorentzian line shape. Since the angular distributions transform as a second-rank tensor, one indeed expects a line shape ($\overline{G_2}$) resembling two unresolved Lorentz curves. The quantities g, $A_2(66)$, and $A_2(360)$ were obtained from each measurement by a least-squares fit using the explicit form of $\overline{G_2}$. A reduction in each A_2 was found, ascribed tentatively to unexpected perturbations in the target used. The results obtained for the g factor agree within the error of the field determinations (±0.05%). Correcting approximately for the Knight shift (+0.3%), we obtain g = 1.146±0.007. This identifies the isomer unambiguously as a $g_{9/2}$ proton state and is consistent with other states in this region.

The technique described may be applicable to accurate measurements of the hyperfine interaction for a variety of elements and host materials, including combinations which are chemically unstable. It offers advantages over the "stroboscopic" technique[3] if the experiment requires a holding field, or if there is sizeable inhomogeneous broadening.

Footnotes and References

†Condensed from Phys. Letters 30B, 329 (1969); UCRL-18871.
*On leave from Institut für Technische Kernphysik, Technische Hochschule, Darmstadt. Present address: IV. Physikalisches Institut, Freie Universität, Berlin, W. Germany.
1. Hyperfine Interactions Detected by Nuclear Radiations, ed. by E. Matthias and D. A. Shirley (North-Holland Publishing Co., Amsterdam, 1968), Chap. X.
2. B. A. Olssen, E. Matthias, and R. M. Steffen, report UUIP 583 (Uppsala, 1968); see also Ref. 1.
3. J. Christiansen, H.-E. Mahnke, E. Recknagel, D. Riegel, G. Weyer, and W. Witthun, Phys. Rev. Letters 21, 554 (1968).

STUDIES OF MACROMOLECULES IN SOLUTION USING PERTURBED ANGULAR CORRELATIONS OF GAMMA RADIATIONS†

D. A. Shirley

The rotational correlation time, τ_c, of a biological macromolecule in solution is a quantity of fundamental importance, and several techniques exist for studying it. These techniques tend to be macroscopic in nature, however, and thus are relatively insensitive. We have developed a more sensitive method for determining τ_c, based on the perturbed angular correlations of γ rays.

These "rotational tracer" experiments are carried out by binding a suitable radioactive nucleus to a macromolecule. Both ^{111}In and ^{111}Cd^{m} have been used. A decay scheme is given in Fig. 1. The nucleus decays through a γ-ray cascade. The first γ ray in the cascade is observed, and then the molecule rotates or "tumbles" during the lifetime of the intermediate state. This tumbling affects the subsequent direction of emission of the second γ ray, and the angular correlation pattern is thereby perturbed. The theory for this perturbation was developed by Abragam and Pound,[1] for very fast tumbling. For very slow tumbling a stationary theory may be used, while the intermediate tumbling-time case is more complicated and has not been treated explicitly. Figure 2 illustrates the approximate behavior to be expected for various values of τ_c. The perturbation factor $G_{22}(t)$ decays exponentially for short τ_c (Abragam-Pound limit), while a very long correlation time would be expected to give the stationary behavior shown in panel 8 of Fig. 2. Intermediate cases are also indicated, although these curves are only qualitatively correct.

Early measurements were made by using the ^{111}In parent bonded to macromolecules.[2] Results obtained by using this isotope are less quantitative than those obtained by using ^{111}Cd^{m}, because of chemical changes accompanying electron-capture decay. Still, valuable qualitative information can be obtained with ^{111}In.

In later work the 49-minute isomer was employed,[3] using a 4-detector angular correlation system designed and built by Mr. George Gabor. This system facilitated the rapid acquisition of angular correlation data that is necessary when such a short-lived parent is used. Chemical changes were avoided by using the isomeric state.

When $^{111}Cd^{m}$ was bound to bovine serum albumin, a biological macromolecule of molecular weight 10^5, the $G_{22}(t)$ function behaved as indicated in Fig. 3. This time dependence is similar to the theoretical curve in panel 8 of Fig. 2, indicating a very long τ_c, as expected, for this slowly tumbling large molecule. Similar behavior was found for equine apo-carbonic anhydrase, in which $^{111}Cd^{m}$ went into zinc-ion positions.

In EDTA (ethylenediaminetetracetic acid) of molecular weight $\approx$ 500, $^{111}Cd^{m}$ was tightly bound and $G_{22}(t)$ decayed very slowly (Fig. 4), indicating a short correlation time. The biologically important molecule ATP, which is larger, shows a slower decay of $G_{22}(t)$ (Fig. 5), and thus a longer correlation time, than EDTA. These two curves may be compared with panels 1 and 2 in Fig. 2.

Finally, $^{111}Cd^{m}$ was bound to n-benzyliminodiacetic acid (NBIDA), with which it forms dichelates, with the formula $Cd(NBIDA)_2^{2+}$. At ordinary temperatures this complex tumbles very slowly in solution. It thus has a relatively large τ_c and a rapid exponential decay of $G_{22}(t)$. This behavior is evident in Fig. 6, in which $G_{22}(t)$ resembles the theoretical curve in panel 3 of Fig. 2. When a solution containing this complex is frozen, however, the "static" curve (panel 8, Fig. 2) is observed.

The assistance of Mr. George Gabor, Mrs. Winifred Heppler, Mrs. Penny Fink, and Dr. Lloyd Robinson is gratefully acknowledged.

Footnotes and References

†The work on which this report is based was done in collaboration with J. D. Baldeschwieler, Robert G. Bryant, Thomas K. Leipert, and Claude F. Meares of the Chemistry Department, Stanford University.

1. A. Abragam and R. V. Pound, Phys. Rev. 92, 943 (1953).
2. T. K. Leipert, J. D. Baldeschwieler, and D. A. Shirley, Nature 220, 907 (1968).
3. Claude F. Meares, Robert G. Bryant, John D. Baldeschwieler, and David A. Shirley, Study of Carbonic Anhydrase Using Perturbed Angular Correlations of Gamma Radiation, submitted to Proceedings of the National Academy of Sciences, U. S. (1969).

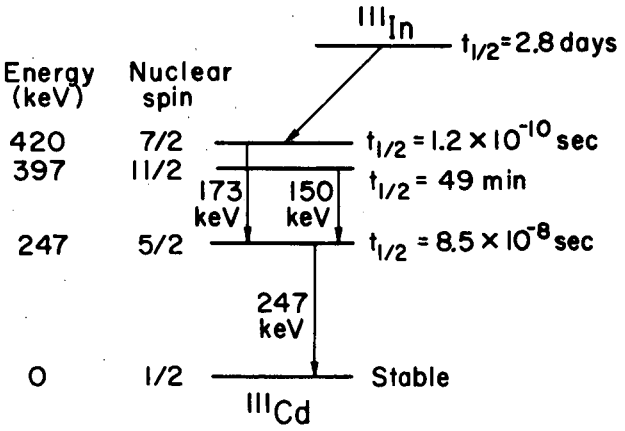

Fig. 1. The decays of 2.8-day ^{111}In and 49-min $^{111}Cd^{m}$. (XBL702-2386)

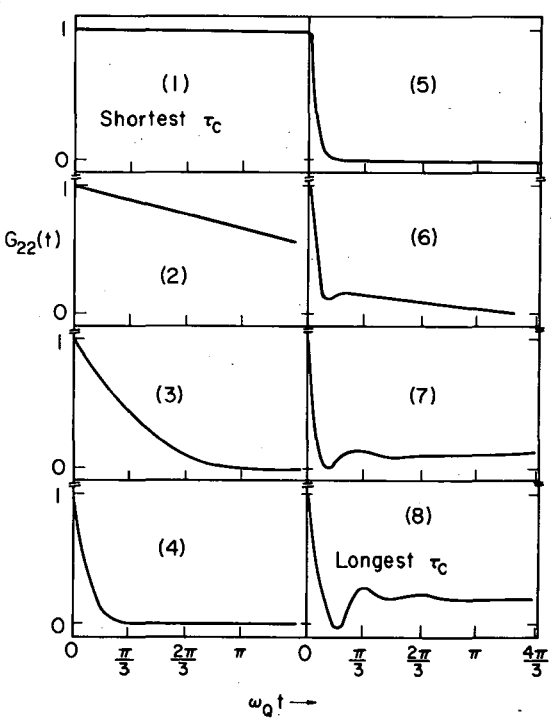

Fig. 2. Theoretical time dependences of correlation factors $G_{22}(t)$ as correlation time τ_c increases monotonically. (XBL695-2888)

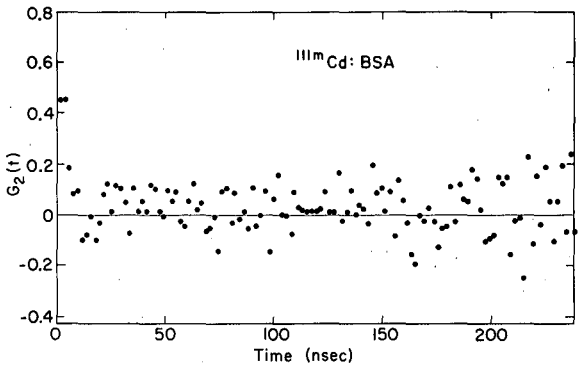

Fig. 3. The $G_{22}(t)$ function for bovine serum albumin. (XBL695-2850)

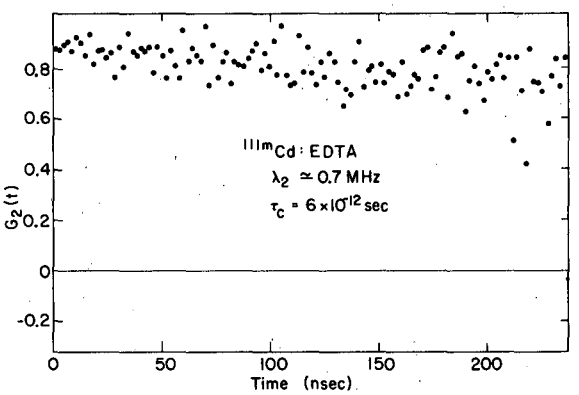

Fig. 4. The $G_{22}(t)$ function for $^{111}Cd^{m}$ bound to the small molecule EDTA. (XBL695-2852)

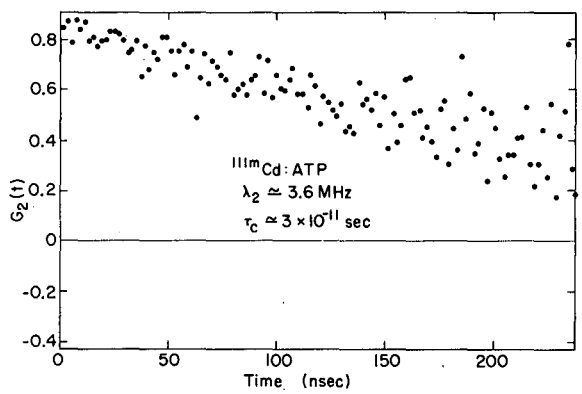

Fig. 5. The $G_{22}(t)$ function for $^{111}Cd^{m}$ bound to the ATP molecule. (XBL695-2853)

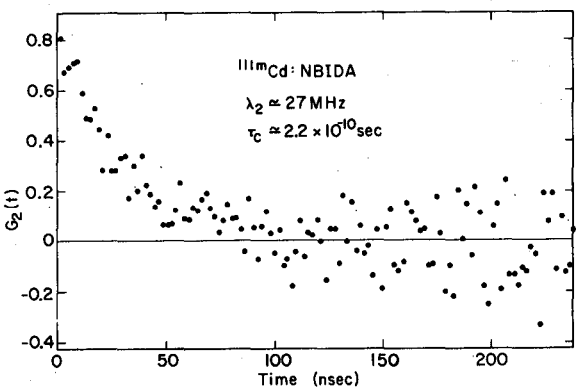

Fig. 6. The $G_{22}(t)$ function for $^{111}Cd^{m}$ bound to N-benzyliminodiacetic acid (NBIDA). (XBL695-2855)

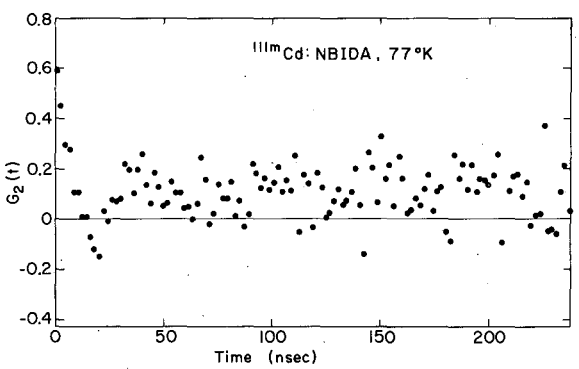

Fig. 7. As in Fig. 6, but at 77°K. (XBL695-2848)

PERTURBED ANGULAR CORRELATIONS IN FERROMAGNETS: THE ^{100}RhNi CASE

S. Koički,† T. A. Koster, R. Pollak, D. Quitmann,* and D. A. Shirley

When the intermediate state in an angular correlation cascade interacts with a magnetic field by dipole coupling,

$$\mathcal{H} = -\vec{\mu}\cdot\vec{H} = -\gamma\vec{I}\cdot\vec{H},$$

the nuclear moment precesses about $\vec{H}$ at the Larmor frequency

$$2\pi\nu_L = \gamma H,$$

where γ is the nuclear gyromagnetic ratio. Consequently the angular correlation pattern, which for dipole transitions has the form

$$W(\theta) = 1 + A_2 P_2(\cos\theta),$$

becomes

$$W(\theta,t) = 1 + A_2 P_2[\cos(\theta - 2\pi\nu_L t)] \ .$$

Because $W(\theta)$ has period π, the modulation frequency in $W(\theta,t)$ is $2\nu_L$. The determination of ν_L is a problem of central importance in the application of perturbed angular correlations to solid-state physics. In this report we describe two ways in which the techniques for determining ν_L with high accuracy for the test case ^{100}RhNi have been developed in this Laboratory.

Before 1966, an accurate determination of ν_L for ^{100}RhNi would have been impossible. Fast timing techniques were too slow for this case ($\nu_L \approx 340$ MHz), and the long lifetime ($\tau_{1/2} = 235$ nsec; see Fig. 1) precluded time-integral measurements. The problem was overcome by the development of the nuclear magnetic resonance–perturbed angular correlation (NMR-PAC) technique,[1] which was first demonstrated on the ^{100}RhNi case.

The first NMR-PAC experiments, while qualitatively successful, left several questions unanswered. In particular, the observed 2% effect was smaller than expected, and the resonance line width of 20 MHz (Fig. 2a) was far greater than the 0.94 MHz natural line width dictated by the intermediate-state lifetime. Further studies[2] served only to confirm these results; in fact, the asymmetric line was later resolved into two components (Fig. 2b).

We now understand these early results. The line width and small effect were mainly attributable to inhomogeneous broadening caused by impurities in the samples. Chemical analysis revealed Pd in the Rh metal from which ^{100}Pd was prepared by the ^{103}Rh(p, 4n) reaction. This Pd went through the chemical separations with the ^{100}Pd activity and appeared as a 1% impurity in the Ni samples. From Budnick's work[3] we would expect a ^{100}Pd atom within 2 or 3 lattice positions of a Pd impurity atom in a nickel lattice to exhibit resonance at a frequency $\approx$ 5% below the main line, and substantial line broadening would also be expected. The early spectra are fully consistent with Budnick's results for an alloy with 1% impurity.

Higher-purity alloys were prepared and further NMR-PAC experiments were carried out with the temperature and rf field intensity more carefully controlled. The resonance lines were much narrower and the NMR-PAC effect was greater, as shown in Fig. 2c. The remaining 4-MHz line width can be attributed partially to inhomogeneous broadening. ($\Delta\nu_L/\nu_L \approx 10^{-2}$ is typical for NMR line widths in ferromagnetic metals.) Power broadening is probably also of some importance and relaxation broadening may also be present. We conclude that in ferromagnets NMR-PAC can produce resonance lines that are essentially equivalent to those observed by conventional NMR.

The second approach for the determination of ν_L consists in simply improving the fast resolving time of the coincidence circuit until the precession can be observed time-differentially. With Ge(Li) detectors in earlier work,[4] the resolving time for the 84-keV — 75-keV cascade in ^{100}Rh had previously been brought down to 11 nsec FWHM. Further improvements in the Ge(Li) system have now improved this figure to 6.3 nsec FWHM. This is still too slow for the ^{100}RhNi case, since for a ν_L of 340 MHz the coincidence rate oscillates through a full cycle in only 1.5 nsec. With an unpolarized source a component with period $1/\nu_L$ = 3 nsec is present,[5] but this is still too fast for the Ge(Li) system. The highest-frequency oscillations previously observed by using low-energy γ rays were reported by Hohenemser et al.[6] for ^{57}FeNi, with ν_L = 42 MHz. The resolving time of their circuit (4.75 nsec FWHM) is too slow for the ^{100}RhNi case, however.

To solve the fast timing problem, an apparatus was built that employs Sn-doped plastic scintillators together with RCA C31000D photomultiplier tubes. The (unresolved) photopeak associated with the 84-keV — 75-keV cascade could be observed directly and a fast resolving time of 1.20 nsec FWHM was achieved. On application to an unpolarized ^{100}RhNi source, this system resolved the slow (340-MHz) component very well. A time-differential curve is shown in Fig. 3.

The data may be analyzed most conveniently by Fourier transforming them into the frequency domain. This was accomplished by procedures analogous to those described previously,[4,7] except that an analog time-to-amplitude converter and a pulse-height analyzer were used in this case. The Fourier cosine transform of the autocorrelation function of the coincidence counting rate is shown in Fig. 4. This curve is similar to an NMR line, but there is of course no rf field present. The residual line width of 4 MHz FWHM is still in excess of the natural line width (0.94 MHz). It is tempting to attribute this line width to inhomogeneous broadening, for two reasons. First, it agrees well with the NMR-PAC result of 4 MHz. Second, this width ($\Delta\nu_L/\nu_L = 10^{-2}$) is about what one would expect from experience with conventional NMR in ferromagnetic metals. It is also possible, however, that additional line broadening is introduced through relaxation processes, instrumentally, or in the rather involved data-reduction procedures. This broadening might be approximately equivalent to the effects of relaxation and power broadening in the NMR-PAC spectrum, and the good agreement of the 4-MHz line widths would then be in part fortuitous. Thus it seems best at least tentatively to regard the 4-MHz line width as an upper limit for inhomogeneous broadening.

Two other points deserve special comment. First, the resonance frequencies ν_L derived from the NMR-PAC curves in Fig. 2 and from the Fourier transform curve in Fig. 4 are different. This is attributable to inductive heating in the NMR-PAC experiments, since ν_L in ferromagnets decreases with increasing temperature. Second, an unpolarized source should exhibit a high-frequency oscillation in $W(\theta,t)$ at frequency $2\nu_L$. This component is directly apparent in the $W(\theta,t)$ curve in Fig. 3, where its most pronounced effect is to give the low-frequency peaks a "cusped" appearance. It should show up even more clearly in the Fourier transform function. That it does so is demonstrated in Fig. 5. Although the signal-to-noise ratio is smaller than for the resonance at ν_L, the resonance at $2\nu_L$ is unmistakably present. This frequency ($2\nu_L$ = 680 MHz) is over an order of magnitude higher than any observed previously by perturbed angular correlations.

It is a pleasure to thank Dr. E. Matthias for his continued interest in, and contributions to, the development of this field, Mr. George Gabor for his contributions to the development of both the NMR and the fast timing apparatus, Miss Claudette Rugge and Mrs. Esther Schroeder for writing the computer programs used in our analysis, and Mrs. Winifred Heppler for carrying out and improving the sample preparation.

Footnotes and References

†On leave from Boris Kidrič Institute, Beograd, Yugoslavia.
*On leave from Institut für Technische Kernphysik, Technische Hochschule, Darmstadt. Present address: IV. Physikalisches Institut, Freie Universität, Berlin, W. Germany.

1. E. Matthias, D. A. Shirley, M. P. Klein, and N. Edelstein, Phys. Rev. Letters 16, 974 (1966).
2. E. Matthias, D. A. Shirley, N. Edelstein, H. J. Körner, and B. A. Olsen, Resonance Destruction of Angular Correlations: ^{100}Rh in Fe and Ni, in Hyperfine Structure and Nuclear Radiations, ed. by E. Matthias and D. A. Shirley (North-Holland Publishing Co., Amsterdam, 1968).
3. J. Budnick, Nuclear Resonance in Metallic Ferromagnets, in Magnetic Resonance and Radio-frequency Spectroscopy, ed. by P. Averbuch (North-Holland Publishing Co., Amsterdam, 1969).
4. G. N. Rao, E. Matthias, and D. A. Shirley, Phys. Rev. 184, 325 (1969).
5. E. Matthias, S. S. Rosenblum, and D. A. Shirley, Phys. Rev. Letters 14, 46 (1965).
6. C. Hohenemser, R. Reno, H. C. Benski, and J. Lehr, Phys. Rev. 184, 298 (1969).
7. E. Matthias and D. A. Shirley, Nucl. Instr. Methods 45, 309 (1966).

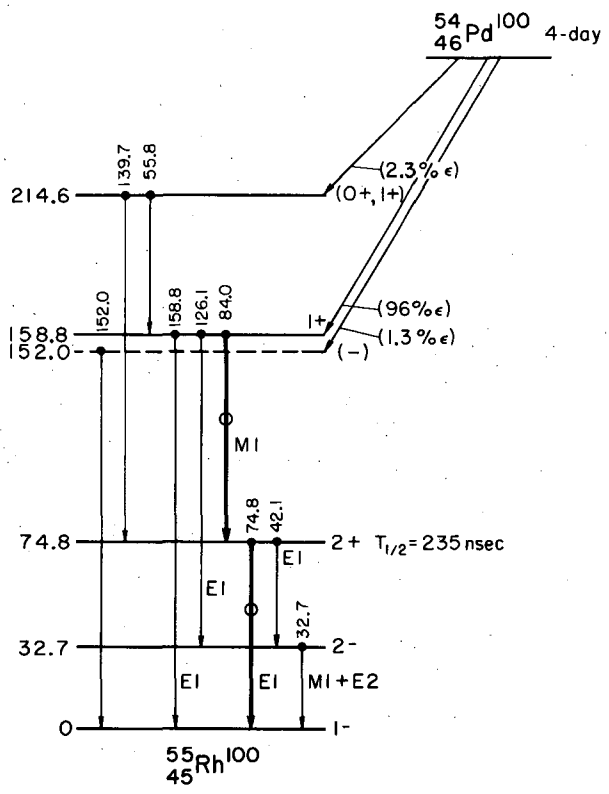

Fig. 1. Decay scheme of ^{100}Pd → ^{100}Rh. (MUB-6309)

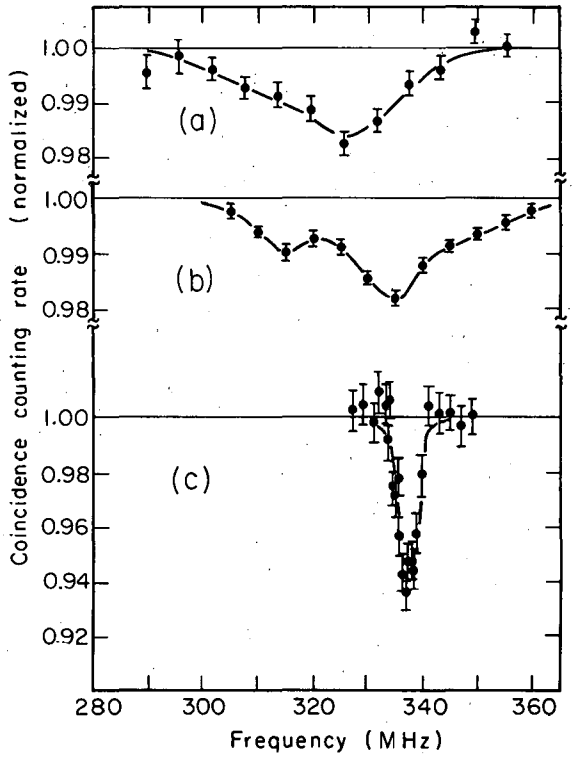

Fig. 2. NMR/PAC spectra for ^{100}RhNi: (a) Reference 1 (1966), (b) Reference 2 (1968), and (c) unpublished (1969). In (a) and (b) the wide and asymmetric absorption areas are attributed to the presence of Pd impurities in the Ni host. In (c), the low frequency component is no longer present and the effect is tripled to 6%. (XBL701-2204)

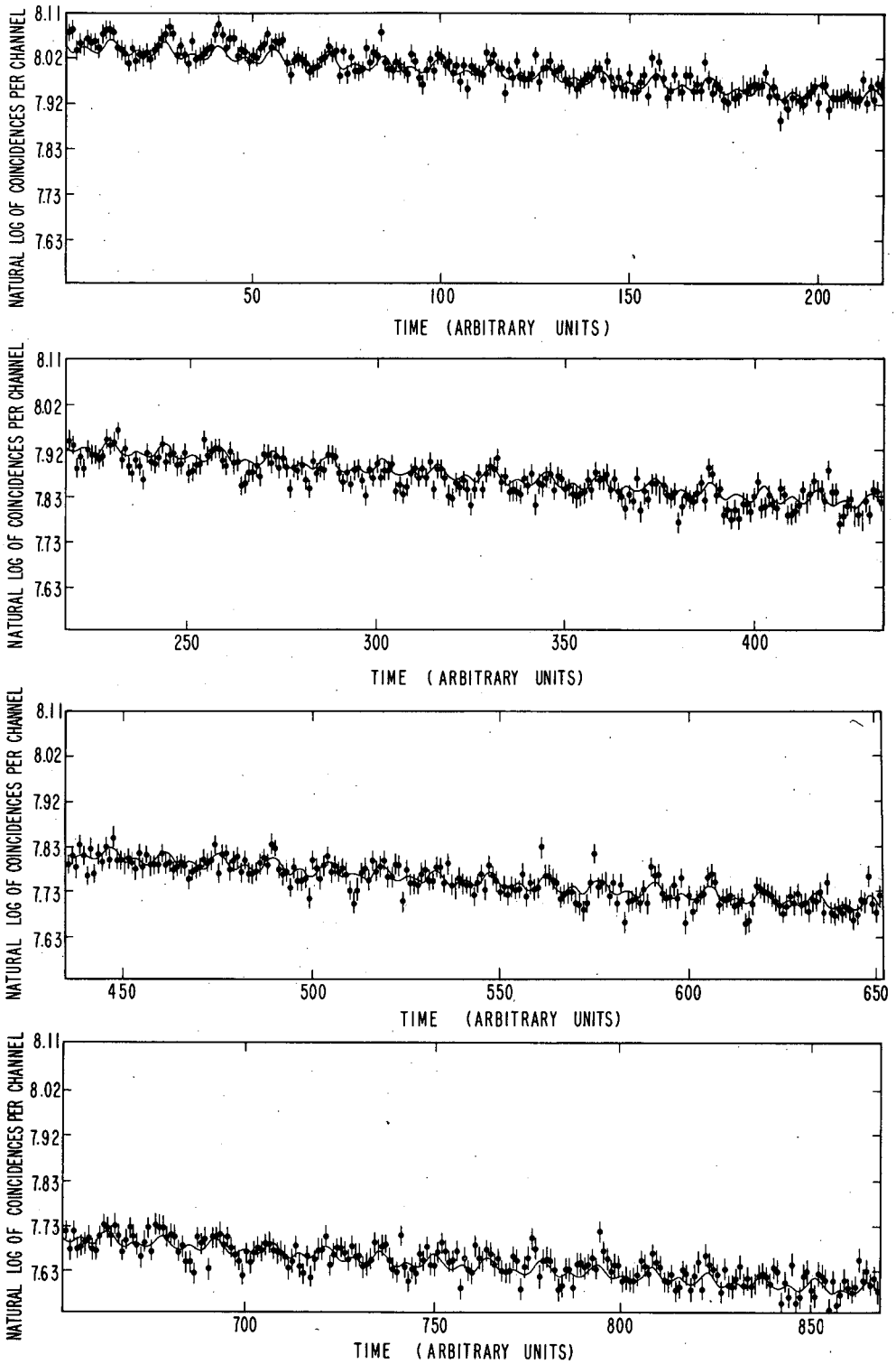

Fig. 3. Time-differential perturbed angular correlation spectrum for the 74.8-keV, 2^+ state of ^{100}Rh in Ni. (XBL702-297, -296, -299, -298)

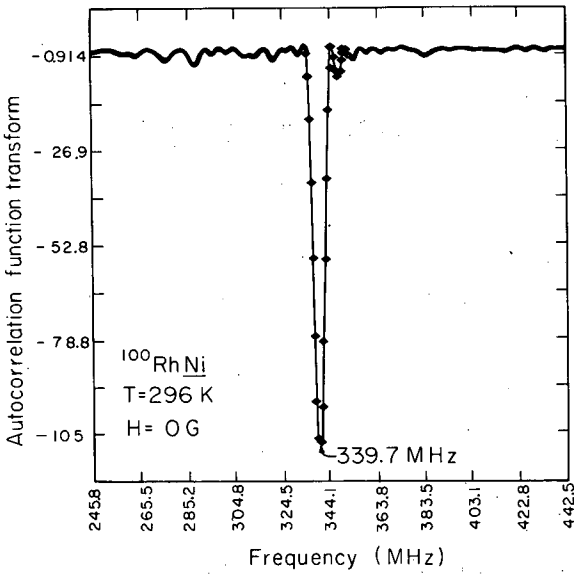

Fig. 4. Fourier cosine transform of the autocorrelation function of the coincidence counting rate showing the Larmor resonance frequency ν_L = 339.7±1.2 MHz, yielding a hyperfine field $|H_{hf}|$ = 207.2±1.1 kG. (XBL701-2206)

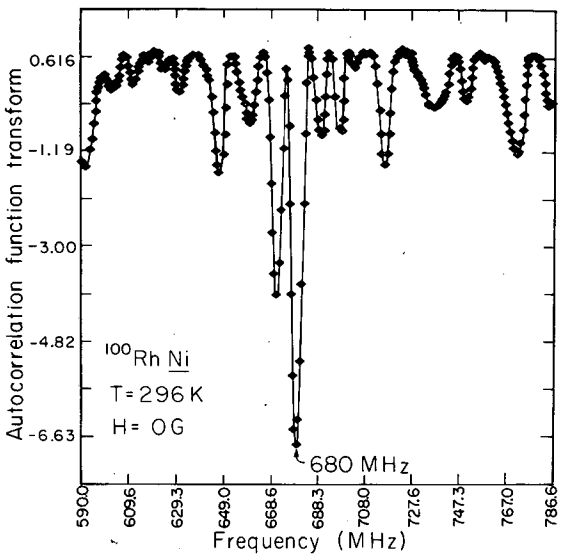

Fig. 5. Fourier cosine transform of the autocorrelation function of the coincidence counting rate showing the high frequency component at $2\nu_L$ = 680 MHz. (XBL701-2205)

THEORETICAL STUDIES OF ATOMIC AND MOLECULAR HYPERFINE STRUCTURE

Henry F. Schaefer III

Recent advances in ab initio quantum-mechanical calculations have made it increasingly practical to make qualitative and even quantitative predictions of atomic and molecular hyperfine parameters. During the past six months we have completed three studies[1-3] which illustrate the present "state of the art" in theoretical predictions of hyperfine structure.

At present the simplest and therefore most appropriate nonempirical method by which to study a polyatomic molecule such as SiH_4 is the self-consistent-field (SCF) molecular orbital approximation. Using a large basis set of s-, p-, and d-type contracted Gaussian functions, we have made the first accurate SCF studies[1] of polyatomic molecules containing second-row atoms. For SiH_4, PH_3, H_2S, and HCl, we obtained total energies estimated within 0.04 Hartree atomic units of the true Hartree-Fock energies. In addition, a large number of molecular properties were computed, including dissociation energies, ionization potentials, molecular multipole moments, magnetic susceptibilities, magnetic shielding, chemical shifts, and electric field gradients. In particular the calculated electric field gradients were used in conjunction with experimental quadrupole coupling constants[4] to deduce the nuclear electric quadrupole moments of ^{33}S (0.065 b), ^{35}S (-0.045 b), ^{35}Cl (-0.080 b), and ^{37}Cl (-0.063 b). The above quadrupole moments are the most reliable yet obtained for these four nuclei and are expected to be within 10% of the exact quadrupole moments.

The spin density $|\psi(0)|^2$, or Fermi contact interaction,

$$|\psi(0)|^2 = \langle J = L+S,\ M_J = J | \sum_i \delta(\vec{r}_i) S_{zi} | J = L+S,\ M_J = J \rangle \ , \qquad (1)$$

is one of the most difficult expectation values to calculate quantum-mechanically. Nonvanishing spin densities for p^n and d^n atomic configurations are commonly explained as a manifestation of "core polarization." Core polarization is most often described quantum-mechanically within the unrestricted Hartree-Fock (UHF) approximation. However, such calculations[5] have been of

varying accuracy and carried out for only a small number of atoms. Therefore, we have carried out[2] high accuracy numerical UHF calculations for the ground states of the atoms Li through Br and the ions Sc^{2+} through Cu^{2+}. This work establishes clearly that the UHF method is capable of reproducing experimental trends (such as the increase in spin density across the transition metal series), but that the UHF spin densities differ by as much as a factor of 2.5 from the experimental values.

The next logical step beyond the UHF approximation is configuration interaction (CI). In previous work[6] we have introduced two limited types of CI wave functions, the polarization and first-order wave functions. In particular it was found that the polarization wave function yielded values of the hfs parameters $\langle r_\ell^{-3} \rangle$, $\langle r_s^{-3} \rangle$, and $\langle r_q^{-3} \rangle$, within 2% of experiment. In this most recent work,[3] polarization and first-order functions have been used to study the positive and negative ions of first-row atoms. The results[3] are of interest because (a) hfs parameters yield important basic information concerning the structure of an electronic state and (b) it now appears[7] that experimental measurements of hfs constants will soon be possible for positive ions such as O^+.

References

1. S. Rothenberg, R. H. Young, and H. F. Schaefer, Ground State Self-Consistent-Field Wave Functions and Molecular Properties for the Isoelectronic Series SiH_4, PH_3, H_2S, and HCl, J. Am. Chem. Soc. (in press).
2. P. S. Bagus, B. Liu, and H. F. Schaefer, Contact Hyperfine Structure from Spin Unrestricted Hartree-Fock Wave Functions for Li to Br and Sc^{2+} to Cu^{2+}, Phys. Rev. (in press).
3. H. F. Schaefer and R. A. Klemm, Atomic Hyperfine Structure IV. Positive and Negative First Row Ions, Phys. Rev. (in press).
4. C. A. Burrus and W. Gordy, Phys. Rev. 92, 274 (1953); C. A. Burrus, W. Gordy, B. Benjamin, and R. Livingston, Phys. Rev. 97, 1661 (1955).
5. R. E. Watson and A. J. Freeman, in Hyperfine Interactions, ed. by A. J. Freeman and R. B. Frankel (Academic Press, Inc., New York, 1967), p. 53.
6. H. F. Schaefer, R. A. Klemm, and F. E. Harris, Phys. Rev. 176, 49 (1968); 181, 137 (1969).
7. J. S. M. Harvey, private communication.

HYPERFINE STRUCTURE OF TRIVALENT Pu†

N. M. Edelstein and R. J. Mehlhorn*

Values of the nuclear dipole moment of ^{239}Pu derived from different types of measurements varied widely when the data were first analyzed. Subsequent analyses showed these results could be brought into agreement by a complete theoretical treatment including intermediate coupling and core polarization effects.[1] Attempts to explain the sign of the core polarization term with basis wave functions obtained from the central field model of atomic structure proved inadequate until admixtures of continuum states were included.[1] Unfortunately, this type of calculation is very difficult. Exchange-polarized Hartree-Fock calculations were able to account for the sign and approximate magnitude of core polarization effects in the lanthanide series.[2] In this paper, using the known nuclear dipole moment of ^{239}Pu,[3] we derive values for the core polarization term and $\langle 1/r^3 \rangle$ for trivalent Pu. The latter quantity is compared with values calculated from various theoretical models.

The electron paramagnetic resonance spectra of Pu^{3+}, $5f^5$, have recently been measured in cubic symmetry sites in CaF_2, SrF_2, and BaF_2. The Zeeman splitting factors (g values) have been interpreted by calculating the crystalline field mixing of the first excited J = 7/2 state with ground J = 5/2 state.[4] In this paper the hyperfine structure associated with the ^{239}Pu nucleus (I = 1/2) is interpreted in a similar manner. From this analysis we obtain the hyperfine coupling constants for two different J levels in the crystal and deduce values for $\langle 1/r^3 \rangle$ and core polarization.

In Table I we list the experimental data for Pu^{3+} in various alkaline earth fluorides that we will need for this analysis.

For the nonrelativistic theory that we shall use, A, the hyperfine constant may be divided into two parts:

$$A = A_f + A_c,$$

where

$$A_f = \theta \langle \psi | \Sigma \underset{\sim}{N}_i | \psi \rangle,$$

$$A_c = \langle \psi | \Sigma \underset{\sim}{s}_i | \psi \rangle C,$$

and $\theta = [4\beta\beta_N\mu_N/I]\langle 1/r^3 \rangle$ and C is the parameter combining relativistic and core polarization effects. The parameter $\langle 1/r^3 \rangle$ is the expectation value of this quantity for the f electrons and may be compared to theoretical calculations. The operators $\underset{\sim}{N}$ and $\underset{\sim}{s}$ for the ith electron are the appropriate hyperfine operators and are defined in the paper of Bordarier et al.[5] The values of the necessary matrix elements for Pu^{3+} in CaF_2, SrF_2, and BaF_2 are given in Table II. From the quantities in Tables I and II we determine $\theta = 9.810\times10^{-3}$ cm^{-1} and C = - 0.0147 cm^{-1}. Using these values we calculate the hyperfine parameters for pure J = 5/2 and J = 7/2 free ion states that are given in Table III. From this table we derive for Pu^{3+} free ion:

$$a_c = -(556\pm42)\frac{\mu_N}{I} \text{ MHz}.$$

From the value of θ we calculate

$$\langle 1/r^3 \rangle_{Pu^{3+}} = (7.57\pm0.5) \text{ au}.$$

Dr. D. T. Cromer has sent us the wave functions obtained from his Dirac-Slater calculations.[6] We have integrated these wave functions and find $\langle 1/r^3 \rangle_{Pu^{3+}} = 6.77$ au. Our results show that core polarization is much larger for a trivalent ion of the actinide series than the lanthanide series,[7] and that a Dirac-Slater calculation appears to give too low a value for $\langle 1/r^3 \rangle_{Pu^{3+}}$.

Footnotes and References

†Condensed from a manuscript in preparation.

*Present address: Department of Genetics, University of California, Berkeley, California.

1. J. Bauche and B. R. Judd, Proc. Phys. Soc. 83, 145 (1964) and references contained in this paper.
2. A. J. Freeman, in Hyperfine Structure and Nuclear Radiations, ed. by E. Matthias and D. A. Shirley (North-Holland Publishing Company, Amsterdam, 1968), p. 427.
3. J. Faust, R. Marrus, and W. A. Nierenberg, Phys. Letters 16, 71 (1965).
4. N. Edelstein, H. Mollet, W. Easley, and R. Mehlhorn, J. Chem. Phys. 51, 3281 (1969).
5. Y. Bordarier, B. R. Judd, and M. Klapisch, Proc. Roy Soc. (London) A289, 81 (1965).
6. We wish to thank Dr. D. Cromer for sending us his calculated wave functions.
7. B. Bleaney, in Proceedings of the Third International Congress on Quantum Electronics, ed. by P. Grivet and N. Bloembergen (Columbia University Press, New York, 1964), p. 595.

Table I. Spin Hamiltonian parameters for Pu^{3+} in various alkaline earth fluorides.

Ion	Matrix	|g|	|A| ($cm^{-1} \times 10^{-3}$)
Pu^{3+}	CaF_2	1.297±0.002	6.72±0.06
Pu^{3+}	SrF_2	1.250±0.002	8.45±0.1
Pu^{3+}	BaF_2	1.187±0.004	10.2 ±0.3

Table II. Matrix elements for Pu^{3+} in various alkaline earth fluorides.

Ion	Matrix	$\langle \psi \vert \Sigma \bar{N}_i \vert \psi \rangle$	$\langle \psi \vert \Sigma \bar{s}_i \vert \psi \rangle$
Pu^{3+}	CaF_2	-0.644	0.0276
Pu^{3+}	SrF_2	-0.733	0.0858
Pu^{3+}	BaF_2	-0.832	0.154

Table III. Hyperfine parameters for Pu^{3+} free ion J states.

	a ($cm^{-1} \times 10^{-3}$)	a_f ($cm^{-1} \times 10^{-3}$)	a_c ($cm^{-1} \times 10^{-3}$)
J = 5/2	11.51	7.21	4.30
J = 7/2	6.18	5.18	1.00

Photoelectron Spectroscopy

MULTIPLET SPLITTING OF METAL CORE-ELECTRON BINDING ENERGIES†

C. S. Fadley, D. A. Shirley, A. J. Freeman,* P. S. Bagus,‡ and J. V. Mallow*

In any atomic system with unpaired valence electrons, the exchange interaction affects core electrons with spin up and spin down differently. This interaction is responsible for the well-known core polarization contributions to magnetic hyperfine structure.[1] The binding energies of core electrons are also affected. For example, spin-unrestricted Hartree-Fock (SUHF) calculations predict large splittings in the core electron energy eigenvalues of transition-metal ions[2] (≈ 12 eV for the 3s level of atomic iron), and it has been pointed out that these splittings should be reflected in measured binding energies.[3] By use of x-ray photoelectron spectroscopy such splittings were sought in core-level peaks from iron and cobalt metal, but with negative results.[3] Recently, splittings of ≈1 eV have been observed in the 1s photoelectron peaks of the paramagnetic molecules O_2 and NO.[4] We report here the observation of ≈6 eV splittings in the 3s levels of Mn and Fe in various magnetic solids.[5,6] Theoretical calculations for free atoms[5,6] and small clusters[7] predict the essential features of these splittings.[8] Photoelectron spectra from gaseous Eu also show some evidence for these effects.[6]

The experimental procedure has been described previously.[3,9] Samples were bombarded with x rays of ≈1 keV energy (primarily $MgK\alpha_{1,2}$, 1253.6 eV). The ejected electrons were analyzed for kinetic energy in the Berkeley iron-free spectrometer. The kinetic energy distributions so obtained contain photoelectron peaks corresponding to excitation from all the accessible core and valence electronic levels in the sample. If a photoelectron peak involves only the ejection of one electron from the parent system, the observed kinetic energy (E_{kin}) is directly related to the difference in energy between the initial state of the system and the final state after photoemission by

$$h\nu = E_f - E_i + E_{kin} + \text{work function and charging corrections}, \qquad (1)$$

where E_i is the total energy of the initial state, E_f is the total energy of the final state with a hole in some subshell. The quantity $E_f - E_i$ is the binding energy of the electron removed from the subshell, relative to a final state corresponding to E_f. The work function and charging corrections are constant for a given sample and so can be disregarded in the measurement of splittings.[9] If the ejection of an electron from a given subshell can result in several final states of the system, a corresponding number of photoelectron peaks is observed.

Measurements were made on Mn levels in MnF_2, MnO, and MnO_2, and on Fe levels in FeF_3, Fe metal, and $K_4Fe(CN)_6$. Figure 1 shows the spectra obtained from these materials in the region corresponding to ejection of 3s and 3p electrons from the transition-metal atoms. Also noted are significant peaks in these spectra resulting from the weaker $MgK\alpha_3$ and $MgK\alpha_4$ x rays. All samples were studied at room temperature at a pressure of approximately 10^{-5} torr with the exception of iron metal, which was heated in a hydrogen atmosphere to clean its surface.[3]

Table I summarizes our experimental results for the 3s region, and for convenience of interpretation presents the free-ion electron configurations. We see that the $3d^5$ compounds exhibit two peaks, denoted 3s(1) and 3s(2). MnO_2 shows a somewhat weaker 3s(2) peak at smaller separation, and $K_4Fe(CN)_6$ shows essentially no 3s(2) peak. Iron metal exhibits a distinct shoulder (not observed in earlier work because of poor statistics[3]) which persists with no appreciable change from 810°C above the Curie point) to 565°C. All spurious sources of an extra peak in the 3s region can be ruled out.[5] The separations and relative intensities of these peaks as derived by least-squares fits of standard peak shapes[6] are presented in Table I. Also noted in Fig. 1 and Table I are those cases in which known properties and the observation of broadening of certain photoelectron peaks seem to indicate slight chemical reaction within the thin (≈ 10^{-6} cm) surface layer that produces photoelectrons in the full-energy inelastic peaks. These results are consistent with the two peaks 3s(1) and 3s(2) representing two final states of the Mn(Fe) ion split primarily by the exchange interaction. That is, the 3s(2) peak is observed for cases in which d electrons are known to couple to a high-spin ground state (MnF_2, MnO, FeF_3, and ferromagnetic Fe) and is reduced in separation and intensity relative to 3s(1) for cases in which the number of unpaired 3d electrons is smaller (MnO_2) or the transition-metal ion exists in a diamagnetic ground state [$K_4Fe(CN)_6$].

Also consistent with this interpretation is an analogous spectrum from Cu metal (d-electron configuration $3d^{10}$), which shows a narrow, single 3s line such as observed in $K_4Fe(CN)_6$.

We now consider such splittings theoretically, using the free Mn^{2+} ion as an illustrative example. The initial state is $3d^5\ ^6S$, and the ejection of a 3s or 3p electron gives rise to final states which we denote as $Mn^{3+}[3s]$ and $Mn^{3+}[3p]$ respectively. In first approximation, we can make use of Koopmans' theorem, which states that the binding energies of ejected electrons are given by their one-electron energy eigenvalues, ϵ_i, calculated for the ground-state configuration of Mn^{2+}. Since a detailed allowance for exchange predicts that, for any shell $\epsilon_i^\alpha \neq \epsilon_i^\beta$ (where α, β denote spin directions), two peaks are predicted for photoemission from both the 3s and 3p levels. The simplest estimate for this effect treats the exchange interaction as a perturbation which splits the restricted Hartree-Fock (RHF) 3s and 3p one-electron eigenvalues, and yields the values given in Table II, line 1. SUHF calculations represent a higher-order estimate, but the energy splittings are not appreciably altered (see Table II, line 2).

This use of Koopmans' theorem to equate binding energies to ϵ_i is known to have shortcomings. The correct definition of electron binding energy is given as the difference between computed total energies for initial and final states (cf. Eq. 1). The possible final states are ^7S and ^5S for $Mn^{3+}[3s]$, and ^7P and ^5P for $Mn^{3+}[3p]$. But, unlike the other final states just given, the ^5P state can be formed in three different ways from parent d^5 terms of ^6S, ^4P, and ^4D. This multiplicity predicts four final states for $Mn^{3+}[3p]$ instead of two final states as in the SUHF scheme, and rules out the simple connection of 3p photoemission splittings (or splittings of any non-s electron) to ground-state one-electron energies. We have calculated the total energies of these final states, using two "multiplet hole theory" (MHT) methods: diagonalization of the appropriate energy matrix, assuming Coulomb and exchange integrals to be given by RHF single-determinant values for the initial state (a frozen orbital approximation), and more accurate multiconfiguration Hartree-Fock calculations on the final hole states (an optimized orbital calculation). The results are presented in Table II, lines 4 and 5. The agreement between frozen orbital and optimized orbital estimates is very good, with slightly larger splittings for the optimized orbitals. These results confirm the essential equivalence between the MHT and exchange polarization views for the splittings of s electron levels. No such equivalence exists for non-s electron levels.

The results of Table II are borne out qualitatively by our 3s spectra from MnF_2, MnO, and FeF_3. The 3s region shows a doublet whose weaker component lies at lower kinetic energy, in agreement with a calculated ratio of 7:5 for ^7S:^5S relative intensities based on one-electron transitions in photoemission.[6] However, the observed separation of approximately 6 eV is only about half the value predicted by the free-ion calculations. Although electron-electron correlation acts to reduce the theoretical splittings,[3] a greater reduction is expected from the effects of covalency in chemical bonding. This effect can be estimated from the spin- and orbital-unrestricted Hartree-Fock (UHF) calculation by Ellis and Freeman[7] for the $(MnF_6)^{4-}$ cluster. Their predicted splittings of energy eigenvalues, listed in Table II, line 3, show a substantial decrease from the free-ion values and rather remarkable agreement with the measured splittings in MnF_2. The reduced splitting (5.7 eV) in MnO is consistent with the well-known effects of covalency in that oxygen coordination is more covalent than fluorine coordination. On the other hand, the larger splitting observed for FeF_3 over MnF_2 is consistent with free-ion calculations that give a greater exchange splitting for Fe^{3+} than for Mn^{2+}. The measured ratio of separations for MnF_2 and MnO_2 (1.41:1.00) is larger than the computed free-ion ratio for Mn^{2+} and Mn^{4+} (1.22:1.00), as expected from covalent bonding effects.

The observed 3s(1):3s(2) intensity ratio of ≈2.0:1.0 for MnF_2 and MnO does not agree with the ^7S:^5S ratio of 1.4:1.0 obtained from a free-atom calculation based on one-electron transitions. The 1.5:1.0 ratio for FeF_3 does agree, but the apparent surface reaction indicates that this agreement is probably fortuitous. There are, however, several reasons for a discrepancy between such simple estimates and experiment.[5]

The 3p regions of the spectra in Fig. 1 show several extra peaks, which have been labeled. The peaks 3p(2) and 3p(3) of $K_4Fe(CN)_6$ appear to be associated with two-electron transitions of potassium, and are not observed in similar spectra from $Na_4Fe(CN)_6$ and $(NH_4)_4Fe(CN)_6$. The extra peaks for MnF_2, MnO_2, and FeF_3 may be related to multiplet splittings, however. There is at least qualitative agreement with the predictions of our MHT calculations in that peaks resulting from p-electron ejection are spread out in intensity over a broad region. However, further experimental and theoretical study will be necessary to assign the observed 3p peaks to specific final hole states.

Similar effects should also be observed in photoelectron spectra from gaseous metals, and

recent work[6] indicates that this is at least qualitatively the case. Atomic Eu, with a half-filled 4f shell, should exhibit multiplet splittings analogous to those of Mn^{2+}, with a half-filled 3d shell. The nearby atoms Xe and Yb, with filled outer shells, should not show these effects. Unfortunately, the 4s levels of these atoms (for which the splittings should be largest and have the simplest interpretation) do not give photoelectron peaks with sufficient intensity to be studied at present. Figure 2 presents the more intense 4d spectra from gaseous Xe, Eu, and Yb.[6] The basic structure of the spin-orbit doublet is observed for all three, and the separation of the two components is close to that predicted by theory.[10] The increase in linewidth from Xe to Eu to Yb can be ascribed to a decrease in the lifetime of the 4d hole state. The only obvious peculiarity in the Eu spectrum is that the left component of the doublet is definitely weaker than for Xe or Yb. The intensity ratios of these two components as derived by least-squares fits are: X, 1.47:1.00; Eu, 2.29:1.00; and Yb, 1.55:1.00. The theoretical ratio for a simple spin-orbit doublet is 1.50:1.00, in agreement with the ratios for Xe and Yb. A further anomaly in Eu is that the experimental separation of the two peaks is 4.8 eV, compared with 5.8 eV for solid Eu_2O_3 (for which covalency might be expected to reduce multiplet effects). Thus, although no theoretical calculations are available for the Eu^{1+}[4d] hole state, the experimental results indicate that multiplet effects may be present in the photoelectron spectrum of gaseous Eu.

Footnotes and References

†Work partially supported by the Air Force Office of Sponsored Research and Advanced Research Projects Agency, through the Northwestern University Materials Research Center.
*Department of Physics, Northwestern University, Evanston, Illinois 60201.
‡IBM Research Laboratory, San Jose, California 95114.
1. A. J. Freeman and R. E. Watson, Magnetism, Vol. IIA, ed. by G. Rado and H. Suhl (Academic Press, Inc., New York, 1965), p. 167.
2. J. H. Wood and G. W. Pratt, Jr., Phys. Rev. 107, 995 (1957); R. E. Watson and A. J. Freeman, Phys. Rev. 120, 1125, 1134 (1960); and P. S. Bagus and B. Liu, Phys. Rev. 148, 79 (1966).
3. C. S. Fadley and D. A. Shirley, Phys. Rev. Letters 21, 980 (1968), and C. S. Fadley and D. A. Shirley, in Nuclear Chemistry Annual Report, 1968, UCRL-18667, Jan. 1969, p. 247.
4. J. Hedman, P.-F. Hedén, C. Nordling, and K. Siegbahn, Phys. Letters 29A, 178 (1969).
5. C. S. Fadley, D. A. Shirley, A. J. Freeman, P. S. Bagus, and J. V. Mallow, Phys. Rev. Letters 23, 1397 (1969).
6. Charles S. Fadley, Core and Valence Electronic States Studied With x-Ray Photoelectron Spectroscopy (Ph. D. thesis), UCRL-19535, Feb. 1970.
7. D. E. Ellis and A. J. Freeman, in preparation.
8. The splittings reported here are probably not of precisely the same origin as previously reported "electrostatic" splittings of core levels in heavy metals [T. Novakov and J. M. Hollander, Phys. Rev. Letters 21, 1133 (1968)].
9. C. S. Fadley, S. B. M. Hagström, M. P. Klein, and D. A. Shirley, J. Chem. Phys. 48, 3779 (1968).
10. F. Herman and S. Skillman, Atomic Structure Calculations (Prentice-Hall, Inc., Englewood Cliffs, N. J., 1963).

Table I. Transition metal ion electron configuration for the solids indicated in Fig. 1, together with experimental separations and ratios of the 3s photoelectron peaks.

Atom	Compound	Electron configuration	3s(1)-3s(2) separation (eV)	3s(1):3s(2) intensity ratio
Mn	MnF_2	$3d^5\ ^6S$	6.5	2.0:1.0
	MnO	$3d^5\ ^6S$	5.7	1.9:1.0
	MnO_2[a]	$3d^3\ ^4F$	4.6	2.3:1.0
Fe	FeF_3[b]	$3d^5\ ^6S$	7.0	1.5:1.0
	Fe	$(3d^6\ 4s^2)$	4.4	2.6:1.0
	$K_4Fe(CN)_6$	$(3d^6)$	---	>10:1

a. Probably slightly reduced; often a nonstoichiometric compound.
b. Probably slightly reduced.

Table III. Theoretical predictions of core electron binding energy splittings (eV).

Final state:	Mn^{3+}[3s]		Mn^{3+}[3p]	
Description:	3sα hole	3sβ hole	3pα hole	3pβ hole
(1) RHF + exchange perturbation (Mn^{2+})	11.1	0	13.5	0
(2) SUHF (Mn^{2+})	11.3	0	13.7	0
(3) UHF, $(MnF_6)^{4-}$ cluster (Ref. 7)	6.8	0	8.1	0

Description:	^5S	^7S	$^5P_1$	$^5P_2$	$^5P_3$	^7P
(4) MHT, frozen orbital[a]	13.3	0	22.4	8.5	3.6	0
(5) MHT, optimized orbital[b]	14.3	0	23.8	9.4	4.0	0

a. Orbitals obtained from an RHF calculation on Mn^{2+} $3d^5$ ^6S.
b. Values based on multiconfiguration Hartree-Fock calculations for Mn^{3+}[3s] and Mn^{3+}[3p].

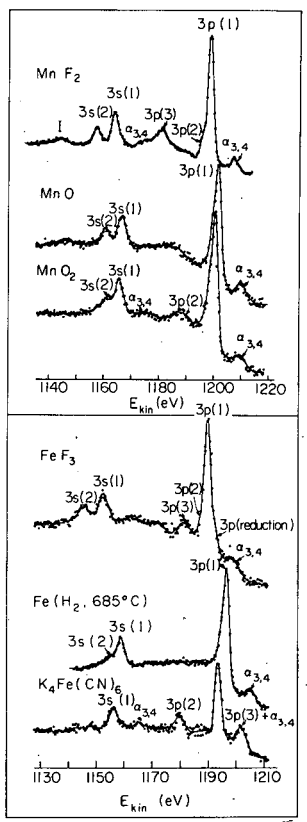

Fig. 1. Photoelectron spectra in the region corresponding to ejection of 3s and 3p electrons from Mn and Fe in various solids. MgKα radiation was used for excitation. (XBL 698-3635)

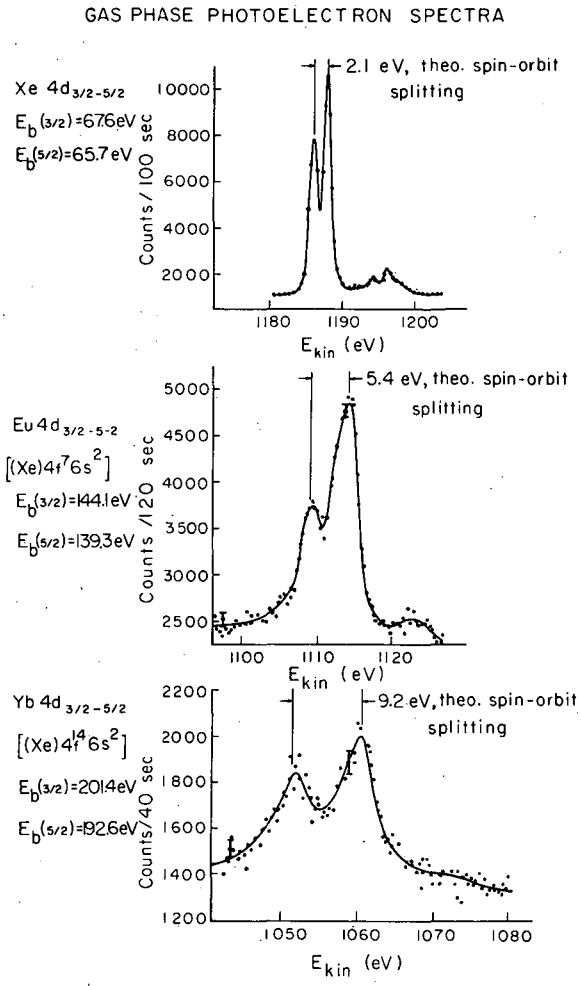

Fig. 2. Photoelectron spectra corresponding to ejection of 4d electrons from gaseous Xe, Eu, and 4b. The valence electron configurations and binding energies of the $d_{3/2}$ and $d_{5/2}$ components are also given. The weaker peaks ≈ 10 eV to the right of the main peaks are due to $MgK\alpha_{3,4}$ x rays. The theoretical spin-orbit splittings are from Ref. 10. (XBL 694-2448)

ELECTRONIC DENSITIES OF STATES FROM x-RAY PHOTOELECTRON SPECTROSCOPY†

C. S. Fadley and D. A. Shirley

In x-ray photoelectron spectroscopy (XPS), a sample is exposed to low-energy x rays (approximately 1 keV), and the resultant photoelectrons are analyzed with high precision for kinetic energy. Corrections can be made for the effects of inelastic scattering of photoelectrons and weak satellite x rays by using a core-level photoelectron peak as a reference.[1,2] Core-level peaks can also be used to ascertain the chemical state of the sample.[1] A corrected XPS spectrum in the region of the valence levels of a solid should reflect the valence-band density of states. All features in this spectrum should be modulated by appropriate photoelectric cross sections, and there are several final-state effects which could complicate the interpretation even further.

In comparison with the closely related experimental technique, ultraviolet photoelectron spectroscopy (UPS),[3] XPS has the following advantages for obtaining density-of-states information: (a) the inelastic scattering correction is more straightforward and less essential, (b) chemical effects on core levels are not accessible to UPS, (c) surface conditions are not so critical in XPS,[1,4] and (d) the free electron states involved in the photoemission process do not introduce significant distortions in an XPS spectrum, whereas they do in UPS. At present UPS has the decided advantage of approximately fourfold higher resolution, however. Thus, XPS seems capable of giving a

more reliable description of the general shape of the density-of-states function, but one that may be lacking in some of the fine-structure details present in UPS results.

We have used XPS to study the densities of states of the metals Fe,[1] Co,[1] Ni,[1] Cu,[1] Ru, Rh, Pd, Ag, Os, Ir, Pt.[1] and Au, as well as the compounds ZnS, $CdCl_2$, and HgO. The metal surfaces were cleaned by heating in hydrogen.[1] These fifteen solids illustrate trends observed as the 3d, 4d, and 5d levels are filled, becoming core-like states. Figure 1 indicates the portion of the periodic table represented. Peaks due to the d bands of these solids are the dominant feature of the XPS spectra near the Fermi energy (E_f), and these are presented in Fig. 2. Table I summarizes relevant data for the core reference levels and the d-band peaks.

Within a 3d, 4d, or 5d series, the XPS results show systematic variation, giving somewhat wider d band for Fe, Ru, and Os than for Cu, Ag, and Au, respectively, and even narrower core-like states $\approx$ 10 eV below E_f for ZnS, $CdCl_2$, and HgO. This variation is consistent with the filling of the d bands. The 4d bands studied are only slightly wider than their 3d counterparts; the 5d bands are considerably wider and show gross structure.

Within two isomorphous series--Rh, Pd, Ag and Ir, Pt, Au, all members of which are face-centered cubic--there is sufficient similarity of the shapes of the d-band peaks to suggest a rigid-band model for $\rho(E)$. If $\rho(E)$ of Ag can be used to generate $\rho(E)$ of Rh and Pd, or $\rho(E)$ of Au to generate $\rho(E)$ of Ir and Pt, simply by lowering the Fermi energy to allow for partial filling of the d bands, then this model applies. The peaks for Rh and Pd are too wide to be represented by a Ag $\rho(E)$, but the shapes of both could be very roughly approximated in this manner. The similarity of the two-peak structure for the three metals Ir, Pt, and Au gives more evidence for the utility of a rigid band model, especially as the uncorrected XPS results for Ir show the peak near E_f to be narrower (as though it were a broader peak cut off by the Fermi energy).

The d-band peaks for Ag, Pt, Au, and HgO have a similar two-component shape, with the more intense component lying near E_f. To estimate the intensity ratios of these components more accurately, we have least-squares-fitted two Gaussian peaks of equal width to our data for these four solids. The ratios and separation so derived are: Ag--1.51:1.00, 1.8 eV; Pt--1.60:1.00, 3.3 eV; Au--1.48:1.00, 3.1 eV; and HgO--1.39:1.00, 1.8 eV. As our accuracy in determining these ratios is $\pm$0.15, they could all be represented by a value of 1.50:1.00. One possible significance of this value is that it is the expected (and observed) intensity ratio for a spin-orbit split d level. In fact, the separation for HgO is in good agreement with a free-atom theoretical spin-orbit splitting.[5] Thus, one might argue that as the 4d and 5d shells move nearer to the Fermi energy with decreasing Z, they must go continuously from core states to valence states, perhaps retaining some degree of simple spin-orbit character in the process. The observed separations for Ag, Pt, and Au are 1.5 to 2.5 times as large as free-atom predictions,[5] but the various perturbations of the lattice might be responsible for this. Speaking against such a simple interpretation, however, is our observation (verified in UPS results[6, 7]) that for Au the component nearer E_f is broader. In view of this, our intensity ratio estimates based on two peaks of equal width may not have fundamental significance, and the agreement of these ratios, particularly between Ag and Pt or Au, could be somewhat accidental. Nonetheless, the similarity in shape of our results for the d levels of Ag, Pt, Au, and Hg is rather striking.

We have compared our results with the predictions of one-electron band theory where possible (for Fe, Co, Ni, Cu, Pd, and Pt). The widths and shapes of the XPS curves are in fair agreement with theory, but several differences can be noted. In particular, the two-peak structure observed for Pt is not reproduced very well in the theoretical curve[8] (see Fig. 3).

Where comparisons are possible, the results of other experiments agree reasonably well with XPS, though there are some significant discrepancies. Recent UPS work on Cu, Ag, and Au[7] (at somewhat higher photon energies than have normally been used) is in very good basic agreement with XPS.

Footnote and References

†Condensed from UCRL-18953 (to appear in J. Res. Natl. Bur. Std. A).

1. C. S. Fadley and D. A. Shirley, Phys. Rev. Letters 21, 980 (1968); J. Appl. Phys. 40, 1395 (1969); and UCRL-18667, p. 247.
2. C. S. Fadley, Core and Valence Electronic States Studied With x-Ray Photoelectron Spectroscopy (Ph. D. thesis) UCRL-19535, Feb. 1970.
3. C. N. Berglund and W. E. Spicer, Phys. Rev. 136, A1030 and A1044 (1964).
4. D. E. Eastman, J. Appl. Phys. 40, 1387 (1969).

5. F. Herman and S. Skillman, Atomic Structure Calculations (Prentice-Hall, Inc., Englewood Cliffs, New Jersey, 1963).
6. W. F. Krolikowski and W. E. Spicer, Phys. Rev. (to be published).
7. D. E. Eastman and J. K. Cashion, Phys. Rev. Letters 24, 310 (1970).
8. F. M. Mueller, J. W. Garland, M. H. Cohen, and K. H. Benneman, Phys. Rev. (to be published).

Table I. Summary of pertinent results for the 15 solids studied. The reference core levels used for inelastic scattering correction are listed, along with their binding energies and widths. The widths of the d-band peaks are also given, along with the spacing of the two components in these peaks (if observed).

Solid	Reference core levels	Ref. core level binding energy[a] (eV)	FWHM of core levels[b] (eV)	FWHM of d-band peak (eV)	Separation of 2 components in d-band peak (eV)
Fe	$3p_{1/2-3/2}$ (unresolved)[c]	52	2.3	4.2	---
Co	$3p_{1/2-3/2}$	57	2.5	4.0	---
Ni	$3p_{1/2-3/2}$	66	3.4	3.0	---
Cu	$3p_{1/2-3/2}$	75	4.2	3.0	---
ZnS	$3p_{1/2-3/2}$	90	5.4	1.7	---
Ru	$3d_{3/2-5/2}$	280	1.1	4.9	---
Rh	$3d_{3/2-5/2}$	307	1.3	4.4	---
Pd	$3d_{3/2-5/2}$	335	1.3	4.1	---
Ag	$3d_{3/2-5/2}$	368	1.0	3.5	1.5-1.8
$CdCl_2$	$3d_{3/2-5/2}$	408	1.2	2.0	---
Os	$4f_{5/2-7/2}$	50	1.3	6.5	---
Ir	$4f_{5/2-7/2}$	60	1.4	6.3	3.3
Pt	$4f_{5/2-7/2}$	71	1.5	5.8	3.3
Au	$4f_{5/2-7/2}$	84	1.2	5.7	3.1
HgO	$4f_{5/2-7/2}$	103	1.5	3.8	1.8

a. Binding energy of the $\ell + 1/2$ component, relative to the Fermi energy.
b. Equal widths assumed for both components in the least-squares fits for 3d and 4f levels.
c. The theoretical spin-orbit splitting for the 3p levels in this series ranges from 1.6 eV for Fe to 3.1 eV for Zn (Ref. 5). The partially resolved doublet in ZnS is found to have a separation of 2.8 eV, in good agreement.

26 $3d^6 4s^2$ Fe bcc	27 $3d^7 4s^2$ Co fcc	28 $3d^8 4s^2$ Ni fcc	29 $3d^{10} 4s^1$ Cu fcc	30 $3d^{10} 4s^2$ Zn --
44 $4d^7 5s^1$ Ru hcp	45 $4d^8 5s^1$ Rh fcc	46 $4d^{10}$ Pd fcc	47 $4d^{10} 5s^1$ Ag fcc	48 $4d^{10} 5s^2$ Cd --
76 $5d^6 6s^2$ Os hcp	77 $5d^9$ Ir fcc	78 $5d^{10}$ Pt fcc	79 $5d^{10} 6s^1$ Au fcc	80 $5d^{10} 6s^2$ Hg --

Fig. 1. The portion of the periodic table studied in this work. The atomic number, free-atom electronic configuration, and metal crystal structures are given. Zn, Cd, and Hg were studied as compounds. The crystal structures are those appropriate at the temperatures of our metal experiments (700–900°C). (XBL 701-2073)

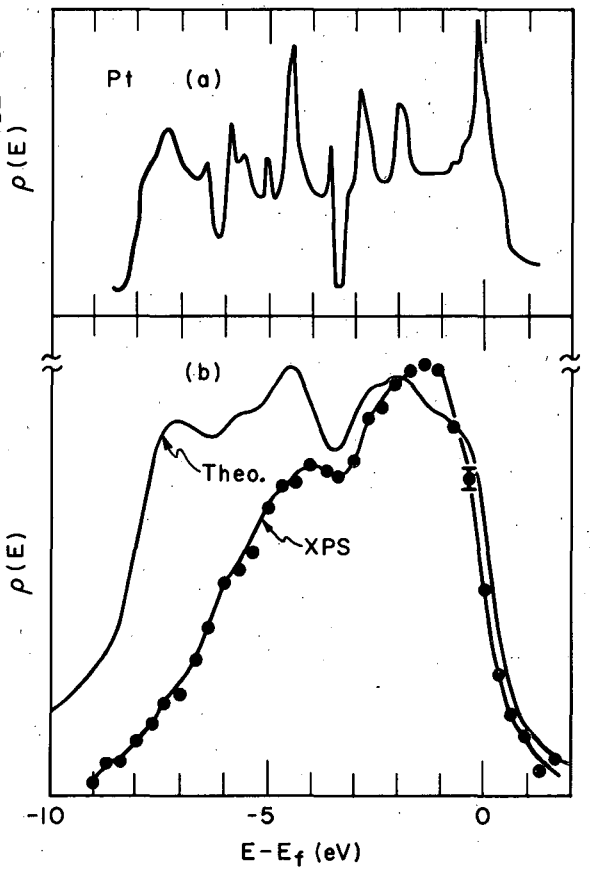

Fig. 3. Comparison of Pt XPS results with theory: (a) the theoretical density-of-states function of Ref. 8; (b) comparison of the broadened theoretical curve with our XPS results. (XBL 701-2062)

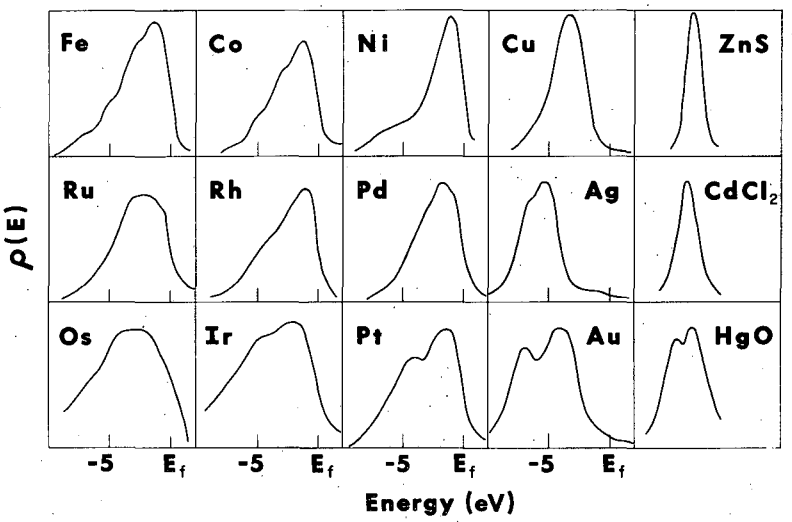

Fig. 2. Summary of the XPS results for the 15 solids studied (cf. Table I). The peaks for ZnS, $CdCl_2$, and HgO lie at $E-E_f \approx -13$ eV, -14 eV, and -12 eV, respectively. (701-2059)

COMPARISON OF CORE-LEVEL BINDING ENERGY SHIFTS IN MOLECULES WITH PREDICTIONS BASED ON KOOPMANS' THEOREM

D. W. Davis, J. M. Hollander, D. A. Shirley, and T. D. Thomas†

x-Ray photoelectron spectroscopy allows the determination of core-electron binding energies, which exhibit environment-sensitive "chemical shifts."[1] That core-electron binding energies increase with oxidation is well known,[1-5] but there have been few rigorous theoretical calculations with which to compare the experimental shifts. Recently, however, SCF-MO calculations on several small molecules have become available.[6-8] We here compare experimental values of shifts of carbon, nitrogen, and oxygen 1s binding energies in some of these molecules with theoretical estimates from these calculations.

Core-electron binding energies obtained by photoemission experiments in atoms are much closer to those computed for an "adiabatic" process than for a "sudden" process.[9] The adiabatic process can be thought of as taking place in two (fictitious) steps: (i) The photoelectron is ejected suddenly, leaving a hole in the K shell and leaving the other (passive) electrons "frozen" in their initial ground-state orbitals, and (ii) the passive orbitals quickly relax toward the positive hole, accelerating the outgoing electron.

By Koopmans' Theorem,[10] "sudden" values of binding energies may be obtained from Hartree-Fock calculations: they are just the one-electron orbital energies. Adiabatic binding energies are harder to calculate, because for these the energies of both the initial state and the (unstable) final "hole state" must be evaluated. It is of interest to learn if the one-electron energies are adequate for predicting chemical shifts. This would be the case if electronic relaxation in the chemical environment either were negligible or constant. In contrast, if electronic relaxation in the molecule is significant, a differential, structure-dependent violation of Koopmans' Theorem should be noted.

The measurements were made on gases at room temperature in the Berkeley iron-free spectrometer, using Mg k$\alpha_{1,2}$ x rays. Pressures in the sample chamber were maintained at about 0.02 torr; the observed kinetic energy values were, however, relatively insensitive to pressure. Every compound was compared directly with a standard compound. The observed shifts are summarized in Table I.

In Fig. 1 the experimental 1s-electron binding-energy shifts, $\Delta E = E(C, N, \text{ or } O) - E(CH_4, NH_3, \text{ or } H_2O)$, are plotted against "sudden" values based on SCF calculations.[6-8] Two conclusions may be drawn from this comparison. First, the SCF calculations by Basch and Snyder give quite good predictions of the shifts. The agreement is encouraging; it suggests that a rigorous theoretical understanding of core-level chemical shifts may not be far in the future.

Second, however, the agreement between ΔE_{expt} and ΔE_{sudden} for these molecules is not perfect. An average deviation of about 1 eV is noted for the elements studied (with ΔE_{sudden} being larger in each case), and the rms spread about this deviation is also about 1 eV. The cause of this almost constant deviation is not presently known. In all three elements, the hydride was chosen as the standard molecule.

The data do show that there are no significant structure-dependent deviations from the SCF "frozen orbital" values. It is concluded that these calculations can be used to give estimates of the binding energy shifts in these molecules to within about 1 eV.

Footnote and References

†Permanent address: Department of Chemistry, Princeton University, Princeton, New Jersey.

1. S. B. M. Hagström, C. Nordling, and K. Siegbahn, Z. Physik 178, 433 (1964).
2. K. Siegbahn, C. Nordling, A. Fahlman, R. Nordberg, K. Hamrin, J. Hedman, C. Johansson, T. Bergmark, S.-E. Karlsson, I. Lindgren, and B. Lindberg, ESCA, Atomic, Molecular, and Solid State Structure Studied by Means of Electron Spectroscopy (Almqvist and Wiksell, Uppsala, 1967), 97-137.
3. J. M. Hollander, D. N. Hendrickson, and W. L. Jolly, J. Chem. Phys. 49, 3315 (1968).
4. R. Nordberg, R. G. Albridge, T. Bergmark, U. Ericson, J. Hedman, C. Nordling, K. Siegbahn, and B. J. Lindberg, Arkiv Kemi 28, 257 (1967).
5. K. Hamrin, G. Johansson, A. Fahlman, C. Nordling, and K. Siegbahn, Chem. Phys. Letters 1, 557 (1968).

6. Tae-Kyu Ha and L. C. Allen, Intern. J. Quantum Chem. 1S, 199 (1967).
7. H. Basch and L. C. Snyder, Chem. Phys. Letters 3, 333 (1969).
8. H. Basch (Scientific Research Staff, Ford Motor Co., Detroit, Michigan), private communication, Dec. 1969.
9. P. S. Bagus, Phys. Rev. 139, A619 (1965).
10. T. Koopmans, Physica 1, 104 (1933).
11. It is noted that the Basch and Snyder calculations (Ref. 7) made use of a "double zeta" set of Gaussian functions, whereas Ha and Allen (Ref. 6) used a minimal basis set.
12. W. L. Jolly (University of California-Berkeley), private communication, Oct. 1969.

Table I. Binding energy shifts (in eV) of 1s electrons from C, O, and N compounds, relative to CH_4, H_2O, and NH_3.

Compound	ΔE(expt)[a]	ΔE(sudden)[b]	Compound	ΔE(expt)[a]	ΔE(sudden)[b]
C 1s shift			O 1s shift		
C_2H_6	-0.2[c]	0.2	C_2H_4O	-1.05(5)	0.2
C_2H_4	-0.1[c]	0.9	CH_3OH	-0.80(10)	-0.2
C_2H_2	0.4[c]	1.4	CO_2	1.44(5)	3.2
C_2H_4O	2.01(5)	2.4	HCO_2H[d]	0.67(5) -0.95(5)	2.0 0.8
CH_3OH	1.9(2)	2.0	N_2O	1.54(10)	2.9
HCO_2H	4.99(10)	6.0	CO	2.94(10)[e]	3.3
CO_2	6.84(5)	8.3			
CO	5.4[e]	5.5	O_2, $^4\Sigma$	3.47(5)	---
CH_3F	2.8[f]	3.0[g] 4.9[h]	O_2, $^2\Sigma$	4.59(5)	---
Cyclo-propane	-0.23(5)	0.5	O_2, wtd ave	3.84(6)	4.3
CHF_3	8.3[f]	9.4[g] 15[h]	N 1s shift		
CF_4	11.0[f]	12.7[g]	N_2	4.35(20)	5.4
HCN	2.6(2)[i]	2.8	N_2O	3.17(10), 7.04(5)	6.1 9.3
			HCN	0.55(20)[i]	3.0

a. Error in last place given parenthetically. From this work unless otherwise noted. Shifts positive if no sign given.
b. From Ref. 7, unless otherwise indicated.
c. T. D. Thomas, J. Chem. Phys. 52, 1373 (1970).
d. Two lines of equal intensity, hence two possible ways to assign lines.
e. T. D. Thomas, in preparation.
f. T. D. Thomas, submitted to J. Am. Chem. Soc.
g. Ref. 8.
h. Ref. 6.
i. P. Finn, J. M. Hollander, and W. L. Jolly, unpublished data.

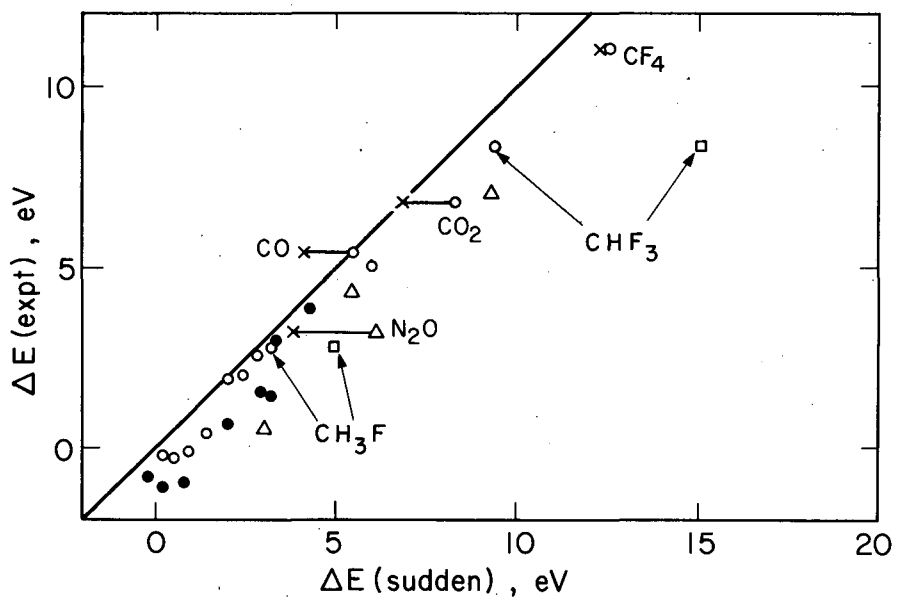

Fig. 1. Experimental binding-energy shifts vs "sudden" estimates for carbon 1s (open circles), oxygen 1s (filled circles), and nitrogen 1s (triangles) electrons in compounds listed in Table I. For $\Delta E_{expt} = \Delta E_{sudden}$ points would lie on the solid line. Carbon values from Ref. 6 are indicated by open squares (Ref. 11). W. L. Jolly has made thermochemical estimates (Ref. 12) for several compounds; these are indicated by X's. (XBL 6911-6303)

A STUDY OF THE "GOLD 5d BANDS" IN $AuAl_2$ AND $AuGa_2$ BY PHOTOELECTRON SPECTROSCOPY*

P. D. Chan and D. A. Shirley

x-Ray photoelectron spectroscopy has been extended to studies of the valence electrons in solids and gaseous molecules.[1,2] The spectra obtained provide direct determination of N(E), the density of states near the Fermi level. We have studied in particular N(E) of $AuAl_2$ and $AuGa_2$.

$AuAl_2$ is purple and $AuGa_2$ is greyish, and these interesting optical properties are often attributed to the proximity of Au 5d electrons to the Fermi energy, E_F. In a recent proposal by Switendick and Narath,[3] which was based on the band-structure calculations for a solution for the "$AuGa_2$ dilemma,"[4] it was found that the positions of the gold d-band states were at about E_F-7 eV in $AuAl_2$ and at similar energies in $AuGa_2$ and $AuIn_2$.[3] If these Au 5d states really lay 7 eV below E_F, and the density of state peak were as narrow as the calculation indicated, then they could scarcely affect the compounds' optical properties. We describe here our XPS work on density of states of these two compounds in order to help resolve this "d-band dilemma."[4]

The experimental aspects of XPS have been reviewed in detail elsewhere.[1] In this work, Mg $K\alpha_{1,2}$ (1253.6 eV) were used as the excitation source, and the photoelectrons emitted were magnetically analyzed for kinetic energy in the Berkeley iron-free spectrometer. The samples were prepared by heating stoichiometric amounts of pure metals in vacuo, and then spark-cut and polished.

The XPS spectra for $AuAl_2$ and $AuGa_2$ taken near the Fermi level, along with the least-squares fittings with a linear sloping background plus a Gaussian with a constant tail on the low-energy side, are shown in Figs. 1 and 2, respectively.

The spectra of $AuAl_2$ showed one dominant peak at E_F -6 eV which we attribute to the Au 5d band with considerable confidence. The "d-band" peak appeared to be slightly asymmetric. However, two-Gaussian fitting gave only a very weak higher-energy peak of variable position and shifted the main peak only a few tenths eV, and so only the one-Gaussian fittings are used. The final value of $AuAl_2$ position is E_F -(6.0 ± 0.3) eV, and the full width at half maximum, FWHM, is (4.1 ± 0.5) eV.

The spectra and Gaussian fitting of $AuGa_2$ showed a Ga 3d peak at E_F -20 eV, and a Au 5d-band peak at E_F -6 eV. The Au 5d-band peak was quite symmetric. The Ga 3d peak was asymmetric and appeared to consist of two peaks each of width 2 eV FWHM and spaced about 2 eV apart, with the higher-energy peak about 0.4 as intense as the lower-energy peak. We attribute the higher-energy peak to free Ga, which we think came from nonstoichiometry. The Au $4f_{5/2}$ and $4f_{7/2}$ doublet showed no evidence of a second phase at the gold sites, and gave support to the Au 5d-band results. The final value of the Au 5d-band position is E_F -(5.7 ± 0.2) eV, and FWHM is (4.6 ± 0.4) eV.

We interpret the results from $AuGa_2$ and $AuAl_2$ as giving strong (but qualitative) support for Switendick's band-structure calculations: the positions of these peaks are in good agreement with his predictions. However, the experimental "d bands" are at higher energy (E_F -6 eV) than the theoretical value (E_F -7 eV), and the experimental line width (4 eV) is about twice theoretical.

In the particular case of $AuAl_2$, our results agree also basically with those of Al ($L_{2,3}$) soft x-ray emission work by Williams et al.,[5] who took their spectra as support of Switendick's calculations. However, there are small differences among the two experimental results and the theoretical. The soft-x-ray work showed a peak at E_F -8.3 eV, whereas the XPS peak is at E_F -6.0 eV, and the peak positions calculated by Switendick are E_F -8.0 eV for Al 3s-like states and E_F -7.1 eV for the peak in the total density of states.[6] We attribute the difference to the fact that XPS is most sensitive to d electrons whereas the soft-x-ray work is sensitive to bands with s symmetry at the Al sites. Another point of disagreement is the position of the Al 2p state. Switendick predicted E = E_F -(73.8 ± 0.1) eV,[6] and he quoted an experimental value of E_F -(73.5 ± 0.5) eV, whereas our spectra showed the peak at E_F -(75.1 ± 0.2) eV.

In spite of the points of disagreement among Switendick's theoretical work, the soft-x-ray emission work of Williams et al., and our XPS results, we conclude that these three investigations all concur on one major point: the gold 5d bands in the $AuAl_2$-type alloy lie 6 to 8 eV below the Fermi level.

Footnote and References

*Condensed from P. D. Chan and D. A. Shirley, A Note on the Position of the "Gold 5d Bands," in Proceedings of the Density-of-States Symposium at the National Bureau of Standards, Nov. 3-6, 1969.

1. C. S. Fadley and D. A. Shirley, Phys. Rev. Letters 21, 980 (1968).
2. K. Hamrin et al., Chem. Phys. Letters 1, 613 (1968).
3. A. C. Switendick and Albert Narath, Phys. Rev. Letters 22, 1423 (1969).
4. V. Jaccarino, M. Weber, J. H. Wernick, and A. Menth, Phys. Rev. Letters 21, 1811 (1968).
5. M. L. Williams, R. C. Dobbyn, J. R. Cuthill, and A. J. McAllister, Soft x-Ray Emission Spectrum of Al in $AuAl_2$ in Proceedings of the Density-of-States Symposium (see Ref. 1).
6. A. C. Switendick, Orbital Symmetry Contributions to Electronic Density of States of $AuAl_2$, in Proceedings of the Density-of-States Symposium (see Ref. 1).

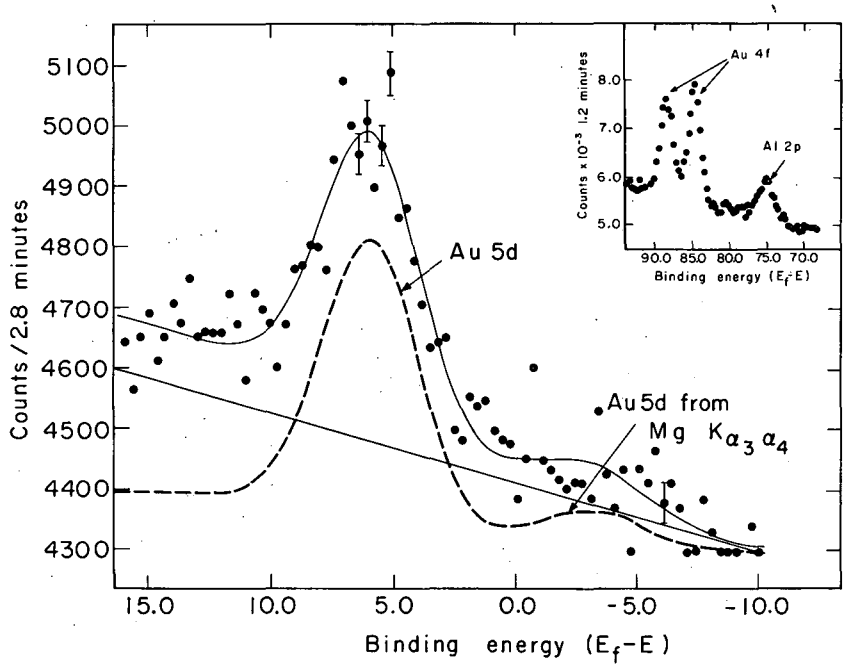

Fig. 1. Typical x-ray photoemission spectrum for $AuAl_2$ near the Fermi energy. Filled circles represent data points. Top solid curve was fitted to the data. It was composed of background, indicated by sloping solid line, plus a response curve indicated by dashed curve. The main peak of this dashed curve arises through photoemission from the "gold 5d" bands by Mg $K\alpha_{12}$ radiation. Core-level peaks in inset indicate chemical purity of sample. (XBL 6912-6330)

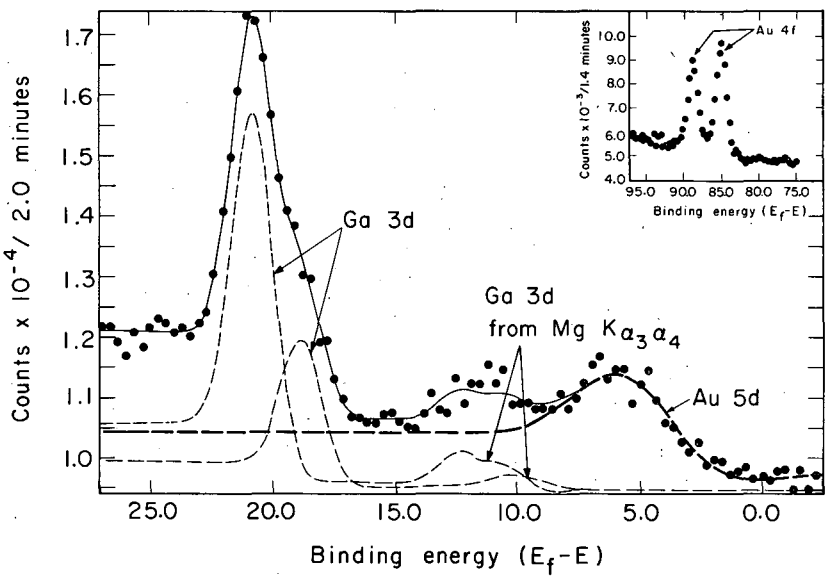

Fig. 2. Typical x-ray photoemission spectrum from $AuGa_2$ near the Fermi energy. (XBL 6912-6331)

x-RAY PHOTOELECTRON SPECTROSCOPY: A TOOL FOR RESEARCH IN CATALYSIS †

W. N. Delgass,* T. R. Hughes,‡ and C. S. Fadley

Chemical shifts in x-ray photoelectron spectra can be related to charges on atoms in the sample, while peak areas yield an approximate chemical analysis. Because of its general applicability and the semisurface nature of measurements on solids, x-ray photoelectron spectroscopy (XPS) has high potential for research in catalysis. The purpose of this work has been to explore this potential in several specific areas.

Figure 1 shows N(1s) photoelectron spectra of NH_4-Y zeolite. Spectrum 1(a) gives a binding energy for nitrogen in good agreement with that for NH_4 in NH_4NO_3. Spectrum 1(b) resulted when the sample was heated in the vacuum of the photoelectron spectrometer. The decrease in intensity and broadening of the line are consistent with partial deammoniation of the sample and a change in the chemical state of some of the residual nitrogen. Similar effects were seen for NH_3 adsorbed on silica-alumina and H-Y zeolite. Spectrum 1(c) resulted when the sample was heated in the spectrometer to 450° C, cooled to 120° C, and exposed to approximately 5 torr of pyridine. The left line of the broad doublet was shown in a separate experiment to be due to residual nitrogen from NH_4-Y, and the right peak was assigned to adsorbed pyridine. The shift of the residual nitrogen line in 1(c) with respect to 1(a) shows a further change in the chemical state of the original nitrogen as a consequence of heating and the resulting dehydration of the zeolite.

The ability of XPS to provide information concerning the chemical states of supported metal catalysts is demonstrated in the Ni($2p_{3/2}$) spectra of 6% Ni on silica-alumina, Fig. 2. Spectrum 2(a) is characteristic of NiO. The left peak, an "extra feature" of the spectrum, is not yet fully understood, but it may be due to Ni^{3+}. The right peaks of spectra 2(b) and 2(c) show in situ reduction and subsequent reoxidation of the supported nickel. Spectrum 2(d) is for a sample treated in a stream of H_2 plus H_2S to sulfide the nickel. As expected, this spectrum is different from the characteristic NiO spectrum. Spectrum 2(e) shows that even after a CO stripping treatment and exposure to air during transfer to the spectrometer, some Ni metal was still present on the catalyst. This result may be due to passivation of the Ni surface by oxygen before the CO treatment. A more precise identification of the left peaks in the spectra of Fig. 2 is a topic of interest for further study.

In other experiments (a) an effect of particle size on the oxidizability of Pt and (b) chemical changes in the surface layer of FeV_2O_4 after use as a catalyst were observed. It was also found that Eu^{3+} exchanged into zeolites could be reduced to Eu^{2+} in the presence of H_2 at 450° C, whereas a similar treatment of Eu_2O_3 had no observable effect. This result suggests that further studies of the chemistry of rare earths in zeolites may be useful in the understanding of zeolite activity.

On the basis of these experiments we feel that such subjects as catalyst characterization, activation, aging, and poisoning, as well as adsorption and surface segregation in multicomponent systems, should be fruitful. At this stage in the development of the technique, investigation of chemical effects involving large changes in the charge on atoms of interest has the best chance for success. More subtle chemical changes will become amenable to quantitative study with more accurate charging and band-bending corrections, improved methods for dealing with the Fermi level energy reference in solids, and improved vacuum conditions in the spectrometer.

An Air Force Office of Scientific Research Postdoctoral Research Award to W. N. D. in support of this research, under the direction of Professor David A. Shirley, is gratefully acknowledged. We are indebted to many colleagues for helpful discussions and the donation of samples.

Footnotes

†Summary of UCRL-18968, submitted to Catalysis Reviews.

*Present address: Yale University, New Haven, Connecticut 06520.
‡Chevron Research Corporation, Richmond, California 94802.

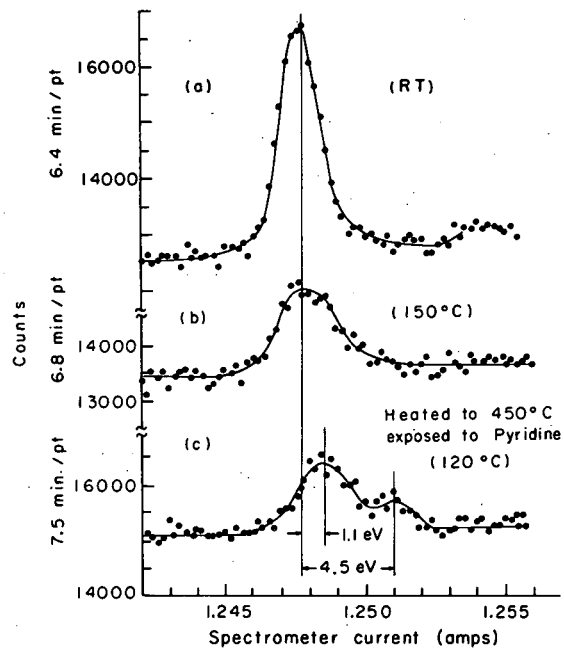

Fig. 1. N(1s) photoelectron lines from NH_4-Y zeolite as a function of treatment in situ. (XBL 699-3709)

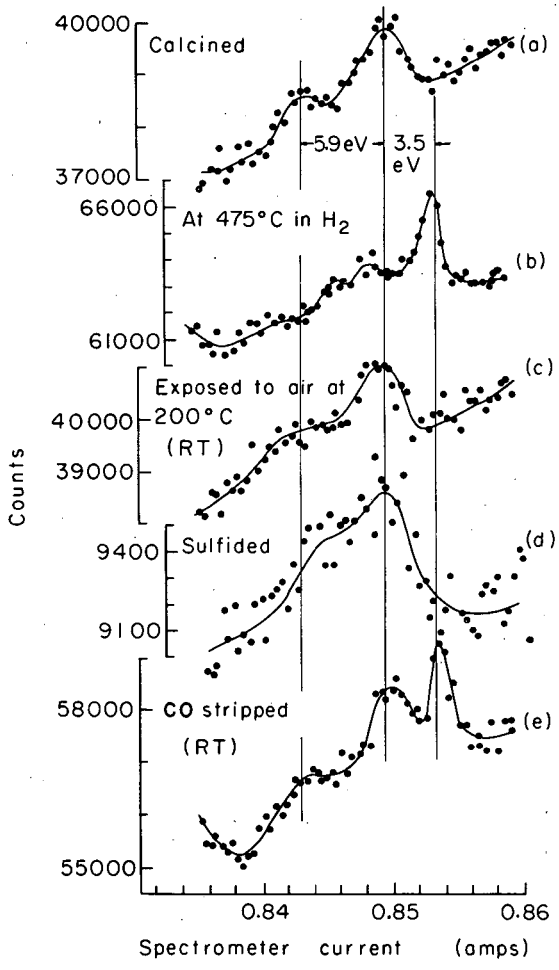

Fig. 2. Ni($2p_{3/2}$) photoelectron lines from 6% Ni on silica-alumina. (XBL 699-3703)

SPLITTING OF GOLD $p_{3/2}$ CORE LEVELS BY CHEMICAL BONDING†

G. R. Apai, W. N. Delgass,* J. M. Hollander, T. Novakov,‡ and D. A. Shirley

Through the use of x-ray photoelectron spectroscopy, Novakov and Hollander[1] have recently observed a splitting of atomic-core $p_{3/2}$ levels in compounds of thorium and uranium. In the uranium compounds, the magnitude of the splitting varied from 3 to 10 eV (the latter in uranyl acetate). The splittings were interpreted as arising from crystal fields or from specific interactions with the bonding orbitals.

In an effort to gain more information, photoelectron spectra from some gold compounds were studied.[2] These compounds were chosen because their chemical bonding schemes had recently been characterized by Faltens and Shirley.[3] In their study of nuclear quadrupole splitting of linear gold compounds (by Mössbauer spectroscopy) these authors had interpreted the splitting as arising from the participation of 6p orbitals in the X-Au-X bonds, producing a field gradient at the nucleus. They inferred that the magnitude of the splitting is proportional to the degree of sp covalency of the bond.

In our experiments, solid samples were irradiated with Mg K_α x rays (1253.6 eV). The ejected photoelectrons were analyzed with a magnetic spectrometer. Figure 1 shows spectra for the $4f_{5/2}$ (N_{VI}), $4f_{7/2}$ (N_{VII}), and $5p_{3/2}$ (O_{III}) levels of Au metal, AuCN, and $KAu(CN)_2$. All the peaks of gold metal appear to have the normal line shape; a least-squares program gave good fits to these peaks by use of single Gaussians. However, the $5p_{3/2}$ peaks of AuCN and $KAu(CN)_2$ show splittings. The energy splittings $\Delta E(5p_{3/2})$ for these two cases, along with other parameters in the fitting routine, are given in Table I. Since the $5p_{3/2}$ electrons of Au are not usually regarded as participating in chemical bonding, the origin of composite structure in the $5p_{3/2}$ peak was not obvious.

Table I. Spectral parameters derived from the least-squares fitting of the photoelectron spectra. Errors in the last place are given parenthetically.

Compound	Peak	Energy[a] (eV)	FWHM[b] (eV)	Relative intensity[c]
Au	$4f_{5/2}(N_{VI})$	1163.27(1)	1.57(3)	
	$4f_{7/2}(N_{VII})$	1166.90(1)	1.58(3)	1.25
	$5p_{3/2}(O_{III})$	1194.1(1)	3.6 (2)	
AuCN	$4f_{5/2}(N_{VI})$	1160.42(1)	1.56(3)	
	$4f_{7/2}(N_{VII})$	1164.09(1)	1.65(2)	1.34
	$5p_{3/2}(O_{III})(1)$	1190.1(2)	2.4(3)	
	$5p_{3/2}(O_{III})(2)$	1191.8(2)	2.4(3)	1.2
$KAu(CN)_2$	$4f_{5/2}(N_{VI})$	1158.98(3)	1.80(7)	
	$4f_{7/2}(N_{VII})$	1162.64(2)	1.79(5)	1.29
	$5p_{3/2}(O_{III})(1)$	1188.4(2)	2.3(2)	
	$5p_{3/2}(O_{III})(2)$	1190.3(2)	2.3(2)	0.97

a. Kinetic energies only--binding energies could be deduced only if corrections for source charging were known.
b. Full width at half maximum height of fitted Gaussian.
c. Relative to peak immediately above.

We believe that whatever detailed mechanism is responsible, splitting of the $5p_{3/2}$ level in linear gold compounds must result from (a) Coulombic interaction of electrons in the $5p_{3/2}$ level with electrons both in the ligand bonding gold orbitals and in the carbon atom, and (b) nuclear attraction of the $5p_{3/2}$ electrons to the carbon nucleus. The observation of splitting in linear $[NC\text{-}Au\text{-}CN]^-$ and its absence in cubic Au metal are consistent with this interpretation. (A $p_{3/2}$ state can form only one irreducible representation of a cubic group.) In an attempt to explain the observed splitting in detail we restrict ourselves to the $Au(CN)_2^-$ case.

The observed splitting must be in the final hole states left after ejection of the $5p_{3/2}$ electron. If we take the symmetry axis of the ion as the quantization axis, then we may denote the states as $\psi(\pm 1/2)$, which represents an $m_j = \pm 1/2$ hole in the Au $5p_{3/2}$ shell, and $\psi(\pm 3/2)$, which represents an $m_j = \pm 3/2$ hole. By using first-order perturbation theory, $\Delta E = E(\pm 3/2) - E(\pm 1/2)$ can be calculated. Since the $p_{3/2}$ shell has one hole, it can be treated as a one- (rather than three-) electron state. We assign this state a definite magnetic quantum number (+3/2 or +1/2). Now we calculate the interaction of the $5p_{3/2}$ ($m = +3/2$ or $m = +1/2$) state with one CN group and double the resulting ΔE.

In our model we assume 6s6p hybridization in Au as well as 2s2p hydridization in the carbon of the CN group. The antisymmetrized wave functions describing the $5p_{3/2}$ electron plus the bond may be written as a linear combination of Slater determinants composed of atomic orbitals, such as

$$\psi(3/2,+3/2) = \left[\begin{array}{l} \frac{1}{\sqrt{2}} A(1\text{-}1)\,|\,511(1)\rangle\,\alpha(1)\,|\,2p\pi(2)\rangle\,\alpha(2)\,|\,2p\pi(3)\rangle\,\beta(3) \\ \qquad |\,q(4)\rangle\,\beta(4)\,|\,\ell(5)\rangle\,\alpha(5)\,|\,k(6)\rangle\,\beta(6)\,|\,1S(7)\rangle\,\alpha(7)\,|\,1S(8)\rangle\,\beta(8) \\ -\frac{1}{\sqrt{2}} A(1\text{-}1)\,|\,511(1)\rangle\,\alpha(1)\,|\,2p\pi(2)\rangle\,\alpha(2)\,|\,2p\pi(3)\rangle\,\beta(3) \\ \qquad |\,q(4)\rangle\,\alpha(4)\,|\,\ell(5)\rangle\,\beta(5)\,|\,k(6)\,\alpha(6)\,|\,1S(7)\rangle\,\alpha(7)\,|\,1S(8)\rangle\,\beta(8) \end{array}\right]$$

Here $|q\rangle$ refers to the carbon hybrid orbital $\frac{1}{\sqrt{2}}(|200\rangle - |210\rangle)$; $|\ell\rangle$ refers to the other hybrid of carbon $\frac{1}{\sqrt{2}}(|200\rangle + |210\rangle)$, and $|k\rangle$ denotes the gold hybrid $\frac{1}{\sqrt{2}}(|600\rangle + |610\rangle)$. We may expand $\psi(3/2, +1/2)$ in the $|\ell_z S_z\rangle$ representation

$$\psi(3/2,+1/2(1)) = (1/3)^{1/2}\,|\,510(1)\rangle\,\alpha(1) + (2/3)^{1/2}\,|\,511(1)\rangle\,\beta(1).$$

The wave function for the gold-nitrogen interaction is written similarly. The relevant part of the perturbing Hamiltonian is

$$\mathcal{H} = \sum_{i>j=1}^{8} \frac{e^2}{|r_{ij}|} - \sum_{i=1}^{8} \frac{Z(r_{iC})\,e^2}{|r_{iC}|}.$$

Here r_{iC} is the distance of an electron in an Au atomic orbital from the carbon nucleus and $Z(r_{iC})$ is the total carbon nuclear charge. Splitting will arise only if electron i or j is in a 5p orbital. Hence we have, for two Au-C bonds,

$$\Delta E = 2\,\{\langle\psi(3/2,+3/2)|\,\mathcal{H}\,|\psi(3/2,+3/2)\rangle - \langle\psi(3/2,+1/2)|\,\mathcal{H}\,|\psi(3/2,+1/2)\rangle\}.$$

The calculations for our two center integrals were carried out with use of a diatomic restricted SCF program.[4]

The electron hole–nucleus sum in $\mathcal{H}$ tends to lower the energy of the $m_j = +3/2$ state relative to that of the $m_j = +1/2$ state, whereas the electron–electron hole sum has the opposite effect. Table II lists the contributions to the splitting of the $5p_{3/2}$ level that we find by preliminary calculation. The total calculated splitting is therefore only -0.24 eV. Recent Mössbauer results[5] on transition metal cyanides indicate that back-donation of the dxz and dyz electrons to π-antibonding orbitals on the carbon atoms may be important. Our calculations indicate this effect would lead to a negligible contribution.

Table II. Contributions to $5p_{3/2}$ splitting for $\Delta E = E(\pm 3/2) - E(\pm 1/2)$.

Interaction	ΔE (eV)
$\Delta E_{Z(r_{iC})\,e^2}$	-2.96
$\Delta E_{Z(r_{iN})\,e^2}$	-0.92
ΔE_{ee} (1-center Au 5p-6s6p)	+0.15
ΔE_{ee} (2-center Au 5p-C electrons)	+2.56
ΔE_{ee} (2-center Au 5p-N electrons)	+0.93

Therefore, although the model correctly predicts a splitting in the $5p_{3/2}$ state, it falls short by a rather large factor of giving quantitative agreement with experiment. An orbital unrestricted Hartree-Fock calculation on $Au(CN)_2^-$ would be a more realistic theoretical approach, but such a calculation is not yet feasible.

Footnotes and References

†Condensed from G. R. Apai, W. Nicholas Delgass, J. M. Hollander, T. Novakov, and D. A. Shirley, in preparation.
*Present address: Yale University, New Haven, Connecticut 06520.
‡Present address: Shell Development Company, Emeryville, California 94608.

1. T. Novakov and J. M. Hollander, Phys. Rev. Letters 21, 1133 (1968).
2. T. Novakov and J. M. Hollander, Bull. Am. Phys. Soc. 14, 524 (BM4) (1969).
3. M. O. Faltens and D. A. Shirley, in preparation.
4. We express our appreciation to Dr. H. F. Schaefer for the use of his computer program for diatomic calculations and also for help concerning its use.
5. G. Kaindl, W. Potzel, F. Wagner, Ursel Zahn, and R. L. Mossbauer, Z. Physik 226, 103 (1969).

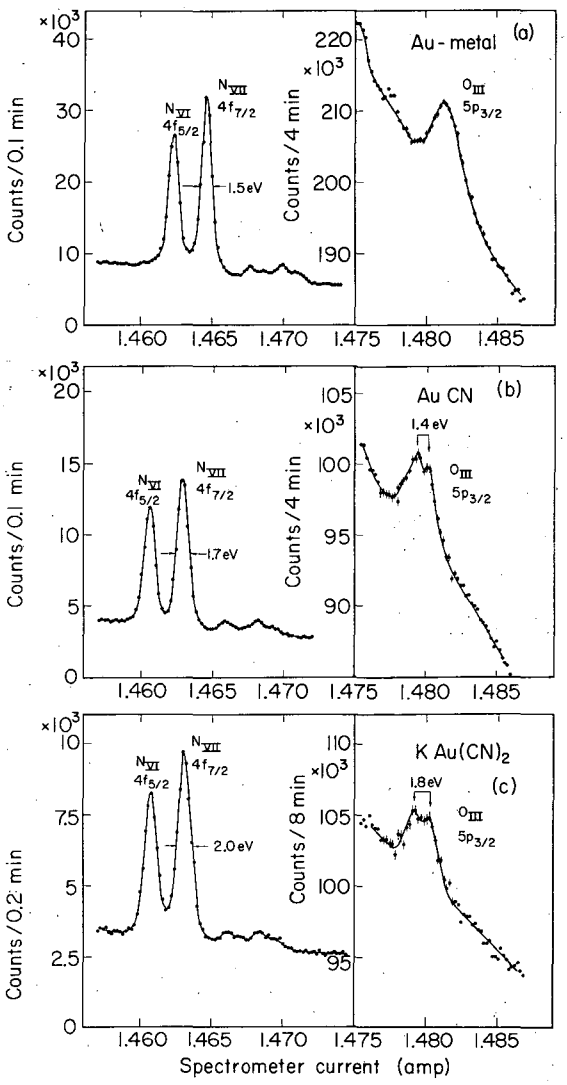

Fig. 1. Photoelectron spectra of gold compounds. (XBL 694-2338)

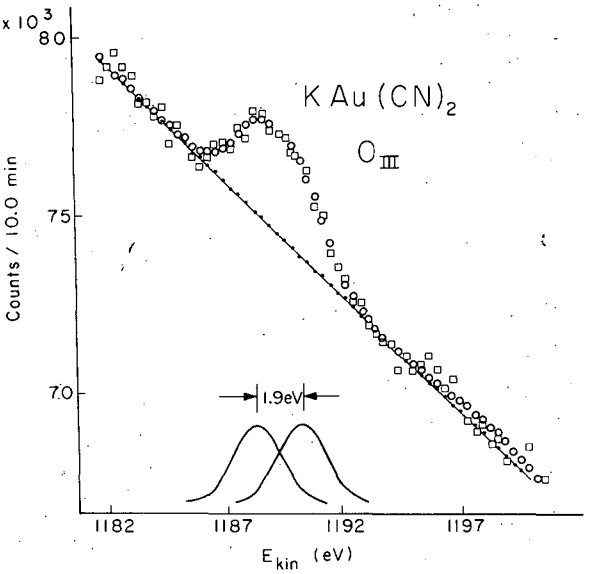

Fig. 2. A typical least-squares fit, showing the requirement of two equally intense split peaks in the $KAu(CN)_2$ spectrum. Here □ represent data points; O, least-squares fitted points; and ●, background. For data points with no corresponding fitted point, both coincide in the figure. (XBL 701-2269)

x-RAY PHOTOELECTRON SPECTROSCOPY OF COMPOUNDS CONTAINING CARBON

T. Darrah Thomas†

It is likely that one of the important areas of applicability of x-ray photoelectron spectroscopy will be the study of carbon-containing compounds. The present resolution of the technique (about 1.2 eV for the 1s level of carbon) is sufficient to show the gross differences between different carbons in a variety of compounds, and even the rather fine differences between the carbons in methane and ethane. The ultimate limiting resolution is determined by the natural line width for the carbon 1s level, and is calculated to be about 0.06 eV. At this resolution one should probably be able to resolve the CH_3 carbon from the CH_2 carbon in propane, and many other closely spaced lines.

The following summaries cover a series of investigations I made, while a visitor to Berkeley, on the x-ray photoelectron spectroscopy of compounds containing carbon. The first of these, on hydrocarbons, is concerned with the effects on the carbon 1s binding energy due to changes of bond type, hydrogenation of multiple bonds, and replacement of hydrogen by carbon. The second, on halomethanes, deals with the effects of replacing hydrogen with electronegative ligands, specifically halogens. The third is concerned with the binding energies of all the electrons on carbon monoxide, and also discusses what sort of information may be obtained from intensity data.

A. x-Ray Photoelectron Spectroscopy of Simple Hydrocarbons*

Carbon 1s ionization potentials for methane (290.8 eV), ethane (290.6), ethylene (290.7), acetylene (291.2), cyclohexane (290.3), benzene (290.4), 2,2-dimethylpropane (290.4), and fluoroform (299.1), together with the fluorine 1s ionization potential for fluoroform (694.1) and ionization potentials for the $2a_g$ and $2a_u$ orbitals of ethylene (24.5 ± 1 and 19.5 ± 1) and for the $2\sigma_g$ and $2\sigma_u$ orbitals of acetylene (23.5) and 18.5), have been measured. These values, together with those from other measurements, are compared with orbital energies obtained by use of Koopmans' theorem. The comparison indicates that this method of calculation gives orbital energies that are about 5% larger than the experimental ionization potentials for carbon 1s electrons and 10 to 15% greater for the outer electrons. These differences are consistent with calculations of the ionization potentials of carbon atoms. The carbon 1s binding energy decreases with hydrogenation and when a hydrogen is replaced by an alkyl group. The first of these results is consistent with theoretical calculations and with other chemical evidence. There is an apparent discrepancy between the second result and the result of theory or other chemical evidence.

B. x-Ray Photoelectron Spectroscopy of Halomethanes‡

Carbon 1s ionization potentials, relative to that of methane (290.8 eV), have been measured for

(a)	CH_3F (2.8 eV)	CF_4 (11.0 eV)	CH_2Cl_2 (3.1 eV)	CCl_4 (5.5 eV)
	CHF_3 (8.3 eV)	CH_3Cl (1.6 eV)	$CHCl_3$ (4.3 eV)	CH_3Br (1.0 eV)
(b)	CH_3F (692.4 eV)	CHF_3 (694.1 eV)	CF_4 (695.0 eV)	
(c)	CH_3Cl (277.2 eV)	CH_2Cl_2 (277.6 eV)	$CHCl_3$ (277.7 eV)	CCl_4 (278.0 eV)

The carbon and halogen binding energies increase linearly with the number of halogens. Comparison of the fluorocarbon results with binding energies based on use of Koopmans' theorem indicates a substantial error between experiment and theory that increases with the number of fluorines. This discrepancy arises because Koopmans' theorem does not allow for relaxation of electrons and polarization of the ligands when the ion is formed from the neutral molecule. The measured binding energies are found to vary linearly with the sum of differences between the electronegativities of the ligands and that of hydrogen.

C. x-Ray Photoelectron Spectroscopy of Carbon Monoxide††

The ionization potentials for all the electrons on carbon monoxide have been measured by x-ray photoelectron spectroscopy. The values found (in eV) are 1σ (oxygen 1s), 542.3; 2σ (carbon 1s), 296.2; 3σ, 38.9; 4σ, 19.8; 1π, 17.2; and 5σ, 14.0. The 1σ ionization potential is 1.2 eV less than the 1s ionization potential for molecular oxygen; the 2σ ionization potential is 5.4 eV greater than the 1s ionization potential in methane. These results indicate a positive charge on the carbon of carbon monoxide and a negative charge on the oxygen, in agreement with the relative electronegativities, but opposite to what might be expected from the dipole moment of carbon monoxide. The ionization potentials for the three least bound electrons are in agreement with those found by other techniques, provided that allowance is made for the fact that these values represent vertical (rather than adiabatic) ionization potentials. Although the relative intensities of the photoelectrons reflect the atomic photoelectric cross sections and the molecular orbital composition in a qualitative way, there is not quantitative agreement between the measured intensities and theoretical cross sections.

Footnotes

†Permanent address: Princeton University, Princeton, New Jersey.
*J. Chem. Phys., Feb. 1970.
‡Submitted to J. Am. Chem. Soc.
††Submitted to J. Chem. Phys.

CORE-ELECTRON BINDING ENERGIES FOR SOLID COMPOUNDS OF BORON, CHROMIUM, NITROGEN, AND PHOSPHORUS†*

D. N. Hendrickson,‡ J. M. Hollander, and W. L. Jolly††

We have previously reported data on the chemical shifts of core-electron binding energies of nitrogen compounds, together with a correlation of these data with values of atomic charge calculated by the CNDO-MO method.[1] This work has now been extended to include compounds of boron, chromium, and phosphorus, and the calculations of atomic charge have been done by the extended Hückel MO method[2] as well as by the CNDO method.

The experiments were done with the Berkeley 50-cm iron-free spectrometer, utilizing magnesium K_α x rays (1253.6 eV). The binding energy data on boron, chromium, nitrogen, and phosphorus are plotted against calculated atomic charge values in Figs. 1 through 7.

The results of these correlation studies are summarized as follows:

Boron. A fair linear correlation is obtained between measured 1s electron binding energies and boron atom charge obtained from the EHMO calculations (Fig. 1). It is found that the EHMO method tends to overemphasize charge separation in these molecules, as compared with the CNDO-calculated charges (see Fig. 2). This is probably the result of using charge-independent Coulomb integrals in the EHMO calculations.

Chromium. Preliminary iterative EHMO calculations were done for a few of the chromium compounds, with different input parameters, but only a rough correlation was found between chromium 3p binding energy and calculated charge (see Fig. 3).

The chromium 3p binding energies of $K_3[Cr(CN)_6]$ and $K_3[Cr(CN)_5NO]$ are identical, and therefore one might conclude that the latter is a Cr(III) compound, contrary to its usual formulation as a Cr(I) compound. The assignment of the +3 oxidation state to chromium corresponds to a formal NO^- group. This conclusion is consistent with our nitrogen 1s work, in which we found the charge on the NO nitrogen in $K_3[Cr(CN)_5NO]$ to be more negative than expected for an NO^+ group.

Nitrogen. Extended Hückel MO calculations were completed for 28 nitrogen compounds, and Fig. 4 demonstrates the linear correlation that is found between nitrogen 1s binding energies and the EHMO nitrogen charges. The nitrogen charges obtained from the EHMO calculations range from -1.7 to almost +2.6. As noted above for boron, this range of charge is much greater than that obtained from the CNDO molecular orbitals. A characteristic of the CNDO plot (Fig. 5) is the presence of two lines--one for anions, and the other for neutral molecules and possibly

cations. This is probably an artifact of the CNDO method, arising from an inherent overemphasis of electron repulsion in the CNDO calculations of anionic molecules.

Phosphorus. Phosphorus 2p binding energies were obtained for more than 50 phosphorus compounds. The range of binding energy shifts was about 8 eV. For about half the compounds, EHMO calculations were made of phosphorus atomic charge. The calculations were done both with and without inclusion of 3d orbitals on the phosphorus atom, but the results were not appreciably different. The correlation between the phosphorus 2p binding energies and the EHMO-calculated charges is poor (see Figs. 6 and 7) in contrast to the nitrogen work, in which a reasonably good correlation was found with the same variations of the Hückel method.

Footnotes and References

†The work on phosphorus compounds was done with the assistance of M. Pelavin.

*This report is condensed from publications on

boron and chromium [D. N. Hendrickson, J. M. Hollander, and W. L. Jolly, UCRL-19083, Sept. 1969],

nitrogen [D. N. Hendrickson, J. M. Hollander, and W. L. Jolly, UCRL-19027, Aug. 1969; J. Chem. Phys. 49, 3315 (1968); Inorg. Chem. 8, 2642 (1969)], and

phosphorus [M. Pelavin, D. N. Hendrickson, J. M. Hollander, and W. L. Jolly, UCRL-19044, Aug. 1969].

‡Present address: California Institute of Technology, Pasadena, California 91109.

††Inorganic Materials Research Division, Lawrence Radiation Laboratory.

1. J. A. Pople, D. P. Santry, and G. A. Segal, J. Chem. Phys. 43, S 129, S 136 (1965); P. M. Kuznesof and D. F. Shriver, J. Am. Chem. Soc. 90, 1683 (1968).

2. R. Hoffman, J. Chem. Phys. 39, 1397 (1963); P. C. Van der Voorn and R. S. Drago, J. Am. Chem. Soc. 88, 3255 (1966).

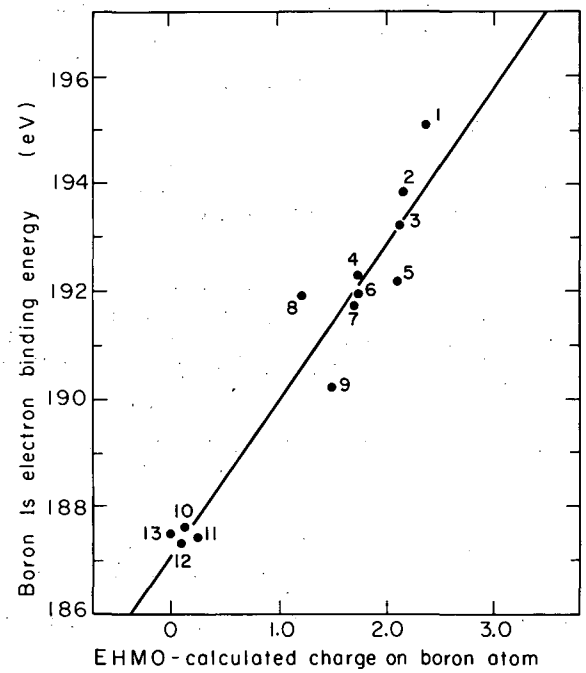

Fig. 1. Plot of boron 1s binding energy vs extended Hückel-calculated charges on boron atoms. (XBL 697-3245)

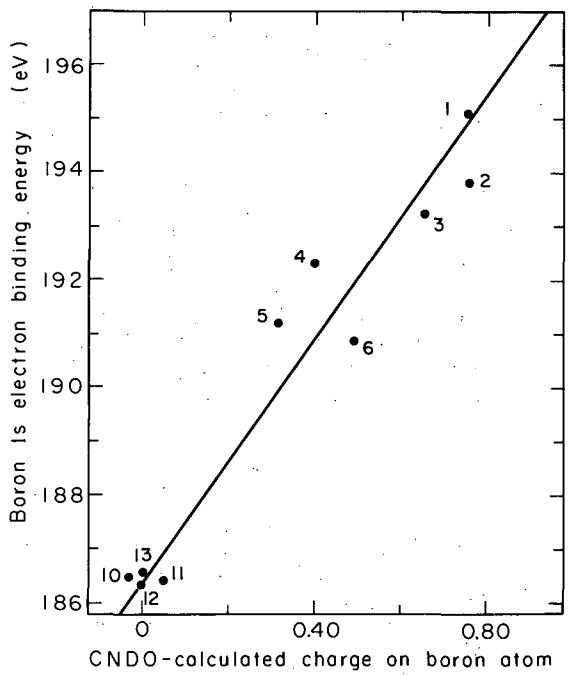

Fig. 2. Plot of boron 1s binding energy vs CNDO-calculated charges on boron atoms. (XBL 697-3247)

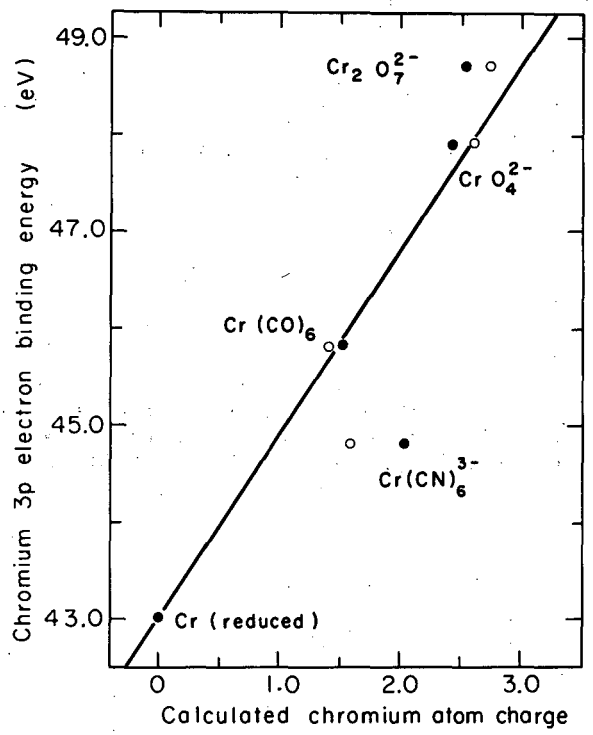

Fig. 3. Plot of chromium 3p binding energies vs iterative extended Hückel-calculated charges on chromium atoms. The symbols ● and o refer to two different sets of input data.
(XBL 697-2248)

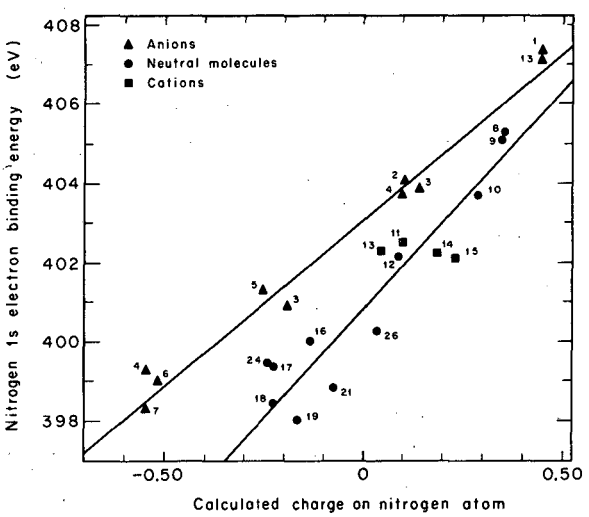

Fig. 5. Plot of nitrogen 1s binding energies vs CNDO calculated charges on nitrogen atoms.
(XBL 695-2642)

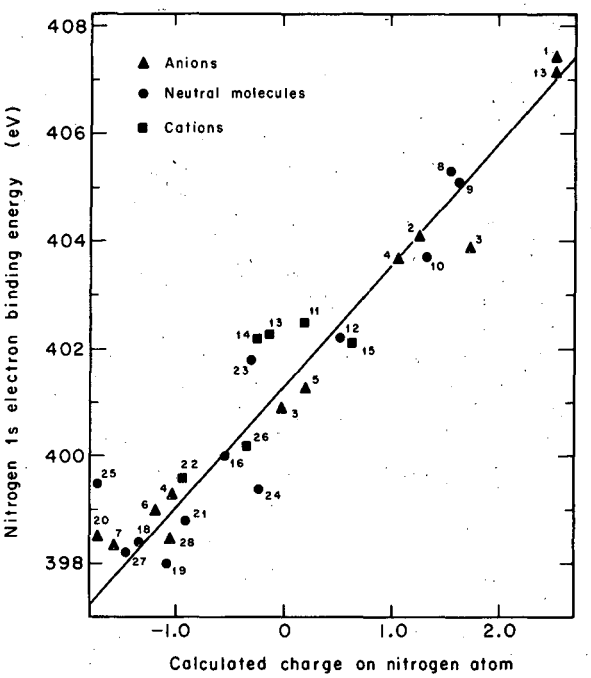

Fig. 4. Plot of nitrogen 1s binding energies vs extended Hückel-calculated charges on nitrogen atoms. (XBL 695-2645)

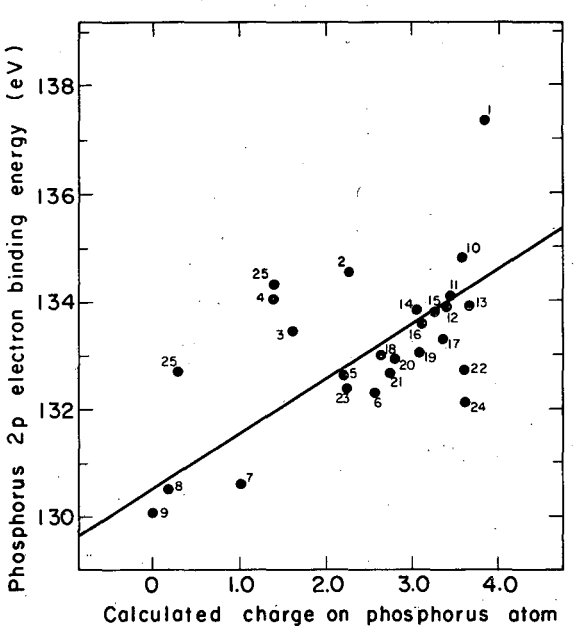

Fig. 6. Plot of phosphorus 2p binding energies vs noniterative extended Huckel-calculated charges on phosphorus atoms. (XBL 696-2987)

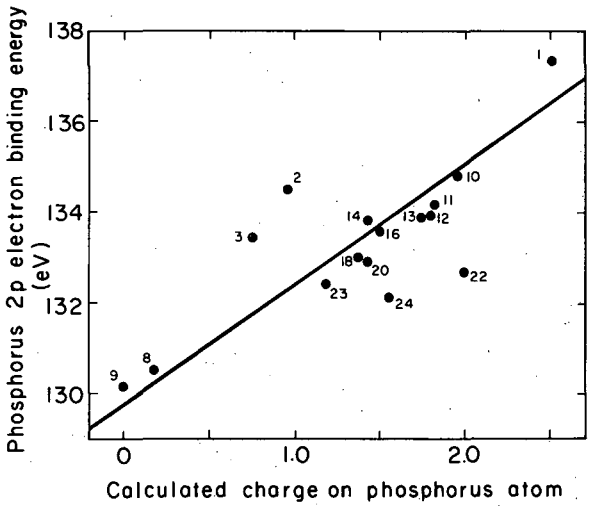

Fig. 7. Plot of phosphorus 2p binding energies vs iterative extended Hückel-calculated charges on phosphorus atoms. (XBL 696-2990)

III. Physical, Inorganic, and Analytical Chemistry

x-Ray Crystallography

THE STRUCTURE OF Di-π-CYCLOOCTATETRAENEURANIUM (URANOCENE)†

Allan Zalkin and Kenneth N. Raymond*

Streitwieser and Mueller-Westerhoff have recently reported the synthesis and characterization of bis(cyclooctatetraene)uranium.[1] As the name "uranocene" implies, this compound was proposed to be a new type of sandwich metal complex homologous with ferrocene.[2] We have completed an x-ray diffraction analysis of a single crystal of this material which shows it is indeed a π sandwich compound with a molecular symmetry of D_{8h}, as shown in Fig. 1.

The deep green compound crystallizes in $P2_1/n$ (an alternative setting of $P2_1/c$, C_{2h}^5) with $a = 7.084(3)$,[3] $b = 8.701(3)$, $c = 10.631(5)$ Å, $\beta = 98.75$ deg(3), $V = 6476(10)$ Å^3. For two formula units in the cell, the calculated density of 2.29 g/cm^3 is in the range expected from comparison with heavy metal compounds which have similar formulas. Several of the extremely air-sensitive crystals were sealed within thin-walled quartz capillaries (0.3 mm in diameter) under a carefully purified nitrogen atmosphere. Intensity data were collected by the stationary crystal–stationary counter method on a manually operated diffractometer using Zr-filtered Mo Kα radiation out to a Bragg 2θ angle of 35 deg. These data were corrected for absorption.

With two formula units in the cell the molecule may be unambiguously placed on the origin with $\bar{1}$ (C_i) crystallographic point symmetry. The uranium atoms then contribute only to structure factors F(h, k, l) for which h + k + l is even. Those structure factors with h + k + l odd are due entirely to the scattering of the carbon and hydrogen atoms. For this class of reflections the problem is virtually the same as a light-atom structure. Assignment of phases for these reflections is then difficult, but their magnitudes are very sensitive to the carbon atom positions.

An origin-removed sharpened Patterson map showed very little ripple, and the strongest eight peaks in this map for vectors in the range 1.6 to 3.0 Å all had lengths of about 2.6 Å and clearly showed the sandwich structure of the molecule with virtually no significant distortion. The coordinates from the Patterson map were directly used in subsequent least-squares refinements. The present level of refinement for all 540 reflections with $F^2 > \sigma(F^2)$ corrected for absorption gives R and wt R as 3.3 and 3.9%, respectively.

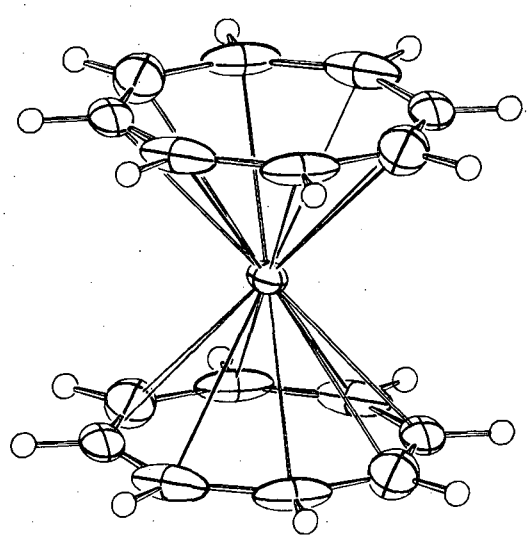

Fig. 1. A perspective drawing of $(C_8H_8)_2U$, di-cyclooctatetraeneuranium. (XBL701-18)

Since the molecule lies on the origin with $\bar{1}$ (C_i) crystallographic point symmetry, the two planar C_8H_8 rings are then constrained to be parallel and eclipsed. The orientations of the carbon atom thermal ellipsoids (Fig. 1) show a preferential oscillation of the rings about the molecular symmetry axis, as expected in a compound of this type. The U–C and C–C bond lengths are all equivalent to within the present level of refinement. The average U–C bond length is 2.648(5) Å, with the assigned standard deviation estimated from the variance. The average C–C bond length is 1.395(15) Å. The averages for alternating sets of four bonds are 1.391 and 1.398 Å. The eight carbon atoms of an individual ring all lie within about 0.02 Å of the least-squares plane. This planarity and the equality of alternate bond lengths

leaves no question that this is a pseudoaromatic ring and that di-π-cyclooctatetraene-uranium or "uranocene" is an authentic π sandwich complex of the 5f transition series.

Footnotes and References

†Condensed from J. Am. Chem. Soc. 91, 5667 (1969).
*Chemistry Department, University of California, Berkeley 94720.
1. A. Streitwieser and U. Mueller-Westerhoff, J. Am. Chem. Soc. 90, 7364 (1968).
2. Although other complexes of planar cyclooctatetraene dianion are known [see, for example, M. A. Bennett, Advan. Organometal. Chem. 4, 376 (1966); H. Breil and G. Wilke, Angew. Chem. Intern. Ed. Engl. 5, 899 (1968)], these compounds contain rather weakly bound C_8H_8 dianions and show chemical behavior characteristic of ionic bonding.
3. The standard deviation in the least significant digits is given in parentheses.

REDETERMINATION OF THE BETAINE HYDROCHLORIDE STRUCTURE, $[(CH_3)_3NCH_2COOH]^+Cl^-$

Mark S. Fischer,† David H. Templeton, and Allan Zalkin

The structures of compounds of choline, $[(CH_3)_3NCH_2CH_2OH]^+X^-$, and of betaine, $[(CH_3)_3NCH_2COOH]^+X^-$, are of interest because of both the unusual radiation sensitivity of choline chloride[1] and the frequent occurrence of these compounds in biological systems. They are components of complex lipids, and they can act as transmethylating agents. The related acetylcholine is essential to nerve impulse transfer.

Related structures which have been determined previously include choline chloride,[2] muscarine iodide,[3] and acetylcholine bromide.[4] Clastre[5] has published a preliminary structure report for betaine hydrochloride, but it is not very accurate. We undertook this structure investigation to provide an accurate structure, to locate the positions of the hydrogen atoms, and to investigate the packing.

Small colorless crystals of betaine hydrochloride were kindly supplied to us by Dr. R. M. Lemmon. These were then recrystallized in the form of colorless needles by the evaporation of a water-methanol solution to dryness at room temperature. The unit cell parameters (at 23 deg) are $a = 7.428 \pm 0.002$, $b = 9.108 \pm 0.005$, $c = 11.550 \pm 0.003$ Å, and $\beta = 96.71 \pm 0.03$ deg. The space group is $P2_1/c$. The crystal used measured $0.09 \times 0.09 \times 0.43$ mm. The four most prominent faces were (100), (001), ($\bar{1}00$), and (00$\bar{1}$). The observed density of 1.314 ± 0.005 g/cm^3, which was determined by flotation in a chloroform–ethylene dichloride mixture, agrees well with the value of 1.313 g/cm^3 calculated for four formula units per unit cell. Integrated intensities (θ–2θ scans) were measured with a card-controlled automated General Electric XRD-5 diffractometer. Copper Kα radiation was used to collect 794 independent reflections.

The structure was deduced from Patterson and Fourier calculations and was refined by full-matrix least squares. The final R value was 0.027. All nonhydrogen atoms were refined with anisotropic thermal parameters. The twelve hydrogens were located and refined with isotropic thermal parameters. A stereoscopic view of one molecule is presented in Fig. 1. The atomic positions found in this investigation differed from those found by Clastre[5] [by as little as 0.02 Å for the chlorine atom to as much as 0.16 Å for atom C(2)]. The mean difference was 0.07 Å, which is more than 20 times the estimated standard deviations in this investigation. Clastre made no statement concerning the precision of his results.

The orientations of the methyl and methylene groups are very near to being staggered around each of the four C-N bonds. The entire cation conforms within about 0.1 Å to the symmetry of a noncrystallographic mirror plane. The mirror plane passes through (or near) atoms O(1), O(2), C(5), C(4), N, C(3) and relates C(1) to C(2). The carboxyl group is planar within experimental error. The carboxyl group is twisted around bond C(4)-C(5) in such a way that atom O(2) is almost as close to and O(1) as far from the nitrogen atom in the same molecule as is possible. This results in an extended shape for the molecule in which the carboxyl hydrogen atom is remote from the positively charged ammonium group. The molecular packing is shown in Fig. 2.

Footnote and References

†Present Address: Medical School, University of Wisconsin, Madison, Wisconsin 53706.

1. B. M. Tolbert, P. T. Adams, E. L. Bennett, A. M. Hughes, M. R. Kirk, R. M. Lemmon, R. M. Noller, R. Ostwald, and M. Calvin, J. Am. Chem. Soc. 75, 1867 (1953).
2. M. E. Senko and D. H. Templeton, Acta Cryst. 13, 281 (1960).
3. F. Jellinek, Acta Cryst. 10, 277 (1957).
4. F. G. Canepa, P. Pauling, and H. Sörum, Nature 210, 907 (1966).
5. J. Clastre, Compt. Rend. 259, 3267 (1964).

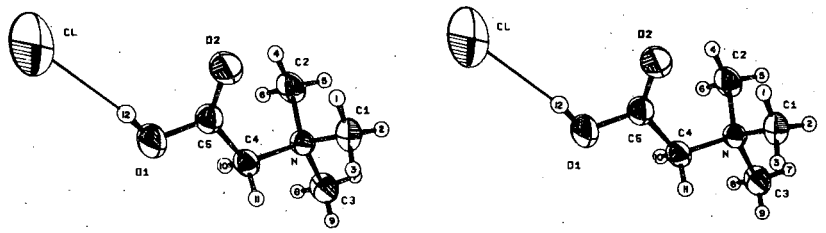

Fig. 1. Stereoscopic view of one molecule of betaine hydrochloride.
(XBL692-255)

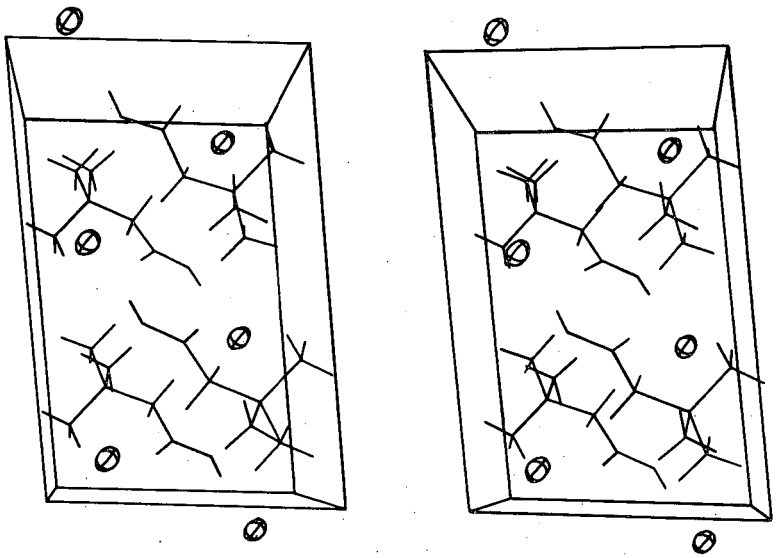

Fig. 2. Stereoscopic view of one unit cell of betaine hydrochloride.
(XBL692-254)

THE CRYSTAL STRUCTURE OF $Ni(B_9C_2H_{11})_2$, A NICKEL(IV) COMPLEX OF THE DICARBOLLIDE ION

David St. Clair,† Allan Zalkin, and David H. Templeton

Another in the series of transition-metal complexes of the dicarbollide ion, $(B_9C_2H_{11})^{-2}$, has been prepared.[1,2] This complex, $Ni(B_9C_2H_{11})_2$, is a neutral molecule in which the nickel is in a formal +4 valence state. Warren and Hawthorne predicted the structure as having the nickel ion sandwiched between the open fivefold faces of two $(B_9C_2H_{11})^{-2}$ icosahedral fragments. Because of the unusual chemical and spectral properties of this compound, observed for only this molecule and an analogous $Pd(B_9C_2H_{11})_2$ neutral molecule,[3] an unusual structure was expected.

We report the results of a single-crystal x-ray analysis which confirms the sandwich-type structure in the molecule, shown in Fig. 1. We show that there are two enantiomorphic rotational configurations present in the crystal and that the cages are staggered. The structure is novel among the unsubstituted metallocarboranes containing two dicarbollide ions in that the pairs of carbon atoms in opposite cages are as close to each other as is possible in this staggered configuration, so that the molecule has the symmetry of only a twofold axis. A similar configuration of carbon atoms has been observed, however, in a double-icosahedral-cage cobalt metallocarborane in which the two cages are linked by a S-C-S bridge,[4] and in a metallocarborane containing three linked icosahedra.[5]

The yellow crystals are monoclinic with unit cell dimensions, measured at room temperature (≈22°), $a = 13.371 \pm 0.003$ Å, $b = 10.398 \pm 0.005$ Å, $c = 13.556 \pm 0.003$ Å, $\beta = 119.16 \pm 0.04$ deg. There are four molecules of $Ni(B_9C_2H_{11})_2$ in the unit cell. The calculated density, $\rho = 1.31$ g/cm^3, agrees well with the observed density, $\rho = 1.30$ g/cm^3, measured by flotation. The space group is $P2_1/c$. A total of 3242 intensities was measured by the $\theta-2\theta$ scan technique using a G.E. card-controlled automatic x-ray diffractometer equipped with a Cu x-ray tube and a scintillation counter.

The location of the Ni atom was determined from a study of a pattern of strong and weak reflections in the data. A Fourier map phased on the nickel disclosed the rest of the structure. All the positional parameters were refined by a full-matrix least-squares procedure. All nonhydrogen atoms were given anisotropic thermal parameters. The final refinement gave a conventional R value 0.035 for the 2724 non-zero-weighted data, and $R = 0.051$ calculated by using all 3242 data.

As shown by the stereoscopic pair drawing in Fig. 1, this neutral molecule is a double-cage carborane having the nickel atom sandwiched between the cages by bonding to the open fivefold faces of the two icosahedral fragments. Each of the carbon and boron atoms in the cages has a hydrogen atom pointing out radially from the cage approximately along a line from the atom to which it is attached to the atom directly opposite it in the cage. The carbon pairs in the cages on opposite sides of the metal are as close as is possible with the cages staggered. The carbons allow only C_2 point symmetry for the molecule. This lack of reflection and inversion symmetry permits the existence of enantiomorphic rotational isomers. Ni-C distances vary from 2.065 to 2.077 Å; N-B distances from 2.085 to 2.105 Å; C-C distances from 1.601 to 1.610 Å; C-B distances from 1.670 to 1.732 Å; and B-B distances from 1.753 to 1.843 Å.

The molecular packing is shown by the stereoscopic pair drawing of the unit cell in Fig. 2. There are only six intermolecular H-H distances less than 2.60 Å.

Footnote and References

†Present address: Shell Oil Company, P. O. Box 262, Wood River, Illinois.

1. L. F. Warren and M. F. Hawthorne, J. Am. Chem. Soc. 89, 470 (1967).
2. M. F. Hawthorne, D. C. Young, T. D. Andrews, D. V. Howe, R. L. Pilling, A. D. Pitts, M. Reintjes, L. F. Warren, Jr., and P. A. Wegner, ibid. 90, 879 (1968).
3. L. F. Warren and M. F. Hawthorne, J. Am. Chem. Soc. 90, 4823 (1968).
4. M. R. Churchill, K. Gold, J. N. Francis, and M. F. Hawthorne, ibid. 91, 1222 (1969).
5. D. St. Clair, A. Zalkin, and D. H. Templeton, Inorg. Chem. 8, 2080 (1969).

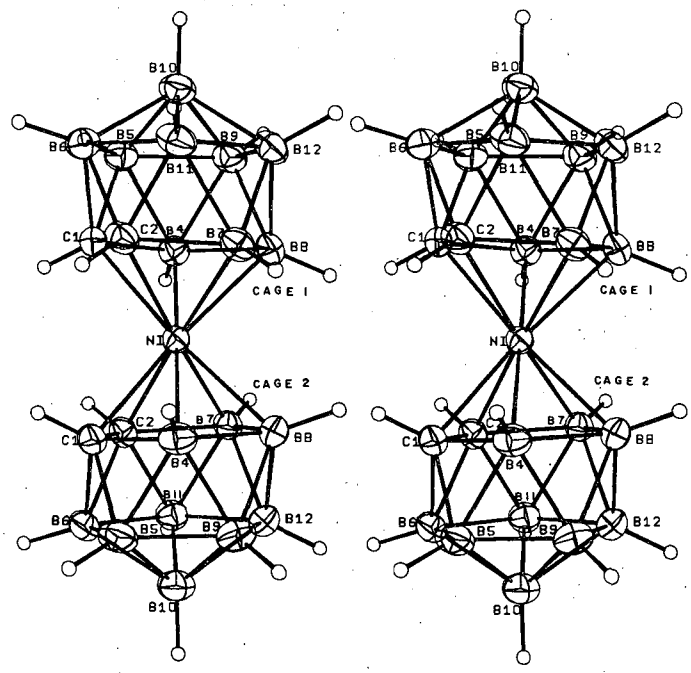

Fig. 1. Stereoscopic pair drawing of a complete $Ni(B_9C_2H_{11})_2$ molecule. Thermal ellipsoid boundaries are at the 40% probability level. For this drawing the hydrogens were given artifical thermal parameters, $\underline{B} = 0.5$. (XBL6811-6215)

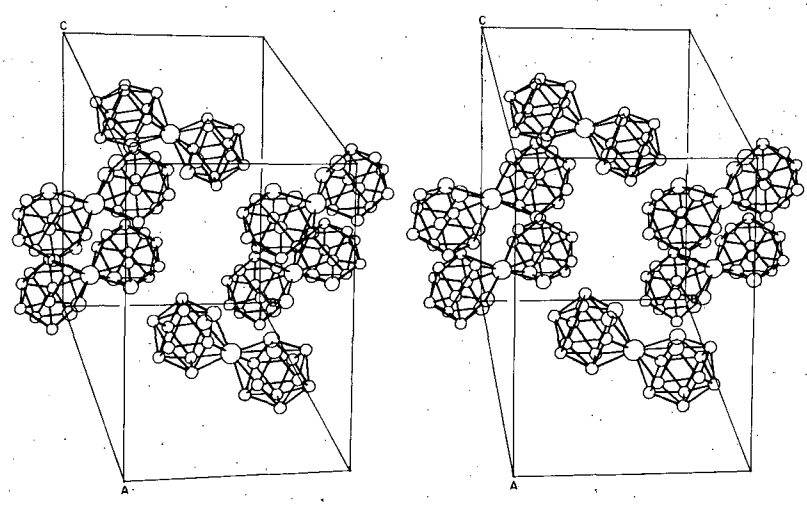

Fig. 2. Stereoscopic pair drawing of the unit cell (hydrogen atoms not shown). The origin is at the left rear corner of the unit cell. All thermal ellipsoids here are artificial. Nickel atoms are shown as the largest circles, carbon atoms as medium-size circles, and boron atoms as the smallest circles. (XBL 691-93)

THE CRYSTAL STRUCTURE OF $CsCr[B_9C_2H_9(CH_3)_2]_2 \cdot H_2O$, A HYDRATE OF A CHROMIUM METALLOCARBORANE SALT

David St. Clair,† Allan Zalkin, and David H. Templeton

Ruhle and Hawthorne have recently reported[1] the preparation of $Cr[B_9C_2H_9(CH_2]_2^-$, another in the series of transition-metal derivatives of the dicarbollide ion, $(B_9C_2H_{11})^{-2}$. In this anion the chronium is in a formal +3 valence state and is bonded to two icosahedral dicarbollide ions in which the hydrogen atoms on the carbons of the $(B_9C_2H_{11})^{-2}$ have been replaced by methyl groups. It was expected that the complex would have a sandwich-type structure in which the chromium would simultaneously occupy an apex in each of two icosahedra.

The crystal structure determination of the monohydrate of the cesium salt of the metallocarborane anion, $CsCr[B_9C_2H_9(CH_3)_2]_2 \cdot H_2O$, is reported here. The sandwich nature of the anion structure, shown in Fig. 1, is confirmed, and it is shown that the cages are staggered across the chromium with the carbon atoms of one cage rotated as far as possible from those in the other.

The dark red crystals of $CsCr[B_9C_2H_9(CH_3)_2]_2 \cdot H_2O$ were very well formed in the shape of square prisms elongated along the c axis. The largest faces were the rectangular-shaped (110) faces. Data were collected on a card-controlled General Electric XRD-5 diffractometer using $\theta-2\theta$ scans and Cu Kα radiation. A total of 2233 intensities was measured.

The unit cell is tetragonal with cell dimensions a = 9.938 ± 0.004 Å and c = 22.739 ± 0.007 Å. With four formula units, $CsCr[B_9C_2H_9(CH_3)_2]_2 \cdot H_2O$, in the unit cell, the density is calculated to be 1.55 g/cm^3. The space group was found to be $P4_12_12_1$.

The structure was determined from Patterson and Fourier maps and then refined by using a full-matrix least-squares calculation. Anisotropic temperature factors were applied to all the nonhydrogen atoms. All the hydrogen atoms except those of the water molecule were included with two isotropic temperature factors, one for the hydrogens attached to the boron cage and another for the methyl group hydrogens. The refinement gave $R = 0.047$ for the 1957 data having $I > \sigma(I)$.

The structure of the $Cr[B_9C_2H_9(CH_3)_2]_2^-$ anion skeleton is shown without hydrogen atoms in Fig. 1. The complete anion including hydrogen atoms is shown by the stereoscopic pair drawing in Fig. 2. The anion consists of two complete icosahedra linked through the chromium atom which simultaneously occupies an apex position in each cage. Each of the carbon atoms in the cage has a methyl group attached, and each boron has a hydrogen pointing out radially from the cage. The anion has an approximate mirror plane passing through atoms Cr, B(6), B(8), and B(10) in each cage. The point symmetry 2 is required for the anion by the space group, but the anion is observed to have $C_{2h}(2/m)$ point symmetry to within ± 0.02 Å.

The molecular packing is shown in Fig. 3 by the stereoscopic pair drawing of the unit cell looking approximately down the b axis. Each of the dumbbell-like anions is tilted out of the ab plane until its axis, B(10) in one cage to B(10) in the cage on the opposite side of the chromium, makes an angle of about 20 deg with the c axis. The water molecule has no neighbors suitable for hydrogen bonding, and therefore it is not surprising that it is observed to have large amplitudes of thermal motion, nor that we failed to detect its hydrogen atoms.

Footnote and Reference

†Present address: Shell Oil Company, P. O. Box 262, Wood River, Illinois 62095.

1. H. W. Ruhle and M. F. Hawthorne, Inorg. Chem. 7, 2279 (1968).

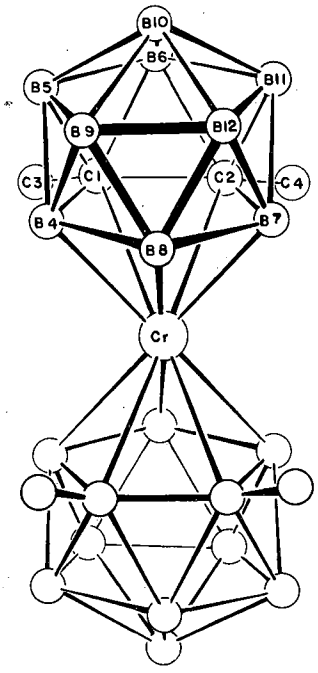

Fig. 1. Skeletal drawing of the $Cr[B_9C_2H_9(CH_3)_2]_2^-$ anion (hydrogen atoms not shown), including the numbering system. (XBL692-164)

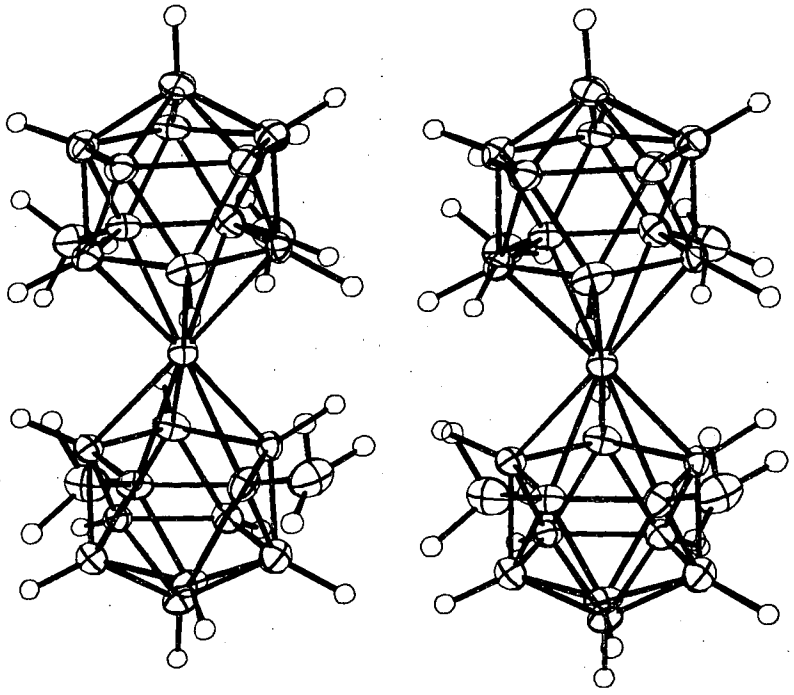

Fig. 2. Stereoscopic pair drawing of the complete $Cr[B_9C_2H_9(CH_3)_2]_2^-$ anion. (XBL692-166)

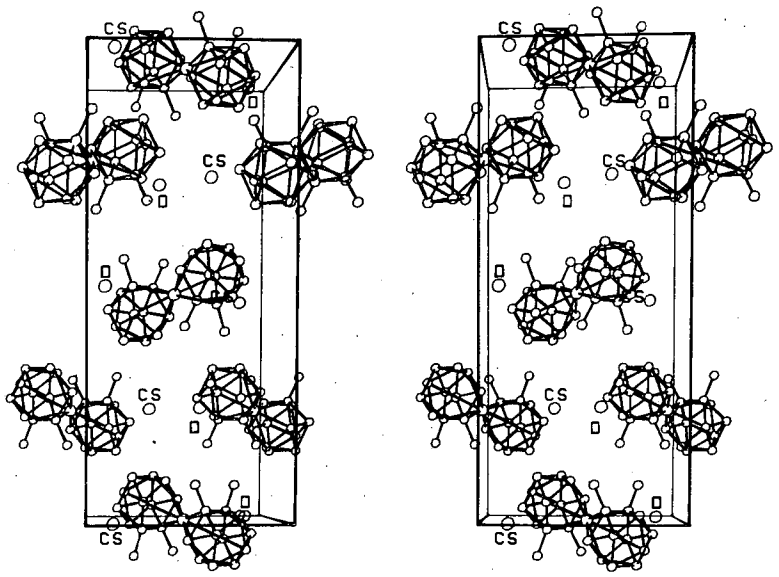

Fig. 3. Stereoscopic pair drawing of the unit cell of $CsCr[B_9C_2H_9(CH_3)_2 \cdot H_2O$ (hydrogens not shown) looking down the b axis. The a axis is horizontal and the c axis is vertical in the plane of the paper. The sets of two $Cr[B_9C_2H_9(CH_3)_2]_2^-$ anions appearing at $z = 1/4$ and $z = 3/4$ for the chromium atom should be in both the rear and the fore of the unit cell, but for clarity only one set of each pair is shown in the drawing. (XBL692-165)

THE CRYSTAL AND MOLECULAR STRUCTURE OF THE HEPTACOORDINATE COMPLEX TRIS(DIPHENYLPROPANEDIONATO)AQUOHOLMIUM, $Ho(C_6H_5COCHCOC_6H_5)_3 \cdot H_2O$†

Allan Zalkin, David H. Templeton, and David G. Karraker*

Holmium in the trivalent state, like other rare earths, reacts with dibenzyolmethane[1] to form a complex with the structure

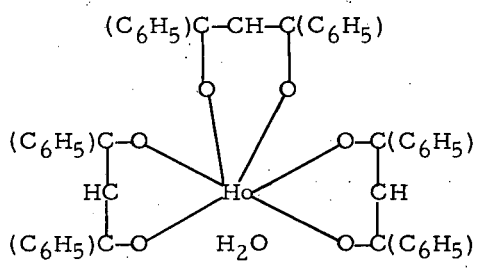

The water molecule is known to be firmly bound, and Hoard[2] in 1961 suggested this heptacoordinate structure for some similar complexes. The structure determination was undertaken in order to ascertain the coordination geometry about the holmium atom, and to investigate the nature of the hydration of the water molecule in this material. Recently the structures of tris(1-phenyl-1,3 butanedionato)aquoyttrium,[3] ytterbium acetylacetonate monohydrate,[4] and tris(acetylacetonato)-aquoytterbium hemibenzene[5] were reported, which also have sevenfold coordination.

$Ho(C_6H_5COCHCOC_6H_5)_3 \cdot H_2O$ was prepared by adding an aqueous solution of holmium trichloride to a refluxing mixture of dibenzoylmethane, acetone, and potassium hydroxide. Yellow crystals of the compound crystallized from the filtered and cooled solution.

A set of x-ray-diffraction data was taken manually, using the stationary-crystal stationary-counter technique with Cu $K\alpha$ x rays; 1365 independent intensities were used in the structure determination.

The space group of the crystal is R3 and contains a single formula unit in the rhombohedral unit cell. The cell dimensions of the triply primitive hexagonal cell at 23° are: $a_h = 22.713 \pm 0.012$ and $c_h = 6.334 \pm 0.004$ Å. The observed density from flotation in a mixture of ethylene dichloride and carbon tetrachloride at 25° is 1.48 g/cm^3, and the calculated x-ray density is 1.501 ± 0.005 g/cm^3.

The structure was determined[5] from Fourier maps and refined by full-matrix least squares. The concluding refinement of the structure resulted in a final R factor of 0.031, using all 1365 data. A refinement of the inverse structure resulted in an increase in R to 0.046. This is confirmation that the absolute configuration of the molecule in this particular crystal is correct. We have not made a correlation of the absolute configuration with respect to morphology or any other physical property.

The basic unit in this structure is a unimolecular species that consists of all the atoms in the chemical formula. A projection of the molecule down the threefold axis is shown in Fig. 1. The holmium atom, on the threefold axis, is surrounded by a distorted octahedron of six oxygen atoms from the organic ligands and a seventh oxygen from the water. The overall complex resembles a right-handed three-bladed propeller, this being the absolute configuration of this particular crystal. The phenyl rings are twisted from the plane of the propanedionato portion of the complex. This twisting is discernible in the stereographic representation in Fig. 2. Figure 3 shows the geometry in one blade of the molecule.

Footnotes and References

†Condensed from Inorg. Chem. 8, 2680 (1969).
*Present Address: Chemistry Department, E. I. DuPont Company, Savannah River, Georgia.

1. L. R. Melby, N. J. Rose, E. Abramson, and J. C. Caris, J. Am. Chem. Soc. 86, 5117 (1964).
2. J. L. Hoard, G. S. Smith, and M. Lind, Advances in the Chemistry of the Coordination Compounds, in Proceedings of the Sixth International Conference on Coordination Chemistry, ed. by Stanley Kirscher (MacMillan Company, New York, 1961), p. 296.
3. F. A. Cotton and P. Legzdins, Inorg. Chem. 7, 1777 (1968).
4. J. A. Cunningham, D. E. Sands, W. F. Wagner, and M. F. Richardson, Inorg. Chem. 8, 22 (1969).
5. E. D. Watkins II, J. A. Cunningham, T. Phillips II, D. E. Sands, and W. F. Wagner, Inorg. Chem. 8, 29 (1969).

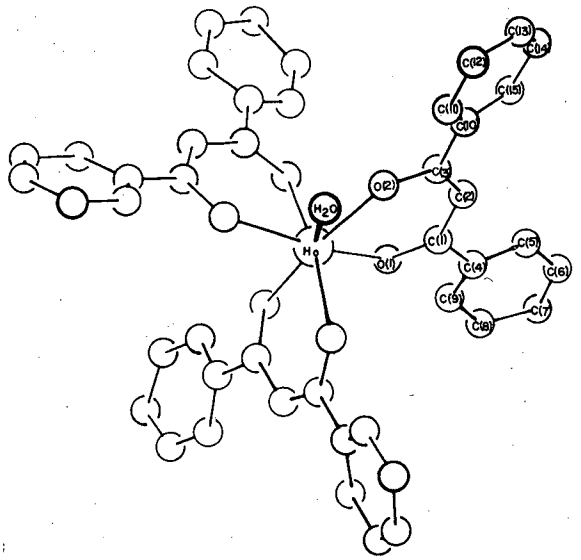

Fig. 1. The molecular unit of tris(diphenyl propanedionato)aquoholmium projected down the threefold axis. The water molecule is directly above Ho but has been displaced slightly in this drawing to better show the structure (XBL 678-4409)

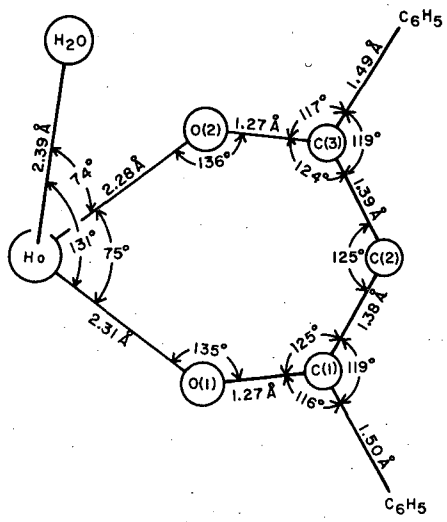

Fig. 3. Some distances and angles of the ligands about holmium. The estimated standard deviation of the angles is about 0.5 deg, and of the distance is about 0.02 Å. (XBL 6811-6173)

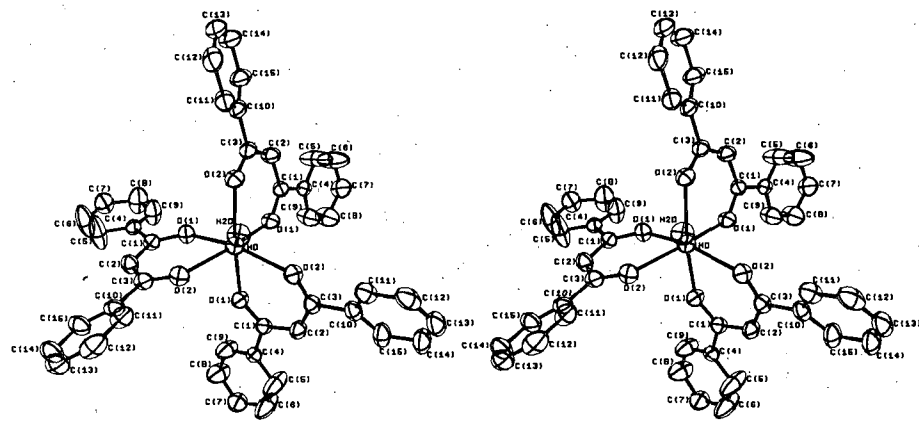

Fig. 2. A stereographic pair drawing of the molecule of tris(diphenyl propanedionato)aquoholmium. (XBL 6810-6058)

Physical and Inorganic Chemistry

$^{261}_{104}$Rf: NEW ISOTOPE OF ELEMENT 104

Albert Ghiorso, Matti Nurmia, Kari Eskola,† and Pirkko Eskola*

As part of our research program on the properties of element 104, rutherfordium, we have positively identified the nuclide ^{261}Rf. It was synthesized by bombarding a target containing 47 μg of ^{248}Cm with ^{18}O ions from the Berkeley Hilac. The gas-jet system used to deposit the product atoms on the periphery of a digitally stepped wheel for α-particle spectroscopy has been described before.[1,2]

In place of the simple two-crystal shuttle system used in the identification of ^{257}Rf and ^{259}Rf,[3] we employed a more advanced mechanism with two movable and two stationary crystals at each detector position (Fig. 1). This system permits the simultaneous recording of alpha-decay events taking place on the wheel, and the collection and study of the daughter nuclei ejected from the wheel.

A series of "mother" spectra recorded by the movable crystals while facing the wheel is shown in Fig. 2. The individual spectra obtained at each of the five detector positions around the stepped wheel are shown in numerical order with a sum spectrum at top. It can be seen that the α-particle energy of ^{261}Rf, approximately 8.25 MeV, largely coincides with that of its daughter, ^{257}No, but that the half-life of the combined peak clearly exceeds that of ^{257}No, 26 sec.

An analysis of the observed daughter counts from a number of similar experiments is presented in Fig. 3. These counts were recorded while the mother crystals were facing the stationary daughter crystals and were shielded from the activity on the wheel.

The diagram at the right shows the distribution of the daughter counts between the five detector positions. From these numbers, the half-life of the mother can be determined to be approximately 70 sec.

The time distribution of the summed daughter counts is shown at the left in the figure, and it is consistent with the 26-sec half-life of ^{257}No. We have also looked for a spontaneous-fission branching in the decay of ^{261}Rf, but without conclusive results. At this point we can only set an upper limit of approximately 10% for such a branching.

In our opinion this experiment clearly demonstrates the genetic relationship between ^{261}Rf and its daughter, ^{257}No. ^{261}Rf is thus the third isotope of element 104 that has been discovered and positively identified by our group. Its use in the first chemical experiments on rutherfordium will be described elsewhere.[4]

ADDENDUM: NAMING OF ELEMENT 104

The following statement was made by Albert Ghiorso at the Conference on Transuranium Elements, Houston, Texas, November 17-19, 1969:

"We have established with great confidence the alpha-decay properties of the isotopes 104-257, 104-259, and 104-261, and there is reasonable probability that we have characterized the spontaneously fissioning isotope 104-258.

"We have chemically separated element 104 by an aqueous method from the other transuranium elements, and shown that it behaves like hafnium and zirconium, as expected.

"We have searched diligently for an isotope of element 104 that decays by spontaneous fission with a half-life of 0.3 second (the originally reported Russian finding) without success. We have repeated these experiments with higher sensitivity, but find equally negative results for a half-life down to 0.1 second (the revised Russian finding).

"We are suggesting that element 104 be called rutherfordium (Rf) after Lord Rutherford, the great pioneer of nuclear science. If in the course of further experiments, contrary to our expectations, we do confirm the earlier findings of the Dubna group of an approximately 0.3-second

spontaneous fission activity, we will withdraw our suggested name and accept that proposed by the Russian group, kurchatovium."

Footnotes and References

†On leave from Department of Physics, University of Helsinki, Finland.
*Guest Scientist supported by the National Research Council of Sciences, Helsinki, Finland.

1. A. Ghiorso, T. Sikkeland, and M. J. Nurmia, Phys. Rev. Letters 18, 401 (1967).
2. A. Ghiorso and T. Sikkeland, Phys. Today 20, 25 (1967).
3. A. Ghiorso, M. Nurmia, J. Harris, K. Eskola, and P. Eskola, Phys. Rev. Letters 22, 1317 (1969).
4. Robert Silva, James Harris, Matti Nurmia, Kari Eskola, and Albert Ghiorso, First Chemical Separation of Rutherfordium, following paper.

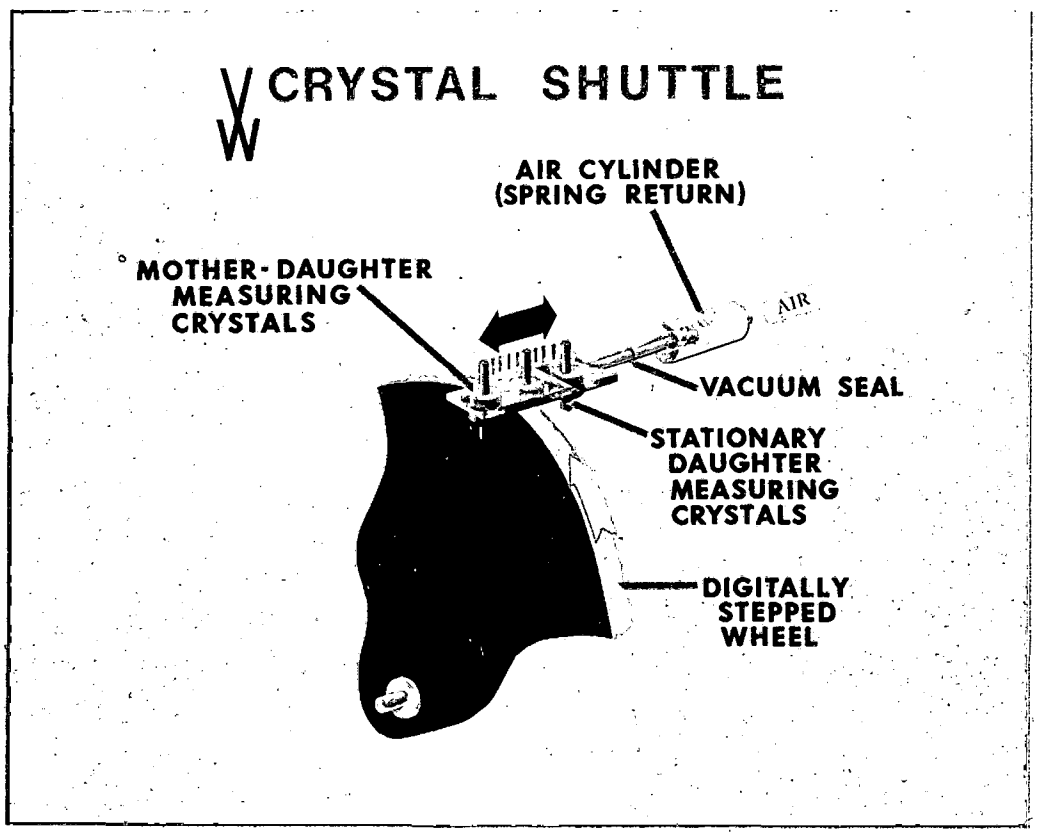

Fig. 1. Four-crystal shuttle system used in the study of genetically related alpha-decay events. (CBB698-5321)

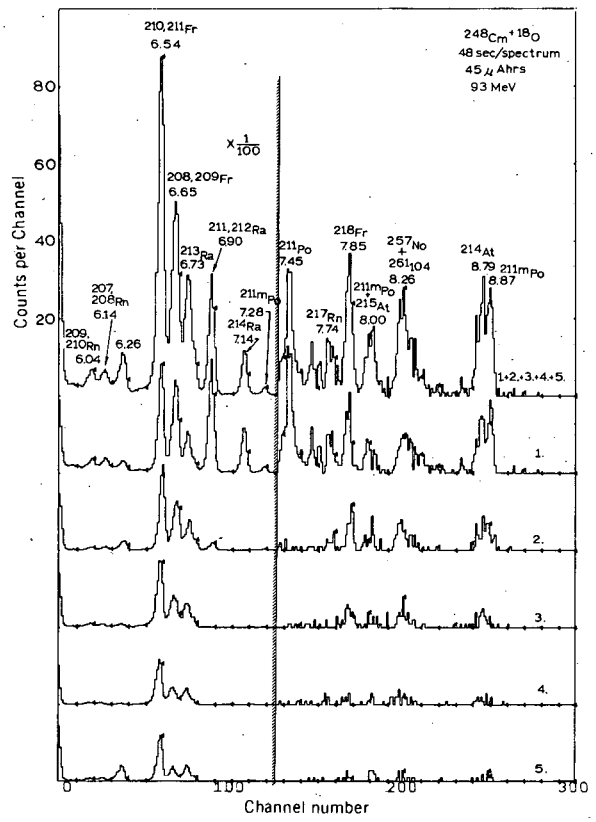

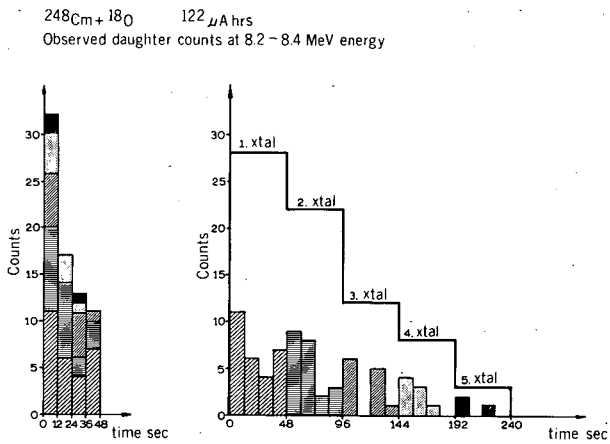

Fig. 3. The time distribution of alpha-decay events due to the 26-sec ^{257}No daughter of ^{261}Rf. (XBL701-6105)

Fig. 2. A series of alpha spectra resulting from bombarding ^{248}Cm with ^{18}O ions. Most of the alpha peaks are due to minute Hg and Pb impurities in the target. (XBL6911-4925)

FIRST CHEMICAL SEPARATION OF RUTHERFORDIUM

Robert Silva, † James Harris, Matti Nurmia, Kari Eskola, * and Albert Ghiorso

The discovery of rutherfordium-261, [1] with half-life of ≈ 70 sec and α-particle energy of 8.25 to 8.40 MeV, has made it possible to carry out aqueous chemical separations using standard tracer techniques. A total of 17 significant alpha decay events was observed in approximately 250 experiments performed by bombarding 47 μg of curium-248 with 92-MeV oxygen-18 ions from the Berkeley Hilac. Details of the bombardment assembly, fast sample-transfer system, and experimental procedures have been described elsewhere. [2]

Assuming element 103, Lr, to be the last member of the actinide series, element 104 would be expected to fall into the group IV B elements of the periodic table, i.e., to be eka-hafnium. It is predicted to have a valence and ionic radius similar to Zr and Hf, [3,4] and therefore exhibit similar chemical properties.

Previous studies with actinide elements show that cation-exchange columns using chelating agents as eluants can provide rapid chemical separations on one atom at a time, and yield sources suitable for alpha energy analysis. Under experimental conditions described below, a high percentage of tracer quantities of Zr and Hf were washed through the ion-exchange column with the first few column volumes of eluant, as shown in Fig. 1. In contrast, trace quantities of the 3+ ions Tm, Cf, and Cm required more than 100 column volumes to elute. One would expect Lr to be the first 3+ actinide [5,6] to be removed from the column and to elute in about the same position as Tm. Divalent nobelium and the alkaline earth elements are retained even more strongly by the resin column than the actinides. [7] Experiments with trace quantities of Bi (< 3%), Ra (< 1%), Fr (< 1%), Th (< 1%), Np (< 5%), Pu (≈ 50%), and Pa (≈ 50%) showed that only the latter two elements were present to any appreciable extent in the column fractions taken for α-particle analysis.

In our experiments, the rutherfordium recoil atoms were washed from an NH_4Cl-coated platinum catcher foil with ≈ 50 λ of ammonium alpha hydroxisobutyrate (0.1 M, pH 4.0) onto the top of a 2-mm-diameter by 2-cm-long heated (80 °C) column of Dowex-50 X 12 resin. This solution was forced into the resin and, after more eluant was added, the washing was continued. The first two drops (free column volume) contained little or no activity and were discarded. The next four drops (taken in two-drop fractions) were collected on platinum disks, evaporated to dryness, and heated to 500 °C. The alpha particles emitted from the sources were detected with Si(Au) detectors, and the number, energy, and time distribution of α particles with energies between 6 and 12 MeV were recorded in a PDP-9 computer. The average time from beam off to counting was 60 sec.

Figure 2 shows a summary of data accumulated over a 3-week period. Although the actual time of occurrence as well as the energy of each α-particle event was recorded, the time distributions given in Fig. 2 are broken up into four sequential 1-min decay intervals. Summations of the four individual energy spectra are also given. Figure 2a shows a summation of energy spectra obtained directly from the platinum catcher foils (i. e., no chemistry), from which the production rates of element 104 and impurity activities were determined. Figure 2b shows the accumulated energy spectra obtained after chemical separation. As can be seen, 17 α-particle events in the energy region 8.2 to 8.4 MeV were detected. Approximately half of these events are probably due to the decay of ^{257}No [$T_{1/2}$ = 26 sec, E_α = 8.22 (55%), 8.27 (26%), 8.32 (19%) MeV], the daughter of separated ^{261}Rf. In two experiments, two alpha decay events occurred in the 8.2 to 8.4 MeV region within a time interval of 1 min--most probably the first one due to ^{261}Rf and the second due to the daughter ^{257}No. This is consistent with the number of pair events expected in the counting system used.

The data indicate that the ion-exchange column behavior of the activity assigned to element 104 with mass 261 is consistent with that of Hf and Zr, but that it differs entirely from the chemical behavior of the trivalent and divalent actinide elements.

The authors thank Jean Rees for her considerable help in the chemical separations and the Hilac staff for their excellent support.

Footnotes and References

†Present address: Chemistry Division, Oak Ridge National Laboratory, Oak Ridge, Tennessee 37830.
*On leave from University of Helsinki, Finland.

1. Kari Eskola and Pirkko Eskola, The 158th National Meeting of the American Chemistry Society, Division of Nuclear Chemistry & Techniques, New York, N. Y., September 7-12, 1969, Paper 44.
2. R. J. Silva, M. Nurmia, T. Sikkeland, and A. Ghiorso, in Chemistry Division Annual Report, 1968, UCRL-18667, Jan. 1969, p. 299; A. Ghiorso, T. Sikkeland, and M. Nurmia, Phys. Rev. Letters 18, 11, 401 (1967); A. Ghiorso and T. Sikkeland, Phys. Today 20, 25 (1967).
3. G. T. Seaborg, American Chemical Society, Mendeleev Centennial Symposium, Minneapolis, Minnesota, April 15, 1969.
4. B. B. Cunningham, Robert A. Welch Conference on Chemical Research, XIII, The Transuranium Elements, Houston, Texas, November 17-19, 1969.
5. G. R. Choppin and R. J. Silva, J. Inorg. Nucl. Chem. 3, 153 (1956).
6. G. R. Choppin, B. G. Harvey, and S. G. Thompson, J. Inorg Nucl. Chem. 2, 66 (1956).
7. J. Maly, T. Sikkeland, R. Silva, and A. Ghiorso, Science 160, 1114 (1968).

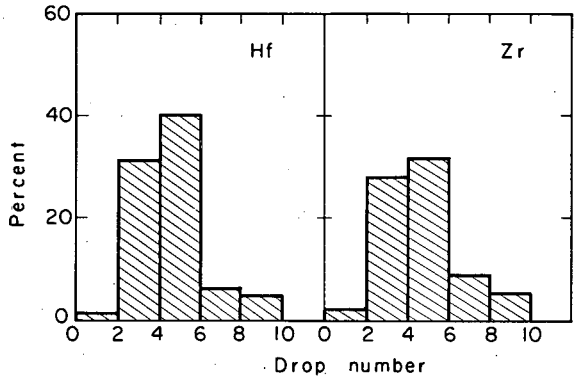

Fig. 1. Percent recovery of Hf and Zr tracer added to the column vs the volume of eluant passed through the column. (XBL702-2325)

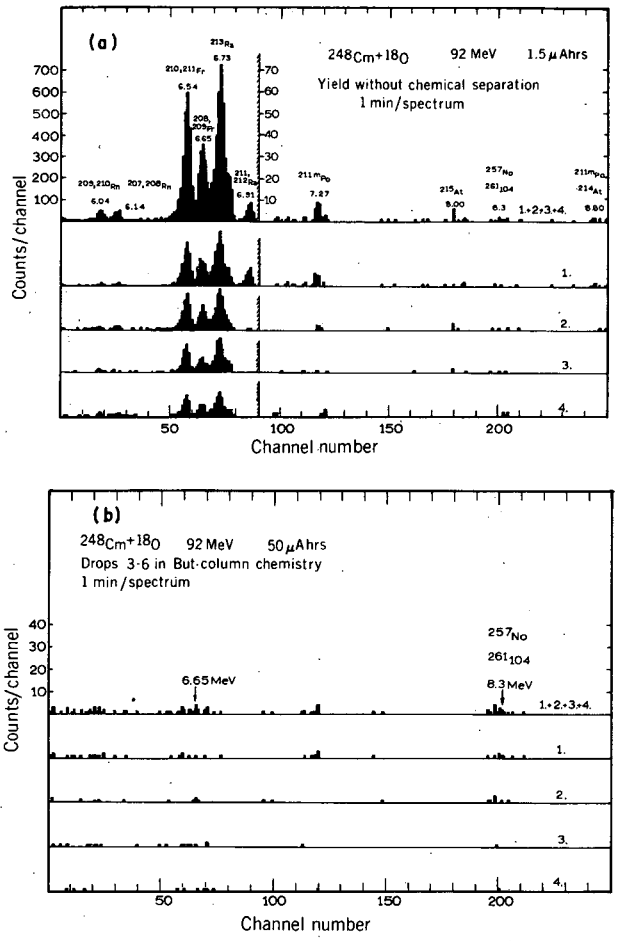

Fig. 2. The accumulated number and energy of α particles emitted in four decay intervals of 1-min duration. (a) Sum of ten bombardments without chemical separation. (b) Sum of all bombardments with chemical separation. (XBL701-6104 and 6103)

SEARCH FOR SUPERHEAVY ELEMENTS IN NATURE VIA THEIR NEUTRON EMISSION

E. Cheifetz,† H. R. Bowman, and S. G. Thompson

We are at present using a large gadolinium-loaded liquid scintillator with 85% efficiency for detecting neutrons in an attempt to observe the spontaneous fission of superheavy elements. Calculations by Nix[1] indicate that superheavy elements with atomic numbers in the range Z = 110 to 114 emit about 10 neutrons when they undergo spontaneous fission decay. The emission of such a large number of neutrons from each single fission event is then a very distinctive indicator of the presence of superheavy elements, because this property does not occur in any of the presently known spontaneously fissioning species in nature. Furthermore, these evaporated neutrons are expected to have kinetic energies in the region 0.5 to 7 MeV, and thus would have considerable penetration depth; consequently large amounts of materials can be examined with great sensitivity.

The system and its operation have been described previously.[2] It consists of a cylinder 103 cm in diameter and 83 cm long filled with 680 liters of the scintillating liquid. Sixteen photomultipliers of 5-in. diam connected in two banks are placed around the cylinder. The samples are placed in a hollow tube of 11.5 cm diam at the axis of the chamber. The detection system is operated in two ways. For calibration, a fission signal derived from a solid-state detector generates a 36-μsec gate after a 1-μsec delay. Pulses that are in coincidence between the two banks with time resolution of 50 nsec and corresponding to energy greater than ≈ 1 MeV are registered if

they appear within the fission gate. The pulse pair resolution is ≈ 200 nsec. For the actual measurements, we generate the 36-μsec gate for any pulse that arrives in the system when the gate is not activated. If a superheavy element decays the gate will be generated either by the prompt gammas or by the first neutron. Since the gate opens for any gamma signal above ≈ 1 MeV, the system is very sensitive to the environmental radiation, which consists of γ rays from natural radioactivity (e. g. uranium, thorium, and potassium) and cosmic-ray-induced radiation. The probability of observing a multiple event caused by the natural radiation behaves according to the Poisson distribution and falls very rapidly for increasing multiplicity. For a single counting rate of 2000/sec, less than 0.1 count/day is expected for multiplicities of six or more. High energy particles in cosmic rays induce (xn) reactions in heavy elements, and thus appear as multiple events. A reduction in the cosmic-ray effect was observed by rejecting multiple events that included very large pulses. The distributions of multiplicities obtained with and without a lead sample are shown in Fig. 1. The tail at multiplicities of six and above is consistent with the cosmic radiation fluxes and amounts to 0.15 event/kg of lead/min. Such a tail appears also when other heavy elements such as tungsten and tantalum are placed inside the detector. The tail corresponding to the high multiplicities in the background measurement is consistent with cosmic-ray-induced reactions in the gadolinium.

It is planned to install a counter similar to the one described above in a 250-m-deep tunnel, which should eliminate the cosmic ray events. The system will then be used to investigate the reported presence of enhanced spontaneous fission in lead samples[3] and to investigate a host of other possibilities.

Footnote and References

†On leave from Weizmann Institute of Science, Rehovoth, Israel.

1. J. R. Nix, Phys. Letters 30B, 1 (1969).
2. V. J. Ashby, H. C. Catron, L. L. Newkirk, and C. J. Taylor, Phys. Rev. 111, 616 (1958).
3. G. N. Flerov, Joint Institute of Nuclear Research (Dubna) Report E15-4651, Aug. 1969.

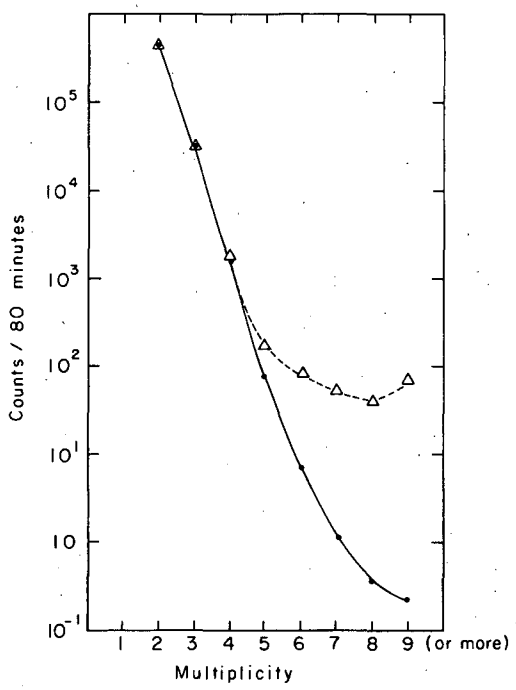

Fig. 1. Distribution of the multiplicities in the detector. The single count rate is 4.1×10^3 counts/sec. The average of 16 measurements with 25 kg lead is denoted by △. The average of 13 measurements with no sample is shown by ●. (XBL6912-6387)

SEARCH FOR POLAROGRAPHIC REDUCTION IN SOLUTIONS OF CALIFORNIUM(III) AND EINSTEINIUM(III)

B. B. Cunningham, L. R. Morss,† and T. C. Parsons

Experimental evidence has been accumulating that heavy actinides, beginning with Cf, have increasingly more stable divalent oxidation states (with respect to the trivalent states). Sufficient quantities of ^{249}Cf and ^{253}Es were available to attempt to observe the M(III)-M(II) reduction of these elements polarographically.

The polarographic microcell consisted of a 4-mm-i. d. Pyrex tube of working volume ≈ 150 μl, with a hole near its bottom so that mercury accumulating from the dropping mercury electrode could flow into a much larger reservoir (thus maintaining nearly constant mercury level). The cell, reservoir, and calibrated dropping mercury electrode were all contained in an inert-gas enclosure.

The apparatus was tested with 0.001 M solutions of Eu^{3+} and Yb^{3+} in a supporting electrolyte of 0.1 N NH_4Cl. Polarograms of the reduction of these ions reproduced similar experiments reported in the literature.[1,2] In the presence of alpha radioactivity equivalent to 20 μg of ^{249}Cf, the Eu and Yb polarograms could be reproduced without interference from radiolysis products; however, in the presence of alpha activity equivalent to 2 μg of ^{253}Es, peroxide built up so rapidly that a continually increasing current was observed at voltages more negative than -0.8 V vs NHE, even when surfactant (Triton X) and free-radical scavenger (4% methanol) were present.

Solutions were prepared (in 0.1 N NH_4Cl) of purified 0.001 M $^{249}Cf^{3+}$ and 0.0002 M $^{253}Es^{3+}$ and scanned polarographically within minutes of dissolution. No polarographic reduction waves were observed in either of these solutions, thereby setting approximate upper limits to the standard electrode potentials as follows:

$$Cf^{3+} + e^- = Cf^{2+}, \qquad E^0 < -1.4 \text{ V vs NHE},$$

$$Es^{3+} + e^- = Es^{2+}, \qquad E^0 < -0.5 \text{ V vs NHE}.$$

As a check on the Cf experiment, Yb was added directly to the ^{249}Cf polarographic solution to make both Cf^{3+} and Yb^{3+} concentrations 0.001 M. As before, the Yb reduction wave was observed, with the expected half-wave potential and diffusion current, thereby confirming that the Cf(III)-Cf(II) potential is more negative than that of Yb (-1.15 V).

Footnote and References

†Present address: Department of Chemistry, Purdue University, Lafayette, Indiana 47907.

1. H. N. McCoy, J. Am. Chem. Soc. 58, 1577 (1936).
2. H. Laitinen, J. Am. Chem. Soc. 64, 1133 (1942).

THERMOCHEMISTRY OF RARE-EARTH CHLOROCOMPLEX COMPOUNDS, Cs_2NaMCl_6

L. R. Morss†

Several chlorocomplex compounds of trivalent metals, Cs_2NaMCl_6, have been prepared; all have been characterized as face-centered cubic.[1] Compounds for the rare-earth elements Y, La, Ce, Nd, Gd, Dy, Er, Lu, and Pu were prepared as single crystals by gradient solidification of a melt of the anhydrous chlorides. x-Ray powder patterns of these crystals yielded diffraction lines all of which could be indexed (with respect to angle and intensity) as face-centered cubic.

By use of a gold-plated copper microcalorimeter of 30-ml volume, duplicate heats of solution were measured at 25 °C for all these compounds. Heats of solution were measured in 0.001 M HCl

(to avoid hydrolysis) and the final molality of Cs_2NaMCl_6 following each dissolution was about 0.004. The averaged heats of solution, corrected to infinite dilution, of the lanthanide compounds are displayed in Fig. 1a; corresponding values for Cs_2NaYCl_6 and $Cs_2NaPuCl_6$ are -18.7 and -13.4 kcal/mol.

From these heats of solution, the heats of formation of these complex compounds were calculated by making use of literature values for heats of formation and solution of the binary chlorides. The enthalpies of complexing,

$$MCl_3(c) + 2CsCl(c) + NaCl(c) = Cs_2NaMCl_6(c),$$

were calculated from the respective heats of formation; these enthalpies for the lanthanide compounds are plotted in Fig. 1b; corresponding values for Y and Pu compounds are -25.6 and -9.0 kcal/mol.

By means of appropriate Born-Haber cycles, with experimental values from the literature and from this research as well as calculated lattice energies for Cs_2NaMCl_6, the sum of the first three ionization potentials of the lanthanide atoms, and the absolute heats of hydration of the trivalent lanthanide ions, were estimated. These useful empirical data are plotted in Fig. 2; the third ionization potentials of the lanthanides were estimated by subtracting recent experimental values of the first and second ionization potentials.

Footnote and Reference

†Present address: Department of Chemistry, Purdue University, Lafayette, Indiana 47907.

1. L. R. Morss, M. Siegal, L. Stenger, and N. Edelstein, Preparation of Cubic Chlorocomplex Compounds of Trivalent Metals, UCRL-18973, Aug. 1969.

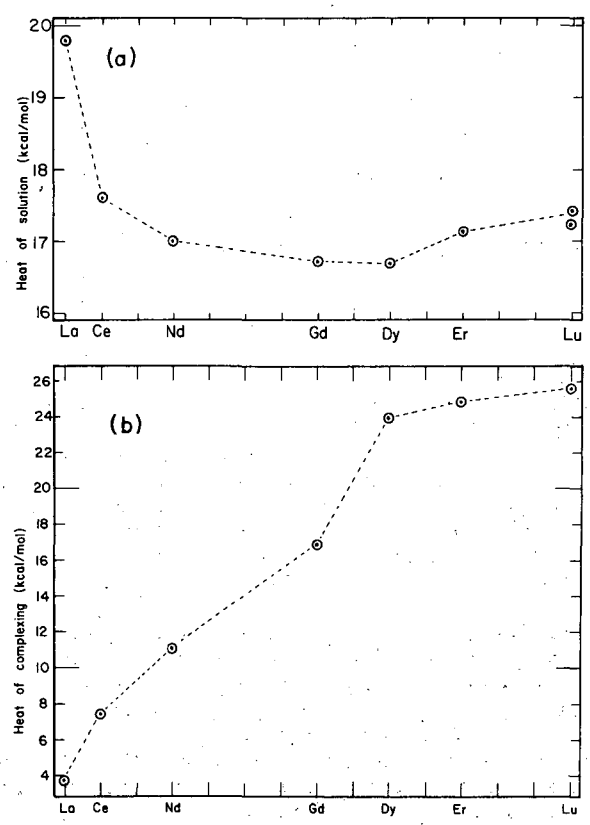

Fig. 1. (a) Heat of solution (exothermic) of Cs_2NaMCl_6.
(b) Heat of complexing (exothermic) of Cs_2NaMCl_6. (XBL697-1076)

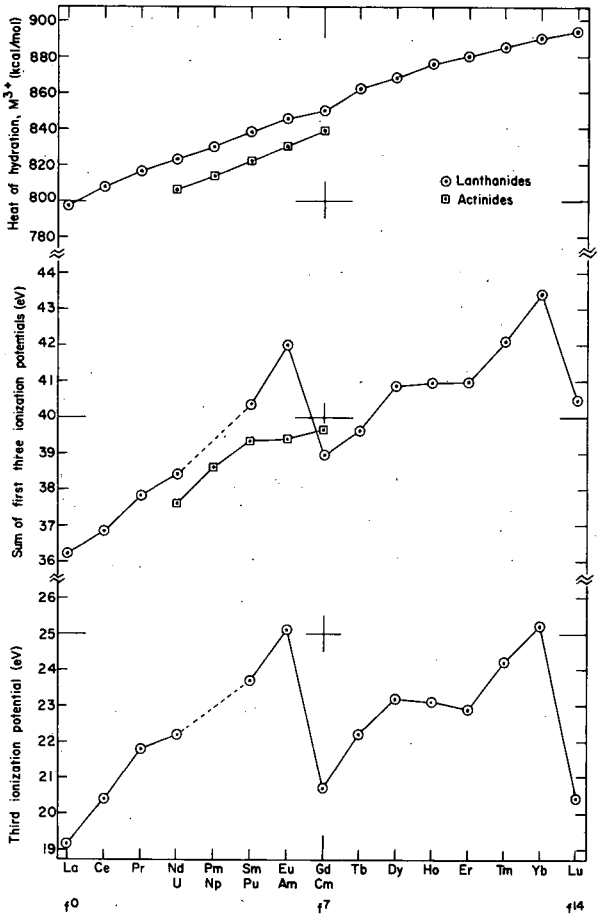

Fig. 2. Ionization potentials of lanthanide atoms and heats of hydration of trivalent lanthanide ions. (XBL697-1074)

DETERMINATION OF VALENCE STATES OF IRON IN GLASS AND OF URANIUM IN CALCIUM FLUORIDE SINGLE CRYSTALS†

Ursula Abed

As the result of high-temperature electrochemical experiments with iron-containing sodium disilicate glasses, a determination of the ferrous and ferric oxide distribution became necessary. The analytical approaches cited in the literature usually consisted of dissolving the glass under an inert atmosphere, followed by a titration of ferrous ion with an oxidant. The total iron content was determined by any of the conventional means, the value for ferrous ion was subtracted from it, and thus ferric ion was found by difference. Although the reproducibility of the total iron results was acceptable, widely scattered data were obtained for the ferrous ion determination. A slight modification of the method selected, i. e., an attempt to prevent air-oxidation of the ferrous ion by working in a glove box under N_2, did not improve the precision.

The procedure presented here is based upon the fact that the cerate ion is stable for an extended period over the temperature range from 20 to 100 °C in a HF-H_2SO_4 acid mixture. This permits the instantaneous oxidation of the released ferrous ion by a known excess of standard cerate during the dissolution of the glass, and thus obviates the need for an inert atmosphere. The results obtained on glass samples ranging from < 0.1 to 26% in ferrous ion were precise, and the accuracy of the determination, as ascertained with the aid of simulated samples consisting of iron-free quartz wool and semimicro quantities of known, standard ferrous ion, was 99% or better. The method, omitting HF, found further application in the determination of ratios of ferrous oxide to

ferric oxide in magnesium oxide crystals which were used in electron paramagnetic resonance studies. The analytical results agreed well with the calculated values.

An estimation of the formal oxidation potentials of the Ce(III)-Ce(IV) and Fe(II)-Fe(III) couples in HF-H_2SO_4 proved that the Ce(III)-Ce(IV) potential (≈ 0.8 V) obtained is sufficiently positive to oxidize Fe(II) (0.5 V) under the conditions employed.

A study was made to correlate the particle size of a commercial glass with the time required for dissolution, and to investigate whether there exists any relationship between the particle size and the ferrous ion content found. No air-oxidation occurred during prolonged grinding (5 days), and minimum dissolution time requirements were established for 100 mesh, 80 mesh, 48 mesh, 20 mesh, and > 20 mesh.

The same method, with minor changes, was used in the determination of valence states of semimicro amounts of U in CaF_2 single crystals, the properties of which are being studied by optical spectroscopy. The overall error in the initial-valence determination was ± 5% and included the instantaneous oxidation of a lower valence state of U to the U^{+6} oxidation state with subsequent back-titration of the excess standard cerate present in the solvent system, a neutron-activation analysis in duplicate, and a spectrophotometric determination in duplicate for total U.

Obviously, the method cannot be used without modification if mixtures of several valences, or reducing substances, or both, are present. I thank Mrs. H. Michel and Dr. F. Asaro for their neutron-activation analyses, which confirmed the results obtained for total U by spectrophotometry. I am indebted to Dr. E. H. Huffman for stimulating discussions.

Footnote

†Condensed from Anal. Chim. Acta 47, 495 (1969).

OXIDATION STATES AND SITE SYMMETRIES OF CaF_2:U CRYSTALS†

R. McLaughlin, U. Abed, John G. Conway, N. Edelstein, and E. H. Huffman

When CaF_2 crystals are grown containing small amounts of U, crystals which display many different colors result: brown, green, yellow, and red of various shades, displaying various EPR absorptions, have all been reported. Work described in this report was undertaken in an effort to determine the manner in which various oxidation states and site symmetries of the U ion might be responsible for the many different properties of these crystals. A major effort was made to minimize the uncertainty of the valence of the U ion in the crystals investigated. This was accomplished by designing the experiment so that no valence change would be expected in the process of making the crystal, and by determining the oxidation state of U by chemical analysis[1] after spectral measurements on the crystal had been completed.

A small carbon resistance furnace, which operated under vacuum, was supplied with a 0.25-in. o.d. graphite tube which had a 1-in.-long bathtub section cut in its center. The center section was filled with mixtures of U and CaF_2 and heated until the material melted. An observation port allowed one to turn off the power as soon as the mixture became liquid, and thus minimize the possibility of reaction with the graphite tube or gases in the system. If the power was turned off as soon as melting occurred the pressure did not exceed 5×10^{-4} torr. However, if the sample was held in the molten state for several minutes the pressure might increase as high as 3×10^{-2} torr. Small crystals were grown starting with the following mixtures: (a) crystalline CaF_2 + 2 wt % PbF_2 + 1 wt % UF_4, (b) crystalline CaF_2 + 2 wt % PbF_2 + 1 wt % UO_2, and (c) powdered CaF_2 + 1 wt % $UO_2(NO_3)_2 \cdot 6H_2O$.

The spectral data were recorded by use of a Cary model 14 and a Jarrell-Ash model 75 f/6.3 spectrograph.

A major source of confusion about the nature of the different CaF_2:U crystals is that reactions occur during crystal growth which are not understood. The equipment described here was used to

grow crystals in the hope that minimizing the time that the material was in the molten state would minimize the occurrence of unknown high-temperature reactions. Early attempts were unsuccessful; the results were not reproducible. By increasing the sample size and the U concentration and improving the vacuum, reproducibility was finally achieved. It was noted that a different, but not understood, result was obtained the first time a heating element was used after being machined, so crystals produced under these conditions are ignored in the discussion that follows.

After many samples had been run the following results were clearly established:
(a) If the starting material is crystalline CaF_2, 2 wt % PbF_2, and 1 wt % UF_4 a green crystal is obtained whose spectrum is identical to the spectrum of the green crystals described by W. A. Hargreaves[2] and explained as due to U^{2+}. The spectra are shown in Fig. 1.
(b) If the starting material is crystalline CaF_2, 2 wt % PbF_2, and 1 wt % UO_2 a brown crystal is obtained whose spectrum is displayed in Fig. 2.
(c) If the starting material is powdered CaF_2 (Baker and Adamson reagent grade) and 1 wt % $UO_2(NO_3)_2 \cdot 6H_2O$ a yellow crystal is obtained whose spectrum is identical to the yellow crystal described in Ref. 2 and explained as due to U^{4+}. These spectra are shown in Fig. 3. Samples of the green and yellow crystals were generously supplied by W. A. Hargreaves of Optovac Inc.

There was indication of reaction occurring in the UO_2 doped crystals. If these crystals were kept in the molten state for periods of time longer than 1 min a mixture of the brown and yellow spectra was obtained. If the power to the furnace was turned off as soon as the material melted a crystal containing brown particles of undissolved UO_2 resulted. Crystals free of UO_2 particles and of the yellow spectrum were grown by keeping the material in the molten state for about 10 sec.

By repeating the crystal-growing processes several times, enough of the UO_2 and $UO_2(NO_3)_2 \cdot 6H_2O$-doped crystals were accumulated to make a valence determination possible. This determination revealed the U in the yellow crystal to be in the 6+ state, the U in the green crystal to be in the 4+ state, and the U in the brown crystal to be a mixture of valence states (the actual result was 4.4). We interpret this last result to mean most of the U is in the 4+ state, however, some is present with a valence of 6+. This method was also applied to the red CaF_2: U, with the expected results that U^{3+} predominates in this crystal.

The fact that UF_4 produces a green crystal and UO_2 a brown one suggests that the spectral differences between these two crystals are caused by a different method of charge compensation. EPR experiments[3] indicate that the U ion in the brown crystal is situated in a crystal field of trigonal symmetry and has $g_{\parallel} = 4.02$ and $g_{\perp} \leq 0.1$. Similar experiments[4] on green crystals indicate again trigonal symmetry with $g_{\parallel} = 3.27$ and $g_{\perp} = 0$. One possible explanation of these results, when combined with this work, is the following. When the U^{4+} ion substitutes for the Ca^{2+} ion at the center of a cube of F^- ions in the brown crystal, charge compensation is achieved by the substitution of two O^{2-} ions for the two F^- ions at the opposite corners of the cube, whereas in the green crystal compensation results from two F^- ions occupying the centers of the cubes whose corners are common with the opposite corners of the cube containing the U^{4+} ion. That the spectral differences between the two crystals are so large is not surprising when compared with differences between U^{4+} compounds (i. e., U^{4+} in zircon[5]).

Results of this paper indicate the interpretation of the work on CaF_2: U^{2+} (Ref. 6) to be invalid, and may affect the interpretation of work done on a U^{4+} crystal[7, 8] which probably contained a large amount of U^{6+}.

Discussions with Burris Cunningham were invaluable.

Footnotes and References

†Condensed from UCRL-18999.

1. U. Abed, Anal. Chim. Acta 47, 495 (1969).
2. W. A. Hargreaves, Phys. Rev. 156, 331 (1967).
3. S. D. McLaughlan, Phys. Rev. 150, 118 (1966).
4. R. S. Title, P. P. Sorokin, M. J. Stevenson, G. D. Pettit, J. E. Scardefield, and J. R. Landard, Phys. Rev. 128, 62 (1962).
5. I. Richman, P. Kisliuk, and E. Y. Wong, Phys. Rev. 155, 212 (1967).
6. P. F. McDonald, E. L. Wilkinson, and R. A. Jensen, J. Phys. Chem. Solids 28, 1629 (1967).
7. Grover C. Wetsel, Jr., and Earle T. Kitts, Jr., Phys. Rev. Letters 18, 841 (1967).
8. Grover C. Wetsel, Jr., J. Appl. Phys. 39, 692 (1968).

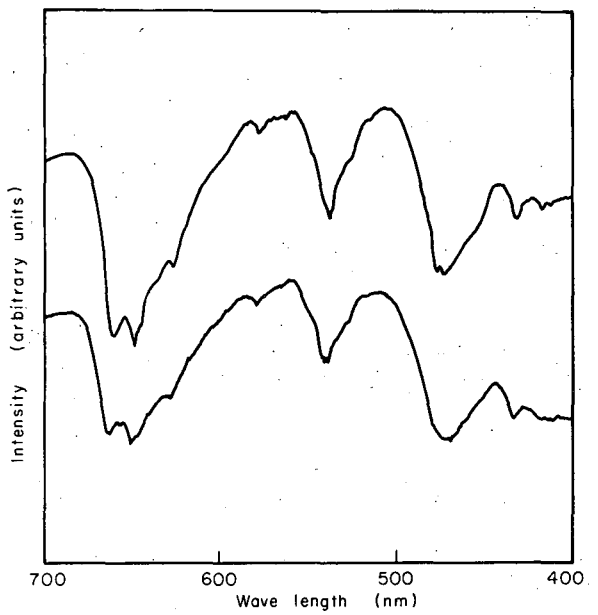

Fig. 1. Upper spectrum: crystal made from 1% UF_4, 2% PbF_2 in CaF_2. Lower spectrum: green crystal described in Ref. 2. (XBL6912-6380)

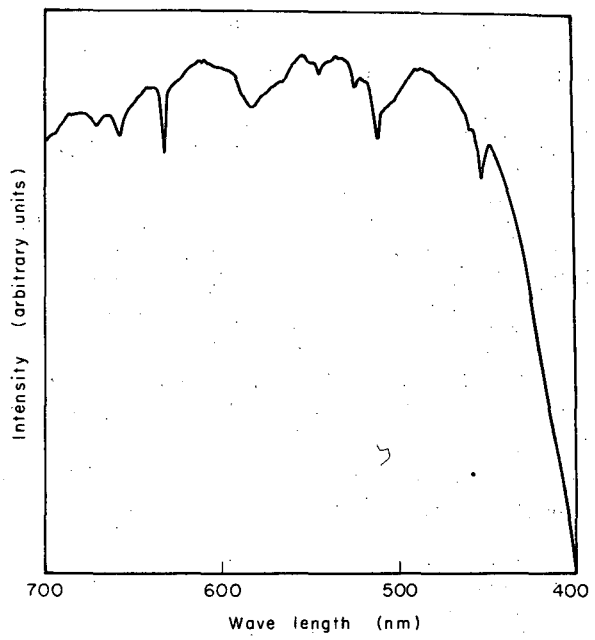

Fig. 2. Spectrum of crystal made from 1% UO_2, 2% PbF_2 in CaF_2. (XBL6912-6382)

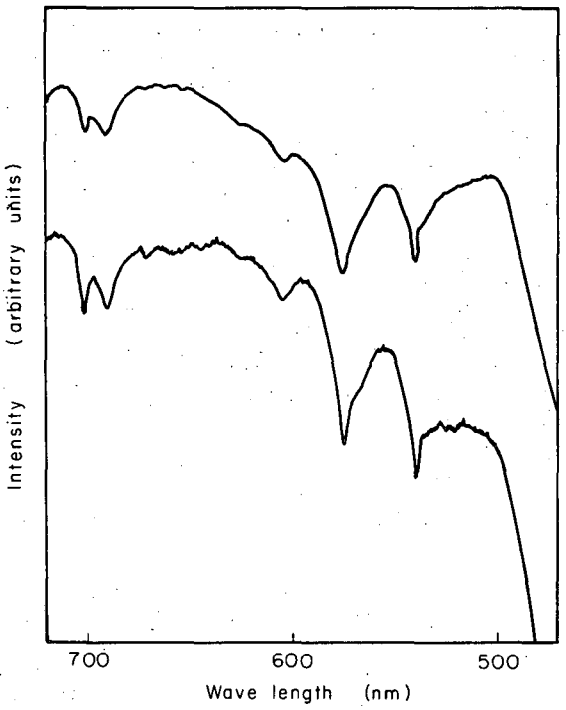

Fig. 3. Upper spectrum: crystal made from 1% $UO_2(NO_3)_2$ in CaF_2. Lower spectrum: yellow crystal described in Ref. 2. (XBL6912-6381)

POTTERY ANALYSIS BY NEUTRON ACTIVATION†

I. Perlman and F. Asaro

This study is a detailed evaluation of the accuracy attainable by neutron-activation analysis employing a germanium γ-ray spectrometer. When pottery samples are irradiated with neutrons, many radioactive species are formed and the mixture produces very complex γ-ray spectra. Analysis of a spectrum gives information which can be converted to the abundances of those elements measured. For a large number of analyses, the data processing becomes so tedious that the use of a computer is virtually mandatory.

Addressed to problems in archaeology, there were no a priori guidelines for the accuracy required nor the number and kinds of elements for which data would be useful. The questions so posed are still not completely answered. However, the initial premise–that the highest possible accuracy on the largest number of elements is desirable–seems borne out.

It should be clear that in activation analysis as in others, the accuracy of analysis for each element cannot be better than that for the particular element in the standard. This would suggest that in constructing a composite standard, the typically weak peaks of pottery should be enhanced in the standard, whereas each strong peak should be minimized to a level which still gives good counting statistics. (The overall γ-ray intensity should be kept to a minimum because the Compton distributions from all γ rays contribute to the background under the peaks, and this is a major source of error for many elements.) In principle, these objectives could be reached by formulating a completely synthetic standard from appropriate compounds. This approach was rejected because of the anticipated difficulty of homogenizing the material and keeping it so. If we consider standards weighing 100 mg with some elements present to less than 1 ppm, this means that 0.1 μg of that element must be dispersed in a statistically satisfactory number of particles, say 10 000 or more. There seemed to be no method of accomplishing this and knowing that it had been accomplished other than by trial and error. Since the calibration of the standard was expected to take at least 6 months, we were not encouraged to pursue a trial-and-error approach.

Since fine pottery clay is already a highly dispersed system presumably containing the elements of interest, it was decided to start with this as the basis for the standard. A clay was selected and found (fortunately) to contain a number of the weakly activated elements in amounts more than normal and such strongly activated elements as manganese, sodium, and iron in low amounts. Its single largest drawback was the presence of scandium in "normal" amount which is more than necessary. As expected of any particular clay, it was undesirably deficient in a few elements, a problem to be handled separately.

The clay was first ground wet in a ball mill for 40 hours. Then the wet mix was put through a 60-mesh screen, and dried. The clay was broken up, ground wet for 10 hours, and then spiked with a water solution containing desired amounts of cobalt, nickel, bromine, and arsenic. The original clay was deficient in these substances and it was thought that by adding them in this fashion, they would be uniformly dispersed by coating the large surface area of the clay particles. The "doped" clay was then ground wet for 26 hours, strained with a 120-mesh screen, cast into convenient shapes, dried, and fired to 705 °C for half an hour. The fired ceramic was ground in the ball mill for 9 hours, yielding a final product of about 2 kg of fine powder.

Before the laborious task of calibration was undertaken, eight random samples were pressed into standard pills, irradiated, and analyzed for uniformity. Each of several radioactive species agreed virtually within counting statistics, so the pottery was considered suitable for calibration and use as a standard.

For calibrating the standard pottery, known quantities of chemicals representing each of 38 elements were separately pressed into pills and irradiated with the standard pottery. At least two independent sources of each compound were employed, and where attested primary standards were not available, conventional chemical analysis was employed to establish the absolute content of the element. This turned out to be a long process, because most compounds are not stoichiometric with the nominal formula and many preparations and irradiations were required.

During the course of these calibrations there was ample opportunity to test the reproducibility of the entire analytical process, which was found to be about 0.4%. This value is low enough to permit concentration on the assessment of other errors and finally the real differences between potteries.

Tables I and II give the composition of the standard pottery in terms of the elements detected by neutron-activation analysis as well as constituents determined by other means.

Footnote

†Condensed from Archaeometry 11, 21 (1969).

Table I. Composition of major components in standard pottery.

Component	Composition		Assumed oxide
	Element (%)	Oxide (%)	
SiO_2		60.4±0.3	(SiO_2)
Al	15.9±0.2	29.9	(Al_2O_3)
K	1.45±0.04	1.75	(K_2O)
Fe	1.02±0.01	1.5	(Fe_2O_3)
Ti	0.79±0.03	1.3	(TiO_2)
Mg	0.5 ±0.2	0.8	(MgO)
Na	0.26±0.01	0.3	(Na_2O)
Ba	0.072±0.003	0.08	(BaO)
Σ Trace elements		0.1	
Volatile components		3.99±0.10	
Total components		100.1	

Table II. Composition[a] of standard pottery.

Element	Species studied	Technique[b]	Composition		Chemical symbol
			Diff. techniques	Best value	
Aluminum	^{28}Al	neut act 1		$(15.9\pm0.2)\times10^{-2}$	Al
Antimony	^{122}Sb	neut act 3	$(1.66\pm0.12)\times10^{-6}$		
	^{124}Sb	neut act 4	$(1.73\pm0.06)\times10^{-6}$	$(1.71\pm0.05)\times10^{-6}$	Sb
Arsenic	^{76}As	neut act 3		$(3.08\pm0.22)\times10^{-5}$	As
Barium	^{139}Ba	neut act 2	$(7.13\pm0.32)\times10^{-4}$	$(7.12\pm0.32)\times10^{-4}$	
	^{131}Ba	neut act 4	$(7.0\pm1.1)\times10^{-4}$	$(7.12\pm0.32)\times10^{-4}$	Ba
Bromine	^{82}Br	neut act 3		$(2.3\pm0.9)\times10^{-6}$	Br
Calcium	^{47}Ca	neut act 3	$<1\times10^{-2}$		
		opt spec	$<1\times10^{-3}$		
		wet chem	$<2\times10^{-4}$	$<2\times10^{-4}$	Ca
Carbon	CO_2	C-H anal		$(3\pm3)\times10^{-4}$	C
Cerium	^{141}Ce	neut act 4		$(8.03\pm0.39)\times10^{-5}$	Ce
Cesium	^{134}Cs	neut act 4		$(8.31\pm0.55)\times10^{-6}$	Cs
Chlorine	^{38}Cl	neut act 1		$<1.3\times10^{-4}$	Cl
Chromium	^{51}Cr	neut act 4		$(1.151\pm0.038)\times10^{-4}$	Cr
Cobalt	^{60}Co	neut act 4		$(1.406\pm0.015)\times10^{-5}$	Co
Copper	^{64}Cu	neut act 2	$(6.0\pm0.8)\times10^{-5}$		
	Cu	wet chem	$(5.8\pm0.5)\times10^{-5}$	$(5.9\pm0.5)\times10^{-5}$	Cu
Dysprosium	^{165}Dy	neut act 2		$(4.79\pm0.19)\times10^{-6}$	Dy
Europium	$^{152m1}Eu$	neut act 2	$(1.418\pm0.048)\times10^{-6}$		
	^{152}Eu	neut act 4	$(1.477\pm0.047)\times10^{-6}$	$(1.448\pm0.034)\times10^{-6}$	Eu
Gallium	^{72}Ga	neut act 2		$(4.44\pm0.46)\times10^{-5}$	Ga
Gold	^{198}Au	neut act 3		$\leq1\times10^{-8}$	Au
Hafnium	^{181}Hf	neut act 4		$(6.23\pm0.44)\times10^{-6}$	Hf
Hydrogen	H_2O	C-H anal		$(5.4^{+0.0}_{-0.5})\times10^{-3}$	H

Iron	^{59}Fe	neut act 4		$(1.017\pm0.012) \times 10^{-2}$	Fe
Lanthanum	^{140}La	neut act 3		$(4.490\pm0.045) \times 10^{-5}$	La
Lutetium	^{177}Lu	neut act 3		$(4.02\pm0.36) \times 10^{-7}$	Lu
Magnesium	^{27}Mg	neut act 1	$(5\pm2) \times 10^{-3}$		
		opt spec	$(7\pm2) \times 10^{-3}$	$(5\pm2) \times 10^{-3}$	Mg
Manganese	^{56}Mn	neut act 2		$(4.09\pm0.05) \times 10^{-5}$	Mn
Nickel	^{58}Co	neut act 4		$(2.79\pm0.20) \times 10^{-4}$	Ni
Potassium	^{42}K	neut act 2		$(1.45\pm0.04) \times 10^{-2}$	K
Rubidium	^{86}Rb	neut act 4		$(7.00\pm0.63) \times 10^{-5}$	Rb
Samarium	^{153}Sm	neut act 3		$(5.78\pm0.12) \times 10^{-6}$	Sm
Scandium	^{46}Sc	neut act 4		$(2.055\pm0.033) \times 10^{-5}$	Sc
Silicon dioxide	SiO_2	wet chem		$(6.04\pm0.03) \times 10^{-1}$	SiO_2
Sodium	^{24}Na	neut act 2		$(2.61\pm0.04) \times 10^{-3}$	Na
Strontium	^{87m}Sr	neut act 2		$(1.45\pm0.22) \times 10^{-4}$	Sr
Tantalum	^{182}Ta	neut act 4		$(1.550\pm0.044) \times 10^{-6}$	Ta
Thorium	^{233}Pa	neut act 4		$(1.396\pm0.039) \times 10^{-5}$	Th
Titanium	^{47}Sc	neut act 3		$(7.82\pm0.34) \times 10^{-3}$	Ti
Uranium	^{239}Np	neut act 3		$(4.82\pm0.44) \times 10^{-6}$	U
Ytterbium	^{175}Yb	neut act 3		$(2.80\pm0.36) \times 10^{-6}$	Yb
Zinc	^{65}Zn	neut act 5		$(0.51\pm0.08) \times 10^{-4}$	Zn

[a] These compositions and all others in this paper refer to the elements unless otherwise noted.

[b] The entries in this column have the following meanings: neut act 1, neutron-activation measurement with special irradiations for very short half-lives; neut act 2, usual neutron-activation measurement for half-lives less than 1 day; neut act 3, usual neutron-activation measurement for half-lives from 1 to 6 days, neut act 4, usual neutron-activation measurement for half-lives longer than 6 days; neut act 5, special neutron-activation measurement about 8 months after irradiation; opt spec, measurement with optical spectograph; wet chem, measurement by wet chemical analysis; C-H anal, measurement of carbon and hydrogen by combustion analysis.

PROVENIENCE STUDIES OF TEL ASHDOD POTTERY EMPLOYING NEUTRON-ACTIVATION ANALYSIS†

I. Perlman, Frank Asaro, and J. D. Frierman*

There is evidence that pottery made from different clay sources will reveal differences in composition if subjected to sufficiently detailed chemical analysis. The only feasible types of analysis are those which can determine many elements simultaneously and which are sensitive enough to measure accurately a considerable number of those present only in trace amounts. A method which meets these criteria is neutron-activation analysis.[1]

A system has been worked out for measuring more than 30 elements in pottery without resorting to chemical fractionation in the laboratory. Only about 100 mg of powdered pottery is used for each analysis.

The results presented here concern a small collection of sherds from Tel Ashdod on the coast of Israel, which are expected to be the forerunner of a more detailed analysis of the site. The collection comprises only five "local" Philistine sherds, four of Cypriote White Slip II Ware and two Mycenaean III B pieces. These pieces are surface finds (or of unstratified context), but are well correlated through stratified counterparts: Philistine sherds – mainly Stratum XII; Cypriote and Mycenaean sherds – mainly XV and XIV.

Philistine Ware

In Table I are shown analytical results on 18 elements for the five Tel Ashdod Philistine sherds. Particular attention is called to the "error limits" employed. The limits shown on the elemental abundances for the individual sherds are the standard errors of the respective measurements. Each entry in parentheses is the mean value for an element in the pottery group and the standard deviation (σ) encountered in the group for that element. These latter numbers are used to determine whether any sherd belongs to the group.

The second set of data shown in Table I pertains to five pieces of Philistine pottery excavated from tombs at Tel Eitum, about 25 miles inland from Ashdod. Only the mean values with their standard deviations are shown for this group. (Ten other pieces from Tel Eitun were analyzed but none of these belong to this particular group.) When this Tel Eitun group is compared statistically with that from Tel Ashdod, they are found to be indistinguishable.

To provide contrast with the above-mentioned materials, Table I also shows results on two Philistine vessels from Tel Eitun of a different chemical type (ETN3 and ETN13). Of the major constituents, it is seen that the calcium content of these is considerably higher and the iron appreciably lower. Most of the trace elements are also well outside the standard deviations of the reference materials. If we assume that the five Tel Ashdod and five Tel Eitun pieces constitute a single chemical group, then the odds that ETN3 and ETN13 belong to this group are very, very small.

Cypriote Ware

The results for the Cypriote White Slip II Ware (four sherds) are tabulated as the upper group in Table II. These do not by any means make up a close-knit pottery group, but they share some characteristics which make them highly distinctive. Although we cannot refer to a typical chemical pottery type, this Cypriote ware has extreme divergences for a number of elements from values obtained on a large variety of pottery analyzed from many sites. This particular Cypriote ware, for example, has the lowest values yet seen anywhere for U, La, Hf, Th, and Rb; at the same time they have about the highest values for Fe and Sc.

We have begun a rather ambitious program of analyzing pottery excavated on Cyprus, embracing major stylistic types from 16 sites. The same distinctive chemical profile as the Tel Ashdod material has turned up, but we are not yet ready to attempt determination of the exact place of origin. Not enough sites have yet been examined, and where this has been done several different pottery groups are emerging all with the same general characteristics as the White Slip Ware described above. One such "group" from Ayios Jakovos is shown in summary form in Table II. This "group" consists of seven sherds, but it is possible that they all came from only two vessels. The agreement between this group and the Cypriote sherd ASH5 is very good. Other ware from Ayios Jakovos as well as from Enkomi and Milia is of this same distinctive chemical type, and illustrations could be given which encompass the compositions of the other Cypriote pieces from Tel Ashdod. Pottery of this style from still other sites on Cyprus has not yet been available for analysis.

One conclusion is unmistakable. Wherever the various groups of White Slip Ware may have been made, the potters selected a particular type of clay for this ware, because other styles of Cypriote ware were distinctly different in chemical composition. The Tel Ashdod White Slip Ware is of a distinctive composition thus far encountered only in eastern Cyprus.

Mycenaean Ware

The two Mycenaean sherds from Tel Ashdod, which have their counterparts in materials already analyzed in our laboratory, are from bowls or kraters classified LM III B. The results for the individual pieces are given in Table III. The Mycenaean reference materials are sparse, consisting of a small collection of five sherds.

Of the two pieces from Tel Ashdod, one of them (ASH 12) matches the reference very well. The other sherd, ASH 3, is made from a closely similar clay, but it does not quite "belong" to the reference group. In view of the meagerness of the collection with which we are dealing, it is not possible to ascribe a different provenience to this sherd.

It seems rather puzzling that six out of seven Mycenaean III B found in three different places have proved to be closely enough alike to be classed as a group. A hasty explanation is that all of these have a common place of origin. However, one must also consider the possibility that they came from more than one place but that the clay sources are indistinguishable by our analysis. A much more ambitious effort must be undertaken before questions of origin of Mycenaean pottery can be answered.

Conclusions

The analysis of this small collection of Tel Ashdod sherds has yielded no surprises, but suggests that a much amplified study could help provide a detailed picture of contacts between this settlement and others in the vicinity and at a distance.

The Philistine sherds of Level XI have chemical counterparts in a group found in tombs at Tel Eitun suggesting (but not yet proving) a common origin. Other Philistine pieces found at Tel Eitun were different. The Cypriote White Slip II sherds were not homogeneous, but belong to a highly distinctive type of clay so far found only in similar ware from three tomb sites in eastern Cyprus. Two sherds of Mycenaean III B ware were similar to each other and to a small collection of typologically similar ware said to have been excavated at Mycenae and also one sherd found on Kea. The Mycenaean reference materials in particular are too meager to allow one to draw firm inferences about the uniqueness of assignment.

Table I. Philistine Pottery

Code*	Fe (%)	Sc	Ta	Co	Cs	Cr	Hf	Th
ASH 1	3.80±0.04	12.42±0.04	1.195±0.048	17.59±0.27	1.49±0.18	122.0±1.2	10.58±0.19	7.13±0.05
ASH 4	3.84±0.04	12.66±0.04	1.166±0.046	19.30±0.29	1.61±0.19	119.2±1.2	12.75±0.21	7.84±0.05
ASH 6	3.89±0.04	13.01±0.04	1.263±0.050	19.20±0.30	1.58±0.19	120.8±1.3	12.89±0.21	7.83±0.05
ASH 8	3.83±0.04	12.76±0.04	1.187±0.051	18.97±0.30	1.86±0.20	128.3±1.3	16.48±0.26	8.58±0.06
ASH 10	3.96±0.04	13.12±0.04	1.189±0.046	20.43±0.29	1.65±0.18	129.9±1.3	14.44±0.23	9.04±0.05
Mean value ASH 1,4,6,8	(3.86±0.10)	(12.79±0.32)	(1.200±0.037)	(19.10±0.97)	(1.64±0.14)	(124.0±6.0)	(13.43±2.41)	(8.08±0.86)
Mean value ETN 1,6,7,9,14	(3.70±0.07)	(12.85±0.13)	(1.137±0.034)	(17.01±1.15)	(1.64±0.15)	(114.5±1.9)	(11.57±0.73)	(7.38±0.54)
ETN 3	3.01±0.03	10.72±0.03	0.857±0.031	13.43±0.15	1.24±0.12	118.8±0.9	7.75±0.12	6.12±0.04
ETN 13	3.10±0.03	10.66±0.02	0.856±0.028	13.41±0.14	0.88±0.10	125.2±0.9	8.13±0.13	5.95±0.04

All abundances of elements are in parts-per-million except those designated "%". Numbers in parentheses are mean values for the group of the standard deviations for the group. The other numbers refer to individual measurements and the standard errors of the gamma-ray counting only.

Table II. Cypriote Pottery from

Code*	Fe (%)	Sc	Ta	Co	Cs	Cr	Hf	Th
ASH 2	6.23±0.06	36.39±0.07	0.353±0.056	34.44±0.45	0.69±0.29	181.5±1.8	2.22±0.18	2.52±0.06
ASH 11	7.09±0.06	40.00±0.08	0.423±0.056	37.29±0.48	0.74±0.36	202.4±2.0	2.17±0.19	2.61±0.07
ASH 5,9 **	7.74±0.05	41.30±0.05	0.192±0.032	46.10±0.35	0.35±0.18	260.7±1.4	1.77±0.11	1.91±0.04
ASH 7	7.09±0.06	46.39±0.07	0.346±0.037	52.99±0.51	0.90±0.23	839.6±5.2	1.83±0.13	3.03±0.05
Mean value JAK 9,12,14,15, 17,18,20†	(8.02±0.48)	(41.30±1.36)	(0.254±0.063)	(44.37±2.27)	(0.75±0.32)	(242.2±51.1)	(1.67±0.31)	(1.70±0.07)

*All pieces designated ASH are Cypriote White Slip II Ware from Tel Ashdod; those designated JAK are similar ware from Ayios Jakovos, Cyprus. Mean values are not given for the Tel Ashdod pieces because they cannot be placed in a group even though they share certain distinctive characteristics.

Table III. Mycenaean Pottery from

Code*	Fe (%)	Sc	Ta	Co	Cs	Cr	Hf	Th
ASH 3	5.39±0.05	23.12±0.05	0.837±0.042	35.63±0.39	8.56±0.24	295.4±2.1	3.60±0.13	12.01±0.06
ASH 12	5.25±0.05	21.21±0.05	0.812±0.046	29.17±0.36	9.13±0.26	245.6±2.0	3.91±0.15	11.31±0.06
Mean value MYC 1,2,3,6	(5.21±0.23)	(21.84±1.36)	(0.769±0.066)	(30.74±2.01)	(9.42±0.40)	(229.4±16.6)	(3.60±0.51)	(11.19±0.83)

*ASH 3 and ASH 12 from Tel Ashdod are characterized as Late Mycenaean IIIB. MYC 2, 3, and 6 are similar ware said to come from Mycenae. MYC 1 is also similar and it is described as an import found on Kea. Another sherd from Kea is not included here and is different in composition.

For those unfamiliar with viewing analytical data of the kind shown in this paper, it is perhaps worth calling attention to the large differences in composition between the Philistine, Cypriote, and Mycenaean ware illustrated in the Tel Ashdod material. The distinctions we have been trying to make in judging the provenience of the respective wares are minuscule compared with the differences between the different wares.

Footnotes

†Condensed from UCRL-18957, July 1959, Atiqot (to be published).
*Present address: Museum of Ethnic Arts and Technology, University of California–Los Angeles.

from Tel Ashdod and Tel Eitun.

Ba	Rb	Sb	U	Lu	La	Ti (%)	Ca (%)	Mn	Na (%)
228±23	53±5	0.447±0.059	2.57±0.11	0.372±0.010	29.47±0.29	0.584±0.034	7.6±0.7	755±16	0.614±0.010
333±26	51±5	0.329±0.059	1.95±0.11	0.441±0.011	28.24±0.29	0.693±0.034	3.8±0.6	777±16	0.655±0.011
384±26	54±6	0.395±0.061	2.11±0.11	0.418±0.011	27.88±0.28	0.683±0.033	3.1±0.6	742±16	0.611±0.011
476±30	60±6	0.430±0.068	2.02±0.11	0.449±0.011	30.15±0.31	0.773±0.036	3.6±0.6	810±17	0.610±0.011
490±28	46±6	0.432±0.061	1.99±0.11	0.454±0.011	30.56±0.31	0.754±0.036	5.1±0.6	924±19	0.628±0.011
(382±121)	(53±5)	(0.407±0.053)	(2.13±0.26)	(0.427±0.038)	(29.26±1.42)	(0.697±0.079)	(4.6±2.0)	(802±77)	(0.624±0.021)
(549±206)	(53±2)	(0.357±0.064)	(1.52±0.10)	(0.410±0.021)	(27.92±1.14)	(0.667±0.024)	(5.2±1.1)	(733±48)	(0.668±0.088)
687±24	32±4	0.354±0.040	1.90±0.10	0.348±0.009	26.52±0.26	0.484±0.031	14.2±0.6	560±8	0.499±0.009
1148±33	43±4	0.414±0.059	2.07±0.10	0.388±0.009	26.57±0.27	0.443±0.030	13.9±0.6	595±7	0.554±0.008

*ASH 1, 4, 5, 8, 10 are Philistine pieces from Tel Ashdod; ETN 1, 6, 7, 9, 14 are Philistine pieces from Tel Eitun closely similar to the Tel Ashdod ware as explained in the text. ETN 3 and ETN 13 are Philistine pieces different in composition from the others in this table.

Tel Ashdod and Ayios Jakovos (Cyprus).

Ba	Rb	Sb	U	Lu	La	Ti (%)	Ca (%)	Mn	Na (%)
142±40	30±8	0.493±0.097	0.73±0.15	0.340±0.012	9.01±0.21	0.407±0.029	2.5±0.5	779±16	1.131±0.016
87±44	19±8	0.469±0.108	0.78±0.15	0.300±0.012	8.48±0.21	0.427±0.029	2.0±0.5	875±19	1.149±0.016
101±25	36±4	0.524±0.060	1.19±0.11	0.309±0.009	5.66±0.14	0.376±0.020	1.6±0.4	1102±17	1.060±0.011
88±32	29±6	0.300±0.073	0.67±0.25	0.324±0.013	8.01±0.27	0.479±0.035	2.3±0.5	1020±22	0.745±0.012
(111±79)	(34±11)	(0.387±0.236)	(0.31±0.16)	(0.308±0.015)	(5.79±0.31)	(0.374±0.028)	(2.3±0.6)	(1193±36)	(1.223±0.135)

**ASH 5 and ASH 9 are two sherds analyzed separately but which proved to come from the same vessel. The values listed are mean values with standard errors of gamma-ray counting.
†As explained in the text, these seven sherds may have come from only two bowls but have been treated here as independent pieces. This "group" is closely similar to ASH 5, 9.

Tel Ashdod with Comparative Material.

Ba	Rb	Sb	U	Lu	La	Ti (%)	Ca (%)	Mn	Na(%)
307±31	150±9	0.695±0.072	2.22±0.16	0.390±0.012	34.95±0.37	0.496±0.038	9.2±0.7	1003±21	0.601±0.011
367±34	156±9	0.658±0.080	2.20±0.15	0.345±0.011	31.42±0.34	0.486±0.035	8.6±0.7	953±20	0.547±0.010
(359±14)	(161±15)	(0.789±0.238)	(2.34±0.34)	(0.362±0.013)	(32.59±2.31)	(0.485±0.076)	(9.0±2.0)	(945±52)	(0.419±0.186)

SURFACE PROFILE ANALYSIS BY ^{3}He ACTIVATION: OXYGEN IN SILICON

James F. Lamb, Diana M. Lee, and Samuel S. Markowitz

^{3}He activation has been used for oxygen surface-profile analysis of high-purity silicon. The ability to preferentially activate sample constituents which lie within the first few mg/cm^2 of surface of a sample is a feature almost unique to charged-particle activation. Because its nucleus is loosely bound, enabling nuclear reactions to proceed with minimum-energy bombardment, ^{3}He is well suited as the activating particle.

Analysis of oxygen in silicon was based upon the combined reactions $^{16}O(^3He,p)^{18}F$ and $^{16}O(^3He,n)^{18}Ne \rightarrow {}^{18}F$. The total production cross section is almost 400 mb at its maximum near 7-MeV bombarding energy.[1-4] The ^{18}F activity induced decays predominantly by positron emission ($T_{1/2}$ = 110 min), and can be conveniently detected nondestructively by γ-ray spectrometry of the 511-keV β^+ annihilation radiation. The short-lived activities induced in the silicon sample matrix contribute no interference with ^{18}F detection.

The distribution of induced ^{18}F activity as a function of depth from the sample surface is distorted by recoil of the reaction products. The recoil energy depends upon the mechanism of the nuclear reaction, but for ^{3}He activation analysis it is practical to assume complete linear momentun transfer and to calculate the maximum recoil energy from[5]

$$E_r = [A_i A_p/(A_i + A_t)]\ E_i ,$$

where E_r is the recoil energy, and A_i, A_p, and A_t are the mass numbers of the incident particle, the product nucleus, and the target nucleus, respectively; E_i is the incident beam energy. Figure 1 shows the total path-length ranges of recoiling ^{18}F in various nongaseous stopping media as calculated by using the computer code of Steward.[6]

The predicted maximum recoil ranges of ^{18}F in aluminum were tested experimentally by bombarding targets composed of 1-mg/cm^2 Mylar foils sandwiched within a deck of aluminum foil recoil catchers, each 100 μg/cm^2 thick, at incident ^{3}He energies of 5, 10, 20, and 25 MeV. The activation data for the 10-MeV bombardment is shown in Fig. 2. The almost constant ^{18}F activities in foils 8 through 13 may be interpreted as resulting from activation of the surface oxide coating on aluminum. The combined data from all bombardments calculated in terms of the percent of forward recoiling ^{18}F remaining "in beam" after each catcher foil is shown in Fig. 3.

The maximum range in silicon of ^{18}F induced by 8-MeV ^{3}He ions is about 0.5 mg/cm^2, approximated from Fig. 1. Because the oxide coating on high-purity silicon is known to be only about 10 Å thick,[7] activity of ^{18}F following 8-MeV ^{3}He bombardment should be contained within a layer about 0.5 mg/cm^2 from the surface of the sample. To test this prediction, a sample of high-purity zone-refined silicon was irradiated with 8-MeV ^{3}He ions. The decay of the 511-keV annihilation radiation from the activated sample was followed until short-lived activities had decayed to a negligible level. A thin surface layer of the silicon was then removed by grinding against a glass plate with 600-mesh silicon carbide powder, its thickness determined by weight difference, and the remaining activity redetermined. This process was repeated until the activity per unit thickness of silicon removed remained constant. The results are shown in Fig. 4. The ordinate of the figure represents the parts of oxygen per million parts effective-thickness silicon remaining after each surface grinding. The oxygen concentration was determined by using a Ta_2O_5 comparison standard in a subsequent irradiation, and the effective thickness of silicon is the thickness necessary to degrade the incident beam to $\approx$ 2 MeV, at which energy no further activation of ^{16}O takes place. The 1 ppm oxygen concentration determined for bulk silicon agrees well with the data of Saito et al.,[8] who used ^{4}He activation analysis at beam energies greater than 20 MeV.

Footnote and References

†Condensed from Anal. Chem. 42, 212 (1970).

1. S. S. Markowitz and J. D. Mahony, Anal. Chem. 34, 329 (1962).
2. R. L. Hahn and E. Ricci, Phys. Rev. 146, 650 (1966).
3. O. D. Brill', Sov. J. Nucl. Phys. 1, 37 (1965).
4. D. M. Lee, J. F. Lamb, and S. S. Markowitz, UCRL-17989.

5. L. Winsberg and J. M. Alexander, Phys. Rev. 121, 518 (1961).
6. P. G. Steward, Stopping Power and Range for Any Nucleus in the Specific Energy Interval 0.01 to 500 MeV/amu in Any Nongaseous Material (Ph. D. Thesis), UCRL-18127, May 1968.
7. R. J. Archer, J. Electrochem. Soc. 104, 619 (1957).
8. K. Saito, T. Nozaki, S. Tanaka, M. Furukawa, and Hwasheng cheng, Intern. J. Appl. Radiation Isotopes 14, 357 (1963).

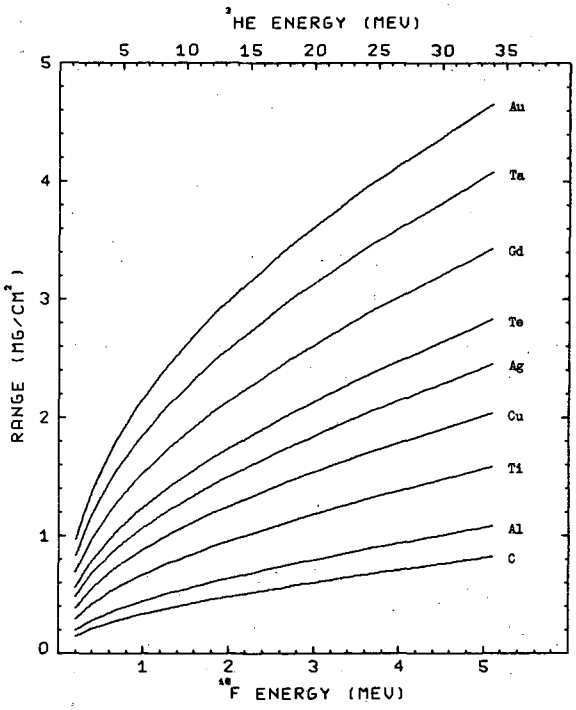

Fig. 1. Range of ^{18}F in various stopping media. The upper scale is the ^{3}He energy corresponding to the total momentum transfer ^{18}F energy shown on the lower scale as calculated by Eq. (1). (XBL697-1024)

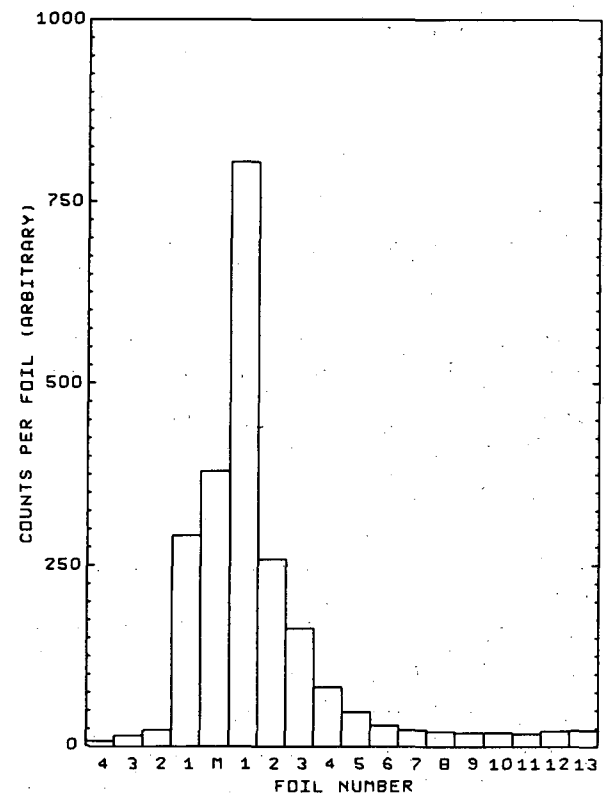

Fig. 2. Distribution of recoiling ^{18}F in 100-μg/cm^2 Al catcher foils. M designates Mylar target. ^{3}He energy = 10 MeV. (XBL697-1025)

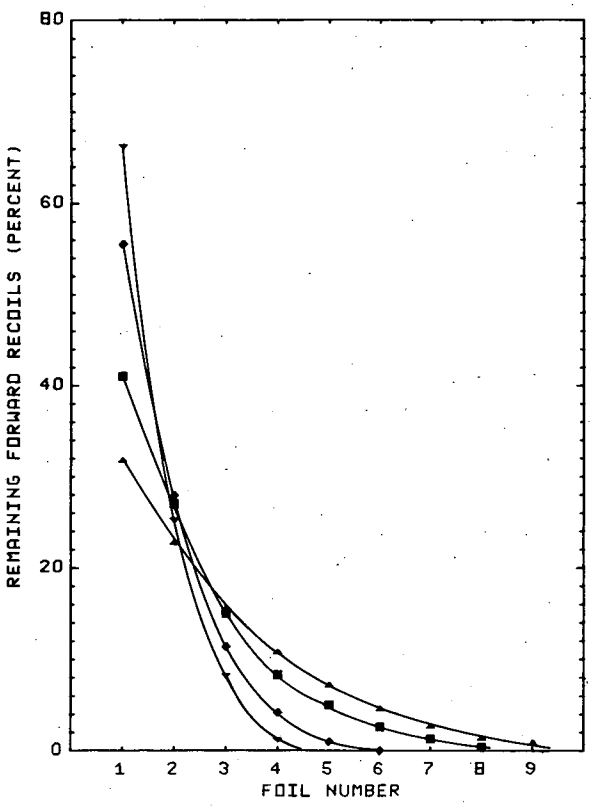

Fig. 3. Percent of recoil ^{18}F passing through each catcher as a function of the number of 100-μg/cm^2 Al catcher foils. ▼ = 5 MeV, ◆ = 10 MeV, ■ = 20 MeV, ▲ = 25 MeV. (XBL697-1026)

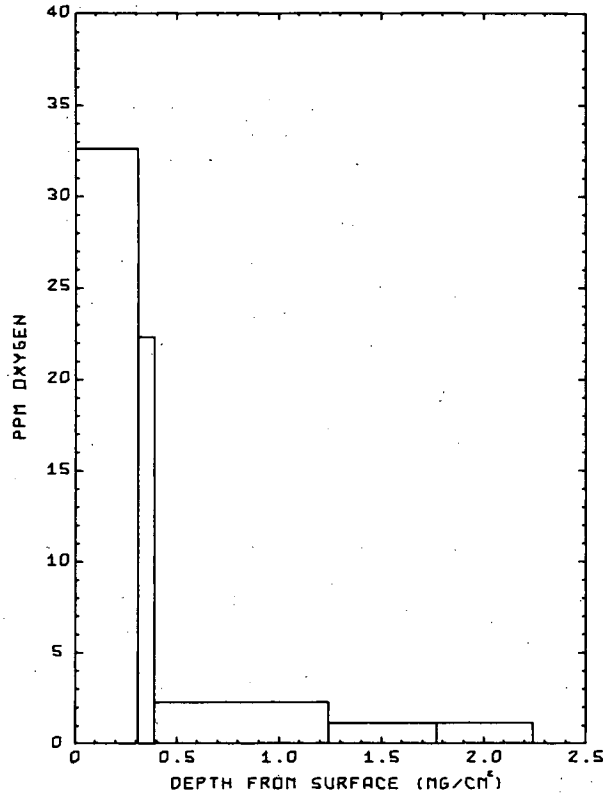

Fig. 4. Surface oxygen profile of high-purity silicon determined by ^3He activation. (XBL697-1027)

DETERMINATION OF OXYGEN IN COPPER BY ^{3}He ACTIVATION ANALYSIS†

Diana M. Lee, Cynthia V. Stauffacher, and Samuel S. Markowitz

A radioactivation method using ^3He as the bombarding particle has been developed to determine trace concentrations of oxygen in copper. The limits of detection extend to about 0.35 part per billion, with a sensitivity of approximately 29 dpm/ppb of radioactive 110-min ^{18}F, which is used as the "signal" for ^{16}O. The ^{18}F is produced by the nuclear reaction of ^{16}O with low-energy (4 to 10 MeV) ^3He ions. The 0.51-MeV annihilation radiation from the ^{18}F is detected by a NaI scintillation spectrometer, or by a Ge γ-ray spectrometer. At ^3He energies below 6.3 MeV, no interfering radioactivities from reactions with the Cu matrix are present, so the analysis is nondestructive. If necessary, destructive analysis may be carried out; a rapid, clean procedure for radiochemical separation of ^{18}F as PbF_2 is presented. The method is calibrated either absolutely through measurement of beam intensity, detection coefficient, cross section, and bombardment time, or through a comparative method based upon standards of known oxygen content prepared by anodic oxidation of tantalum foils. The oxygen content of 0.1-mil Cu foil was measured and found to be 550±30 ppm. The relative standard deviation was 5%. Only a fraction of a milligram of sample is required.

Activation analyses, especially those involving ^3He as the incident particle,[1-5] ^3He reactions with copper,[6] and preparations of oxygen standards by anodic oxidation of Ta (Ref. 7) have been discussed.

Spectra of copper foils irradiated at various ^{3}He energies (with no radiochemical separation) are displayed in Figs. 1 and 2. The upper spectrum in each figure indicates gamma photopeaks from isotopes of Cu and Ga present in large amounts. The predominant high-energy gamma peaks diminish as the incident energy of ^{3}He decreases to below 6 MeV, as shown in both Fig. 1 and Fig. 2. Figure 3 shows a comparison of two copper samples irradiated by 11.4-MeV ^{3}He; the upper spectrum was obtained from direct counting of one of the copper foils and the lower spectrum was obtained from $Pb^{18}F_2$, which was chemically separated. The experiment demonstrates radiochemical separation even in the presence of a very high intensity of unwanted activities.

Decay curves of the 0.51-MeV photopeak from copper activated by ^{3}He ions of various energies are plotted in Fig. 4. The slope of the decay curves for ^{3}He energies below 6 MeV corresponds to a half-life of 110 minutes with negligible interference. As the energy of ^{3}He is increased, the shape of the decay curve changes with the appearance of a long-life component corresponding to a half-life between 9.5 and 10 hours. Analyses of the decay curves indicate that the long-life component is a mixture of 9.5-h ^{66}Ga and 12.8-h ^{64}Cu. Some ^{61}Cu (3.3 h) was also present at ^{3}He energies higher than 8 MeV. Elimination of interference solely by decay-curve analysis of the annihilation gamma for the energies of ^{3}He above 8.5 MeV was found to be inaccurate, because of the large amount of interfering activity from long-life components and because ^{61}Cu has a half-life different from ^{18}F by less than a factor of two. As the energy of ^{3}He decreases, the ratio of activity of ^{18}F to the long-life component (^{64}Cu + ^{66}Ga) increases, and production of ^{61}Cu decreases very rapidly; ratios of ^{18}F to (^{64}Cu + ^{66}Ga) were approximately 2 at 8.5 MeV, 9 at 7.5 MeV, and 90 at 6.3 MeV. Some cross sections for production of ^{18}F from ^{16}O are listed in Table I. The ratio of ^{18}F cross section at 6.3 MeV to that at 7.5 MeV is approximately 0.9; the relative activity, however, of ^{18}F to the interfering activity for these two energies is 10. Therefore, a nondestructive analysis of oxygen in copper can be measured with minimum interference and maximum sensitivity at the incident energy of ^{3}He of about 6.3 MeV.

Table I shows results of eleven analyses obtained from four different irradiations for the nondestructive analysis of oxygen in copper foils. The average analyses for 0 in Cu based on Ta_2O_5 as the oxygen comparative standard and on the absolute method are $0.054_6 \pm 0.003\%$ and $0.055_9 \pm 0.003\%$ by weight, respectively. A comparison of destructive and nondestructive analysis of oxygen in copper foil is listed in Table II for the same average incident energies of ^{3}He. The average chemical yield of $Pb^{18}F_2$ was approximately 50%. The results indicated $0.052 \pm 0.009\%$ 0 in Cu.

In this research, we have demonstrated the method of oxygen analysis in copper by both destructive and nondestructive means. By control of the incident ^{3}He energy, however, we show that nondestructive analysis can be successfully carried out, eliminating the need for chemical separation. At ^{3}He energies of 4.7 to 6.3 MeV (Table I), the cross section for the $^{16}O \longrightarrow {}^{18}F$ remains high, i.e., 165 to 350 mb. Because the sensitivity is very high, reduction of the beam energy eliminates Cu-induced interference without seriously decreasing sensitivity. The depth of penetration decreases, of course.

References

1. B. A. Thompson, Anal. Chem. 33, 583 (1961).
2. S. S. Markowitz and J. D. Mahony, ibid. 34, 329 (1962).
3. K. Saito, T. Nozaki, S. Tanaka, M. Furukawa, and Hwashing Cheng, Intern. J. Appl. Radiation Isotopes 14, 357 (1963).
4. E. Ricci and R. L. Hahn, Anal. Chem. 39, 795 (1967).
5. J. F. Lamb, D. M. Lee, and S. S. Markowitz, in Proceedings of the 2nd Conference on Practical Aspects of Activation Analysis with Charged Particles, Liège, 1967 (Euratom, Brussels, 1968), 1, 225.
6. E. A. Bryant, D. R. F. Cochran, and J. D. Knight, Phys. Rev. 130, 1512 (1963).
7. J. F. Lamb, D. M. Lee, and S. S. Markowitz, Anal. Chem. 42, 212 (1970).

Table I. Results from nondestructive analysis of oxygen in copper foils by ^3He ions at various energies.

Beam intensity ≈ 1.5 μA. Length of bbt ≈ 10 min. ODC = 4.2%.

Copper foil	^3He energy (MeV)	Cross section σ (mb)	A_0 ^{18}F (counts per min)	Oxygen found in Cu based on Ta_2O_5 std. (%)	Oxygen found in Cu based on absolute method (%)
1	3.7	55	1842±50	0.051	0.056
2	4.5	140	5089±327	0.061	0.064
3[a]	4.7	165	5322±186	0.053	0.056
4	4.7	165	5473±90	0.055	0.054
5[a]	5.3	230	7331±110	0.053	0.054
6	5.3	230	7011±110	0.052	0.051
7	5.7	290	9577±105	0.056	0.056
8	6.3	350	10603±113	0.053	0.055
9	7.5	390	12218±109	0.054	0.055
10	7.8	350	11065±220	0.053	0.053
11	8.5	335	11610±1205	0.060	0.061
			Average	0.054_6±0.003%	0.055_9±0.003%

[a]Samples 3 and 5 were etched with dilute HNO_3 for a few seconds.

Table II. Comparison of destructive and nondestructive analyses at the same ^3He energies and identical counting conditions.

^3He energy (MeV)		Oxygen in Cu with chemical separation (%)	Chemical yield (%)	Oxygen in Cu without chemical separation (%)
6.3		0.054	37.4	0.053
7.5		0.046	50.2	0.054
8.5		0.045	49.7	0.060
9.6		0.046	58.4	-----
11.4		0.069	37.4	-----
	Average	0.052±0.009%		0.056±0.003%

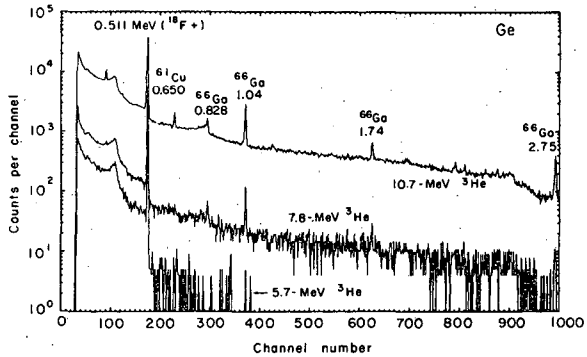

Fig. 1. Gamma-ray spectra of copper foil irradiated by 10.7-, 7.8-, and 5.7-MeV ^{3}He ions: Ge detector, no chemical separation. (XBL6910-3991)

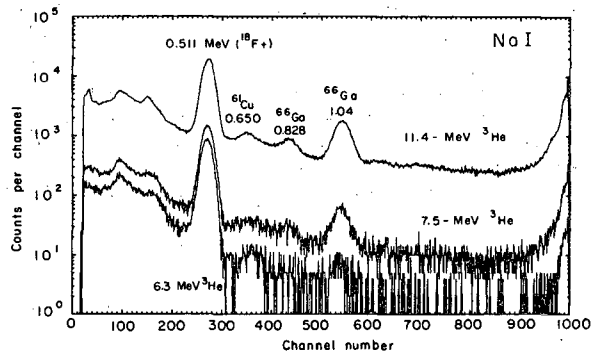

Fig. 2. Gamma-ray spectra of copper foil irradiated by 11.4-, 7.5-, and 6.3-MeV ^{3}He ions: NaI detector, no chemical separation. (XBL6910-3990)

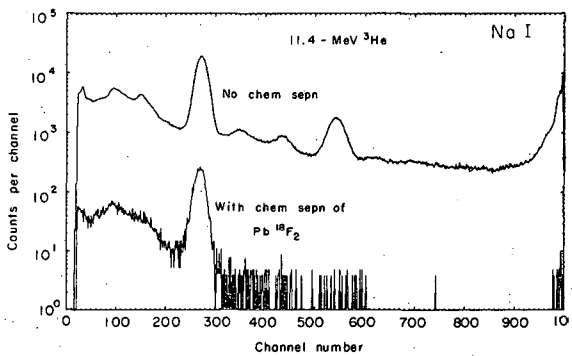

Fig. 3. Comparison of γ-ray spectrum of chemically separated $Pb^{18}F_2$ with that of copper foil counted without chemical separation of ^{18}F. Irradiated by 11.4-MeV ^{3}He; NaI detector. (XBL6910-3988)

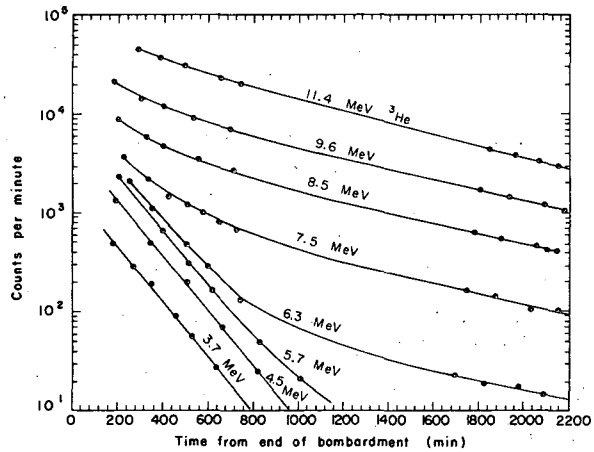

Fig. 4. Decay curves of 0.51-MeV annihilation radiation photopeak at various ^{3}He incident energies. (XBL690-3987)

EXTRACTION OF $HReO_4$ AND $HAuCl_4$ BY TRIOCTYL PHOSPHINE OXIDE IN CARBON TETRACHLORIDE AND CYCLOHEXANE

J. J. Bucher and R. M. Diamond

A previous study[1] of $HClO_4$ extraction by dilute solutions of trioctyl phosphine oxide (TOPO) in CCl_4 indicated that an acid complex involving three TOPO molecules was found in the organic phase. This study also showed that at least one water molecule was co-extracted. With these two results and making an analogy with a similar system using the less basic tributyl phosphate as extractant, tributyl phosphate-CCl_4-$HClO_4$,[2] we suggested that the acid complex with TOPO had a hydronium core around which three TOPO molecules (the maximum number) were coordinated. More recent work dealing with the extraction of perrhenic and chloroauric acid ($HAuCl_4$) by TOPO in benzene, chloroform, sym-triethyl benzene, nitro-benzene,[3] and 1,2-dichloroethane[3] indicated that the extraction complex was solvated by only two TOPO molecules and insufficient water was co-extracted to allow the formation of a hydronium ion core. The cation was a proton bound to two TOPO molecules. It was thus of interest to reexamine the extraction of $HReO_4$ by TOPO in CCl_4 to determine if by such a simple change of diluent the acid complex could indeed be so radically changed to a hydronium-based complex. It was also desired to extend the survey of TOPO extraction to one additional type of diluent, namely an aliphatic hydrocarbon. Cyclohexane was

chosen, as it has less tendency for third-phase formation than the straight or branched-chain hydrocarbons.

Instead of using acid-base titration methods for determining the amount of extracted $HClO_4$ acid, as was done in the previous work, radioactive $^{186}ReO_4^-$ tracer was employed. Use of the tracer technique allows determination of much lower organic-phase acid concentrations, so that extraction of $HReO_4$ into more dilute TOPO concentrations can be studied. Gold tracer in the form of chloroauric acid, $H^{198,199}AuCl_4$, was also used, as it was considered likely that this anion would be essentially anhydrous, so that any water co-extracted would be on the cation or dissolved in the (new) solvent consisting of the organic-phase salt solution. The solutions of $HAuCl_4$ were always kept in 0.010 M HCl.

Extraction of the acid as an ion pair may be expressed as

$$H^+ + X^- + xH_2O + nTOPO\ (org) = H^+ \cdot nTOPO \cdot xH_2O \cdots X^-\ (org),$$

with the corresponding equilibrium constant

$$K_n^a = (H^+ \cdot nTOPO \cdot XH_2O \cdots X^-)_o / [TOPO]_o^n\ (H_2O)^x\ (H^+X^-),$$

where [ ] denotes concentrations, ( ) signifies activities, and the subscript o denotes the organic phase.

From log-log plots of the organic-phase acid concentration, $[H^+]_o$, vs the aqueous-acid activity, with the TOPO concentration held constant, it can be determined whether the extracting species is dissociated, an ion pair, or a higher aggregate. With CCl_4 (ϵ = 2.24 at 20 °C) and cyclohexane (ϵ = 2.02 at 20 °C) as diluents, ion-pair species are to be expected. Figure 1 shows such a log-log plot for 0.10 and 0.01 M TOPO in CCl_4 with $HReO_4$ acid; the limiting slopes of unity in this figure do indicate that ion pairs are formed over most of the organic-phase concentration range observed. The dashed portion of the 0.10 M TOPO–CCl_4 curve is an attempt to correct the data for the TOPO used up by extracted acid, and deviates upward from the curve of unit slope established at lower $[H^+]_o$ concentrations. The deviation suggests the possibility that aggregation is occurring at the higher concentrations. Figure 2 for 0.10 and 0.010 M TOPO in cyclohexane with $HAuCl_4$ in 0.010 M HCl shows more conclusively that aggregation is occurring. The dashed line indicates what the data would be if only ion pairs existed. Both figures indicate that the stoichiometric limit of $[H^+]_o$ is about one-half the initial TOPO concentration and not one-third, the value necessary if a three-TOPO complex were being formed.

From log-log plots of the organic acid vs the equilibrium TOPO concentration at a fixed aqueous activity, the number n of TOPO molecules involved in the extraction complex can be determined. Figure 3 is such a log-log plot for TOPO-CCl_4-$HReO_4$, and shows limiting slopes of 2; n = 2, and a 2 TOPO-acid complex is indicated. At the upper end of each curve deviations upward from this line of slope 2 occur. In Fig. 4, a log-log plot of the distribution coefficient of tracer ReO_4^- vs TOPO concentration at a fixed aqueous HCl activity of 9.3×10^{-5} also indicates deviations at higher TOPO concentrations. Remembering that the limiting ratio of extracted acid to TOPO concentration in Fig. 1 is one-half, we suggest that this deviation in Fig. 4 is due to a decreasing activity coefficient for the extracted 2:1 TOPO-acid complex and not to formation of a 3:1 species. That is, above about 2×10^{-2} M TOPO, the presence of the polar TOPO molecules makes the CCl_4 diluent more suitable for the introduction of the extracted ion pairs. (There is solvent sorting around the ion pairs.) We feel that this effect is a major cause of the deviation observed in curves 2 and 3 in Fig. 3, and that the deviation does not signify a 3:1 complex, even though the data can be resolved into a component of slope $\approx$ 3 as shown on curve 3. It is also probable that a decrease in the acid complex activity coefficient occurs at moderate concentrations of the complex in the organic phase, and this is represented by the aggregation already mentioned in connection with Figs. 1 and 2. The deviation of curve 1 in Fig. 3 is probably due to such aggregation. Curves 1 and 2 in Fig. 4 also show limiting slope values of 2 for chloroauric acid extraction by TOPO in CCl_4 and in cyclohexane, and indicate considerably less ideal solutions in cyclohexane than in CCl_4.

The amount of water co-extracted by the organic-phase acid complex (after subtraction of the diluent- and TOPO-associated water from the total organic-phase water) was found to be approximately one-half molecule per extracted proton in TOPO-CCl_4-$HAuCl_4$ and to vary from 1.6 to 0.1

for TOPO-cyclohexane-$HAuCl_4$. Most of the measured ratios for the cyclohexane system were less than unity. This result, coupled with the limiting loading curves and the TOPO variation curves already described, suggests that the extraction of these acids by TOPO in these two types of diluents is based on the same cationic complex as found previously in other TOPO–diluent systems, an anhydrous $2TOPO \cdot H^+$ species. The principal differences between the extraction behavior with CCl_4 and cyclohexane diluents and the other solvents studied are the occurrence of ion aggregation in the organic phase and the significant changes in the acid complex activity coefficients at higher TOPO concentrations; both features complicate the slope analysis of the data.

In the previous $HClO_4$-TOPO-CCl_4 study, the TOPO concentrations were restricted to these higher values, where the analysis is confusing, and plots of the TOPO dependence gave slopes of about 3. We now believe that the assumption of a 3:1 complex based on a hydronium ion core--as is valid for TBP extractions--was false, and that the more basic TOPO molecule yields a $2TOPO \cdot H^+$ cation intermediate to the anhydrous R_3NH^+ cation achieved by the still more basic trialkyl amine extractants.

References

1. T. J. Conocchioli, M. I. Tocher, and R. M. Diamond, J. Phys. Chem. 69, 1106 (1965).
2. D. C. Whitney and R. M. Diamond, J. Phys. Chem. 67, 209 (1963).
3. J. J. Bucher, T. J. Conocchioli, and R. M. Diamond, in Nuclear Chemistry Annual Report, 1968, UCRL-18667, Jan. 1969, pp. 307-309.

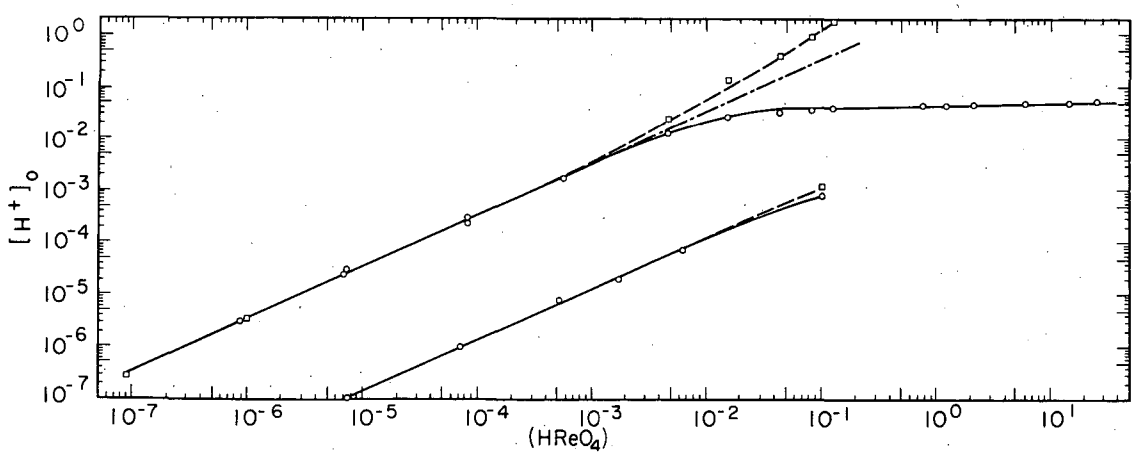

Fig. 1. Variation of acid content of CCl_4 phase with aqueous $HReO_4$ activity for TOPO concentrations of 0.10 M (upper line) and 0.010 M (lower line). o, uncorrected data; ■, data corrected for used-up TOPO. (XBL701-2203)

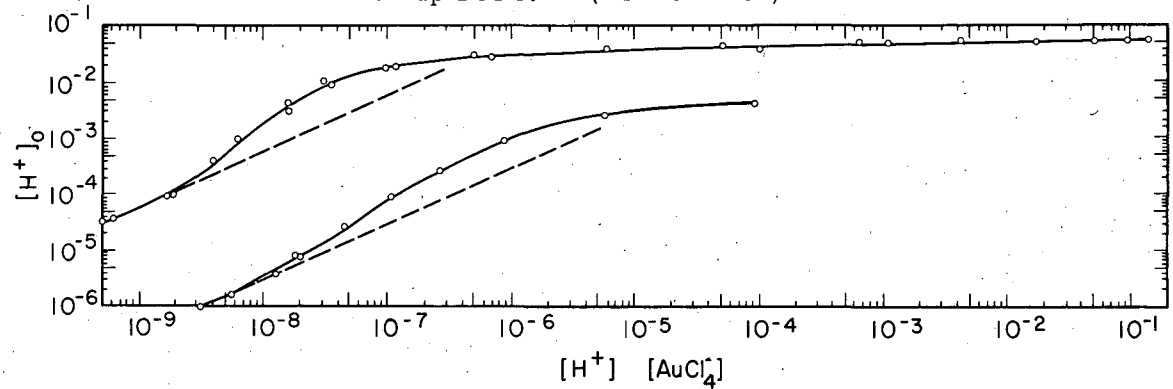

Fig. 2. Variation of acid content of cyclohexane phase with aqueous $HAuCl_4$ activity in 0.010 M HCl for TOPO concentrations of 0.10 M (upper line) and 0.010 M (lower line). o, uncorrected data; the dashed line indicates the extrapolation of unit slope for an ion-paired species. (XBL701-2194)

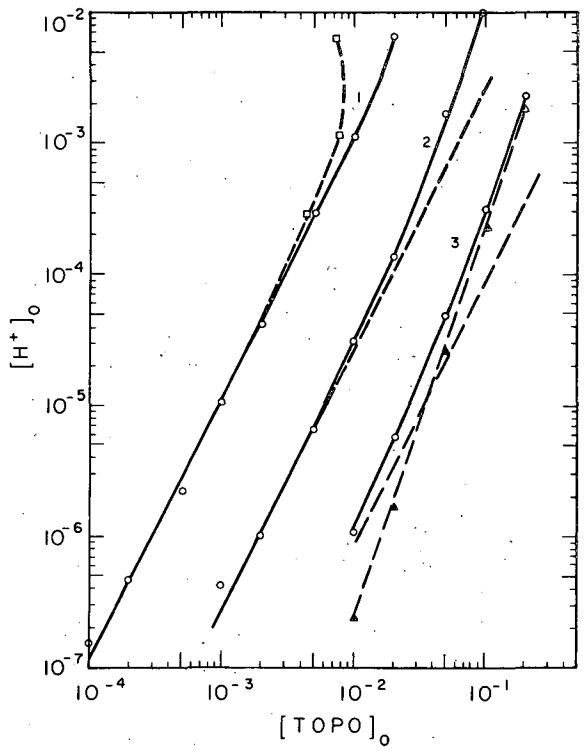

Fig. 3. Variation of acid content of CCl_4 phase with TOPO concentration for aqueous $HReO_4$ solutions of 0.437 M (line 1), 0.060 M (line 2), and 0.010 M (line 4). o, uncorrected data; □, data corrected for used-up TOPO; ▽, resolved n = 3 line (see text for explanation). (XBL701-2195)

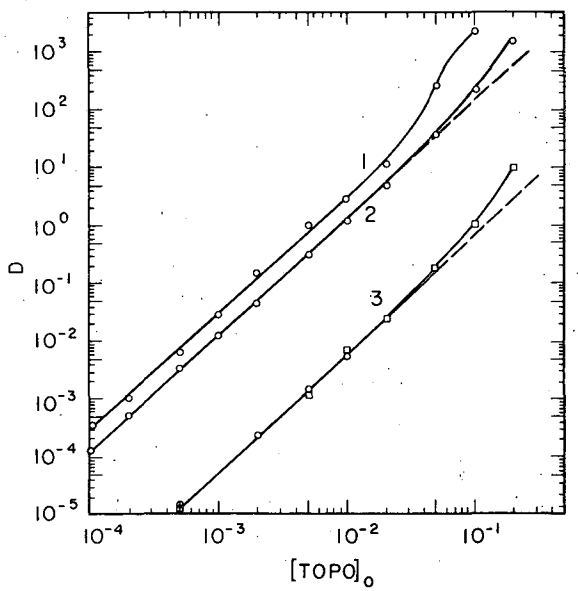

Fig. 4. Distribution ratio: D vs total TOPO concentration for (line one) cyclohexane with 1×10^{-5} M $HAuCl_4$, 0.010 M HCl; (line two) CCl_4 with 5.5×10^{-5} M $HAuCl_4$, 0.010 M HCl; and (line three) CCl_4 with 1×10^{-8} M (□) and 2×10^{-6} M (○) $HReO_4$, 0.50 M HCl. (XBL701-2196)

EXTRACTION OF $HClO_4$ AND $HReO_4$ BY TRI-2-ETHYLHEXYL PHOSPHATE IN ISOOCTANE AND 1,2-DICHLOROETHANE

J. J. Bucher, R. W. Zuehl,† and R. M. Diamond

A previous survey[1,2] of perrhenic and perchloric acid extraction by tributyl phosphate (TBP) in a variety of diluents (isooctane, CCl_4, 1,2-dichloroethane, benzene, and $CHCl_3$) showed a hydronium ion core–TBP complex was formed in each system. Depending upon the choice of diluent and TBP concentration the acid complex could be a saturated 3:1 TBP-acid species or a lower complex. In isooctane, principally the 3:1 ion-paired species was found; in 1,2-dichloroethane only a dissociated $3TBP\cdot H_3O^+$ complex was observed. In the other diluents, appreciable or predominant amounts of $2TBP\cdot H_3O^+$ were observed in the range of TBP concentrations studied.

In this paper our study of strong acid extraction by trialkyl phosphates is extended by using a bulky, branched extractant: tris(2-ethylhexyl) phosphate (TEHP), which might show steric problems. Only the TEHP-isooctane and TEHP-1,2-dichloroethane systems are examined; these two diluents should sufficiently bracket the possible extraction behavior for $HClO_4$ and $HReO_4$ acid, as will be discussed.

Tracer $^{186}ReO_4^-$ was used out of either macro $HClO_4$ or $HReO_4$ acids to determine organic-phase acid concentrations to much lower values than is possible with ordinary acid-base titrations.

The extraction of $HClO_4$ or $HReO_4$ by solutions of TEHP in a diluent may be expressed as

$$H^+ + x^- + xH_2O + nTEHP\ (org) = \begin{cases} H^+ \cdot nTEHP \cdot xH_2O \cdots X^-\ (org), \\ H^+ \cdot nTEHP \cdot xH_2O\ (org) + X^-\ (org), \end{cases}$$

with the corresponding equilibrium constants

$$K^a = [H^+ \cdot nTEHP \cdot xH_2O \cdots X^-]_o / [TEHP]_o^n\ (H_2O)^4\ (HX),$$

$$K^d = [H^+ \cdot nTEHP \cdot xH_2O]_o\ [X^-]_o\ y_\pm^2 / [TEHP]_o^n\ (H_2O)^4\ (HX),$$

where [ ] denotes concentrations, ( ) signifies activities, $y_\pm$ is a mean molar activity coefficient, and the subscript o indicates organic-phase quantities.

From a log-log plot (not shown) of organic-phase acid concentration vs aqueous $HClO_4$ activity at constant TEHP concentration, it was determined that the extracting species in isooctane was an ion pair. From previous work[1] it is assumed that the complex in 1,2-dichloroethane is dissociated. Then from the slope of log-log plots of organic acid vs equilibrium TEHP concentration at fixed aqueous activites, the TEHP solvation number n can be determined. In Fig. 1 such a plot for TEHP-isooctane has a slope of 2; two TEHP are involved in each extraction complex at least up to TEHP concentrations of 0.10 M. Figure 2 is a similar plot for TEHP-1,2-dichloroethane. The dashed line indicates the correction for activity coefficients calculated by the method of Poirier,[3] and has a slope of 1.5. From previous work with this solvent it is assumed that the extracted species is dissociated, so that $n/2 = 1.5$ or $n = 3$. The complex has three TEHP molecules per extracted proton. This is the same as for TBP-1,2-dichloroethane-$HReO_4$. However, the magnitude of K_3^d with TEHP is different. For TEHP the value is 2.9×10^{-5}, while for TBP $K_3^d = 2.4 \times 10^{-4}$, both evaluated under similar dilute conditions. This tenfold smaller constant probably reflects the steric interference of the more bulky, branched hydrocarbon tails of TEHP, as expected. With the TEHP-isooctane system, however, even taking into account the fact that for tracer ReO_4^- out of macro perchloric acid the extraction constant is higher than for the tracer out of macro perrhenic acid by a factor which may be as large as 2, the constant for the 2:1 complex is practically the same as for the TBP-isooctane system:[1] $K_2^a = 5 \times 10^{-3}$. We would have expected the TEHP system to have shown a lower extraction constant than for the TBP system, as the TEHP does in 1,2-dichloroethane. The explanation may be that the problems of steric hindrance do not arise with the 2:1 complex, but only when three of the TEHP molecules are to be packed around the hydronium ion core. This same difference between straight-chain and bulkier branched phosphates has been observed in a dodecane diluent system, when three phosphate molecules have to be placed around $Th(NO_3)_4$ for extraction; but not when metal nitrates requiring only two phosphate molecules for extraction [for example, $UO_2(NO_3)_2$] are involved.[4] Perhaps similarly the 3:1 TEHP-$HReO_4$ complex is unfavorably hindered and cannot form in isooctane, at least below 0.1 M TEHP, whereas with TBP in isooctane the amount of 3:1 complex equals the 2:1 complex at a TBP concentration of $\approx 7 \times 10^{-3}$ M.

It remains to explain why the 2:1 complex did not show up in 1,2-dichloroethane with TEHP. We think it would, if we could go to low enough TEHP concentrations, and would also show up at still lower concentrations for TBP in dichloroethane. The reason for appearance of the 2:1 complex only at much lower phosphate concentrations in 1,2-dichloroethane than in isooctane is because the anion is dissociated from the complex in the former solvent. In isooctane, a low-dielectric-constant medium, the anion is ion-paired to the cation complex, and when one site on the H_3O^+ core is free, as in the 2:1 complex, the anion can go there and provide electrostatic solvation (a tighter ion pair) and thus compensate part of the loss in solvation suffered by the H_3O^+ upon losing a phosphate molecule. But this cannot happen in 1,2-dichloroethane where the ions are dissociated, and so that saturated 3:1 complex is relatively favored.

Footnote and References

†Undergraduate summer visitor from Ripon College, Wisconsin, 1969.

1. J. J. Bucher and R. M. Diamond, J. Phys. Chem. 73, 675 (1969).
2. J. J. Bucher and R. M. Diamond, J. Phys. Chem. 73, 1494 (1969).
3. J. C. Poirier, J. Chem. Phys. 21, 965 (1953).
4. T. H. Siddall III, J. Inorg. Nucl. Chem. 13, 151 (1960).

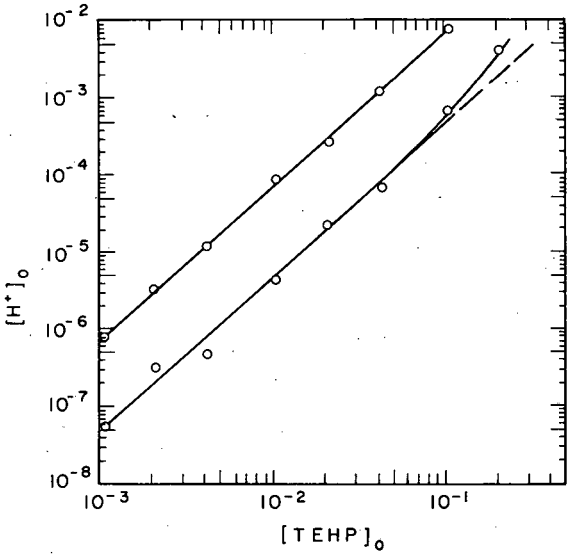

Fig. 1. Variation of acid content of organic phase with TEHP in isooctane for aqueous $HClO_4$ concentrations of 4.0 M (upper line) and 2.0 M (lower line). (XBL 701-2198)

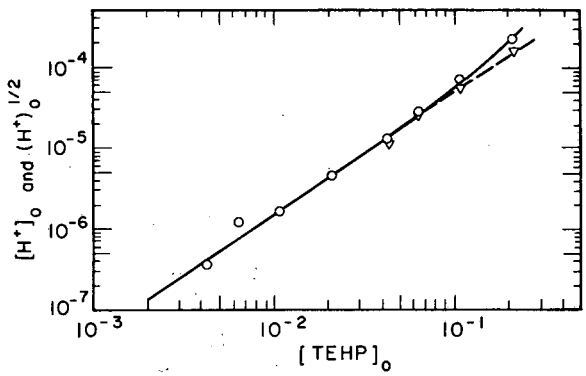

Fig. 2. Variation of acid content of organic phase with TEHP in 1,2-dichloroethane for aqueous $HReO_4$ concentration of 0.30 M. ö, uncorrected data; ∇, data corrected for activity coefficients. (XBL 701-2197)

EXTRACTION OF $HReO_4$, $HClO_4$, and $HAuCl_4$ BY TRIOCTYL PHOSPHINE OXIDE IN BENZENE, 1,3,5-TRIETHYL BENZENE, AND CHLOROFORM

J. J. Bucher, R. C. Laugen,† and R. M. Diamond

An earlier study[1] of the extraction of perrhenic acid ($HReO_4$) by trioctyl phosphine oxide (TOPO) in two diluents having relatively high dielectric constants, nitrobenzene (ϵ = 34.8 at 25° C) and 1,2-dichlorethane (ϵ = 10.4 at 25° C), demonstrated that very little or no water was co-extracted. In both diluents the extracted species was dissociated, and the cation, $2TOPO{\cdot}H^+$, was based on the bare proton and not on the hydronium ion. It was concluded that the extraction behavior of alkyl phosphine oxides was intermediate between two other common classes of extractants: the more basic alkyl amines, in which only one extractant molecule coordinates with a bare proton; and the less basic trialkyl phosphates, which are not strong enough to remove the proton from a water molecule and so have two or three molecules coordinated with a hydronium ion (H_3O^+) core. It was thought desirable to examine the extraction of acids by TOPO into other diluents that have different characteristics than just a high dielectric constant. In this paper benzene and 1,3,5-triethyl benzene, representing two basic, low-dielectric-constant aromatic solvents (one somewhat hindered), and chloroform, and acidic solvent, are examined. To minimize cation-anion interactions perrhenic and chloroauric ($HAuCl_4$) acids were used. Instead of using acid-base titration methods for determining the distribution data, we employed radioactive $^{186}ReO_4^-$ and $^{198,199}AuCl_4^-$ tracers wherever possible.

The extraction may be expressed as

$$H^+ + X^- + xH_2O + nTOPO\ (org) = H^+ \cdot nTOPO \cdot xH_2O \cdots X^-\ (org),$$

with a corresponding equilibrium constant

$$K^a = (H^+ \cdot nTOPO \cdot xH_2O \cdots X^-)_o / [TOPO]_o^n\ (H_2O)^x\ (H^+X^-),$$

where [ ] denotes concentration, ( ) signify activities, and the subscript o means the quantity is

in the organic phase.

From log-log plots of the organic-phase acid concentration, $[H^+]_o$, vs the aqueous acid activity, with the TOPO concentration and the water activity held constant, it can be determined whether the extracting species is an ion pair or higher aggregate. Such plots are shown in Figs. 1 and 2 for TOPO extractions of $HReO_4$, $HClO_4$, and $HAuClO_4$ in both benzene and chloroform. The slope of unity for TOPO-benzene, $CHCl_3$, -$HReO_4$, and $HClO_4$ indicates only ion pairs are extracted. The limiting slope of unity in TOPO-benzene -$HAuCl_4$ indicates only ion pairs are found if the organic-phase acid concentrations are sufficiently low. Above approximately 10^{-3} M acid, however, the slope is greater than one, indicating that aggregation is occurring.

The value(s) of n, the number of coordinated TOPO molecules, can be determined from log-log plots of organic acid vs equilibrium TOPO concentration at a fixed aqueous acid activity. Such plots are shown in Figs. 3 and 4 for $HReO_4$ and $HAuCl_4$ in benzene and $CHCl_3$. In each plot the slope is 2. Thus only two TOPO molecules, as in the nitrobenzene and 1,2-dichloroethane system, are involved in the extraction complex. It can be seen in Figs. 1 and 2 that the stoichiometric loading limit is one-half the fixed TOPO concentration, again indicating n = 2.

Several approximations have been made to calculate the constants in Table I. Mainly organic-phase activities have been replaced by molar concentrations. However, the constants are evaluated at dilute concentrations, that is, along straight-line portions of the plots, and are thus probably at least proportional to a true-equilibrium constant.

Table I. Constants for the extraction of $HReO_4$ and $HAuCl_4$.

Diluent	Acid	K_2^a
Benzene	$HReO_4$	1.2×10^3
	$HAuCl_4$	2.5×10^6
Triethyl benzene	$HReO_4$	1.0×10^3
Chloroform	$HReO_4$	5.8

A comparison of the various constants gives several interesting results. The use of $CHCl_3$ as diluent decreases the extraction of mineral acids by a large factor even though the dielectric constant of $CHCl_3$ (ϵ = 4.8 at 20° C) is considerably larger than the other two diluents (ϵ = 2.28 at 20° C for benzene and sym-triethyl benzene). This occurs because the chloroform interacts with TOPO to form a hydrogen-bonded complex, $R_3P{=}O\cdots HCCl_3$, which, of course, lowers the activity of the TOPO. Chloroauric anion, being somewhat larger than either ReO_4^- or ClO_4^-, is more easily forced out of the aqueous phase, giving considerably better extraction. ($AuCl_4^-$ may also be better tolerated in the organic phase due to better dispersion-free interactions.)

The difference in extraction of $HReO_4$ by TOPO in benzene and sym-triethyl benzene is surprisingly small compared with its extraction by alkyl amines[2] or trisubstituted phosphates[3] in these same diluents. In triethyl benzene, trialkyl amines (for the ion-paired amine salt) are extracted only one hundreth as much as they are in benzene. With tributyl phosphate the triethyl benzene system lowers (by a factor of four) the extraction of the 2TBP complex common to both diluents and also allows the formation of a 3TBP complex. Triethyl benzene in both extractant systems acts somewhat like the poorer aliphatic hydrocarbon solvents. Yet for TOPO the constants differ only by some 20%. The activity of TOPO in triethyl benzene is probably higher than in benzene. But the most important effect is likely that the protonic charge in the $2TOPO\cdot H^+$ cation is considerably shielded from direct diluent interactions, in particular with the π electrons of both diluents, and thus cannot be solvated appreciably better by the less sterically hindered and more dense π electrons of benzene.

Studies of the water coextracted with $HReO_4$ and $HAuCl_4$ by 0.1 M TOPO solution in benzene and $CHCl_3$ show that for $HReO_4$-benzene the ratio of H_2O per extracted proton is from 0.8 to 0.6; for $CHCl_3$-$HReO_4$ the value varies from 0 to 0.4; and for $HAuCl_4$-benzene, the value is approximately zero, even though in the concentration range of organic-phase acid examined the complex is aggregated. These data suggest that the acid complex cation extracted in these three diluents is anhydrous. It is not built around a hydronium ion core, but is the same TOPO solvate found in nitrobenzene and 1,2-dichloroethane systems; the acid complex in these three diluents differs only in being either ion-paired or aggregated, and not dissociated. The additional water found in these diluent systems may be associated with the perrhenate anion, loosely bound into the ion aggregates, or both.

Footnote and References

†Summer visitor, 1965, NSF High School Teachers Research Participation Program.

1. J. J. Bucher, T. J. Conocchioli, and R. M. Diamond, in Nuclear Chemistry Annual Report, 1968, UCRL-18667, Jan. 1969, pp. 307-309.
2. J. J. Bucher and R. M. Diamond, J. Phys. Chem. 69, 1565)1965).
3. J. J. Bucher and R. M. Diamond, J. Phys. Chem. 73, 1494 (1969).

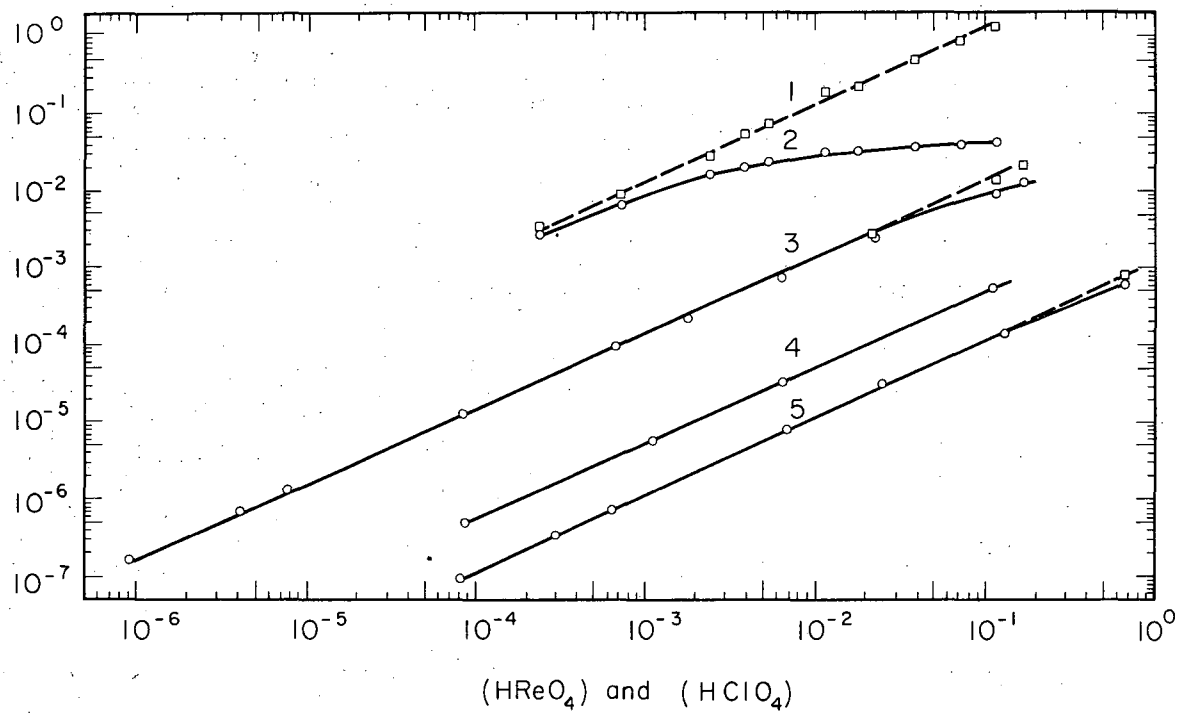

Fig. 1. Variation of acid content of organic phase with aqueous HReO, and $HClO_4$ for TOPO-benzene and -$CHCl_3$. Lines 2 and 3 are for 0.1 M TOPO in benzene and $CHCl_3$ respectively; line 4 is for 0.0020 M TOPO in benzene and line 5 is for 0.01 M TOPO in $CHCl_3$. Line 1 shows the result after correction to a constant TOPO concentration of 0.1 M. O, uncorrected data; □, corrected data. (XBL 701-2202)

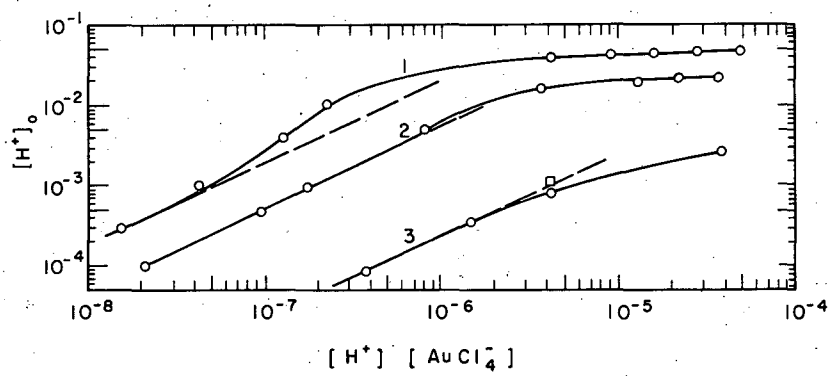

Fig. 2. Variation of acid content of organic phase with aqueous $HAuCl_4$ in 0.010 M HCl for 0.10 M (line 1), 0.050 M (line 2), and 0.01 M (line 3) TOPO-benzene. O, uncorrected data; □, corrected data. The dashed line indicates the extension of slope-one line. (XBL 701-2201)

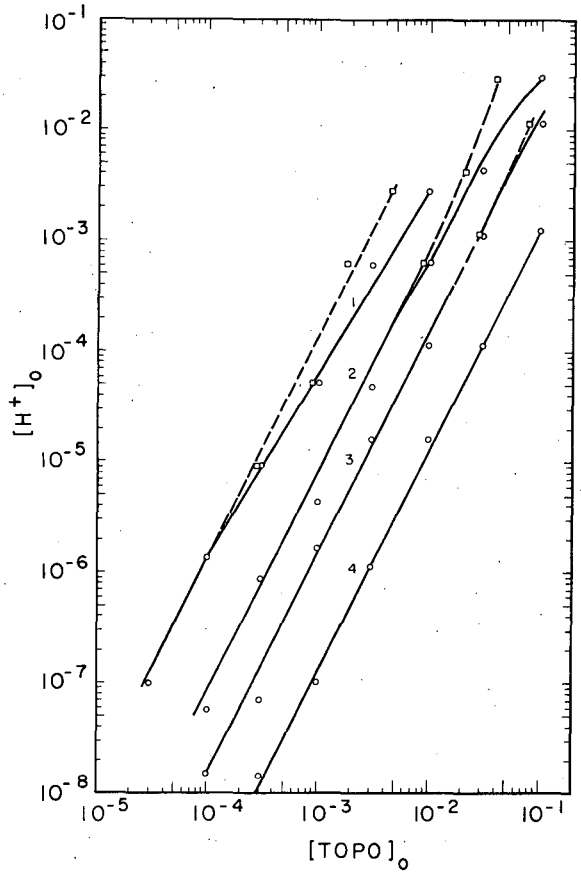

Fig. 3. Variation of acid content of organic phase with TOPO in benzene for aqueous $HReO_4$ concentrations of 0.437 M (line 1), 0.10 M (line 2), 0.040 M (line 3), and 0.010 M (line 4). O, uncorrected data; □, corrected to equilibrium TOPO. (XBL 701-2199)

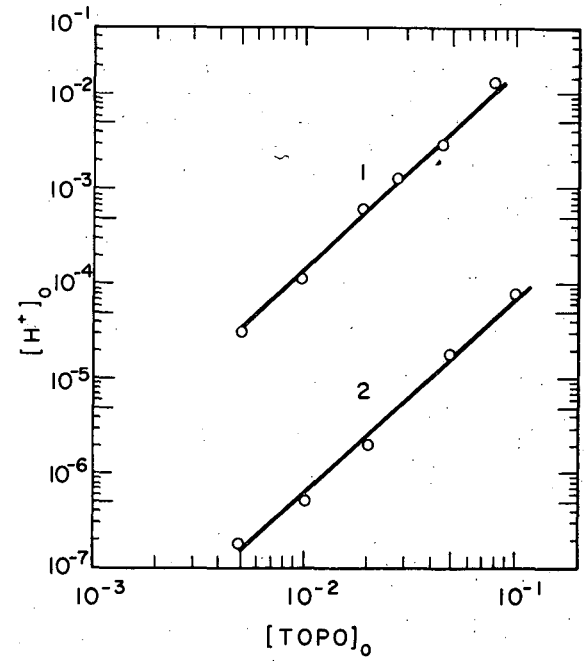

Fig. 4. Variation of acid content of organic phase with TOPO in $CHCl_3$ for aqueous $HReO_4$ concentrations of 0.514 M (line 1) and 0.040 M (line 2). (XBL 701-2200)

ANION EXCHANGE IN MIXED ORGANIC-AQUEOUS SOLUTIONS. I. DIOXANE-WATER

C. H. Jensen† and R. M. Diamond

The idea has been developed in earlier papers[1-3] that ion-exchange selectivity occurs as the result of a competition between the exchanging ions for solvation. That ion whose need is the more urgent goes into that phase which provides the better solvation, and so forces the remaining ion into the other phase, even though the latter ion also prefers the better solvating phase. Water molecules usually provide the main means of ionic solvation, and so for the usual conditions of a dilute external solution and a (concentrated) resin phase with strongly acidic or basic exchange groups, the external solution furnishes the most favorable medium. For a family of similar ions such as the halides, the smallest ion goes into the aqueous phase and the largest ion is pushed into the resin phase. Thus the dilute-solution anion exchange selectivity order expected for the halides and ReO_4^- would be $F^- < Cl^- < Br < I^- < ReO_4^-$, and this is indeed observed.

But as dioxane replaces water in the system, the mixed external solution becomes a poorer solvating agent for a number of reasons. First of all, dioxane does not possess any (acidic) hydrogen capable of bonding to the (basic) anions as does the water molecule. Secondly, the dioxane molecule acts as a base towards the water molecule, competing with the anions for hydrogen

bonding to the water, and breaking up the hydrogen-bonded water structure. Finally, the addition of dioxane, because of its own low dielectric constant and because of the destruction of the water structure, causes an increasingly marked drop in the dielectric constant of the mixed solvent. For all these reasons, the dioxane solution provides a much poorer solvating medium for anions than the original water solution (both chemically and electrostatically), and the effect is more marked the more the anion needs solvation.

But obviously, then, to be able to predict the effect of dioxane on the selectivity order of a family of anions, one must first determine the distribution of dioxane between the resin phase and the external solution. Figure 1 shows that with Dowex 1-X4, Cl^- form, the resin phase preferentially rejects dioxane and takes up water. Thus, as the concentration of dioxane in the total system increases, the resin phase absorbs a higher proportion of water than exists in the external solution, and the superiority of the external phase over the resin phase for solvating anions decreases.

With water alone as the solvent medium, anions obtain the best solvation in the dilute external phase, and so choose that phase in the order of their need for solvation, resulting in the resin selectivity order $F^- < Cl^- < Br^- < I^- < ReO_4^-$. But as dioxane is added to the system, the external solution becomes increasingly richer in dioxane (compared with the resin phase), and so less desirable to the (smaller) anions with the greatest need for solvation. They are held less tightly in the external phase, and so the degree of separation or selectivity among the anions should decrease. Under the proper conditions the selectivity order might even be reversed.

This is precisely the behavior observed with Dowex-1 with 0.0100, 0.0300, and 0.100 M LiCl as the macro-electrolyte and with F^-, Br^-, I^-, and ReO_4^- tracers, and shown in Fig. 2 for 0.0300 M LiCl. The values of D for ReO_4^- and F^- from water solution differ by more than 1000, but by the time one gets down to 20% mol-fraction dioxane this factor has decreased to about 15 and by 50% mol-fraction to about 3.

Thus, it seems that the expectations based on the suggested model have been fulfilled. Actually, of course, other factors must also be taken into account with the addition of dioxane to the system. Two of the most important of these are (a) the increase of nonexchange or "resin-invasion" electrolyte, and (b) the occurrence of ion pairing in the system with the decrease in dielectric constant. As a result of considering these effects, in particular the second, it was expected that a still greater trend toward reversal of the "normal" selectivity order would be observed with $N(CH_3)_4Cl$ as the macro-electrolyte instead of LiCl, and this was found to be true, Fig. 3. Actual reversal was obtained with the use of a weakly basic resin, Dowex 3-X4, and $N(CH_3)_4Cl$, as had been hoped.

Although the only anions treated in this paper are the monoatomic halide ions and one stable complex ion, ReO_4^-, the arguments presented are quite general and should hold for all other simple and stable anions. Since the agreement between expectation and experiment has been good in the systems studied, we believe, in fact, that this will prove to be true for other anions, with one important caution. Consideration of complex metal anions such as $GaCl_4^-$, $FeCl_4^-$, $InBr_4^-$, $ZnCl_4^-$, etc., which must be produced in the solution by replacement of the first hydration shell of the metal cation with the ligand of the supporting electrolyte, has this additional feature of complex-formation to take into account as the organic solvent replaces water in the system. This can be done, leading to somewhat different predictions, but that is another story.

Footnote and References

†Summer visitor, 1965, NSF College Teachers Research Participation Program.
Permanent address: Cabrillo College, Aptos, California.

1. B. Chu, D. C. Whitney, and R. M. Diamond, J. Inorg. Nucl. Chem. 24, 1405 (1962).
2. C. H. Jensen and R. M. Diamond, J. Phys. Chem. 69, 3440 (1965).
3. R. M. Diamond and D. C. Whitney, Resin Selectivity in Dilute to Concentrated Aqueous Solutions, in Ion Exchange, Vol. 1, edited by J. Marinsky (M. Dekker, New York, 1966).

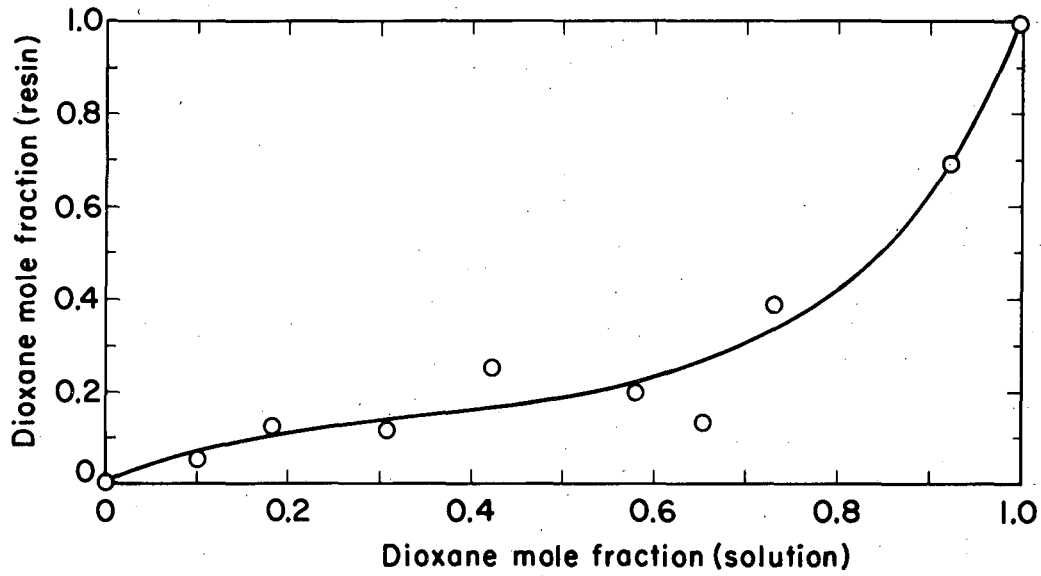

Fig. 1. The mol-fraction of dioxane in the resin phase for Dowex-1-X4 vs the mol-fraction of dioxane in the equilibrium solution. (XBL 702-2296)

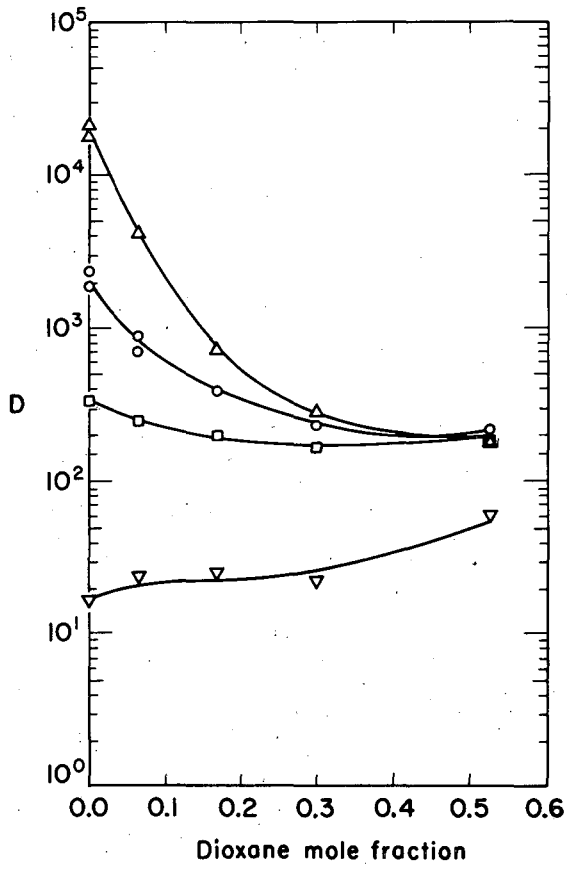

Fig. 2. Plot of D vs dioxane mol-fraction in the solution for 0.0311 M LiCl and Dowex-1-X4 resin and the tracer anions F^-, ∇; Br^-, I^-, O; and ReO_4^-, Δ. (XBL 701-2081)

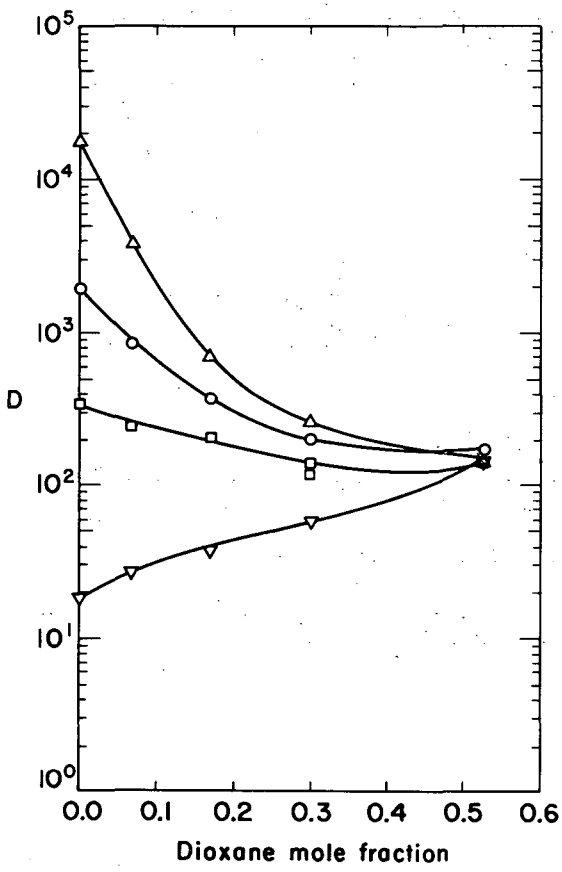

Fig. 3. Plot of D vs dioxane mol-fraction in the solution for 0.0303 M $N(CH_3)_4Cl$ and Dowex-1-X4 resin and the same tracer anions as in Fig. 2.
(XBL 701-2080)

HYDRATION OF ClO_4^-, $B\phi_4^-$, AND NO_3^- IN ORGANIC SOLVENTS

T. Kenjo† and R. M. Diamond

The distribution of salts between water and an organic phase can be made relatively high if either the cation or anion is large and hydrophobic enough. In particular, the extraction of anions can be studied by using large tetraalkylammonium cations. Other reports[1,2] describe studying the organic-phase complexing of F^- and Cl^- in such salts by water-immiscible phenols and alcohols. From the fact that definite complexes were indicated, we wondered if distribution of the salts alone and determination of the water co-extracted would not yield information on the first-shell hydration of the anions.

It would be advantageous in such a study if the extracted salt were dissociated into independent ions, for then if one ion could be shown to be anhydrous or to have a definite amount of water associated with it in a particular solvent, the determination of the total water extracted by a salt containing that ion yields the water bound to the co-ion (after subtraction of the water distributing into the volume-fraction of pure solvent alone). For this purpose a solvent of high dielectric constant was chosen, namely nitrobenzene (ϵ = 34.8 at 25°C).

It has been shown in a different type of study[3] that ClO_4^- in nitrobenzene is essentially anhydrous, so tetrapropylammonium perchlorate was the first salt studied. Figure 1 shows a log-log plot of the organic-phase salt concentration vs the equilibrium aqueous concentration. But even with a dielectric constant of 35, the decrease in the activity coefficients from unity at the higher organic-phase concentrations becomes significant. So they were calculated by the method of

Poirier,[4] and as can be seen in Fig. 1, the corrected points at the higher concentrations fall on the same straight line of unit slope extended from the more dilute solutions where the corrections are negligible. Since the salt is surely dissociated in the dilute aqueous phase, the slope of 1 observed shows that it is also dissociated in the organic phase over the range of concentration studied.

Table I shows the results of determining by Karl Fischer titrations the water co-extracted by three concentrations of tetrapropylammonium perchlorate in nitrobenzene. Approximately 1/3 mol of water appears per mol of extracted salt. It is not clear whether this water is (a) associated with the cation, (b) associated with the anion, or (c) just an increase in water dissolved in the nitrobenzene solvent because of the presence of the dissolved salt. To help understand this, a still larger anion was studied, the tetraphenyl boride ion. Table I shows the results; essentially zero water is involved. Since the salts are dissociated in the nitrobenzene medium, this means that no water is bound with the tetraalkylammonium cation, so that the 1/3 mol of water in Table I either is bound to ClO_4^- or is just excess water due to the changed nature of the solvent with the salt present.

Table I. Water co-extracted with tetraalkylammonium salts into nitrobenzene.

Salt	Molarity of salt (org)	Ratio of water to salt molarity (org)
Tetrapropylammonium perchlorate	1.39×10^{-1}	0.33
	5.43×10^{-2}	0.32
	2.66×10^{-2}	0.33
Tetrabutylammonium tetraphenyl boride	9.96×10^{-2}	0.08
	3.98×10^{-2}	0.04
	1.99×10^{-2}	0.07
Tetrabutylammonium nitrate	2.04×10^{-1}	1.45
	9.11×10^{-2}	1.41
	4.12×10^{-2}	1.40
	1.52×10^{-2}	1.27

If the latter, one might expect that changing to a lower-dielectric-constant solvent and going to conditions under which the extracted species is aggregated would change the water uptake. So the water uptake for tetrabutylammonium perchlorate in 20 volume % benzene and in dichloroethane was studied; the extraction curve shows that in these solvents and at these concentrations the salt has aggregated to the ion-quadrupole stage and beyond. But the water co-extracted is still 1/2 mol per mol of salt.

These results seem to indicate that this small amount of water may be on the ClO_4^-, and, at least, that it is not on the tetraalkyl ammonium cation. So it should be possible to study the water carried into nitrobenzene by the distribution of other anions. Figure 2 shows a log-log plot of the organic-phase concentration of tetrabutylammonium nitrate vs the aqueous-phase value. After activity coefficient corrections are made for the most concentrated organic solutions, by use of the expressions of Poirier,[4] a straight line of unit slope results for the entire range of concentrations studied, indicating for that range dissociation of the salt in the nitrobenzene. Table I lists values for the water co-extracted with the NO_3^- (the water distributing into the solvent alone has been subtracted). Between 1.4 and 1.1 mols of water are involved with the NO_3^-, depending upon how the 1/3 mol of water with the perchlorate salt is assigned. Some 1:2 complex is possible, or--perhaps less likely--there is some extra water extracted into the organic phase because the presence of the salt changes the nature of the solvent. In any case, a predominance of $NO_3^- \cdot H_2O$ species is suggested. This monohydration can be compared with the alcoholation number found in an extraction study of tetrabutylammonium nitrate into 1, 2-dichloroethane with decanol.[5] Only one alcohol complexed the NO_3^-, but in that study it was not possible to determine the water uptake to better than 1 ± 1 water molecule, so that it is not yet clear what the nitrate ion coordination number is.

Footnote and References

†Permanent address: Department of Chemistry, Tokyo Institute of Technology, Tokyo, Japan.

1. D. J. Turner, A. Beck, and R. M. Diamond, J. Phys. Chem. 72, 2831 (1968).
2. T. Kenjo and R. M. Diamond, following paper.
3. J. Bucher, T. J. Connochioli, and R. M. Diamond, in Nuclear Chemistry Annual Report, 1968, UCRL-18667, Jan. 1969, p. 307; submitted to J. Phys. Chem.
4. J. C. Poirier, J. Chem. Phys. 21, 965 (1953).
5. D. J. Turner and R. M. Diamond, J. Inorg. Nucl. Chem. 30, 3039 (1968).

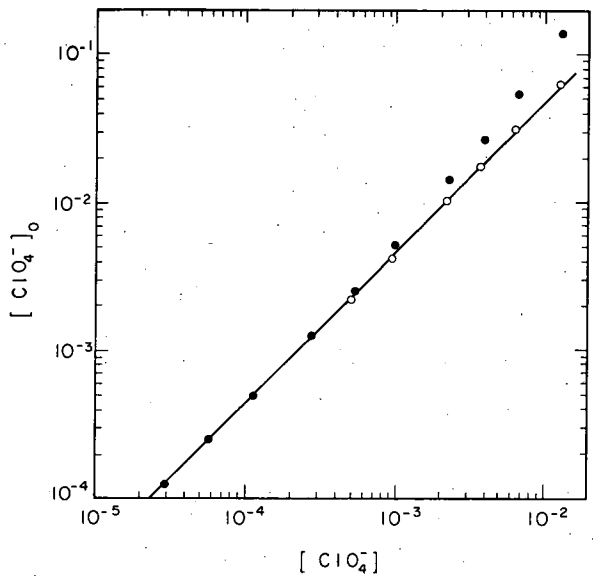

Fig. 1. The tetrapropylammonium perchlorate concentration in nitrobenzene vs the aqueous ammonium perchlorate concentration; organic-phase concentration, ●; organic-phase activity by the method of Poirier (Ref. 4), O. (XBL 701-2192)

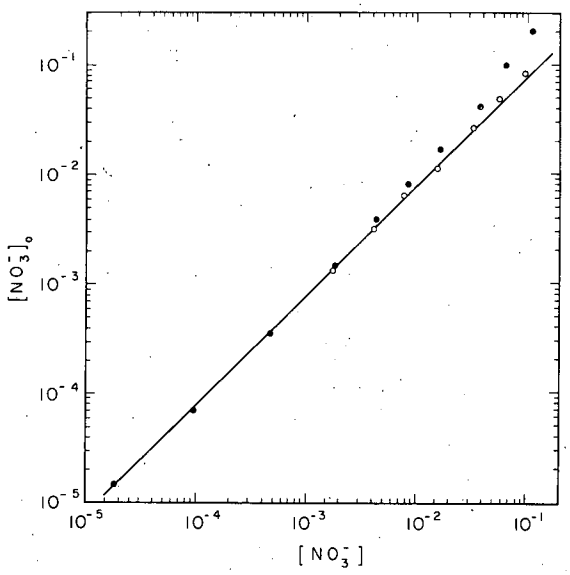

Fig. 2. The tetrabutylammonium nitrate concentration in nitrobenzene vs the aqueous ammonium nitrate concentration, ●; organic-phase activity by the method of Poirier (Ref. 4), O. (XBL 701-2193)

COORDINATION OF FLUORIDE AND CHLORIDE ANIONS WITH ALCOHOL AND PHENOL

T. Kenjo† and R. M. Diamond

A recent paper[1] on the extraction of tetraheptylammonium fluoride into toluene by alcohol and naphthol showed that definite integral numbers of the extractant molecules were involved in the organic-phase species. These molecules were surely hydrogen-bonded to the F^-, as little interaction would be expected with large quaternary ammonium cations. Four benzyl or decyl alcohol molecules were required, and two or four molecules of naphthol or phenylphenol, depending upon the phenol concentration. This indicates the stepwise complexing of the F^- by phenol, as is commonly observed with metal cations and simple ligands, but with the 3:1 species in vanishingly small abundance.

It was of interest to see if the same alcoholation number would be obtained with a different diluent, and if the fluoride-alcohol data in toluene could be extended to more dilute alcohol concentrations to look for lower alcohol complexes. We were also curious whether Cl^- would show the same behavior or indicate a larger alcoholation number; the Cl^- ion is larger and could accommodate a larger number of molecules around itself, but on the other hand it is less basic than F^-, and so needs less solvation.

The procedure was essentially similar to earlier work, but organic-phase salt concentrations were usually determined spectrophotometrically by picrate extraction with the alkylammonium cation.[2] Logarithmic plots of the organic salt concentration vs the equilibrium aqueous concentration established the ion-pair nature of the extracted species, and the slope of log-log plots of the organic salt concentration vs the equilibrium alcohol or phenol concentration gave the number of such molecules bound to the extracted anion.

It was found by extending the previous F^- study to lower benzyl alcohol concentrations in toluene that there was, indeed, a lower 2:1 complex just as with phenol, and again there was little evidence for a 3:1 complex. The concentration of extractant yielding about equal amounts of the 2:1 and 4:1 species was ≈ 2 to 3×10^{-3} for the phenols and ≈ 8 to 9×10^{-2} for the benzyl alcohol.

The results for the extraction of tetrapentylammonium chloride into toluene with benzyl alcohol show the same general behavior; at low alcohol concentrations a 2:1 alcoholate is indicated, and at higher concentrations a 4:1 species predominates, with little evidence for a 3:1 complex. Equal amounts of the 2:1 and 4:1 species occur at ≈ 0.2 M alcohol, compared to 8 to 9×10^{-2} M for the F^-; the weaker solvation needed by Cl^- would seem to be the reason.

If a different diluent were used, it might be expected that the relative proportions of 2:1 and 4:1 complexes at a given alcohol concentration would differ from those of toluene, and that the magnitude of the extraction would change. If a more inert diluent, for example isooctane, were used instead of toluene, it might be expected that extraction would be poorer, and that the range of alcohol concentration in which the 4:1 complex predominated over the 2:1 might extend to lower values. This would be because the loss of the generalized solvation furnished the 2:1 complex by the dispersion-force interactions of the π electrons of toluene has to be made up in isooctane by coordination with (more) extractant molecules. These latter molecules, too, are more available for complexing because isooctane is not so good an electron donor as toluene toward them, and so does not interact so strongly with them.

Both predictions were verified. To obtain satisfactory extraction of Cl^- into isooctane, the larger tetrahexylammonium cation had to be used. A log-log plot of the organic-phase salt concentration vs the equilibrium aqueous salt concentration for 0.20 M (upper curve) and 0.080 M (lower curve) benzyl alcohol is shown in Fig. 1. Both curves rise initially with a slope of 2, indicating extraction of ion pairs, and then abruptly level off and actually decrease slightly. This latter behavior is probably due to the formation of salt micelles in the aqueous phase at the higher salt concentrations, and the solubilization therein of some of the benzyl alcohol from the organic phase. The effect becomes larger, the higher the concentration of aqueous salt and of organic-phase alcohol. Figure 2, a log-log plot of extracted chloride salt concentration vs the alcohol concentration for 2.30×10^{-2} M (upper curve) and 5.75×10^{-3} M (lower curve) aqueous tetrahexylammonium chloride solutions, shows that over the range of alcohol concentrations studied, 0.2 to 5×10^{-3} M, only a slope of 4, indicating a 4:1 complex, occurs. (At the highest alcohol concentration with the more concentrated salt solution, solubilization into the aqueous micelles occurs.) This confirms the prediction that the use of a more inert diluent would enhance the range of the 4:1 alcohol-chloride complex to make up for the poorer solvation of the 2:1 species by the diluent.

In a similar way, the extraction of tetraheptylammonium fluoride into isooctane by benzyl alcohol shows only a 4:1 alcoholate over the limited range of alcohol concentration accessible, 0.2 to 0.05 M. And again the extraction is poorer than with toluene as the diluent.

It appears from this (and the preceding) study that the alcoholates and phenolates of F^- and Cl^- do form stepwise complexes, but not smoothly. There is a marked preference for the 2:1 and 4:1 species. The larger value, 4, may be an indication of the first-shell hydration number for these anions in aqueous solution; at least it should be a lower limit. It also appears that the changes in the extraction behavior caused by changing the diluent lend themselves to rather simple interpretations.

Footnote and References

†Permanent address: Department of Chemistry, Tokyo Institute of Technology, Tokyo, Japan.

1. D. J. Turner, A. Beck, and R. M. Diamond, J. Phys. Chem. 72, 2831 (1968).
2. R. R. Grinstead and J. C. Davis, Annual Summary Progress Report, 1966-1967, from the Dow Chemical Company to the Office of Saline Water, p. 65.

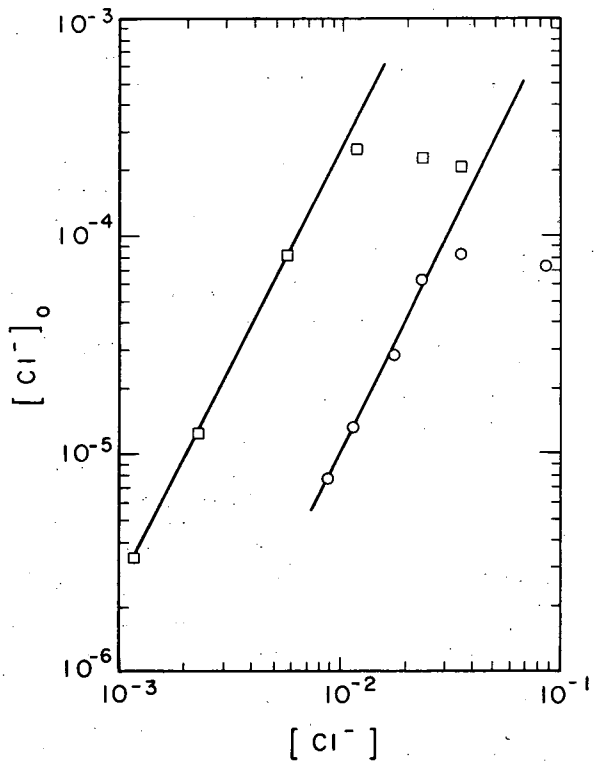

Fig. 1. A log-log plot of the tetrahexylammonium chloride concentration in isooctane vs the aqueous salt concentration for 0.20 M benzyl alcohol, □; and 0.080 M alcohol, O. (XBL 701-2191)

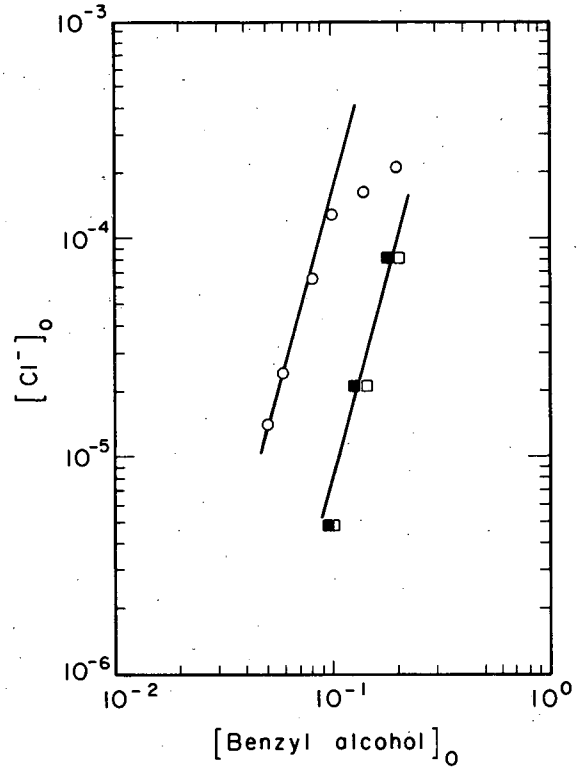

Fig. 2. A log-log plot of the tetrahexylammonium chloride concentration in isooctane vs the benzyl alcohol concentration for 2.30×10^{-2} M aqueous salt, O; and for 5.75×10^{-3} M aqueous salt, □. In the latter case, correction for the alcohol bound to water gives the solid symbols, ■.
(XBL 701-2190)

Radiation Chemistry

RADIOLYTIC OXIDATION OF THE PEPTIDE MAIN CHAIN IN DILUTE AQUEOUS SOLUTION: CHEMISTRY OF THE PEROXY RADICAL, $RCONHC(\dot{O}_2)R_2$†

M. J. Kland-English, H. A. Sokol, and W. M. Garrison

The radiolytic oxidation of the peptide main chain in dilute aqueous solution containing O_2 has been described[1] in terms of the radiation-induced step[2, 3]

$$H_2O \longrightarrow H_2O_2,\ H_2,\ OH,\ H,\ e^-_{aq},\ H^+ \qquad (1)$$

followed by

$$OH + RCONHCHR_2 \longrightarrow RCONH\dot{C}R_2 + H_2O, \qquad (2)$$

$$O_2 + RCONH\dot{C}R_2 \longrightarrow RCONHC(\dot{O}_2)R_2. \qquad (3)$$

The reducing species formed in reaction (1) are scavenged by O_2 via

$$e^-_{aq}(H) + O_2 \longrightarrow O_2^-(HO_2), \qquad (4)$$

where the products of reaction (4) are related by the equilibrium[4] $HO_2 \rightleftharpoons H^+ + O_2^-$. The simplest scheme for subsequent radical removal involves

$$HO_2 + RCONHC(\dot{O}_2)R_2 \longrightarrow RCONHC(O_2H)R_2 + O_2, \qquad (5)$$

$$H_2O + RCONHC(O_2H)R_2 \longrightarrow RCONH_2 + R_2CO + H_2O_2 \qquad (6)$$

to give amide and carbonyl functions.

We have completed a detailed study of the degradation products formed in the γ radiolysis of the peptide N-acetylalanine in oxygenated solution. Major products and their yields are summarized in Table I. Amide is produce in the expected yield, $G(CH_3CONH_2) \approx G_{OH} \approx 2.8$. The pyruvic acid (plus acetaldehyde) yield is, however, much less than that predicted on the basis of reaction (5) as the major radical-removal step.

The evidence is that the $RCONHC(\dot{O}_2)R_2$ radicals derived from N-acetylalanine are removed predominantly via[5]

$$2RCONHC(\dot{O}_2)R_2 \longrightarrow 2RCONHC(\dot{O})R_2 + O_2 \qquad (7)$$

in competition with reaction (5). Reaction (7) is then followed by

$$RCONHC(\dot{O})(C(=O)OH)R + O_2 \longrightarrow RCONHCOR + CO_2 + HO_2 \qquad (8)$$

to give the diacetamide derivative, which is hydrolytically labile and on mild differential hydrolysis of the irradiated solution yields acetamide and acetic acid.[6] The HO_2 radicals formed via reactions (4) and (8) are removed via

$$2HO_2 \longrightarrow H_2O_2 + O_2. \qquad (9)$$

The sequence of reactions (1) to (4) followed by reactions (7) to (9) satisfies both the qualitative and quantitative requirements of the present system. The data of Table I were obtained at pH 3, under which condition the hydroperoxy radical is predominantly in the HO_2 form.[4] Although the yield for main-chain degradation is essentially the same at pH 3 and at pH 7 (Fig. 1), the relative contributions of reactions (5), (6) and (7), (8) may be pH dependent. Such effects are now being evaluated.

For O_2-saturated solutions of poly-DL-alanine we find $G(NH_3) \approx 3.8$.[7] With this oligopeptide (mol wt 2000) we assume random attack of OH at the main chain and envisage the analogue of reaction (8) as involving the enol form of an adjacent peptide linkage,

$$\mathrm{RCONHC(\dot{O})(R)-C(OH)=N-R} + O_2 \longrightarrow \mathrm{RCOHNCOR} + \mathrm{O{=}C{=}N{-}R} + HO_2, \qquad (10)$$

where

$$\mathrm{O{=}C{=}N{-}R} + H_2O \longrightarrow CO_2 + RNH_2$$

follows essentially instantaneously.

Footnotes and References

†Condensed from UCRL-18983, Sept. 1969, presented at the 158th National Meeting of the American Chemical Society, New York, September 7-12, 1969.

1. For a recent review see W. M. Garrison, Current Topics in Radiation Research, ed. by M. Ebert and A. Howard, Vol. IV (North-Holland Publishing Co., Amsterdam, 1968), p. 45-94.
2. C. J. Hochanadel and R. Casey, Radiation Res. 25, 198 (1965), report $G_{OH} = 2.59$, $G_{e^-_{aq}} = 2.58$, $G_H = 0.55$, $G_{H_2} = 0.45$, $G_{H_2O_2} = 0.72$. The maximal OH yield at high solute concentration appears to be $G_{OH} \approx 2.9$ (Ref. 3).
3. E. Hayon, Trans. Faraday Soc. 61, 723 (1965); G. Czapski, Adv. Chem. Ser. 81, 106 (1968).
4. G. Czapski and H. J. Bielski, J. Phys. Chem. 67, 2180 (1963).
5. In an earlier study we found reaction of the type $2RO_2 \longrightarrow O_2$ to be of major importance in the radiolytic oxidation of acetic acid in dilute aqueous solution [Radiation Res. 10, 273 (1959)]. Such reaction of RO_2 was invoked in earlier studies of radical-initiated oxidation of gaseous hydrocarbons by Vaughan and co-workers [J. Am. Chem. Soc. 73, 15 (1951)].
6. The maximal acetic acid yield as measured by vapor-phase chromatography was obtained after the solutions were made 1 N in sodium hydroxide and allowed to stand at room temperature for 15 min. Amide ($RCONH_2$) hydrolysis is negligible under these conditions.
7. We find (W. Bennett-Corniea, H. A. Sokol, and W. M. Garrison; to be published) that the $G(NH_3)$ values obtained in the γ radiolysis of dilute oxygenated solutions of oligopeptides and polypeptides are consistently greater than G_{OH}. Our interpretation of this effect is that with such compounds a fraction of the RO radicals formed via reaction (7) react intramolecularly with an adjacent C-H locus of the main chain, $RO + RH \longrightarrow ROH + R$. This leads then to an enhancement in the observed yield for amide production. With small molecules containing a single amino acid residue (e. g., N-acetylalanine) the equivalent RO chemistry can occur only intermolecularly and is of negligible importance in dilute solution.

Table I. Product yields in the γ radiolysis of 0.05 M N-acetylalanine, O_2-saturated, pH 3.

Product	Yield (G)[4]
NH_3	2.9
CH_3COOH	2.8
H_2O_2	2.2
(ROOH)	≈0.5[b]
$CH_3COCOOH$	≈0.5
CH_3CHO	

[a]Product yields are independent of dose up to ≈ 2×10^{19} eV/ml.
[b]Unspecified.

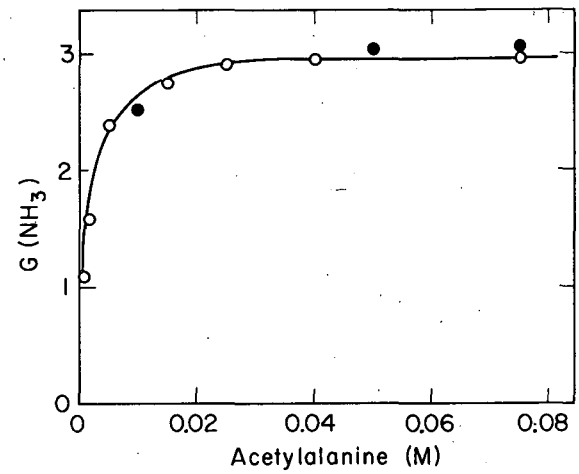

Fig. 1. Effect of solute concentration in the γ radiolysis of N-acetylalanine in O_2-saturated solution; pH 7, 0; pH 3, 0. Dose = 1.5×10^{19} eV/ml. (XBL698-3505)

RECONSTITUTION ("REPAIR") MECHANISMS IN THE RADIOLYSIS OF AQUEOUS BIOCHEMICAL SYSTEMS: INHIBITIVE EFFECTS OF THIOLS†

John Holian* and Warren M. Garren

The hydrated electron, e^-_{aq}, and the OH radical are the principal products of the radiation-induced decomposition of liquid water; with γ rays the 100-eV yields[1] of these reactive intermediates are approximated by the values $G_{e^-_{aq}} \approx G_{OH} \approx 2.6$.

In the γ radiolysis of oxygen-free solutions of the pyrimidine bases, both e^-_{aq} and OH add preferentially to the 5, 6 double bond,[2, 3]

$$e^-_{aq} + B + H_2O \longrightarrow \dot{B}H + OH^-, \quad (1)$$

$$OH + B \longrightarrow \dot{B}OH, \quad (2)$$

where the rate constants[4, 5] k_1, k_2 fall in the range 10^9 to 10^{10} M^{-1} sec^{-1}. Yet, the observed yield for base destruction in millimolar solutions is uniformly low with G(-B) < 0.9. The evidence is that a back-reaction[3]

$$\dot{B}H + \dot{B}OH \longrightarrow 2B + H_2O \quad (3)$$

leads to a reconstitution of the base.

Similarly, in the radiolysis of primary amides and monosubstituted primary amides (peptides) in oxygen-free neutral solution, the reducing and oxidizing species e^-_{aq} and OH are removed through reactions of the type[6]

$$e^-_{aq} + RCONHR + H_2O \longrightarrow R\dot{C}(OH)NHR + OH^- , \quad (4)$$

$$OH + RCONHR \longrightarrow RCONH\dot{C}R_2 + H_2O , \quad (5)$$

where k_4, k_5 are in the range 10^7 to 10^8 M^{-1} sec^{-1}.[6,7] Combination of $R\dot{C}(OH)NHR$ with like species or with the radical $RCONH\dot{C}R_2$ would lead to formation of ketonic products. However, the combined yield of such products is low, with $G(>CO) \approx 0.2$; the evidence is that the reconstitution reaction

$$R\dot{C}(OH)NHR + RCONH\dot{C}R_2 \longrightarrow 2RCONHR \quad (6)$$

represents the major stoichiometry for removal of organic radical in such systems.[6,7]

We find that labile species such as cysteine and ascorbic acid effectively block the reconstitution reactions 3 and 6 through

$$\dot{B}H + R'H \longrightarrow BH_2 + R', \quad (7)$$

$$R\dot{C}(OH)NHR + R'H \longrightarrow RCHO + NH_2R + R'; \quad (8)$$

yield data are summarized in Table I.

We find that (a) the presence of cysteine and ascorbic acid (which ordinarily function as protective agents both in radiation chemistry and in radiation biology) leads at low concentrations to a very marked enhancement in the radiolytic lability of the pyrimidine and peptide moieties in oxygen-free solution, and that (b) such enhancement arises as a consequence of the blocking by the second solute of the reconstitution reactions formulated in Eqs. 3 and 6.

Footnotes and References

†Condensed from Nature 221, 57 (1969).

*Present address: 19 Stanley Avenue, Chesham, Buckinghamshire, England.

1. G. Czapski, Advan. Chem. Ser. 81, 106 (1968).
2. J. Weiss, Nucleic Acid Res. and Mol. Biol. 3, 103 (1964).
3. A. Kamal and W. M. Garrison, Nature 206, 1315 (1965).
4. E. J. Hart, J. K. Thomas, and S. Gordon, Radiation Res., Suppl. 4, 74 (1964).
5. P. Scholes, P. Shaw, R. L. Willson, and M. Ebert, Pulse Radiolysis (Academic Press, New York, 1965), p. 151.
6. R. L. S. Willix and W. M. Garrison, Radiation Res. 32, 452 (1967).
7. M. A. J. Rodgers and W. M. Garrison, J. Phys. Chem. 72, 758 (1968).

Table I. Effect of cysteine and ascorbic acid (R'H) on the γ-ray-induced reduction of pyrimidine (C=C) and peptide (C=O) linkages in oxygen-free solutions.[a]

Solution	R'H[b]	$G(BH_2)$
A. Cytosine ⟶ dihydrouracil (BH_2) + ammonia[c]		
0.05 M Cytosine, pH 7	none	< 0.9
0.05 M Cytosine, pH 7	cysteine, 2.5×10^{-3} M	2.8
0.05 M Cytosine, pH 7	ascorbic acid, 1.5×10^{-3} M	2.9
B. N-ethylacetamide ⟶ acetaldehyde (RCHO) + ethylamine		
1M N-ethylacetamide, pH 7	none	< 0.1
1M N-ethylacetamide, pH 7	cysteine, 4×10^{-4} M	2.8

a. At dosages below ≈ 2.5×10^{18} eV/gm.
b. The indicated concentrations of R'H give the maximum enhancement in the yield of reduced products.
c. Dihydrocytosine is unstable and hydrolyzes spontaneously to yield dihydrouracil and ammonia.

RADIATION CHEMISTRY OF BIOCHEMICAL COMPOUNDS†

Warren M. Garrison

Radiation-chemical reactions of biochemical compounds in aqueous solution and in the solid state are reviewed. A brief introductory survey is given of the radiation-induced reactions of water that lead to formation of the hydrated electrons, e^-_{aq}, and the OH radical as major decomposition products. Reactions of these reactive species with amino acids, peptides, purines, and pyrimidines in dilute aqueous solution are outlined.

Particular emphasis is given to the concept of reductive deamination of amino acids and peptides in radiolysis. The evidence is that electrons produced in the ionization act are chemically trapped through addition to C=O double bonds. Dissociation of the reduced intermediate then ensues:

$$e^- + NH_3^+CH(R)COO^- \longrightarrow NH_3^+CH(R)\dot{C}(O^-)(O^-) \longrightarrow NH_3 + \dot{C}H(R)COO^-, \quad (1)$$

$$e^- + NH_3^+CH(R)CONHR \longrightarrow NH_3^+CH(R)\dot{C}(O^-)NHR \longrightarrow NH_3 + \dot{C}H(R)CONHR. \quad (2)$$

For reductive deamination to occur, the C=O linkage must be in the α position to the NH_3^+ group. Such reaction occurs in the radiolysis of both aqueous and solid-state systems.

Evidence for the role of excited-molecule reactions in the radiolysis of peptides in concentrated aqueous solution and in the solid state is reviewed. Decomposition of excited species, which leads to cleavage of the peptide main chain, is of the form

$$RCONHCHR_2^* + RCONHCHR_2 \longrightarrow RCONH\dot{C}R_2 + R\overset{OH}{C}{=}NH + \dot{C}NR_2 , \qquad (3)$$

where $R\overset{OH}{C}{=}NR$ represents the end form of the amide function. Experimental findings suggest that $RCONHCHR_2^*$ represents a long-lived triplet state with an excited electronic level of $\approx$ 3 eV.

Specific roles of ionization and excitation in the radiolysis of a number of amino acid and peptide systems are summarized.

Footnote

†Abstract of review paper presented at the annual meeting of Radiological Research Society of North America, Chicago, December 1-5, 1969.

Chemical Engineering

THE GROWTH RATE OF MICROORGANISMS AS THE FUNCTION OF A SINGLE LIMITING SUBSTRATE

J. N. Dabes, R. K. Finn,† and C. R. Wilke

We have developed a simplified model of a cell consisting of a series of linked reversible enzymatic reactions dependent on the concentration of a single external substrate. The general mathematical solution of this system of reactions has been found. This general solution confirms the concept of a master reaction in biological systems as first proposed by Blackman.[1] The maximum rate of an enzymatic system is determined by, and equal to, the maximum rate of the slowest forward reaction in the series. This is a consequence of the fact that enzymatic reactions approach zero-order kinetic behavior as they near their maximum rate.

Of greater practical interest in modeling the growth rate of cells as a function of a single limiting substrate are three cases developed from the above general model of a cell. The first and simplest special case results in the Monod equation[2]

$$\mu = \frac{\mu_{max}[S]}{B + [S]} ,$$

where μ is the specific growth rate, time^{-1}; μ_{max} is the maximum specific growth rate, time^{-1}; $[S]$ is the concentration of the external limiting substrate, mass/volume of external phase; and B is a constant, mass/volume of external phase. The Monod equation results when the maximum forward rate of one enzymatic reaction in the cell is much less than the maximum forward rate of any other enzymatic reaction. The Monod equation is presently used by most workers modeling the growth of microorganisms.

A more realistic model is the case in which more than one enzymatic reaction is slow. When these enzymatic reactions are separated from each other by any number of fast reactions which overall have a large equilibrium constant, the Blackman form results:

$$\mu = [S]/A, \text{ when } [S] < A\mu_{max}$$

$$\text{and} \quad \mu = \mu_{max}, \text{ when } [S] > A\mu_{max},$$

where A is a constant, mass $\times$ time/volume of external phase.

Unlike the Monod and Blackman forms, which contain only two arbitrary constants, the three-constant form contains three arbitrary constants,

$$[S] = \mu A + \frac{\mu B}{(\mu_{max} - \mu)} ,$$

where the specific growth rate, μ, is implicitly expressed. This case results when two slow enzymatic steps are separated by an equilibrium constant that is not large. The Monod and Blackman forms can readily be seen to be special cases of this third form.

Twelve sets of experimental data from the literature were examined.[3] The Monod equation gave poorer fit of the data than the Blackman form in 9 of the 12 cases, as determined by a non-linear least-squares fitting technique.

On Figs. 1, 2, and 3 are presented data of Monod,[2] Shelef et al.,[4] and Johnson,[5] respectively. Also shown are the "best-fit" curves for the three models. Table I summarizes statistical data for the three sets of data as compared with the three models. SUMSQ in Table I is the sum of the squares of the deviations of the data from the particular model in question in the direction of the

dependent variable, μ. The units associated with the quantities μ_{max}, A, and B are those that result from the original data as taken[2, 4, 5] and as shown on the figures.

It is concluded that workers modeling the growth of microorganisms should not accept the Monod equation without question, as many apparently do today.

Footnote and References

†Present address: School of Chemical Engineering, Cornell University, Ithaca, New York 14850.

1. F. F. Blackman, Ann. Bot. 19, 281 (1905).
2. J. Monod, Recherches sur la croissance des cultures bactériennes (Hermann et al., Paris, 1942).
3. J. N. Dabes, R. K. Finn, and C. R. Wilke, Lawrence Radiation Laboratory Report (in preparation).
4. G. Shelef, W. J. Oswald, and C. J. Golueke, SERL report no. 68-4, University of California, Berkeley, 1968.
5. M. J. Johnson, J. Bacteriol. 94, 101 (1967).

Table I. The best fit of three sets of data against the Monod, the Blackman, and the three-constant forms.

	μ_{max}	A	B	Number of data points	SUMSQ
Monod—glucose					
Monod form	1.440	0	11.97	27	0.363
Blackman form	1.229	17.63	0	27	0.207
Three-constant form	1.256	16.46	0.701	27	0.1941
Shelef et al. —nitrate					
Monod form	5.41	0	2.09	24	1.297
Blackman form	4.09	0.748	0	24	1.844
Three-constant form	4.61	0.412	0.585	24	0.985
Johnson—oxygen					
Monod form	1.116	0	0.823	15	0.0440
Blackman form	0.886	1.499	0	15	0.0212
Three-constant form	0.935	1.248	0.0851	15	0.00493

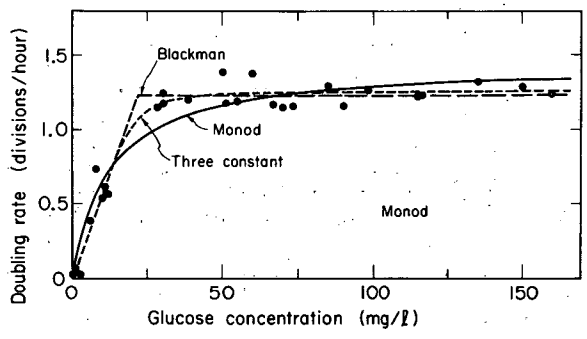

Fig. 1. Doubling rate of E. coli at 37°C limited by glucose concentration. Data from Monod (Ref. 2). (XBL698-3637)

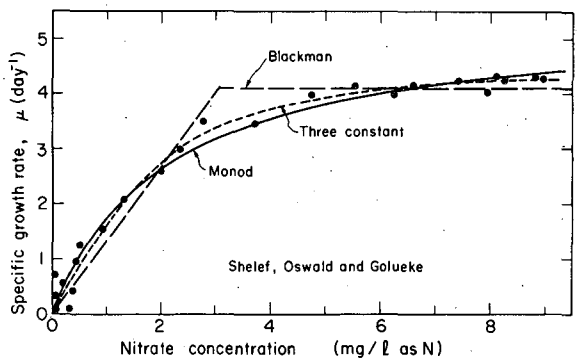

Fig. 2. The specific growth of Chlorella pyrenoidosa 71105 at 35 °C in continuous culture as a function of nitrate concentration as limiting substrate. The light intensity was above saturation. Data from Shelef, Oswald, and Golueke (Ref. 4). (XBL698-3640)

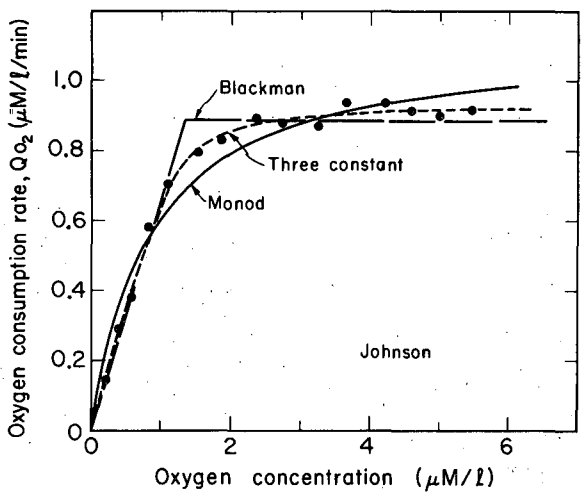

Fig. 3. The rate of oxygen uptake of Candida utilis at 30 °C as a function of oxygen concentration. The data presented here are for cells grown at 0.97×10^{-6} M O_2. Data from Johnson (Ref. 5). (XBL698-3645)

GAS-ABSORPTION CHARACTERISTICS OF AGITATED AQUEOUS ELECTROLYTE SOLUTIONS†

C. W. Robinson and C. R. Wilke

The performance capability of a stirred-tank gas absorber traditionally has been characterized by empirically correlating the overall volumetric mass transfer rate coefficient ($K_L a$) for a given gas-liquid system with the process variables, superficial gas velocity (v_S) and agitation power input per unit volume (P_G/V_L). Previous work has been confined largely to pure liquid absorbents[1-3] or to model chemically reactive systems,[3-6] the physicochemical properties of which differ from many systems of present or potential industrial importance. One example of the latter is the production of microbial biomass from alkanes dispersed in dilute aqueous electrolyte solution, a process in which the agitation power requirement is well above levels heretofore studied. The value of $K_L a$ is strongly influenced by the physicochemical properties of the liquid phase. One such property, the effect of which has not been previously fully characterized, is the ionic strength of the solution.

A 2.5-liter liquid volume stirred-tank gas-absorption system was designed and constructed to measure the variation of $K_L a$ with agitation power and aeration rate for physical transfer of oxygen into several electrolytic solutions and oxygen transfer rates with chemically reactive sodium sulphite solution. Both continuous-feed steady-state and semi-batch unsteady-state absorption or desorption techniques were used to evaluate $K_L a$ at 30 °C. Liquid-phase oxygen tension or its rate of change was measured by means of a Teflon-membrane oxygen probe. Because of the diffusion lag in the membrane, the probe response to unsteady-state oxygen tensions cannot be used directly to determine the rate of change of the liquid-phase oxygen tension; the combined response of the liquid phase and the probe output has been mathematically modeled, and $K_L a$ is determined by means of a nonlinear least-squares computer program which fits the experimental response data to the theoretical behavior.

For the solutions studied so far, we find that $K_L a$ for oxygen transfer correlates logarithmically with the power input according to $(P_G/V_L)^{n_j}$, where the exponent depends upon the ionic strength, but appears to be independent of composition, as shown in Fig. 1. Medium A-1 consisted of 1.6 g K_2HPO_4, 0.48 g $MgSO_4 \cdot 7H_2O$, 4.6 g NH_4Cl, and 0.02 g NaCl per liter of distilled water (a fermentation medium); the sodium sulphite solution contained $4(10^{-3})$ M $CuSO_4$. From the form of Fig. 1, it appears that

$$n_j = 0.40 + 2.38\,\Gamma_T, \qquad 0 \le \Gamma_T < 0.21,$$

$$n_j = 0.90, \qquad \Gamma_T \ge 0.21,$$

where Γ_T is the total ionic strength. $K_L a$ is also dependent upon $(v_S)^{m_j}$ in range $0 \le v_S \le 0.015$ ft/sec, where m_j varies somewhat with the solution type (m_j = 0.35 for distilled water, 0.43 for KOH, 0.39 for Na_2SO_4, and 0.38 for Na_2SO_3).

A new simultaneous measurement technique involving concurrent pseudo steady-state absorption of carbon dioxide and unsteady-state desorption of oxygen was developed for separately evaluating the liquid film coefficient (K_L) and the interfacial area per unit volume of clear liquid, a. Ten percent CO_2-90% N_2 gas is sparged into 0.06M KOH solution, which is initially saturated with oxygen from air; the CO_2 absorption is accompanied by chemical reaction in a regime intermediate between the slow and fast reaction regimes as defined by Astarita[7] or Danckwerts.[8] Based on the random surface renewal model of mass transfer, the value of $K_L a$ determined from the oxygen probe transient response is used in conjunction with the rate of CO_2 absorption determined from a gas-phase material balance to calculate the value of a ; then, $K_L = K_L a/a$.

Preliminary results for K_L and a at one gas sparging rate are given in Fig. 2, where the line representing the overall behavior of K_L was computed from the least-squares lines for $K_L a$ and a . It is clear that the value of K_L decreases with increasing power input, in contrast to the results of others at lower agitation levels[6] or in nonelectrolytic liquids.[2] We attribute this to the much smaller bubble diameters produced in ionic solutions (which inhibit bubble coalescence) and at the higher power inputs used in this study.

It should be possible to extend the use of this simultaneous absorption-desorption technique to any normally nonreactive electrolyte solution by replacing a portion of the original electrolyte(s) with hydroxide while keeping the total ionic strength constant, thereby separately evaluating the effect of ionic strength upon K_L and a . Work is in progress on this aspect of the investigation.

Footnote and References

†Condensed from paper submitted to Chemical Engineering Conference Australia 1970, August 18-26, 1970, Melbourne and Sydney, Australia.

1. P. H. Calderbank, Trans. Inst. Chem. Engrs. (London) 36, 443 (1958).
2. ibid, 37, 173 (1959).
3. F. Yoshida, A. Ikeda, A. Imakawa, and Y. Miura, Ind. Eng. Chem. 52, 435 (1960).
4. C. M. Cooper, G. A. Fernstrom, and S. A. Miller, Ind. Eng. Chem. 36, 504 (1944).
5. K. R. Westerterp, L. L. van Dierendonck, and J. A. de Kraa, Chem. Eng. Sci. 18, 157 (1963).
6. F. Yoshida and Y. Miura, Ind. Eng. Chem. Process Design Develop 2, 263 (1963).
7. G. Astarita, Mass Transfer with Chemical Reaction (Elsevier Publishing Co., Amsterdam, 1967).
8. P. V. Danckwerts, Ind. Eng. Chem. 43, 1460 (1951).

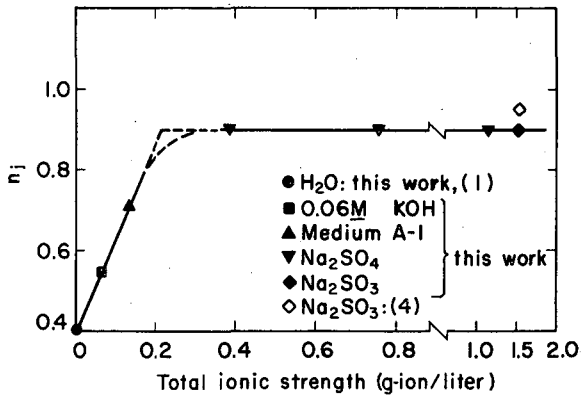

Fig. 1. Effect of ionic strength on power/unit volume exponent. (XBL6912-6365)

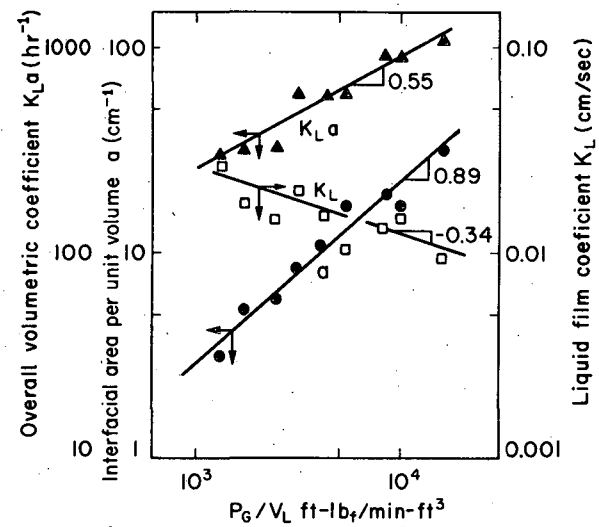

Fig. 2. Oxygen mass transfer parameters in potassium hydroxide solution: superficial gas velocity 0.015 ft/sec. (XBL6912-6366)

CONTINUOUS LIGAND ELECTROCHROMATOGRAPHY OF RARE EARTH IONS†

Louie Nady* and Theodore Vermeulen

Electrochromatography has been investigated as a possible separation process for ions, particularly for lanthanides and actinides. Following a review of previous work, two new advances were developed. One is a proposed new device in which a stable broad-band concentration gradient is developed by applying a dc voltage to a packed bed of ion-exchange resin confined by ion-exchange membranes. The resulting separation depends on solution-phase and resin-phase mobilities of the ions and on the resin selectivity for the ions.

Because resin-phase mobilities play an important part, bed conductivity measurements were made for Dowex 50W-X4 resin in equilibrium with solutions of NaCl, $AgNO_3$, $La(NO_3)_3$, $Ce(NO_3)_3$, $Nd(NO_3)_3$, $Ho(NO_3)_3$, and mixtures of $AgNO_3$ + $La(NO_3)_3$, and $AgNO_3$ + $Ce(NO_3)_3$. Particle conductivities were then calculated by use of Bruggeman's equation. Electrolyte sorption of these same ions into Dowex 50W-X4, and of $La(ClO_4)_3$ into Dowex 50W-X2, X4, X8, and X12 were investigated. The resulting identification of all species in the resin phase made it possible to determine resin-phase mobilities for the individual ions.

The second advance is the development and operation of a continuous preparative-scale ligand electrochromatograph, shown in Fig. 1. The central separating section is a rectangular bed packed with inert polystyrene beads as "anticonvectant," having fluid flow lengthwise through the bed and electrophoretic flow of ions in the transverse direction. In the mode of operation shown by Fig. 1, complexing agent enters the unit across the entire inlet end, partly in combination with an excess of "retainer-species" ions R (an excess of R assures practically total conversion of ligand to the complex form) and partly with the feed mixture. The complexes formed are neutral and have zero electrophoretic mobility when the uncomplexed ligand and the ions to be separated have equal but opposite valences; otherwise, the electrophoretic migration of complexes must also be accounted for. "Chaser-species" ions C are introduced along the side of the unit by electrophoretic migration through a porous diaphragm. The affinity of C for ligand is greater, and that of R is less, than the affinities of the ions undergoing separation. A second mode of operation involves feeding retainer-ligand mixture across the entire inlet end, and introducing uncomplexed feed mixture along the side of the unit, upstream of the chaser species.

Continuous separation is achieved as a result of transverse electrophoretic migration of excess feed ions across the laminar flow of complexing agent. Selective complex formation of the

ion mixture (with a resultant marked mobility change for the complexed species) causes the net electrophoretic migration rates to differ for each component, hence separates them.

Figure 2 shows the resulting exit-end and side-compartment offtake patterns for a mixture of $La(NO_3)_3$, $Ce(NO_3)_3$, and $(EDTA)Na_2$ fed over the entire entrance-end region. Chaser ion (Cu^{2+}) is fed to all the anode-side compartments. The offtake patterns for such a case should consist of pure Cu^{2+} in end offtake groove 1, Ce^{3+} and Cu^{2+} in groove 2, pure Ce^{3+} in groove 3, mostly Ce^{3+} with a little La^{3+} in groove 4, and La^{3+}-rich mixtures of both rare earths in all cathode-side compartments. Except for some trailing of La^{3+} into grooves 2 and 3, this result is achieved.

Footnotes

†L. Nady and T. Vermeulen, UCRL-19526, Apr. 1970.

*Present address: Stauffer Chemical Co., Richmond, California.

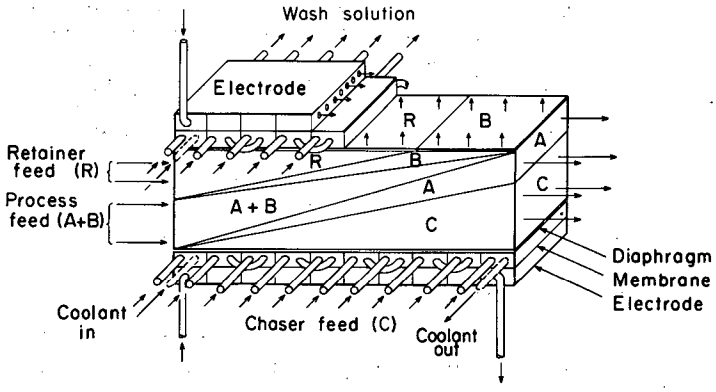

Fig. 1. Schematic diagram of the ligand electrochromatograph. (XBL701-2208)

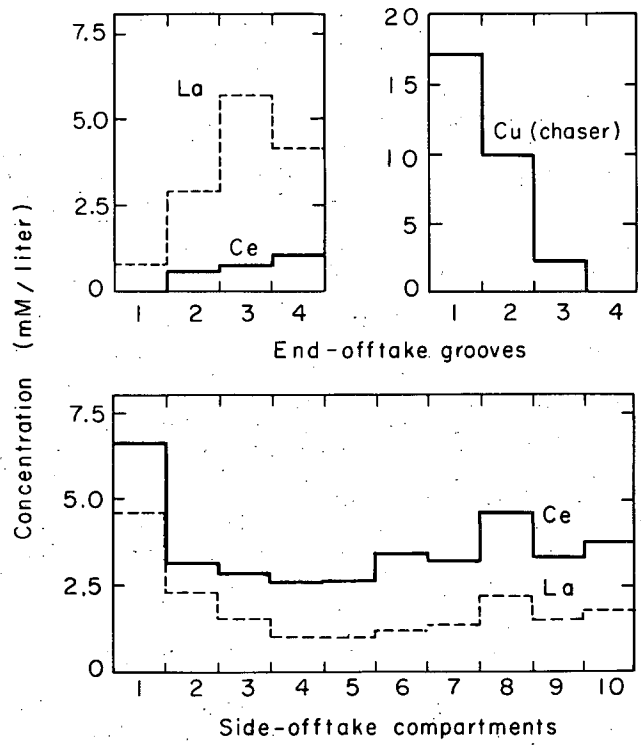

Fig. 2. Offtake patterns after one residence time for Ce-La separation; end feed; uncomplexed/complexed ratio, 0.5; bed potential, 12 V. (XBL701-2207)

FOAM FRACTIONATION OF RARE EARTH ELEMENTS†

George H. Robertson* and Theodore Vermeulen

The foam fractionation of rare earth elements Nd, Sm, and Ce by extraction of their EDTA chelates with a cationic surfactant, and the foam fractionation of an anionic surfactant, were studied. The objective was to determine the usefulness of the foaming technique in fine separations and to examine quantitatively the properties of transient foaming in producing the separation.

The model of "persistent" foaming did not apply to most of the foaming conditions which were found in this study to favor foam formation, extraction, and fractionation. Therefore a two-property classification was adopted, the type being determined by the persistence or transience of surface area, and the mode by the constancy or depletion of specific liquid content with foam height or age.

In a preliminary study fixed-height foaming from aqueous solutions of an anionic surfactant (Aerosol-22) was used to evaluate the effect of gas rate on the relative transiency and separation performance. Foaming of Aerosol-22 in a transient regime of gas rates yielded the best enrichments and extraction. The foam liquid fraction was proportional to the 0.20 power of the gas velocity in the transient regime and to the 0.71 power in the persistent regime.

No previous foam fractionation between rare earth elements has been reported. As with ion exchange or extraction, chelation or similar complexing appears essential for providing reasonable separations between rare earths (or between actinides) in foam fractionation. Although a surfactant that also enters into selective complex formation might be found, these two functions were served in the present experimental program by a cationic surfactant (Hyamine 1622) and by EDTA. To obtain foaming, both free surfactant and surfactant-EDTA-metal complex (or basic surfactant) were required. Foaming of this system shows transient surface-area behavior and diminishing liquid content per unit area; transiency increases as surfactant concentration decreases.

Rare earth enrichments increased continuously with height in the foam. In the 50-mm-diam experimental column, effective extraction rates were constant at foam heights above 17 cm. Constancy of extraction, in spite of surface loss, was viewed as a conservation of total rare earth mass on the diminishing surfaces. Separation factors (α) for the Nd/Ce separation were 1.9, and for Sm/Ce 3.85 above 17 cm. The separation factor drops sharply toward 1.0 at shorter heights. Evidence of nonspecific coadsorption of rare earth was observed, since the value of α expected on the basis of the liquid-phase equilibrium was not reached. The lowest surfactant concentration (0.03 g/liter) that will still produce foaming (of the most transient type), also yields the best separation factor and enrichment at constant height. Extraction rates increase proportionately to increasing EDTA concentration at fixed rare earth and surfactant levels, but are accompanied by decreasing selectivity.

At a relatively high EDTA solution concentration (1.3×10^{-4} M), a light-colored precipitate (believed to contain EDTA, rare earth, and surfactant) forms. This condition is operationally undesirable and also departs from pure foam fractionation, therefore setting an upper limit to the allowable EDTA level which appears to be relatively insensitive to the variations allowable in rare-earth and surfactant levels. A pool-liquid pH above 6.9 causes bulk precipitation of rare earth hydroxides. Maximum separation and extraction are obtained adjacent to this limit. Hence a pH near 6.7 is recommended as optimum.

Reflux inducement by inserting obstructions was effective in improving the separation factor in cases of prolonged distortion of the foam matrix. For plastic bead packings or stacked three-tier stainless steel screens, the α for Nd/Ce was raised from 1.9 to 2.2, and the α for Sm/Ce from 3.1 to 4.8. Single screens and single finely perforated plates were found to reduce drainage and increase the foam liquid content, but without altering the α. Still other materials (plastic screens and small-mesh stainless steel screens) rejected liquid more completely and hence destroyed the foam. Reflux-inducing devices deserve much broader study with respect to their surface properties, degree of deformation of the foam, and duration of contact.

By contrast to the present study, which focuses upon extraction of complexed rare earth, it appears that higher α values will probably be obtained by using an anionic surfactant which will interact with and co-adsorb only unchelated rare earth cations. Also, the low surface area typical of many anionic surfactants may provide higher molar concentrations per unit surface area,

and thus lead to greater enrichments.

The overall prospects for foam fractionation of lanthanides or actinides are directly related to the following features:

(a) It operates in a low concentration range.
(b) High degrees of purification are possible.
(c) Product recovery is easy.
(d) Supplementary processing to recover surfactant from the concentrated foam liquid is accessible.
(e) The process consumes a minimum of materials and produces little waste.
(f) It is operationally very simple.
(g) Power requirements are low because of very low pressure drops through the equipment.

Footnotes

†G. H. Robertson and T. Vermeulen, Foam Fractionation of Rare Earth Elements, UCRL-19525, Dec. 1969.

*Present address: U. S. Department of Agriculture, Western Regional Laboratory, Albany, California.

IMPROVED METHODS FOR CONTACTING FLUID PHASES IN SEPARATION PROCESSES

Edward J. Palkot, Jr.† and C. Judson King

This project was described to a large extent in the 1968 Annual Report. The aim was to evaluate various novel cocurrent flow gas-liquid contacting devices for absorption separation processes of practical importance. Such devices have the general characteristic of decreasing the size and complexity of equipment required at the possible expense of additional operating costs. This trend in design requirements is frequently of interest in nuclear processing in view of the shielding problem.

Cocurrent flow devices are usually capable of providing a closer approach to equilibrium in a given stage than can be obtained with either a countercurrent or a crosscurrent device. The action of a modest number of cascaded stages may still be achieved economically by assembling a number of devices into a countercurrent pattern while maintaining cocurrent flow within each device. Specific processes investigated in the present work are (a) the absorption of carbon dioxide into catalyzed potassium carbonate solutions and (b) the absorption of hydrogen chloride into water.

A report on the project was issued during the year.[1] Figure 1, taken from that report, shows the power consumption (proportional to operating costs) of each device considered, along with the total internal surface areas (assumed proportional to investment costs) for the CO_2 absorption case. Figure 2 is a similar plot for the HCl absorption case. An economically favored device will be indicated on such a plot by a point relatively close to the origin. From Fig. 1 it may be seen that staged annular-flow contactors and froth-flow contactors are most attractive for CO_2 absorption and warrant further pilot-scale investigation. From Fig. 2, cocurrent packed columns appear to warrant further developmental studies for HCl absorption.

Footnote and Reference

†Present address: Esso Research & Engineering Co., Florham Park, New Jersey.

1. E. J. Palkot and C. J. King, The Design of an Improved Device for Absorption with Chemical Reaction, UCRL-18918, June 1969.

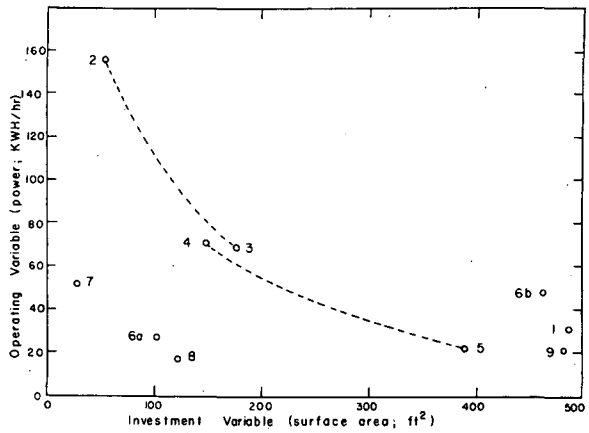

Fig. 1. Operating and investment variables for absorbers to reduce the CO_2 level in 862.9 lb moles/hr of inlet gas from 19.6 to 1.0%.

1. Sieve-tray tower.
2. Single cocurrent packed column; D = 1.33 ft.
3. Single cocurrent packed column; D = 2.66 ft.
4. Staged cocurrent packed columns; D = 1.33 ft.
5. Staged cocurrent packed columns; D = 2.66 ft.
6a. Staged annular-flow contactors (50% of driving force corresponding to droplet equilibration assumed).
6b. Staged annular-flow contactors (10% of driving force corresponding to droplet equilibration assumed).
7. Single froth-flow contactor.
8. Staged froth-flow contactors.
9. Staged spray towers. (XBL695-567)

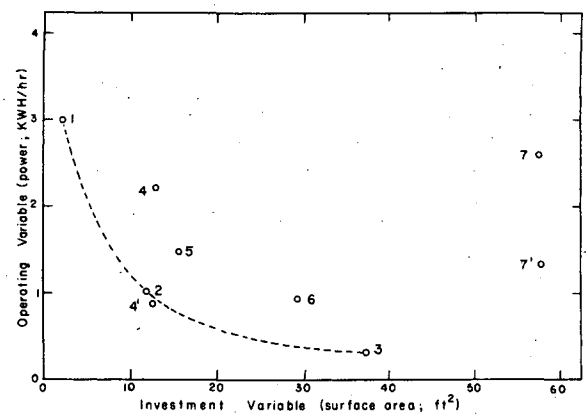

Fig. 2. Operating and investment variables for absorbers to reduce the HCl level in 150 lb moles/hr of inlet gas from 20.0 to 1.0%.

1. Single cocurrent packed column; D = 0.5 ft.
2. Single cocurrent packed column; D = 0.888 ft.
3. Single cocurrent packed column; D = 1.5 ft.
4. Staged cocurrent packed columns; D = 0.888 ft.
4'. Staged cocurrent packed columns; D = 0.888 ft (cooling water costs neglected).
5. Single froth-flow contactor.
6. Single annular-flow contactor.
7. Staged annular-flow contactors.
7'. Staged annular-flow contactors (cooling water costs neglected).

(XBL695-568)

MASS TRANSFER BETWEEN FLUID PHASES; INFLUENCES OF INTERFACIAL INSTABILITY AND HIGH RATES OF MASS TRANSFER

William H. Brown† and C. Judson King

Previous work on this project has been described in the 1966 and 1967 Annual Reports. The experimental device employed for contacting a gas and a liquid in stratified flow is a horizontal channel of high aspect ratio. This channel device has demonstrated adherence to the predictions of simple convective diffusion theory for both gas- and liquid-phase controlled mass transfer in cocurrent and countercurrent flow[1,2] with dilute systems, and for heat transfer in the absence of mass transfer.[3] Rates of evaporation of ethyl ether, n-pentane, and cyclopentane from tridecane into nitrogen were anomalously high.[3,4] This behavior arose at solute mole fractions above 0.01 to 0.07 and was shown to be directly attributable to interfacial cellular convection caused by unstable surface tension gradients developing during the evaporation process.[3,4] This cellular motion has little effect upon the gas-phase mass transfer coefficient but can accelerate the liquid-phase mass transfer coefficient by factors of up to 10 or 20. Results for different solutes have been correlated in terms of the ratio of the Thompson number to the critical value of the Thompson number.[3,4]

More recent work[5] has investigated the influence of liquid flow conditions on the contribution of interfacial mixing cells to the mass transfer coefficient for the evaporation of ethyl ether from

tridecane. Figure 1 shows the increase in liquid-phase mass transfer coefficient caused by interfacial convection vs. solute mole fraction for three different liquid flow conditions.[5] Figure 2 shows the same results, expressed as the ratio of the observed coefficient to the coefficient predicted by simple convection diffusion theory, with the ratio of the Thompson number to the critical value of the Thompson number (at which the effects of cellular action are first observed) as the independent variable.[5] The dashed curve in both figures represents the results of Clark and King[3,4] at a relatively low liquid flow rate which gave a smooth liquid surface. The circular data points represent results obtained in the present study at a liquid flow rate nearly 6 times greater, where ripples were apparent upon the surface of the flowing liquid. The triangular data points are results obtained in the present study at an intermediate flow rate where the liquid surface was still smooth.

At the higher liquid flow rate with a rippling surface the effect of interfacial mixing in increasing k_L becomes evident at a lower value of the Thompson number (approximately the same value of solute mole fraction). Also the increase in mass transfer coefficient due to interfacial mixing at solute mole fractions or values of the Thompson number just above the critical is greater at the higher liquid flow rate than at the lower one. This behavior suggests a synergistic effect between the rippling action and the interfacial mixing cells. At higher mole fractions or Thompson numbers further above the critical, on the other hand, the augmentation of the mass transfer coefficient is much less at the higher flow rate than at the lower flow rate. This result indicates that the rippling of the surface at higher flow rates may prevent the interfacial cellular convective circulation patterns from attaining a full scale of development. The results at the intermediate flow rate—where the liquid surface was still smooth—are much more similar to the low flow rate data than to the high flow rate data, indicating that the differences in behavior at high and low flow rates reflect the specific effect of rippling.

One particularly noteworthy result is that the liquid-phase mass transfer coefficient at an ether mole fraction of 0.30 is 0.011 cm/sec at 2.3 gpm liquid flow rate and is 0.029 cm/sec at 0.4 gpm. Thus the detrimental interaction of rippling and interfacial cellular convection has actually caused the mass transfer coefficient to decrease by a factor of more than 2 as the flow rate is increased. This is a highly unusual result.

A paper based upon Reference 5 will be presented at the National Meeting of the American Institute of Chemical Engineers in Denver in August 1970.

These studies are of benefit in developing an understanding of the effect of spontaneous interfacial mixing cells upon mass transfer coefficients and hence upon equipment sizes for gas absorption, liquid-liquid extraction, and related separation processes. This phenomenon is known to have a marked effect upon mass transfer coefficients, but there are no design procedures available to allow for it.

Footnote and References

†Present address: Crown Zellerbach Corp., Camas, Washington.

1. C. H. Byers and C. J. King, Convective Transfer Processes in Laminar Gas-Liquid Channel Flow, UCRL-16535, May 1966.
2. C. H. Byers and C. J. King, Gas-Liquid Mass Transfer With a Tangentially Moving Interface: I-Theory, II-Experimental, UCRL-16926, July 1966; A. I. Ch. E. Journal 13, 628, 637 (1967).
3. M. W. Clark and C. J. King, Mass and Heat Transfer Processes in Laminar, Two-Phase Flow, UCRL-17527, June 1967.
4. M. W. Clark and C. J. King, Evaporation Rates of Volatile Liquids in a Laminar Flow System: I-Pure Liquids, II-Liquid Mixtures, UCRL-17655, UCRL-17656, Dec. 1967; A. I. Ch. E. Journal, Jan. 1970.
5. W. H. Brown and C. J. King, Interfacial Mixing Cells and Mass Transfer in Turbulent Flow, UCRL-18974, Aug. 1969.

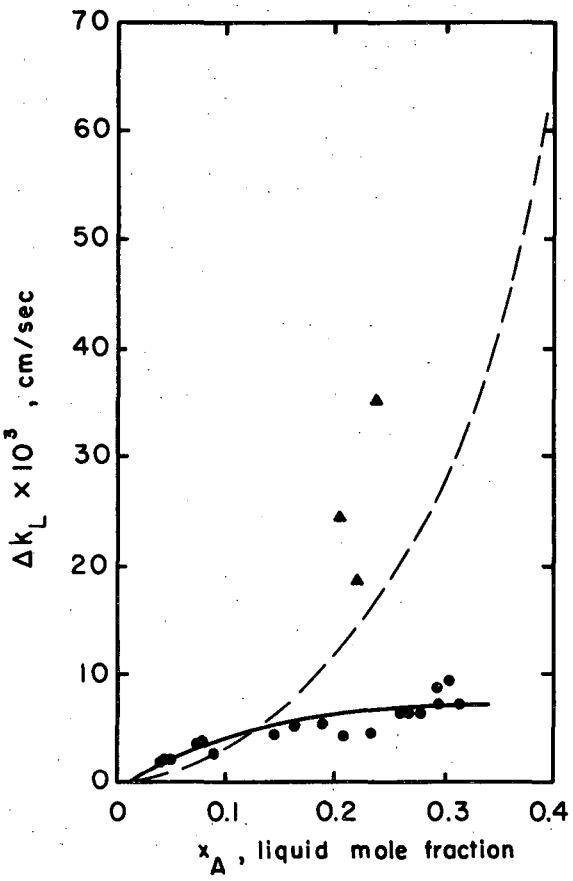

Fig. 1. Increase in value of liquid-phase mass transfer coefficient above convective diffusion prediction vs. solute mole fraction for evaporation of ethyl ether from tridecane into nitrogen. • indicates 2-3 gpm data; ▲ indicates 0.96 gpm data; dashed curve indicates 0.4 gpm data of Clark and King (Refs. 3, 4). (XBL698-1166)

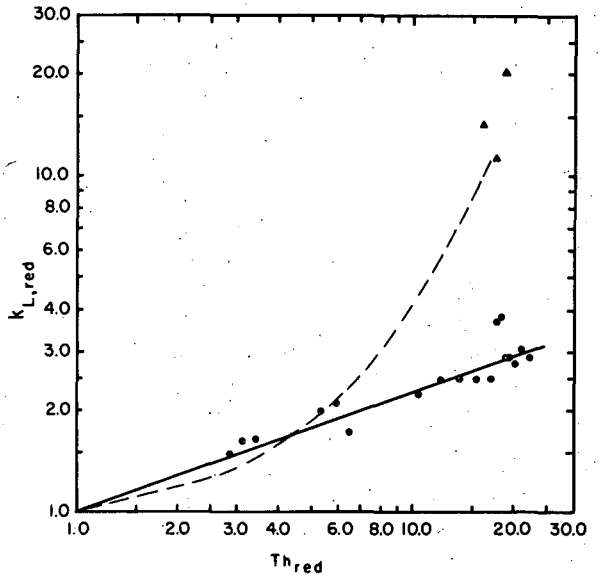

Fig. 2. Results of Fig. 1, expressed as ratio of liquid-phase mass transfer coefficient to the value predicted by simple convective diffusion theory. (XBL698-1167)

CYCLING ZONE ADSORPTION—A NEW SEPARATION PROCESS

B. Baker, D. Blum, and R. L. Pigford

Cyclic changes in concentration are produced in a fluid mixture which flows through a fixed bed of solid adsorbent owing to temperature or pressure cycling of the bed. The product stream is collected separately during the periods of positive and negative deviations from the feed composition. The separation is increased by using separate zones in series, the temperatures or pressures in adjacent zones being out of phase. The separation is governed by the temperature and concentration wave properties of the beds. Figure 1 illustrates the use of successive zones in series, the arrows representing heat flow directions.

A short paper [Pigford, Baker, and Blum, Ind. Eng. Chem., Fund. Quarterly 8, 848-51 (1969)] describing the new process was published and a U. S. Patent was applied for. Report UCRL-18967 by B. Baker demonstrated that the staging idea and the use of thermal inputs of various kinds produced good separation of acetic acid–water mixtures using activated carbon as the adsorbent. Some of the data are shown in Fig. 2.

Work is continuing on multicomponent separations and on the use of certain recycle schemes in order to produce pure products.

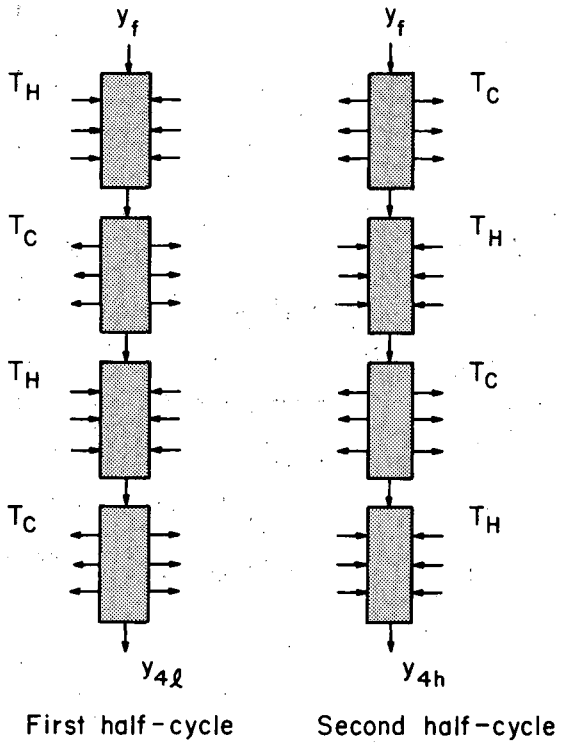

Fig. 1. Multiple-zone standing-wave operation of cycling zone adsorber. (XBL694-2397)

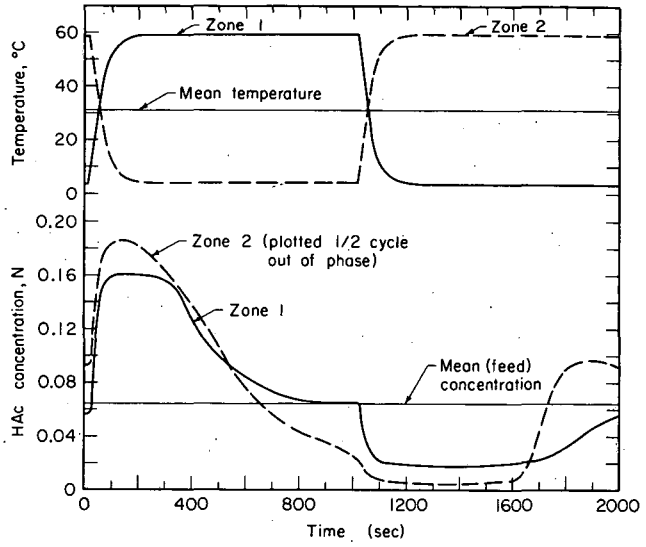

Fig. 2. Comparison of single- and dual-zone standing square-wave cycling.
(a) Temperature profiles.
(b) Effluent-concentration profiles.
(XBL694-2399)

SEPARATION OF ORGANIC LIQUID MIXTURES BY FRACTIONAL FREEZING

C. T. Cheng and R. L. Pigford

By using a special hot stage under a microscope the growth of crystals has been observed quantitatively in order to determine the deviations from equilibrium phase diagram behavior which occur, primarily owing to interface rate limitations. The apparatus incorporates features for producing diffraction fringes, the displacement of which can be related to instantaneous liquid and solid compositions at the moving surface of a crystal.

Data were reported in UCRL-19512† for several binary mixtures. Some of the most interesting results are those for two compounds of nearly the same molecular structure, dibenzyl and stilbene, which differ only by the presence of a double bond in one. These substances form solid solution crystals over a wide range of compositions as shown in the phase diagram, Fig. 1. Figure 2 shows observed solid and liquid mole fractions as a function of growth rate at bulk mole fractions of stilbene ranging from 0.15 to 0.45. The large enrichment of stilbene in the crystals according to the phase diagram is shown by the pairs of points on the vertical axes; at finite though small rates of growth the enrichment is very much reduced, as shown.

This behavior appears to be in accord with expectations based on theories of such rate processes for complex organic substances. Separations of such materials by fractional freezing will always be difficult.

Footnote

†Cheng and Pigford, Purity of Crystals Grown from Binary Organic Melts, UCRL-19512, Nov. 1969.

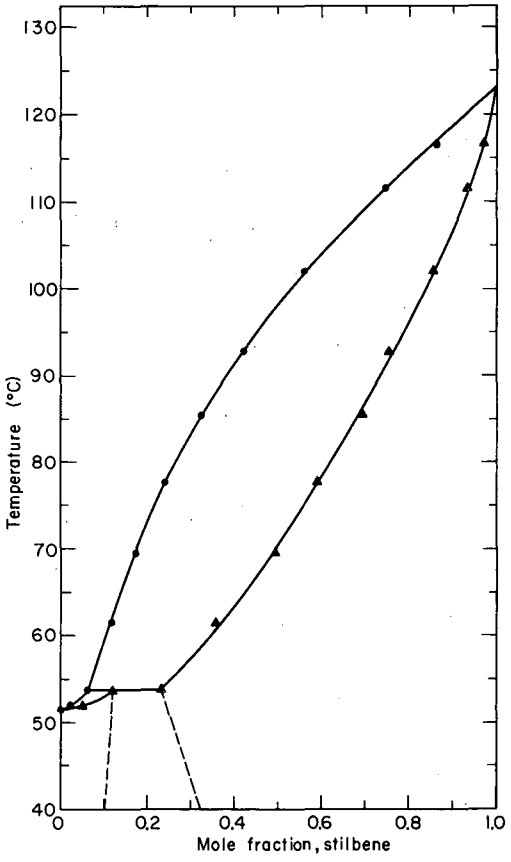

Fig. 1. Phase diagram of dibenzyl-stilbene system. (XBL6911-6190)

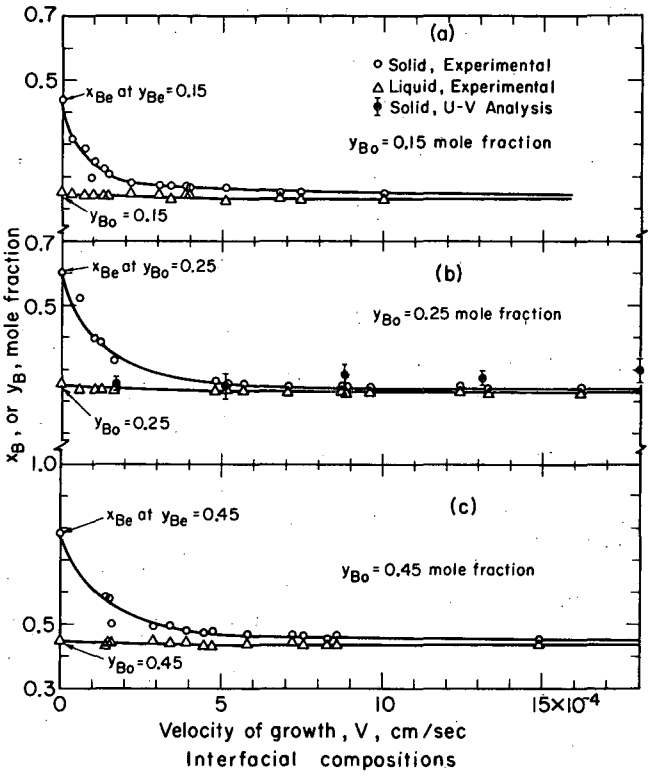

Fig. 2. Interfacial compositions, dibenzyl and trans-stilbene system. (XBL6911-6177)

THE INTERFACE IMPEDANCE BRIDGE

T. G. Springer and R. L. Pigford

Figure 1 [from Ind. Eng. Chem., Fund. Quarterly 8, 823-27 (1969)] shows a new experimental method which we are using to measure gas-liquid interface rate phenomena more accurately than has been possible heretofore. It consists of two chambers, each filled with water and with pure SO_2 gas. The chambers connect to two cylinders which are driven from a common shaft and which produce in-phase sinusoidal variations in the gas pressure in the chambers. When the two interfaces offer equal resistances to the passage of soluble SO_2 through the interfaces there is no pressure difference and the bridge is balanced. When the surfaces are different, as when one is stirred or is covered with a surfactant layer, a pressure difference signal develops and is a function of the frequency.

The apparatus has been used to study (a) the ability of certain surfactants to inhibit mass transfer and (b) the statistical character of the fluid particles that compose a turbulent interface. The results are reported in UCRL-18995. They show that not all surfactants offer any measurable resistance. The ones that do are those nearly insoluble in water and, like cetyl alcohol, able to form a condensed cross-linked film on the interface. Such surfactant films are very easily destroyed, however, by gentle fluid movement from below. Soluble surfactants, on the other hand, offer negligible mass transfer resistance themselves but inhibit fluid motion and thereby indirectly reduce mass transfer rates.

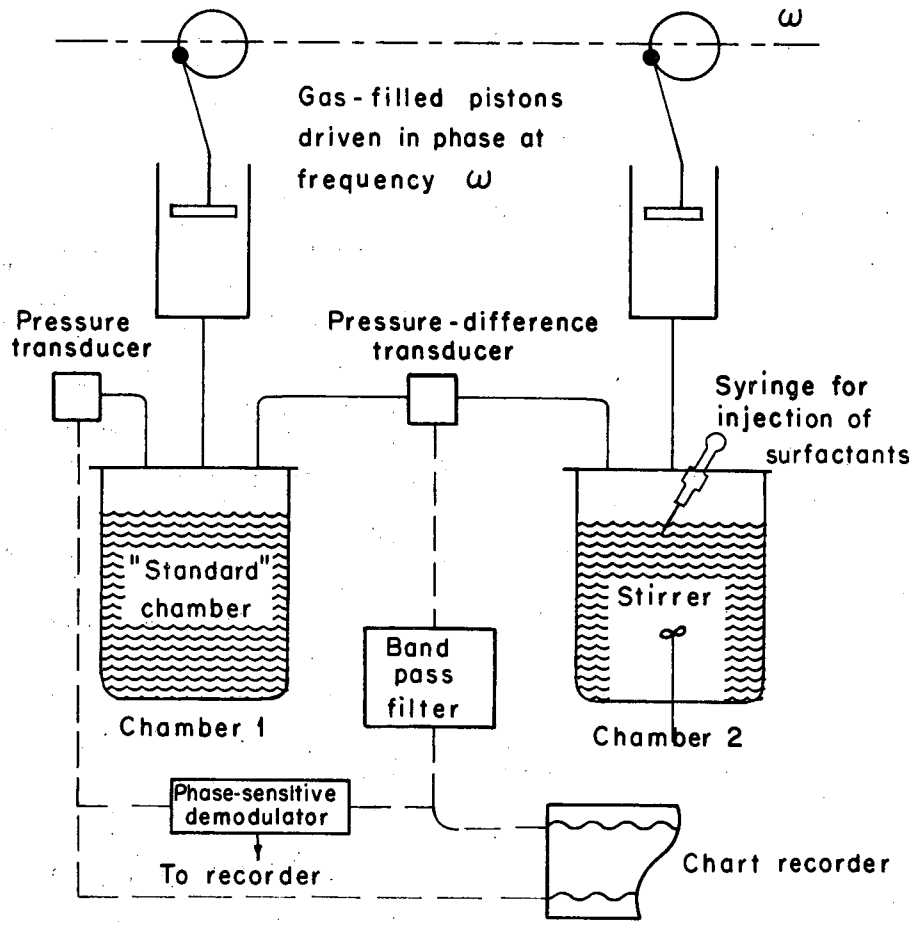

Fig. 1. Diagram of interface impedance bridge. (XBL695-2743)

IV. Instrumentation and Systems Development

Electronic Instrumentation and Semiconductor Devices

DIGITAL POLAROGRAPHY—COULOMETRY AND INPUT CHARGE DIGITIZATION IN NUCLEAR-EVENT-SENSITIVE AMPLIFIERS

William Goldsworthy

Two projects have been pursued in the past year. These are the development of electro-chemical analysis instruments and systems for the Analytical Chemistry Group in collaboration with Raymond Clem and a study into the techniques needed to achieve accurate metering and digitization of the amount of recharging needed to neutralize nuclear-event-liberated charges directly at the output of a nuclear-event detector.

Digital Polarography—Coulometry

An electro-chemical system capable of performing accurate and sensitive coulometric and polarographic measurements has been developed for the Analytical Chemistry group. It is now being used by Raymond Clem for chemical analysis.

Three important features make the apparatus unique. Charge information is digitized directly by an integration technique that virtually eliminates the usual capacitor hysteresis and linearity errors; charge-related information is processed in digital form to provide the functions of integration, differentiation, signal sampling and averaging, storage, display, and readout; and acquisition of data is time-synchronized with the DME cell period during polarographic studies.

Details of design and performance of this apparatus were presented at the 13th Conference on Analytical Chemistry and Nuclear Technology at Gatlinburg, Tennessee, on October 2, 1969 and are described in report UCRL-18939 entitled "A Digitized Time Synchronized Sampling System for Polarographic and Coulometric Studies" by William Goldsworthy and Raymond Clem.

Input Charge Digitization in Nuclear-Event-Sensitive Amplifiers

Since October of 1968 I have been studying the feasibility of metering and digitizing the recharge necessary to maintain balance at a nuclear detector's output following the occurrence of a nuclear event. Improvements in energy resolution, sensitivity, linearity, and overload capability could easily result if this objective can be successfully accomplished, since the amplifier circuitry need only be capable of accurately indicating a null, and since the usual functions of metering, integration, differentiation, storage, and readout could be performed digitally.

Investigations are currently being made into the techniques necessary for average input balance stabilization of high-resolution systems and into those necessary to provide rapid and accurate metering and digitization of the differential detector charges produced by nuclear event occurrences in order to assess the problems involved.

Several methods are currently being examined and compared to provide average input balance stabilization. These consist of input charge reinjection by resistive, radiation-induced, and electronic means. Pulsed operation of these means is also under study to ascertain whether further resolution improvement can be achieved by using the time interval between events for input rebalance and by finding solutions for fast system-overload recovery.

Techniques of rapid digitization, of accurate pre- and post-event base-line determination, and of accurate metering of reinjected charge are being carefully examined for possible application in direct and accurate digitization of detector output charge.

A preliminary written disclosure on this subject was submitted to the Lawrence Radiation Laboratory patent division in October 1968.

DATA LINK BETWEEN PDP-9 AND CDC-6600

Michiyuki Nakamura and John A. Mendes

A Data Link between a PDP-9 and the CDC-6600 has been completed for the Nuclear Fission Group. The PDP-9 and the CDC-6600 are manufactured by Digital Equipment Corporation (DEC) and Control Data Corporation (CDC) respectively. The Data Link[1] was designed to work with the DEC PDP-5 and PDP-8 for high-energy physics experiments. A channel synchronizer placed directly near the CDC-6600 communicates with the 6600. A device synchronizer placed near the small computer communicates with the small computer (PDP-5 or -8) and with the channel synchronizer over long twisted-pair telephone wires.[2,3] The CDC-6600 is located in our main computer center two buildings away.

We designed a new device synchronizer to communicate with the PDP-9 and to follow all of the procedures laid down for PDP-5 or -8 system so that the new device synchronizer could communicate with the same channel synchronizer without modification to the original system. Since the PDP-5 or -8 and the peripheral processor unit (PPU) of the CDC-6600 have word lengths of 12 bits, it was relatively easy to communicate between the small computers and the PPU's. The PDP-9, on the other hand, is an 18-bit word machine, so we had to combine two PDP-9 words to form three 12-bit words for the PPU's to handle. Care must be taken to ensure exchange of the correct number of PDP-9 and PPU words.

Gerald M. Litton is doing all of the required programming for the PDP-9 and the CDC-6600. Several tests have yet to be made to check the long-term reliability of the system and its ability to transfer data back and forth without error. To date, the Data Link has been performing very well.

Data rates of one word (12 bits) every 15 μsec are typical. Errors detected in the Data Link will slow this rate because the word must be retransmitted each time an error is detected.

Use of the Data Link will allow quick turnaround in the analysis of data from experiments by using existing programs written for the CDC-6600. Some of these programs are complex sophisticated programs that the PDP-9 could not execute. The availability of mass store devices at the computer center opens up the possibility of storing the large volumes of data required in a typical multiparameter experiment by using the Data Link. The vast computational facilities of the CDC-6600 open up many potential applications of the Data Link to on-line checks during the setting-up process of the experiment as well as the experimental results while the experiment is in progress.

References

1. S. W. Andreae, A Computer Data Link for High Energy Physics Experiments, UCRL-17918, Nov. 1967.
2. A. E. Oakes, Transmission of Link Data over Telephone Lines, UCRL-17960, Nov. 1967.
3. R. W. Lafore, Error Checking and Other Aspects of Data Link Organization, UCRL-17934, Nov. 1967.

RECENT RESULTS ON THE OPTOELECTRONIC FEEDBACK PREAMPLIFIER†

F. S. Goulding, J. T. Walton, and R. H. Pehl

Work on ultrahigh-resolution spectrometer systems using semiconductor detectors has been excessively time-consuming and, for the most part, frustrating. For some areas—specifically for high-energy γ rays (i.e., > 500 keV)—statistics of charge production in the detector have become a large and perhaps dominant contributor to the resolution, and the preamplifier noise is a minor factor. However, at lower energies electronic noise is still the major limitation.

The frustrating aspects of work in this area stem in part from our total dependence on chance developments in other areas of electronics, such as low-noise field-effect transistors. This means

that our work involves evaluating and selecting components, which is made more complicated by our use of components at low temperatures, a factor which at once renders manufacturer's specifications meaningless, and furthermore makes the testing cycle long and tedious.

The optoelectronic feedback system represents a significant attempt to remove one frustrating element from the game—namely the high-valued biasing resistor in the input circuit. As with all new ideas that see the light of day, we have gained substantially in performance—the idea would have been rejected had that not been so—but new questions, both philosophical and practical, have arisen.

In the optoelectronic system shown in Fig. 1, the feedback resistor is replaced by light feedback obtained by connecting a light-emitting diode to the output of the stage and directing some of the light from it onto a reverse-biased photodiode that connects to the input of the stage. It can be seen that the current in the photodiode is proportional to the output voltage if the light intensity is proportional to the current through the light-emitting diode, which is true over a small range of currents and if the photodiode response is linear. We can therefore regard the circuit as being equivalent to a feedback resistor whose value can be varied by adjusting the light coupling. Equivalent resistor values ranging from 10^8 to 10^{12} Ω can be achieved. Unlike practical high-valued resistors, the response times of the light-emitting diodes and photodiodes are very short, and the combination results in an equivalent feedback resistor value that is constant up to 10 MHz or more.

A further refinement is possible since the drain-gate diode of the FET is photosensitive and can be used as the photodiode. This eliminates the additional component in the gate circuit, thereby reducing the stray capacity to a minimum. In practice, this means removing the FET from its case—a procedure which seemed doubtful at first sight but which has been executed very successfully in about 25 samples. Moreover, the elimination of the gate-lead feed-through has apparently removed a source of noise, and more consistent results are obtained from a group of transistors after removal from the case.

The change in resolution of a typical system as a function of time constant using an equal RC integrator-differentiator shaper is shown in Fig. 2, and is compared with the results obtained in a standard resistor feedback system. The main improvement in performance is at the longer time constants. Figure 3 shows a typical spectrum for a Si detector on low-energy x rays produced by x-ray fluorescence in a target containing a number of elements.

The counting-rate behavior for Mn x rays in a typical system is shown in Fig. 4 to illustrate the performance for various peaking times in the Gaussian shaper. Serious degradation of performance occurs at about 2000 Hz for the 16-μsec peaking time and at appropriately higher rates for the shorter peaking times. These results suggest that fluctuations of baseline in the dc restorer are responsible for the degradation in performance. However, further study reveals that a new aspect of the high-counting-rate behavior causes about half the degradation in resolution.

In the optoelectronic feedback system shown in Fig. 1, the effect of the negative feedback is to make the average current in the photodiode equal to the average current in the detector. In the absence of radiation this means that the photodiode current is equal to the detector leakage current, and the total noise due to the two currents, which are not correlated, is $\sqrt{2}$ times that due to the detector leakage alone. At high counting rates the average detector current increases, causing an increase in the photodiode average current which introduces additional noise.

Since a counting rate of 10^4 Hz of 20-keV x rays produces an average current of 10^{-11} A, whereas the normal detector leakage is only about 10^{-13} A, this effect is not negligible. If the shaping network has a long time constant, fluctuations in the feedback photodiode current can become the dominant source of noise. The contribution of this component of the resolution should increase in proportion to (counting rate)$^{1/2}$, and the curve in Fig. 4 for a 16-μsec Gaussian shaper does behave approximately in this way. Calculation of this contribution indicates that it causes almost half the degradation in resolution at 8000 Hz; presumably, the remainder is due to base-line fluctuations, and possibly nonlinear behavior of the amplifier chain.

Therefore, we are apparently observing a new and interesting phenomenon that causes a degradation of resolution at high counting rates. From a practical point of view we can eliminate this problem by using some method of pulsed light feedback like that of Kandiah and Stirling,[1] rather than dc feedback, to maintain the charge-sensitive stage near its correct operating point. Logical techniques can then be used to eliminate the false signals that appear at the output of the amplifier when the feedback system is pulsed. Since the photodiode then passes no average current, this noise source is eliminated. Even dc current in the photodiode, which normally balances the detector leakage, is eliminated; so the resolution at low counting rates is improved.

Footnote and Reference

†Presented at 16th Nuclear Science Symposium, San Francisco, Oct. 29-31, 1969; also to be published in IEEE Trans. Nucl. Sci. NS-14, No. 1 (1970).

1. K. Kandiah and A. Stirling, A Direct-Coupled Pulse Amplifying and Analyzing System for Nuclear-Particle Spectroscopy, in Semiconductor Nuclear-Particle Detectors and Circuits (National Academy of Sciences, Publication 1593, 1969), p. 495.

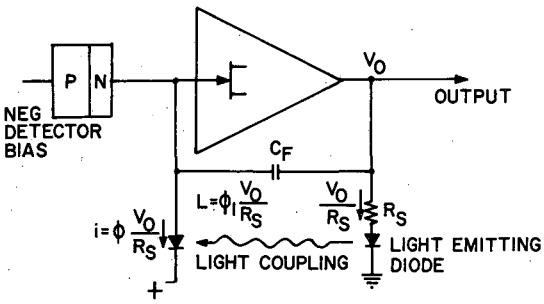

Fig. 1. Block diagram of optoelectronic feedback system. (XBL692-171)

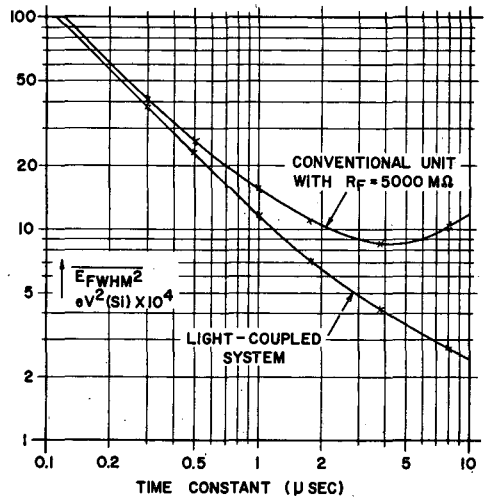

Fig. 2. Change in resolution with time constant for the two systems using equal RC integrator-differentiator shaping networks. (XBL692-173)

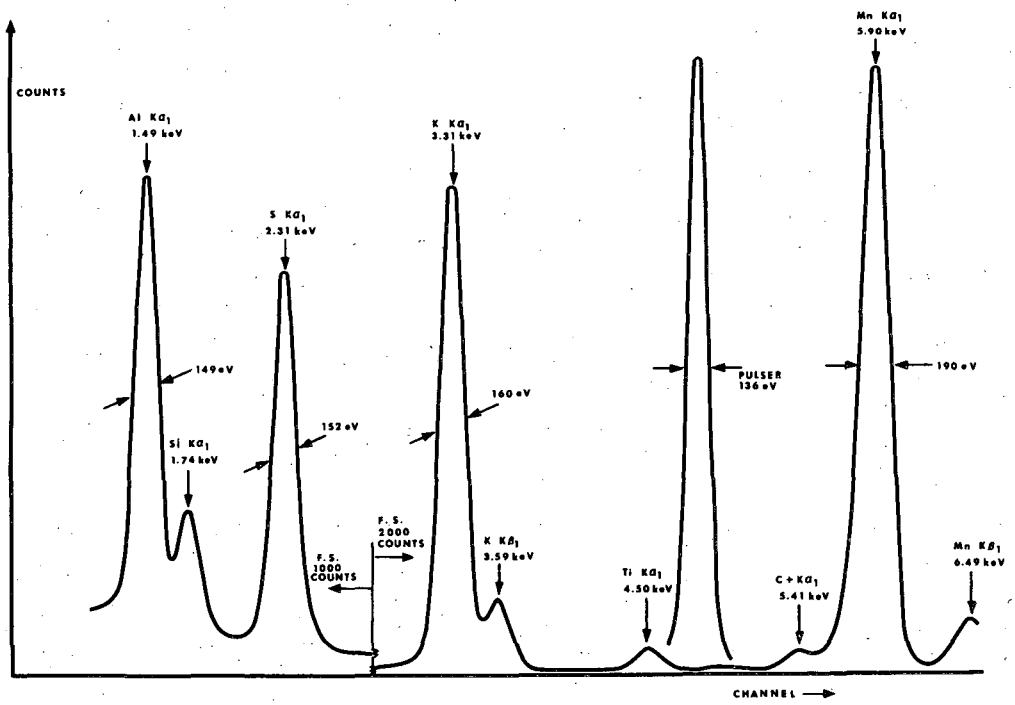

Fig. 3. Low-energy x-ray spectrum. The source is aluminum potassium sulphate glued to an Al backing plate by silicone varnish. Fluorescence excitation is provided by the Mn x rays from an ^{55}Fe source. (XBL702-345)

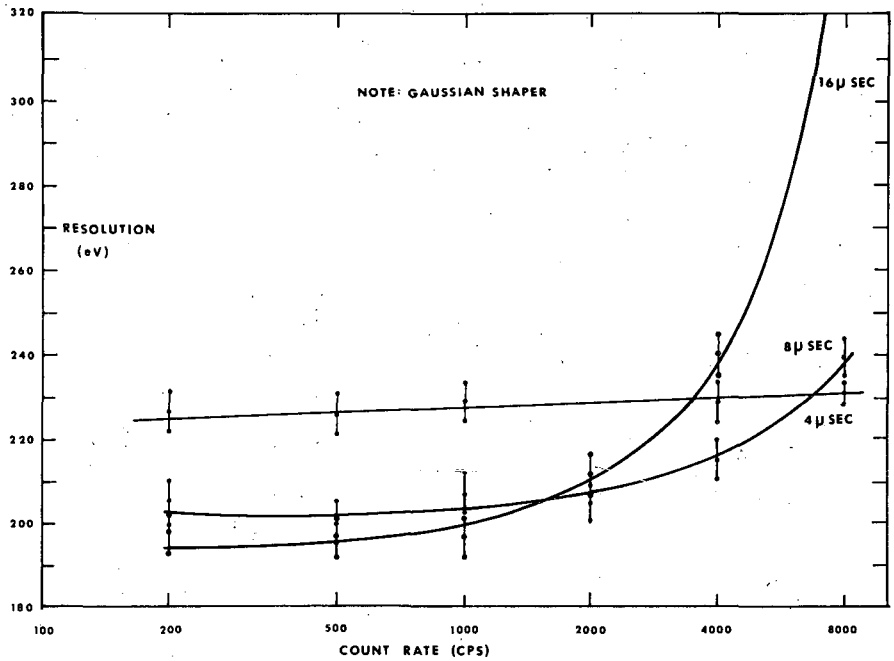

Fig. 4. System behavior at different counting rates for Mn x rays. (XBL6910-5807)

RECENT OBSERVATIONS ON THE FANO FACTOR IN GERMANIUM†

Richard H. Pehl and Fred S. Goulding

The Fano factor has been something of a "phantom factor"[1] to many workers in the field of semiconductor detectors. However, the extensive work of Bilger[2] appeared to clarify the situation in germanium and put an end to the era of plunging experimental values as summarized by Klein.[3]

The objective of this brief note is to conclusively demonstrate that the intrinsic Fano factor for germanium is appreciably less than the 0.129 value obtained by Bilger.[2] For several years we occasionally have observed detectors, invariably having relatively small dimensions, whose resolution was significantly better than could be accounted for unless the Fano factor was less than 0.10. However, lack of time prevented us from studying these detectors extensively enough to warrant reporting these results. With the advent of our high-resolution optoelectronic feedback preamplifier[4] the opportunity to make a relatively simple assessment of the Fano factor became available. Early results from use of this technique are described in the following paragraphs.

Measurements were carried out by using several small thin-window lithium-drifted germanium detectors (intrinsic area of 4×4 mm, and a drift of 4 mm) that exhibited a leakage current of about 5×10^{-13} A at a bias of 1000 V. It is quite possible that the energy resolution at high energies is degraded by charge-collection problems, but our purpose here is only to obtain an upper limit for the Fano factor, and our result may therefore be considered conservative. The detectors were made from a germanium ingot grown by W. Hansen.

The electronic resolution of the complete system, measured with a Gaussian shaper peaking at 8 μsec, was 140 eV. Both pulser and rms noise-meter measurements gave essentially the same value.

From 8 to 1333 keV our results establish a maximum value of 0.08 for the Fano factor. We emphasize that this is a maximum value, as it is easy for extraneous problems to broaden peaks but the reverse is an unlikely possibility. At energies higher than 122 keV the pulser peak is

spread over so few analyzer channels that an accurate determination of the pulser resolution could not be made. However, this presents no serious problem, since the electronic resolution becomes an almost negligible component of the observed gamma peak width at higher energies. Consequently the safe assumption was made that the pulser resolution remained at the value determined at lower energies. Table I summarizes our results.

We plan to extend these measurements over a larger energy range and to survey a number of detectors made from different germanium ingots. Present indications are that the measured peak widths in earlier experiments are not representative of the intrinsic statistical processes in germanium and are affected in some manner by properties of the particular piece of germanium.

Footnote and References

†Condensed from UCRL-19439; to be published in Nucl. Instr. Methods.

1. F. J. Walter, Comments on Measurements of Epsilon and the Fano Factor, in Semiconductor Nuclear-Particle Detectors and Circuits (National Academy of Sciences, Publication 1593, 1969), p. 63.
2. H. R. Bilger, Phys. Rev. 163, 238 (1967).
3. C. A Klein, IEEE Trans. Nucl. Sci. NS-15, No. 3, 214 (1968).
4. F. S. Goulding, J. Walton, and D. F. Malone, Nucl. Instr. Methods 71, 273 (1969); F. S. Goulding, J. T. Walton, and R. H. Pehl, to be published in IEEE Trans. Nucl. Sci. NS-17, No. 1, (1970).

Table I. Resolution of the germanium detector system at various energies. A pulser resolution of 140 eV was used throughout for the calculation of the Fano factor.

Source	Energy	Resolution	Fano factor
^{60}Co	1333 keV	1.30 keV	0.076
^{60}Co	1173 keV	1.23 keV	0.077
^{137}Cs	662 keV	924 eV	0.077
^{57}Co	122 keV	420 eV	0.078
^{241}Am	59.54 keV	310 eV	0.078
Br $K\beta_1$ x ray	13.3 keV	195 eV	0.084
As K_α x ray	10.53 keV	183 eV	0.080
Cu K_α x ray	8.04 keV	175 eV	0.083

SELECTION OF GERMANIUM FOR LITHIUM-DRIFTED RADIATION DETECTORS BY OBSERVATION OF ETCH-PIT DISTRIBUTIONS†

W. L. Hansen, R. H. Pehl,
E. J. Rivet,* and F. S. Goulding

Our own observations, and those made by other groups, show that conventional semiconductor material parameters provide no indication of the quality of radiation detectors that can be made from different germanium crystals. Wide variations in performance are observed both between detectors made from different crystals and between detectors made from different parts of the same crystal. Charge trapping (which may be exaggerated by electric field nonuniformities) has been shown to be the mechanism causing poor performance.

Because the manufacture of detectors in order to evaluate a crystal is a time-consuming, frustrating, and expensive process, it is important to find a simple measurement that correlates with detector performance. We have found that etch-pit distributions provide a virtually infallible guide to crystal quality (vacuum-grown crystals excepted) for detector use. At least a major source of

problems in detectors is revealed by this very simple technique, although we have accurately discriminated between crystals from which detectors showing small differences in performance were made.

Almost any chemical etch that attacks germanium will reveal screw-axis dislocations on the 111 face. However, the overall appearance of the etched faces is greatly variable for most etches. Consequently, we selected a standard etch routine that would be least affected by time-temperature variations. A standard etch routine has the added feature that variations in etch-pit size are due to real variations in the energy distribution around a dislocation rather than to external chemical variables.

The crystal slice is first lapped with 600-grit carborundum and then polish etched to produce a smooth background with minimum pit size. Since most of the crystals used have a fairly low dislocation density we can develop the etch pits to a large size for unmagnified observation. This is done with a 15-minute Billig[1] etch, which produces large sharp pits. Billig etch decomposes on heating in the presence of germanium, and the same solution cannot be used for more than one etching.

The samples are illuminated for photography by placing three lights at an angle of about 60 deg to the sample surface, and at 120 deg with respect to one another, and the crystal is rotated to achieve maximum pit brightness.

The etch-pit photographs for a number of germanium crystals are presented in Figs. 1 through 5. These represent a very small selection out of approximately 300 detectors made from nearly 100 crystals (20 commercial and 80 made in our laboratory). The results given here are representative of the larger sample.

The following general observations can be made about the relationship between etch pits and crystal quality:

1. Good material is always characterized by a uniform distribution of etch pits.
2. No clear relation has been seen between the etch-pit density and quality except in the case of zero-dislocation crystals, which are always poor.
3. A ring-shaped area depleted of etch pits always signifies poor material.
4. A minor degree of slip does not seem to be detrimental to detector performance but gross lineage is unacceptable.

The crystals that we have grown have, in general, a similar evolution of the etch-pit pattern. The seed end of the crystal generally has a uniform pit distribution, often with minor slip. The slip usually disappears shortly after the full diameter is reached and a uniform good-quality region of variable length follows. The ring structure depleted of etch pits gradually appears and the quality deteriorates. The tail end almost always shows the ring figure, often with slip.

Footnotes and Reference

†Presented at an AEC progress meeting July 29 and 30, 1969, at Germantown, Maryland (proceedings to be published); also to be published in Nucl. Instr. Methods.
*Present address: E. I. du Pont de Nemours and Co., Wilmington, Delaware, 19898.
1. E. Billig, Proc. Roy. Soc. (London) A 235, 37 (1956).

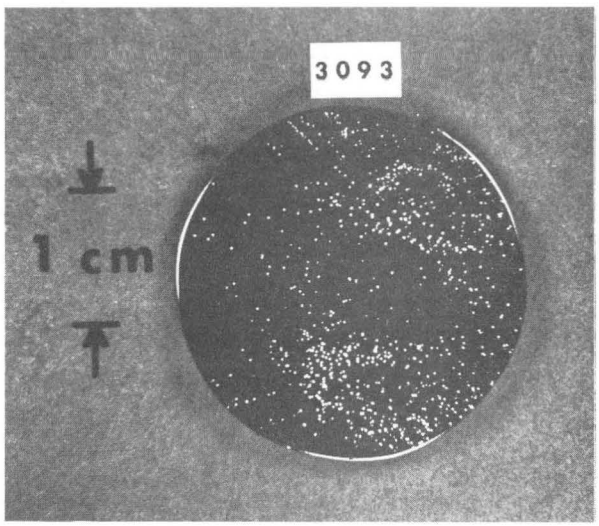

Fig. 1. A Hoboken crystal from which outstanding detectors were produced. The etch-pit distribution is reasonably uniform with no apparent pattern. (XBL699-5892)

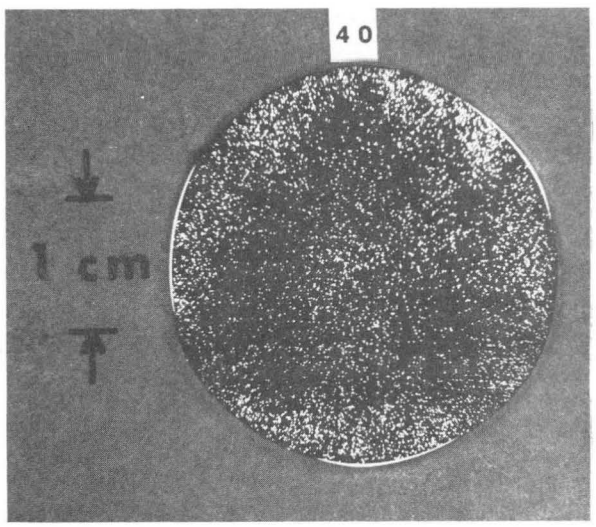

Fig. 2. Crystal No. 40 grown at LRL from which outstanding detectors were produced. The dislocation density is clearly much higher than that of Fig. 1, but the distribution is reasonably uniform. (XBL699-5893)

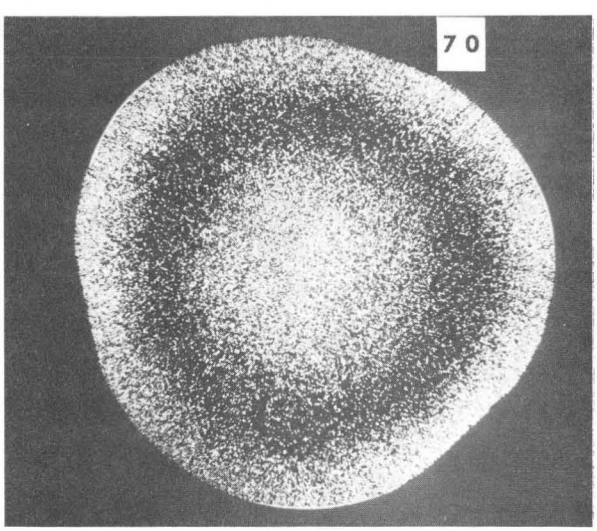

Fig. 3. A slice taken near the middle of crystal No. 70 grown at LRL. The pronounced ring structure indicates a poor-quality crystal, and detectors made from the middle of this crystal were not acceptable. (XBB699-5898)

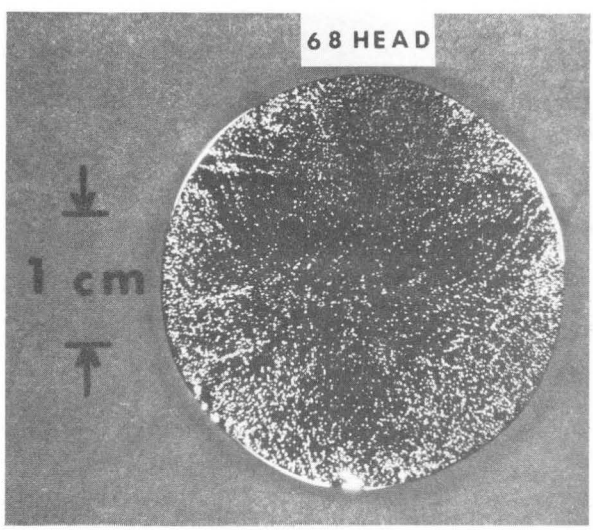

Fig. 4. Head end of crystal No. 68 grown at LRL. Some slip is visible, but the etch-pit distribution is reasonably uniform, and an excellent detector was made from this slice. (XBB699-5899)

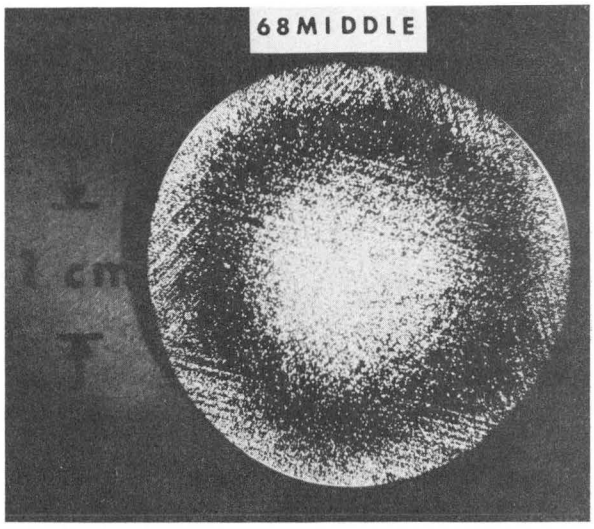

Fig. 5. Middle of crystal No. 68. A pronounced ring structure is present and detectors made from this region are worthless. (XBB699-5900)

THIN-WINDOW GERMANIUM DETECTORS: FALLACY AND FACT†

R. H. Pehl, F. S. Goulding,
W. L. Hansen, and R. C. Cordi

The purpose of this brief note is to refute some erroneous and misleading statements recently published in this journal by Dearnaley et al. [1] We speak from our own experience but would like to note that other groups observe similar results, and that devices similar to ours are commercially available.

For more than 5 years we have been routinely making thin-window detectors by using the gold surface-barrier technique. [2] About 40 successful detectors have been produced and used without a single failure caused by the surface-barrier contact. * These detectors are commonly used for photon measurements, and occasionally for charged-particle measurements.

Figure 1 compares a typical voltage-current curve for one of our detectors against the "low reverse current" detector of Dearnaley et al. [1] This dramatically demonstrates that "excessive" reverse current is not present in our surface-barrier detectors, and that the detector described in Ref. 1 would not be considered acceptable by our reverse current standards. A possible explanation of the shape of the V-I curve presented in Ref. 1 is that the gallium implanted layer is not providing a sufficiently p^+ contact.

As for the unstable characteristics of germanium surface-barrier devices alluded to in Ref. 1, the detector shown in Fig. 1 has been in almost continuous operation for nearly 4 years, and we have about 10 other detectors that have been in operation over 2 years. In fact there has been no case where detector degradation has forced removal of a thin-window detector (except due to radiation damage in detectors used near accelerators).

In 1965 we used these thin-window germanium detectors to measure protons up to 40 MeV. [3,4] Similar work was reported by Bertrand et al. [5] Although this program has received little emphasis, a total system resolution of 17 keV for 42-MeV protons has now been obtained. [6] (This includes the

*We would like to differentiate here between the conventional type of gold surface barrier used on n-type material and its use as a p^+ termination of the intrinsic region in a lithium-drifted detector. In the latter case, at least in silicon detectors, our observations strongly indicate that the performance is much less sensitive to the environment, damage, and edge effects than in the conventional surface barrier. This has led us to question whether the mechanism of operation of the barrier is the same in the two cases.

cyclotron beam-energy spread, electronic noise, detector statistics, and other sources of signal spread.)

As discussed previously,[7] maintenance of an extremely thin window presents some problems, but we have no difficulty maintaining a considerably thinner window than Dearnaley et al.[1] Figure 2 shows a ^{228}Th alpha-particle energy spectrum obtained by using a surface-barrier entrance window; a comparison of this spectrum with the alpha-particle spectrum presented in Fig. 3 of Ref. 1 is quite enlightening. Our nearly symmetric peak at 5.427 MeV with a resolution of 14 keV compares quite favorably with their very asymmetric peak with a resolution of 200 to 300 keV.

Figure 3 shows the type of high-quality gamma-ray spectrum that can be obtained with surface-barrier thin-window detectors. This spectrum was recently obtained from the detector discussed in conjunction with Fig. 1. Somewhat better resolution has been obtained by using a smaller detector surrounded by a cold shield to reduce IR-induced leakage current.

In conclusion we would like to say that our purpose in this note is to emphasize to other groups that the surface-barrier technique can provide a very satisfactory method of achieving the p^+ entrance window for lithium-drifted germanium detectors. We do not wish to indicate any lack of interest in ion-implantation, which has its own attractive features independent of techniques which compete in a particular application.

Footnote and References

†Published in Nucl. Instr. Methods 75, 175 (1969).
1. G. Dearnaley, A. G. Hardacre, and B. D. Rogers, Nucl. Instr. Methods 71, 86 (1969).
2. F. S. Goulding and B. V. Jarrett, A Method of Making Thin-Window Germanium Detectors, UCRL-16480, January 1966.
3. R. H. Pehl, D. A. Landis, F. S. Goulding, and B. V. Jarrett, Phys. Letters 19, 945 (1965).
4. R. H. Pehl, D. A. Landis, and F. S. Goulding, IEEE Trans. Nucl. Sci. NS-13, No. 3, 274 (1966).
5. F. E. Bertrand, R. W. Peele, T. A. Love, R. J. Fox, N. W. Hill, and H. A. Todd, IEEE Trans. Nucl. Sci. NS-13, No. 3, 279 (1966).
6. E. A. McClatchie, M. S. Zisman, A. D. Bacher, C. Glashausser, R. H. Pehl, E. J. Rivet, and F. S. Goulding (Lawrence Radiation Laboratory), unpublished data, 1968.
7. R. H. Pehl, F. S. Goulding, D. A. Landis, and M. Lenzlinger, Nucl. Instr. Methods 59, 45 (1968).

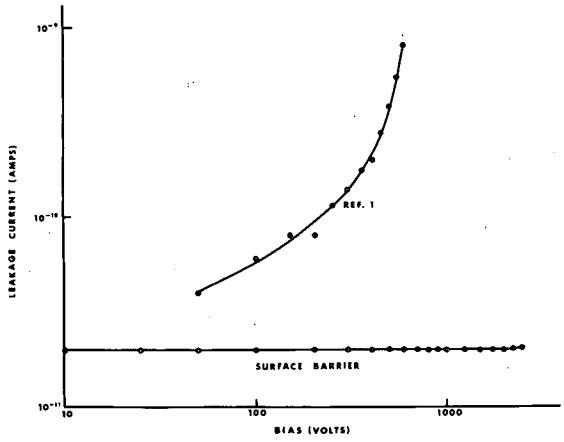

Fig. 1. Comparison of the voltage-current curves for a gold surface-barrier thin-window lithium-drifted germanium diode against the device shown in Ref. 1. (XBL697-1066)

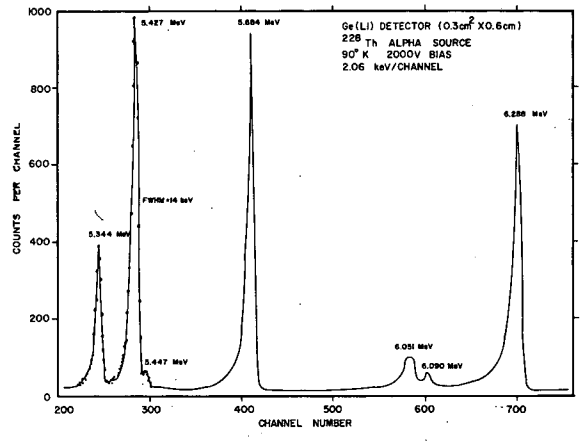

Fig. 2. Partial alpha-particle energy spectrum from a ^{228}Th source. (XBL678-4738)

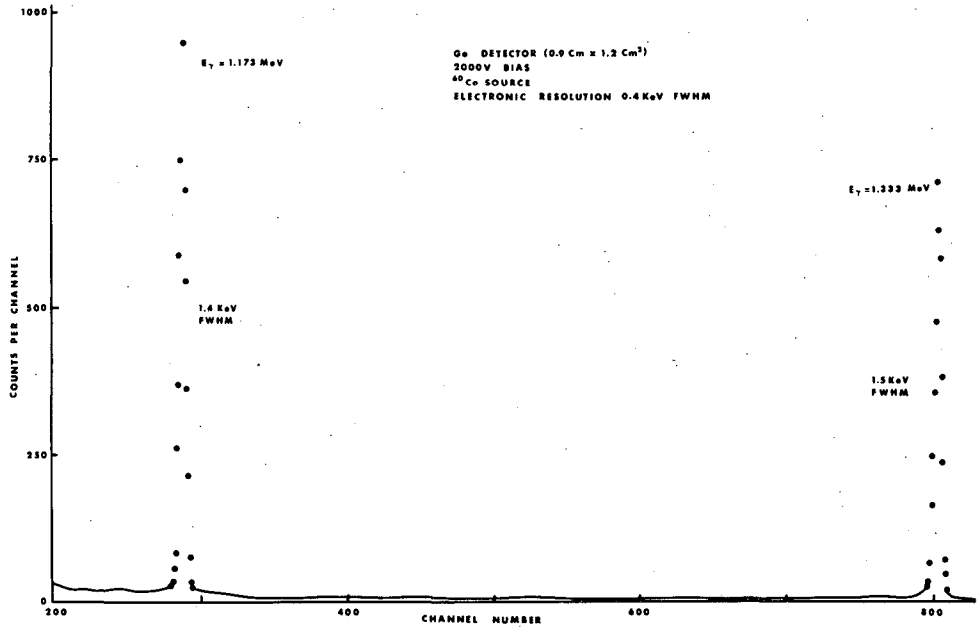

Fig. 3. Spectrum for ^{60}Co gamma rays in the gold surface-barrier thin-window detector discussed in conjunction with Fig. 1. (XBL697-1065)

General Instrumentation and Development

SURVEY OF EXTERNAL INJECTION SYSTEMS FOR CYCLOTRONS†

D. J. Clark

Internal cyclotron ion sources produce large currents of light ions such as protons, deuterons, and α particles, but for many other ions an internal ion source is either impossible or of low intensity. Sources of polarized ions are much too large to put in the center of a cyclotron. To make heavy ions with the high charge states necessary for high cyclotron energy, the ion source needs high arc power input, which is supplied more easily in an external source. For negative-ion acceleration, high gas flow and low pressure are needed, indicating the advantage of an external source. For such ions a number of groups have built or are planning injection from external sources. For polarized beams a few installations have used neutral-beam injection. However, most polarized beam systems and all heavy-ion and negative-ion systems use ion injection because of better beam control during transport, and no loss of beam in charge exchange. The ion beams are brought in either axially through the magnet pole, or radially along the median plane. The larger cyclotrons being planned for 200 to 500 MeV provide adequate space, in the usually crowded center region, for transport and inflection of beams from external injection systems. This paper compares and summarizes the various external injection systems operating or under construction for cyclotrons up to 500 MeV.

The status of most of these systems is summarized in Table I. Both axial and radial ion injection work well, with overall transmission from source to extracted beam in the region of 1 to 5%. In the larger machines being built, the higher injection energies and smaller phase-space areas promise efficiencies of up to 30%, starting with a dc beam.

Footnote

†Condensed from UCRL-18980; presented at the International Cyclotron Conference, Oxford, England, September 17-19, 1969.

TABLE I. EXTERNAL INJECTION SYSTEMS, SPECIFICATIONS

	CYCLOTRON ENERGY (MeV)	INJECTOR STATUS	SOURCE TYPE	SOURCE ENERGY(kV)	SOURCE POL.	SOURCE CURRENT	TRANSPORT MODE	TRANSPORT FOCUSING	TRANSPORT INFLECTOR	TRANSPORT BUNCHER	CYCLOTRON BEAM ACCEL.	CYCLOTRON BEAM EXTERNAL	TRANSMISSION SOURCE TO: ACCEL. (%)	TRANSMISSION SOURCE TO: EXT. (%)	COMMENTS
ATOMIC BEAM															
Saclay	22d	Shutdown 1969	Pol.	Thermal	.5 d		Radial	None	Ionizer	No		.03 nA			
Czech.	12d	Inst. 1969	Pol.	40 p,d	.3 d	.3 μA	Radial	None	Stripping	rf					.1 nA external beam pred.
AXIAL ION															
Birmingham	12d	Oper.	Pol.	12 d	.55 d	.2 μA	Axial	Ein. Lens	Grid-mirror	rf	20 nA*	4 nA*	10*	2*	Grids in center region
		Shutdown	rf	12 d	0	600 μA	"	" "	" "		21 μA		3		1962 tests only
Cycl. Corp.	15 H^-	Oper.	Ehlers	10-14 H^-	0	2.5 mA	Axial	Elec. Quads	Grid-mirror	rf	120 μA*	40 μA*	5*	1.5*	Sold to LRL Livermore
Duke	15 H^-,8 H_2^+	Oper.	Ehlers	17 H^-,10 H_2^+	0	2.5 mA	Axial	Elec. Quads	Grid-mirror	rf	80 μA*	30 μA*	3*	1.5*	Built by Cycl. Corp.
Grenoble	60 p,..	Oper.	Pol.	13 p	.78 p	1.9 μA	Axial	Mag. Q.+ Ein.L.	Channel	rf(study)	23 nA	7 nA	1.2	.4	22 Mag. Quads + 8 Ein. L.
		Oper.	Duoplas.	13 p	0	3 mA	"	" "	"	"	20 μA	4.2 μA			Space Charge comp.
Philips	14 p,7.5 d	Testing	Penning	7.5 d	0	5 mA	Axial	Elec. Quads	Grid-mirror	rf(const.)	30 μA		2		Prelim. results
Berkeley	55 p,65 d	Oper.	Pol.	12 p	.7 p	1.4 μA	Axial	Elec. Quads	Grid-mirror	rf(const.)	50 nA	20 nA	3.5	1.5	Old line tested 1966
		Oper.	Duoplas.	10 p	0	40 μA-p	"	" "	" "	"	3.6 μA	1.8 μA	9	4.5	New duoplas. since 1966
Harwell-VEC	53 p,40 d	Inst. 9-69	P.I.G.	30 p,He	0	200 mA	Axial	Mag. Quads	Mirror	No					Space Charge comp.
Groningen	70 p,..	Inst. 1969					Axial	Mag. Lens	Mirror						90% transm. in inj. line
ORNL-ORIC	65 p,40 d	Inst. 11-69	Pol.	15 p,d	.9 p	5 μA	Axial	Elec. Quads	Grid-mirror	Sawtooth					Heavy-ion Source planned
TRIUMF	500 H^-	Inst. 1972	Ehlers	300 H^-	0	5 mA	Axial	Elec. Quads	Channel	rf	1.5 mA*†	1.5 mA*†	30*†	30*†	Polarized source planned
UCLA	48 p	Const.	Ehlers	15 H^-	0	2 mA	Axial	Elec. Quads	Mirror						
Manitoba	48 p,24 d	Const.	Duoplas.	H^-,D^-	0		Axial	Elec. Quads	Grid-Mirror						
C.S.F.	Model	Study			0		Axial		Mirror						Electron Model Tests
A.E.G.	Model	Study		10	0		Axial	Quads	Channel						Ion model tests.
RADIAL ION															
Lebedev	.15 p,.3 d	Oper.	Penning	15 p,30 d	0	5 μA	Troch.	Sector gradient	Channel	No	1.0μA		20		Operating 1964
M.S.U.	56 p,..	Study		250 p			Troch.	Sector gradient							Good optical quality
Saclay	27 p,..	Oper.	Pol.	5 p	.9 p	5 μA	E ⊥ B	Ein. Lens		rf	200 nA*	70 nA*	4*	1.4*	Heavy ion source-constr.
Orsay	140 H^{+5},..	Const.	Linac	1 MeV/A	0		Radial		Strip.						
Zurich	585 p	Inst. 1973/74	AVF Cycl.	70 MeV p	0	100 μA	Radial	Mag. Quads	Channel	No	100 μA†	100 μA†			Proj. complete 1974
Indiana Inj.	15 p,..	Inst. 3-70	Duoplas.	500 p	0	50 μA	Radial	Elec.,Mag. Q.	Channel	rf	10 μA*†	10 μA*†			Building pol. He^3 source
Indiana Fin.	200 p,..	Inst. 3-70	AVF Cycl.	15 MeV p	0	10 μA	Radial	Mag. Quads	Channel	No	10 μA†	10 μA†	90†	90†	Cyclotron complete 1-72

*Buncher used. †Design goal.

GRAPHICAL CALCULATION OF WAIST-TO-WAIST TRANSFER IN PARTICLE OPTICS†

A. U. Luccio*

A graphical method is described to calculate waist-to-waist transfer in thin-lens particle optics.

Perhaps the most important result of an optical transfer-line calculation for charged particles is the location of the "waists" or minima in the beam section and the determination of their phase-space shape. Formulas for waist-to-waist transfer in thin-lens optics are given, e.g., in Banford's book.[1] These formulas are quite general, since all optical elements--such as lenses and beam-bending devices--can be reduced to appropriate systems of thin lenses and drift spaces.[2] Unfortunately, if the elements are many, the use of these formulas is rather tedious, because of the large number of parameters to be adjusted, and very often becomes impossible in practice.

The procedure can be greatly expedited by the use of charts and nomograms, of which good examples are due to Banford,[3] Smith,[4] Randle,[5] and Resmini.[6] If the line contains some accelerating element, however, the above methods cannot be utilized; it appeared desirable to us to develop a very general method for waist-to-waist transfer calculation. In doing so, our aim has been simplicity of reading and use, so that the fundamental properties of waists could appear as explicitly as possible. The results of graph calculations are accurate enough for many purposes and, in any case, can be considered as a good starting point for more refined computer calculations.

The graphs presented here are an improved and generalized version of a method already described.[7]

Waist-to-Waist Transfer for a Thin Accelerating Lens

Let us refer the beam in a meridian section to the axes Z (longitudinal) and Y (transverse) (Fig. 1). Subscripts 1 and 2 mean upstream and downstream from a lens, subscript 0 refers to a waist.

The following definitions are used:

Y_0, Y_0'	= phase-space coordinate of a waist,
$\epsilon = Y_0 Y_0'$	= emittance of a waist,
$X = Y_0/Y_0'$	= characteristic length of a waist,
$\mu = Y_{02}/Y_{01}$	= linear magnification,
z_1, z_2	= distance of a point from the lens, upstream and downstream,
z_{01}, z_{02}	= distance of the waists from the lens ($z_0 < 0$ corresponds to a virtual waist),
f	= focal length (positive for a converging lens),
$\eta^2 = V_2/V_1$	= acceleration factor.

The thin lens we are discussing is considered as composed of a thin nonaccelerating lens (L) followed or preceded by a thin accelerating gap (A), which changes the energy eV_1 of an incoming particle into eV_2. This lens changes the emittance of the beam, and therefore the characteristic length of the second waist, according to $\epsilon_2 = \epsilon_1/\eta$, $X_2 = \mu^2 \eta X_1$.

We define $u = z_{01}/X_1$, $v = z_{02}/X_1$, and $\phi = f/X_1$.

Analysis shows that

$$X_2 = \mu^2 \eta X_1, \quad v = \eta\phi \frac{u(u-\phi)+1}{(u-\phi)^2+1}, \quad \mu^2 = \frac{\phi^2}{(u-\phi)^2+1}.$$

The function $v(u,\phi)/\eta$ is plotted in Fig. 2 for positive values of u and v. Negative values of u and v are shown in the full paper (UCRL-18977). The function $\mu^2(u,\phi)$ is plotted in Fig. 3.

The graphs can be used quite generally to deal with real and virtual waists and with converging and diverging lenses.

The following well-known features of W-W transfer show clearly from Fig. 2: to a given position of the source waist, there corresponds a focal length for which v, positive or negative, is maximum. Locus of maxima is indicated by the dashed lines. This is an important property; it means, e.g., that in order to obtain a real image waist at a given position downstream, the source waist should be located not too close to the lens, upstream.

In Fig. 3 the magnification μ^2 has a maximum for each positive u, corresponding to a definite focal length. The locus of maxima is shown by a dashed line.

Let us show an example of the use of the graphs. In Fig. 4 is sketched a line composed by an ion gun with proper (accelerating) optics, plus another (nonaccelerating) lens, e.g., an "einzel" lens. The purpose of the line is to transfer a crossover (waist) of given characteristics near the ion source to a given point at a given distance. Let us refer to the geometrical data of Fig. 4 and to these properties of the starting waist: $Y_{01} = 0.5$ cm, $Y'_{01} = 0.100$ rad, $\epsilon_1 = 0.05$ cm-rad, $X_1 = 5$ cm. Then the calculation can run as shown below.

First lens. For $\eta = 2$, $z_{01} = 10$ cm, and accordingly, for $u = z_{01}/X_1 = 10/5 = 2$, a reasonable value for z_{02}, corresponding to a second waist midway between the first and the second lens, is $z_{02} = 24$ cm. This value corresponds to $v/\eta = z_{02}/\eta X_1 = 2.4$, which can be obtained from the graph of Fig. 2 with $\phi = 1.5$; or $f = 7.5$ cm. The corresponding values for μ^2 and X_2 obtained from the graph of Fig. 3 are $\mu^2 = 1.8$, $X_2 = \mu^2 \eta X_1 = 18$ cm.

Second lens. For $\eta = 1$, $z_{01} = 25$ cm, $X_1 = 18$ cm, and accordingly for $u = z_{01}/X_1 = 25/18 = 1.4$ we can obtain (Fig. 2) a value $z_{02} = 21$ cm, or $v/\eta = z_{02}/\eta X_1 = 21/18 = 1.17$, with $\phi = 0.95$; or $f = 17$ cm. The resulting magnification (Fig. 3) is $\mu^2 = 0.8$; the overall magnification is $\mu_{ov} = (0.8 \times 1.8)^{1/2} = 1.2$; and the final emittance is $\epsilon_{ov} = \epsilon_{in}/\eta = 0.025$ cm-rad.

A second example of a beam-bending line arrangment and quadrupoles is described in the original paper (UCRL-18977).

Footnotes and References

†Condensed from UCRL-18977; submitted to Nucl. Instr. Methods.
*Present address: University of Milan, Milan, Italy.

1. A. P. Banford, The Transport of Charged Particle Beams (E. and F. N. Spon, Ltd., London, 1966).
2. Ibid; p. 40.
3. A. P. Banford, A Circle Diagram for Beam Transport Calculations, Rutherford Laboratory Report NIRL/R/8, 1961.
4. W. I. B. Smith, Beam-Transport Calculations Using Graphs, MIT Report CEAL-1002, 1963.
5. T. C. Randle, Two Graphical Constructions for Beam-Transport Problems, Nucl. Instr. Methods 41, 319 (1966).
6. F. G. Resmini, A Simple Method for Determining Waist-to-Waist Transfer Properties of Quadrupole Doublets and Triplets, Nucl. Instr. Methods 68, 235 (1969).
7. A. U. Luccio, Waist-to-Waist Transfer in Thin-Lens Optics, UCRL-18217, May 1968.

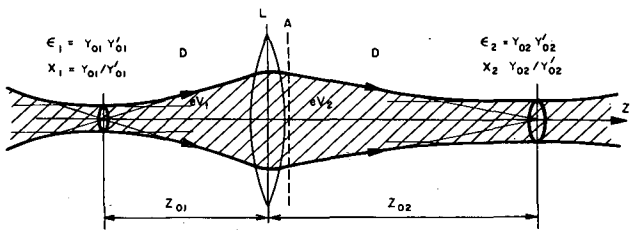

Fig. 1. A thin accelerating lens.
(XBL684-2601)

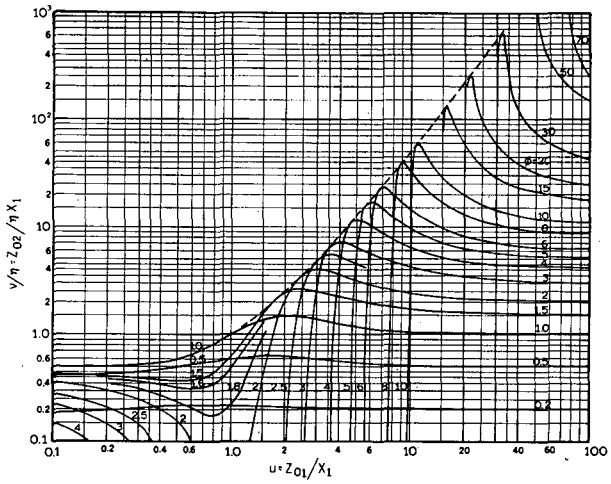

Fig. 2. The function $v(u, \phi) > 0$ for $u > 0$. (XBL692-4803)

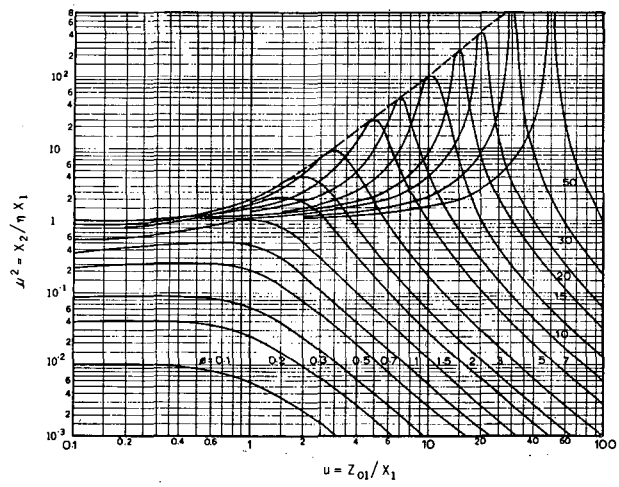

Fig. 3. The magnification function $\mu^2(u, \phi)$ for $u > 0$. (XBL692-4805)

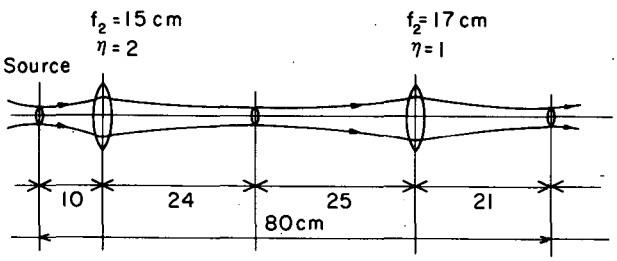

Fig. 4. Example of application. (XBL684-2600)

DESIGN AND CONSTRUCTION OF THE AXIAL INJECTION SYSTEM FOR THE 88-INCH CYCLOTRON†

D. J. Clark, R. Burger, A. Carneiro, D. Elo, P. Frazier, A. Luccio,*
D. Morris, M. Renkas, and F. Resmini*

A new axial injection system for the 88-inch cyclotron has been constructed. It transports beams from external ion sources axially through the magnet yoke to the median plane of the cyclotron. The optical elements include a bending magnet, electric quadrupoles, and the magnetic field of the cyclotron. Beam monitoring is done with scanning wires, phosphor plates, and Faraday cups.

The old axial line[1] of 1966 used an ion source mounted directly on the line axis, and had electric quadrupole doublet lenses with a 3.0-cm aperture. The new line, Fig. 1, accepts beam from either a polarized ion source on axis, or a duoplasmatron source used with a 90-deg bending magnet. The aperture has been increased to 7.3 cm, and quadrupole triplets are used for greater matching flexibility. This paper describes the system down to the median plane. The new inflector and center-region electrodes will be the subject of a future paper.

Since the polarized source is a complex structure, it was placed above the 7-ft-thick concrete roof of the cyclotron vault, to allow construction and testing during cyclotron operation. The duoplasmatron source and future sources should also be at a convenient distance above the shielding to allow for expansion. The injection line is required to transport the beam about 15 ft from the source to the median plane.

When one uses an injection voltage that increases with cyclotron field as $V_i \propto QB^2/M$, where Q and M are particle charge and mass, one has "scaled operation," as shown by the diagonal lines in Fig. 2, for example. All beams on one line then have the same trajectories through the magnetic "hole lens" approaching the median plane, and in the first turn up to the first acceleration gap. The dee voltage must be kept proportional to injection voltage, so the orbit pattern in the cyclotron is also constant. The main advantage of this type of operation is that once the beam optics has been optimized in the injection line, hole lens, and cyclotron center region for one point on the line, all the other cyclotron energies and particles can be obtained easily by the proper variation of injection and dee voltage.

The polarized ion source[2] is of the usual atomic beam type, using a dissociator, a sextupole, rf transitions, and a strong-field ionizer. We expect that it will produce polarized beam for experiments of 100 to 1000 times the intensity and much better quality than that available with the α-p scattered beam used during the past several years.

The duoplasmatron source[3] produces intensities of more than 500 μA of protons, H_2^+, H_3^+, and similar deuteron beams. It is being used to test the performance of the transport line for efficiency under low- and high-intensity conditions. Its output of doubly charged ions is small, a few μA, so a PIG source is planned to give a higher α-particle output for pulsed-beam work.

The 90-deg bending magnet brings the duoplasmatron beam into the axial line. It gives equal focusing in both planes, with a flat field and edges cut at 36 deg to the beam normal.

Three quadrupole triplet lenses were chosen to transport the beam efficiently down the column to the median plane.[4] They give versatile transformation of phase-space ellipses to match the ion sources to the cyclotron, and transmit beam currents of more than 500 μA at 10 kV injection voltage. Space between triplets is used for steering plates, scanning wires, phosphor plates, and Faraday cups. A buncher will be placed in the space between the last two triplets to match the dc beam from the source to the rf time acceptance of the cyclotron. A sine-wave buncher is being planned at present, rather than the more ideal but more difficult sawtooth buncher suggested previously.[5]

The mechanical structure consists of 6-in. -diameter tubes containing the lenses, inside an evacuated column of 12-in. -square cross section, as shown in Fig. 1. To reduce neutron leakage, as much shielding as possible is replaced around the injection line.

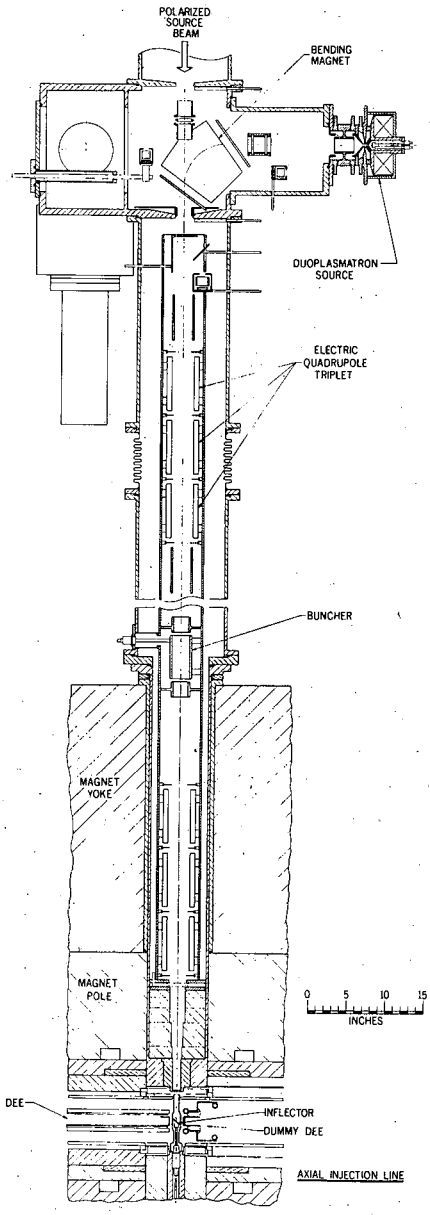

Fig. 1. Schematic drawing of axial injection line for 88-inch cyclotron. An additional quadrupole triplet is located in the omitted section above the magnet. (XBL692-252)

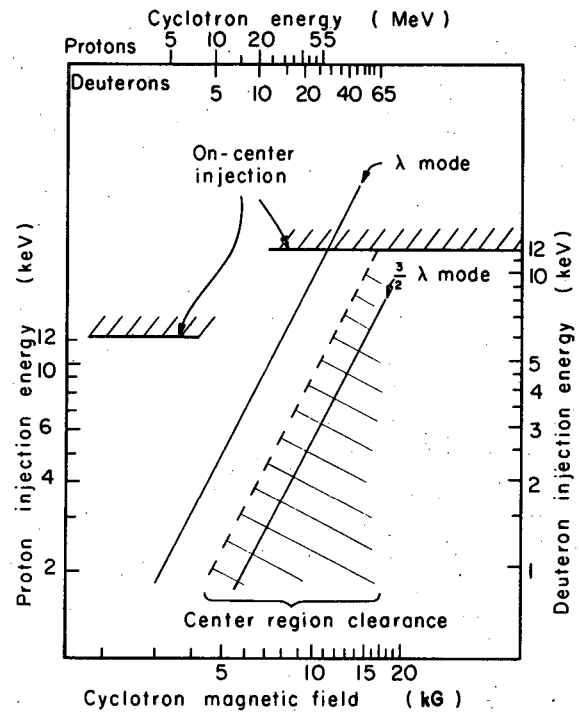

Fig. 2. Chart of operating parameters for injection line. Forbidden regions are shaded: at the right because of the clearance requirement for inflected beam in the first turn, and at the top because of the orbit-centering requirement. (XBL692-2032)

The beam entering the strong magnetic field of the cyclotron is focused to periodic waists by this half solenoid or "hole lens." Calculations were made on particle trajectories for various phase-space shapes and waist positions.[6] They showed that several discrete operating modes (Fig. 2) produce the desired beam size, in the median plane, of 2 to 3 mm diameter. The "λ mode" is obtained by starting with a small waist, about 14 cm before the median plane, which is then transferred to the median plane by the strong axial magnetic field.

Footnotes and References

†Condensed from UCRL-18608; presented at the 1969 Particle Accelerator Conference, Washington, D. C., March 5-7, 1969.
*Present address: University of Milan, Milan, Italy.

1. R. Burger et al., Machine Development at the Berkeley 88-Inch Cyclotron, IEEE Trans. Nucl. Sci. NS-13 [4], 365 (1966).
2. A. Luccio et al., A Polarized Ion Source for the Berkeley 88-Inch Cyclotron, Abstract for 1969 Particle Accelerator Conference, Washington, D. C., 5-7 March 1969.
3. C. D. Moak et al., Duo Plasmatron Ion Source for Use in Accelerators, Rev. Sci. Instr. 30 [8], 694 (1959), and drawings supplied by C. D. Moak.
4. F. G. Resmini and D. J. Clark, Beam Optics and Space-Charge Effects in the Axial Injection Line for the 88-Inch Cyclotron, Abstract for 1969 Particle Accelerator Conference, Washington, D. C., 5-7 March 1969.
5. F. Resmini and D. J. Clark, A Proposed Sawtooth Buncher for the 88-Inch Cyclotron Axial Injection System, UCRL-18125, March 1968.
6. A. U. Luccio, Axial Injection Studies on the 88-Inch Cyclotron "Hole Lens," UCRL-18016, Jan. 1968.

SPACE-CHARGE EFFECTS IN THE AXIAL INJECTION LINE FOR THE 88-INCH CYCLOTRON†

F. Resmini* and D. J. Clark

A new axial injection beam transport line has been designed for the 88-inch cyclotron (Fig. 1). The line beam optics[1] and construction[2] have been described previously. In this report we give the results of space-charge calculations at higher beam intensities in this line.

In treating the problem of matching external sources to the cyclotron acceptance, it is convenient to refer to the phase-space representation. The two phase spaces, (x, x') and (y, y'), are associated with the beam, traveling along the z axis. The units used here for position (x and y) and for divergence (x' and y') are mm and mrad. The x-z plane is defined parallel to the dee edge in the center of the cyclotron, and the polarities of the quadrupoles are so chosen that the motion in the x-z plane generally corresponds in a triplet to the sequence DFD (defocusing-focusing-defocusing), and in the y-z plane to FDF.

The beam is at a waist, along a drift length, when the representative ellipses in phase space are upright, i.e., their axes coincide with x, x' or (y, y') axes. However, the waist positions for the two phase spaces do not necessarily coincide along the line.

In discussing the matching requirements we describe the beam, at a waist, through the characteristic length of the phase-space ellipses, defined as $X_x = x_0/x'_0$ and $X_y = y_0/y'_0$, where the subscripts (0) refer to the semiaxes of the ellipses at the waist.

Interest in studying in some detail the optics of the line with space-charge effects also taken into account arises because of the advantages of injecting very intense (nonpolarized) beams. In some cases--e.g., α particles or heavy ions--this possibility would allow for overcoming the intensity limits of conventional cyclotron sources and eventually lead to more intense accelerated beams. Although the feasibility of such a scheme has not yet been proved, it is nevertheless worthwhile to get some insight into the problem. The aim of the calculations presented here is therefore to (a) evaluate the desirable characteristics, such as emittance and initial phase-space shaping of such beams, and (b) determine the range of currents that can be transmitted through the line--still satisfying, however, some reasonable requirements on phase-space matching. The program BEAMCAL, developed at Los Alamos,[3] was used to perform the Runge-Kutta integration of the Vladimirskiy-Kapchinskiy equations.[4]

In the injection of intense beams it is intended to use the first triplet, T_0, in the $M_x = M_y = 1$ magnification mode, performing a symmetric beam transfer over the length of 1.4 meters. It has been found that this mode of operation is generally possible, if the quadrupole voltages are properly corrected. The main results can be summarized as follows.

The initial shaping in phase space for a given emittance is far more critical than in the zero-current approximation, from the point of view of transmission efficiency. The effect is illustrated in Fig. 2, where beam envelopes are plotted for 10-keV protons and a 200-mm-mrad emittance, for different beam currents. For example, two extreme X_{in} values have been chosen, $X_{in} = 1$

and 0.14. It is clear that although 800 μA can be transmitted in the first case, 400 μA exceeds the available aperture in the second. This, of course, reflects the fact that space-charge effects are less pronounced for a large-diameter nearly parallel beam.

Footnotes and References

†Condensed from UCRL-18596; presented at the 1969 Particle Accelerator Conference, Washington, D. C., March 5-7, 1969.
*Present address: University of Milan, Milano, Italy.

1. F. Resmini, Optics of the Axial Injection Line for the 88-Inch Cyclotron, UCRL-18442, Sept. 1968.
2. D. J. Clark et al., Design and Construction of the Axial Injection System for the 88-Inch Cyclotron, UCRL-18608, March 1969.
3. P. W. Allison (Los Alamos Scientific Laboratory), private communication.
4. I. M. Kapchinskiy and V. V. Vladimirskiy, Limitations of Proton Beam Current In a Strong-Focusing Linear Accelerator Associated with the Beam Space Charge, in Proceedings of the International Conference on High Energy Accelerators, CERN, 1959, p. 274.

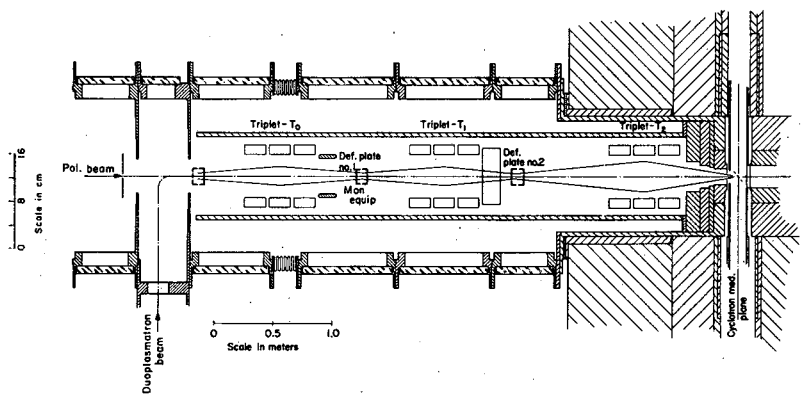

Fig. 1. Layout of the axial injection line. Only schematic beam envelope is shown.
(XBL683-2219A)

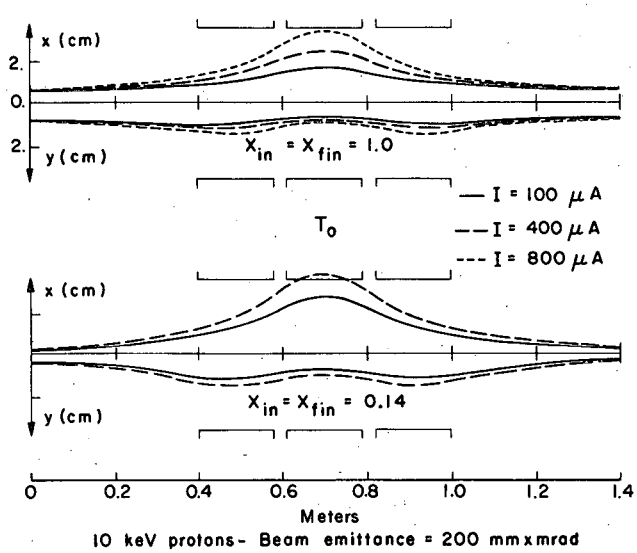

Fig. 2. Beam envelopes through triplet T_0 for 10-keV protons and different beam currents.
(XBL692-1998)

OPERATION OF THE POLARIZED-ION SOURCE AND AXIAL INJECTION SYSTEM FOR THE BERKELEY 88-INCH CYCLOTRON†

D. J. Clark, A. U. Luccio,* F. Resmini,* and H. Meiner‡

A polarized-ion source for protons and deuterons is now in operation at the Berkeley 88-inch cyclotron. The source is of the atomic beam type, using rf transitions and a strong field ionizer. It is mounted vertically above the cyclotron roof shielding. A new axial injection transport system, whose optical elements are electrostatic quadrupole triplets, replaces the previous system,[1] and brings the beam down to the cyclotron median plane. A duoplasmatron source can inject unpolarized protons through a 90-deg bending magnet. A gridded electrostatic mirror inflects the beam into the dummy dee. Electrodes inserted into the dummy dee and dee give narrow accelerating gaps to allow the beam to clear the mirror. They are designed to unplug at vacuum for easy conversion between axial injection and internal source operation.

A polarized-ion source, shown in Fig. 1, was constructed.[2] To allow for future development it is designed for easy replacement of components and has a large pumping capacity to handle high gas loads. It is located in a low-radiation area above the cyclotron shielding roof for convenient maintenance and development. Its axis is vertical, to match the injection line without spin rotation.

The beam transport line,[3] shown in Fig. 2, brings beams from the ion sources 4.5 meters down to the cyclotron. It is composed of three sets of electric quadrupole triplet lenses. It accepts beams from either the polarized-ion source, on axis, directly above, or from the duoplasmatron test source[4] through the 90-deg bending magnet.

The optics of the line[5] was designed to transport beams of up to 800 mm-mrad emittance at energies of 5 to 20 kV, and to allow flexible matching between the external beams and the cyclotron phase-space acceptance. Calculations on high-current beams including space-charge forces show[6] that this line will transmit 600 to 800 μA of protons if the beam has a suitable emittance shape.

A sine-wave buncher is placed between the second and third triplets. It is a drift tube with a drift length of 3/2 cyclotron period. It is located near the cyclotron end of the line to minimize debunching from polarized-ion source energy spread. We use the sine-wave rather than the previously proposed sawtooth-wave shape[7] because of its ease of construction, and because its performance would closely approach the sawtooth type after addition of a higher-harmonic drift tube.

The beam enters the cyclotron through a half-solenoid "hole lens," the region where the cyclotron magnetic field increases from near zero to its median-plane value of 5 to 17 kG. Calculations of phase-space beam trajectories[8] show that several modes of operations are possible, depending on injection energy and cyclotron magnetic field.

When the beam reaches the median plane of the cyclotron, it must be bent through 90 deg into the horizontal plane and enter the dee accelerating gaps in such a way as to be centered radially on the cyclotron center. To inflect the axial beam into the median plane, we use an electrostatic mirror oriented at 45 deg to the median plane.

The center region geometry is shown in plane view in Fig. 3, along with the calculated orbit for the highest-energy α-particle beam. A baffle across the median plane in the dee shields the beam from the dee-mirror electric field. A "half-turn collimator" is provided in the dummy dee to select phase on the first turn, but is normally retracted for polarized-ion injection, because maximum transmission is desired.

This axial injection geometry is not compatible with the normal internal ion source, since the source would have to come through the dummy dee. So a "plug-in" concept was adopted, in which the central parts of the dee and dummy dee out to a 14 cm radius--the "inserts"--are removable at vacuum through the dee stem.

The first test of the entire system of polarized-ion source, axial injection system, and cyclotron acceleration was in April 1969. The best results of system operation in September 1969 are given in Table I.

Footnotes and References

†Condensed from UCRL-18934; presented at the International Cyclotron Conference, Oxford, England, September 17-19, 1969.
*Present address: University of Milan, Milano, Italy.
‡Present address: University of Basel, Basel, Switzerland.

1. R. Burger et al., IEEE Trans. Nucl. Sci. NS-13 [4], 364 (1966).
2. A. U. Luccio, D. J. Clark, D. Elo, P. Frazier, H. Meiner, D. Morris, and M. Renkas, IEEE Trans. Nucl. Sci. 16 [3], 140 (1969).
3. D. J. Clark et al., IEEE Trans. Nucl. Sci. 16 [3], 471 (1969).
4. C. D. Moak et al., Rev. Sci. Instr. 30, 694 (1959).
5. F. Resmini, Optics of the Axial Injection Line for the 88-Inch Cyclotron, UCRL-18442, Sept. 1968.
6. F. Resmini and D. J. Clark, IEEE Trans. Nucl. Sci. 16 [3], 465 (1969).
7. F. Resmini and D. J. Clark, A Proposed Sawtooth Buncher for the 88-Inch Cyclotron Axial Injection System, UCRL-18125, March 1968.
8. A. U. Luccio, Axial Injection Studies on the 88-Inch Cyclotron: "Hole Lens," UCRL-18016, Jan. 1968.

Table I. System tests with 22-MeV protons.

	Ion source		
	Polarized		Duoplasmatron
Injection energy (keV)	12	12	10
Source current, FC_0 (μA)	1.4	2	40
Accelerated current (nA)	50	145	3.6
External current (nA)	20	60	1.8
Transmission:			
Source-external beam (%)	1.5	3	4.5
Polarization (%)	70	80	0
Buncher used?	No	Yes	No

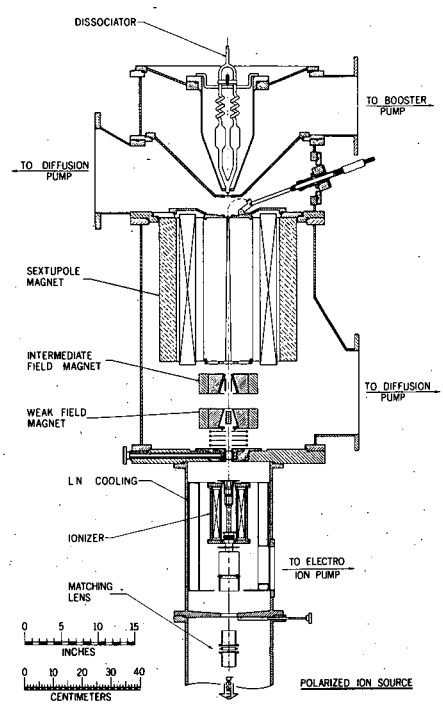

Fig. 1. Polarized-ion source schematic cross section, showing principal components and vacuum pump ports. (XBL681-1702)

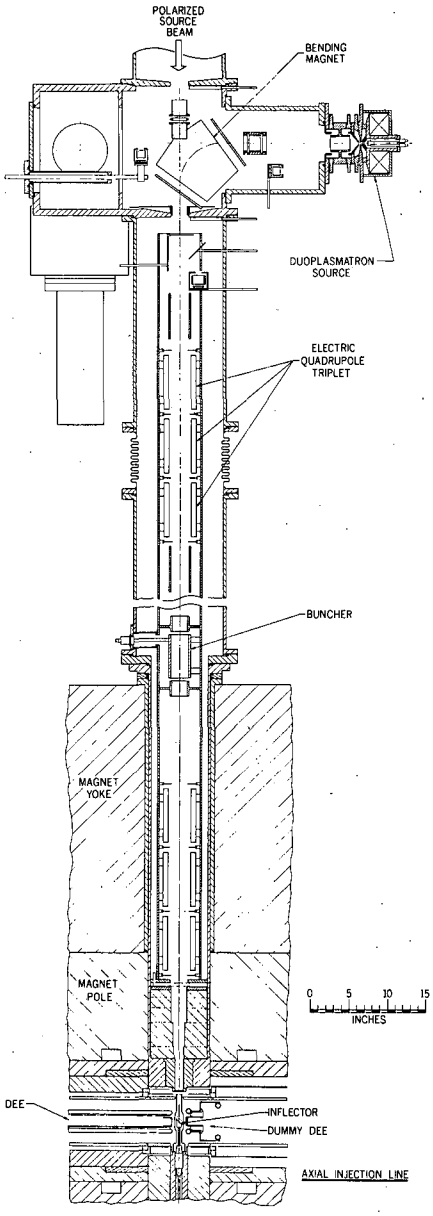

Fig. 2. Axial-injection transport line schematic cross section, showing components. Note that one quadrupole triplet lens has been omitted. (XBL692-252)

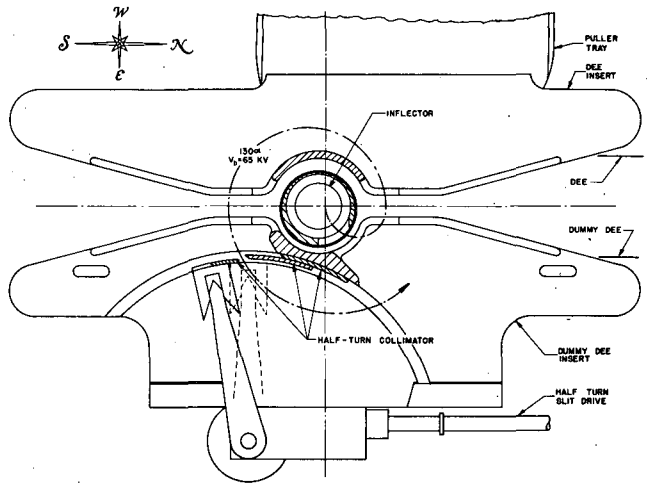

Fig. 3. Plan view (June 1969), of axial-injection center region showing smallest beam trajectory for maximum-energy α particles. "Plug-in" dee and dummy-dee inserts are shown. (XBL698-1229)

ACCELERATION OF FISSION FRAGMENTS†

E. Cheifetz,* R. C. Gatti, R. C. Jared, S. G. Thompson, and A. Wittkower‡

The fission fragments emitted by a 6-μg source of ^{252}Cf were accelerated in a Model MP tandem Van de Graaff accelerator at the High Voltage Engineering Corporation in Burlington, Massachusetts. In order to prevent contamination of the surroundings the source was placed inside a 1-in.-diameter tube and was covered with aluminum and two thin protective foils. A schematic drawing of the experimental arrangement is shown in Fig. 1. Quadrupole magnets are used to focus the fragments both at the source and at the end of the accelerator. The

fragment energy distribution was measured by using a 4.5-cm^2 surface barrier silicon detector 17 m from the source.

The fragments were accelerated as was expected; the energy spectra as a function of terminal voltage are shown in Fig. 2, in which the channel numbers correspond rather closely to units of MeV. The maximum voltage on the terminal in our experiments was 6 MV.

Because of their larger initial charges, the energies of the heavy fragments increase more rapidly than the energies of the light fragments. At a voltage of 2 MV there is still a difference, as indicated by the shoulder on the spectrum. At 4 MV the two groups are indistinguishable. At 6 MV the average energy of the fragments was about 200 MeV and the width of the energy distribution (FWHM) was $\approx$ 45 MeV. As the acceleration voltage increased the widths of the two energy distributions of californium fragments increased, as would be expected on the basis of a distribution in the charge states of the fragments.

An accurate determination of the energy spectra depends on an accurate calibration of channel number versus energy. Therefore some knowledge of the pulse-height response of solid-state detectors to heavy ions is necessary. As a basis for this calibration we used the well-known energy spectrum obtained from a ^{252}Cf standard source located in front of our detector. The energies obtained on the basis of the following two assumptions were then compared: (a) a linear response of the detector was assumed and the average energies of the light and heavy peaks were taken to be those given by Fraser et al.,[1] (b) the "Schmitt calibration procedure," which prescribes a mass-dependent pulse-height response, was assumed.[2]

The mean values of the energy spectra are shown in Fig. 3. Some ambiguity due to the uncertainty in exact positions of the light and heavy peaks occurs in the Schmitt calibration, and is indicated by the small bars. It can be seen that there is a discrepancy of more than 10 MeV between the two calibration methods at an energy of $\approx$ 200 MeV. Therefore we have obtained two different values for the overall average charge state of the fragments: $\bar{q}$ = 19.2 is obtained by the Fraser calibration,[1] and $\bar{q}$ = 21.0 is obtained by using the Schmitt calibration.[2] Information about the mean charge of the light and heavy fragments separately was obtained from the data taken at a voltage of 2 MV, where the two peaks could still be resolved. These results also depend on the choice of a calibration procedure, and are $\bar{q}$ = 17.5 to 18.8 for the light fragments and 20.8 to 23.0 for the heavy ones.

The mean charges of the heavy fragments are in agreement with the values obtained from the data of experiments performed at High Voltage Engineering Corporation by Grodzins et al.[3] and Moak et al.[4] Comparisons of the mean charge state were made at the same ion velocities (appropriate corrections were made for the 13 amu difference between stable ^{127}I and fission-fragment ^{140}I). For the light fragments the above reference would predict a mean charge of 21.0, whereas our experimental value is 18 ± 1. This difference may be due to the effect of selection by the focusing magnet at the source.

The intensity of the beam of fragments at the end of the 17-meter acceleration path is shown as a function of terminal voltage in the upper part of Fig. 3. The observed increase in intensity as a function of voltage exceeds the expected increase due to electrostatic focusing of a perfectly aligned system. Increased electrostatic focusing tends to reduce the effect of errors in alignment. These results show that the system was not well aligned to begin with, and indicate that additional intensity could have been obtained. The source emitted 5×10^8 fragments/min into 4π solid angle, and at 6 MV we obtained 2.25×10^3 fragments/min. The transmission factor, therefore, was 4.5×10^{-6}, as compared with a geometrical transmission of 1.3×10^{-7}.

Footnotes and References

†Condensed from paper to be published in Phys. Rev. Letters.
*On leave from the Weizmann Institute, Rehovoth, Israel.
‡High Voltage Engineering Corporation, Burlington, Massachusetts 01803.

1. J. S. Fraser, J. C. D. Milton, H. R. Bowman, and S. G. Thompson, Can. J. Phys. 41, 2080 (1963).
2. H. W. Schmitt, W. E. Kiker, and C. W. Williams, Phys. Rev. 136, B837 (1965).
3. L. Grodzins, R. Kalish, D. Murnick, R. J. Van de Graaff, F. Chmara, and P. H. Rose, Phys. Letters 24B, 282 (1967).

4. C. D. Moak, H. O. Lutz, L. B. Bridwell, L. C. Northcliffe, and S. Datz, Phys. Rev. 176, 427 (1968).

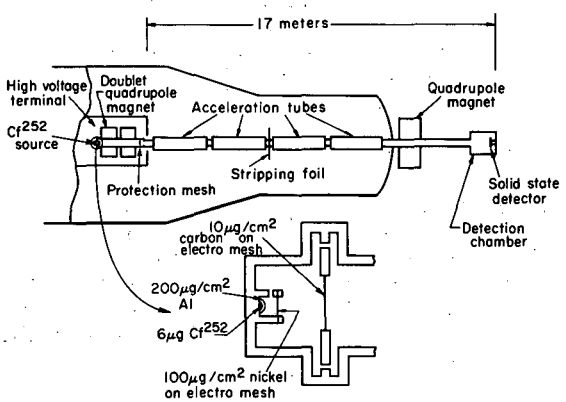

Fig. 1. Experimental arragement. The californium source holder with its protective foils is shown in detail in the insert. (XBL6911-6259)

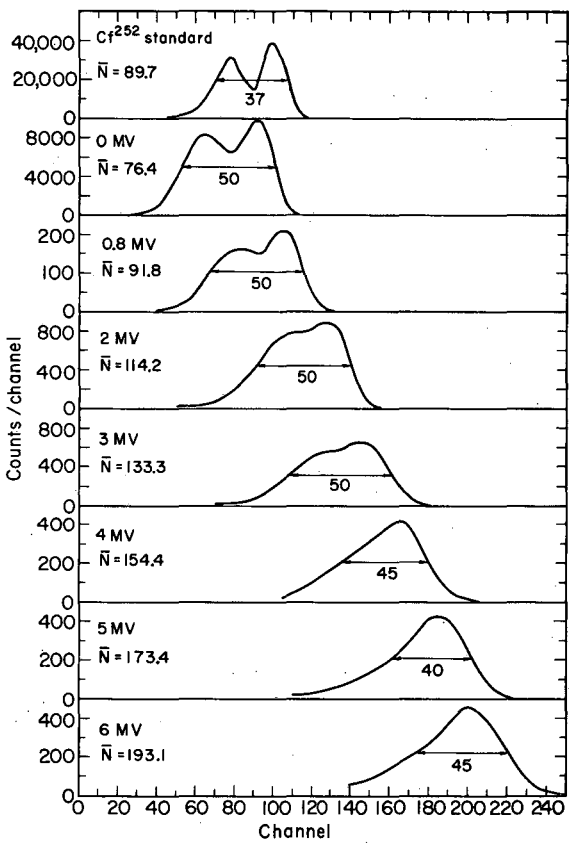

Fig. 2. Spectra of the fragments for several terminal voltages. The standard source shown in the upper part is not covered with any protective foils. 1 channel ≈ 1 MeV. $\bar{N}$ is the mean value of the distribution in channel numbers. (XBL6911-6260)

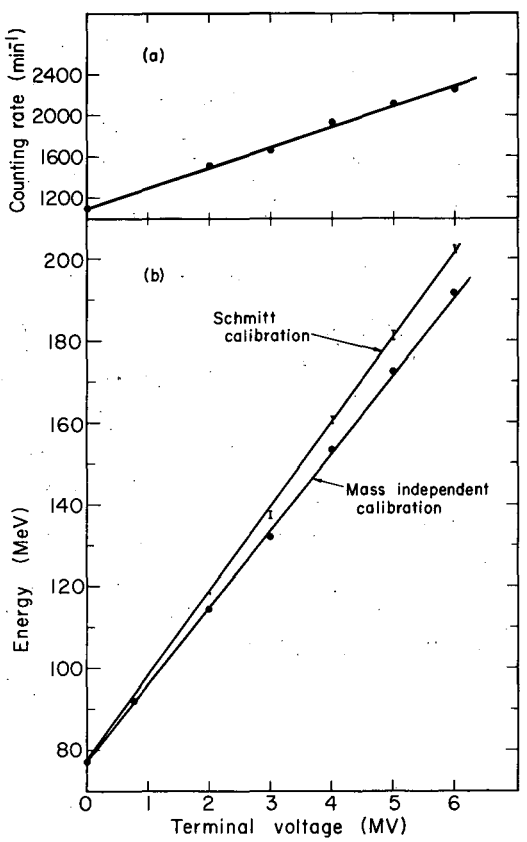

Fig. 3. (a) Intensity as a function of terminal voltage. (b) The mean energy as a function of the terminal voltage for two calibration procedures as explained in the text. (XBL6911-6258)

INITIAL SEPARATION-FACTOR MEASUREMENTS ON CASCADE ISOTOPE SEPARATOR

M. C. Michel

During the continuing testing and evaluation of the performance of the first stage of the Cascade Isotope Separator,[1] direct mass-spectrometric measurements of the enrichment factor for neighboring isotopes were made.

For the purposes of this report, the enrichment factor (F) of isotope 1 with respect to isotope 2 is defined as

$$F = (i_1/i_2)_f / (i_1/i_2)_i \quad ,$$

with i_1/i_2 being the relative abundance of the two isotopes, and f and i referring to post- and preseparation measurements.

Since the preliminary electrical measurements indicated a rather high enrichment, it seemed reasonable to avoid the possibility of natural chemical contamination of separated samples by direct collection of the sample on a mass-spectrometer filament in the separator collector chamber. The filament containing this sample was then made part of a standard double-filament ion source, and isotopic analysis was performed on a 60-deg single-direction-focusing mass spectrometer of high sensitivity. Because direct collection of the 40-keV ion beam resulted in burial of the sample to a depth of the order of 0.1 μ, the mass analysis was complicated by emission of the sample over a broad range of temperature, resulting in decreased beam intensities. Then because of the saturation effect of direct collection[2] the sample size could not exceed ≈ 0.2 μg (determined by the filament area), and this further limits the beam intensity. As a result, the mass analysis can as yet only set an upper limit to the presence of unwanted isotopes (or a lower limit to the enrichment factors).

The measurements discussed here were made with lead, a rather easy element to run in the modified axial-extraction plasma ion source, but its low ionization efficiency in the mass spectrometer served to further limit the mass spectrometer performance. In order to optimize the mass spectrometer runs, ^{204}Pb was chosen as the collected isotope, since this low-abundance isotope would yield samples of minimum isotopic ratio for analysis. Of course, lead is of sufficiently high mass to be a good test of the separator performance, since the dispersion decreases with increasing mass number. Separations were made at total lead ion currents of ≈ 10 to 15 μA, with 2-mm collector slits.

Table I gives limits on the values of the separation factors as measured by this technique for the various lead isotopes. Unfortunately, the adjacent mass number is vacant, and the enrichment is determined only at positions more than one mass number away from the collected isotope. It will be noted that the limits rise rapidly as one goes away from the collected isotope; it is felt from behavior of the mass spectrometer that this is at least partly an artifact of the mass spectrometer analysis, not necessarily an indication of the separator performance. Measurements now in progress should extend the limits or determine the exact levels of contamination.

For comparison, Table II lists some selected values of enrichment factor for other machines, either from direct measurements (obs) or by integration of published beam profiles over a 2-mm slit width (calc). Note that much better separations are to be expected at lower mass number.

Apparently the present instrument is performing at least as well as the best previous reports. Since there are some significant differences in operating conditions, continued effort will be made to determine the actual separation factors and the causes of the observed contamination.

References

1. M. C. Michel and F. L. Reynolds, in Nuclear Chemistry Annual Report, 1968, UCRL-18667, Jan. 1969, p. 355.
2. O. Almén and G. Bruce, Nucl. Instr. Methods 11, 279 (1961).
3. H. Fabricius, K. Freitag, and S. Göring, Nucl. Instr. Methods 38, 64 (1965).
4. W. L. Rautenbach and K. Lubbinge, Nucl. Instr. Methods 38, 61 (1965).
5. J. Lerner, Nucl. Instr. Methods 38, 116 (1965).
6. J. Uhler, Arkiv Fysik 24 [24] 329 (1963).
7. T. Alväger and J. Uhler, Characteristics of the Electromagnetic Separator at the Nobel Institute, in Electromagnetic Separation of Radioactive Isotopes, M. J. Higatsberger and F. P. Viehböck, editors (Springer-Verlag, Vienna, 1961), p. 166.
8. R. Bernas, J. L. Sarrouy and J. Camplan, Double Magnetic Deflexion Isotope Separator for the Production of Very High Parity Isotopes, in Electromagnetic Separation of Radioactive Isotopes, M. J. Higatsberger and F. P. Viehböck, editors (Springer-Verlag, Vienna, 1961), p. 121.

Table I. Separation factor limits, cascade isotope separator (first stage only).

M (mass collected)	ΔM	Contaminating isotope	Separation factor
204	+2	206	⩾ 43 000
204	+3	207	⩾130 000
204	+4	208	⩾200 000

Table II. Separation factors from published reports.

M, mass collected	ΔM	Contaminating isotope	Separation factor	Comments	Ref.
204	+1	205	7 600	calc from electrical measurements	3
204	+2	206	16 700		
204	+3	207	27 800		
204	+4	208	33 300		
84	+1	85	10 000	calc	4
83	+2	85	≈50 000		
211	+1	212	2 500	obs in radioactive collection	3
213	-1	212	5 000		
84	+1	85	20 000	calc from data of Uhler (Ref. 6)	5
86	-1	85	4 700		
83	+2	85	50 000		
82	+3	85	120 000		
130	+1	131	2 500	obs in radioactive collection	7
129	+2	131	10 000		
128	+3	131	16 700		
53	-1	52	52 000 to 70 000	obs in two-stage separator	8
87	+1	88	20 000		
153	-2	151	5 000		
174	+2	176	10 000–12 000		
235	+3	238	14 000		

DIRECTLY HEATED SAMPLE OVEN FOR ISOTOPE SEPARATOR ION SOURCE

M. C. Michel and F. L. Reynolds

Ion sources used in isotope separators, often of the low-voltage electron-supported-plasma type, usually require the ability to ionize elements all of whose compounds are solids of relatively low vapor pressure. This is usually accomplished by operating the entire source at a considerably elevated temperature and vaporizing the sample material into the plasma chamber. Commonly, the vaporization rate of the sample is adjusted by positioning it nearer to or farther away from the source within a connecting tube, allowing conducted or radiated heat from the source itself to vaporize the sample.

Since this obviously requires physical motion of a sample at high temperature, in vacuum, and also at high electrical potential, it is not easily done from a remote location. A directly heated metallic oven system is shown in Fig. 1 which is adaptable to rapid insertion through vacuum locks and gives easy remote control of sample temperature. The tantalum tubes are flared by a simple hydraulic die system and, along with the blocking foil, spot-welded temporarily in preparation for a vaportight TIG weld done in an inert atmosphere enclosure. The sample (often in a secondary crucible to avoid chemical attack of the main tube) is then placed in the longer end, the open end inserted in a tapered hole in the ion-source wall (graphite) which establishes both vapor seal and electrical contact. A suitable holder at the other (short) open end is connected to a power supply (current regulated), and the sample may now be heated by direct resistance heating.

When graphite end plates are used on the ion source the tapered hole makes a graphite-tantalum joint which gives satisfactorily vaportight seals repeatedly with the same oven. One has been used more than 20 times without failure, yet they are sufficiently inexpensive if made in quantity to be disposable for radioactive source work. Measured collection efficiencies indicate that the vapor seal keeps the loss in yield negligible.

Because of the high conductivity of the metallic tube (compared with quartz or other insulators used previously), it is difficult to keep extremely volatile samples cool enough without excessively long tubes to reduce the heat flow. Proper redesign of the system to introduce a large heat sink could easily solve this problem.

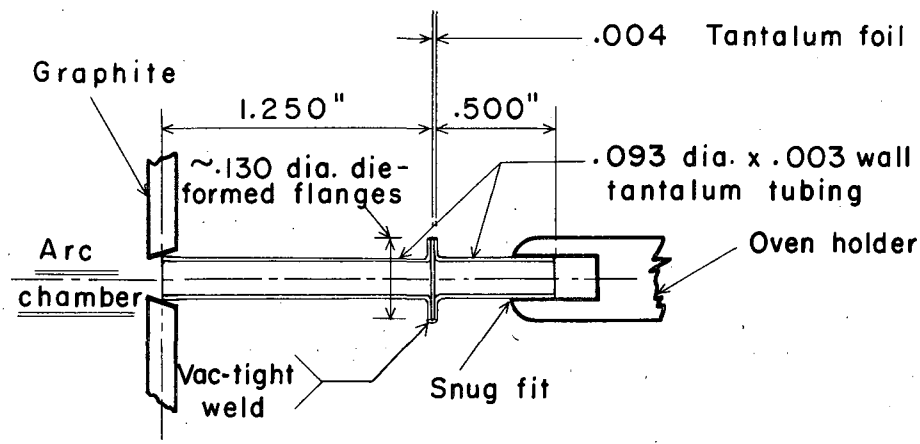

Fig. 1. Directly heated source oven for isotope separator.
(XBL701-2282)

DESIGN OF A MAGNETIC SPECTROMETER FOR PHOTOELECTRON SPECTROSCOPY†

C. S. Fadley, C. E. Miner, and J. M. Hollander

We present the results of a computer design study for an iron-free double-focusing magnetic spectrometer specifically intended for photoelectron spectroscopy. With single detector operation the proposed design is more efficient than any existing magnetic double-focusing spectrometer, and the focal-plane characteristics allow more than a 100-fold increase in data-accumulation rate with a multichannel detector. This design also has very high physical accessibility near the source and detector areas, and it is compatible with either normal or ultrahigh-vacuum operations.

Precise energy analysis of photoelectrons expelled by x rays[1-3] and ultraviolet radiation has been used extensively in the last few years to obtain fundamental information about organic and inorganic solids and gases. In an instrument designed specifically for photoelectron spectroscopy a number of primary features are desirable. The most important of these are: (a) high energy resolution (approximately 1 part in 10^4) for electron energies in the range 1 to 2 000 eV, (b) high overall electron collection efficiency, as defined by the fraction of electrons leaving the source which can be energy-analyzed and detected simultaneously, (c) unrestricted physical access to the source and detector areas, so as to be compatible with a variety of sample arrangements (heated or cooled solids, gases, reaction chambers, etc.) and radiation sources (e.g., x ray or uv) as well as complicated detector systems, (d) possibility of ultrahigh-vacuum operation in the source area for control of surface conditions in work with solids, and (e) relative simplicity of construction. We have carried out a computer design study of an iron-free double-focusing magnetic spectrometer in which the above features were considered as design objectives.[6, 7] Previous experience has shown that, with careful construction, such studies provide results that agree excellently with experimental performance.[8, 9]

Energy analysis in such a double-focusing spectrometer is accomplished by magnetically deflecting the electrons in roughly circular orbits centered on the symmetry axis of a cylindrically symmetric field. This magnetic field, which decreases approximately as $1/\sqrt{r}$ near the optic circle of the instrument, has the property that electrons with both axial and radial departure angles are focused to first order at the same distance around the optic circle (corresponding to $\pi\sqrt{2}$ radians $\approx$ 254 deg). We treat here the "high aperture" field wherein axial departure angles can be larger than radial departure angles (a higher-order focusing property).[7] A further property of the high-aperture field is that it possesses a focal plane;[8, 10] that is, electrons of different energies are brought to a focus at different radii along a plane at $\pi\sqrt{2}$. Therefore, more than one energy (channel) can be detected at a time without significant loss of resolution and the overall collection efficiency thereby increased. Due to detector limitations it has been practical in the past to exploit the focal-plane properties of double-focusing electron spectrometers to the extent of only four- to five-channel detection.[3] However, we look forward to the development of detector arrays with the order of several hundred channels in the near future.[11]

The basic design problem is to find a set of cylindrically symmetric coils that reproduces the chosen theoretical field with sufficient accuracy over the region occupied by the electron orbits to give the desired focusing properties.[12] We note several features of this work that differ significantly from previous design studies: (a) the theoretical "optimum" field[10] was fitted over a region corresponding to much higher axial departure angles, in order to achieve a larger usable solid angle, (b) the locations of all coils were constrained to be entirely inside (i.e., at smaller radius than) the vacuum chamber housing the electron orbits, so as to permit good access to source and detector areas, and (c) the focal-plane properties of several theoretical fields, of existing spectrometers, and of our own design were studied in detail to determine relative overall collection efficiencies with multichannel detection.

The coil geometry of a typical design case, shown in Fig. 1(a), consists of one main coil with four pairs of smaller coils wound on it.[6] Coil dimensions are consistent with integral numbers of turns of fixed-diameter wire, and all coils are in series so that only one power supply is needed. With the choice of 30 cm for the optic circle radius, the height of the main coil is approximately 200 cm and its outer radius is 20 cm. Our calculations indicate that coil winding and positioning need only be done to reasonable tolerances (± 0.025 cm). For operation at energies up to 2000 eV, no cooling of the coils should be required. An important feature of this design is that vacuum chambers can be easily interchanged for different types of experiments.

The electron optical properties of this design have been calculated in terms of contours of equal focusing aberration of monoenergetic electrons in the plane of radial and axial depature angles.[7] The optimum field exhibits only negative aberration (electrons at angle $\pi\sqrt{2}$ fall at smaller radius than the optic circle radius), but in most real designs the effective solid angle is determined by how high a vertical departure angle one can use before unacceptably high positive aberrations are encountered. Our design case has a vertical acceptance window for operation at 0.02% energy resolution of approximately ± 17 deg, compared with ± 22 deg for the theoretical optimum field, ± 14 deg for the $1/\sqrt{r}$ field, ± 9 deg for the Chalk River spectrometer (four pairs of coils),[8] and ± 3 deg for a recent Uppsala spectrometer (two pairs of coils).[9]

In the single-channel mode of operation (detection of one narrow electron energy interval at a time) the relative collection efficiency of a spectrometer is proportional to the fractional solid angle into which electrons can be emitted without exceeding the desired resolution because of focusing aberrations. This solid angle is in practice controlled by baffles. In Fig. 1(b) we show resolution–fractional-solid-angle curves for the two primary theoretical fields for the two previously mentioned spectrometers, and for our design case. The present design approaches theoretical optimum performance much more closely than the existing spectrometers, and is better in performance than the $1/\sqrt{r}$ field.

We have also studied the focal-plane behavior of the cases in Fig. 1(b). In general, it is found that as the range of energies analyzed increases (that is, as the radial width of the detector increases), it is necessary to decrease the vertical acceptance angle of the common electron baffle to avoid introducing significant line broadening at the edges of the detector. The radial acceptance angle of the baffle, on the other hand, can be kept roughly constant. Furthermore, the distance of the baffle from the electron source must be decreased as the range of energies is increased in order to accurately discriminate all particles on the basis of departure angles. Where comparison with previous focal plane studies[8,9] is possible, the agreement is good.

The overall collection efficiency for multichannel operation will be proportional to the fractional solid angle times the number of channels in the detector. A channel width is defined to be the width of the image of a monoenergetic beam of electrons on the optic circle at $\pi\sqrt{2}$. Efficiency estimates were made on the basis of a multichannel detector centered on the optic circle. In Fig. 2 we plot the relative overall collection efficiencies of the design cases of Fig. 1, of 0.02% energy resolution, as a function of detector width (expressed as ΔE = detection bandwidth in % of mean energy). From these curves it is clear that data-accumulation rates can be increased by at least two orders of magnitude if multichannel detection is fully exploited. Our design case is essentially equivalent to theoretical optimum, and is approximately twice as efficient as the Chalk River spectrometer[8] up to $\Delta E \approx 8\%$. It also represents a marked improvement over the Uppsala spectrometer,[9] especially for $\Delta E > \approx 4\%$. We also note that for multichannel operation at $\Delta E > \approx 2\%$, the $1/\sqrt{r}$ field gives superior performance to the theoretical optimum field; this behavior was qualitatively predicted by Lee-Whiting and Taylor.[10]

We gratefully acknowledge the assistance of R. N. Healey, J. S. Colonias, S. J. Sackett, and B. R. Burkhart in the preparation of computer programs.

Footnote and References

†Appl. Phys. Letters 15, 223 (1969).

1. C. S. Fadley, S. B. M. Hagström, M. P. Klein, and D. A. Shirley, J. Chem. Phys. 48, 3779 (1968).
2. J. M. Hollander, D. N. Hendrickson, and W. L. Jolly, J. Chem. Phys. 49, 3315 (1968).
3. K. Siegbahn et al., Electron Spectroscopy for Chemical Analysis - Atomic, Molecular, and Solid State Structure Studies by Means of Electron Spectroscopy (Almqvist and Wiksells AB, Stockholm, Sweden, 1967).
4. D. W. Turner, in Physical Methods in Advanced Inorganic Chemistry, edited by M. A. O. Hill and P. Day (Interscience Publishers, Inc., London, 1968), Chap. 3.
5. W. E. Spicer and R. C. Eden, in Proceedings of the International Conference on the Physics of Semiconductors, Moscow, 1968 (Nauka, Leningrad, 1968), Vol. 1, p. 65.
6. A detailed account of this study is now in preparation.
7. For a review of work up to 1965 on this type of spectrometer see K. Seigbahn, in Alpha-, Beta-, and Gamma-Ray Spectroscopy, edited by K. Siegbahn (North-Holland Publishing Co., Amsterdam, 1965), Chap. 3.
8. R. L. Graham, G. T. Ewan, and J. S. Geiger, Nucl. Instr. Methods 9, 245 (1960).

9. C. Besev et al., Nucl. Instr. Methods 62, 125 (1968).
10. G. E. Lee-Whiting and E. A. Taylor, Can. J. Phys. 35, 1 (1957).
11. Bundles of glass channel electron multipliers represent one possibility in this area. See, for example, W. C. Wiley and C. F. Hendee, IRE Trans. Nucl. Sci. NS-9 103 (1962), and J. Adams and B. W. Manley, Philips Tech. Rev. 28, 156 (1967).
12. B. Castman, T. Groth, B. Olsen, and G. Pettersson, Uppsala University Institute of Physics Report No. UUIP-585, Uppsala, Sweden.

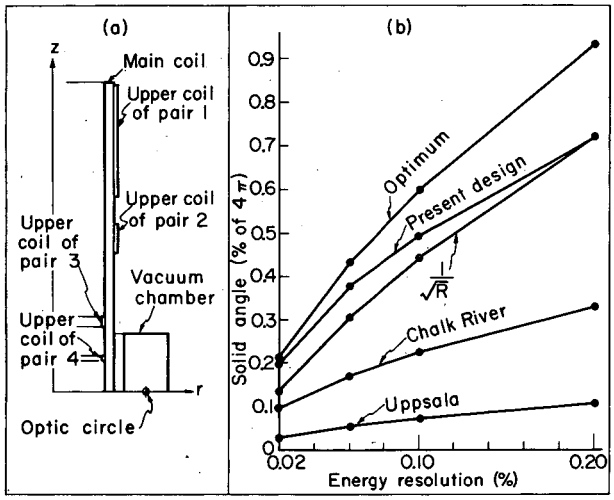

Fig. 1. (a) Coil geometry for the proposed spectrometer design. Only one quadrant of cross section is shown.
(b) Fractional solid angle of acceptance plotted against resolution for various theoretical fields and spectrometers. (Single-channel detection.) (XBL698-3331)

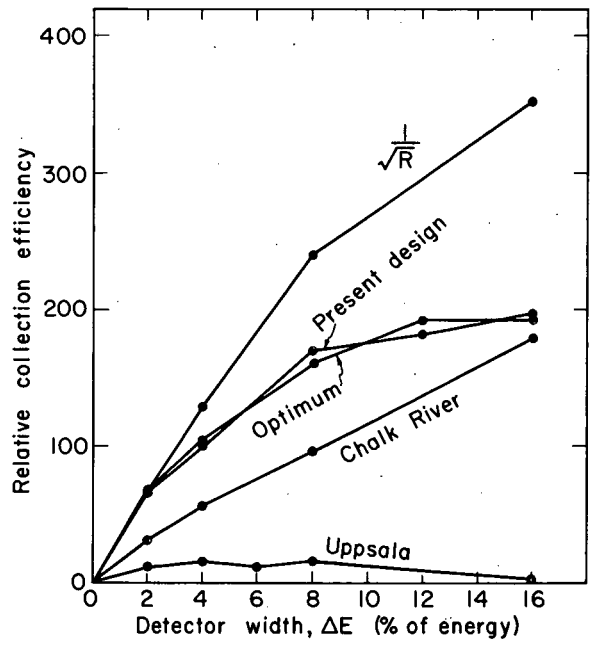

Fig. 2. Relative collection efficiency for multi-channel detection at 0.02% energy resolution plotted against width of detector array in % of mean kinetic energy. All values divided by the theoretical optimum efficiency for single-channel detection. (XBL698-3330)

COMPUTER CONTROL SYSTEM FOR THE FIELD-FREE SPECTROMETER

Joseph E. Katz

A computer control system that utilizes a Digital Equipment Corporation PDP-8 computer has been in operation over the past year. The computer control system is used to collect and display data as well as to control the operation of the field-free spectrometer. Many experiments have been performed on an around-the-clock basis with a high degree of reliability; more than 7 000 hours of operation have been logged during the past year.

The reliability of the system has been increased by utilizing solid-state power controllers in many of the peripheral devices. In particular, the mean time between failures of the ASR 33 teletype has been significantly increased by not running the drive motor needlessly.

Another significant improvement in the computer system has been the addition of a hardware bootstrap loader. Users of small computer systems are well aware of the inconvenience and frustration in having to repeatedly key in the bootstrap loader while testing or loading programs. The hardware bootstrap loader used is based on a design described by Morgan.[1]

Reference

1. G. B. Morgan, A Hardware Bootstrap Loader for the PDP-8 Series Computers, Nucl. Instr. Methods 74, 165 (1969).

COMPUTER ANALYSIS OF SPECTRA†

C. M. Lederer

Recent work on the analysis of multichannel spectra is reviewed, with emphasis on assessing the level of accuracy attainable in the determination of energies and intensities. A major portion of the review deals with the fundamental process of peak shape fitting of single and complex peaks. As an example Fig. 1 shows some fits to a single peak with two different types of peak shapes. Figure 2 shows the accuracy with which a doublet can be resolved when these shapes are used. From the analysis of results such as these and calibration procedures, it is concluded that γ-ray energies can generally be determined to a few eV.

Techniques for automated analysis, including peak-finding methods, are reviewed less critically, and examples of three different programs in current use at Berkeley are given. The complete review was published in Hamilton's book.

Footnote

†Condensed from a contribution to J. Hamilton, Radioactivity in Nuclear Spectroscopy (Gordon and Breach, New York, 1970).

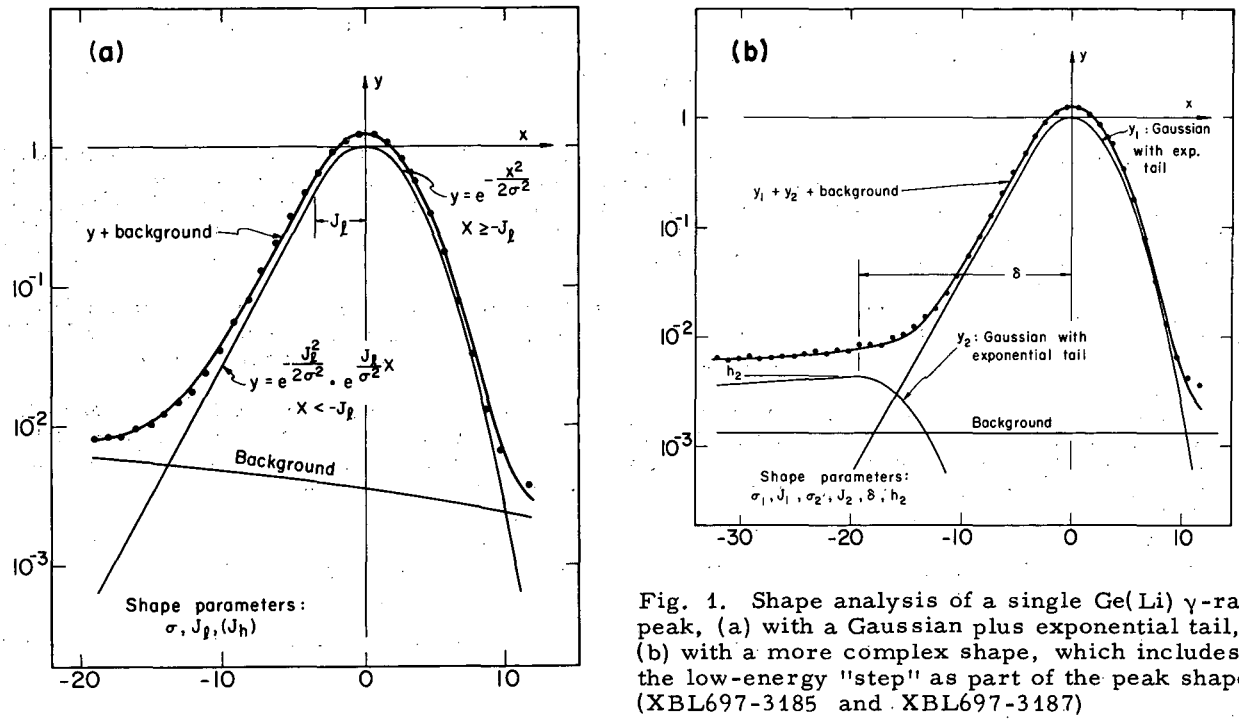

Fig. 1. Shape analysis of a single Ge(Li) γ-ray peak, (a) with a Gaussian plus exponential tail, (b) with a more complex shape, which includes the low-energy "step" as part of the peak shape. (XBL697-3185 and XBL697-3187)

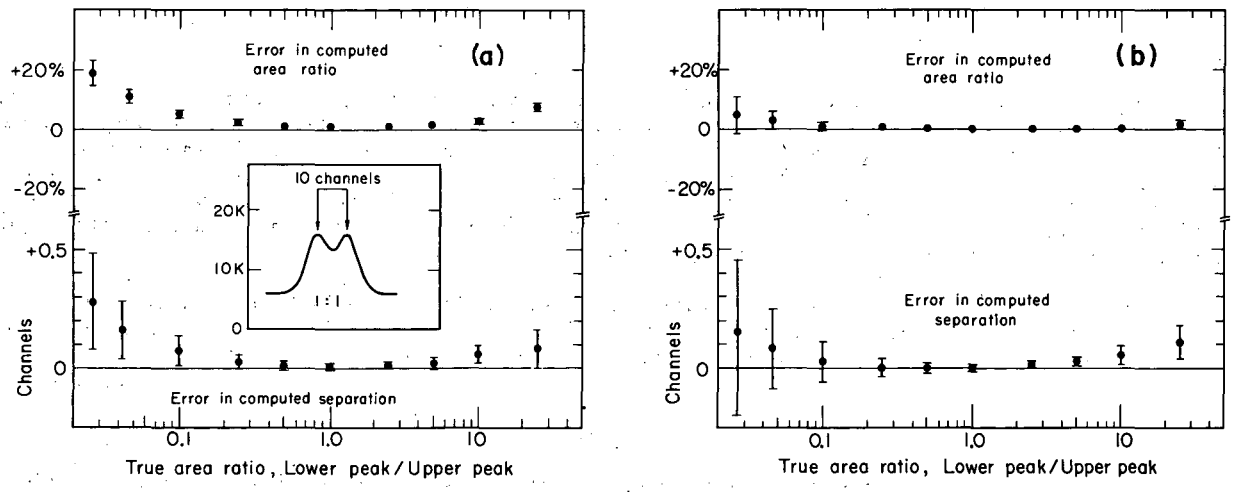

Fig. 2. Analysis of a doublet synthesized by displacing and adding spectra. The peak separation is 1.86 times FWHM. (a) With peak shape 1(a), (b) with peak shape 1(b). (XBL697-3190 and XBL697-3191)

SOME USES OF DIGITAL POLAROGRAPHY

Ray G. Clem and W. W. Goldsworthy

The general-purpose electrochemical instrumentation here presented is digital, and, since it is modular, permits the performance of a variety of electrochemical methods of analysis in keeping with the nonroutine nature of our analytical work by simple changes in the interconnections of the modules. The fact that the data are recorded in a 1024-channel pulse-height analyzer (PHA), equipped with a data processor (DP), allows some arithmetic manipulation of the stored data. Important advantages accrue.

Coulometry

A potentiostat is used in conjunction with a current amplifier and a digital current integrator to perform constant-potential or constant-current coulometric analyses. Coulombs consumed in an oxidation or reduction at constant potential can be displayed on a scaler. A rate-meter is used to gate the scaler off at a preselected counting rate (current level). Alternatively, the coulometric data can be gated by a flip-flop between two scalers at equal, preselected time intervals by a pulse obtained from the time-base oscillator (TIBO). Either way, the operator is freed from attending the instrument during the analysis. Sufficient data are accumulated to permit calculation of the titration end point with a small desk computer in considerably less time than that necessary for the complete electroreduction or oxidation.

During the development or evaluation of a coulometric procedure, it is oftentimes helpful to have a log current-time display of the current decay curve. This display is readily obtained by storing the digital data in a PHA, using the TIBO to provide a channel advance signal at preselected time intervals. The DP gives a five-cycle log display and, if the data are stored in the first half of the memory, allows one to determine the linear region of the decay curve and to integrate selected channel regions for the calculation or direct determination of the end point. This log-display approach also allows one to deal, in some cases, with interferring substances coreduced with the ion of interest (Fig. 1).

Polarography

In addition to the instrumentation used in the preceding section, a multifunctional ramp generator, a digital differentiator, a drop sensor, a wait gate, and an interface to a PHA are required to do polarography. Unlike analogue instruments, ours does not require the use of a drop time controller, a residual current compensator, an active differentiator, or signal filters; however, it does embrace some of the fundamental features of existing instruments. Our instrument uses an incrementing-voltage scan; the increment is applied at the beginning of the drop. The sample gate width and wait interval are freely variable from about 1 msec to 1.8 sec. We have the ability to store digital information in a PHA and to do some data processing as described earlier. The stored data are not a measure of the instantaneous cell current, as with some other methods, but rather a digital current-time integral which amounts to signal averaging on each drop. Also the measuring devices used--the current amplifier, the digital current integrator, and the wait gate--are all precise to 0.05% or less.

Table I indicates the sensitivity and precision obtainable using different time slices of a drop. Generally one uses a 1-sec drop time, a wait interval of 450 to 500 msec, and a gating interval of 400 msec, provided maxima are absent. The high reproducibility for both the signal and background, coupled with an ability to subtract background, results in a high difference sensitivity. Thus we are able to detect the reduction of Cd^{2+} at $< 10^{-8}$ M levels. Table II shows the reproducibility obtainable on consecutive sweeps.

The phenomena of maxima have long plagued the field of classical polarography at the dropping mercury electrode (DME). Explanations for their existence are various and measures to contend with them have long been used.[2,3] An examination of a scope trace of the current-time behavior of a mercury drop in the maximum potential region revels normal behavior at the beginning of the drop, but rapid current increase and finally erratic behavior as the drop nears completion (Fig. 2). Gating in the region of erratic current gives a polarogram with a pronounced maximum (Fig. 3A). Gating early in the drop life sacrifices some sensitivity, but yields a normal polarogram (Fig. 3B).

Possible Future Developments and Uses

Digital polarography is highly amenable to computerization. Some 30 to 40 cations and anions could be determined by this approach. If calibration sweeps, including background, were made for these cations and anions in several different supporting electrolytes and Ilkovic capillary transfer function ($m^{2/3} t^{1/6}$) were recorded, the task of analysis would be ameliorated. Also, interrogation of the computer's memory file of elements in different supporting electrolytes should result in the selection of the appropriate electrolyte, furnishing maximum separation of the half-wave potentials for complex mixtures of cations and anions. The computer's ability to do complex mathematics quickly, coupled with the high precision of digital data obtainable, should allow one to use kinetics as a practical approach to chemical analysis.

The digital instrument is called polarograph only because we use a potentiostat and work with electrochemical cells. If the equipment were connected to a spectrophotometer, for example, it could be used for colorimetry, flame emission, or atomic absorption of fluorescence. Its ability to signal-average could greatly enhance the spectra of weakly absorbing compounds, thereby increasing sensitivity and precision.

References

1. L. Meites, Anal. Chem. 31, 1285 (1959)
2. V. A. Levich, Physicochemical Hydrodynamics (Prentice-Hall, Englewood Cliffs, New Jersey, 1962).
3. L. Meites, Polarographic Techniques, Second edition (Interscience, New York, 1965).

Table I. Gating effects on the signal-to-background ratio (1-sec drop time, 0.1 M KCl, 2 ppm Cd, E = -0.750 vs SCE, average for 50 drops).

Gate interval (% of drop life)	Counts		Signal bkgd	ppm Cd for signal/bkgd = 1
	Signal	Background		
90-98	1186 ± 1	89 ± 2	13.33	0.150
80-98	2505 ± 2	197 ± 1	12.72	0.157
70-98	3588 ± 3	284 ± 1	12.64	0.158
60-98	4671 ± 3	419 ± 1	11.15	0.179
50-98	5732 ± 7	529 ± 1	10.84	0.185
40-98	6667 ± 7	627 ± 1	10.63	0.188
ungated	11354 ± 42	1374 ± 18	8.26	0.242
90-99	1277 ± 5	118 ± 1	10.82	0.184
80-90	1266 ± 2	120 ± 1	10.55	0.189
70-80	1256 ± 2	121 ± 1	10.38	0.193
60-70	1254 ± 2	124 ± 1	10.11	0.198
50-60	1250 ± 2	127 ± 1	9.84	0.203
40-50	1246 ± 2	131 ± 1	9.51	0.210
30-40	1244 ± 2	137 ± 2	9.08	0.220
20-30	1245 ± 2	146 ± 2	8.53	0.234
10-20	1213 ± 2	163 ± 2	7.44	0.269
0-10	920 ± 2	216 ± 2	4.26	0.469

Table II. Reproducibility of consecutive sweep on the same solution. Polarograms obtained with triplicate runs on the same solution: 8.88×10^{-5} M Cd, 0.100 M KCl; total volume; 50 ml, gate, 400 msec, wait 450 msec; open-circuit drop time, 1.02 sec.

	Derivative			Integral		
Run	1	2	3	1	2	3
	642	660	658	29 699	29 693	29 654
	797	797	841	29 684	29 677	29 654
	980	1 015	1 024	29 685	29 673	29 635
	1 163	1 167	1 141	29 672	29 670	29 634
	1 283	1 273	1 273	29 679	29 663	29 635
	1 322	1 324	1 329	29 644	29 642	29 609
	1 292	1 283	1 285	29 657	29 650	29 586
	1 186	1 179	1 181	29 666	29 634	29 629
	1 032	1 028	1 002	29 593	29 627	29 598
	845	825	803	29 634	29 626	29 603
	667	651	662	29 624	29 616	29 594
Σ	11 209	11 202	11 199	326 237	326 171	325 861

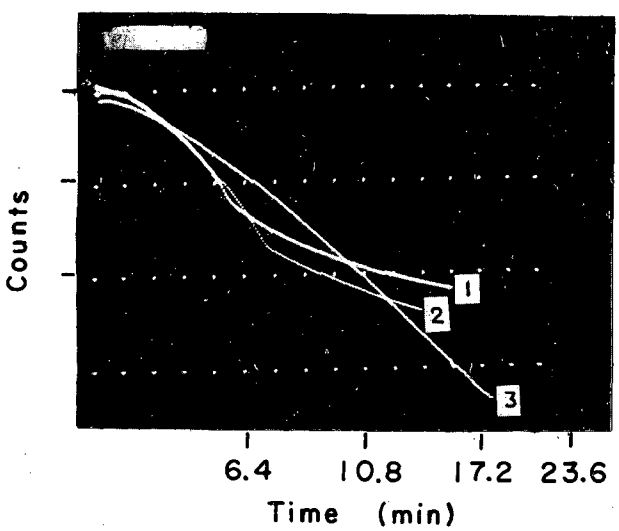

Fig. 1. Current-decay curves.
1. Reduction of 4 mg Pd^{4+} in the presence of 108 mg Pt^{4+}.
2. Reduction of 4 mg Pd^{4} in the presence of 54 mg Pt^{4+}.
3. Reduction of 4 mg Pd^{4+} alone.
End points of Pd^{4+} titration in curves 2 and 3 are found by locating the channel at the intersection of the extrapolated descending and horizontal branches and summing all preceding channels to this points.
Reaction:

$$Pd^{4+} + 2e^{-} \rightarrow Pd^{2+}$$
$$Pt^{4+} \rightarrow Pt^{2+} + 2e^{-}$$
$$Pt^{2+} + Pd^{4+} \rightarrow Pt^{4+} + Pd^{2+}$$

Supporting electrolyte: 0.05 M N_3^-, 0.24 M phosphate buffer, pH 6.85. (XBB702-673)

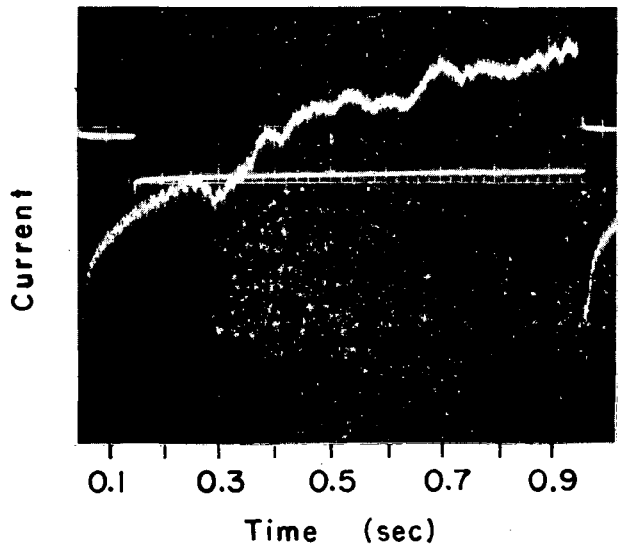

Fig. 2. Maximum phenomenon. Current-time curve of: 8.8 ppm Ni^{2+} in 1 M NH_3, 1 M NH_4Cl; E = -1.101 V vs. SCE.
(XBB702-670)

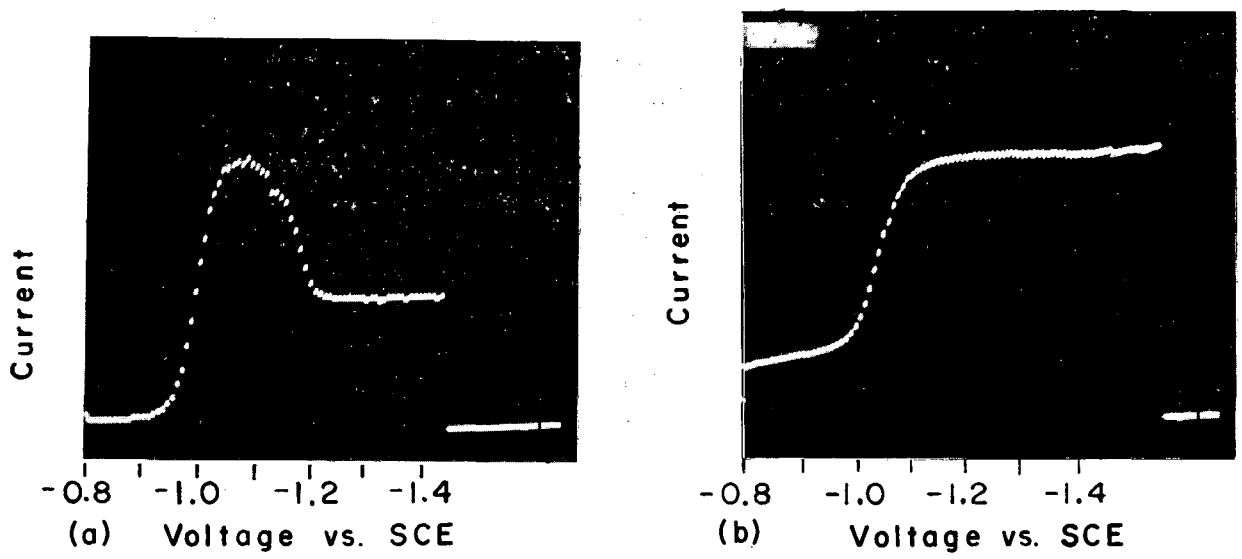

Fig. 3. Polarographs with and without a maximum.
a. Polarographic maximum present: wait, 580 msec; gate, 100 msec.
b. Polarographic maximum absent: wait, 3 msec; gate, 100 msec.
(XBB702-671 and XBB 702-672)

PREPARATION OF ISOTOPIC OXYGEN TARGETS FOR CHARGED-PARTICLE ACTIVATION ANALYSIS†

James F. Lamb,* Diana M. Lee, and Samuel S. Markowitz

A method has been developed for the preparation of oxygen comparison standards for charged-particle activation analysis, particularly for the use of ^{3}He as the activating particle, by anodic oxidation of tantalum foil. The isotopic composition of the oxide is varied by using isotopically enriched water in the electrolyte, which is 0.1% potassium chloride. The current passing through the cell is held constant at 40 mA while the voltage is allowed to vary. The thickness of the oxide film produced is a smooth function of time and is reproducible to within a few percent. Oxide films have been produced which vary in thickness from 0.5 mg/cm^2 for a 1-min anodization to more than 35 mg/cm^2 for an anodization time of 3 hours. The uniformity of the anodized foil and the oxygen content have been verified by ^{3}He activation analysis. Standards for activation analysis may be made by this method which reproduce any beam degradation in a sample from negligible energy loss to the complete stopping of a 10-MeV ^{3}He beam. These standards have been used for isotopic oxygen analysis of several materials and for measuring excitation functions for the production of ^{19}O and ^{20}F from ^{18}O and for production of ^{18}F, ^{15}O, ^{11}C, and ^{17}F plus ^{14}O from ^{16}O.

The apparatus used is shown in Fig. 1. The reasons for the rather interesting shape of the voltage curve in Fig. 2 and the mechanism of the process remain to be explored. The thickness of oxide coating as a function of plating time is shown in Fig. 3.

Footnotes

†Condensed from Anal. Chem. 42

*Present address: Biomedical Department, Donner Laboratory, University of California–Berkeley.

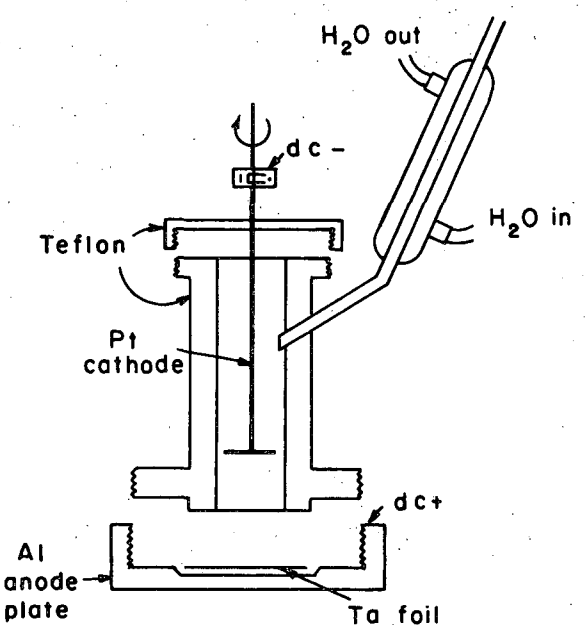

Fig. 1. Electrolytic cell for anodization of Ta foils at the electrolyte boiling point, ≈ 100°C. (XBL671-345)

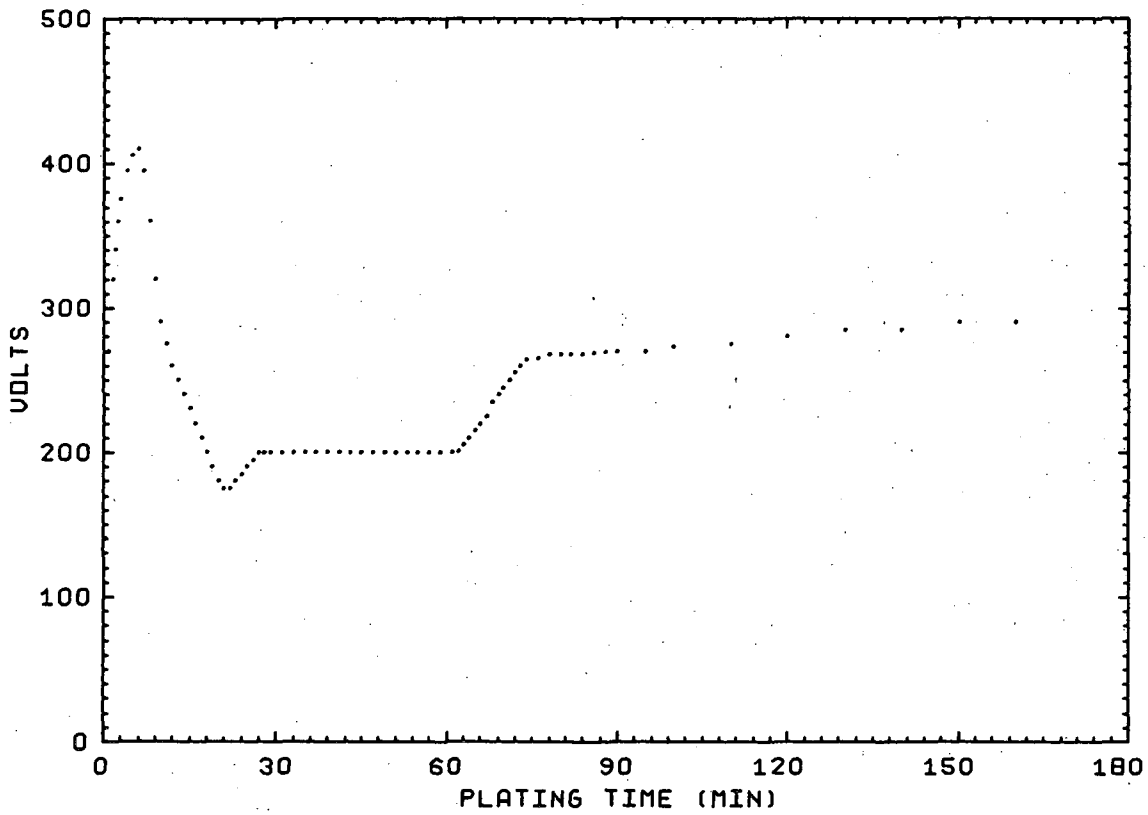

Fig. 2. Variation in the applied voltage during boiling-point anodization of Ta foil. Current = 40 mA, temperature ≈ 100°C. (XBL697-1032)

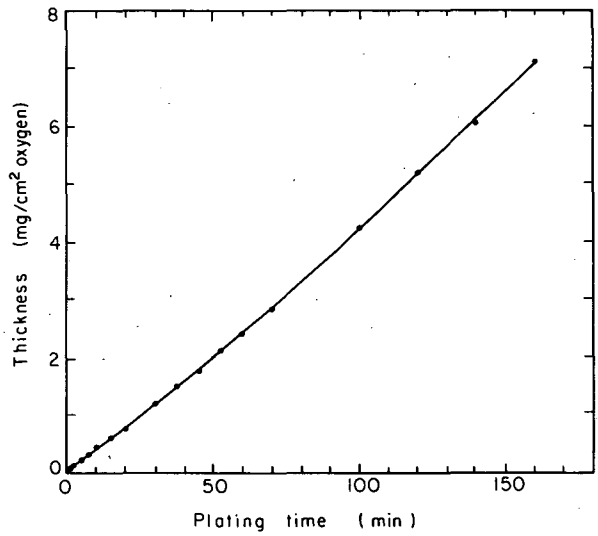

Fig. 3. Thickness of oxide coating produced by anodization of Ta foils in 0.1% KCl. Current = 40 mA, temperature ≈ 100°C. (XBL671-346)

V. Thesis Abstracts

On the following pages the abstracts of theses issued in 1968 are given as they appeared in the original documents.

CYCLING ZONE ADSORPTION SEPARATION BY THERMAL-WAVE PROPAGATION

Burke Baker III
(Ph. D. Thesis)

(From UCRL-18967)

It is demonstrated that proper utilization of the wave-propagational properties of fixed-bed adsorption systems can result in separation processes based on the imposed cyclic variation of certain intensive variables in the system. Mathematical and experimental evidence for this conclusion is presented, and a cyclic temperature-driven process based on this conclusion is proposed.

SPIN-LATTICE RELAXATION BY NUCLEAR MAGNETIC RESONANCE ON ORIENTED NUCLEI

John Arthur Barclay
(Ph. D. Thesis)

(From UCRL-18986)

Nuclear magnetic resonance was detected at 0.004 - 0.010° K by perturbation of the gamma-ray anisotropy of Co^{60} in Fe, Co, and Ni. Shirley's work on the response functions describing the perturbation in the presence of homogeneous broadening has been extended to include inhomogeneous broadening. The existence of a "hard core" value at resonance is demonstrated in this case also. Frequency modulation of the inhomogeneous line was necessary in order to perturb all of the spin packets in the broadened lines. The optimum conditions for frequency modulation were found by varying the modulation bandwidth and modulation frequency. A simple model was proposed to explain the observed degree of perturbation. In addition, nuclear spin-lattice relaxation times have been measured in the 0.004 - 0.010° K temperature range. Interpretation of the data was done by fitting the data with a sum of exponentials. Precise T_1 results are obtained but the accuracy was uncertain due to the uncertainty of the initial conditions.

I. THE $|\Delta K| = 1$ ELECTRIC DIPOLE TRANSITIONS IN ODD-MASS DEFORMED NUCLEI II. THE DECAY OF Ta^{176} TO LEVELS IN Hf^{176}

Frederick Michael Bernthal
(Ph. D. Thesis)

(From UCRL-18651)

In Part I we combine elements of the collective and single-particle nuclear models to provide a unified model interpretation of the $|\Delta K| = 1$ electric dipole transitions in odd-A deformed nuclei. Attention is focused on the uniquely informative set of E1 transitions in Hf^{177} that results from decay of the singular Lu^{177m} nucleus. We show that the influences of Coriolis coupling, pairing, and octupole vibration-particle coupling may be used to successfully account for the anomalous E1 transition rates in Hf^{177}, and by implication, in other odd-A deformed nuclei. Precise experimental data have been gathered for comparison with the theory.

In Part II we describe a detailed experimental study of the decay of Ta^{176} to levels in Hf^{176}. Numerous semiconductor detection systems have been employed in conjunction with an on-line PDP-7 data acquisition system to gather γ-ray singles, conversion electron, and γ-γ coincidence data on this remarkably complex decay. Over 300 transitions have been observed to follow the Ta^{176} decay, and some 140 of these have been placed in the proposed Hf^{176} level scheme. We compare the experimental data on levels in Hf^{176} with contemporary theoretical expectations.

We also call attention to the exceptional quantity and quality of information on nuclear properties that can now be expected from the timely marriage of semiconductor-detector and on-line computer technology. The techniques and problems associated with precision γ-ray spectroscopic data acquisition and analysis are discussed.

WEAK INTERACTION STUDIES BY NUCLEAR ORIENTATION

William D. Brewer
(Ph. D. Thesis)

(From UCRL-19533)

The technique of low temperature nuclear orientation has been applied to two problems involving weak nuclear decays. Nuclei of ^{119}Sb were polarized in an iron lattice and the angular distribution of inner bremsstrahlung photons emitted during the electron capture decay was observed. The distribution fit the correlation function $W(\theta) = 1 + A_1 G_1 P_1 (\cos\theta)$ and the asymmetry coefficient had the theoretical value of ± 1.0 near the spectrum endpoint. However, some energy dependence of A_1 was observed, in contrast to theoretical expectations. Possible origins of the energy dependence are discussed. Nuclear orientation was also carried out with three isotopes which under go 1st forbidden beta decays: ^{186}Re, ^{188}Re, and ^{194}Ir. The source nuclei were polarized in iron lattices and the angular distributions of both beta particles and gamma rays were observed. Lithium-drifted germanium counters were used to detect the beta particles. The beta particle angular distribution coefficients A_1 and A_2 are reported as functions of energy. The results are in general agreement with those of previous workers, although the experimental errors have been considerably reduced. The attenuation of the gamma ray anisotropies gives a measure of the relative size of the $\int B_{ij}$ matrix element in the preceeding $1^- \rightarrow 2^+$ beta decays and values for this attenuation are reported. The $\int B_{ij}$ matrix element was found to make a finite contribution in the decays of the two Re isotopes, but to be zero in the ^{194}Ir decay. The combined data may be used to determine the nuclear matrix elements entering the decays and to test the Conserved Vector Current hypothesis of weak interactions.

INTERFACIAL MIXING CELLS AND MASS TRANSFER IN TURBULENT FLOW

William H. Brown
(M. S. Thesis)

(From UCRL-18974)

The effect of a rippling interface upon surface tension-driven cellular convection was experimentally investigated by contacting ethyl ether in tridecane solvent with nitrogen, both phases flowing in a cocurrent, stratified manner. These experiments were conducted in a horizontal, rectangular duct with a high aspect ratio. Under laminar flow conditions in both phases, it is known for various systems that interfacial cellular convection caused by surface tension gradients will dramatically increase the liquid-phase mass-transfer coefficient. This type of cellular convection has been termed the Marangoni effect.

In order to determine the influence of interfacial rippling upon Marangoni cells the liquid volumetric flow rate was increased until the interface was visibly disturbed by wavelets. The individual liquid-phase mass-transfer coefficient was obtained from the experimental mass-transfer data by assuming that the gas-phase resistance to mass transfer was equal to that resistance measured in the absence of or suppression of resistance in the liquid phase. At low liquid mole fractions, the increase in the liquid-phase mass-transfer coefficient due to cellular motion was greater than for the corresponding laminar-flow results of Clark and King; hence, it appears that interfacial rippling enhances the formation of Marangoni cells and their resultant effect upon the mass-transfer coefficient. However at high values of the liquid mole fraction, the experimental liquid-phase mass-transfer coefficients were only one-third as large as those for the laminar-flow case, an unusual result considering only the difference in flow rates. Here, at high liquid mole fractions, interfacial rippling appears to have a severe dampening effect on the contribution of Marangoni cells to the liquid-phase mass-transfer coefficient.

THE (p, t) AND (p, ^{3}He) REACTIONS ON (2s-1d) SHELL NUCLEI

Heinz Brunnader
(Ph. D. Thesis)

(From UCRL-18716)

The excitations of high isospin (T = 2) analogue states in the $T_z = 0$ and the $T_z = +1$ A = 4n nuclei have been measured for the entire (sd) shell using the (p, t) and (p, ^{3}He) reactions induced by 45 MeV protons. Also the reactions ^{40}Ar(p, t)^{38}Ar and ^{40}Ar(p, ^{3}He)^{38}Cl were utilized to observe the first T = 3 analogue states in the $T_z = 1$ and $T_z = 2$ nuclei. In addition to these high T states, a number of T = 1 analogue states were also observed. The ratio of the observed cross sections for these T = 1 analogue states was compared with the ratio predicted from the DWBA cross section expressions. This predicted ratio is found to depend on the type of transition by which the final analogue states are formed, and hence may be used to provide structural information on the analogues without the use of detailed wave functions. The (p, t) reaction was further utilized to extend the range of known excitations in the nuclei ^{18}Ne and ^{34}Ar. All Coulomb displacement data in the (1p) and ($1d_{5/2}$) shells, including those derived from this work, were fitted to parameterized Coulomb displacement energy formulae derived in the jj-coupling low seniority and Wigner supermultiplet schemes. The results were used to predict the masses of yet unmeasured neutron deficient nuclei in this region.

MÖSSBAUER RESONANCE STUDIES OF GOLD COMPOUNDS

Marjorie O. Faltens
(Ph. D. Thesis)

(From UCRL-18706)

Mössbauer experiments were performed at liquid helium temperature on linear gold(I) compounds and square-planar gold(III) compounds. A linear relationship was established between the isomer shift and quadrupole splitting values for both the aurous and auric compounds. These results are explained in terms of the comparable electric field gradient values of the 5d and 6p electrons of gold and the differences in the ionic character of the compounds. The nuclear factor $\delta R/R$ for Au 197 was determined to be 3.1×10^{-4}. A scale was established to indicate the number of 6s electrons on gold which corresponds to a given isomer shift and the number of 6p electrons and 5d electron holes which are responsible for the observed quadrupole splittings.

AN X-RAY CRYSTALLOGRAPHIC STUDY OF CHLOROPHYLL ANALOGUES AND OTHER BIO-ORGANIC COMPOUNDS

Mark S. Fischer
(Ph. D. Thesis)

(From UCRL-19524)

The crystal and molecular structures of two analogues of chlorophyll have been determined by x-ray diffraction. The monohydrated dipyridinated magnesium phthalocyanin crystallizes in space group $P2_1/n$ with cell dimensions $\underline{a} = 17.098$ Å, $\underline{b} = 16.951$ Å, $\underline{c} = 12.449$ Å, and $\beta = 105.88^\circ$. All hydrogen atoms were located, and the final R-value is 0.050 for the 3323 independent non-zero reflections which were peak-counted on a diffractometer. The asymmetric unit contains one magnesium phthalocyanin molecule in which the magnesium atom is also coordinated to the oxygen atom of a water molecule. The hydrogens of the water molecule are hydrogen-bonded to two pyridine molecules of crystallization. The phthalocyanin ring deviates significantly from a plane, and the magnesium atom is 0.496 Å out of the plane of the inner nitrogen atoms and towards the water molecule. The biosynthesis and possible non-planarity of chlorophyll are discussed.

The chlorophyll derivative methyl pheophorbide $\underline{a}$ crystallizes in space group $P2_1$ with cell dimensions $\underline{a} = 8.035$ Å, $\underline{b} = 28.531$ Å, $\underline{c} = 7.320$ Å, and $\beta = 110.96^\circ$ and with two molecules in the unit cell. The final R-value is 0.051 for the 1616 independent non-zero reflections collected on a diffractometer. The inner hydrogen atoms are disordered. The Ring I vinyl and Ring V carbonyl groups are in conjugation with the nearly flat chlorin ring. There are no chlorin-chlorin intermolecular contacts less than 3.5 Å. We propose a detailed model for the arrangement of chlorophyll in photosynthetic lamellae, in which non-parallel chlorophyll molecules are related by a 2_1 screw axis and are linked by water molecules.

With the use of molecular orbital calculations, we predict a correlation between the phosphorescence energy of metalloporphyrins and the ionic radius of the central metal atom. This prediction is in agreement with data in the literature. Since the metallic ionic radius depends on its coordination geometry, we suggest that phosphorescence spectra of metalloporphyrins be used to infer the environment of the central metal atom.

Unsuccessful attempts to crystallize chlorophyll and a successful synthesis of zinc methyl chlorophyllide are described.

We have determined the structures of two choline chloride analogues in detail as well as listed space group information on the phosphonium analogue of choline chloride and on choline bromide. Betaine hydrochloride crystallizes in space group $P2_1/c$ with cell parameters $\underline{a} = 7.428$ Å, $\underline{b} = 9.108$ Å, $\underline{c} = 11.550$ Å, and $\beta = 96.71^\circ$ and with four molecules in the unit cell. The final R-value has been reduced to 0.026. The cation assumes a completely staggered conformation with the acidic hydrogen atom as far away as possible from the nitrogen atom. Because of space group difficulties, we present only an approximate structure of choline iodide. Iodide-choline interactions determine the packing arrangement. The configuration of the choline cation is nearly identical for choline chloride and choline iodide. The mechanism for the unique radiation sensitivity of choline chloride is discussed.

We have determined the crystal structure of 7-chloromercurinaphthalene-1-sulfonyl fluoride, a possible protein label, by x-ray diffraction. It crystallizes in space group $P2_1/m$ with the molecule lying in the mirror plane. The unit cell dimensions are $\underline{a} = 9.725$ Å, $\underline{b} = 6.836$ Å, $\underline{c} = 8.351$ Å, and $\beta = 90.99^\circ$, and there are two molecules in the unit cell. The conventional R-value is 0.027 for the 1055 independent data collected on a scanning counter diffractometer and corrected for acute absorption effects. The fluorine atom always lies near a hydrogen atom of the naphthalene ring.

We present space group data for triphenyl oxaziridine and N-(p-bromophenyl)-C, C-diphenyl-oxaziridine. A glossary of crystallographic terms is attached in the Appendix.

SOME MAGNETIC, SPECTROSCOPIC, AND CRYSTALLOGRAPHIC PROPERTIES OF BERKELIUM, CALIFORNIUM, AND EINSTEINIUM

Dennis Ken Fujita
(Ph. D. Thesis)

(From UCRL-19507)

The work reported here is part of a continuing study of the physical and chemical properties of the transcurium elements. During the course of these studies, ~100 μg ^{249}Bk, ~40 μg ^{249}Cf, and ~15 μg ^{253}Es were made available. Procedures for the purification, assay, and evaluation of sample purity are discussed in detail.

The experimental techniques used to study the magnetic susceptibilities of berkelium metal, Bk^{3+}, and Cf^{3+} are described. The susceptibilities of Bk^{3+} and Cf^{3+} follow the Curie-Weiss relationship with $\mu_{eff}(Bk^{3+}) = 9.40 \pm 0.06$ B. M. and $\mu_{eff}(Cf^{3+}) = 9.14 \pm 0.06$ B. M. Among three samples of berkelium metal both ferromagnetism and antiferromagnetism were detected at low temperature; at higher temperatures the susceptibilities follow the Curie-Weiss law. Effective magnetic moments derived from the high temperature data suggest that greater than three electrons per atom occupy bonding orbitals. The effective moment of the most pure Bk metal sample (8.83 B. M.) corresponds to a metallic valence of ~3.4.

A recently-developed, light-pipe microabsorption cell used to obtain the solution absorption spectra of Bk^{3+} and Es^{3+} in dilute HCl solutions is described. The confirmatory experiments have verified most of the previously-detected Bk^{3+} and Es^{3+} absorption peaks. Seven additional Bk^{3+} and 12 new Es^{3+} absorption bands are reported. The most intense Es^{3+} peaks are observed at 4225 Å and 4950 Å.

Techniques to prepare several ^{249}Bk, ^{249}Cf, and ^{253}Es compounds on the microgram scale are discussed. Standard x-ray diffraction powder methods are applied in the determinations of the crystal structures and lattice parameters of the Bk and Cf compounds. The extremely high specific radioactivity of ^{253}Es required the development of special techniques for the preparation and x-ray analysis of Es compounds.

Face-centered cubic Bk metal ($a = 4.987 \pm 0.001$ Å) is prepared by Li vapor reduction of BkF_3. Attempts to prepare Cf metal by similar reductions of CfF_3 with Li and K were unsuccessful due to the high vapor pressure of elemental Cf. CfF_3 samples exhibiting the orthorhombic YF_3-type structure ($a = 6.651 \pm 0.007$ Å, $b = 7.040 \pm 0.002$ Å, and $c = 4.393 \pm 0.004$ Å) are prepared. The monoclinic lattice constants of $CfBr_3 \cdot 6H_2O$ are $a = 9.992 \pm 0.053$ Å, $b = 6.716 \pm 0.025$ Å, $c = 8.146 \pm 0.006$ Å, and $\beta = 93.50 \pm 0.14$ Å. $CfBr_3$ crystallizes in a structure that remains uncharacterized; however, similar structure have been observed in $BkBr_3$ and $GdBr_3$. CfOBr and CfOI exhibit the tetragonal PbFCl-type structure. Lattice constants of CfOBr are $a = 3.900 \pm 0.003$ Å and $c = 8.110 \pm 0.007$ Å. CfOI lattice parameters are $a = 3.97 \pm 0.02$ Å and $c = 9.13 \pm 0.08$ Å. Thermal expansion coefficients for CfOCl are reported: $\alpha_a = (1.14 \pm 0.01) \times 10^{-5}\,^{\circ}C^{-1}$ and $\alpha_c = (1.85 \pm 0.03) \times 10^{-5}\,^{\circ}C^{-1}$. Our unsuccessful attempts to prepare $CfCl_2$ by hydrogen reduction of $CfCl_3$ contradict tracer experiments which have been interpreted as evidence for a moderately-stable +2 oxidation state of Cf.

The first compounds of ^{253}Es are reported. $EsCl_3$ exhibits the hexagonal UCl_3-type structure between 400 - 450° C; the lattice parameters corrected to 20° C are $a = 7.40 \pm 0.02$ Å and $c = 4.07 \pm 0.02$ Å. EsOCl crystallizes in the tetragonal PbFCl-type structure at 400 - 450° C. The lattice constants at 20° C are $a = 3.948 \pm 0.004$ Å and $c = 6.702 \pm 0.019$ Å.

T = 0 AND T = 1 PAIRING IN LIGHT NUCLEI

Alan L. Goodman
(Ph. D. Thesis)

(From UCRL-19514)

A generalized quasiparticle transformation is presented which includes n-n, p-p, and n-p (T = 0 and T = 1) pairing correlations. The quasiparticle co-ordinates are required to be complex. The resulting gap equations for N = Z even-even nuclei are solved for the nuclei in the sd shell. To permit interaction between the Hartree-Fock (HF) and pair potentials, the Hartree-Fock-Bogoliubov (HFB) equations, including both T = 0 and T = 1 pairing, are also solved for these nuclei.

Although T = 1 pairing correlations are not significant, T = 0 pairing correlations play a very important role, rectifying many of the failures of the HF theory in this region. T = 0 pairing restores axial symmetry to the equilibrium shapes of Mg^{24} and S^{32} and explains the vibrational nature of Ar^{36}. These conclusions are reproduced by the following nucleon-nucleon interactions: the Yale t-matrix (s-p-sd), the Nestor-Davies-Krieger-Baranger effective interaction (s-p-sd and s-p-sd-pf), and the Rosenfeld effective interaction (sd).

Evaluation of various approximations to HFB is facilitated by deriving the canonical form of the density matrix and the pairing tensor for generalized isospin pairing. The general quasiparticle transformation is equivalent to the product of three transformations: (1) an isospin-conserving rotation in particle space (canonical basis), (2) an isospin-generalized "special" quasiparticle transformation, (3) a rotation in quasiparticle space.

The canonical basis often bears no resemblance to the corresponding HF basis. The third transformation may not be approximated by the unit transformation, nor is the pair potential diagonal in the canonical basis. The BCS approximation of neglecting elements of the pair potential connecting different spatial orbitals is therefore unjustified. Iterating between the HF and the BCS equations in an attempt to permit both degrees of freedom to interact with one another is an even worse approximation to HFB than merely solving the BCS equations with the trivial HF basis.

The HFB equations are derived by a variational principle. The self-consistent symmetries of the HFB solutions are discussed. Usage of the same effective interaction in both the HF and the pair potential is justified.

DEVELOPMENT OF A JET-MIXED EXTRACTION COLUMN

Daniel R. Kahn
(M. S. Thesis)

(From UCRL-18679)

A jet-mixed extraction column has been developed which incorporates most advantages of existing column-type extractors, while eliminating the need for internal moving parts. The column was designed to provide high rates of mass transfer, with only normal or even decreased extents of unwanted longitudinal dispersion ("axial mixing"). A guide to some of the more important experimental studies involving longitudinal dispersion in various column-type extractors, and two theoretical models which describe the combined effect of mass transfer and longitudinal dispersion, are presented.

The concept of a jet-mixed column is discussed, and the apparatus employed in the present study is described. The column utilizes uniformly spaced, horizontal, tubular, jetting and intake rings at the inner and outer boundaries of an annular cross-section. At each level, both rings are perforated so as to promote nearly straight-line radial flow between the jetting and intake rings. Externally these rings are connected by way of a small centrifugal circulating pump.

Semiquantitative tests of the column in single-phase and two-phase operation have been made to study the effects of number, size, and position of the ring ports, compartment height, jetting circulation rate, and longitudinal flow rates, upon the vortex patterns, the extent of interception (desired) of the discontinuous phase, and the extent of colloidal dispersion (undesired) of discontinuous phase.

Further experimentation, involving a complete mass-transfer analysis using two different solvent-solute systems and a larger number of jet-mixed stages, is needed to complete the performance evaluation of this new design.

EPR-STUDIES OF TRIVALENT PLUTONIUM IN CaF_2, SrF_2, AND BaF_2

Heinz Friedrich Mollet
(M. S. Thesis)

(From UCRL-18922)

The electron paramagnetic resonance spectra (EPR) of the ground state of $^{239}Pu^{+3}$ in the three lattices CaF_2, SrF_2, and BaF_2 have been measured at helium temperatures at frequency $\nu \cong 9$ Gc/sec. The observed isotropic spectrum was fitted to a spin-Hamiltonian

$$H = g \beta \vec{\mathcal{H}} \cdot \vec{S'} + A\vec{I} \cdot \vec{S'}$$

with $S' = 1/2$, $I = 1/2$ and the spin Hamiltonian parameters:

Pu^{+3}/CaF_2	$\|g\| = 1.297 \pm 0.001$	$\|A\|/h[^{239}Pu] = 201 \pm 2$ Mc/sec
Pu^{+3}/SrF_2	$\|g\| = 1.250 \pm 0.003$	$\|A\|/h[^{239}Pu] = 253 \pm 3$ Mc/sec
Pu^{+3}/BaF_2	$\|g\| = 1.187 \pm 0.004$	$\|A\|/h[^{239}Pu] = 306 \pm 9$ Mc/sec

We have interpreted the measured g-values using the concepts of intermediate coupling and crystal field J-mixing.

The free ion ground state of $^{239}Pu^{+3}$ (electron configuration [Rn] $5f^5$) is a $J = 5/2$ state which splits into a doublet Γ_7 and a quartet Γ_8 in a cubic crystalline field. We have calculated $\beta_{5/2}$, the 4th-order operator equivalent factor using an intermediate coupling ground state wave function. This showed that $\beta_{5/2}$ is negative as required for the isotropic Γ_7 to be the ground state.

The observed g-values indicate that there is an appreciable amount of crystal field J-mixing. The calculated g-value for the Γ_7 doublet neglecting J-mixing is $|g| = 0.70$. The amount of J-mixing required to fit the experimental data was calculated including the next term ($J = 7/2$) which splits into a Γ_6, a Γ_7 and a Γ_8 state in a cubic crystal field. This in turn allows one to calculate the 4th-order crystal field parameter for a given ratio of B_6^0/B_4^0. Assuming $B_6^0/B_4^0 = -0.2$, we obtain

Pu^{+3}/CaF_2	$B_4^0 = -6300\ cm^{-1}$
Pu^{+3}/SrF_2	$B_4^0 = -5400\ cm^{-1}$
Pu^{+3}/BaF_2	$B_4^0 = -4500\ cm^{-1}$

The true values are most likely with $\pm 25\%$ of the values given.

For Pu^{+3}/CaF_2 and Pu^{+3}/SrF_2 the most intense EPR spectrum observed was due to Pu^{+3} in cubic sites, whereas, for Pu^{+3}/BaF_2 the cubic spectrum was always accompanied by a much stronger trigonal spectrum which was fitted to the spin Hamiltonian.

$$H = g_{\|}\beta H_z S'_z + g_{\perp}\beta (H_x S'_x + H_y S'_y) + A_{\|} I_z S'_x + A_{\perp} (I_x S'_x + I_y S'_y)$$

with $S' = 1/2$, $I = 1/2$ and the parameters

$\|g_{\perp}\| = 1.300 \pm 0.005$	$\|A_{\perp}\|/h = 678 \pm 8$ Mc/sec	$(A_{\perp}/g_{\perp}\beta = 372 \pm 4$ gauss)
$\|g_{\|}\| = 0.80 \pm 0.03$	$\|A_{\|}\|/h = 365 \pm 15$ Mc/sec	$(A_{\|}/g_{\|}\beta = 326 \pm 13$ gauss)

$A_{\perp}/g_{\perp}$ is not equal to $A_{\|}/g_{\|}$, which again indicates the importance of crystal field J-mixing.

CRYSTALLOGRAPHY AND THERMOCHEMISTRY OF SOME CHLOROCOMPLEX COMPOUNDS OF THE LANTHANIDE AND ACTINIDE ELEMENTS

Lester Robert Morss
(Ph. D. Thesis)

(From UCRL-18951)

Several complex compounds containing lanthanide and actinide (III) or (IV) ions in sixfold chloride coordination have been prepared in amounts ranging from several grams to one microgram. Preparative techniques for compounds Cs_2NaMCl_6 (M = trivalent cation) and Cs_2MCl_6 (M = tetravalent lanthanide or actinide cation) are discussed. Structures of these compounds have been studied by the X-ray powder method. All compounds Cs_2NaMCl_6 which have been prepared are face-centered cubic; the lattice parameter of $Cs_2NaBkCl_6$ is 10.805(3) Å. The synthesis and chemical analysis of a new compound of Bk(IV), Cs_2BkCl_6, are described; this compound is hexagonal, with $a = 7.450(3)$, $c = 12.098(5)$ Å. (Error limits represent 95% confidence.)

The principles of design and the experimental operation of some solution microcalorimeters are described. The most versatile microcalorimeter has a capacity of 30 ml, a thermal leakage modulus of 0.0009^{min-1}, and a sensitivity of 2×10^{-4} cal. Heats of solution of standard substances of lanthanide and actinide metals, and of compounds Cs_2NaMCl_6, are reported.

The crystallographic and thermochemical measurements on chlorocomplex compounds have been combined with auxiliary data to yield heats of formation of lanthanide and actinide chlorides, chlorocomplex compounds, and ions; redox potentials for lanthanide and actinide species; ionization potentials for several lanthanide and actinide ions; hydration energies for lanthanide and actinide (II) and (III) ions; and a set of ionic radii based upon sixfold chloride coordination. Comparative stabilities and crystal structures of chlorocomplex compounds are discussed and systematized.

IN-BEAM PROTON-GAMMA RAY COINCIDENCE STUDIES USING A LARGE COAXIAL Ge(Li) DETECTOR

Joel M. Moss
(Ph. D. Thesis)

(From UCRL-18902)

Two different applications were made of particle-gamma ray coincidence techniques: first, in the $^{54}Fe(p, p')^{54}Fe$ reaction at 10 MeV and then, in the reactions $^{54, 56}Fe(p, p')^{54, 56}Fe$ at 19.6 MeV. In both experiments a large coaxial Ge(Li) counter was used to detect the gamma rays.

In the $^{54}Fe(p, p')^{54}Fe$ reaction at 10 MeV, the angular correlation of gamma rays coincident with protons detected near 180^{o} was measured. On the basis of this information, unambiguous spin assignments were made to the 3.345(3), 4.074(2), 4.781(3), and 4.949(4) MeV states. Model-dependent assignments and spin limitations were made for several other states. The angular correlation analysis also yielded multipole mixing ratios for several transitions and branching ratios for the decay of all states of ^{54}Fe below 5 MeV. From an analysis of the observed Doppler shifts of the coincident gamma rays, mean lifetimes were derived for the 1.409, 2.959, 3.164, 3.836, 4.048, 4.074, 4.265, 4.287, 4.781, and 4.949 MeV states.

Coincident gamma rays perpendicular to the reaction plane, as a function of proton scattering angle, were observed in the reactions $^{54, 56}Fe(p, p')^{54, 56}Fe$ at 19.6 MeV. Analysis of these data yielded angular distributions of the spin-flip probability in the inelastic excitation of the first 2^{+} states in both nuclei. The spin-flip probabilities were compared to the predictions of both the collective and microscopic models of inelastic proton scattering. Also included in the theoretical analysis were high precision differential cross section measurements made here, and inelastic asymmetry data from Saclay.

THE DESIGN OF AN IMPROVED DEVICE FOR ABSORPTION WITH CHEMICAL REACTION

Edward J. Palkot, Jr.
(M. S. Thesis)

(From UCRL-18918)

When absorption is accompanied by chemical reaction in the liquid phase, the nature of the gas-liquid equilibrium data is often such that a high degree of gas purification may be accomplished in one or a very few equilibrium stages. Examples of such absorption systems that were considered in this study are the scrubbing of CO_2 from gas streams using hot, catalyzed potassium carbonate and the scrubbing of HCl from gas streams using water. The scrubbing of CO_2 is important in the manufacture of high purity hydrogen for process uses such as the manufacture of ammonia, and HCl absorption is important in many processes, including a scheme for the reprocessing of enriched reactor fuels which has been considered by the AEC. Less commonly used devices for carrying out these absorption processes were considered which had features likely to result in high absorption rates and, consequently, high efficiency. The implementation of devices with these characteristics might be expected to result in considerable savings in investment and/or operating costs when compared to equipment currently used to effect the desired gas purifications.

The devices considered were the co-current packed column, open pipe contractors with co-current flow of gas and liquid in the froth and annular regimes, and the spray tower. Based on information dealing with these devices in the literature and models which were proposed to fill gaps in the literature, device sizes necessary to scrub gases of quantities and compositions likely to be encountered in industry were calculated. Hierarchies of attractiveness of the devices for each of the systems studied were determined by assigning relevant cost variables to each contractor. It was shown that some of the devices could well be attractive in reducing the costs of absorption in the processes considered.

FOAM FRACTIONATION OF RARE-EARTH ELEMENTS

George H. Robertson
(Ph. D. Thesis)

(From UCRL-19525)

The foam fractionation of rare-earth elements Nd, Sm, and Ce by extraction of their EDTA chelates with a cationic surfactant, and the foam fractionation of an anionic surfactant were studied. The objective was to determine the usefulness of the foaming technique in fine separations and to examine quantitatively the properties of transient foaming in producing the separation.

The model of "persistent" foaming did not apply to most of the foaming conditions which were found in this study to favor foam formation, extraction, and fractionation. Therefore, a two-property classification was adopted; the type being determined by the persistence or transience of surface area, and the mode by the constancy or depletion of specific liquid content with foam height or age.

In a preliminary study, fixed-height foaming from aqueous solutions of an anionic surfactant (Aerosol 22) was used to evaluate the effect of gas rate on the relative transiency and separation performance. Foaming of Aerosol 22 in a transient regime of gas rates yielded the best enrichments and extraction. The foam liquid fraction was proportional to the 0.20 power of the gas velocity in the transient regime and to the 0.71 power in the persistent regime.

No previous foam fractionation between rare-earth elements has been reported. For rare-earth separation, separate cationic surfactant (Hyamine 1622) and chelating agent (EDTA) were employed to obtain good foaming and extraction as well as selectivity. Experimental studies were made of solution variables (surfactant concentration, EDTA concentration, total rare-earth concentration) and of physical variables (foam height and column packings) on the relative foam stability, total rare-earth enrichment, separation factor, extraction rate, and foam liquid content.

Transient foaming for rare-earth separations was observed for all concentrations of surfactant tested; transiency increased as the surfactant concentration decreased. Enrichments of rare earth were best for the most transient foaming (lowest surfactant concentration). Separation factor (1.9 for Nd/Ce and 3.1 for Sm/Ce) was invariant above 17 cm and decreased sharply to 1.0 below 17 cm. Extraction, constant above 17 cm, was best in the most transient foams.

TEMPERATURE DEPENDENCE OF THE HYPERFINE INTERACTION IN DILUTE NICKEL ALLOYS USING GAMMA-GAMMA PERTURBED ANGULAR CORRELATION

Stephen Saul Rosenblum
(Ph. D. Thesis)

(From UCRL-18675)

Perturbed angular correlation studies of temperature-dependent hyperfine fields at ^{111}Cd, ^{99}Ru, and ^{100}Rh solutes in nickel above and below the Curie point are presented. For ^{111}Cd$\underline{\text{Ni}}$ it is found that the hyperfine field is proportional to the lattice magnetization over the entire range of temperatures studied. For ^{99}Ru$\underline{\text{Ni}}$ this is not the case, and a molecular field model is described which accounts for this behavior by postulating a local moment on the ruthenium atom. For ^{100}Rh$\underline{\text{Ni}}$ all data was taken for $T_c \lesssim T \leq 1.2\ T_c$ and the hyperfine field was found to be proportional to the lattice magnetization. In addition, a time dependent interaction is seen in this case, which is accounted for by a model based on the exchange-narrowing of a broadened Zeeman transition. Angular-correlation apparatus capable of 0.1% accuracy and a furnace capable of $\pm 0.5^{\circ}$C stability over 24 hours for use with this apparatus are also described.

THE INFLUENCE OF SURFACE TURBULENCE AND SURFACTANTS ON GAS TRANSPORT THROUGH LIQUID INTERFACES

Thomas G. Springer
(Ph. D. Thesis)

(From UCRL-18995)

An apparatus called an interface impedance bridge is described for the observation of the resistance to passage of a soluble gas through a gas-liquid interface under dynamic conditions. The apparatus resembles an electrical a. c. bridge circuit and permits measurements to be made over a range of frequencies.

The interface impedance bridge is used to measure passage of a soluble gas through a gas-liquid interface under varying conditions. Measurements over a range of frequencies of gas pressure oscillations allowed one to test interface mass transfer mechanisms, including the effects of soluble and insoluble surfactants on both stagnant and turbulent liquid surfaces.

Analysis of the turbulent interface of a clean liquid shows that a Danckwerts type distribution function of surface ages may be used to describe the statistical characteristics of the interface under the conditions of these experiments.

Addition of a soluble surfactant to the liquid produced no measurable change in the mass transfer rate through a stagnant gas-liquid interface, but reduced the intensity of turbulence at the interface when the liquid was stirred from beneath. It was found that the statistical nature of the interface could still be described reasonably well with the Danckwerts random distribution function.

Placement of an insoluble surfactant on the surface of a clean stagnant surface reduced the mass transfer rate of soluble gas through it. The film resistance was found to be a function of the surface concentration. The film resistance was found to be a function of the surfactant's surface concentration. An insoluble surfactant had no effect on the mass transfer rate when the liquid was stirred from beneath.

The nature of surface films and their stability in the presence of interfacial turbulence is discussed.

METALLOCARBORANE STRUCTURE INVESTIGATION BY SINGLE-CRYSTAL X-RAY ANALYSIS

David John St. Clair
(Ph. D. Thesis)

(From UCRL-18910)

The solid state structures of four two-carbon metallocarboranes have been determined by analysis of the X-ray diffraction patterns from single-crystals of $(C_2H_5)_4NCo(B_7C_2H_9)_2$, $CsCr\left[B_9C_2H_9(CH_3)_2\right]_2 \cdot H_2O$, $Ni(B_9C_2H_{11})_2$, and $Cs_2(B_9C_2H_{11})Co(B_8C_2H_{10})Co(B_9C_2H_{11}) \cdot H_2O$.

Crystals of the salt, $(C_2H_5)_4NCo(B_7C_2H_9)_2$, are tetragonal, space group P4/n, with $\underline{a} = 16.556$ Å and $\underline{c} = 8.580$ Å. There are four molecules in the unit cell and the calculated density is $\rho = 1.15$ g/cc. Using the 926 independent X-ray intensity data collected by counter methods and the point counting technique, the structure was refined by least squares to a conventional $\underline{R}$ value of 9.6%. The anion, $Co(B_7C_2H_9)_2^-$, has the shape of two distorted bicapped square antiprisms which have one corner in common. This shared corner is occupied by the cobalt atom which lies on a crystallographic inversion center. The point symmetry of the anion is 2/m (C_{2h}). Half of the $(C_2H_5)_4N^+$ ions lie on special positions having 4-fold rotational point symmetry and are disordered. One of the carbons in each B_7C_2 fragment was located at an apex position but the other appeared to be disordered between two positions. Very anisotropic thermal parameters were found for most of the atoms. This result may be attributed in part to effects of the disorder, especially among the atoms in the B_7C_2 fragments.

Crystals of the hydrated salt, $CsCr\left[B_9C_2H_9(CH_3)_2\right]_2 \cdot H_2O$, are tetragonal, space group $P4_12_12$, with $\underline{a} = 9.938$ Å and $\underline{c} = 22.739$ Å and with four molecules in the unit cell. The calculated density is $\rho = 1.55$ g/cc. For 1957 independent reflections measured by counter methods and the θ-2θ scan technique, the model was refined by least squares to a conventional $\underline{R}$ value of 4.7%. The metallocarborane anion consists of two icosahedra linked by a chromium atom which simultaneously occupies an apex position in each cage. Each icosahedron is composed of the chromium atom, nine boron atoms each having a hydrogen pointing out radially from the cage, and two carbon atoms each having a methyl group attached. The carbon atoms in the cage are bonded to each other and to the chromium atom. The pair of methyl groups in one cage are as far as possible from the pair of methyl groups in the other cage in a single molecule. The anion has exactly point symmetry 2 (C_2) and approximately point symmetry 2/m (C_{2h}).

Crystals of the neutral molecule, $Ni(B_9C_2H_{11})_2$, are monoclinic, space group $P2_1/c$, with $\underline{a} = 13.371$ Å, $\underline{b} = 10.398$ Å, $\underline{c} = 13.556$ Å, and $\beta = 119.16°$. There are four molecules in the unit cell and the calculated density is $\rho = 1.31$ g/cc. 3242 independent X-ray reflections measured by counter methods using the θ-2θ scan technique were used and the model was refined by least squares to a conventional $\underline{R}$ value of 3.5%. The molecule has the shape of two icosahedra, each composed of nine boron atoms, two carbon atoms and a nickel atom, which have one vertex position, occupied by the nickel, shared in common. The positions of the carbon atoms in the cage were determined and all hydrogen atoms were located. The carbon atoms in opposite cages are as close to each other as is possible in the staggered configuration. The molecule has C_2 point symmetry. There are two enantiomorphic rotational isomers present in the crystal.

Crystals of $Cs_2(B_9C_2H_{11})Co(B_8C_2H_{10})Co(B_9C_2H_{11})\cdot H_2O$ are monoclinic, space group $P2_1/c$, with $\underline{a} = 7.089$ Å, $\underline{b} = 19.240$ Å, $\underline{c} = 20.682$ Å, and $\beta = 98.00°$. There are four molecules in the unit cell and the calculated density is $\rho = 1.87$ g/cc. Using 3649 independent X-ray reflections measured by counter methods by the point count technique, the model was refined to a conventional $\underline{R}$ value of 3.4%. The carborane anion consists of three linked icosahedra. Two corners of a central ten-light-atom icosahedron are occupied by cobalts each of which is common to another icosahedron containing eleven light atoms. Five of the carbon atoms were localized but one was disordered between two positions. The cages are staggered across the cobalts and all carbons are as close to each other as is possible in this configuration. All hydrogen atoms except those in the water molecule were located.

Correlations between these structures and those of other metallocarboranes are made. Metallocarboranes and metallocenes are qualitatively compared concerning the possibility of free rotation of the ligands.

HIGH-RESOLUTION GAMMA AND X-RAY SPECTROSCOPY ON UNSEPARATED FISSION PRODUCTS

Jerry Barnard Wilhelmy
(Ph. D. Thesis)

(From UCRL-18978)

X-ray and γ-ray studies were made on the short-lived products formed from the spontaneous fission of ^{252}Cf. The fission fragments from an ~10-μg source of ^{252}Cf (3.7×10^8 fissions/minute) were embedded in a continually-moving belt system and transported past a detection point located some 19 inches from the source. By varying the velocity of the tape, spectra were obtained for transit times ranging from 0.27 seconds to 4.8 hours.

Three individual experiments were performed: 1) K x-ray, γ-ray coincidence studies, 2) high resolution γ-ray singles studies, and 3) high resolution K x-ray singles studies. In the coincidence studies it was possible to follow the decay of approximately 200 transitions and, through the x-ray energies, establish the element emitting the gamma ray for a large number of these. For the γ-ray singles studies 20,000 individual γ-ray peaks were analyzed at the various experimental transit times. From the K x-ray singles measurements it was possible to determine the quantitative K x-ray yields as a function of time for all the elements appreciably populated from the fission of ^{252}Cf (rubidium-europium).

The data from the γ-ray singles experiment were correlated with information from 1) the x-ray, γ-ray coincidence study, 2) the studies on the prompt radiations from the primary fragment, and 3) the reported literature on the decay of fission products. It was possible to assign ~250 of the observed transitions to specific isotopes. New assignments were made to 25 isotopes which were previously unreported or had only been identified by half life. By following the

genetic decay of certain transitions it was possible to deduce charge distribution information on twelve mass chains. Finally, strong experimental information has been presented for the existence of the proposed new region of permanent deformation near ^{110}Ru.

RADIOACTIVATION BY ^{3}He BOMBARDMENT: A PRACTICAL ANALYTICAL SYSTEM

James F. Lamb
(Ph. D. Thesis)

(From UCRL-18981)

Charged-particle activation analysis using 1-30-MeV ^{3}He ions as the nuclear reaction inducing particle is discussed from a practical point of view with emphasis upon the light elements, especially oxygen.

Definitions and expressions fundamental to charged particle activation analysis are given with brief discussions. Also included are convenient ^{3}He activation analysis reference curves for estimating Coulomb barriers and the effects of Rutherford scattering upon the incident beam. Range-energy tables for ^{3}He ions in nongaseous targets of the stable isotopes of all elements and an extensive Q-value table for the more important ^{3}He-induced reactions appear as appendices.

A summary of excitation functions and reaction data for ^{3}He induced reactions in Be, B, C, N, O, F, Na, Mg, Al, Si, Ca, Ti, Fe, Ni, Cu, Ge, Ta, and Au is given which contains our experimental measurements as well as those from the literature. All the excitation functions have been re-drawn to the same scale to permit convenient comparison. A brief discussion of the recognizable trends in the excitation functions for the more important ^{3}He-induced reactions follows the experimental data.

VI. 1969 Publications

PAPERS PUBLISHED AND UCRL REPORTS ISSUED, 1969

ADAMSON, M. G., (See Hopkins, T. E., UCRL-18800)

ARIMA, A., (See McGrath, R. L., UCRL-18940)

ASARO, F., (See Perlman, I., UCRL-18957)

ASARO, F., (See Gorman, D. J., UCRL-18975)

ASARO, F., (See Browne, E., UCRL-19502 Abstract)

ASARO, F., (See Gorman, D. J., UCRL-19503 Abstract)

ASCUITTO, R. J. and N. K. Glendenning
The role of inelastic processes in two-nucleon transfer reactions
UCRL-18874, April 1969
Phys. Rev. 181, 1396 (1969)

BACHER, A. D., F. Resmini, H. E. Conzett, and J. Ernst
Alpha-^{4}He elastic scattering from 30 to 50 MeV
UCRL-18745 Abstract, February 1969
Bull. Am. Phys. Soc. 14, (CG5) 534 (1969)

BACHER, A. D., F. G. Resmini, R. J. Slobodrian, R. de Swiniarski, H. Meiner, and W. M. Tivol
Observation of the ^{3}He(p, n)3p reaction at 25 MeV
UCRL-18929, June 1969
Phys. Letters 29B, 573 (1969)

BACHER, A. D., H. E. Conzett, R. de Swiniarski, H. Meiner, F. G. Resmini, and T. A. Tombrello
^{3}He-^{4}He elastic scattering from 18 to 70 MeV
UCRL-18944 Abstract, June 1969
Meeting of the American Physical Society, Honolulu, Hawaii, 2-4 September 1969

BACHER, A. D., F. G. Resmini, H. E. Conzett, R. de Swiniarski, and H. Meiner
Levels in ^{8}Be from alpha-^{4}He elastic scattering
UCRL-18989 Abstract, September 1969
Meeting of the American Physical Society, Boulder, Colorado, 30 October - 1 November 1969

BACHER, A. D., R. L. McGrath, J. Cerny, R. de Swiniarski, J. C. Hardy, and R. J. Slobodrian
The (^{3}He, ^{6}He) reaction on ^{6}Li and ^{7}Li
UCRL-19521, December 1969
Phys. Letters

BACHER, A., (See de Swiniarski, R., UCRL-18744 Abstract)

BACHER, A., (See Resmini, F. G., UCRL-18822)

BACHER, A., (See Meiner, H., UCRL-18831 Abstract)

BACHER, A., (See de Swiniarski, R., UCRL-18930)

BACHER, A., (See de Swiniarski, R., UCRL-18941)

BAGUS, P. S., (See Fadley, C. S., UCRL-19501)

BAKER III, B.
Cycling zone adsorption - Separation by thermal-wave propagation
UCRL-18967, August 1969
Ph. D. Thesis

BAKER III, B., (See Pigford, R. L., UCRL-18848)

BARCLAY, J. A.
Spin-lattice relaxation by nuclear magnetic resonance on oriented nuclei
UCRL-18986, September 1969
Ph. D. Thesis

BARTLETT, N., (See Karlsson, S.-E., UCRL-18502)

BAR-TOUV, J., (See Goodman, A. L., UCRL-19506)

BENNETT-CORNIEA, W., H. A. Sokol, and W. M. Garrison
Reductive deamination in the radiolysis of oligopeptides in aqueous solution and in the solid state
UCRL-19504, October 1969
Meeting of the American Chemical Society, Houston, Texas, 23 - 27 February 1970

BERGER, R., (See Clark, D. J., UCRL-18608)

BERNTHAL, F. M.
The $|\Delta K| = 1$ electric dipole transitions in odd-mass deformed nuclei II. The decay of Ta^{176} to levels in Hf^{176}
UCRL-18651, February 1969
Ph. D. Thesis

BLAIR, A. G., C. Glashausser, R. de Swiniarski, J. Goudergues, R. Lombard, B. Mayer, J. Thirion, and P. Vaganov
Excitation of collective states in light nuclei by inelastic scattering of 20.3-MeV polarized protons
UCRL-18927, August 1969
Phys. Rev.

BLUM, D. E., (See Pigford, R. L., UCRL-18848)

BORGGREEN, J., (See Valli, K., UCRL-18992)

BOWMAN, H. R., (See Watson, R. L., UCRL-19510)

BREWER, W. D.
Weak interaction studies by nuclear orientation
UCRL-19533, December 1969
Ph. D. Thesis

BROWN, W. H., and C. J. King
Interfacial mixing cells and mass transfer in turbulent flow
UCRL-18974, August 1969
M. S. Thesis

BROWNE, E., and F. Asaro
Energy levels of ^{233}Pa and ^{231}Pa
UCRL-19502 Abstract, October 1969
Meeting of the American Chemical Society, Houston, Texas, 23-27 February 1970

BRUNNADER, H.
The (p, t) and (p, ^{3}He) reactions on 2s-1d shell nuclei
UCRL-18716, January 1969
Ph. D. Thesis

BRUNNADER, H., J. C. Hardy, and J. Cerny
^{34}Ar and T = 1 states in ^{34}Cl from two-nucleon pick-up reactions
UCRL-18921, May 1969
Nucl. Phys. A137, 487 (1969)

BRUNNADER, H., (See Hardy, J. C., UCRL-18873)

BRUNNADER, H., (See Hardy, J. C., UCRL-18942)

BRUNNADER, H., (See Hardy, J. C., UCRL-18943)

CALVIN, M., (See Fischer, M. S., UCRL-18828 Abstract)

CARNEIRO, A., (See Clark, D. J., UCRL-18608)

CERNY, J., R. A. Mendelson, Jr., G. R. Wozniak, J. E. Esterl, and J. C. Hardy
New nuclides ^{19}Na and ^{23}Al observed via the (p, ^{6}He) reaction
UCRL-18724, January 1969
Phys. Rev. Letters 22, 612 (1969)

CERNY, J., (See Mendelson, R. A., Jr., UCRL-18746 A)

CERNY, J., (See Hardy, J. C., UCRL-18774)

CERNY, J., (See Hardy, J. C., UCRL-18873)

CERNY, J., (See Brunnader, H., UCRL-18921)

CERNY, J., (See McGrath, R. L., UCRL-18940)

CERNY, J., (See Hardy, J. C., UCRL-18942)

CERNY, J., (See Hardy, J. C., UCRL-18943)

CERNY, J., (See Mendelson, R., UCRL-18950)

CERNY, J., (See Loiseaux, J. M., UCRL-18990 Abstract)

CERNY, J., (See Bacher, A. D., UCRL-19521)

CHAN, D., and D. A. Shirley
A note on the position of the "gold 5d bands" in $AuAl_2$ and $AuGa_2$
UCRL-19519, December 1969
The Density of States Symposium, National Bureau of Standards, Washington, D. C., 3-6 November 1969

CHEIFETZ, E., R. C. Gatti, R. C. Jared, S. G. Thompson, and A. Wittkower
Acceleration of fission fragments
UCRL-19516, November 1969
Phys. Rev. Letters 24, 148 (1970)

CHENG, C. T., and R. L. Pigford
Experimental study of rates of crystal growth from organic melts
UCRL-19500, December 1969
Rev. Sci. Instr.

CHENG, C. T., and R. L. Pigford
Purity of crystals grown from binary organic melts
UCRL-19512, December 1969
Ind. Eng. Chem. Fundamentals

CHENG, C. T., and R. L. Pigford
An application of Eyring's theory to crystallization kinetics of polyphenyls
UCRL-19513, December 1969

CHENG, C. T.
Rates of growth of crystals from solutions
UCRL-19518, December 1969
Ph. D. Thesis

CIRILOV, S. D., (See Newton, J. O., UCRL-19527)

CLARK, D. J., R. Berger, A. Carneiro, D. Elo, P. Frazier, A. Luccio, D. Morris, M. Renkas, and F. Resmini
Design and construction of the axial injection system for the 88-inch cyclotron
UCRL-18608, March 1969
1969 Particle Accelerator Conference, Washington, D. C., 5-7 March 1969

CLARK, D. J., A. U. Luccio, F. Resmini, and H. Meiner
Operation of the polarized ion source and axial injection system for the Berkeley 88-inch cyclotron
UCRL-18934, August 1969
International Cyclotron Conference, Oxford, England, 17-19 September 1969

CLARK, D. J.
Survey of external injection systems for cyclotron
UCRL-18980, September 1969
International Cyclotron Conference, Oxford, England, 17-19 September 1969

CLARK, D. J., (See Resmini, F., UCRL-18596)

CLARK, D. J., (See Luccio, A. U., UCRL-18607)

CLARK, D. J., (See Resmini, F. G., UCRL-18822)

CLEM, R. G., and W. W. Goldsworthy
Part I. Some advantages of digital polarography
UCRL-18936 Abstract, June 1969
Thirteenth Conference on Analytical Chemistry in Nuclear Technology, Gatlinburg, Tennessee, 30 September - 2 October 1969

CLEM, R. G., (See Goldsworthy, W. W., UCRL-18939)

CONZETT, H. E., (See Bacher, A. D., UCRL-18745 Abstract)

CONZETT, H. E., (See Meiner, H., UCRL-18831 Abstract)

CONZETT, H. E., (See Bacher, A. D., UCRL-18944 Abstract)

CONZETT, H. E., (See Bacher, A. D., UCRL-18989 Abstract)

CUNNINGHAM, B. B., (See Fujita, D. K., UCRL-18861)

DABES, J. N., C. R. Wilke, and R. K. Finn
Master reaction concept: Its validity in integrated biological systems
UCRL-18971, October 1969
Science

DARCEY, W., (See Davies, W. G., UCRL-18686)

DAVIS, D. W., J. M. Hollander, D. A. Shirley, and T. D. Thomas
Comparison of core-level binding energy shifts in molecules with predictions based on Koopmans' theorem
UCRL-19515 Rev, November 1969
J. Chem. Phys.

DAVIES, W. G., J. C. Hardy, and W. Darcey
The $^{31}P(p,t)^{33}P$ reaction and the usefulness of double-stripping in distinguishing between shell model calculations
UCRL-18686, January 1969
Nucl. Phys. A128, 465 (1969)

DELGASS, W. N., T. R. Hughes, and C. S. Fadley
x-Ray photoelectron spectroscopy: A tool for research in catalysis
UCRL-18968, February 1970
Catalysis Reviews

deSWINIARSKI, R., J. Sherman, A. Bacher, C. Glashausser, D. L. Hendrie, and E. A. McClatchie
Inelastic scattering of protons on ^{20}Ne at 24.5 MeV
UCRL-18744 Abstract, February 1969
Bull. Am. Phys. Soc. 14, (CE12) 531 (1969)

deSWINIARSKI, R., C. Glashausser, D. L. Hendrie, J. Sherman, A. D. Bacher, and E. A. McClatchie
Evidence for Y_4 deformation in ^{20}Ne and other s-d shell nuclei
UCRL-18930, June 1969
Phys. Rev. Letters 23, 317 (1969)

deSWINIARSKI, R., A. D. Bacher, C. Glashausser, E. A. McClatchie, F. G. Resmini, and J. Sherman
UCRL-18941, June 1969
Meeting of the American Physical Society, Honolulu, Hawaii, 2-4 September 1969

deSWINIARSKI, R., (See Glashausser, C., UCRL-18677)

deSWINIARSKI, R., (See Resmini, F. G., UCRL-18822)

deSWINIARSKI, R., (See Bacher, A. D., UCRL-18929)

de SWINIARSKI, R., (See Blair, A. G., UCRL-18927)

de SWINIARSKI, R., (See Bacher, A. D., UCRL-18944 Abstract)

de SWINIARSKI, R., (See Bacher, A. D., UCRL-18989 Abstract)

de SWINIARSKI, R., (See Bacher, A. D., UCRL-19521)

DIAMOND, R. M., F. S. Stephens, W. H. Kelly, and D. Ward
Lifetimes of rotational states from heavy-ion reactions
UCRL-18702, January 1969
Phys. Rev. Letters 22, 546 (1969)

DIAMOND, R. M., F. S. Stephens, R. Nordhagen, and K. Nakai
Half-lives of rotational levels in ^{152}Sm
UCRL-18920 Abstract, May 1969
International Conference on Properties of Nuclear States, Montreal, 25-30 August 1969

DIAMOND, R. M., F. S. Stephens, K. Nakai, and R. Nordhagen
Lifetimes of ground-band states in $^{148, 150, 152}Sm$
UCRL-19517, November 1969
Phys. Rev.

DIAMOND, R. M., (See Newton, J. O., UCRL-18358 Rev)

DIAMOND, R. M., (See Nordhagen, R., UCRL-18925)

DIAMOND, R. M., (See Nordhagen, R., UCRL-18931 Abstract)

DIAMOND, R. M., (See Nakai, K., UCRL-18933 Abstract)

DIAMOND, R. M., (See Nakai, K., UCRL-18959)

DIAMOND, R. M., (See Nordhagen, R., UCRL-18965)

DIAMOND, R. M., (See Newton, J. O., UCRL-19527)

DUONG, T. H., R. Marrus, and J. Yellin
Atomic beam study of the rubidium 85, 87 relative isotope shift
UCRL-18309, June 1968
Phys. Letters 27B, 565 (1968)

EASLEY, W. C., (See Edelstein, N., UCRL-18913)

EDELSTEIN, N., H. F. Mollet, W. C. Easley, and R. J. Mehlhorn
Electron paramagnetic resonance of Pu^{3+} in cubic symmetry sites in CaF_2, SrF_2, and BaF_2
UCRL-18913, May 1969
J. Chem. Phys. 51, 3281 (1969)

EDELSTEIN, N., (See Morss, L. R., UCRL-18973)

ELO, D., (See Luccio, A. U., UCRL-18607)

ELO, D., (See Clark, D. J., UCRL-18608)

ENGLISH, M. J., and W. M. Garrison
Radiolytic oxidation of the peptide main-chain in aqueous solution: Chemistry of the peroxy radical $RCONHC(\dot{O}_2)R_2$
UCRL-18905 Abstract, May 1969
Meeting of the American Chemical Society, New York, 7-12 September 1969

ERNST, J., (See Bacher, A. D., UCRL-18745 Abstract)

ERNST, J., (See Meiner, H., UCRL-18831 Abstract)

ESKOLA, K., (See Ghiorso, A., UCRL-18819)

ESKOLA, P., (See Ghiorso, A., UCRL-18819)

ESTERL, J. E., (See Cerny, J., UCRL-18724)

ESTERL, J. E., (See Hardy, J. C., UCRL-18774)

FADLEY, C. S., and D. A. Shirley
Electronic density of states from x-ray photoelectron spectroscopy
UCRL-18953, July 1969
Symposium on Electronic Density of States, Gaithersburg, Maryland, 3-6 November 1969

FADLEY, C. S., C. E. Miner, and J. M. Hollander
Design of a magnetic spectrometer for photoelectron spectroscopy
UCRL-18954, July 1969
Appl. Phys. Letters 15, 223 (1969)

FADLEY, C. S., D. A. Shirley, A. J. Freeman, P. S. Bagus, and J. V. Mallow
Multiplet splitting of core electron binding energies in transition metal ions
UCRL-19501, October 1969
Phys. Rev. Letters 23, 1397 (1969)

FALTENS, M. O.
Mössbauer resonance studies of gold compounds
January 1969, UCRL-18706
Ph. D. Thesis

FARRAGI, H. (See Kossanyi-Demay, P., UCRL-18988 Abstract)

FINN, R. K., (See Dabes, J. N., UCRL-18971)

FISCHER, M. S., D. H. Templeton, and M. Calvin
The crystal structure of magnesium phthalocyanin· H_2O· 2 pyridine
UCRL-18828 Abstract, April 1969
Meeting of the American Crystallographic Association, Seattle, Washington, 23-27 March 1969

FISCHER, M. S., D. H. Templeton, and A. Zalkin
Solid state structure and chemistry of the choline halides and their analogues. Redetermination of the betaine hydrochloride structure, $[(CH_3)_3NCH_2COOH]^+Cl^-$
UCRL-19523, December 1969
Acta Cryst.

FISCHER, M. S.
An x-ray crystallographic study of chlorophyll analogues and other bio-organic compounds
UCRL-19524, December 1969
Ph. D. Thesis

FOWLER, T., and J. Yellin
Stark effect in the resonance lines of indium and thallium
UCRL-18924 Abstract, May 1969
Meeting of the American Physical Society, Honolulu, Hawaii, 2-4 September 1969

FOWLER, T. R., and J. Yellin
Electric field effect in the resonance lines of indium and thallium
UCRL-19337, September 1969
Phys. Rev.

FRAZIER, P., (See Luccio, A. U., UCRL-18607)

FRAZIER, P., (See Clark, D. J., UCRL-18608)

FREEMAN, A. J., (See Fadley, C. S., UCRL-19501)

FRIERMAN, J. D., (See Perlman, I., UCRL-18957)

FUJITA, D. K., B. B. Cunningham, T. C. Parson, and J. R. Peterson
The solution absorption spectrum of Es^{3+}
UCRL-18661, January 1969
Inorg. Nucl. Chem. Letters 5, 245 (1969)

FUJITA, D. K.
Some magnetic spectroscopic, and crystallographic properties of berkelium, californium, and einsteinium
UCRL-19507, November 1969
Ph. D. Thesis

GABRIEL, H.
Effect of radio-frequency fields on Mössbauer spectra
UCRL-18759, February 1969
Phys. Rev. 184, 359 (1969)

GARRISON, W. M., and M. A. J. Rodgers
Role of excited species $(RCONHCHR_2)^*$ in the radiolytic oxidation of the peptide main-chain in aqueous systems
UCRL-18849, April 1969
Int. J. Radiat. Phys. Chem. 1, 541 (1969)

GARRISON, W. M.
Radiation chemistry of biochemical sybstances
UCRL-18906 Abstract, May 1969
Fifty-fifth Scientific Assembly of the Radiological Society of North America, Chicago, 30 November - 5 December 1969

GARRISON, W. M.
Some radiation-induced reactions of amino acids and peptides
UCRL-19511 Abstract, November 1969
18th Annual Meeting of the Radiation Research Society, Dallas, Texas, 1-5 March 1970

GARRISON, W. M., (See English, M. J., UCRL-18905 Abstract)

GARRISON, W. M., (See Kland-English, M. J., UCRL-18983)

GARRISON, W. M., (See Bennett-Corniea, W., UCRL-19504)

GATTI, R. C., (See Cheifetz, E., UCRL-19516)

GHIORSO, A., M. Nurmia, J. Harris, K. Eskola, and P. Eskola
Positive identification of two alpha particle emitting isotopes of element 104
UCRL-18819, April 1969
Phys. Rev. Letters 22, 1317 (1969)

GHIORSO, A., (See Sikkeland, T., UCRL-18674)

GLASHAUSSER, C., R. de Swiniarski, J. Goudergues, R. M. Lombard, B. Mayer, and J. Thirion
Elastic and inelastic scattering of 20.3 MeV polarized protons from ^{90}Zr, ^{92}Zr, and ^{92}Mo
UCRL-18677, March 1969
Phys. Rev. 184, 1217 (1969)

GLASHAUSSER, C., D. L. Hendrie, J. M. Loiseaux, and E. A. McClatchie
Fragmentation of the octupole strength in $^{205}Tl(p, p')^{205}Tl$
UCRL-19528, December 1969
Phys. Letters

GLASHAUSSER, C., (See Moss, J. M., UCRL-18725 Abstract)

GLASHAUSSER, C., (See de Swiniarski, R., UCRL-18744 Abstract)

GLASHAUSSER, C., (See Hendrie, D. L., UCRL-18826)

GLASHAUSSER, C., (See Blair, A. G., UCRL-18927)

GLASHAUSSER, C., (See de Swiniarski, R., UCRL-18930)

GLASHAUSSER, C., (See McClatchie, E. A., UCRL-18937)

GLASHAUSSER, C., (See de Swiniarski, R., UCRL-18941)

GLASHAUSSER, C., (See McClatchie, E. A., UCRL-18945 Abstract)

GLENDENNING, N. K., and R. S. Mackintosh
Non-rigidity in alpha scattering from deformed nuclei
UCRL-18914, May 1969
Phys. Letters 29B, 626 (1969)

GLENDENNING, N. K., and K. Harada
Effects of the octupole vibration on the reactions $^{207}Pb(t, p)^{209}Pb$ and $^{209}Pb(p, t)^{207}Pb$
UCRL-18982, September 1969
Phys. Letters

GLENDENNING, N. K.
Role of inelastic processes in two-nucleon transfer reactions
Proceedings of International Conference on Properties of Nuclear States, ed. by M. Harvey, University of Montreal Press, Montreal, 1969)

GLENDENNING, N. K., (See Ascuitto, R. J., UCRL-18874)

GOLDRING, G., (See Nordhagen, R., UCRL-18925)

GOLDRING, G., (See Nordhagen, R., UCRL-18931 Abstract)

GOLDSWORTHY, W. W., and R. G. Clem
A digitized, time synchronized, and sampling system for polarographic and coulometric studies
UCRL-18939, August 1969
13th Conference on Analytical Chemistry in Nuclear Technology, Gatlinburg, Tennessee, 30 September - 2 October 1969

GOLDSWORTHY, W. W., (See Clem, R. G., UCRL-18936 Abstract)

GOODMAN, A. L., G. L. Struble, J. Bar-Touv, and A. Goswami
Generalized pairing in light nuclei II: Solution of HFB equations with realistic forces and comparison of different approximations
UCRL-19506, December 1969
Phys. Rev.

GOODMAN, A. L.
T = 0 and T = 1 pairing in light nuclei
UCRL-19514, October 1969
Ph. D. Thesis

GORMAN, D. J., and F. Asaro
Tables of Clebsch-Gordan coefficients for odd and even mass deformed nuclei
UCRL-18975, September 1969

GORMAN, D. J., and F. Asaro
Energy levels of ^{235}Np
UCRL-19503 Abstract, October 1969
Meeting of the American Chemical Society, Houston, Texas, 23-27 February 1970

GOSWAMI, A., (See Goodman, A. L., UCRL-19506)

GOTH, G., (See McGrath, R. L., UCRL-18940)

GOUDERGUES, J., (See Glashausser, C., UCRL-18677)

GOUDERGUES, J., (See Blair, A. G., UCRL-18927)

GUSTAFSON, C., (See Nilsson, S.-G., UCRL-18692)

HALBACH, K.
First order perturbation effects in iron-dominated two-dimensional symmetrical multipoles
UCRL-18841, April 1969
Nucl. Instr. Methods 74, 147 (1969)

HALBACH, K., and R. Yourd
Tables and graphs of first order perturbation effects in iron dominated two dimensional symmetrical multipoles
UCRL-18916, May 1969

HALBACH, K.
Fields and first order perturbation effects in two-dimensional conductor dominated magnets
UCRL-18947, July 1969
Nucl. Instr. Methods

HARDY, J. C., H. Brunnader, J. Cerny, and J. Janecke
Isobaric analogue states and coulomb displacement energies in the ($1d_{5/2}$) shell
UCRL-18566, January 1969
Phys. Rev. 183, 854 (1969)

HARDY, J. C., J. E. Esterl, R. G. Sextro, and J. Cerny
Isospin purity and decay of the T = 3/2 analogue state in ^{17}F
UCRL-18774, February 1969
Second Conference on Nuclear Isospin, Asilomar, Pacific Grove, California, 13-15 March 1969

HARDY, J. C., H. Brunnader, and J. Cerny
A simple method for investigating the parentage of states using two-nucleon transfer reactions
UCRL-18873, April 1969
Phys. Rev. Letters 22, 1439 (1969)

HARDY, J. C., H. Brunnader, and J. Cerny
T = 2 and T = 3 analogue states, $28 \leq A \leq 40$
UCRL-18942, June 1969
Phys. Rev.

HARDY, J. C., H. Brunnader, and J. Cerny
Nuclear parentage simply obtained from two-nucleon transfer reactions
UCRL-18943, June 1969
International Conference on Properties of Nuclear States, Montreal, 25-30 August 1969

HARDY, J. C., (See Davies, W. G., UCRL-18686)

HARDY, J. C., (See Cerny, J., UCRL-18724)

HARDY, J. C., (See Mendelson, R. A., Jr., UCRL-18746 Abstract)

HARDY, J. C., (See Brunnader, H., UCRL-18921)

HARDY, J. C., (See McGrath, R. L., UCRL-18940)

HARDY, J. C., (See Mendelson, R., UCRL-18950)

HARDY, J. C., (See Bacher, A. D., UCRL-19521)

HARADA, K., (See Glendenning, N. K., UCRL-18982)

HARRIS, J., (See Ghiorso, A., UCRL-18819)

HARVEY, B. G., (See Lu, C. C., UCRL-18719)

HEBERT, A. J.
Photovoltaic effects in laser diodes
UCRL-18909, May 1969
Appl. Phys. Letters

HEBERT, A. J., (See Melendres, C. A., UCRL-18850)

HENDRICKSON, D. N., J. M. Hollander, and W. L. Jolly
Nitrogen 1s electron binding energies. Correlations with molecular orbital calculated nitrogen charges
UCRL-19027, August 1969
Inorg. Chem.

HENDRICKSON, D. N., (See Pelavin, M., UCRL-19044)

HENDRIE, D. L., C. Glashausser, J. M. Moss, and J. Thirion
The spin flip reaction with 19.6 MeV protons on ^{54}Fe and ^{56}Fe
UCRL-18826, April 1969
Phys. Rev. 186, 1188 (1969)

HENDRIE, D. L., (See Satchler, G. R., Phys. Rev. 187, 1491 (1969))

HENDRIE, D. L., (See Moss, J. M., UCRL-18725 Abstract)

HENDRIE, D. L., (See de Swiniarski, R., UCRL-18744 Abstract)

HENDRIE, D. L., (See de Swiniarski, R., UCRL-18930)

HENDRIE, D. L., (See McClatchie, E. A., UCRL-18937)

HENDRIE, D. L., (See McClatchie, E. A., UCRL-18945 Abstract)

HENDRIE, D. L., (See Glashausser, C., UCRL-19528)

HOLLANDER, J. M.
Photoelectron spectroscopy: A chemical tool from nuclear spectroscopy
UCRL-18972, August 1969
International Conference on Radioactivity in Nuclear Spectroscopy, Vanderbilt University, 11-15 August 1969

HOLLANDER, J. M., (See Jaklevic, J. M., UCRL-18274)

HOLLANDER, J. M., (See Fadley, C. S., UCRL-18954)

HOLLANDER, J. M., (See Hendrickson, D. N., UCRL-19027)

HOLLANDER, J. M., (See Pelavin, M., UCRL-19044)

HOLLANDER, J. M., (See Davis, D. W., UCRL-19515 Rev)

HOPKINS, T. E., A. Zalkin, D. H. Templeton, and M. G. Adamson
The crystal and molecular structure of hexaaquoaluminum hexachlororuthenate tetrahydrate
UCRL-18800, February 1969
Inorg. Chem. 8, 2421 (1969)

HYDE, E. K.
A nuclear chemistry experiment at the Berkeley Bevatron: Fragment emission from complex nuclei bombarded with 5 GeV protons
UCRL-18830 Abstract, April 1969
Meeting of the American Chemical Society, Minneapolis, Minnesota, 14-18 April 1969

HYDE, E. K., (See Valli, K., UCRL-18992)

JACKSON, A. D., A. Lande, and P. U. Sauer
Matrix elements of the lambda-nucleon potential from phase shifts
UCRL-18956, July 1969
Phys. Letters 30B, 233 (1969)

JAKLEVIC, J. M., C. M. Lederer, and J. M. Hollander
A study of levels in ^{92}Mo and ^{94}Ru by in-beam gamma-ray spectroscopy
UCRL-18274, January 1969
Phys. Letters 29B, 179 (1969)

JAKLEVIC, J. M., (See Quitmann, D., UCRL-18743 Abstract)

JAKLEVIC, J. M., (See Lederer, C. M., UCRL-18747)

JAKLEVIC, J. M., (See Quitmann, D., UCRL-18871)

JAKLEVIC, J. M., (See Quitmann, D., UCRL-18946 Abstract)

JAKLEVIC, J. M., (See Quitmann, D., UCRL-18958)

JARED, R. C., (See Watson, R. L., UCRL-19510)

JARED, R. C., (See Cheifetz, E., UCRL-19516)

JOLLY, W. L., (See Hendrickson, D. N., UCRL-19027)

JOLLY, W. L., (See Pelavin, M., UCRL-19044)

KAHN, D. R.
Development of a jet-mixed extraction column
UCRL-18679, February 1969
M. S. Thesis

KARLSSON, S.-E., K. Siegbahn, and N. Bartlett
Charge distribution in xenon fluorides XeF_2, XeF_4, XeF_6, and $XeOF_4$ from electron spectroscopy (ESCA)
UCRL-18502, September 1969
J. Am. Chem. Soc.

KARRAKER, D. G., (See Zalkin, A., UCRL-18701)

KELLY, W. H., (See Newton, J. O., UCRL-18358 Rev)

KING, C. J., (See Palkot, E. J., Jr., UCRL-18918)

KING, C. J., (See Brown, W. H., UCRL-18974)

KLAND-ENGLISH, M. J., H. A. Sokol, and W. M. Garrison
Radiolytic oxidation of the peptide main-chain in dilute aqueous solution: Chemistry of the peroxy radical, $RCONHC(\dot{O}_2)R_2$
UCRL-18983, September 1969
158th National Meeting of the American Chemical Society, New York, 7-12 September 1969

KOSSANYI-DEMAY, P., P. Roussel, H. Farragi, and R. Schaeffer
A microscopic analysis of the (^{3}He, t) charge exchange reaction on N = 28 even nuclei and the two-body interaction
UCRL-18988 Abstract, September 1969
Meeting of the American Physical Society, Boulder, Colorado, 30 October - 1 November 1969

KUMAR, K., and B. Sørensen
Derivation of the radial dependence of the quadrupole force from a Woods-Saxon potential
UCRL-18593, November 1968
Nucl. Phys.

LAMB, J. F., D. M. Lee, and S. S. Markowitz
Preparation of isotopic oxygen targets for charged particle activation
UCRL-18979, September 1969
Anal. Chem. 42, 209 (1970)

LAMB, J. F.
Radioactivation by ^{3}He bombardment: A practical analytical system
UCRL-18981, September 1969
Ph. D. Thesis

LAMB, J. F., D. M. Lee, and S. S. Markowitz
Surface profile analysis by ^{3}He activation: Oxygen in silicon
UCRL-18984, September 1969
Anal. Chem. 42, 212 (1970)

LAMB, W. B., T. G. Springer, and R. L. Pigford
An interface impedance bridge
UCRL-18912, May 1969
Ind. Eng. Chem. Fundamentals 8, 823 (1969)

LAMM, I.-L., (See Nilsson, S.-G., UCRL-18692)

LANDE, A., (See Jackson, A. D., UCRL-18956)

LEE, D. M., (See Lamb, J. F., UCRL-18979)

LEE, D. M., (See Lamb, J. F., UCRL-18984)

LEDERER, C. M., J. M. Jaklevic, and S. G. Prussin
A low-lying 2- state in ^{236}U
UCRL-18747, February 1969
Nucl. Phys. A135, 36 (1969)

LEDERER, C. M.
Computer analysis of spectra
UCRL-18948, September 1969
International Conference on Radioactivity in Nuclear Spectroscopy, Vanderbilt University, Nashville, Tennessee, 11-15 August 1969

LEDERER, C. M., (See Jaklevic, J. M., UCRL-18274)

LEWIS, R. R., Jr.
The perturbing effect of two rotating fields on angular correlations
UCRL-18802, March 1969
Phys. Rev.

LOISEAUX, J. M., G. J. Wozniak, R. A. Mendelson, Jr., and J. Cerny
The new nuclide ^{11}N
UCRL-18990 Abstract, September 1969
Meeting of the American Physical Society, Boulder, Colorado, 30 October - 1 November 1969

LOISEAUX, J. M., (See Glashausser, C., UCRL-19528)

LOMBARD, R. M., (See Glashausser, C., UCRL-18677)

LOMBARD, R. M., (See Blair, A. G., UCRL-18927)

LU, C. C., M. S. Zisman, and B. G. Harvey
High spin states of configuration $(1d_{5/2})^2_{5+,\,0}$ and $(1g_{9/2})^2_{9+,\,0}$ strongly populated by the (α, d) reaction
UCRL-18719, January 1969
Phys. Rev. 186, 1086 (1969)

LUCCIO, A. U., D. J. Clark, D. Elo, P. Frazier, H. Meiner, D. Morris, and M. Renkas
A polarized ion source for the Berkeley 88-inch cyclotron
UCRL-18607, April 1969
Particle Accelerator Conference, Washington, D. C., 5-7 March 1969

LUCCIO, A. U.
Graphical calculation of waist-to-waist transfer in particle optics
UCRL-18977, September 1969
Nucl. Instr. Methods

LUCCIO, A. U., (See Clark, D. J., UCRL-18608)

LUCCIO, A. U., (See Clark, D. J., UCRL-18934)

MACKINTOSH, R. S.
The nature of the gamma band in erbium and dysprosium
UCRL-18919, May 1969
Phys. Letters 29B, 629 (1969)

MACKINTOSH, R. S., (See Glendenning, N. K., UCRL-18914)

MAIN, R.
Proposed modifications of the Berkeley Hilac
UCRL-18790, March 1969
1969 Particle Accelerator Conference, Washington, D. C., 5-7 March 1969

MALLOW, J. V., (See Fadley, C. S., UCRL-19501)

MARKOWITZ, S. S., (See Lamb, J. F., UCRL-18979)

MARKOWITZ, S. S., (See Lamb, J. F., UCRL-18984)

MARRUS, R., E. C. Wang, and J. Yellin
Atomic beam measurement of the potassium 39-41-42 isotope shift
UCRL-19520, December 1969
Phys. Rev. Letters

MARRUS, R., (See Duong, T. H., UCRL-18309)

MATTHIAS, E., (See Rao, G. N., UCRL-18326)

MAYER, B., (See Glashausser, C., UCRL-18677)

MAYER, B., (See Blair, A. G., UCRL-18927)

McCLATCHIE, E. A., C. Glashausser, and D. L. Hendrie
The proton particle-hole states in ^{208}Pb
UCRL-18937, August 1969
Phys. Rev.

McCLATCHIE, E. A., C. Glashausser, and D. L. Hendrie
Fragmentation of the proton single-particle strength in ^{207}Bi
UCRL-18945 Abstract, June 1969
Meeting of the American Physical Society, Honolulu, Hawaii, 2-4 September 1969

McCLATCHIE, E. A., (See de Swiniarski, R., UCRL-18744 Abstract)

McCLATCHIE, E. A., (See Resmini, F. G., UCRL-18822)

McCLATCHIE, E. A., (See de Swiniarski, R., UCRL-18930)

McCLATCHIE, E. A., (See de Swiniarski, R., UCRL-18941)

McCLATCHIE, E. A., (See Glashausser, C., UCRL-19528)

McGRATH, R. L., J. Cerny, J. C. Hardy, G. Goth, and A. Arima
Isospin-forbidden decay properties of the lowest T = 2 states of ^{20}Ne, ^{24}Mg, ^{28}Si, ^{32}S, and ^{40}Ca
UCRL-18940, June 1969
Phys. Rev.

McGRATH, R. L., (See Bacher, A. D., UCRL-19521)

MEADS, P. F., Jr., and F. B. Selph
Extraction and transfer of high quality beams from synchrotrons of the FOOFDOD type from application to the OMNITRON
UCRL-18781, February 1969
1969 Particle Accelerator Conference, Washington, D. C., 5-7 March 1969

MEINER, H., R. J. Slobodrian, H. E. Conzett, A. D. Bacher, J. Ernst, and F. G. Resmini
Determination of the $^1S_0$ neutron-neutron effective-range parameters from final-state interaction
UCRL-18831 Abstract, April 1969
Bull. Am. Phys. Soc. 14, (BG13) 512 (1969)

MEINER, H., (See Luccio, A. U., UCRL-18607)

MEINER, H., (See Bacher, A. D., UCRL-18929)

MEINER, H., (See Clark, D. J., UCRL-18934)

MEINER, H., (See Bacher, A. D., UCRL-18944 Abstract)

MEINER, H., (See Bacher, A. D., UCRL-18989 Abstract)

MEHLHORN, R.
g-Values and transition probabilities for neon I
UCRL-18908, May 1969
J. Opt. Soc. Am. 59, 1453 (1969)

MEHLHORN, R. J., (See Edelstein, N., UCRL-18913)

MELENDRES, C. A., A. J. Hebert, and K. Street, Jr.
Radio-frequency Stark spectra and dipole moment of BaS
UCRL-18550, October 1968
J. Chem. Phys. 51, 855 (1969)

MENDELSON, R. A., Jr., J. C. Hardy, and J. Cerny
The reactions $^{17}O(p, d)^{16}O$ and $^{17}O(p, t)^{15}O$: A test of recent shell model calculations
UCRL-18746 Abstract, February 1969
Bull. Am. Phys. Soc. 14, (CE3) 529 (1969)

MENDELSON, R., J. C. Hardy, and J. Cerny
The structure of ^{16}O and the $^{17}O(p, d)^{16}O$ reaction
UCRL-18950, July 1969
Phys. Rev. Letters

MENDELSON, R. A., (See Cerny, J., UCRL-18724)

MENDELSON, R. A., (See Loiseaux, J. M., UCRL-18990 Abstract)

MILLERON, N., and R. Wolgast
Cryopumping the OMNITRON ultra-vacuum system using heat pipes and metallic conduction
UCRL-18602, March 1969
1969 Particle Accelerator Conference, Washington, D. C., 5-7 March 1969

MILLERON, N.
Proposed: A vacuum standard based on counting and identifying molecules
UCRL-18938 Abstract, June 1969
16th National Vacuum Symposium, American Vacuum Society, Seattle, Washington, 28-31 October 1969

MINER, C. E., (See Fadley, C. S., UCRL-18954)

MÖLLER, P., (See Nilsson, S.-G., UCRL-18692)

MOLLET, H. F.
ERP - Studies of trivalent plutonium in CaF_2, SrF_2, and BaF_2
UCRL-18922, June 1969
M. S. Thesis

MOLLET, H. F., (See Edelstein, N., UCRL-18913)

MORRIS, D., (See Luccio, A. U., UCRL-18607)

MORRIS, D., (See Clark, D. J., UCRL-18608)

MORSS, L. R.
Crystallography and thermochemistry of some chlorocomplex compounds of the lanthanide and actinide elements
UCRL-18951, August 1969
Ph. D. Thesis

MORSS, L. R., M. Siegal, L. Stenger, and N. Edelstein
Preparation of cubic chlorocomplex compounds of trivalent metals: Cs_2NaMCl_6
UCRL-18973, August 1969
Inorg. Chem.

MOSS, J. M., D. L. Hendrie, C. Glashausser, and J. Thirion
Investigation of levels in ^{54}Fe by the $^{54}Fe(p, p'\gamma)^{54}Fe$ reaction
UCRL-18725 Abstract, January 1969
Bull. Am. Phys. Soc. 14, (GE13) 603 (1969)

MOSS, J. M.
In-beam proton-gamma ray coincidence studies using a large coaxial Ge(Li) detector
UCRL-18902, April 1969
Ph. D. Thesis

MOSS, J. M., (See Hendrie, D. L., UCRL-18826)

MYERS, W. D.
Droplet model isotope shifts and the neutron skin
UCRL-18987, September 1969
Phys. Rev. Letters 30B, 451 (1969)

MYERS, W. D.
Droplet model nuclear density distributions and single particle potential wells
UCRL-18997, October 1969
Phys. Rev.

NAKAI, K., F. S. Stephens, and R. M. Diamond
Quadrupole moment of the first excited state of ^{20}Ne
UCRL-18933 Abstract, June 1969
International Conference on Properties of Nuclear States, Montreal, 25-30 August 1969

NAKAI, K., F. S. Stephens, and R. M. Diamond
Quadrupole moments of the first excited states in ^{20}Ne and ^{22}Ne
UCRL-18959, December 1969
Nucl. Phys.

NAKAI, K., (See Diamond, R. M., UCRL-18920 Abstract)

NAKAI, K., (See Nordhagen, R., UCRL-18925)

NAKAI, K., (See Nordhagen, R., UCRL-18931 Abstract)

NAKAI, K., (See Diamond, R. M., UCRL-19517)

NEWTON, A. S., and A. F. Sciamanna
Metastable ions in the mass spectra of N_2, NO, N_2O, and NO_2
UCRL-18726, May 1969
Seventeenth Annual Conference on Mass Spectrometry and Allied Topics, Dallas, Texas, 18-23 May 1969

NEWTON, A. S., and A. F. Sciamanna
Metastable peaks in the mass spectra of N_2O and NO_2. II
UCRL-18928, June 1969
J. Chem. Phys. 52, 327 (1970)

NEWTON, A. S., and A. F. Sciamanna
Metastable ions in the mass spectra of N_2, NO, N_2O, NO_2
UCRL-18768 Abstract, July 1969
International Conference on Mass Spectroscopy, Kyoto, Japan, 8-12 September 1969

NEWTON, J. O., F. S. Stephens, R. M. Diamond, W. H. Kelly, and D. Ward
Gamma-ray de-excitation of compound-nucleus-reaction products
UCRL-18358 Rev, September 1969
Nucl. Phys.

NEWTON, J. O., S. D. Cirilov, F. S. Stephens, and R. M. Diamond
Possible oblate shape of 9/2-isomer in ^{199}Tl
UCRL-19527, December 1969
Nucl. Phys.

NILSSON, B., (See Nilsson, S.-G., UCRL-18692)

NILSSON, S.-G., C. F. Tsang, A. Sobiczewski, Z. Szymanski, S. Wycech, C. Gustafson, I.-L. Lamm, P. Möller, and B. Nilsson
On the nuclear structure and stability of heavy and superheavy elements
UCRL-18692, January 1969
Nucl. Phys. A131, 1 (1969)

NILSSON, S.-G., (See Tsang, C. F., UCRL-18963)

NILSSON, S.-G., (See Tsang, C. F., UCRL-18966)

NORDHAGEN, R., G. Goldring, R. M. Diamond, K. Nakai, and F. S. Stephens
Perturbed angular distributions from $^{120, 122, 124}Sn(^{40}Ar, 4n)^{156, 158, 160}Er$
UCRL-18925, August 1969
Nucl. Phys.

NORDHAGEN, R., G. Goldring, R. M. Diamond, K. Nakai, and F. S. Stephens
The spin dependence of the deorientation of recoiling free atoms
UCRL-18931 Abstract, June 1969
International Conference on Properties of Nuclear States, Montreal, 25-30 August 1969

NORDHAGEN, R., R. M. Diamond, and F. S. Stephens
Isomers in ^{156}Gd, ^{172}Yb, and ^{182}W
UCRL-18965, August 1969
Nucl. Phys. A138, 231 (1969)

NORDHAGEN, R., (See Diamond, R. M., UCRL-18920 Abstract)

NORDHAGEN, R., (See Diamond, R. M., UCRL-19517)

NURMIA, M. J., (See Sikkeland, T., UCRL-18674)

NURMIA, M. J., (See Ghiorso, A., UCRL-18819)

PALKOT, E. J., Jr., and C. J. King
The design of an improved device for absorption with chemical reaction
UCRL-18918, June 1969
M. S. Thesis

PARKINSON, W. C., (See Satchler, G. R., Phys. Rev. 187, 1491 (1969))

PARSONS, T. C., (See Fujita, D. K., UCRL-18661)

PELAVIN, M., D. N. Hendrickson, J. M. Hollander, and W. L. Jolly
Phosphorus 2p electron binding energies correlation with extended Hückel charges
UCRL-19044, August 1969
J. Phys. Chem.

PERLMAN, I., and F. Asaro
Pottery analysis by neutron activation
UCRL-18734, February 1969
Archaeometry 11, 21 (1969)

PERLMAN, I., F. Asaro, and J. D. Frierman
Provenience studies of Tel Ashdod pottery employing neutron activation analysis
UCRL-18957, July 1969
Atiqot

PETERSON, J. R., (See Fujita, D. K., UCRL-18661)

PIGFORD, R. L., B. Baker III, and D. E. Blum
Cycling zone adsorption, a new separation process
UCRL-18848, May 1969
Ind. Eng. Chem. Fundamentals 8, 848 (1969)

PIGFORD, R. L., (See Lamb, W. B., UCRL-18912)

PIGFORD, R. L., (See Springer, T. G., UCRL-18993)

PIGFORD, R. L., (See Springer, T. G., UCRL-18995)

PIGFORD, R. L., (See Cheng, C. T., UCRL-19500)

PIGFORD, R. L., (See Cheng, C. T., UCRL-19512)

PIGFORD, R. L., (See Cheng, C. T., UCRL-19513)

POSKANZER, A. M.
Counter telescope techniques for the identification of heavy ions
UCRL-18935 Abstract, June 1969
Meeting of the American Chemical Society, New York, 7-12 September 1969

PRUSSIN, S. G., (See Lederer, C. M., UCRL-18747)

QUITMANN, D., and J. M. Jaklevic
Measurement of the magnetic moments of isomeric levels in ^{73}As and ^{206}Pb populated by nuclear reactions
UCRL-18743 Abstract, February 1969
Bull. Am. Phys. Soc. 14, (HE9) 624 (1969)

QUITMANN, D., J. M. Jaklevic, and D. A. Shirley
Observation of NMR in an isomeric state following a nuclear reaction
UCRL-18871, April 1969
Phys. Letters 30B, 329 (1969)

QUITMANN, D., J. M. Jaklevic, and D. A. Shirley
Nuclear magnetic resonance in a 6 μsec isomer produced by a nuclear reaction
UCRL-18946 Abstract, June 1969
International Conference on Properties of Nuclear States, Montreal, 25-30 August 1969

QUITMANN, D., and J. Jaklevic
Measurement of the magnetic moments of the microsecond-isomers in ^{73}As and ^{206}Pb
UCRL-18958, July 1969

RAO, G. N., E. Matthias, and D. A. Shirley
Localized moments on rhodium in Pd-Rh alloys
UCRL-18326, March 1969
Phys. Rev. 184, 325 (1969)

RASMUSSEN, J. O., (See Watson, R. L., UCRL-19510)

RENKAS, M., (See Luccio, A. U., UCRL-18607)

RENKAS, M., (See Clark, D. J., UCRL-18608)

RESMINI, F., and D. J. Clark
Space charge effects in the axial injection line for the 88-inch cyclotron
UCRL-18596, May 1969
1969 Particle Accelerator Conference, Washington, D. C., 5-7 March 1969

RESMINI, F. G., A. D. Bacher, D. J. Clark, E. A. McClatchie, and R. de Swiniarski
Slit scattering effects with medium energy alpha particles and protons
UCRL-18822, April 1969
Nucl. Instr. Methods 74, 261 (1969)

RESMINI, F., (See Clark, D. J., UCRL-18608)

RESMINI, F., (See Bacher, A. D., UCRL-18745 Abstract)

RESMINI, F., (See Meiner, H., UCRL-18831 Abstract)

RESMINI, F., (See Bacher, A. D., UCRL-18929)

RESMINI, F., (See Clark, D. J., UCRL-18934)

RESMINI, F., (See de Swiniarski, R., UCRL-18941)

RESMINI, F., (See Bacher, A. D., UCRL-18944 Abstract)

RESMINI, F., (See Bacher, A. D., UCRL-18989 Abstract)

REYNOLDS, F. L.
Surface ionization: An experimental study of strontium and lanthanum on tungsten
UCRL-18233, May 1968
Surface Sci. 14, 327 (1969)

ROBERTSON, G. H.
Foam fractionation of rare-earth elements
UCRL-19525, December 1969
Ph. D. Thesis

ROBINSON, H. P.
Phase detector
UCRL-18926, June 1969

RODGERS, M. A. J., (See Garrison, W. M., UCRL-18849)

ROSENBLUM, S. S.
Temperature dependence of the hyperfine interaction in dilute nickel alloys using gamma-gamma perturbed angular correlation
UCRL-18675, January 1969
Ph. D. Thesis

ROUSSEL, P., (See Kossanyi-Demay, P., UCRL-18988 Abstract)

RUBEN, H., (See Zalkin, A., UCRL-18829 Abstract)

RUGGE, C., (See Watson, R. L., UCRL-19510)

SATCHLER, G. R., W. C. Parkinson, and D. L. Hendrie
The $^{208}Pb(^{3}He, \alpha)^{207}Pb$ reaction at 47.5 MeV
Phys. Rev. 187, 1491 (1969)

SAUER, P. U., (See Jackson, A. D., UCRL-18956)

SCHAEFFER, R., (See Kossanyi-Demay, P., UCRL-18988 Abstract)

SCIAMANNA, A. F., (See Newton, A. S., UCRL-18726)

SCIAMANNA, A. F., (See Newton, A. S., UCRL-18768 Abstract)

SCIAMANNA, A. F., (See Newton, A. S., UCRL-18928)

SEEGMILLER, D. W., and K. Street, Jr.
Angular momentum effects in charged-particle reactions producing the isomer pair ^{119m}Te - ^{119g}Te
UCRL-18952, August 1969
Phys. Rev.

SELPH, F. B.
Beam dynamics problems in a multiparticle rapid cycling synchrotron
UCRL-18778, February 1969
1969 Particle Accelerator Conference, Washington, D. C., 5-7 March 1969

SELPH, F. B., (See Meads, P. F., Jr., UCRL-18781)

SEXTRO, R. G., (See Hardy, J. C., UCRL-18774)

SHERMAN, J., (See de Swiniarski, R., UCRL-18744 Abstract)

SHERMAN, J., (See de Swiniarski, R., UCRL-18930)

SHERMAN, J., (See de Swiniarski, R., UCRL-18941)

SHIRLEY, D. A.
Topics in Mössbauer spectroscopy
UCRL-18684, January 1969
Annual Review of Physical Chemistry, Vol. 20, (Annual Reviews, Inc., Palo Alto, California, 1969)

SHIRLEY, D. A.
Radiative detection of nuclear magnetic resonance
UCRL-18843, April 1969
Anal. Chem. 41, 62A (1969)

SHIRLEY, D. A., (See Rao, G. N., UCRL-18326)

SHIRLEY, D. A., (See Quitmann, D., UCRL-18871)

SHIRLEY, D. A., (See Fadley, C. S., UCRL-18953)

SHIRLEY, D. A., (See Quitmann, D., UCRL-18946 Abstract)

SHIRLEY, D. A., (See Fadley, C. S., UCRL-19501)

SHIRLEY, D. A., (See Davis, D. W., UCRL-19515 Rev)

SHIRLEY, D. A., (See Chan, D., UCRL-19519)

SIEGBAHN, K., (See Karlsson, S.-E., UCRL-18502)

SIEGAL, M., (See Morss, L. R., UCRL-18973)

SIKKELAND, T., R. J. Silva, A. Ghiorso, and M. J. Nurmia
A study of Dy(^{40}Ar, xn)Po reactions
UCRL-18674, September 1969
Phys. Rev.

SILVA, R. J., (See Sikkeland, T., UCRL-18674)

SLOBODRIAN, R. J., (See Meiner, H., UCRL-18831 Abstract)

SLOBODRIAN, R. J., (See Bacher, A. D., UCRL-18929)

SLOBODRIAN, R. J., (See Bacher, A. D., UCRL-19521)

SOBICZEWSKI, A., (See Nilsson S.-G., UCRL-18692)

SOKOL, H. A., (See Kland-English, M. J., UCRL-18983)

SOKOL, H. A., (See Bennett-Corniea, W., UCRL-19504)

SØRENSEN, B.
A comment on the reaction ^{10}B(t, p)^{12}B
UCRL-18663, December 1968
Phys. Letters 28B, 633 (1969)

SØRENSEN, B.
On the description of fermion systems in boson representations. (III) Normal mode construction and the derivation of kinetic and potential energy expansion
UCRL-18691, January 1969
Nucl. Phys.

SØRENSEN, B.
On the description of fermion systems in boson representations. (IV) Numerical calculation of quadrupole excitations in Cd, Sn, Te, Sm, and Pb
UCRL-18903, April 1969
Nucl. Phys.

SØRENSEN, B.
Isospin structure of pairing vibrations
UCRL-18715, January 1969
Second Conference on Nuclear Isospin, Asilomar, Pacific Grove, California, 13-15 March 1969

SØRENSEN, B.
Neutron pairing states in doubly even nuclei
UCRL-18834, April 1969
Nucl. Phys. A134, 1 (1969)

SØRENSEN, B., (See Kumar, K., UCRL-18593)

SORTLAND, L. D., and C. R. Wilke
Growth of Streptococcus faecalus in dense culture
UCRL-18372 Rev, February 1969
Biotech. Bioeng. XI, 805 (1969)

SPRINGER, T. G., and R. L. Pigford
The influence of surface turbulence and surfactants on gas transport through liquid interfaces
UCRL-18993, October 1969
Ind. Eng. Chem. Fundamentals

SPRINGER, T. G.,
The influence of surface turbulence and surfactants on gas transport through liquid interfaces
UCRL-18995, October 1969
Ph. D. Thesis

SPRINGER, T. G., (See Lamb, W. B., UCRL-18912)

ST. CLAIR, D., A. Zalkin, and D. H. Templeton
The crystal structure of $Cs_2(B_9C_2H_{11})Co(B_8C_2H_{10})Co(B_9C_2H_{11}) \cdot H_2O$, a salt of a three-icosahedral-fragment metallocarborane
UCRL-18870, April 1969
Inorg. Chem. 8, 2080 (1969)

ST. CLAIR, D., A. Zalkin, and D. H. Templeton
The crystal structure of $CsCr[B_9C_2H_9(CH_3)_2]_2 \cdot H_2O$, a hydrate of a chromium metallocarborane salt
UCRL-18900, April 1969
Inorg. Chem.

ST. CLAIR, D., A. Zalkin, and D. H. Templeton
The crystal structure of $(C_2H_5)_4NCo(B_7C_2H_9)_2$, a salt of the cobalt derivative of the $(B_7C_2H_9)^{-2}$ carborane ligand
UCRL-18901, April 1969
Inorg. Chem.

ST. CLAIR, D. J.
Metallocarborane structure investigation by single-crystal x-ray analysis
UCRL-18910, May 1969
Ph.D. Thesis

ST. CLAIR, D., A. Zalkin, and D. H. Templeton
The crystal structure of $Ni(B_9C_2H_{11})_2$, a nickel(IV) complex of the dicarbollide ion
UCRL-18911, May 1969
J. Am. Chem. Soc.

STENGER, L., (See Morss, L. R., UCRL-18973)

STEPHENS, F. S.
Spectroscopic information from heavy-ion reactions
UCRL-18964, August 1969
International Conference on Properties of Nuclear States, Montreal, 25-30 August 1969

STEPHENS, F. S., (See Newton, J. O., UCRL-18358 Rev)

STEPHENS, F. S., (See Diamond, R. M., UCRL-18702)

STEPHENS, F. S., (See Diamond, R. M., UCRL-18920 Abstract)

STEPHENS, F. S., (See Nordhagen, R., UCRL-18925)

STEPHENS, F. S., (See Nordhagen, R., UCRL-18931 Abstract)

STEPHENS, F. S., (See Nakai, K., UCRL-18933 Abstract)

STEPHENS, F. S., (See Nakai, K., UCRL-18959)

STEPHENS, F. S., (See Nordhagen, R., UCRL-18965)

STEPHENS, F. S., (See Diamond, R. M., UCRL-19517)

STEPHENS, F. S., (See Newton, J. O., UCRL-19527)

STREET, K., Jr., (See Melendres, C. A., UCRL-18550)

STREET, K., Jr., (See Seegmiller, D. W., UCRL-18952)

STRUBLE, G. L., and S. N. Tewari
The analogues of 4 particle–4 hole state of ^{16}O in 2s, 1d shell nuclei
UCRL-18932 Abstract, June 1969
International Conference on Properties of Nuclear States, Montreal, 25-30 August 1969

STRUBLE, G. L., (See Tewari, S. N., UCRL-18985)

STRUBLE, G. L., (See Goodman, A. L., UCRL-19506)

SZYMANSKI, Z., (See Nilsson, S.-G., UCRL-18692)

TADA, S.
Oscillating-jet measurement of dynamic liquid-liquid interfacial tension
UCRL-18629, November 1968
Ph. D. Thesis

TEMPLETON, D. H., (See Zalkin, A., UCRL-18701)

TEMPLETON, D. H., (See Hopkins, T. E., UCRL-18800)

TEMPLETON, D. H., (See Fischer, M. S., UCRL-18828 Abstract)

TEMPLETON, D. H., (See Zalkin, A., UCRL-18829 Abstract)

TEMPLETON, D. H., (See St. Clair, D., UCRL-18870)

TEMPLETON, D. H., (See St. Clair, D., UCRL-18900)

TEMPLETON, D. H., (See St. Clair, D., UCRL-18901)

TEMPLETON, D. H., (See St. Clair, D., UCRL-18911)

TEMPLETON, D. H., (See Fischer, M. S., UCRL-19523)

TEWARI, S. N., and G. L. Struble
An investigation of the states of 2s-1d shell nuclei based on the four-particle, four-hole state in ^{16}O
UCRL-18985, September 1969
Phys. Rev.

TEWARI, S. N., (See Struble, G. L., UCRL-18932 Abstract)

THIRION, J., (See Glashausser, C., UCRL-18677)

THIRION, J., (See Moss, J. M., UCRL-18725 Abstract)

THIRION, J., (See Hendrie, D. L., UCRL-18826)

THIRION, J., (See Blair, A. G., UCRL-18927)

THOMAS, T. D.
x-Ray photoelectron spectroscopy of simple hydrocarbons
UCRL-18961, July 1969
J. Chem. Phys.

THOMAS, T. D.
x-Ray photoelectron spectroscopy of halomethanes
UCRL-19508, November 1969
J. Am. Chem. Soc.

THOMAS, T. D., (See Davis, D. W., UCRL-19515 Rev)

THOMPSON, S. G., (See Watson, R. L., UCRL-19510)

THOMPSON, S. G., (See Cheifetz, E., UCRL-19516)

TIVOL, W. M., (See Bacher, A. D., UCRL-18929)

TOMBRELLO, T. A., (See Bacher, A. D., UCRL-18944 Abstract)

TOWNER, I., and J. C. Hardy
Direct two-nucleon transfer reactions and their interpretation in terms of the nuclear shell model
Advances in Physics 18, 401 (1969)

TSANG, C. F., and S.-G. Nilsson
Shape isomeric states in heavy nuclei
UCRL-18963, August 1969
Nucl. Phys.

TSANG, C. F., and S.-G. Nilsson
Further theoretical results on the stability of superheavy nuclei
UCRL-18966, August 1969
Nucl. Phys.

TSANG, C. F., (See Nilsson, S.-G., UCRL-18692)

VAGANOV, P., (See Blair, A. G., UCRL-18927)

VALLI, K., E. K. Hyde, and J. Borggreen
Production and decay properties of thorium isotopes of mass 221-224 formed in heavy ion reactions
UCRL-18992, October 1969
Phys. Rev.

VANDEGRIFT, A. E., (See Tada, S., UCRL-18629)

VERMEULEN, T., (See Tada, S., UCRL-18629)

VERMEULEN, T., (See Kahn, D. R., UCRL-18679)

VERMEULEN, T., (See Robertson, G. H., UCRL-19525)

WANG, E. C., (See Marrus, R., UCRL-19520)

WARD, D., (See Newton, J. O., UCRL-18358 Rev)

WARD, D., (See Diamond, R. M., UCRL-18702)

WATSON, R. L., and J. B. Wilhelmy
Calculated fractional independent yields of products formed in the spontaneous fission of ^{252}Cf
UCRL-18632, February 1969

WATSON, R. L., J. B. Wilhelmy, R. C. Jared, C. Rugge, H. R. Bowman, S. G. Thompson, and J. O. Rasmussen
A study of the low energy transitions arising from the prompt deexcitation of fission fragments
UCRL-19510, November 1969
Phys. Rev.

WEIGEL, M.
Linear response theory in nucleon-nucleus scattering
UCRL-18907, May 1969
Nucl. Phys.

WEIGEL, M.
Inclusion of nuclear-structure calculations in nucleon-nucleus scattering
UCRL-18994, September 1969
Phys. Rev.

WILHELMY, J. B.
High-resolution gamma and x-ray spectroscopy on unseparated fission products
UCRL-18978, August 1969
Ph. D. Thesis

WILHELMY, J. B., (See Watson, R. L., UCRL-18632)

WILHELMY, J. B., (See Watson, R. L., UCRL-19510)

WILKE, C. R., (See Sortland, L. D., UCRL-18372 Rev)

WILKE, C. R., (See Dabes, J. N., UCRL-18971)

WITTKOWER, A., (See Cheifetz, E., UCRL-19516)

WOLGAST, R., (See Milleron, N., UCRL-18602)

WOZNIAK, G. J., (See Cerny, J., UCRL-18724)

WOZNIAK, G. J., (See Loiseaux, J. M., UCRL-18900 Abstract)

WYCECH, S., (See Nilsson, S.-G., UCRL-18692)

YELLIN, J., (See Duong, T. H., UCRL-18309)

YELLIN, J., (See Fowler, T., UCRL-18924 Abstract)

YELLIN, J., (See Fowler, T., UCRL-19337)

YELLIN, J., (See Marrus, R., UCRL-19520)

YOURD, R., (See Halbach, K., UCRL-18916)

ZALKIN, A., and K. N. Raymond
The structure of di-pi-cyclooctatetraeneuranium (Uranocene)
J. Am. Chem. Soc. 91, 5667 (1969)

ZALKIN, A., D. H. Templeton, and D. G. Karraker
The crystal and molecular structure of heptadentate coordination complex tris(diphenylpropanedionato)aquoholmium, $Ho(C_6H_5COOCHCOC_6H_5)_3 \cdot H_2O$
UCRL-18701, January 1969
Inorg. Chem. 8, 2680 (1969)

ZALKIN, A., H. Ruben, and D. H. Templeton
The crystal structure of vanadyl sulfate trihydrate
UCRL-18829 Abstract, April 1969
Meeting of the American Crystallographic Association, Seattle, Washington, 23-27 March 1969

ZALKIN, A., (See Hopkins, T. E., UCRL-18800)

ZALKIN, A., (See St. Clair, D., UCRL-18870)

ZALKIN, A., (See St. Clair, D., UCRL-18900)

ZALKIN, A., (See St. Clair, D., UCRL-18901)

ZALKIN, A., (See St. Clair, D., UCRL-18911)

ZALKIN, A., (See Fischer, M. S., UCRL-19523)

ZISMAN, M. S., (See Lu, C. C., UCRL-18719)

VII. Author Index

Author Index

CONTRIBUTORS TO THIS REPORT